frontiers | Research Topics

# Visualization techniques in tribology

**Edited by**
Taisuke Maruyama, Satoru Maegawa, Hikaru Okubo,
Thomas Reddyhoff and Sorin-Cristian Vladescu

**Coordinated by**
Florian Michael Becker-Dombrowsky

**Published in**
Frontiers in Mechanical Engineering

FRONTIERS EBOOK COPYRIGHT STATEMENT

The copyright in the text of individual articles in this ebook is the property of their respective authors or their respective institutions or funders. The copyright in graphics and images within each article may be subject to copyright of other parties. In both cases this is subject to a license granted to Frontiers.

The compilation of articles constituting this ebook is the property of Frontiers.

Each article within this ebook, and the ebook itself, are published under the most recent version of the Creative Commons CC-BY licence. The version current at the date of publication of this ebook is CC-BY 4.0. If the CC-BY licence is updated, the licence granted by Frontiers is automatically updated to the new version.

When exercising any right under the CC-BY licence, Frontiers must be attributed as the original publisher of the article or ebook, as applicable.

Authors have the responsibility of ensuring that any graphics or other materials which are the property of others may be included in the CC-BY licence, but this should be checked before relying on the CC-BY licence to reproduce those materials. Any copyright notices relating to those materials must be complied with.

Copyright and source acknowledgement notices may not be removed and must be displayed in any copy, derivative work or partial copy which includes the elements in question.

All copyright, and all rights therein, are protected by national and international copyright laws. The above represents a summary only. For further information please read Frontiers' Conditions for Website Use and Copyright Statement, and the applicable CC-BY licence.

ISSN 1664-8714
ISBN 978-2-8325-6194-2
DOI 10.3389/978-2-8325-6194-2

## About Frontiers

Frontiers is more than just an open access publisher of scholarly articles: it is a pioneering approach to the world of academia, radically improving the way scholarly research is managed. The grand vision of Frontiers is a world where all people have an equal opportunity to seek, share and generate knowledge. Frontiers provides immediate and permanent online open access to all its publications, but this alone is not enough to realize our grand goals.

## Frontiers journal series

The Frontiers journal series is a multi-tier and interdisciplinary set of open-access, online journals, promising a paradigm shift from the current review, selection and dissemination processes in academic publishing. All Frontiers journals are driven by researchers for researchers; therefore, they constitute a service to the scholarly community. At the same time, the *Frontiers journal series* operates on a revolutionary invention, the tiered publishing system, initially addressing specific communities of scholars, and gradually climbing up to broader public understanding, thus serving the interests of the lay society, too.

## Dedication to quality

Each Frontiers article is a landmark of the highest quality, thanks to genuinely collaborative interactions between authors and review editors, who include some of the world's best academicians. Research must be certified by peers before entering a stream of knowledge that may eventually reach the public - and shape society; therefore, Frontiers only applies the most rigorous and unbiased reviews. Frontiers revolutionizes research publishing by freely delivering the most outstanding research, evaluated with no bias from both the academic and social point of view. By applying the most advanced information technologies, Frontiers is catapulting scholarly publishing into a new generation.

## What are Frontiers Research Topics?

Frontiers Research Topics are very popular trademarks of the *Frontiers journals series*: they are collections of at least ten articles, all centered on a particular subject. With their unique mix of varied contributions from Original Research to Review Articles, Frontiers Research Topics unify the most influential researchers, the latest key findings and historical advances in a hot research area.

Find out more on how to host your own Frontiers Research Topic or contribute to one as an author by contacting the Frontiers editorial office: frontiersin.org/about/contact

# Visualization techniques in tribology

**Topic editors**
Taisuke Maruyama — NSK Ltd., Japan
Satoru Maegawa — Nagoya Institute of Technology, Japan
Hikaru Okubo — Yokohama National University, Japan
Thomas Reddyhoff — Imperial College London, United Kingdom
Sorin-Cristian Vladescu — King's College London, United Kingdom

**Topic coordinator**
Florian Michael Becker-Dombrowsky — Darmstadt University of Technology, Germany

**Citation**
Maruyama, T., Maegawa, S., Okubo, H., Reddyhoff, T., Vladescu, S.-C., Becker-Dombrowsky, F. M., eds. (2025). *Visualization techniques in tribology*. Lausanne: Frontiers Media SA. doi: 10.3389/978-2-8325-6194-2

# Table of contents

05 Editorial: Visualization techniques in tribology
Taisuke Maruyama, Satoru Maegawa, Hikaru Okubo, Thomas Reddyhoff and Sorin-Cristian Vlădescu

08 The 1 μm wear particles entrainment *in situ* observation via fluorescent staining silica particles by silane coupling with Rhodamine B
T. Tokoroyama, M. Okashita, N. Fusetani, M. Murashima, N. Hashizume, R. Tsuboi, H. Shiomi and N. Umehara

17 Visualization of oil-lubrication ball bearings at high rotational speeds
Mamoru Tohyama, Yasuhiro Ohmiya, Michiru Hirose, Hiroki Matsuyama, Takuya Toda, Kenichi Hasegawa, Takaaki Onizuka, Hideaki Sato, Masahiro Yokoi and Norikazu Sato

26 Visualization techniques of grease fluidity
Kazumi Sakai

34 *In-situ* vibrational spectroscopic observation for thermally activated structural changes of 100% cellulose nanofiber molding with ultralow friction
Hikaru Okubo, Tomori Ishikawa, Hiromi Hashiba, Toru Inamochi and Ken Nakano

45 Electrical impedance based condition monitoring of machine elements–a systematic review
Florian Michael Becker-Dombrowsky and Eckhard Kirchner

58 Visualising the lubrication condition in hydrodynamic journal bearings using impedance measurement
Florian Koetz, Florian Schmitt, Eckhard Kirchner and Eduardo Zancul

73 A method for simultaneously measuring friction and gap at metal–lubricant interface by combined use of atomic force microscopy and line-and-space patterned metal films
Naoki Yamashita and Tomoko Hirayama

83 The mechanism of small wear particles entrainment in friction under boundary lubrication
Takayuki Tokoroyama, Masahiro Okashita, Ruixi Zhang, Motoyuki Murashima, Ryo Tsuboi, Takuji Yoshida, Hiroshi Shiomi and Noritsugu Umehara

95 A study of measurement of raceway direct measurement of rolling bearings
Hiromu Tamae, Naoko Ueda and Yasuyoshi Tozaki

107 Impedance measurement of rolling bearings using an unbalanced AC wheatstone bridge
Steffen Puchtler, Julius van der Kuip, Florian Michael Becker-Dombrowsky and Eckhard Kirchner

120 Application of the electrical impedance method to steel/steel EHD point contacts
Taisuke Maruyama, Daichi Kosugi, Shunsuke Iwase, Masayuki Maeda, Ken Nakano and Satoshi Momozono

130 Controlling windscreen wiper vibration through yaw angle adjustments: a study of dynamic contact behavior using fluorescence observation
Chiharu Tadokoro, Hiroaki Kobayashi, Miwa Sueda, Takuo Nagamine, Sorin-Cristian Vlădescu, Tom Reddyhoff and Ken Nakano

141 Studies on dielectric spectroscopy of oxidatively degraded Poly(α-olefin)
Shunsuke Iwase, Taisuke Maruyama, Satoshi Momozono, Satoru Maegawa and Fumihiro Itoigawa

151 The effect of inner ring groove on leakage reduction in dry gas seals and its visualization verification
Masayuki Ochiai and Yuta Ohya

160 Mechanisms of cage noise generation in machine tool bearings
Kazuho Takeshima, Keisuke Mutoh, Kenji Imanishi and Shunichi Oshima

172 An *in situ* experimental method for monitoring the viscosity change and oil amount during the sliding test
Hiroshi Shiomi and Shingo Obara

frontiers | Frontiers in Mechanical Engineering

TYPE Editorial
PUBLISHED 18 March 2025
DOI 10.3389/fmech.2025.1588494

Check for updates

OPEN ACCESS

EDITED AND REVIEWED BY
Roman Pohrt,
Technical University of Berlin, Germany

*CORRESPONDENCE
Taisuke Maruyama,
maruyama-ta@nsk.com

RECEIVED 06 March 2025
ACCEPTED 11 March 2025
PUBLISHED 18 March 2025

CITATION
Maruyama T, Maegawa S, Okubo H, Reddyhoff T and Vlădescu S-C (2025) Editorial: Visualization techniques in tribology.
*Front. Mech. Eng.* 11:1588494.
doi: 10.3389/fmech.2025.1588494

COPYRIGHT
© 2025 Maruyama, Maegawa, Okubo, Reddyhoff and Vlădescu. This is an open-access article distributed under the terms of the Creative Commons Attribution License (CC BY). The use, distribution or reproduction in other forums is permitted, provided the original author(s) and the copyright owner(s) are credited and that the original publication in this journal is cited, in accordance with accepted academic practice. No use, distribution or reproduction is permitted which does not comply with these terms.

# Editorial: Visualization techniques in tribology

Taisuke Maruyama[1,2]*, Satoru Maegawa[3], Hikaru Okubo[4], Thomas Reddyhoff[5] and Sorin-Cristian Vlădescu[6]

[1]Core Technology R&D Center, NSK Ltd., Fujisawa, Japan, [2]NSK Tribology Collaborative Research Cluster, Institute of Science Tokyo, Yokohama, Japan, [3]Department of Mechanical Engineering, Nagoya Institute of Technology, Nagoya, Japan, [4]Faculty of Environment and Information Sciences, Yokohama National University, Yokohama, Japan, [5]Department of Mechanical Engineering, Imperial College London, London, United Kingdom, [6]Department of Engineering, Faculty of Natural, Mathematical and Engineering Sciences, King's College London, London, United Kingdom

KEYWORDS

**computer simulation, tribology, visualization, condition monitoring, EHL, electrical method, optical method, surface analysis**

Editorial on the Research Topic
Visualization techniques in tribology

## Introduction

"Seeing is believing" is a phrase that conveys the idea that people tend to believe something more strongly and confidently when they can actually see it with their own eyes. It suggests that visual evidence or firsthand experience holds a significant level of conviction and trustworthiness, often surpassing what is merely heard or described. The phrase implies that when you witness something directly, you are more likely to accept its reality or truthfulness compared to when you rely solely on descriptions or explanations. In short, the act of seeing something with your own eyes can be a powerful way to persuade and convince yourself or others of its existence or validity. For this reason, techniques to visualize phenomena that are normally invisible are very effective in elucidating phenomena and are utilized in a variety of academic fields. Of course, various visualization techniques are also used in tribology to contribute to the better understanding of complex phenomena. Tribology is a scientific and engineering discipline that studies friction, wear, and lubrication of surfaces in relative motion. Tribology plays an important role in understanding and optimizing the performance, durability, and efficiency of mechanical systems and components, from small-scale equipment to large-scale industrial machinery. That is, tribology aims to investigate the complex interactions between materials under various conditions and to minimize friction and wear through the use of lubricants, coatings, and surface treatments. However, since tribology deals with severe contact conditions that result in thin film thickness (nm order) and high contact pressure (GPa order), the development of visualization techniques is very important to elucidate the phenomena. Moreover, visualization of actual complex phenomena not only verifies existing theories but also provides opportunities for new discoveries and hints for the construction of new theories that emerge from such discoveries. Therefore, in this Research Topic, we have compiled various themes on the visualization techniques developed to elucidate tribological phenomena. The Research Topic consists of 16 papers, which are

broadly categorized into two groups: 1) optical methods (10 papers) and 2) electrical methods (6 papers).

## Optical methods

The first group focuses on optical methods, which leverage light to visualize tribological interactions. Techniques such as high-speed imaging, laser-induced fluorescence, and optical interferometry have been instrumental in capturing real-time data on friction and wear processes. These methods allow researchers to observe surface changes at the micro and nano scales, providing insights into the mechanisms of lubrication and wear.

This Research Topic of articles begins with a review article titled "Visualization techniques of grease fluidity" authored by Sakai. It introduces visualization techniques using advanced optical methods such as fluorescence, particle image velocimetry (PIV), infrared spectroscopy, X-rays, and neutron beams.

Following this, Yamashita and Hirayama present a paper titled "A method for simultaneously measuring friction and gap at metal–lubricant interface by combined use of atomic force microscopy and line-and-space patterned metal films." They propose a method to simultaneously measure friction and gap at the metal-lubricant interface under boundary lubrication conditions using atomic force microscopy. They also visualize the state of adsorption film formation using neutron reflectometry.

Okubo et al. investigated the friction reduction mechanism of 100% cellulose nanofiber (CNF) molded bodies using an *in-situ* Raman tribometer in their paper titled "*In-situ* vibrational spectroscopic observation for thermally activated structural changes of 100% cellulose nanofiber molding with ultralow friction." The *in-situ* Raman observation results during friction visualized the structural changes of the CNF molded body and identified key factors contributing to the ultra-low friction phenomenon observed at high temperatures.

Shiomi and Obara have published a paper titled "An *in-situ* experimental method for monitoring viscosity change and oil amount during sliding test." They propose a method to predict the viscosity and oil amount during sliding tests by visualizing the shape of the meniscus formed ahead of the EHD (elastohydrodynamic) contact area, and found that it can be applied even in vacuum friction tests without returning to atmospheric pressure.

In addition to the above paper, two papers have been published on visualization technology using high-speed cameras. Takeshima et al. have published a paper titled "Mechanisms of Cage Noise Generation in Machine Tool Bearings," where they conducted observation tests using a high-speed camera to visualize the behavior of the cage in ball bearings under grease lubrication. By detailed image processing of the obtained observation results, they clarified specific cage behaviors that affect cage noise. Ochiai and Ohya have published a paper titled "The effect of inner ring groove on leakage reduction in dry gas seals and its visualization verification," investigating the impact of introducing an inner ring groove (IRG) on the leakage characteristics of dry gas seals widely used in turbomachinery such as gas turbines and compressors. They obtained important insights into the optimal design guidelines for seals by applying PIV to visualize the gas flow within the seal gap using images obtained with a high-speed camera.

Moreover, four papers on visualization techniques using fluorescence methods have been reported in this Research Topic. Tokoroyama et al. have published a paper on the visualization of wear particles titled "The 1 μm wear particles entrainment *in situ* observation via fluorescent staining silica particles by silane coupling with Rhodamine B." Specifically, they experimentally investigated the capture of imitation wear particles in the contact area under boundary lubrication conditions. To address optical limitations, they implemented fluorescent staining on these particles. Furthermore, Tokoroyama et al. have also submitted a paper titled "The mechanism of small wear particles entrainment in friction under boundary lubrication." These two studies are expected to provide important insights into the behavior of wear particles under boundary lubrication and form the basis for a more detailed understanding of the impact of particles on friction phenomena. Tadokoro et al. have published a paper titled "Controlling windscreen wiper vibration through yaw angle adjustments: a study of dynamic contact behavior using fluorescence observation," which elucidates the mechanism of friction-induced vibration in passenger car wiper systems. By conducting fluorescence observations, they successfully measured the exact position of the rubber blade tip and the water film thickness at the contact area during operation. Tohyama et al. have submitted a methods article titled "Visualization of oil-lubrication ball bearings at high rotational speeds." They observed the oil film thickness in the contact area of deep groove ball bearings rotating at high speeds and the oil distribution inside the bearings using three-wavelength optical interferometry and fluorescence methods, respectively. The results of this study are expected to contribute to the development of ball bearings used at high speeds required for electric vehicles.

## Electrical methods

The second group encompasses electrical methods, which utilize electrical signals to infer tribological behavior. Techniques such as piezoelectric sensors, capacitance measurements, and electrical resistance monitoring provide valuable data on contact conditions and wear rates. These methods are particularly useful in environments where traditional optical techniques may be limited due to surface roughness or opacity.

In this Research Topic, five papers on visualization techniques using electrical impedance have been submitted. The first is a review article by Becker-Dombrowsky and Kirchner titled "Electrical impedance based condition monitoring of machine elements–a systematic review." It introduces various studies on condition monitoring using electrical impedance and identifies research challenges to be addressed in future studies. The second is a paper by Puchtler et al. titled "Impedance measurement of rolling bearings using an unbalanced AC wheatstone bridge." They indicated that their developed impedance measurement can be used as a sensor for condition monitoring when the bearing is operated in the hydrodynamic lubrication. The third paper, by Koetz et al., is titled "Visualising the lubrication condition in hydrodynamic journal bearings using impedance measurement."

By measuring the electrical characteristics of journal bearings with applied AC, it suggests the possibility of detecting deformation and damage of bearings in mixed lubrication conditions. The fourth paper, by Maruyama et al., is titled "Application of the electrical impedance method to steel/steel EHD point contacts." It discusses the electrical impedance method that can simultaneously measure the thickness and breakdown ratio of oil films in EHD contacts, particularly mentioning the impact of wear generated in mixed lubrication on the accuracy of oil film measurements. The fifth paper, by Iwase et al., is titled "Studies on dielectric spectroscopy of oxidatively degraded Poly (α-olefin)." By sweeping the frequency of the AC applied to the lubricant, they verify the practicality of dielectric spectroscopy (DES) for condition monitoring and predictive maintenance of lubricants.

Finally, as an electrical visualization method other than electrical impedance, Tamae et al. have presented a paper titled "A study of measurement of raceway direct measurement of rolling bearings." The authors developed a method called "dynamic thermocouple method" to measure the temperature of bearing raceways by applying the Seebeck effect, which generates an electromotive force when different metals are in contact and subjected to a temperature difference. Furthermore, this study is unique in that it correlates the temperature rise of the bearing with the behavior of the rolling elements by combining the dynamic thermocouple method with high-speed camera observations.

## Conclusion

The visualization techniques discussed in this Research Topic are essential for advancing our understanding of tribological phenomena. By making the invisible visible, these methods not only validate existing theories but also pave the way for new discoveries that can transform the field of tribology. As we continue to refine these techniques and develop new ones, we can expect significant improvements in the performance of mechanical systems across various industries. This Research Topic of papers serves as a testament to the importance of visualization in tribology and highlights the ongoing efforts to explore and elucidate complex interactions at play in friction, wear, and lubrication.

At the end of this editorial article, we would like to express our heartfelt gratitude to all the authors who have made valuable contributions to this Research Topic of papers on visualization techniques in tribology. We hope that this Research Topic will contribute not only to the field of tribology, which deals with complex phenomena, but also to various other research fields.

## Author contributions

TM: Writing–original draft, Writing–review and editing. SM: Writing–review and editing. HO: Writing–review and editing. TR: Writing–review and editing. S-CV: Writing–review and editing.

## Funding

The author(s) declare that no financial support was received for the research and/or publication of this article.

## Acknowledgments

This Research Topic was done with the collaboration of Florian Becker-Dombrowsky, M. Sc. from the Technical University of Darmstadt. We acknowledge his dedicated contributions.

## Conflict of interest

Author TM was employed by NSK Ltd.

The remaining authors declare that the research was conducted in the absence of any commercial or financial relationships that could be construed as a potential conflict of interest.

## Generative AI statement

The author(s) declare that no Generative AI was used in the creation of this manuscript.

## Publisher's note

All claims expressed in this article are solely those of the authors and do not necessarily represent those of their affiliated organizations, or those of the publisher, the editors and the reviewers. Any product that may be evaluated in this article, or claim that may be made by its manufacturer, is not guaranteed or endorsed by the publisher.

frontiers | Frontiers in Mechanical Engineering

TYPE Original Research
PUBLISHED 28 February 2024
DOI 10.3389/fmech.2024.1371948

Check for updates

OPEN ACCESS

EDITED BY
Sorin-Cristian Vladescu,
King's College London, United Kingdom

REVIEWED BY
Milan Bukvic,
University of Kragujevac, Serbia
Mladen Radojković,
University of Priština in Kosovska Mitrovica, Serbia

*CORRESPONDENCE
T. Tokoroyama,
takayuki.tokoroyama@mae.nagoya-u.ac.jp

RECEIVED 17 January 2024
ACCEPTED 13 February 2024
PUBLISHED 28 February 2024

CITATION
Tokoroyama T, Okashita M, Fusetani N, Murashima M, Hashizume N, Tsuboi R, Shiomi H and Umehara N (2024), The 1 µm wear particles entrainment *in situ* observation via fluorescent staining silica particles by silane coupling with Rhodamine B.
*Front. Mech. Eng* 10:1371948.
doi: 10.3389/fmech.2024.1371948

COPYRIGHT
© 2024 Tokoroyama, Okashita, Fusetani, Murashima, Hashizume, Tsuboi, Shiomi and Umehara. This is an open-access article distributed under the terms of the Creative Commons Attribution License (CC BY). The use, distribution or reproduction in other forums is permitted, provided the original author(s) and the copyright owner(s) are credited and that the original publication in this journal is cited, in accordance with accepted academic practice. No use, distribution or reproduction is permitted which does not comply with these terms.

# The 1µm wear particles entrainment *in situ* observation via fluorescent staining silica particles by silane coupling with Rhodamine B

T. Tokoroyama[1]*, M. Okashita[1], N. Fusetani[1], M. Murashima[2], N. Hashizume[1], R. Tsuboi[3], H. Shiomi[4] and N. Umehara[1]

[1]Department of Micro-Nano Mechanical Science and Engineering, Graduate School of Engineering, Nagoya University, Nagoya, Japan, [2]Department of Mechanical Systems Engineering, Graduate School of Engineering, Tohoku University, Sendai, Japan, [3]Department of Mechanical Engineering, Graduate School of Engineering, Daido University, Nagoya, Japan, [4]Research and Development Directorate, Research Unit II, Japan Aerospace Exploration Agency, Tsukuba, Japan

Observing wear debris during friction is crucial for comprehending the wear behavior of lubrication systems. Despite various techniques attempted for observation, a persistent challenge is the oversight of wear debris with a diameter less than 1 µm, mainly due to limitations in measurement systems. Consequently, we still lack a comprehensive understanding of whether these small particles can infiltrate contact points and serve as abrasives. In this study, we conducted *in-situ* friction tests to investigate the entrainment of imitation wear particles at the contact point under boundary lubrication conditions. These imitation wear particles were glass beads with diameters of approximately 0.8 µm, 1.0 µm, and 3.0 µm, respectively. To address optical limitations, we stained these particles using silane coupling to attach Rhodamine B to the glass beads. We examined the effect of particle diameter on entrainment numbers under varying outside oil film thicknesses. The results showed that the entrainment number was highest when the outside oil film thickness matched the particle diameter. This clearly indicated that the outside oil film thickness significantly influenced the entrainment of particles.

KEYWORDS

***in-situ*, fluorescent staining, Rhodamine B, silane coupling, oil film thickness**

## 1 Introduction

In order to achieve a sustainable global society, the United Nations adopted the Sustainable Development Goals (SDGs) in 2015. This initiative has led to increased awareness regarding the reduction of friction loss, machine maintenance, parts replacement frequency, and the use of lubricants and additives in various regions and companies (UN, 2015). "Sustainable consumption and production" is one of the key global objectives, highlighting the importance of extending the lifespan of machines and their components in the field of tribology. When considering the life expectancy of machines, it becomes evident that the wear of mating parts has a direct impact, with wear debris believed to significantly reduce their operational lifespan. An investigation using an atomic force microscope revealed that the size of wear debris is quite small, typically in the range of

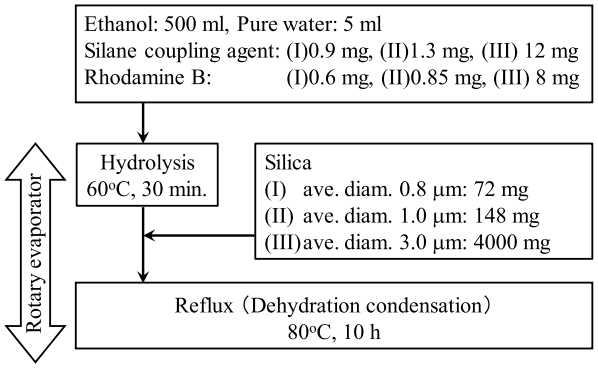


FIGURE 1
Schematic diagram of the florescent staining procedure.

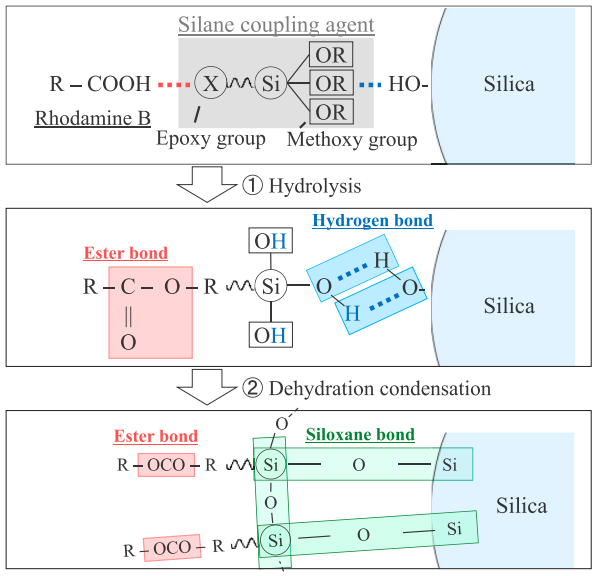


FIGURE 2
Schematic of silane coupling agent acts between the silica and Rhodamine.

several nanometers (approximately 15–40 nm). This was observed in scenarios involving dry friction between identical material pairs, such as an almost pure iron (99.5%) pin against an iron disk, pure capper (99.99%), pure zinc (99.99%), and pure nickel (99.7%). These tiny debris particles eventually aggregate, forming larger particles exceeding 10 μm in size (Mishina et al., 2003). The presence of wear debris or abrasive particles in the surrounding environment contributes to abrasive wear, emphasizing the importance of employing filtration to remove these particles and thereby extend the service life of machinery. Utilizing the ferrography method to determine the size, shape, color and other characteristics of wear debris, coupled with vibration analysis, represents powerful tools for predicting wear patterns at contact points within a tribosystem. This field has been extensively researched over the past 4 decades (Roylance et al., 2000). Recently, real-time measurement of wear debris in lubricating oil has been made possible through a laser–photo diode detector system, which measures particle size distributions and counts along the oil tank–rubbing surface path (Iwai et al., 2010; Hong et al., 2018). This technology enables the detection of wear debris with a diameter larger than 1 μm. As the capability to detect smaller diameters continues to improve, the accuracy of wear amount estimation becomes increasingly precise. However, the challenge remains that wear debris with a diameter less than 1 μm is often overlooked due to limitations in measurement systems. Consequently, we still lack a comprehensive understanding of whether these small particles can enter contact points and function as abrasives.

Over the past few decades, numerous authors have explored the entrainment of particles between sliding surfaces and have sought to determine how these particles can or cannot infiltrate. The inception of this phenomenon, often referred to as "particle entrainment between contacts," has been discussed in several literature sources in the context of lubrication contaminants (Tallian, 1976; Loewenthal and Moyer, 1979; Cusano and Sliney, 1982a; Cusano and Sliney, 1982b). Additionally, it gained prominence with the rise or ceramics bearing technology (Dwyer-Joyce, 1999; Mitchell et al., 2000; Wang et al., 2000; Wang et al., 2007). As a result, there has been a significant focus on carbonaceous hard coatings as an appealing material for reducing friction and wear. However, this approach comes with its share of challenges, including issue related to peeling caused by cyclic impacts (Abdollah et al., 2010; Abdollah et al., 2011; Abdollah et al., 2012a; Abdollah et al., 2012b), droplets emanating from the surface (Lee et al., 2018; Lee et al., 2019; Lee et al., 2020), and oil additives affecting mechano-chemical wear (Kassim et al., 2020; Kassim et al., 2021). It's noteworthy that these particles have been observed to be smaller than 1 μm in diameter (Tokoroyama et al., 2018), underscoring the growing importance of detecting such small wear debris and accurately predicting wear levels. The prediction of wear amounts on surfaces, such as ball or roller bearings, has been accomplished by considering the role of particles acting as abrasives passing through a contact point. This concept involves the removal volume of the surface and its relationship with the hardness between the surface and the particles, a phenomenon known as three-body abrasive wear. Dwyer-Joyce, for instance, reported a bearing mass loss that correlated with particle size, demonstrating an increase in mass loss as the size of diamond particles ranged from 1 to 6 μm in diameter. Notably, when using diamond particles with a diameter less than 1 μm, a mass loss was still observed, implying that diameters less than 1 μm can indeed enter a contact point.

Modeling abrasive wear through wear debris has been a subject of study for many years. Third-body wear caused by such debris is influenced by factors such as debris hardness, normal load between mating surfaces, sliding speed, and so on. However, determining the ratio of particles entrained in the system can be quite challenging, primarily because small-diameter particles result in shallow, narrow, and often undetectable scars. Consequently, a comprehensive understanding of how abrasive wear progresses due to small-diameter particles can only be achieved through *in-situ* observation. *In-situ* direct observation of these particles at a contact point was successfully carried out by Strubel and colleagues (Strubel et al., 2016; Strubel et al., 2017a; Strubel et al., 2017b). Their observations were conducted using particles with diameters of 10 μm or larger, revealing that larger and heavier

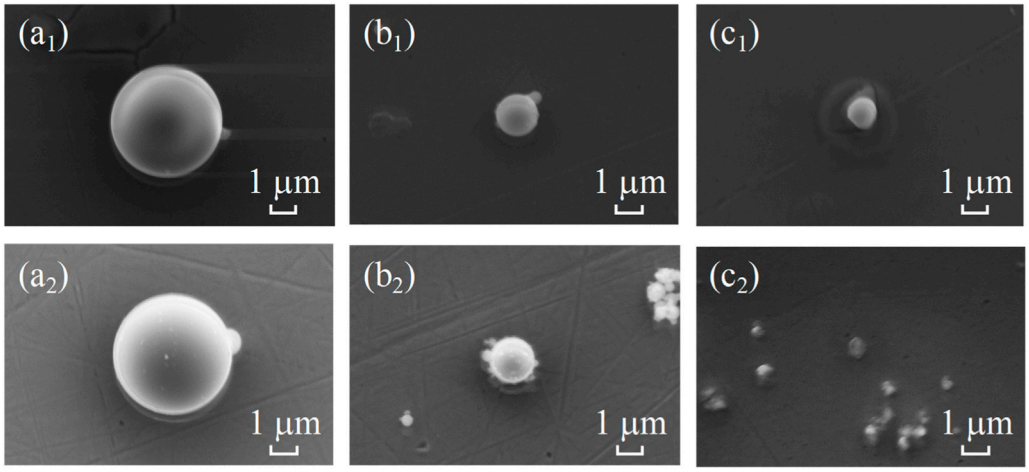


FIGURE 3
The SEM images of before and after staining process; 3.0 μm of before staining **($a_1$)** and after staining **($a_2$)**, 1.0 μm of before **($b_1$)**, and after **($b_2$)**, and 0.8 μm of before **($c_1$)** and after **($c_2$)**.

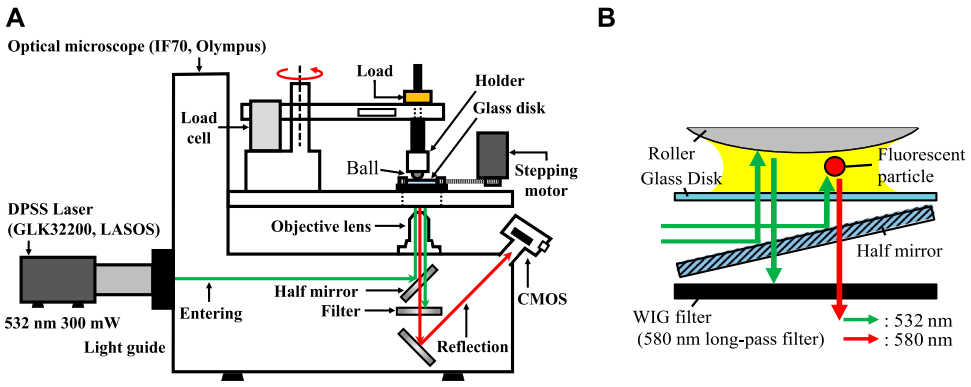


FIGURE 4
**(A)** Schematic of iFlat equipment, **(B)** schematic of inlet laser path through the glass disk to the contact point, and the reflection path through WIG filter.

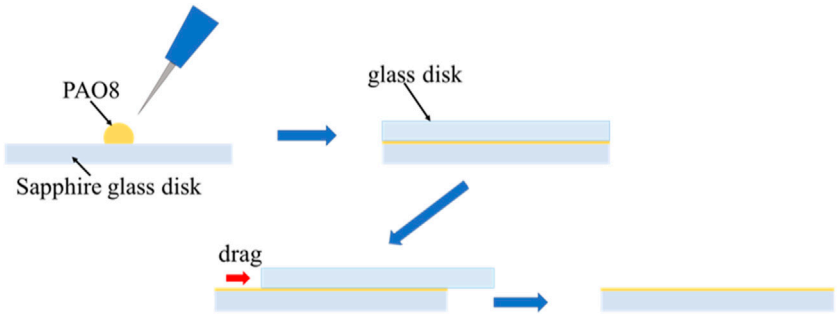


FIGURE 5
Schematic of oil film application on the glass disk before friction test.

particles were more likely to be entrapped than smaller and lighter ones. It was observed that smaller-diameter particles did not enter the system because a reverse flow occurred at a midpoint between mating surfaces, preventing their entrainment in a fully flooded condition. Another critical aspect to consider is the thickness of the oil film outside the Hertzian contact area. Cann et al. reported that a decrease in the oil film thickness ($h_{oil\infty}$) in the vicinity of the sliding track led to a reduction in the oil film thickness at the contact point.

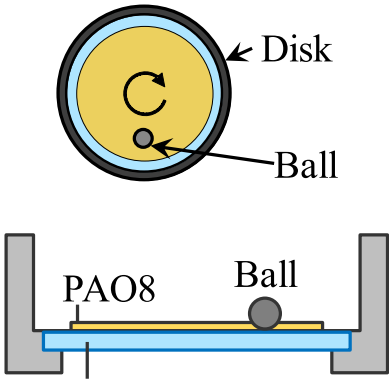


FIGURE 6
Schematic of contact area as top view and side view.

This reduction was attributed to inadequate oil replenishment from the vicinity of the sliding track. Both of these viewpoints—particle entrainment and oil film thickness—intersect and may explain the potential for particle entrainment, even if the particle diameter is around the micro to sub-micro range.

One significant limitation in the observation of micro to sub-micro diameter particles lies in optical constraints. Using white light and a standard CCD camera, particles with diameters less than 0.3 μm cannot be reliably detected. To overcome this optical limitation, particle image velocimetry (PIV) has emerged as a widely-used technique for observing fluid motion by employing fluorescent particles (Kinoshita et al., 2007). In this study, a novel approach was employed, utilizing fluorescent-stained solid particles for direct observation under boundary lubrication conditions. Bright fluorescent particles were obtained through a staining technique involving glass particles (silica) and Rhodamine B (a fluorescent agent) combined with a silane coupling agent to achieve sufficient intensity. With this staining method, it has become possible to directly observe the behavior at the contact surface of particles within 1 μm or less, which sets it apart from other studies the most.

In this study, we examined the quantity of entrainment particles by specifically examining the oil film thickness in the surrounding area beyond the point of contact, which we refer to as the "outside oil film thickness." Subsequently, we utilized silica particles with average diameters of 0.8, 1.0, and 3.0 μm to elucidate the impact of the outside oil film thickness on particle entrainment. Additionally, we conducted dry friction tests to draw comparisons with the lubricated conditions. Furthermore, the establishment of the staining method in this study opens up the possibility of observing the behavior of nanoparticles (Wu et al., 2018; Gao et al., 2021; Nomede-Martyr et al., 2021; Wu et al., 2021; Bukvić et al., 2023), allowing for the investigation of their tribological properties, which have been garnering attention in recent years.

## 2 Experimental procedure

### 2.1 Staining silica particles with fluorescent dyes

The staining of organic materials on inorganic materials, such as glass particles, is being investigated using various staining

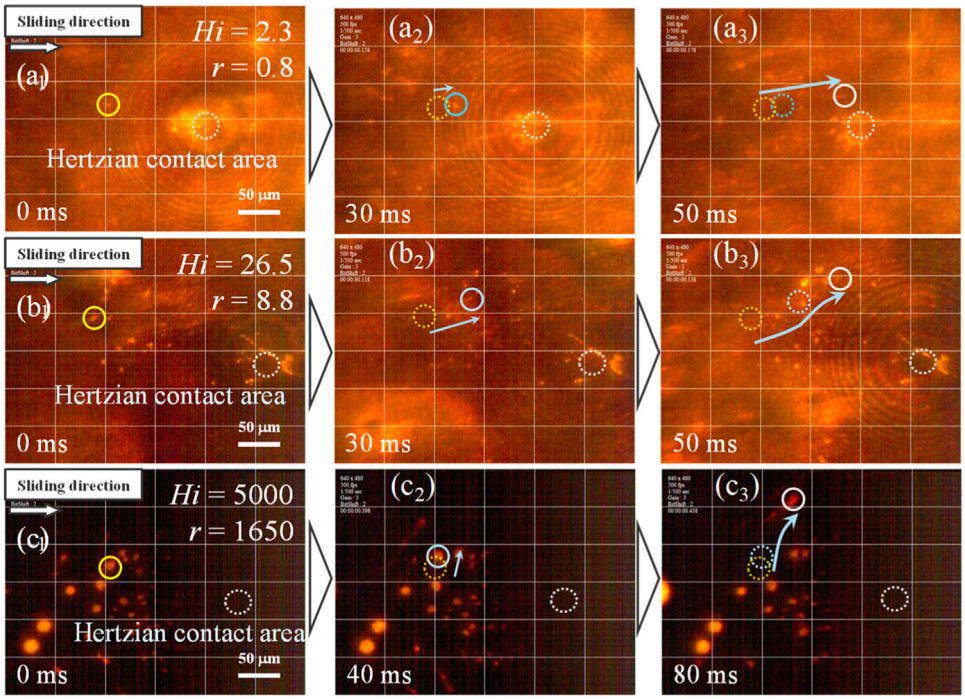


FIGURE 7
The *in-situ* observation results of 3.0 μm diameter particles; **(A)** *Hi* = 2.3 μm, *r* = 0.8; **(B)** *Hi* = 26.5 μm, *r* = 8.8; and **(C)** *Hi* = 5000 μm, *r* = 1650.

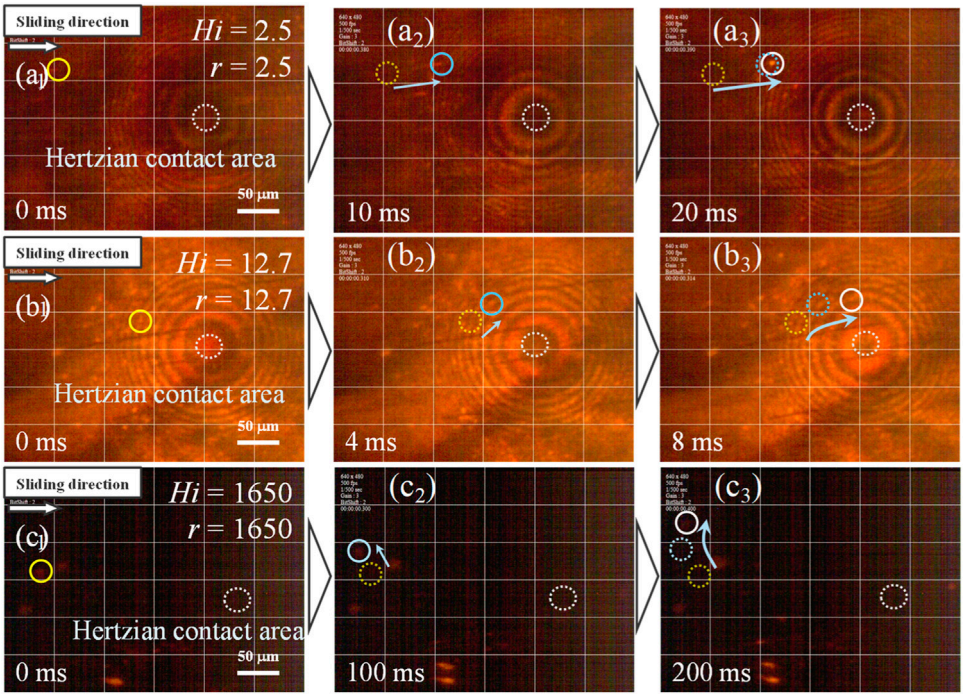


FIGURE 8
The *in-situ* observation results of 1.0 μm diameter particles; **(A)** *Hi* = 2.5 μm, *r* = 2.5; **(B)** *Hi* = 12.7 μm, *r* = 12.7; and **(C)** *Hi* = 1,650 μm, *r* = 1,650.

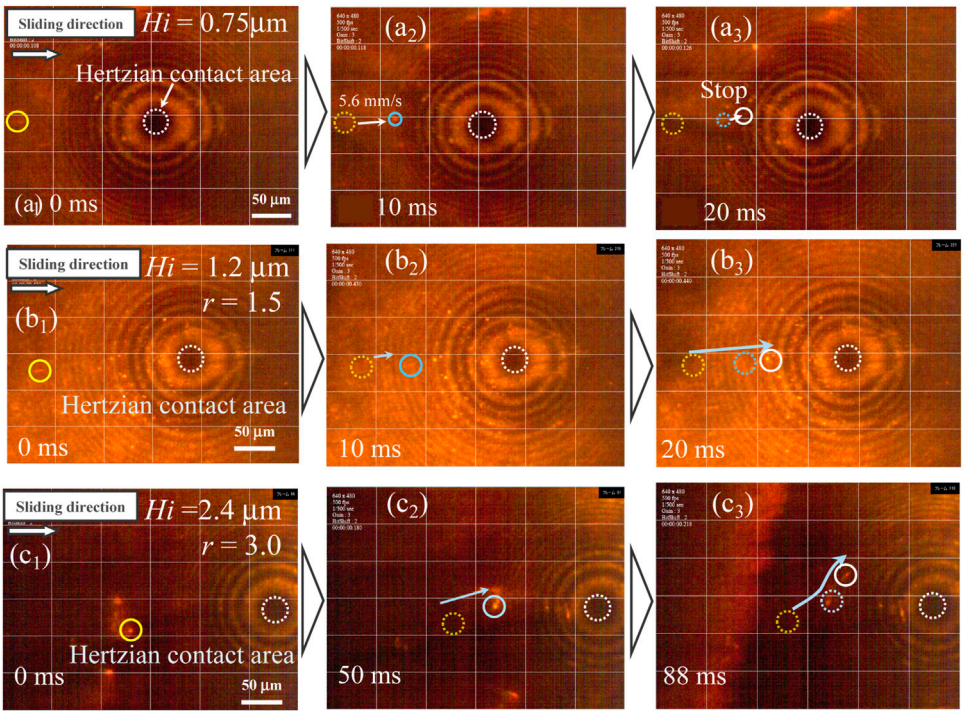


FIGURE 9
The *in-situ* observation results of 0.8 μm diameter particles; **(A)** *Hi* = 0.75 μm, *r* = 0.8; **(B)** *Hi* = 1.2 μm, *r* = 1.5; and **(C)** *Hi* = 2.4 μm, *r* = 3.0.

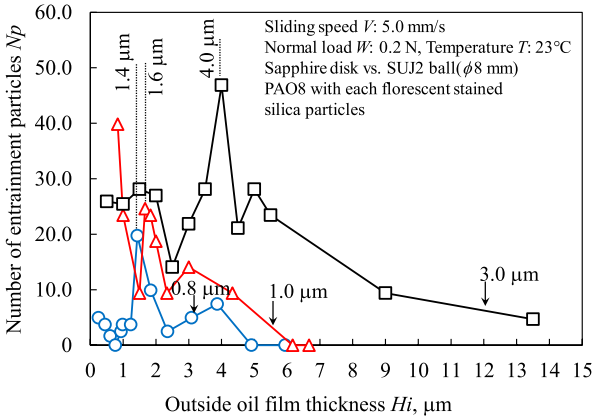


FIGURE 10
The relation between number of entrainment particles and outside oil film thickness.

methods employing silane coupling (Lee et al., 2019; Shi et al., 2023). The fluorescent staining of silica particles was accomplished using a combination of a silane coupling agent (KBM-4803 from Shin-Etsu Silicone, Japan) and Rhodamine B (from Fujifilm Wako Pure Chemical Corporation, Japan). These silica particles came in three sizes, with average diameters of 0.8, 1.0, and 3.0 μm (supplied by Potters Ballotine Co., Ltd., Japan). The process of surface modification for silica particles is illustrated in Figure 1 for each size of silica particles. To achieve this, the silane coupling agent was added to a mixture of ethanol (500 mL), pure water (5 mL), and Rhodamine B. This mixture was then subjected to a 30-min reaction at 60 °C using a rotary evaporator. Following this step, the silica particles were introduced, and a dehydration condensation process was carried out for 10 h at 80°C. The mechanism underlying the silane coupling onto silica and Rhodamine B is depicted in Figure 2. Initially, the epoxy group of the silane coupling agent forms an ester bond with the carboxyl group of Rhodamine B, while the methoxy group on the other side of the silane coupling agent establishes hydrogen bonds with the silica surface. During the subsequent dehydration condensation process, these hydrogen bonds between the silane coupling agent and silica are transformed into siloxane bonds through dehydration. Figure 3 presents representative scanning electron microscope (SEM) images of the fluorescently stained silica particles. Figures 3a$_1$, a$_2$ show the particles before and after staining for 3.0 μm silica, Figures 3b$_1$, b$_2$ for 1.0 μm, and Figures 3c$_1$, c$_2$ for 0.8 μm. In all cases, the staining procedure resulted in a diameter increase of less than 10 nm in radius (Shin et al., 2008), as confirmed by SEM observations, which did not reveal any particles larger than the original diameters of the silica particles.

## 2.2 Observation equipment for *in situ* friction analysis

Friction tests were carried out using an *in-situ* observation system called "iFLAT" (Intelligent Fluorescent Light Assisted Tribometer) (Chiba et al., 2018; Takeno et al., 2020). A schematic of this system is depicted in Figure 4A, with an enlarged view of the observation area shown in Figure 4B. The iFLAT system is equipped with a 532 nm laser source (GLK32200, LASOS, Germany). This laser travels through a light guide from the source, enters an objective lens of an optical microscope, and is directed to the friction area via a sapphire disk (1.0 mm thickness, 50 mm diameter, with a surface roughness of approximately 2.0 nmRa). A fixed SUJ2 bearing ball (approximately 8.0 mm in diameter, with a surface roughness of approximately 7.0 nmRa, it is same property of AISI53200 stainless steel) within a ball holder is placed on a friction cantilever. A dead weight is used to apply a normal load of 0.2 N. The bearing ball reflects the incident laser, and the fluorescently stained particles emit fluorescent light. Both sets of light pass through the sapphire disk before reaching a half-mirror. Subsequently, both lights are directed to a WIG filter, which is a long-pass filter with a cutoff wavelength at 580 nm, effectively eliminating reflected laser light. Finally, the fluorescent light is captured by a CMOS camera, operating at a frame rate of 500 frames per second (fps). The *in-situ* observations were conducted multiple times, and we selected 60 frames (0.12 s) that recorded the highest particle counts within the observation area during the observations.

## 2.3 Preparation and *in situ* friction test observation procedure

The friction test involved the interaction between an SUJ2 ball and a sapphire disk lubricated with PAO8 lubricant,

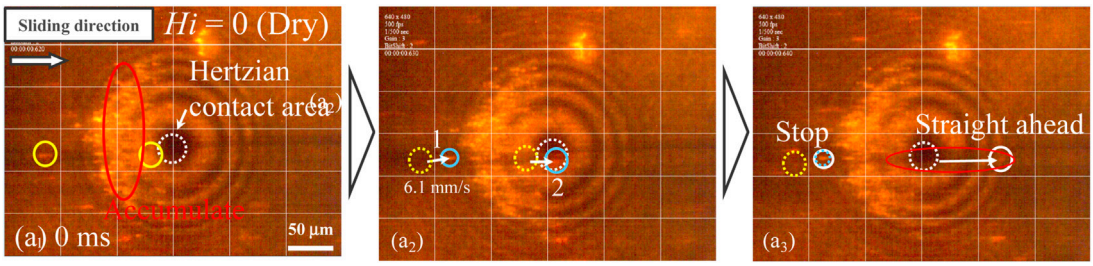


FIGURE 11
The *in-situ* observation under dry conditions.

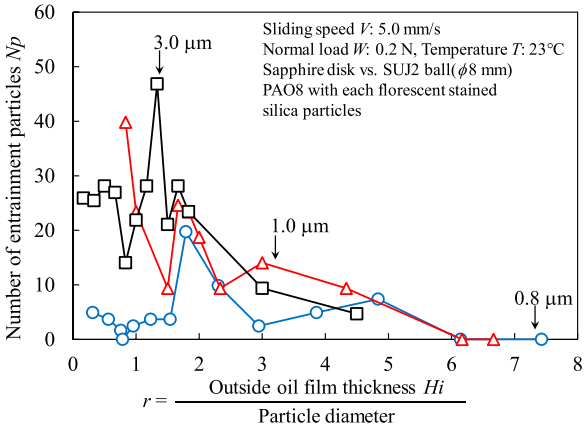


FIGURE 12
The relation between no-dimensional value *r* and number of entrainment particles.

which possesses a viscosity of 46.0 mm$^2$/s at 40 °C. The i-FLAT system was utilized for this test. To prepare for the test, a 2.0–10 μL quantity of lubricant was applied onto the sapphire surface. Another sapphire disk was then placed over the lubricant to achieve a nearly uniform lubricant film. Subsequently, the upper sapphire disk was laterally removed, as illustrated in Figure 5 as a schematic representation. To ascertain the representative lubricant film thickness, ellipsometry was employed to measure the oil film thickness at a distance away from the contact area. The sapphire disk with the lubricant was secured onto the disk holder, with the ball specimen attached to it. A dead weight of 0.2 N was added to the ball specimen. Fluorescently stained particles, comprising a colloidal liquid of ethanol with a volume of 0.1 μL, were applied onto the oil film, positioned at the same radius as the friction test rotation, just ahead of the contact point as depicted in Figure 6. Prior to commencing the *in-situ* friction test, several minutes were allowed to pass to account for ethanol vaporization. The sliding speed was set at 5.0 mm/s (with a rotation radius of approximately 5.0 mm), and the camera operated at a speed of 500 frames per second (fps). We captured a continuous sequence of 60 frames (0.12 s) to tally the number of particles when the highest concentration of particles was observed near the contact point. The sliding distance covered in these 60 frames was approximately 0.6 mm.

# 3 Results

## 3.1 The impact of the oil film thickness Hi on *in situ* observations

The *in-situ* observation results for particles with an average diameter (φ) of 3.0 μm and varying oil film thickness (*Hi*) are presented in Figure 7. The black dotted circle represents the Hertzian contact area, approximately 30 μm in size, under a normal load of 0.2 N. All friction tests were conducted under boundary lubrication conditions, resulting in the gap between the ball specimen and the sapphire disk at the contact point being at the utmost surface roughness level. The representative observation results for 3.0 μm diameter particles under a thin outside oil film thickness (*Hi* = 2.3 μm) are shown in Figures 7a$_1$–a$_3$. The circle marks one particle at 0 m, which then moved linearly along the sliding direction. This trend of linear particle motion remained consistent when the particle diameter was smaller than the outside oil film thickness. However, when the outside oil film thickness exceeded the particle diameter, as shown in Figures 7b$_1$–b$_3$ with *Hi* at 26.5 μm and Figures 7c$_1$–c$_3$ with *Hi* at 5,000 μm, the particle's motion was no longer linear. In the case of the thick outside oil film situation with *Hi* = 5,000 μm, the particle indicated by the circle did not move along with the sliding direction.

Figure 8 presents the results for φ = 1.0 μm diameter particles. In Figures 8a$_1$–a$_3$, where the outside oil film thickness was *Hi* = 2.5 μm, one particle indicated by a circle moved linearly along the sliding direction from Figures 8a$_1$, a$_2$, before stopping at the inlet area of contact as shown in Figure 8a$_3$. However, for outside oil film thicknesses *Hi* = 12.7 μm (Figure 8b$_1$–b$_3$) and *Hi* = 1,650 μm (Figure 8c$_1$–c$_3$), the particles did not exhibit linear motion along the sliding direction. Finally, the results for 0.8 μm diameter particles are shown in Figures 9a$_1$, c$_3$. In cases where the outside oil film thickness was less than the average diameter of the particles, such as in Figures 9a$_1$–a$_3$ with Hi ≤ 0.75 μm, several particles halted just in front of the contact area.

The measured number of entrainment particles, as a function of outside oil film thickness, is summarized in Figure 10. In every situation, the number of entrainment particles decreased with increasing outside oil film thickness, followed by a sharp increase to reach a peak. Subsequently, the number decreased again with greater outside oil film thickness. The peaks were observed at 4.0 μm outside oil film thickness for 3.0 μm diameter silica particles, 1.6 μm thickness for 1.0 μm

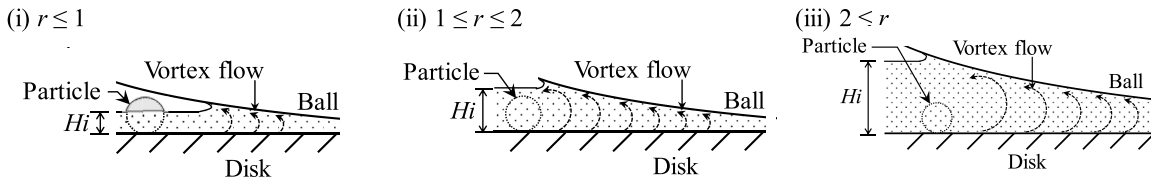


FIGURE 13
The relation between no-dimensional value *r* and number of entrainment particles. **(i-iii)** Schematic of a particle and vortex flow with different outside oil film thickness.

diameter particles, and 1.4 μm thickness for 0.8 μm diameter particles, respectively.

### 3.2 The results of observations under dry conditions

To compare with a lubricated situation, we conducted *in-situ* dry friction tests using silica particles of varying diameters. The representative observation results are shown in Figure 11. In all situation, fluorescently stained particles accumulated in front of the contact area, and these accumulated particles did not move perpendicular to the sliding direction. Instead, they entered the contact point in large numbers.

## 4 Discussion

The relationship between the number of entrained particles and the non-dimensional value "*r*," which represents the outside oil film thickness divided by the particle diameter, is summarized in Figure 12. In dry conditions, a substantial number of particles could enter the contact point regardless of their diameter. However, the entrainment number decreased when the "*r*" value approached approximately 1. Consequently, the maximum number of entrained particles increased within the range of $1 \leq r \leq 2$. Beyond this range, the number of entrained particles gradually decreased. The reason behind this change in the number of entrained particles due to the "*r*" value is believed to be related to reverse flow in front of the contact point. A cross-sectional schematic image illustrating this phenomenon is presented in Figure 13. When "*r*" is less than or equal to 1 as shown in Figure 13i, the reverse flow creates a vortex with a radius smaller than that of the particles because the oil film thickness is less than the particle diameter. As a result, the vortex flow does not significantly affect the motion of particles. In the case where "*r*" falls within the range of $1 \leq r \leq 2$ (Figure 13ii), a vortex flow is generated along the direction from the disk to the oil surface, with a vortex radius equal to the particle radius. Consequently, particles can move from the disk surface to the oil surface and back to the disk surface again. This enhances the maximum number of entrained particles. Finally, for values of "*r*" greater than or equal to 2 (Figure 13iii), the vortex flow radius becomes larger than the particle radius. Thus, once particles attach to the disk surface and follow the vortex flow, they are unable to return to the contact point. Based on the mechanisms described above, specific outside oil film thickness values that enhance the number of entrained particles is suggested.

## 5 Conclusion

- We conducted investigations into the entrainment of glass beads with different diameters, such as 3.0 μm, 1.0 μm, and 0.8 μm. Utilizing a fluorescent staining technique facilitated by silane coupling, we were able to observe the contact point *in-situ*. The high-speed camera effectively detected the number of entrained particles.
- It was observed that particles could enter the contact point even under boundary lubrication conditions.
- The entrainment of particles depended on the thickness of the outside oil film. The non-dimensional value "*r*," expressed as the outside oil film thickness (*Hi*) divided by the particle diameter, exhibited a clear relationship with the entrainment of particles. When "*r*" was less than or equal to 1, particles were capable of entering the contact point. In the range of $1 \leq r \leq 2$, the maximum number of particles entered, while for "*r*" values greater than 2, the number of entrained particles gradually decreased.

## Data availability statement

The raw data supporting the conclusion of this article will be made available by the authors, without undue reservation.

## Author contributions

TT: Conceptualization, Data curation, Formal Analysis, Funding acquisition, Investigation, Methodology, Project administration, Resources, Software, Supervision, Validation, Visualization, Writing–original draft, Writing–review and editing. MO: Writing–original draft, Writing–review and editing. NF: Writing–original draft, Writing–review and editing. MM: Writing–original draft, Writing–review and editing. NH: Writing–original draft, Writing–review and editing. RT: Writing–original draft, Writing–review and editing. HS: Writing–original draft, Writing–review and editing. NU: Writing–original draft, Writing–review and editing.

## Funding

The author(s) declare financial support was received for the research, authorship, and/or publication of this article. This paper is based on results obtained from a project, JPNP20004, subsidized by New Energy and Industiral Technology Development Organization (NEDO).

## Conflict of interest

The authors declare that the research was conducted in the absence of any commercial or financial relationships that could be construed as a potential conflict of interest.

## Publisher's note

All claims expressed in this article are solely those of the authors and do not necessarily represent those of their affiliated organizations, or those of the publisher, the editors and the reviewers. Any product that may be evaluated in this article, or claim that may be made by its manufacturer, is not guaranteed or endorsed by the publisher.

# References


Abdollah, M. F. B., Yamaguchi, Y., Akao, T., Inayoshi, N., Miyamoto, N., Tokoroyama, T., et al. (2012a). Deformation-wear transition map of DLC coating under cyclic impact loading. *Wear* 274–275 (27), 435–441. doi:10.1016/j.wear.2011.11.007

Abdollah, M. F. B., Yamaguchi, Y., Akao, T., Inayoshi, N., Umehara, N., and Tokoroyama, T. (2010). Phase transformation studies on the a-C coating under repetitive impacts. *Surf. Coat. Technol.* 205 (2), 625–631. doi:10.1016/j.surfcoat.2010.07.062

Abdollah, M. F. B., Yamaguchi, Y., Akao, T., Inayoshi, N., Umehara, N., and Tokoroyama, T. (2011). The effect of maximum normal impact load, absorbed energy, and contact impulse, on the impact crater volume/depth of DLC coating. *Tribol. Online* 6 (6), 257–264. doi:10.2474/trol.6.257

Abdollah, M. F. B., Yamaguchi, Y., Akao, T., Miyamoto, N., Tokoroyama, T., Umehara, N., et al. (2012b). Future developments of a deformation-wear transition map of DLC coating. *Tribol. Online* 7 (3), 107–111. doi:10.2474/trol.7.107

Bukvić, M., Gajević, S., Skulić, A., Savić, S., Ašonja, A., and Stojanović, B. (2023). Tribological application of nanocomposite additives in industrial oils. *Lubricants* 12, 6. doi:10.3390/lubricants12010006

Chiba, S., Igami, T., and Tokoroyama, T. (2018). The *in-situ* observation of contact point under boundary lubrication condition with imitation wear particles. *J. Mat. Test. Res. Assoc. Jpn.* 63 (1), 17–21.

Cusano, C., and Sliney, H. E. (1982a). Dynamics of solid dispersions in oil during the lubrication of point contacts, Part I—graphite. *ASLE Trans.* 25 (2), 183–189. doi:10.1080/05698198208983079

Cusano, C., and Sliney, H. E. (1982b). Dynamics of solid dispersions in oil during the lubrication of point contacts, Part II—molybdenum disulfide. *ASLE Trans.* 25 (2), 190–197. doi:10.1080/05698198208983080

Dwyer-Joyce, R. (1999). Predicting the abrasive wear of ball bearings by lubricant debris. *Wear* 233–235, 692–701. doi:10.1016/S0043-1648(99)00184-2

Gao, R., Liu, W., Chang, Q., Zhang, H., and Liu, Y. (2021). Tribological property of biocarbon-based magnesium silicate hydroxide nanocomposite as lubricant additive at different concentrations of additive and dispersant. *Trans. ASME J. Tribol.* 143 (7), 071901. doi:10.1115/1.4048725

Hong, W., Cai, W., Wang, S., and Tomovic, M. M. (2018). Mechanical wear debris feature, detection, and diagnosis: a review. *Chin. J. Aero* 31 (5), 867–882. doi:10.1016/j.cja.2017.11.016

Iwai, Y., Honda, T., Miyajima, T., Yoshinaga, S., Higashi, M., and Fuwa, Y. (2010). Quantitative estimation of wear amounts by real time measurement of wear debris in lubricating oil. *Tribol. Int.* 43 (1–2), 388–394. doi:10.1016/j.triboint.2009.06.019

Kassim, K. A. M., Tokoroyama, T., Murashima, M., Lee, W.-Y., Umehara, N., and Mustafa, M. M. B. (2021). Wear acceleration of a-C:H coatings by Molybdenum-derived particles: mixing and temperature effects. *Tribol. Int.* 159, 106944. doi:10.1016/j.triboint.2021.106944

Kassim, K. A. M., Tokoroyama, T., Murashima, M., and Umehara, N. (2020). The wear classification of MoDTC-derived particles on silicon and hydrogenated diamond-like carbon at room temperature. *Tribol. Int.* 147, 106176. doi:10.1016/j.triboint.2020.106176

Kinoshita, H., Kaneda, S., Fujii, T., and Mari, O. (2007). Three-dimensional measurement and visualization of internal flow of a moving droplet using confocal micro-PIV. *Lab. Chip* 7, 338–346. doi:10.1039/B617391H

Lee, J., Jo, S. H., and Lim, J. (2019b). Effect of surface modification of $CaCO_3$ nanoparticles by a silane coupling agent methyltrimethoxysilane on the stability of foam and emulsion. *J. Industrial Eng. Chem.* 74, 63–70. doi:10.1016/j.jiec.2019.02.002

Lee, W. Y., Jang, Y. J., Umehara, N., Tokoroyama, T., and Murashima, M. (2020). Effect of defects on wear behavior in ta-C coating prepared by filtered cathodic vacuum arc deposition. *Diam. Relat. Mater* 105, 107789. doi:10.1016/j.diamond.2020.107789

Lee, W. Y., Tokoroyama, T., Jang, Y. J., and Umehara, N. (2018). Effect of substrate bias and temperature on friction and wear properties for ta-C coating prepared under different substrate bias voltages with filtered cathodic vacuum arc deposition. *Tribol. Online* 13 (5), 241–247. doi:10.2474/trol.13.241

Lee, W. Y., Tokoroyama, T., Jang, Y. J., and Umehara, N. (2019a). Investigating running-in behavior to understand wear behavior of ta-C coating with filtered cathodic vacuum arc deposition. *J. Tribol.* 23, 38–47.

Loewenthal, S. H., and Moyer, D. W. (1979). Filtration effects on ball bearing life and condition in a contaminated lubricant. *ASME, J. Tribol.* 101 (2), 171–176. doi:10.1115/1.3453307

Mishina, H., Kohno, A., and Akamatsu, A. (2003). Discovery of elemental debris of adhesive wear particles and primary process of wear. *Tribologists* 48 (4), 307–314.

Mitchell, D. J., Mecholsky, J. J., Jr, and Adair, J. H. (2000). All-steel and $Si_3N_4$-steel hybrid rolling contact fatigue under contaminated conditions. *Wear* 239, 176–188. doi:10.1016/s0043-1648(99)00369-5

Nomede-Martyr, N., Bilas, P., Thomas, P., Minatchy, G., and Romana, L. (2021). Tribological performances of graphite and hexagonal boron nitride particles in the presence of liquid. *Trans. ASME J. Tribol.* 143, 071401. doi:10.1115/1.4048550

Roylance, B. J., Williams, J. A., and Dywer-Joyce, R. (2000). Wear debris and associated wear phenomena–fundamental research and practice. *IMechE J. Eng. Trib.* 214, 79–105. doi:10.1243/1350650001543025

Shi, S., Wang, X., Li, Z., Meng, J., Chu, X., Zhang, P., et al. (2023). Multifunctional integrated superhydrophobic coatings with unique fluorescence and micro/micro/nano-hierarchical structures enabled by *in situ* self-assembly. *ACS Appl. Mater. Interfaces* 15 (5), 7442–7453. doi:10.1021/acsami.2c21531

Shin, Y., Lee, D., Lee, K., Ahn, K. H., and Kim, B. (2008). Surface properties of silica nanoparticles modified with polymers for polymer nanocomposite applications. *J. Indust Eng. Chem.* 14, 515–519. doi:10.1016/j.jiec.2008.02.002

Strubel, V., Fillot, N., Cavoret, J., Vegne, P., Mondelin, A., Maheo, Y., et al. (2016). Particle entrapment in hybrid lubricated point contacts. *Tribol. Trans.* 59 (4), 768–779. doi:10.1080/10402004.2015.1106631

Strubel, V., Fillot, N., Ville, F., Cavoret, J., Vergne, P., Mondelin, A., et al. (2017a). Particle entrapment in rolling element bearings: the effect of ellipticity, nature of materials, and sliding. *Tribol. Trans.* 60 (2), 373–382. doi:10.1080/10402004.2016.1168901

Strubel, V., Simoens, S., Vergne, P., Fillot, N., Ville, F., Hajem, M. E., et al. (2017b). Fluorescence tracking and μ-PIV of individual particles and lubricant flow in and around lubricated point contacts. *Tribol. Lett.* 65, 75. doi:10.1007/s11249–017–0859–z

Takeno, H., Tokoroyama, T., Murashima, M., Umehara, N., and Chiba, S. (2020). Enhancement of speed of surface roughness improvement by using a two mixed abrasive slurry method to polish glass surfaces. *J. Jpn. Soc. Abras. Technol.* 64 (8), 428–435. doi:10.11420/jsat.64.32

Tallian, T. E. (1976). Prediction of rolling contact fatigue life in contaminated lubricant: Part I—mathematical Model. *ASME, J. Tribol.* 98 (2), 251–257. doi:10.1115/1.3452814

Tokoroyama, T., Kamiya, T., Ahmed, NSBH, and Umehara, N. (2018). Collecting micrometer-sized wear particles generated between DLC/DLC surfaces under boundary lubricatin with electric field. *JSME Mech. Eng. Lett.* 4, 18–00089. doi:10.1299/mel.18-00089

UN (2015). Transforming our world: the 2030 agenda for sustainable development. Available at: https://sdgs.un.org/2030agenda.

Wang, L., Snidle, R. W., and Gu, L. (2000). Rolling contact silicon nitride bearing technology: a review of recent research. *Wear* 246, 159–173. doi:10.1016/S0043–1648(00)00504–4

Wang, W., Wong, P. L., He, F., and Wan, G. T. Y. (2007). Experimental study of the smoothing effect of a ceramic rolling element on a bearing raceway in contaminated lubrication. *Tribol. Lett.* 28, 89–97. doi:10.1007/s11249–007–9251–8

Wu, C., Yang, K., Chen, Y., Ni, J., Yao, L., and Li, X. (2021). Investigation of friction and vibration performance of lithium complex grease containing nano-particles on rolling bearing. *Tribol. Int.* 155, 106761. doi:10.1016/j.triboint.2020.106761

Wu, H., Li, X., He, X., Lu, J., Wang, L., Zhou, B., et al. (2018). An investigation on the lubrication mechanism of $MoS_2$ nanoparticles in unidirectional and reciprocating sliding point contact: the flow pattern effect around contac area. *Tribol. Int.* 122, 38–45. doi:10.1016/j.triboint.2018.02.013

frontiers | Frontiers in Mechanical Engineering

TYPE Methods
PUBLISHED 07 June 2024
DOI 10.3389/fmech.2024.1416656

Check for updates

OPEN ACCESS

EDITED BY
Taisuke Maruyama,
NSK Ltd., Japan

REVIEWED BY
Aleksandar Ašonja,
Business Academy University, Serbia
Slavica Miladinovic,
University of Kragujevac, Serbia

*CORRESPONDENCE
Mamoru Tohyama,
tohyama@mosk.tytlabs.co.jp

RECEIVED 12 April 2024
ACCEPTED 13 May 2024
PUBLISHED 07 June 2024

CITATION
Tohyama M, Ohmiya Y, Hirose M, Matsuyama H, Toda T, Hasegawa K, Onizuka T, Sato H, Yokoi M and Sato N (2024), Visualization of oil-lubrication ball bearings at high rotational speeds.
*Front. Mech. Eng* 10:1416656.
doi: 10.3389/fmech.2024.1416656

COPYRIGHT
© 2024 Tohyama, Ohmiya, Hirose, Matsuyama, Toda, Hasegawa, Onizuka, Sato, Yokoi and Sato. This is an open-access article distributed under the terms of the Creative Commons Attribution License (CC BY). The use, distribution or reproduction in other forums is permitted, provided the original author(s) and the copyright owner(s) are credited and that the original publication in this journal is cited, in accordance with accepted academic practice. No use, distribution or reproduction is permitted which does not comply with these terms.

# Visualization of oil-lubrication ball bearings at high rotational speeds

Mamoru Tohyama[1]*, Yasuhiro Ohmiya[1], Michiru Hirose[2], Hiroki Matsuyama[3], Takuya Toda[2], Kenichi Hasegawa[2], Takaaki Onizuka[3], Hideaki Sato[4], Masahiro Yokoi[4] and Norikazu Sato[1]

[1]Mechanical System Research-Domain, Toyota Central R&D Labs., Inc., Nagakute, Japan, [2]Engineering Planning Department, Industrial and Bearing Business Unit, JTEKT Corporation, Osaka, Japan, [3]Experimental Validation Department, Industrial and Bearing Business Unit, JTEKT Corporation, Osaka, Japan, [4]Research Instruments Development Research-Domain, Toyota Central R&D Labs., Inc., Nagakute, Japan

Deep-groove ball bearings for the eAxles of electric vehicles must adapt to higher rotational speed conditions because the speed of eAxle motors have been increasing as the size and weight of the motors decrease. Therefore, understanding the oil-lubricated conditions inside ball bearings at high rotational speeds is essential for optimizing their design for eAxles. To clarify the oil-lubricated conditions inside ball bearings at these high speeds, a new test apparatus was developed. This apparatus is capable of simultaneously measuring the friction torque of deep-groove ball bearings, the oil-film thickness on the rolling balls, and observing the oil distributions inside the bearings at rotational speeds up to 20,000 $min^{-1}$. The oil-film thickness was measured using three-wavelength optical interferometry, and the oil distribution was observed using fluorescence. It was found that the oil-film thickness became constant at rotational speed conditions exceeding approximately 7,700 $min^{-1}$. Oil starvations were observed on the raceway around the rolling ball, and these regions increased with increasing rotational speeds. Additionally, in the deep-groove ball bearing with a crown-shaped cage, the oil was mainly supplied to the rolling balls from the inner ring side through the space between the cage claws that held the ball. Moreover, the amount of mixed air tended to increase as the rotational speed increased to approximately 7,700 $min^{-1}$. Those oil starvations and increasing air in oils were considered to be factors that prevent the increase in oil-film thickness. The findings of the reported study will contribute to the development of multibody dynamic technology for high-speed ball bearings necessary in electric vehicles.

KEYWORDS

**ball bearing, lubrication, oil-film thickness measurement, oil distribution, starvation, interferometrytechniques, fluorescence method, EHL (elastohydrodynamic lubrication)**

## 1 Introduction

For electric vehicles (EVs) such as battery, hybrid, plug-in hybrid, and fuel cell EVs, minimizing the mechanical losses in the powertrain system is important for achieving a long driving range with a small battery capacity. The powertrain system of EVs, called the eAxle, includes a gear-train unit (transaxle) to achieve the desired rotational speed and torque at the output shaft from the motor (Nagai et al., 2023). The transaxle primarily comprises gears and rolling bearings (herein referred to as bearings). Because there is a high demand

for reducing friction losses in these components (Hengst et al., 2022), deep-groove ball bearings for EV eAxles should be designed to exhibit low friction–torque properties (Yokota, 2020). Additionally, because the rotational speed of eAxle motors continues to increase as the size and weight of the motors are reduced (Zhang et al., 2019), deep-groove ball bearings are required to be reliable at higher rotational speeds by circumventing excessive wear and seizures.

To optimize the design of high-speed deep-groove ball bearings for eAxles, an understanding of the oil-lubricated conditions inside bearings at higher rotational speeds is required. It has been reported that approximately 50% of all bearing damage results from inadequate lubrication (Desnica et al., 2022). Therefore, it is important to observe the oil distribution and flow inside the bearings and measure the oil-film thickness on the rolling surfaces under high-speed conditions. Many studies have been conducted to determine the lubrication conditions inside bearings using basic ball-on-disk tests under rolling-sliding conditions (Wedeven et al., 1971; Guangteng et al., 1992; Reddyhoff et al., 2010). These studies developed the elastohydrodynamic lubrication (EHL) theories under fully-flooded lubrication conditions (Spikes, 2014), and other various calculation methods for EHL lubrication have been also developed to consider complex factors such as oil starvation due to oil being pushed aw、ay from contact area by rolling balls, oil-reflow to the rolling surface, oil-supply flow rates, inlet oil-film thickness of rolling elements, and other oil flow phenomena (Cann et al., 2004; Maruyama and Tsuyoshi, 2015; Nogi, 2015; Kostal et al., 2017). However, actual bearings comprise an outer ring, inner ring, multiple rolling elements (balls), and a cage to hold the balls. The lubrication conditions within the bearings may differ from those observed in ball-on-disk tests using one or more ball specimens and a single disk specimen. Therefore, observing and measuring the lubrication conditions in actual bearings are important.

Various studies have been conducted to elucidate the lubrication conditions inside actual bearings using optical methods. Wu et al. (2016) observed the oil and air distribution within a 7,210 angular contact ball bearing under oil-jet lubrication conditions at rotational speeds of up to 4,000 $min^{-1}$. Liang et al. (2022) observed the difference in the oil flows and distributions of different cage shapes under extremely low-speed conditions (rotational speed up to 15 $min^{-1}$) using a 7,014 angular contact ball bearing, where the outer ring was replaced with a flat glass ring. Chen et al. (2022) also observed the oil distribution inside of a 7008C angular contact ball bearing using a glass outer ring and a transparent resin cage. They combined laser-induced fluorescence and light emitting diode (LED) illumination with two high-speed cameras and simultaneously observed the radial and axial directions of the bearing up to a rotational speed of 5,000 $min^{-1}$. Chennaoui et al. (2022) measured the oil-film thickness between the ball and outer ring under oil-lubricated conditions using a 6206-type deep-groove bearing with a sapphire outer ring by applying the ultrathin film interferometry method, commonly used in ball-on-disc tests. A triggering system enabled the capture of images when a ball passed the uppermost point of the bearing, independent of the rotational speed, and fluorescence methods were used to observe the oil distribution. To minimize image blurring, they employed an intensified gated camera with a high sensitivity and an exposure time in the nanosecond range, obtaining clear images of the oil-film thickness distribution during rotational motion at a maximum rotational speed of 3,000 $min^{-1}$. Arya et al. (2023a) used transparent resin cages and a test rig, where the inner and outer rings rotated in opposite directions to prevent cage rotation. They observed the oil distribution and flow between the rolling elements (balls) and cage in a 7,311 angular contact ball bearing using a high-speed camera under low-speed conditions (inner ring rotational speed up to 300 $min^{-1}$). Additionally, Arya et al. (2023b) measured the oil flow velocity around a ball using the bubble image velocimetry method, which traces the motion of bubbles generated within the oil during bearing rotation.

For visualizing lubrication conditions inside ball bearings, Noda et al. (2020) and Kamamoto et al. (2022) conducted X-ray computed tomography techniques, although these were used for grease lubrication bearings. However, those observations using X-ray were conducted with bearings made of resins and not of steel, as X-ray penetration through thick steel parts is limited. Sakai et al. (2021a) visualized the grease distribution in a 6204-type deep-groove ball bearing made of metal, using pulsed neutron beam radiography and computed tomography under stationary conditions after rotating the bearings. Sakai et al. (2021b) also observed the inside of a bearing during rotation using the neutron imaging technology. However, the maximum rotational speed for these observations was limited to 2,000 $min^{-1}$, owing to limitations in the time resolution of neutron beam radiography.

A method to measure the electrostatic capacitance to determine oil-film thickness has been reported in several studies for grease-lubricated bearings (Jablonka et al., 2018; Cen and Lugt, 2019; Zhang and Glovnea, 2020). Additionally, Maruyama et al. (2019) developed an electrical impedance method that can measure the oil-film thickness and breakdown ratio of the contact area between the rolling ball and the outer and inner rings, achieving measurements in motor speeds up to 6,000 $min^{-1}$ using 608-type deep-groove ball bearings under oil-lubricated conditions. Electrical measurement methods have an advantage over optical methods because they can be directly applied to bearings without altering the steel materials of the rings. Additionally, ultrasonic methods have been used for measurements (Dwyer-Joyce et al., 2004; Wan Ibrahim et al., 2012), although the rotational speed is limited owing to factors such as transducer frequency. For instance, for the evaluation of a 6410-type deep-groove ball bearing, its maximum rotational speed was limited to 600 $min^{-1}$.

Although various measurement methods have been utilized to observe oil distributions and measure oil-film thickness inside ball bearings, the applied maximum rotational speed is limited to 6,000 $min^{-1}$ or less. Because current EVs feature maximum rotational speeds of 20,000 $min^{-1}$ or higher, the lubricating conditions inside the bearings at rotational speeds exceeding 6,000 $min^{-1}$ have been calculated by computer-aided engineering predictions based on the findings of previous studies (Houpert, 2016; Matsumoto et al., 2021; Chen et al., 2023). However, to validate the accuracy of the previously developed calculation methods for current EVs, actual measurement data under high-speed rotational conditions must be obtained. Therefore, the authors developed a new test apparatus able to measure friction torque and oil-film thickness and observe oil distribution inside oil-lubricated deep-groove ball bearings, up to a shaft rotational speed of

20,000 $min^{-1}$ in the reported study (Tohyama et al., 2023). This report details the measurement and observation methods used in the study, along with the results obtained.

## 2 Observation and measurement methods for high-speed ball bearing

A novel test apparatus capable of measuring the friction torque of a deep-groove ball bearing under oil-lubricated conditions was developed. This apparatus measured the oil-film thickness on the rolling surface using optical interference methods and observed the oil distribution using fluorescence methods at rotational speeds of up to 20,000 $min^{-1}$.

### 2.1 Test apparatus for visualization inside high-speed ball bearing

An outline of the test apparatus is shown in Figure 1. A bearing equipped with a quartz outer ring was incorporated into the bearing housing for observation purposes. The arms used for applying the radial load were connected to the left and right sides of the bearing housing. A radial load on the test bearing was applied by placing weights on these arms. The weights on the left and right sides of the bearing housing and arms were finely adjusted for balance under static conditions. The test bearing was fixed at its outer ring to the bearing housing, and the rotation force of the bearing housing was supported by a load cell for the friction force measurement, enabling the measurement of the friction torque of the test bearing. Although, a test apparatus configuration with two test bearings that support a rotating shaft and apply radial loads to the shaft is commonly used to measure the friction torque of a test bearing (Peterson et al., 2021), considering the relationship between the friction torque and the oil distribution and film thickness, the lubrication conditions of the two test bearings are not always guaranteed to be in the same state. Therefore, the aforementioned structure, which measures the friction torque of a single test bearing, was adopted in this study.

An enlarged cross-sectional view of the bearing housing, including the oil-lubricated structure, is shown in Figure 2. On the test bearing side, an oil supply nozzle with a tip diameter of Φ0.7 mm was installed. Oil was supplied toward the uppermost ball of the test bearing. The oil temperature was controlled to be constant at 60°C at the outlet of the oil supply nozzle by separately adjusting the temperature in an oil bath set. Oil was supplied at a constant rate of 100 mL/min using a roller pump. The oil was a commercially available automatic transmission fluid (ATF: Toyota Auto Fluid WS), which is also used in the transaxles of hybrid EVs. The right side of the bearing housing, shown in Figure 2, was covered with a transparent acrylic cover, whereas the left side was covered with a metal cover. Both covers had clearances between the rotating shafts to prevent contact. An oil drain was placed on one side inside the housing, as shown in Figure 2, and an oil penetration port was placed at a low position in the housing to maintain the oil accumulation below the height of the lower side of the outer ring of the test bearing.

The test bearing featured a transparent quartz outer ring with the same track surface shape as an actual commercial 6008-type deep-groove ball bearing (outer diameter: ø68 mm, inner diameter: ø40 mm, width: 15 mm, 12 balls, crown-shaped resin cage) for optical measurement and observation as described in subsequent sections. The inner ring, balls, and cage were made of steel and resin, respectively, from the actual commercial 6008-type deep-groove ball bearing. The track surface of the quartz outer ring was finished to be very smooth (surface roughness Ra of 0.05 μm or less), which is essential for precise measurements. The outer diameter and width of the quartz outer ring were changed from the shape of the 6008-type bearing to match the shape of the other test bearings (which were not used in this study), resulting in dimensions of ø80 and 18 mm, respectively.

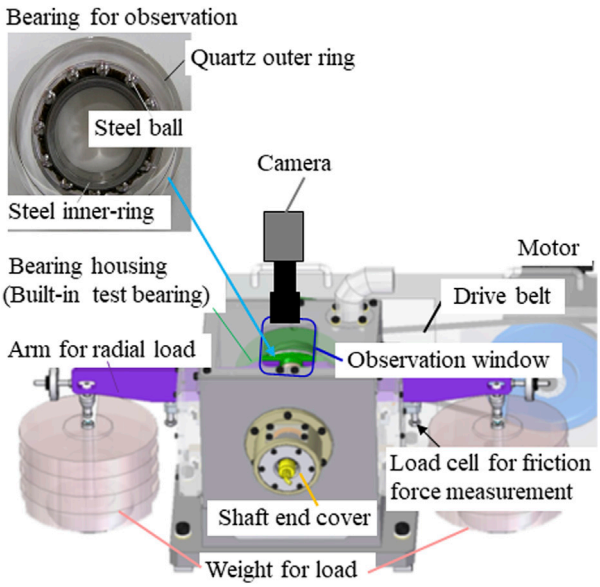


FIGURE 1
Illustration of test apparatus (Tohyama et al., 2023).

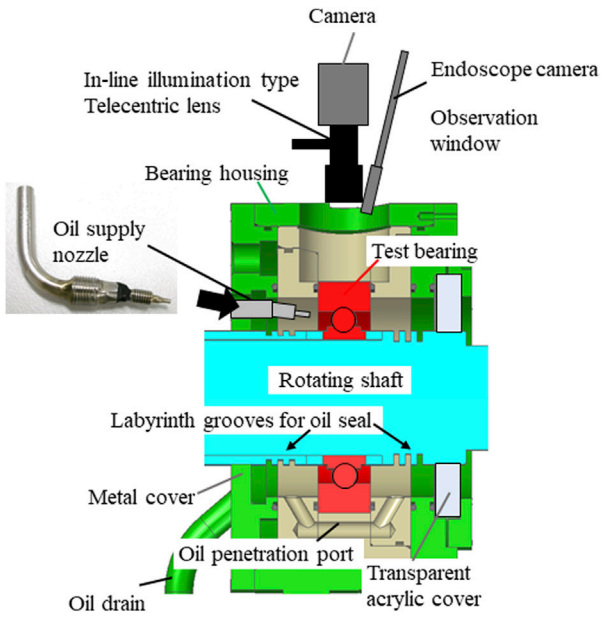


FIGURE 2
Enlarged cross-sectional view of bearing housing (Tohyama et al., 2023).

Thermocouples were attached at four locations around the outer circumference of the outer ring to monitor the temperature of the bearing. The average of these four readings was used to determine the outer-ring temperatures. When conducting tests with varying shaft rotational speeds, to minimize changes in the bearing temperature at each speed, the rotational speed was initially set to the highest value of the test (approximately 20,000 $min^{-1}$) for 2 min before starting measurements, and then the speed was gradually reduced. There was a constant radial load of 300 N.

## 2.2 Oil-film thickness measurements between outer ring raceway and ball surface

The oil-film thickness between the raceway of the quartz outer ring and ball was measured using the three-wavelength optical interference method (Otsuki et al., 2016), as shown in Figure 3. In this method, the three-wavelength light (RGB) was obtained by adjusting white light from a xenon flash lamp through a three-wavelength bandpass filter. These three wavelengths were irradiated onto the ball surface using a liquid light guide and coaxial telecentric lenses, as shown in Figure 2. The raceway of the quartz outer ring was coated with a chromium layer because a partial reflective coating is necessary for the optical interference measurement method. Additionally, silica with a thickness of 300 ± 50 nm (not shown in Figure 3) was coated on top of the chromium layer as a spacer and protective layer. The interference images resulting from the optical path difference between the light reflected by the reflective coating and that reflected by the ball surface (equivalent to half of the oil-film thickness) were captured using a high-resolution 3- complementary metal oxide semiconductor (CMOS) camera for machine vision. The observation area was approximately 3.55 mm (ball rolling direction) × 0.86 mm (axial direction) around the contact area between the ball and raceway on the outer ring of the bearing.

The optical film thickness was determined by comparing the central interference color at the contact surface of the ball with the optical film thickness color chart shown in Figure 3. In cases with significant variations in the interference color within the contact area, a two-dimensional quantitative analysis using the hue method developed by Tomota et al. (2022) was used to calculate the thickness. The calculated optical film thickness includes the thickness of the reflective and spacer films. To measure the total thickness of the reflective and spacer films, the optical film thickness was determined by observing the interference image at the contact surface in a static state by adding a radial load that did not form an oil film. By subtracting this optical film thickness from the experimentally measured optical film thickness of each test condition, the optical film thickness corresponding to the oil-film thickness was obtained. Finally, the oil-film thickness was calculated by dividing the optical film thickness by the refractive index of the ATF (1.45, measured at an oil temperature of 60°C).

A pulsed illumination with a 2 μs irradiation time and 50 Hz repetition rate was employed to reduce image blur during high-speed motion. The frame rate of the 3-CMOS camera was set to 50 fps and synchronized with the pulse illumination. The shaft rotational speed was finely controlled to synchronize the orbit cycle of the ball revolution with the repetition of pulsed illumination. Consequently, although the balls in the bearing were moving at an extremely high speed, the balls in the videos appear to be stopped or moving in orbit very slowly.

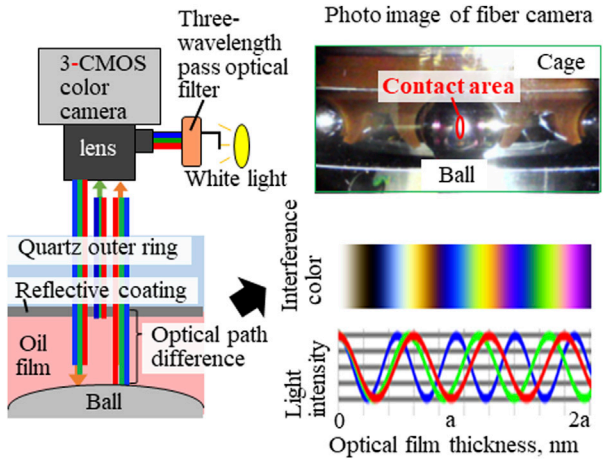


FIGURE 3
Measurement method of oil-film thickness by three-wavelength optical interferometry (Tohyama et al., 2023).

Additionally, an endoscope camera was installed alongside the 3-CMOS camera in the test apparatus, as shown in Figure 2, to observe the white-light image around the rolling ball at approximately 30 and 17 mm in the ball-rolling and axial directions.

## 2.3 Oil distribution observation by fluorescence method

The oil distributions were observed using a fluorescence method. In the fluorescence method, coumarin-6 was added as a fluorescent agent in a 0.05 wt% concentration. For fluorescence excitation, pulsed ultraviolet (UV)-LED illumination at a wavelength of 405 nm was employed. A liquid-light guide was used to direct the emitted light to the focal point where the condenser lens was attached. Unlike interferometry, the excitation light was irradiated from outside the lens onto the observation target. The pulsed UV-LED illumination was configured with a 2 μs irradiation time and 40 Hz repetition rate to reduce image blur. The video recording was synchronized with the camera frame rate set at 40 fps to match the pulse illumination. The 3-CMOS camera was the same as that used for the oil-film measurement. The observation area was approximately 23.6 mm (ball-rolling direction) × 17.7 mm (axial direction). To enhance the sensitivity of the camera, a binning function was applied, which combined four-pixel image sensors to acquire a single image, resulting in a camera resolution of x: 1032, y: 772.

# 3 Results and discussion

## 3.1 Oil-film thickness measurement results

Figure 4 shows examples of interference fringe images caused by oil film formation between the ball and raceway of the outer

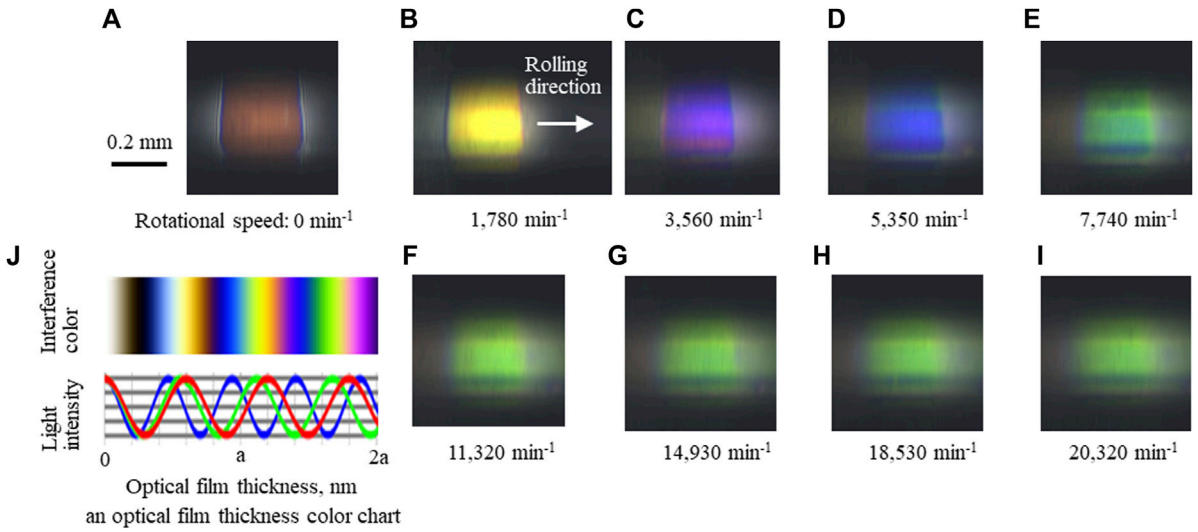


FIGURE 4
Optical interference images of contact surfaces for each rotational speed of **(A)** 0, **(B)** 1,780, **(C)** 3,560, **(D)** 5,350, **(E)** 7,740, **(F)** 11,320, **(G)** 14,930, **(H)**, 18,530, and **(I)** 20,320 $min^{-1}$ and **(J)** is an optical film thickness color chart (Tohyama et al., 2023).

ring under various shaft rotational speed conditions. The interference fringe image at a rotational speed of 0 $min^{-1}$ represents the shape near the center of the Hertz contact ellipse. The brown interference color in the central region for a rotational speed of 0 $min^{-1}$ corresponds to the optical film thickness due to the partially reflective coating (estimated to be a few nanometers thick) and silica coating on the raceway of the quartz outer ring. Focusing on the change in the interference color with increasing rotational speed, color variations from 1,780 to 5,350 $min^{-1}$ can be observed, indicating an increase in the oil-film thickness as the rotational speed increases. However, between 7,740 and 20,320 $min^{-1}$, the interference colors remain similar. These results suggest that the oil-film thickness under high-speed conditions becomes constant. Notably, during the measurement at each speed, changes in the interference color were not observed during the 1-min measurement interval. Therefore, the oil-film thickness on the rolling surface remained stable under steady-state conditions.

In the interference images shown in Figure 4, the upper and lower regions of each image appear dark and interference fringes cannot be observed in these regions. This phenomenon can be attributed to the R-shaped groove on the quartz outer ring, which resembles an actual deep-groove ball bearing. Because of the varying reflection angles caused by the widthwise position of the R-groove and the significant change in distance from the lens, the focus depth deviates, resulting in partial visibility of the interference pattern.

The measured oil-film thickness, calculated from the light interference colors, is shown in Figure 5. For comparison, the dashed line also includes the calculated central oil-film thickness based on the EHL oil-film thickness formula of Chittenden et al. (1985) for fully flooded lubrication conditions. In this calculation, the oil viscosity was estimated to be 0.011 Pa s at a supply oil temperature of 60°C, assuming a constant sliding ratio of 0% for the ball. In these results, the oil-film thickness values at each rotational speed are shown as relative ratios to the calculated central oil-film thickness value at the highest rotational speed of 20,320 $min^{-1}$ in the actual measurement (normalized to 1.0).

At a low-speed range of 1,780–5,350 $min^{-1}$, the measured oil-film thickness values tended to increase as the rotational speed increased, similar to the calculated values. However, at speeds above 7,740 $min^{-1}$, the measured values of the oil-film thickness remained relatively constant regardless of rotational speed. Unlike the assumptions of the EHL theory under fully flooded lubrication conditions, in the high-speed range, the oil-film thickness does not increase, even as the shaft rotation speed (or rolling speed) increases.

Figure 6 shows the friction torque measured simultaneously with the oil-film thickness as a reference, the friction torque obtained during the observation of the oil distribution using the

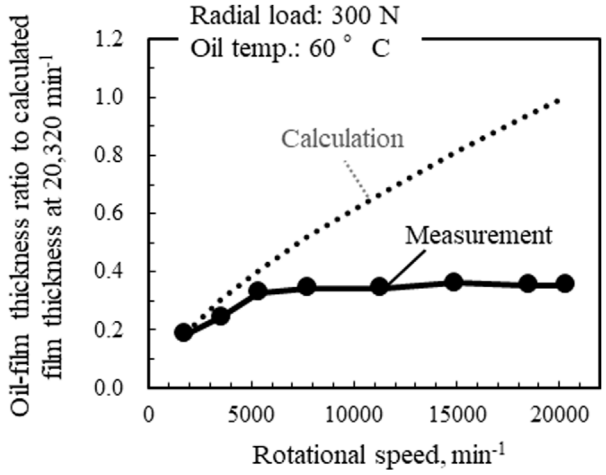


FIGURE 5
Comparison of oil-film thickness between measurement and calculated values (Tohyama et al., 2023).

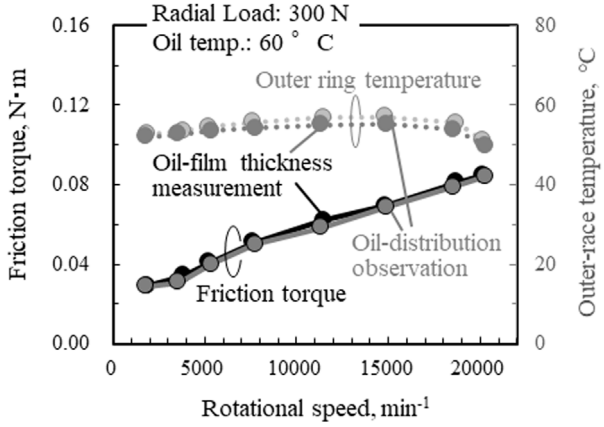


FIGURE 6
Friction torque measured during oil-film thickness measurements and oil-distribution observations (Tohyama et al., 2023).

fluorescence method, and the temperature measurements at the outermost periphery of the quartz outer ring. The measured friction torque values during the oil-film thickness measurement and oil-distribution observation were similar, indicating good reproducibility of the friction torque in this test. The friction torque of the deep-groove ball bearing used in this test tended to increase with rotational speed.

## 3.2 Oil distribution observations using endoscope camera

The oil distribution around the ball was captured using an endoscope camera equipped with pulsed white-light illumination, specifically utilizing three-wavelength light. Snapshot images extracted from the videos are presented in Figure 7. In Figure 7A, the positions of the oil supply nozzle and the outer ring raceway are marked for reference. Figure 7H indicates the cage's shape with brown lines for reference. The red color in the images represents the ATF used in this test. Under the low-speed condition with a rotational speed of 1,780 $min^{-1}$, the area around the rolling ball was nearly fully immersed in oil (ATF). However, at speeds exceeding 3,560 $min^{-1}$, as the rotational speed increased, the oil near the ball inlet (on the right side of the ball) gradually became cloudy white, indicating an increasing presence of air bubbles in the oil due to aeration. The cloudiness of the oils at the ball inlets reveals that the number of air bubbles mixed in the oils tended to rise as the rotational speed approached 7,700 $min^{-1}$. Additionally, oil starvation was observed at the ball outlet (left side of the images), and these oil-starved regions tended to expand with increasing rotational speed. The aeration of the inlet oil and the expansion of the oil-starved regions on the raceway are considered contributing factors that prevent the increase in oil-film thickness under high-speed conditions.

## 3.3 Oil distribution observations using fluorescence method

The oil distributions observed at various rotational speeds using the fluorescence method are depicted in Figure 8. These observations were facilitated by synchronizing the revolution period of the ball with the pulsed illumination, enabling real-time observation. In Figure 8A, the positions of the ball and the edges of the raceway on the outer ring are delineated by dashed lines, with the rolling directions of the balls indicated on the right side of the images. The bright areas signify the presence of substantial amounts of oil. Oil was supplied from the point labeled "oil supply" in Figure 8A towards the ball. Near the

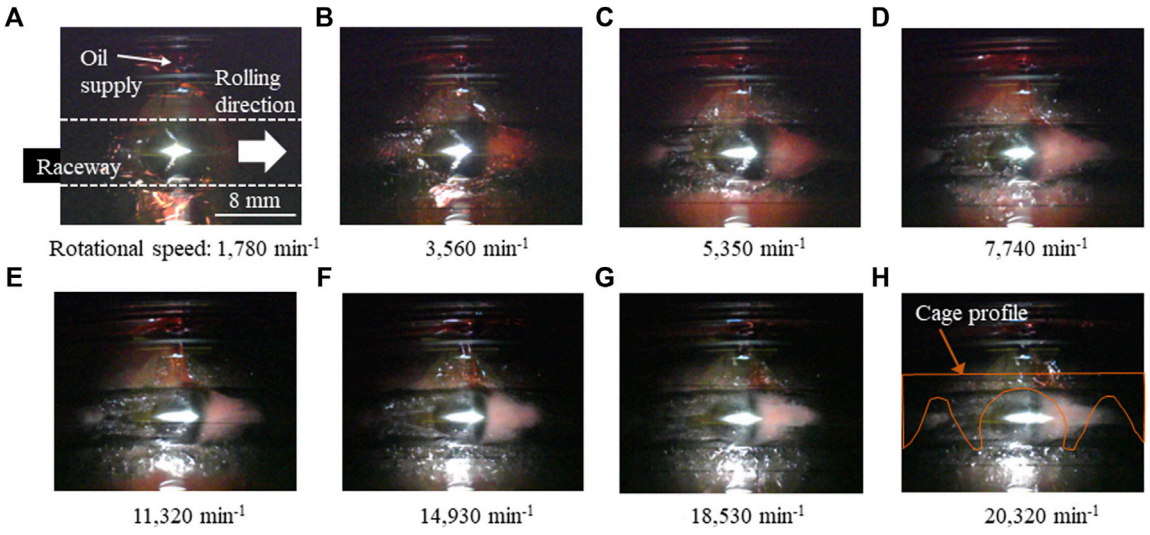


FIGURE 7
White-light images of oil distributions observed by using endoscope camera under rotational speeds of **(A)** 1,780, **(B)** 3,560, **(C)** 5,350, **(D)** 7,740, **(E)** 11,320, **(F)** 14,930, **(G)**, 18,530, and **(H)** 20,320 $min^{-1}$ (Tohyama et al., 2023).

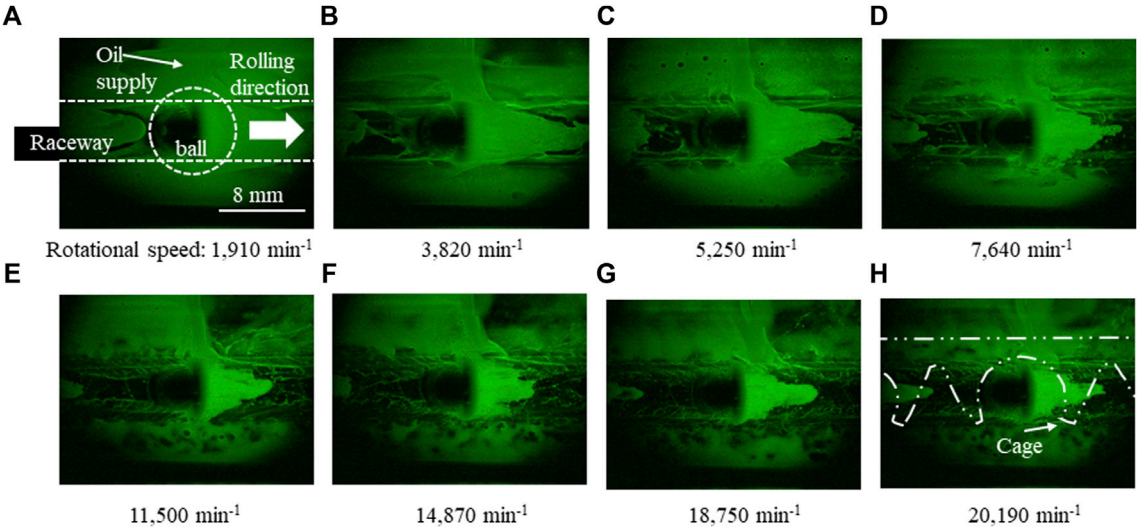


FIGURE 8
Fluorescence images of oil distributions observed by using 3-CMOS camera under rotational speeds of **(A)** 1,920, **(B)** 3,820, **(C)** 5,250, **(D)** 7,640, **(E)** 11,500, **(F)** 14,870, **(G)** 18,750, and **(H)** 20,190 $min^{-1}$ (Tohyama et al., 2023).

center of the ball in the rolling direction, dark regions indicating the absence of oil were consistently observed in all images. These regions are considered the contact areas between the ball and outer ring. The two-dotted dashed line in Figure 8H illustrates the shape of the crown-type cage used for the test bearing.

Under low-speed conditions with a rotation speed of 1,910 $min^{-1}$, similar to the observations made using the endoscope camera described in Section 3.2, the ball inlet (on the right side of the ball) was filled with oil. However, the amount of oil at the ball inlet tended to decrease with increasing rotational speed. Oil starvation occurred at the ball outlet side. As the rotational speed increased, the starvation region tended to expand toward the next ball. Although some details may be difficult to discern in the static image shown in Figure 8, in the captured video for rotational speeds exceeding 7,640 $min^{-1}$ (as shown in Figures 8D–H), the oil flow from the oil supply was deflected by the rolling ball, causing the direct inflow oil supply from the side nozzle to the ball inlet to cease. The oil distribution shape at the ball inlet spread triangularly from the front of the ball toward the ball, and oil was supplied from the space between the cage claws that held the ball in the cage. Therefore, even with oil supply nozzles provided on the side of the ball, the oil supply to the ball in a deep-groove ball bearing during high rotational speeds primarily occurs through the space in the cage, rather than being directly supplied from the side. This oil flow is a specific phenomenon unique to ball bearings and depends on the retainer shape. These results underscore the importance of observations using actual bearing shapes for comprehensive bearing evaluations, as replicating these oil-flow phenomena using simple ball-on-disk tests is challenging.

Focusing on the correlation between the oil distribution and oil-film thickness, it can be assumed that the increment rate in the oil-film thickness decreases with increasing rotational speed, as shown in Figure 4, corresponding to a decrease in the amount of oil at the ball inlet.

These measurements and observations yield new, clarified findings that go beyond speculations or predictions made by many researchers. These findings, which could not be obtained from previous observations at rotational speeds up to 6,000 $min^{-1}$ as described in the introduction section, were made possible by experiments conducted under high-speed conditions up to 20,000 $min^{-1}$. However, the methods introduced above also have limitations, such as the lack of examination of the oil-film thickness between balls and the inner ring, as well as the oil distribution on the inner-ring side. Utilizing other measurement and observation methods evolved from those described in Section 1, along with CAE calculations and prediction techniques improved by incorporating new findings, may also be crucial in fully understanding the lubrication conditions in high-speed ball bearings.

## 4 Conclusion

To clarify the lubrication conditions of deep-groove ball bearings for eAxles of EVs at high rotational speeds, a new test apparatus was developed. This apparatus is capable of simultaneously measuring the friction torque and oil-film thickness on the rolling balls and visualizing the oil distribution around the balls on the raceway of the outer ring at rotational speeds of up to 20,000 $min^{-1}$. Based on the results obtained by measuring the oil-film thickness and observing the oil distribution in a 6008-type ball bearing supplied with oil from a nozzle placed on the side of the bearing (Tohyama et al., 2023), the following findings were obtained.

1) At high rotational speeds, the oil-film thickness on the surface of the rolling ball in deep-groove ball bearings does not increase, in contrast to the EHL theory under fully flooded conditions. The oil-film thickness became constant at rotational speeds exceeding approximately 7,700 $min^{-1}$.
2) At high rotational speeds, oil supplied from the side of the orbit of the rolling ball was obstructed by the moving balls and cage,

incurring oil starvation. In a deep-groove ball bearing with a crown-shaped cage, the oil was mainly supplied to the rolling balls from the inner ring side through the space between the cage claws that held the ball.

3) Oil supplied to the rolling balls from the inner ring side was mixed with air bubbles at rotational speeds exceeding 2,000 $min^{-1}$. The amount of mixed air tended to increase as the rotational speed increased to approximately 7,700 $min^{-1}$.
4) The insufficient oil supply at the ball inlet (resulting in oil starvation) and presence of air bubbles in the oil (causing a decrease in the effective oil viscosity on the rolling surface) were assumed to prevent an increase in oil-film thickness despite increasing rotational speeds in the high-speed range.

The findings of this study will contribute to the development of multibody dynamic technology for high-speed ball bearings necessary in EVs (JTEKT, 2023). The measurement and observation techniques described in this study can be utilized in future studies to enhance the accuracy of computational fluid dynamics analysis methods for calculating oil flow. Moreover, these techniques may enable the design of optimal high-speed deep-groove ball bearings for eAxles, with features such as low friction torque performance and seizure prevention.

## Data availability statement

The original contributions presented in the study are included in the article/supplementary material, further inquiries can be directed to the corresponding author.

## Author contributions

MT: Conceptualization, Investigation, Methodology, Visualization, Writing–review and editing, Validation, Writing–original draft. YO: Data curation, Investigation, Methodology, Visualization, Writing–review and editing. MH: Conceptualization, Supervision, Writing–review and editing. HM: Supervision, Writing–review and editing. TT: Supervision, Writing–review and editing. KH: Supervision, Writing–review and editing. TO: Conceptualization, Project administration, Supervision, Writing–review and editing. HS: Resources, Writing–review and editing. MY: Resources, Writing–review and editing. NS: Conceptualization, Investigation, Project administration, Supervision, Writing–review and editing.

## Funding

The author(s) declare that financial support was received for the research, authorship, and/or publication of this article. This study was funded by Toyota Central R&D Labs., Inc. and JTEKT CORPORATION. The funders were involved in the study titled "Visualization of oil-lubrication ball bearings at high rotational speeds."

## Conflict of interest

Authors MT, YO, HS, MY, and NS are employed by Toyota Central R&D Labs., Inc., while MH, HM, TT, KH, and TO are employed by JTEKT corporation.

The authors declare that this study received funding from Toyota Central R&D Labs., Inc. and JTEKT CORPORATION. The funder had the following involvement in the study: the decision to submit it for publication.

## Publisher's note

All claims expressed in this article are solely those of the authors and do not necessarily represent those of their affiliated organizations, or those of the publisher, the editors and the reviewers. Any product that may be evaluated in this article, or claim that may be made by its manufacturer, is not guaranteed or endorsed by the publisher.

## References

Arya, U., Peterson, W., Sadeghi, F., Meinel, A., and Grillenberger, H. (2023b). Investigation of oil flow in a ball bearing using Bubble Image Velocimetry and CFD modeling. *Tribol. Int.* 177, 107968. doi:10.1016/j.triboint.2022.107968

Arya, U., Sadeghi, F., Aamer, S., Meinel, A., and Grillenberger, H. (2023a). *In situ* visualization and analysis of oil starvation in ball bearing cages. *Tribol. Trans.* 66 (5), 965–978. doi:10.1080/10402004.2023.2253867

Cann, P. M. E., Damiens, B., and Lubrecht, A. A. (2004). The transition between fully flooded and starved regimes in EHL. *Tribol. Int.* 37 (10), 859–864. doi:10.1016/j.triboint.2004.05.005

Cen, H., and Lugt, P. M. (2019). Film thickness in a grease lubricated ball bearing. *Tribol. Int.* 134, 26–35. doi:10.1016/j.triboint.2019.01.032

Chen, H., Liang, H., Wang, W., and Zhang, S. (2023). Investigation on the oil transfer behaviors and the air-oil interfacial flow patterns in a ball bearing under different capillary conditions. *Friction* 11 (2), 228–245. doi:10.1007/s40544-021-0592-3

Chen, H., Wang, W., Liang, H., and Ge, X. (2022). Observation of the oil flow in a ball bearing with a novel experiment method and simulation. *Tri. Int.* 174, 107731. doi:10.1016/j.triboint.2022.107731

Chennaoui, M., Fowell, M., Liang, H., and Kadiric, H. (2022). A novel set-up for *in situ* measurement and mapping of lubricant film thickness in a model rolling bearing using interferometry and ratiometric fluorescence imaging. *Tribol. Lett.* 70 (85), 85. doi:10.1007/s11249-022-01625-z

Chittenden, R. J., Dowson, D., Dunn, J. F., and Taylor, C. M. (1985). A theoretical analysis of the isothermal elastohydrodynamic lubrication of concentrated contacts. II. General case, with lubricant entrainment along either principal Axis of the hertzian contact ellipse or at some intermediate angle. *Proc. R. Soc. A* 397 (1813), 271–294. doi:10.1098/rspa.1985.0015

Desnica, E., Ašonja, A., Radovanović, L., Palinkaš, I., and Kiss, I. (2022). Selection, dimensioning and maintenance of roller bearings. 31st international conference on organization and technology of maintenance (OTO 2022). OTO 2022. *Lect. Notes Netw. Syst.* 592, 133–145. doi:10.1007/978-3-031-21429-5_12

Dwyer-Joyce, R. S., Reddyhoff, T., and Drinkwater, B. W. (2004). Operating limits for acoustic measurement of rolling bearing oil film thickness. *Tribol. Trans.* 47 (3), 366–375. doi:10.1080/05698190490455410

Guangteng, G., Cann, P. M., and Spikes, H. A. (1992). A study of parched lubrication. *Wear* 153 (1), 91–105. doi:10.1016/0043-1648(92)90263-8

Hengst, J., Werra, M., and Küçükay, F. (2022). Evaluation of transmission losses of various battery electric vehicles. *Automot. Innov.* 5, 388–399. doi:10.1007/s42154-022-00194-0

Houpert, L. (2016). Hydrodynamic load calculation in rolling element bearings. *Tribol. Trans.* 59 (3), 538–559. doi:10.1080/10402004.2015.1090043

Jablonka, K., Romeo Glovnea, R., and Jeroen Bongaerts, J. (2018). Quantitative measurements of film thickness in a radially loaded deep-groove ball bearing. *Tribol. Int.* 119, 239–249. doi:10.1016/j.triboint.2017.11.001

JTEKT (2023). JTEKT ENGINEERING JOURNAL No.1019E. Model based development for BEV high-speed ball bearing. Available at: https://www.jtekt.co.jp/e/engineering-journal/1019/1019-17.html (Accessed March 29, 2024).

Kamamoto, S., Murata, J., and Shishihara, Y. (2022). Study on low torque deep groove ball bearing by cage profile optimization. *JTEKT Eng. J. No*. 1018E, 22–34. Available at: https://www.jtekt.co.jp/e/engineering-journal/1018/1018-06.html (Accessed March 30, 2024).

Kostal, D., Sperka, P., Svoboda, P., Krupka, I., and Hartl, M. (2017). Influence of lubricant inlet film thickness on elastohydrodynamically lubricated contact starvation. *J. Tribol.* 139, 051503. doi:10.1115/1.4035777

Liang, H., Zhang, Y., and Wang, W. (2022). Influence of the cage on the migration and distribution of lubricating oil inside a ball bearing. *Friction* 10 (7), 1035–1045. doi:10.1007/s40544-021-0510-8

Maruyama, T., Maeda, M., and Nakano, K. (2019). Lubrication condition monitoring of practical ball bearings by electrical impedance method. *Tribol. Online* 14 (5), 327–338. doi:10.2474/trol.14.327

Maruyama, T., and Tsuyoshi, S. (2015). Relationship between supplied oil flow rates and oil film thicknesses under starved elastohydrodynamic lubrication. *Lubr* 3 (2), 365–380. doi:10.3390/lubricants3020365

Matsumoto, K., Koga, H., Ono, Y., and Mihara, Y. (2021). Calculation of oil film thickness on bearing raceway grooves by measuring raceway outer ring temperature. *SAE Tech. Pap. 2021-01-0342*. doi:10.4271/2021-01-0342

Nagai, H., Kawamoto, N., Horiguchi, K., Yoda, T., Hiyoshi, M., and Yamamoto, M. (2023). Development of powertrain system and battery for BEV. *SAE Tech. Pap. 2023-01-0518*. doi:10.4271/2023-01-0518

Noda, T., Shibasaki, K., Miyata, S., and Taniguchi, M. (2020). X-ray CT imaging of grease behavior in ball bearing and numerical validation of multi-phase flows simulation. *Tribol. Online* 15 (1), 36–44. doi:10.2474/trol.15.36

Nogi, T. (2015). An analysis of starved EHL point contacts with reflow. *Tribol. Online* 10 (1), 64–75. doi:10.2474/trol.10.64

Otsuki, M., Kitagawa, K., Izumi, T., and Tohyama, M. (2016). Development of three-wavelength interferometry (Part 1) -Calibration-less oil thickness profile measurement by thin film interference color analysis-. *Proc. Tribol. Conf. 2016 Spring Tokyo*, B9. (in Japanese).

Peterson, W., Russell, T., Sadeghi, F., and Berhan, M. T. (2021). Experimental and analytical investigation of fluid drag losses in rolling element bearings. *Tribol. Int.* 161, 107106. doi:10.1016/j.triboint.2021.107106

Reddyhoff, T., Choo, J. H., Spikes, H. A., and Glovnea, R. P. (2010). Lubricant flow in an elastohydrodynamic contact using fluorescence. *Tribol. Lett.* 38, 207–215. doi:10.1007/s11249-010-9592-6

Sakai, K., Ayame, Y., Iwanami, Y., Kimura, N., and Matsumoto, Y. (2021a). Observation of grease fluidity in a ball bearing using neutron imaging technology. *Tribol. Online* 16 (2), 146–150. doi:10.2474/trol.16.146

Sakai, K., Iki, H., Ayame, Y., Iwanami, Y., Kimura, N., and Matsumoto, Y. (2021b). Observation of grease fluidity in a ball bearing using neutron imaging technology (Part 2) -*in situ* observation of bearing with rotation-. *Proc. Tribol. Conf. 2021 Autumn Matsue*, D28. (in Japanese).

Spikes, H. (2014). Basics of EHL for practical application. *Lubr. Sci.* 27 (1), 45–67. doi:10.1002/ls.1271

Tohyama, M., Ohmiya, Y., Hirose, M., Matsuyama, H., Toda, T., Hasegawa, K., et al. (2023). Measurement of oil-film thickness and observation of oil-distribution in high-speed deep groove ball bearing. *J. Jpn. Soc. Tribol.* 68 (8), 577–585. (in Japanese). doi:10.18914/tribologist.22-00028

Tomota, T., Tohyama, M., and Yagi, K. (2022). Elucidation of contact state on various rough surfaces via highly robust colorimetric optical interferometry. *Sci. Rep.* 12 (178), 178. doi:10.1038/s41598-021-04104-y

Wan Ibrahim, M. K., Gasni, D., and Dwyer-Joyce, R. S. (2012). Profiling a ball bearing oil film with ultrasonic reflection. *Tribol. Trans.* 55 (4), 409–421. doi:10.1080/10402004.2012.664836

Wedeven, L. D., Evans, D., and Cameron, A. (1971). Optical analysis of ball bearing starvation. *J. Lubr. Tech.* 93 (3), 349–361. doi:10.1115/1.3451591

Wu, W., Hu, C., Jibin Hu, J., and Yuan, S. (2016). Jet cooling for rolling bearings: flow visualization and temperature distribution. *Appl. Therm. Eng.* 105, 217–224. doi:10.1016/j.applthermaleng.2016.05.147

Yokota, K. (2020). Technological trends and outlook of automotive bearing. *JTEKT Eng. J.* 1017E, 25–35. Available at: https://www.jtekt.co.jp/e/engineering-journal/assets/1017/1017e_05.pdf (Accessed March 29, 2024).

Zhang, X., and Glovnea, R. (2020). Grease film thickness measurement in rolling bearing contacts. *Proc. Institution Mech. Eng. Part J J. Eng. Tribol.* 235 (7), 1430–1439. doi:10.1177/1350650120961278

Zhang, Z. C., Song, Q., and Bilal, A. (2019). Innovative design of the cooling topologies for electric vehicle motors. *IOP Conf. Ser. Mater. Sci. Eng.* 533, 012021. doi:10.1088/1757-899X/533/1/012021

frontiers | Frontiers in Mechanical Engineering

TYPE Review
PUBLISHED 26 June 2024
DOI 10.3389/fmech.2024.1408273

Check for updates

OPEN ACCESS

EDITED BY
Taisuke Maruyama,
NSK Ltd., Japan

REVIEWED BY
Milan Bukvic,
University of Kragujevac, Serbia
Toshiaki Iwai,
Idemitsu Kosan, Japan
Takefumi Otsu,
Oita University, Japan

*CORRESPONDENCE
Kazumi Sakai,
sakai.kazumi@eneos.com

RECEIVED 28 March 2024
ACCEPTED 03 June 2024
PUBLISHED 26 June 2024

CITATION
Sakai K (2024), Visualization techniques of grease fluidity.
*Front. Mech. Eng* 10:1408273.
doi: 10.3389/fmech.2024.1408273

COPYRIGHT
© 2024 Sakai. This is an open-access article distributed under the terms of the Creative Commons Attribution License (CC BY). The use, distribution or reproduction in other forums is permitted, provided the original author(s) and the copyright owner(s) are credited and that the original publication in this journal is cited, in accordance with accepted academic practice. No use, distribution or reproduction is permitted which does not comply with these terms.

# Visualization techniques of grease fluidity

Kazumi Sakai*

Grease R&D Group, Lubricants R&D Department, Lubricants Company, ENEOS Corporation, Yokohama, Japan

Energy-saving technology has become increasingly significant as one of the carbon-neutral options for suppressing recent global warming. Grease-lubricated bearings have been used in various automotive and industrial machinery, requiring low torque and long service life for energy-saving performance, which is greatly influenced by grease fluidity. A numerical approach for understanding grease fluidity is very complex since grease is a non-Newtonian fluid with thixotropic properties. Visualization technique is one of the helpful methods to understand the complex grease fluidity and apply it to practical use. This paper describes state-of-the-art visualization techniques, such as fluorescence method, particle imaging velocimetry, infrared spectroscopy, X-rays, and neutron beams.

KEYWORDS

**grease, imaging, bearing, channeling, churning, neutron, particle imaging velocimetry, fluorescence**

## 1 Introduction

The influence of global warming has been serious recently, therefore the environmental preservation programs such as carbon neutrality have been accelerated. The requirements for energy-saving of automotives and industrial machineries have been significant. Among them, rolling element bearings have been used various machineries and required for improvements such as lowering torque and longer service life. Greases are mainly used for lubrication of the bearings and the reduction of energy loss (or torque) caused by grease resistance through bearing rotations could contribute to energy-saving of various machineries. Furthermore, the fluidity of grease affects the service life of bearings, and these factors have been investigated (Vencl et al., 2017; Vasic et al., 2020). Additionally, nanosized additives have been studied to improve bearing lubrication (Abouelkasem et al., 2024; Bukvic et al., 2024).

Nitta et al. (2016) stated that the causes of energy loss in rolling element bearings can be roughly divided into the stirring resistance of lubricants, the viscous rolling resistance, the friction resistance between balls and races, and the friction resistance between balls and cages. It is stated that the stirring resistance is a main factor and largely influenced by grease fluidity in bearings. The grease fluidity can be illustrated by channeling and churning states (Lugt, 2009). In the churning state, a grease is sheared by moving parts such as balls and causes high bearing torque due to drag losses (Hutton, 1975; Lugt, 2016). This continuous grease shearing raises temperature of the bearing. In contrast, in the channeling state, most of grease is pushed away from the running track. The drag losses from grease shearing decrease due to this grease clearing. As a result, the bearing torque reaches steady low values. In the initial phase of a bearing operation, the grease lubricates in the churning state, and a quick transition to the channeling state is promising for developing an energy-saving grease.

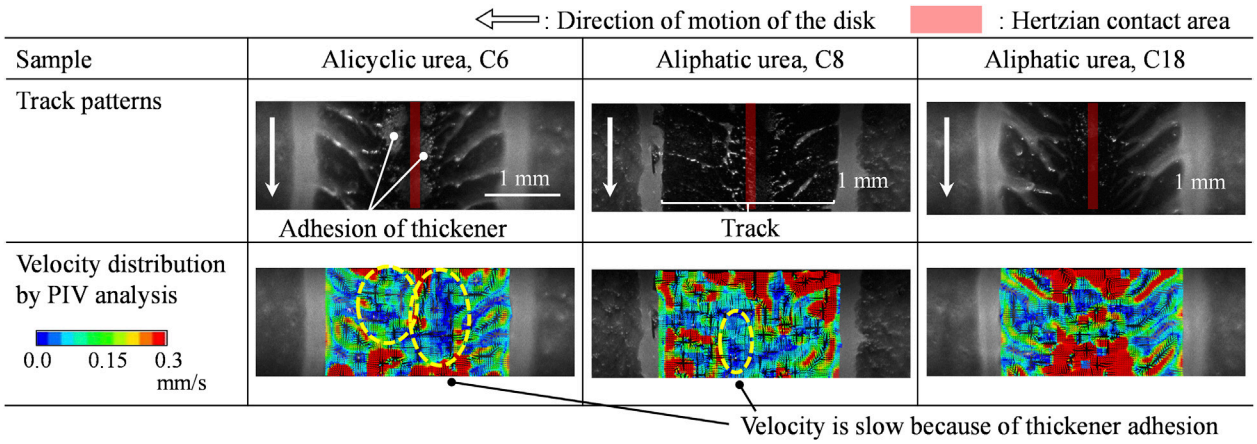


FIGURE 1
Track patterns and velocity distribution by PIV analyses of each type of urea greases (Iki et al., 2022).

For understanding the grease fluidity, it is ideal to visualize grease, especially inside bearings. Papers dealing with the visualization of grease fluidity are limited although those concerning the observation of lubricating oil are more common. This article deals state-of-the-art visualization techniques of grease fluidity, such as fluorescence method, particle imaging velocimetry, infrared spectroscopy, X-rays, and neutron beams. The author hopes that these techniques will enhance the understanding of complex grease behaviors and expedite the development of high-performance greases.

## 2 Fluorescence method

The techniques using fluorescence for the observation of grease fluidity can be roughly divided two types. One is a method using fluorescence particles, and the other is a method using fluorescence dyes dissolved in greases. The former technique is sometimes called PIV (Particle Image Velocimetry). PIV is a fluid visualization technique that involves dispersing tracer particles into a fluid and measuring velocity vectors by capturing the visualized flows. For instance, after dispersing particles that emit fluorescence when irradiated with light of a specific wavelength (fluorescence agent) into an observation target grease, the grease is flowed with irradiation of light containing that specific wavelength and the movement of the generated fluorescence is captured with a high-speed camera. Rhodamine B whose particle size is several to tens of microns can be used as a fluorescent agent Li et al. (2012). Maccioni et al. (2022) and Haruyama et al. (2016) visualized the fluidity of grease in bearings by using bearings with transparent outer rings. Iki et al. (2022), using a ball-on-disk test rig, compared the branch-like patterns (or track patterns) and the flow velocity of greases observed around the running track on the disk as shown in Figure 1, and discussed the correlation between the grease fluidity and the bearing torque behaviors. This method has uncovered the tendencies of thickeners in grease flow; however, the observations were confined to areas outside of the contact point. In other words, it allowed for the observation of grease flows after they had passed the contact point, suggesting that the behaviors within the actual contact area might differ. Instead of PIV using fluorescent particles, Obata and Itoigawa (2022) reported a visualization technique using dye aggregates. They filled greases containing the dye aggregates into bearings and utilized the splitting and coloration of the aggregates caused by the shear generated during bearing rotations to visualize the grease fluidity such as churning and channeling states. This method enabled the visualization of grease shearing within bearings; however, the observation was limited to a side view of the bearing. Consequently, obtaining information about the contact areas still presents some hurdles.

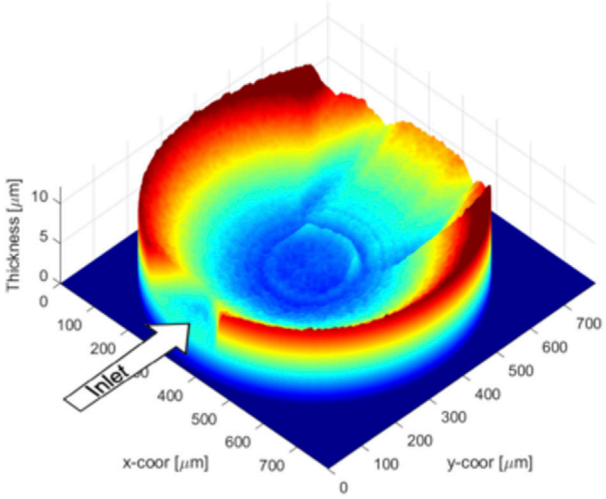


FIGURE 2
Film thickness evaluation (Kostal et al., 2020).

When using fluorescent particles as described above techniques, the particle size is in the micron range, so the techniques visualize the grease fluidity in macro-scale, including relatively thicker films. In contrast, there are also fluorescent dyes that dissolve homogeneously in base oils due to their molecular structures. If

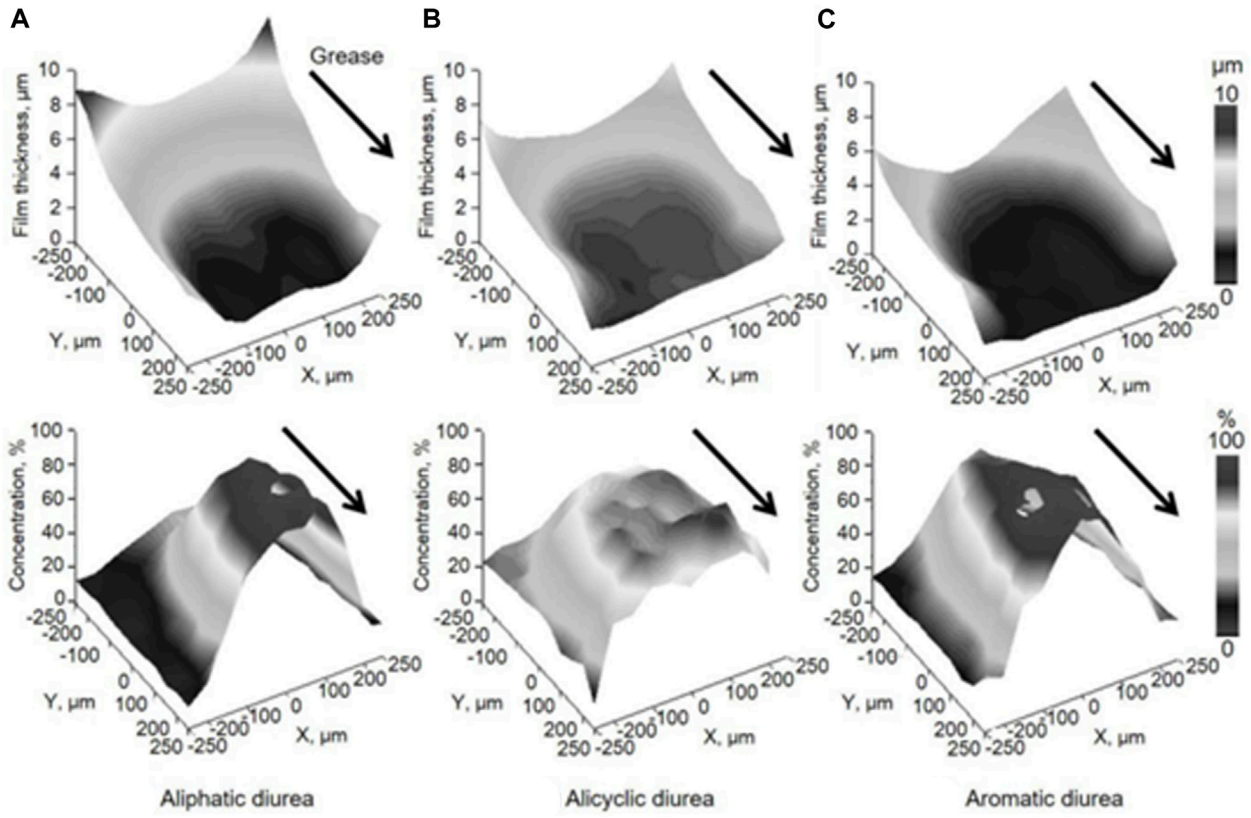


FIGURE 3
3D images of film thickness and thickener concentration (Hoshi et al., 2020).

sufficient fluorescence intensity is obtained, there is a possibility of visualizing the grease fluidity in micro-scale, thinner film in the vicinity of the contact area. The technique using fluorescent dyes for visualization is known as fluorescent staining and is used for observation of cells *in vivo*. Therefore, the fluorescent dyes are often expensive and/or water-soluble. Relatively inexpensive oil-soluble fluorescent dyes that can be applied to lubricants are limited, for instance, pyrene and coumarin-6. The former has a low polarity, while the latter has a high polarity, so it is considered to have a high affinity with low-polarity base oils and high-polarity thickeners, respectively. Since pyrene and coumarin-6 have different fluorescent wavelengths, it could be possible to distinguish the fluidity of base oil and thickeners by blending both fluorescent dyes into the grease. Sakai et al. (2016) observed the grease fluidity using pyrene near the contact area in a ball-on-disk test and discussed the correlation with bearing torque. Kostal et al. (2020) quantified the fluorescence intensity and oil film thickness as shown in Figure 2, and visualized the fluidity of grease near the contact area with relatively thick oil film, although it is difficult to quantify the oil film thickness of the contact area due to the low fluorescence intensity. Suzuki et al. (2020) used coumarin-6 and visualized phenomena of the adhesion and delamination of thickeners to the contact areas in a pin-on-disk test. Yamamoto et al. (2020) visualized the grease fluidity near the EHL (Elastohydrodynamic Lubrication) region using pyrene and coumarin-6. The separation of the base oil and thickeners in the grease during rotations and the backflow of the grease in the front of the contact area were observed. Azetsu (2021) applied the photochromism to the visualization of the movement of oil film on the piston lands of an optical engine. That technique utilizes a photochromic dye dissolved in oil. An arbitrary spot of oil is illuminated with ultraviolet light at an arbitrary timing, which makes a marker in the oil film via a photochromic reaction. This technique has a possibility of the application to visualization of grease fluidity.

## 3 Infrared spectroscopy

In the observations using pyrene and coumarin-6 mentioned in the previous section, these observations were focused on the contact area, which is similar to *in-situ* observation in EHL. There are reports on observation techniques for EHL using FT-IR (Fourier Transform Infrared Spectroscopy) microscopy. In addition to measuring the oil film thickness from the absorbance, information on the chemical structure of the lubricant film present near the contact area can be obtained, allowing for the observation of the concentration ratio of the base oil and thickener. Hoshi et al. (2019); Hoshi et al. (2020) used a ball-on-disk test machine with FT-IR microscopy and confirmed that film thickness of urea grease increased in low-speed ranges and that the thickener is concentrated on the contact area as shown in Figure 3, and discussed the relationship with frictional properties. Mapping with FT-IR microscopy requires a relatively longer duration, for example, 45 s for a line scan, making it challenging to capture grease

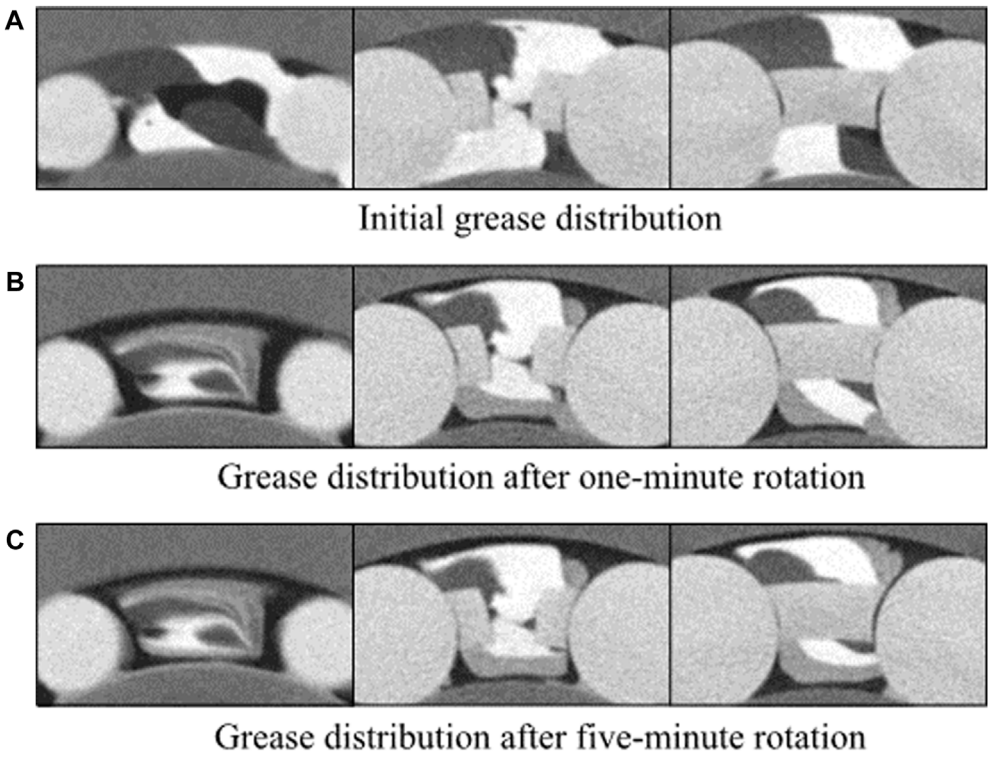


FIGURE 4
Grease internal flow observed from clipped CT images at three different times (Noda et al., 2020).

movement in the vicinity of the contact area within a shorter time span, as is possible with conventional *in-situ* observations in EHL using optical interferometry.

## 4 X-ray CT

Techniques that use X-rays to visualize the inside of the body, such as X-ray photography for medical purposes, barium tests, and CT (Computed Tomography) scans, are generally well-known, but this technology is also used for visualization of grease. Noda et al. (2020) visualized the differences in the fluidity of urea type and barium soap type greases with different X-ray absorption rates using bearings composed of special fluororesin inner and outer rings and special glass balls to pass X-rays through for visualizing the grease fluidity inside the bearing as shown in Figure 4. Additionally, Noda et al. (2022) used USAXS (Ultra-Small-Angle X-ray Scattering) at the large-scale synchrotron radiation facility SPring-8 to observe changes in the scattering pattern that occur when a Barium soap grease is subjected to shear using a rheometer. It is said that structural changes such as the orientation, destruction, and aggregation of thickeners due to shear can be visualized. 3D X-ray micro-CT observations have also been used to identify grease immobilized into geopolymer mortar paste (Campos et al., 2022).

X-rays have a stronger interaction with heavier elements. Therefore, when visualizing the fluidity of grease inside a bearing using X-rays, it is necessary to use special bearings that allow X-rays to pass through, as described above. To increase the sensitivity of the grease, it is also necessary to use barium thickened grease instead of lithium thickened grease, which is commonly used as a grease.

## 5 Neutron imaging

The characteristics of neutrons compared to X-rays are as follows. Neutrons have a strong interaction with light elements such as hydrogen, but a weak interaction with heavy elements such as iron. Therefore, neutrons are potentially effective for visualizing grease, since neutrons can penetrate the inner and outer rings of rolling elements bearings composed mainly of iron and are absorbed by grease composed mainly of light elements. In addition, due to the lower energy of neutrons compared to X-rays, it is expected to cause less damage to samples such as grease. Based on these characteristics, neutrons can be a ground-breaking technique of visualizing grease inside normal bearings, and Ito and Nose (2013) reported visualization of grease inside a bearing using neutrons.

Sakai et al. (2021a) used RADEN, a neutron beamline at the Materials and Life Science Experimental Facility (MLF) of J-PARC (Japan Proton Accelerator Research Complex), to visualize the distribution of grease inside a bearing. The lithium (Li)-based greases were selected for evaluation, Li complex type (Grease A) and single Li soap type (Grease B). Prior to the neutron imaging of the bearing filled with grease, a torque test was performed, and it was confirmed that Grease A provided lower torque. Based on this result, it was speculated that Grease A lubricated in a channeling state, while Grease B lubricated in a churning state. To understand the

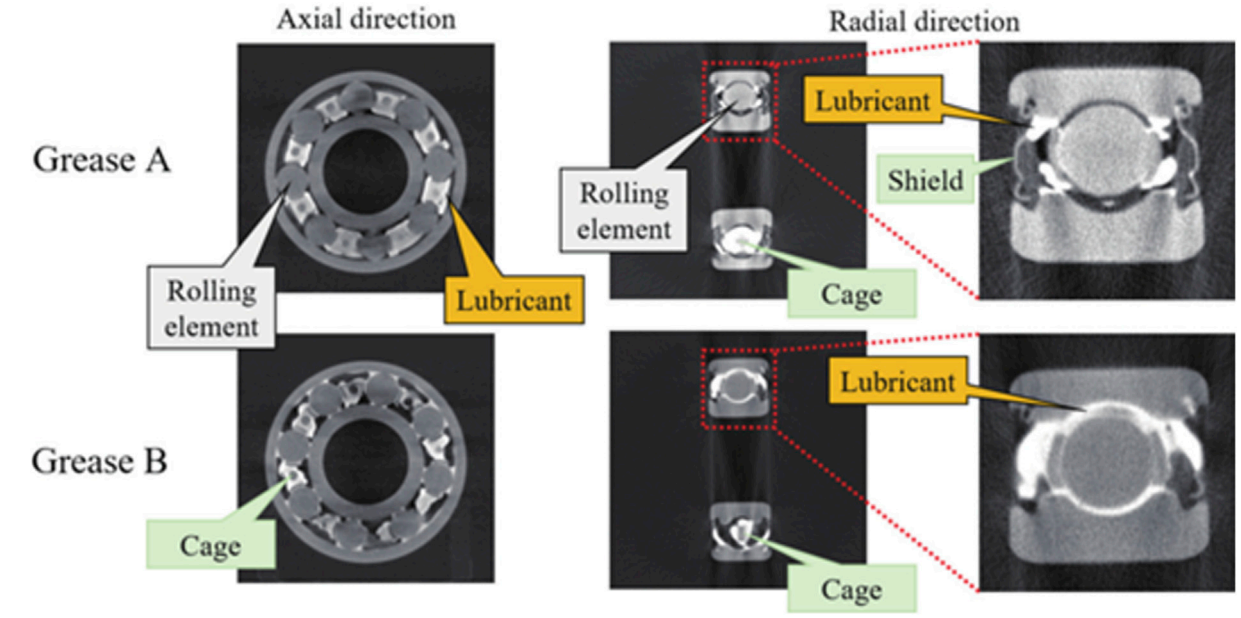


FIGURE 5
Neutron computed tomography of bearings under grease lubrication after rotation (60 min) (Sakai et al., 2021a).

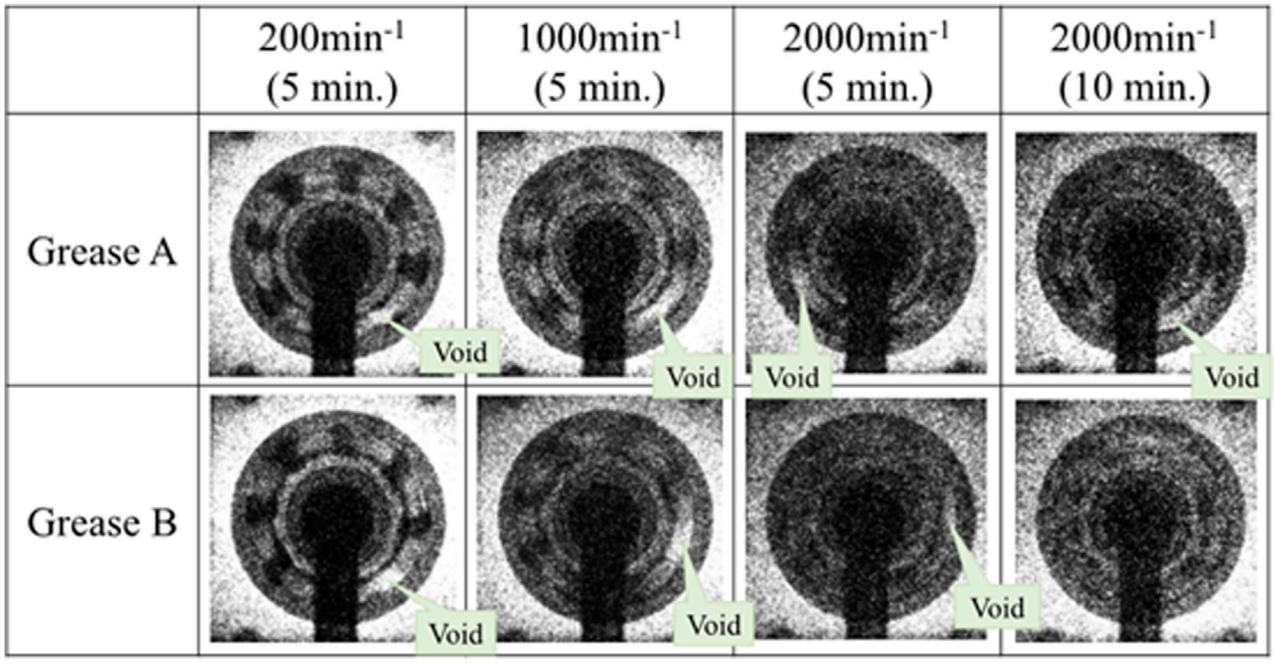


FIGURE 6
*In situ* observation of bearings with rotations using neutron radiography for each rotation speed (Sakai et al., 2021b).

fluidity of the grease in detail, neutron CT imaging was conducted after rotation of the bearing. The axial and radial neutron tomography images of the bearing are shown in Figure 5. The black area indicates a metallic part with low neutron absorption, while the white area indicates the presence of grease or oil with high neutron absorption. Grease A was mainly present on the cage areas, while there was less grease on the cage areas for Grease B. In addition, Grease A showed very little adhesion to the rolling elements, and a gap was confirmed between the inner and outer rings, which corresponds to the channeling state. On the other hand, Grease B showed a lot of adhesion to the rolling elements, which corresponds to the churning state.

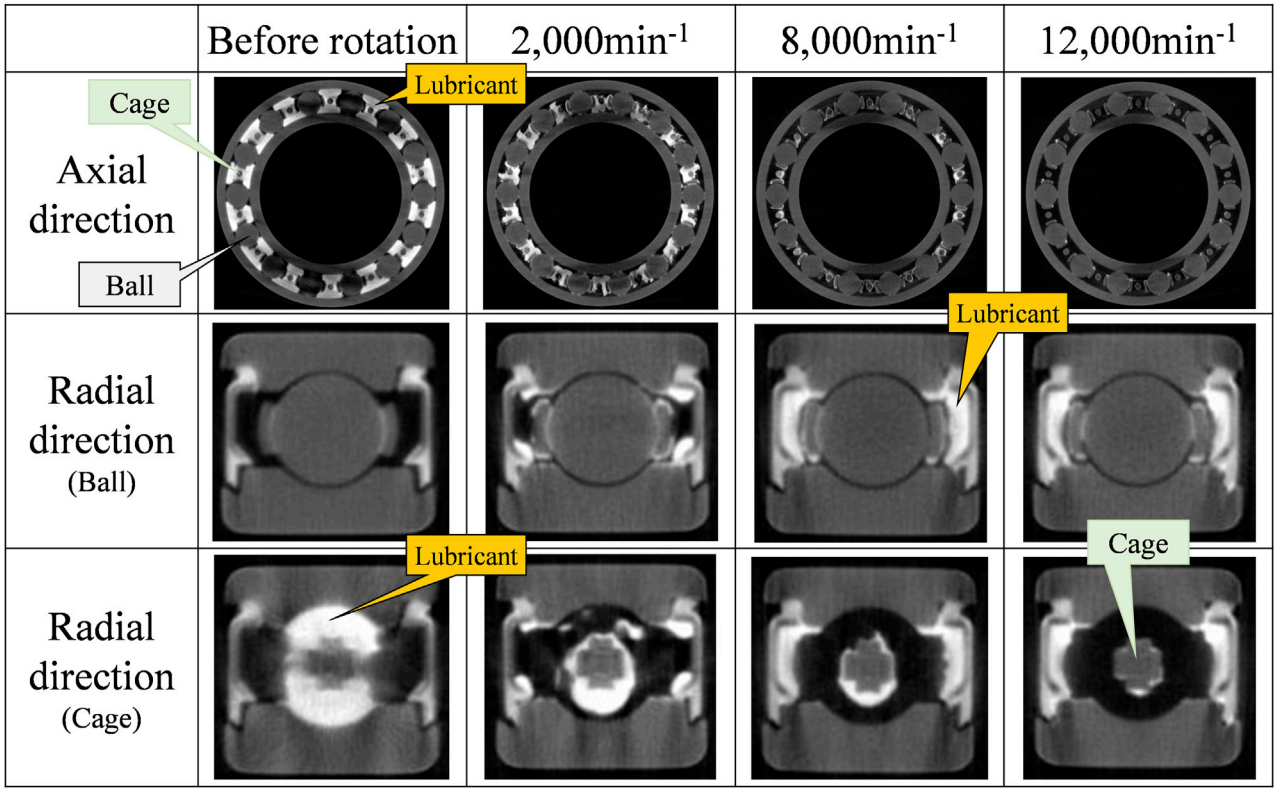


FIGURE 7
Neutron tomography of bearings before/after rotations (Sakai et al., 2022).

Although it was observed that Grease B flew throughout the bearing, it is unclear at which rotational speed and duration it started to flow. To understand this, radiography was conducted on the bearing with rotation at each rotation speed (Sakai et al., 2021b). It should be noted that CT observation is not possible with the rotational condition. The neutron radiography images after 5 or 10 min of rotations at each rotation speed are shown in Figure 6. Unlike the previous images, white areas indicate metallic parts with low neutron absorption, while black areas indicate grease or oil with high neutron absorption. In addition, by leaving one of the eight locations in the cages areas unfilled with grease to create a void (white area), it is easier to understand the fluidity of the grease and the rotation of the bearing. For both Grease A and B, the voids remained and greases mainly stayed on the cage areas at 200 and 1,000 $min^{-1}$. On the other hand, at 2,000 $min^{-1}$, Grease A maintained the same state as at lower rotation speeds, while in Grease B, the grease spread throughout the entire bearing, and the contrast between the grease and the metallic parts gradually decreased as the void disappeared. After 10 min of rotation, it became difficult to distinguish the void. With pulsed neutrons obtained at J-PARC, it is difficult to obtain clear images due to insufficient irradiation frequency and exposure time relative to the rotation speed of the bearing. However, it is speculated that observation of the fluidity of grease at the macro-scale is possible. Increasing the irradiation frequency of the neutron beam is expected to enable observation at high speeds, and one method to achieve this is to use the facilities at the Japan Research Reactor (JRR-3).

Recently, with the electrification of automobiles, the high-speed rotation of bearings used for small and high-output electric motors is required. In order to obtain knowledge of how the grease distribution changes at higher speeds, CT observation was conducted on a 6010 bearing filled with Grease A after rotating it up to 12,000 $min^{-1}$ (Sakai et al., 2022). The results are shown in Figure 7. The black area indicates a metallic part with low neutron absorption, while the white area indicates the presence of grease or oil with high neutron absorption. With increasing rotation speed, the movement of grease from cage areas to the shield was confirmed. As above mentioned, it was also confirmed that there was little adhesion of grease to the rolling elements. Considering the torque and temperature measured separately during bearing rotation, it is speculated that with the increase in rotation speed of the bearing, the torque first decreases and then the bearing temperature also decreases due to the movement of grease from the cage areas to the shield. It was expected that the adhesion of grease to the rolling elements would have a significant impact on the torque, but it is suggested that the grease present on the cage areas can also be a torque factor at high speeds. Furthermore, visualization suggests that the degree of grease exclusion from the rolling elements and cage areas is significant at high speeds, and there is a high possibility of reaching starvation lubrication.

## 6 Conclusion

This article reviewed recent visualization techniques for grease, including the use of fluorescence, IR, X-rays, and neutrons as summarized in Table 1. Each technique covers the visualization of

TABLE 1 Summary of visualization techniques of grease fluidity.

| Basic method | Mechanical configuration | Major findings | Drawbacks | References |
|---|---|---|---|---|
| Fluorescence particles, PIV | Ball on disk | Thickener dependence of grease flow tendency around raceway | Outside of contact area | Iki et al. (2022) |
| Fluorescence particles | Bearing | Grease shearing in bearing | Limited to side view of the bearing | Obata and Itoigawa (2022) |
| Fluorescence dye | Ball on disk | Grease distribution around contact including thickener adhesion and delamination | Weak intensity, limited to outside of contact area | Kostal et al. (2020), Sakai et al. (2016) |
| FT-IR (EHL) | Ball on disk | Urea thickener condensation on the contact area | Longer duration for measurement | Hoshi et al. (2019), Hoshi et al. (2020) |
| X-ray CT | Bearing with plastic | Transition from churning to channeling in bearing | Special materials required for bearing and grease | Noda et al. (2020) |
| Neutron imaging | Conventional bearing | Distribution difference between churning and channeling<br>Distribution change in bearing at high speeds | Limited to bulk grease movement | Sakai et al. (2021a), Sakai et al. (2021b), Sakai et al. (2022) |

limited areas, therefore it is difficult to fully understand the complex flow of grease with only one observation technique. For example, X-ray CT and neutron imaging are effective for understanding bulk grease distribution within machine elements such as bearings. Fluorescence methods can visualize grease flows in the vicinity of the contact areas. Additionally, FT-IR is beneficial for observing EHL to identify the chemical composition of grease around the contact point. Considering the main application of grease for bearings, it is expected that efforts will be made to combine visualization techniques and complementary evaluation methods, and to provide feedback to practical applications. The author hopes that the techniques will contribute not only to the development of grease products but also to achieving carbon neutrality.

## Author contributions

KS: Writing–review and editing, Writing–original draft, Visualization.

## Funding

The author(s) declare that no financial support was received for the research, authorship, and/or publication of this article.

## Conflict of interest

Author KS is employed by ENEOS Corporation.

## Publisher's note

All claims expressed in this article are solely those of the authors and do not necessarily represent those of their affiliated organizations, or those of the publisher, the editors and the reviewers. Any product that may be evaluated in this article, or claim that may be made by its manufacturer, is not guaranteed or endorsed by the publisher.

## References

Abouelkasem, Z. A., Nassef, G. A., Abdelnaeem, M., and Nassef, M. G. A. (2024). Enhancing the elastohydrodynamic lubrication and vibration behavior of rolling bearings using a hybrid bio-grease blended with activated carbon nanoparticles. *Tribol. Lett.* 72, 46. doi:10.1007/s11249-024-01847-3

Azetsu, A. (2021). Observation of oil film behavior using photochromic visualization method. *J. Jpn. Soc. Tribol.* 66 (11), 803. (in Japanese). doi:10.18914/tribologist.66.11_803

Bukvic, M., Gajevic, S., Skulic, A., Savic, S., Asonja, A., and Stojanovic, B. (2024). Tribological application of nanocomposite additives in industrial oils. *Lubricants* 12 (1), 6. doi:10.3390/lubricants12010006

Campos, M. D., Reeb, C., Davy, C. A., Hosdez, J., and Lambertin, D. (2022). Solidification/stabilization (S/S) of high viscosity organics in geopolymers. *J. Nucl. Mater.* 571, 153979. doi:10.1016/j.jnucmat.2022.153979

Haruyama, H., Sawada, N., and Nanri, K. (2016). Visualization of grease flow using fluorescent particle -1st: grease flow of bearing race way. *Proc. JAST Tribol. Conf. Niigata*, B34. (in Japanese).

Hoshi, Y., Takiwatari, K., Nanao, H., and Mori, S. (2020). *In situ* observation of transient responses in grease lubrication by micro infrared spectroscopy. *Tribol. Online* 15 (4), 201–208. doi:10.2474/trol.15.201

Hoshi, Y., Takiwatari, K., Nanao, H., Yashiro, H., and Mori, S. (2019). *In situ* observation of EHL films of greases by micro infrared spectroscopy. *Tribol. Online* 14 (2), 53–59. doi:10.2474/trol.14.53

Hutton, J. F. (1975). The influence of flow elasticity on the bearing performance of lubricating grease. *Proc. JSLE-ASLE Int. Lubr. Conf.*, 707.

Iki, H., Sakai, K., Hoshino, K., Sato, R., Nishizawa, K., Miwa, R., et al. (2022). Observation of grease fluidity on raceway by particle image velocimetry. *J. Jpn. Soc. Tribol.* 67 (10), 727. (in Japanese). doi:10.18914/tribologist.22-00007

Ito, A., and Nose, H. (2013). Visualization of grease 3D distribution in rolling bearing by neutron radiography. *Proc. JAST Tribol. Conf. Fukuoka*, B19. (in Japanese).

Kostal, D., Onitsuka, S., Tanaka, H., Sugimura, J., Krupka, I., and Hartl, M. (2020). Use of pyrene for quantitative fluorescence observation of Li-grease around EHL contacts. *Tribol. Online* 15 (3), 117–125. doi:10.2474/trol.15.117

Li, J. X., Hoglund, E., Westerberg, L. G., Green, T. M., Lundstrom, T. S., Lugt, P. M., et al. (2012). μPIV measurement of grease velocity profiles in channels with two different types of flow restrictions. *Tribol. Int.* 54, 94–99. doi:10.1016/j.triboint.2012.03.007

Lugt, P. M. (2009). A review on grease lubrication in rolling bearings. *Tribol. Trans.* 52 (4), 470–480. doi:10.1080/10402000802687940

Lugt, P. M. (2016). Modern advancements in lubricating grease technology. *Tribol. Int.* 97, 467–477. doi:10.1016/j.triboint.2016.01.045

Maccioni, L., Chernoray, V. G., Bohnert, C., and Concli, F. (2022). Particle image velocimetry measurements inside a tapered roller bearing with an outer ring made of

sapphire: design and operation of an innovative test rig. *Tribol. Int.* 165, 107313. doi:10.1016/j.triboint.2021.107313

Nitta, M., Tsuda, T., Arai, H., Sakamoto, K., and Sakai, K. (2016). Effects of transition point of viscoelasticity of diurea grease and molecular structure of thickener on running torque of the ball bearing -effects of alkyl chain length of aliphatic diurea-. *J. Jpn. Soc. Tribol.* 61, 699. (in Japanese). doi:10.18914/tribologist.61.10_699

Noda, T., Shibasaki, K., Miyata, S., and Taniguchi, M. (2020). X-ray CT imaging of grease behavior in ball bearing and numerical validation of multi-phase flows simulation. *Tribol. Online* 15 (1), 36–44. doi:10.2474/trol.15.36

Noda, T., Takayama, Y., Kuwamoto, S., Sonoda, K., and Washizu, H. (2022). Structural changes of thickener and rheological properties of lubricating greases under shear flow. *Proc. JAST Tribol. Conf. Fukui*, B36. (in Japanese).

Obata, T., and Itoigawa, F. (2022). Quantitative observation of grease behavior for rolling bearings using splitting phenomena of colorant. *J. Jpn. Soc. Tribol.* 67 (1), 54. (in Japanese). doi:10.18914/tribologist.21-00012

Sakai, K., Ayame, Y., Iwanami, Y., Kimura, N., and Matsumoto, Y. (2021a). Observation of grease fluidity in a ball bearing using neutron imaging technology. *Tribol. Online* 16 (2), 146–150. doi:10.2474/trol.16.146

Sakai, K., Iki, H., Ayame, Y., Iwanami, Y., Kimura, N., and Matsumoto, Y. (2021b). Observation of grease fluidity in a ball bearing using neutron imaging technology (Part 2) -*in situ* observation of bearing with rotation-. *Proc. JAST Tribol. Conf. Matsue*, D28. (in Japanese).

Sakai, K., Ogata, R., Kimura, N., and Matsumoto, Y. (2022). Observation of grease fluidity in a ball bearing using neutron imaging technology (Part 3) -effect of rotation speed. *Proc. JAST Tribol. Conf. Fukui*, C5. (in Japanese).

Sakai, K., Tokumo, Y., Ayame, Y., Shitara, Y., Tanaka, H., and Sugimura, J. (2016). Effect of formulation of Li greases on their flow and ball bearing torque. *Tribol. Online* 11 (2), 168–173. doi:10.2474/trol.11.168

Suzuki, M., Maruyama, K., Ando, T., Monna, T., Arakawa, K., and Takeichi, Y. (2020). Behavior observation of grease thickener during compressing and initial sliding using fluorescence microscopy. *Proc. JAST Tribol. Conf. Beppu*, F40. (in Japanese).

Vasic, M., Stojanovic, B., and Blagojevic, M. (2020). Failure analysis of idler roller bearings in belt conveyors. *Eng. Fail. Anal.* 117, 104898. doi:10.1016/j.engfailanal.2020.104898

Vencl, A., Gasic, V., and Stojanovic, B. (2017). Fault tree analysis of most common rolling bearing tribological failures. *IOP Conf. Ser. Material Sci. Eng.* 174, 012048. doi:10.1088/1757-899x/174/1/012048

Yamamoto, T., Tanaka, H., and Sugimura, J. (2020). Observation of base oil and thickener of grease with fluorescent agents. *Proc. JAST Tribol. Conf. Beppu*, F43. (in Japanese).

frontiers | Frontiers in Mechanical Engineering

TYPE Original Research
PUBLISHED 09 July 2024
DOI 10.3389/fmech.2024.1422412

Check for updates

OPEN ACCESS

EDITED BY
Qiang Li,
Technical University of Berlin, Germany

REVIEWED BY
Milan Bukvic,
University of Kragujevac, Serbia
Saša Milojević,
University of Kragujevac Faculty of Engineering, Serbia

*CORRESPONDENCE
Hikaru Okubo,
okubo-hikaru-xp@ynu.ac.jp

RECEIVED 24 April 2024
ACCEPTED 14 June 2024
PUBLISHED 09 July 2024

CITATION
Okubo H, Ishikawa T, Hashiba H, Inamochi T and Nakano K (2024), *In-situ* vibrational spectroscopic observation for thermally activated structural changes of 100% cellulose nanofiber molding with ultralow friction. *Front. Mech. Eng* 10:1422412. doi: 10.3389/fmech.2024.1422412

COPYRIGHT
© 2024 Okubo, Ishikawa, Hashiba, Inamochi and Nakano. This is an open-access article distributed under the terms of the Creative Commons Attribution License (CC BY). The use, distribution or reproduction in other forums is permitted, provided the original author(s) and the copyright owner(s) are credited and that the original publication in this journal is cited, in accordance with accepted academic practice. No use, distribution or reproduction is permitted which does not comply with these terms.

# *In-situ* vibrational spectroscopic observation for thermally activated structural changes of 100% cellulose nanofiber molding with ultralow friction

Hikaru Okubo[1]*, Tomori Ishikawa[1], Hiromi Hashiba[2], Toru Inamochi[2] and Ken Nakano[1]

[1]Faculty of Environment and Information Sciences, Yokohama National University, Yokohama, Japan, [2]Chuetsu Pulp & Paper Co Ltd., Takaoka, Japan

This paper reports the thermally activated ultralow friction of 100% cellulose nanofiber (CNF) molding. The mechanism of friction reduction was investigated using a laboratory-built *in-situ* Raman tribometer. Our experimental results showed that a CNF molding exhibited an ultralow friction coefficient of below 0.04 in a CNF ring and steel disk tribopair under high-temperature conditions ($T >$ 100°C). The results of the temperature-rise friction test showed that the friction coefficient of the CNF molding strongly depended on the temperature and decreased linearly with increasing temperature. The *in situ* tribo-Raman monitoring results, during friction, indicated a change in the structure of the CNF molding. Therefore, the crystallinity indices and lengths of the CNF fibers gradually changed as the temperature increased. Moreover, transfer tribofilms were observed on the counter-steel surface against the CNF rings. When the CNF molding exhibited thermally activated ultralow friction, the tribofilm was mainly composed of cellulose and graphitic carbon. Our results suggest that the thermal and friction-activated structural transformations of CNF molding and CNF-derived transfer film formation are pivotal factors contributing to the ultralow friction phenomenon observed in CNF molding at high temperatures.

KEYWORDS

**cellulose nanofibers, CNF, ultralow friction, Raman, *in-situ*, transfer film**

## 1 Introduction

Cellulose nanofibers (CNFs) have recently been studied and developed as next-generation industrial biomass material (Posada et al., 2020). CNF is a biomass material with a fiber-like structure composed of cellulose microfibrils, which are aggregates of cellulose molecules. These molecules are five times stronger than steel and has a low specific density of 1/5. Owing to these excellent properties, CNFs are increasingly used as substitutes for petroleum-derived materials in industries. Especially, CNF offers a wide range of applications in many fields, including sensor technology, cosmetics, catalysis, energy production, water remediation, near-paper industry, petroleum industry and applications, and medicine (Zhang et al., 2019; Sanad et al., 2023) A novel use of CNF is a "100% CNF molding" (hereafter referred to as "CNF molding"), which is composed entirely of CNF. CNF molding is a biomass molding material

characterized by high strength, light weight, high thermal conductivity, and high processability. It is fabricated by pressurizing and dehydrating CNF dispersion liquids (Chuetsu Pulp and Paper Co, 2021). Although CNF moldings have strengths comparable to those of typical mechanical materials, such as steel and plastics, few studies have been conducted on the application of a CNF molding to fabricate mechanical elements, especially sliding mechanical elements that are expected to be used under severe operating conditions. However, the green transformation of sliding mechanical elements can be accelerated if CNF moldings are used to fabricate them.

A previous study reported the tribological properties of a CNF molding under various sliding conditions (Okubo et al., 2023a; Okubo et al., 2023b). In particular, the authors showed that a CNF molding exhibited a superlow friction coefficient of less than 0.01 when lubricated with a fatty-acid-containing oil, owing to the formation of a specific CNF swollen layer (Okubo et al., 2023b). Hence, controlling the structural transformation of a CNF molding at the frictional interface plays an important role in achieving ultralow friction in the molding. CNF moldings exhibit considerable potential as a ultralow-friction biomass material for various industrial applications. Numerous studies regarding low-friction materials, such as diamond-like carbon (DLC) and other carbon-related materials, have shown that conventional low-friction phenomena are often triggered by "thermal factors" (Enke, 1981; Zeng et al., 2015; Okubo et al., 2017; Zhu et al., 2021). In DLCs, $sp^3$ bonds transition to the more energetically stable $sp^2$ bonds with increasing thermal energy (Enke, 1981). In particular, under high-temperature conditions, DLC films at frictional interfaces undergo rapid structural evolutions owing to the complex interaction of the thermal, mechanical, and chemical effects due to friction. This results in ultralow friction owing to the formation of $sp^2$-rich tribofilms (Enke, 1981; Zeng et al., 2015; Agustin,et al., 2016; Okubo et al., 2017; Zhu et al., 2021). Several researchers have reported the thermal responses of CNFs under static conditions (non-friction) (Rubentheren et al., 2016; Okubo et al., 2019; Yang et al., 2019; Gan et al., 2020; Niskanen et al., 2022), and it is well known that high-temperature conditions cause changes in the crystalline structure of cellulose and in the breakdown of its networked structure. In our previous study, we confirmed that the amortization of a CNF molding was accelerated at tribological contacts under high-temperature conditions (Okubo et al., 2023a). However, the effects of temperature on the tribological properties of CNF molds are unclear.

The time-resolved observation of frictional surfaces is a promising method for understanding the lubrication mechanisms of tribological materials (Okubo and Sasaki, 2017; Okubo et al., 2020a; Okubo et al., 2020b). In our previous studies, we conducted "*in-situ* tribo-Raman spectroscopic measurements," which can be used to monitor the tribochemical reactions at the frictional interfaces during friction processes, to reveal the lubrication mechanisms of tribological materials (Okubo and Sasaki, 2017; Okubo et al., 2020a; Okubo et al., 2020b). The *in situ* tribo-Raman method can be used to effectively reveal the lubrication mechanisms of a material because the time-resolved Raman signals derived from the frictional interface can provide the degree of structural and compositional changes in materials during operation. Therefore, the operando tribo-Raman method has the potential to reveal the lubrication mechanism of CNF moldings.

In this study, the effect of test temperature on the tribological properties of a CNF molding was investigated. Tribological tests were performed using a ring-on-disk tribometer for a CNF ring and steel disk tribo-pairs under dry sliding conditions. To elucidate the effect of temperature on the tribological properties of the CNF molding, temperature rise and fall tests were conducted using a lab-built *in-situ* Raman tribometer (Okubo and Sasaki, 2017; Okubo et al., 2020a; Okubo et al., 2020b) that monitors frictional behavior. Additionally, time-resolved Raman spectra were obtained from the CNF ring under friction. Our results suggest that the thermal and friction-activated structural transformations of CNF molding and CNF-derived transfer film formation are pivotal factors contributing to the ultralow friction phenomenon. Moreover, our results accelerate the social implementation of the CNF molding as 100% biomass tribological materials for the sliding components.

# 2 Materials and methods

## 2.1 Materials

AISI52100 bearing steel (HV750, $S_a$:0.05 μm) was used for the steel disk (20 mm square) specimen. A CNF molding (nanoforest-CMB, JP, density = 1.41 g/cm$^3$, $S_a$ = 0.05–0.1 μm, nanoindentation hardness = 0.37 GPa, XRD crystallinity = 80%, molecular weight *M*w = 133,000) was made from CNF water dispersions, which were prepared via the aqueous counter collision method (nanoforest, Chuetsu Pulp and Paper Co, 2021). The molding was used as a ring specimen ($\varphi$ 20 mm × $t$ 5 mm). The procedure for preparing the CNF molding has been described in previous studies (Okubo et al., 2023a; Okubo et al., 2023b).

## 2.2 Test apparatus and test procedures

A ring-on-disk friction tester equipped with a Raman spectroscope (Raman Touch YNU, Nanophoton Co., JP) was used for the friction tests, as shown in Figure 1A. To investigate the effects of the test temperature on the frictional properties and structure of the CNF molding, two friction tests were conducted: a constant-temperature friction test and a temperature-rise *in-situ* Raman friction test. The constant-temperature friction test was conducted under the following experimental conditions: load = 10 N, temperature: 30°C and 100°C, Hertz maximum contact pressure ≈0.15 GPa, relative humidity = 50–70%, sliding speed = 10 mm/s, and sliding time = 30 min. For the temperature-rise friction test, the friction test and Raman imaging analysis were performed alternately and intermittently at each of the following temperatures: 30, 50, 60, 70, 80, 90, 100, 110, and 120°C, as shown in Figure 1B. The friction test conditions (S1–S9 in Figure 1B) were as follows: load = 10 N, Hertz maximum contact pressure ≈0.15 GPa, relative humidity = 50–70%, sliding speed = 10 mm/s, and sliding time = 60 s at each temperature. Raman imaging (R0–R9 in Figure 1B) was performed on the CNF ring using a laser line scanning system (wavenumber: 532 nm, glid: 600 g/mm, exposure time: 1.0 s, and accumulated time: 1). Each image of

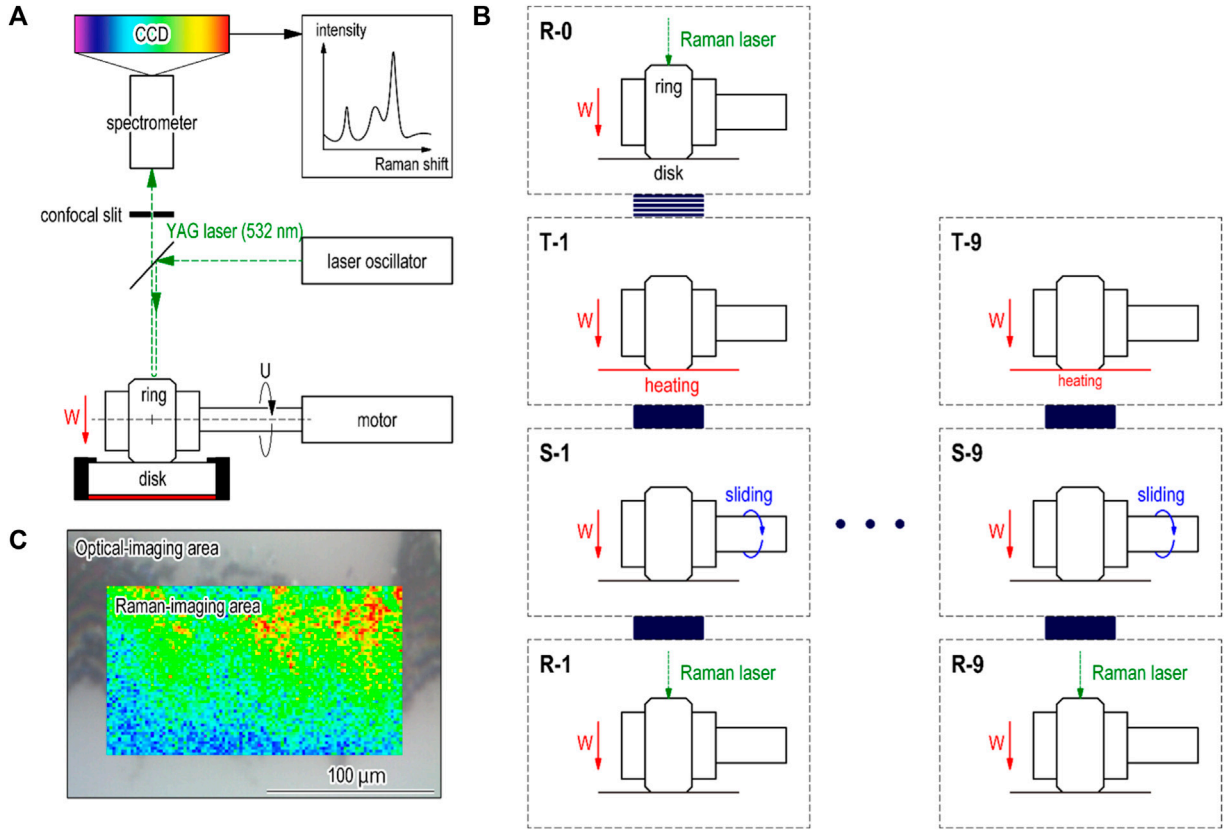


FIGURE 1
**(A)** Schematic of the developed apparatus for *in situ* Raman spectroscopy for observing frictional processes, **(B)** procedure of the temperature-rise friction test, and **(C)** a representative Raman-imaging result.

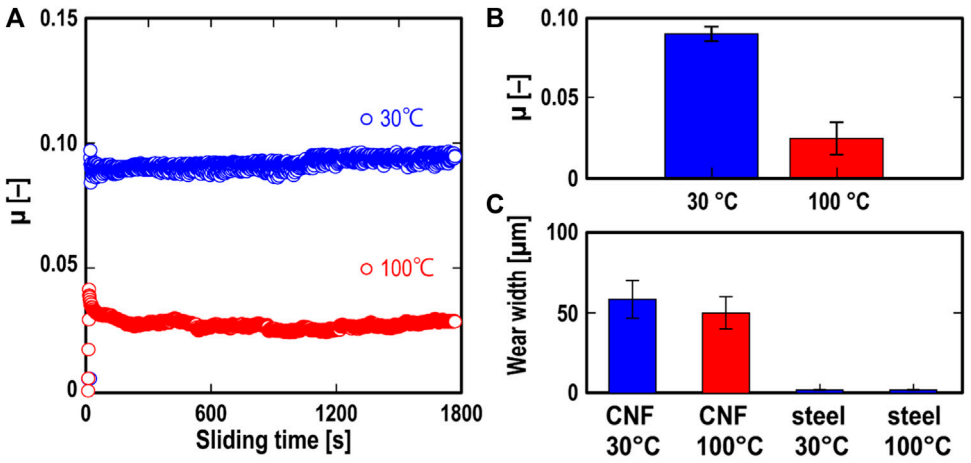


FIGURE 2
**(A)** Frictional behavior of the CNF/steel tribopair at test temperatures of 30°C and 100°C, **(B)** the average friction coefficient over 600 s calculated for each type of frictional behavior shown in Figure 1A, **(C)** the wear width of the CNF molding and steel surface.

the Raman spectrum consists of 5,000–6,000 pixels, with the pixel dimensions of height × width = 1.9 μm × 1.6 μm, as shown in Figure 1C. Atomic force microscopy (AFM) measurements (MultiMode8, Bruker Co., United States) were conducted on the worn steel surfaces to characterize the tribofilm using a pyramidal cantilever (PPP-NCHR AFM Probe, Nanosensor Co., CHE).

In this study, all friction tests and surface analyses were conducted more than three times to confirm the repeatability.

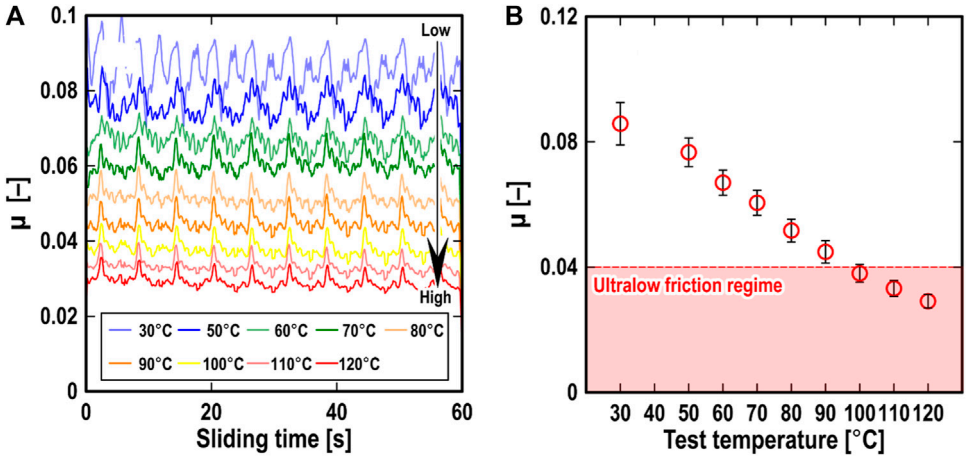


FIGURE 3
**(A)** Frictional behavior of the CNF/steel tribopair at test temperatures of 25°C and 100°C, **(B)** average friction coefficient over 600 s calculated for each type of frictional behavior shown in Figures 1A, C the wear width of the CNF molding and steel surface.

# 3 Results

## 3.1 Constant temperature friction test

Figure 2 shows the friction and wear properties of the CNF ring and steel disk tribopair at the temperatures of 30°C and 100°C. As shown in Figures 2A, B, the frictional properties of the CNF molding considerably differ between the temperatures of 30°C and 100°C. At 30°C, the friction coefficient exhibits an almost stable value of 0.095 during the tests. The friction coefficient is also stable at 100°C but has a value of 0.035 during the test, which is in the ultralow friction regime (below 0.04).

Figure 2C shows the wear widths of the CNF ring and steel disk under each condition. No significant difference is observed between the wear properties of each specimen (CNF ring and steel disk) at the temperatures of 30°C and 100°C, although the frictional performance strongly depended on the temperatures, as mentioned above. In the subsequent sections, we focus only on the friction properties of CNF molding because the wear performance is independent of the test temperature.

## 3.2 Temperature-rise friction test

Figures 3A, B show the frictional behavior and average friction coefficient of the CNF ring and steel disk tribopair, respectively, at each temperature in the temperature-rise friction test (the procedure is shown in Figure 1B). As shown in Figures 3A, B, the friction coefficient of the CNF ring and steel disk tribopair strongly depends on the test temperature, decreasing gradually from 0.09 to 0.025 as the temperature increases from 30°C to 120°C. The results of the temperature-rise friction test show that the frictional performance of CNF molding strongly depends on the test temperature, and thermal effects play a crucial role in achieving ultralow-friction performance of CNF molding.

## 3.3 *In situ* Raman monitoring

Figure 4 shows the representative *in situ* Raman spectra of the as-molded and worn surfaces of the CNF molding at each temperature. As shown in Figure 4A, the shifts in the Raman spectrum from 200 to 1,200 $cm^{-1}$ indicate the presence of CNF-derived peaks. The peaks observed at 380, 430–450, 510, 891, 990, 1,057, and 1,090 $cm^{-1}$ are assigned to CCC, CCO, and CO ring deformations, CCC and CCO ring deformations, COC glycosidic link deformation, vibration of the cellulose lateral unit at the crystal regions, $CH_2$ deformation, $CO_2$ alcohol stretching, and COC glycosidic link deformation, respectively (Li and Renneckar, 2011). Moreover, as shown in Figure 4B, the peaks observed at 2,890 and 3,200 $cm^{-1}$ are assigned to the CH and $CH_2$ stretching vibrations and the OH stretching vibrations of water and cellulose, respectively (Li and Renneckar, 2011; Rossetti et al., 2023). Cellulose is a crystalline polymer, and its higher-order structure consists of a crystalline component with a regular arrangement and an amorphous component with a disordered structure. Raman analysis can be used to evaluate the factors related to the crystalline regions of cellulose using several methods (Agarwal et al., 2010). Following previous studies, the Raman-peak-height intensity ratios $I_{370}/I_{1057}$ and $I_{3200}/I_{2892}$ were used as indices of the crystallinity of the CNF-molded surfaces. Moreover, the peak intensities at 510 $cm^{-1}$ and 890 $cm^{-1}$ correspond to the lengths of the COC glycosidic chains (Li and Renneckar, 2011). Hence, the Raman-peak-height intensity ratios $I_{510}/I_{1057}$ and $I_{891}/I_{1057}$ were used as indices for the length of the COC glycosidic chains on the CNF molding surfaces.

Figure 5 shows the optical images and Raman imaging results of all indices obtained from the worn surface of the CNF molding for each temperature in the temperature-rise friction test. Figure 6 shows the temperature-dependent behavior of the average value of all indices obtained from the intensity ratio of the Raman spectrum for each pixel in the Raman images. As shown in Figure 5, the higher the intensity ratio in the images, the higher the crystallinity or the longer the COC glycosidic chain length in the

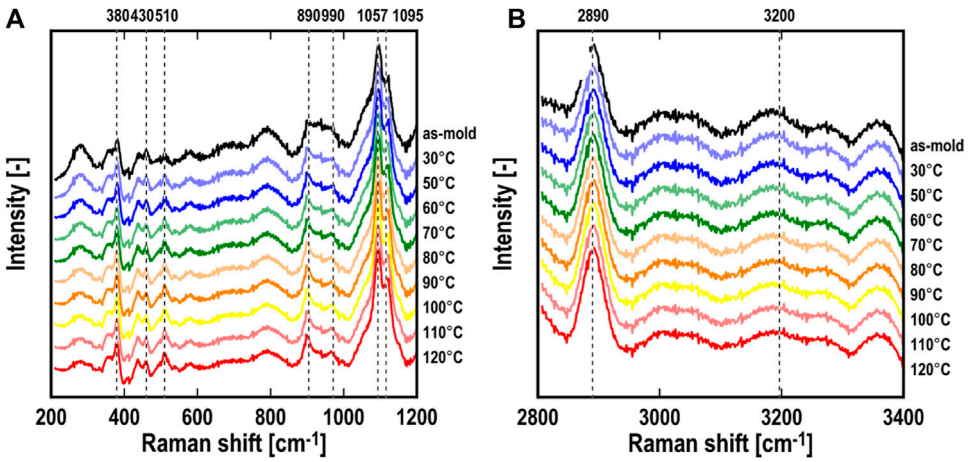


FIGURE 4
**(A)** *In situ* Raman spectra from 200 to 1,200 $cm^{-1}$ for each temperature in the temperature-rise friction test, and **(B)** *in situ* Raman spectra from 2,800 to 3,400 $cm^{-1}$ for each temperature in the temperature-rise friction test.

CNF molding, and *vice versa*. As shown in Figure 5, the values of all the indices in the image uniformly and gradually decrease with increasing test temperature, indicating that the crystallinity and COC glycosidic chain length in the CNF molding gradually decrease with increasing test temperature. Hence, thermally activated structural changes in CNF molding occur at frictional interfaces, and these changes occur easily at relatively high temperatures.

Figure 7 shows the optical images of the worn surfaces of the steel disk after the temperature-rise friction test and the Raman spectrum of the transfer region. As shown in Figure 7A, a transfer film is formed on the steel surface. Figure 7B shows the CNF-derived Raman peaks observed at 1,057 (similarly to the Raman spectra in Figure 4) and 1,430 $cm^{-1}$. These peaks are related to the CH deformation of the CNF (Li and Renneckar, 2011) and indicate that the tribofilm is a transfer film derived from the CNF molding. Two specific peaks, a D peak induced by disorder $sp^2$ carbon and a first-order graphite-induced G peak at 1,352 and 1,580 $cm^{-1}$, respectively, which are assigned to carbon crystals (Zeng et al., 2015; Okubo et al., 2017), are observed, although these peaks were not observed for the CNF molding surfaces. Details of the composition of the transfer film are discussed later.

## 3.4 AFM measurement

In the previous sections, the transfer film formation was observed on the steel surface. Therefore, AFM measurements were performed on the CNF-derived transfer films to evaluate their characteristics. Figure 8 shows the AFM topographical images and distance curves of the out-of-the-transfer and transfer-film regions. As shown in Figures 8A, B, the transfer film has a thickness of approximately 300 nm. Moreover, as shown in Figures 8C, D, the AFM force-distance curve derived from the transfer film region indicates that the approach and retraction curves are separated because of the positive and negative squeeze forces. However, such behavior is not observed outside the tribofilm region. Miklozic and Spikes also observed this phenomenon in tribofilms derived from zinc dialkyl dithiophosphate on steel surfaces. Additionally, from the squeeze behavior in the force-distance curve (Miklozic and Spikes, 2005), the tribofilms on the outermost layer were inferred to exist as a viscous film. According to a previous report, a CNF-derived transfer film exists as a viscous film on a frictional surface.

# 4 Discussion

In this study, the thermally activated ultralow friction phenomena of CNF molding were observed, as shown in Figures 2, 3. The thermally activated structural changes in the CNF molding and transfer-film formation were observed using the *in situ* Raman monitoring method, as shown in Figures 5–7. In this section, the mechanisms of thermally activated ultralow friction in CNF molding are discussed.

As shown in Figures 5, 6, the Raman peak height intensity ratios $I_{370}/I_{1057}$, $I_{510}/I_{1057}$, $I_{890}/I_{1057}$, and $I_{3200}/I_{2892}$ gradually decrease with increasing test temperature, indicating the occurrence of amorphization and a decrease in the length of the COC glycosidic chains of the CNF molding at the frictional interface. These changes proceeded easily at higher temperatures. It is well known that the amortization of CNF, that is, their defibration, is caused by mechanical (Iwamoto et al., 2008; Liu et al., 2020), chemical (Azizi Samir et al., 2005; Bondeson et al., 2006), and thermal processes (Niskanen et al., 2022). Hence, the synergistic mechanical and thermal effects accelerated the amorphization of CNF molding at the frictional interfaces.

By contrast, a thick and viscous CNF-derived transfer film was observed on the steel surface, as shown in Figures 7, 8. For various tribological materials, transfer film formation is a key factor in reducing friction under dry sliding conditions because the transfer film acts as a sacrificial layer to disperse frictional energy at the frictional interface. The friction-reduction mechanisms of DLC coatings under dry sliding conditions have often been explained

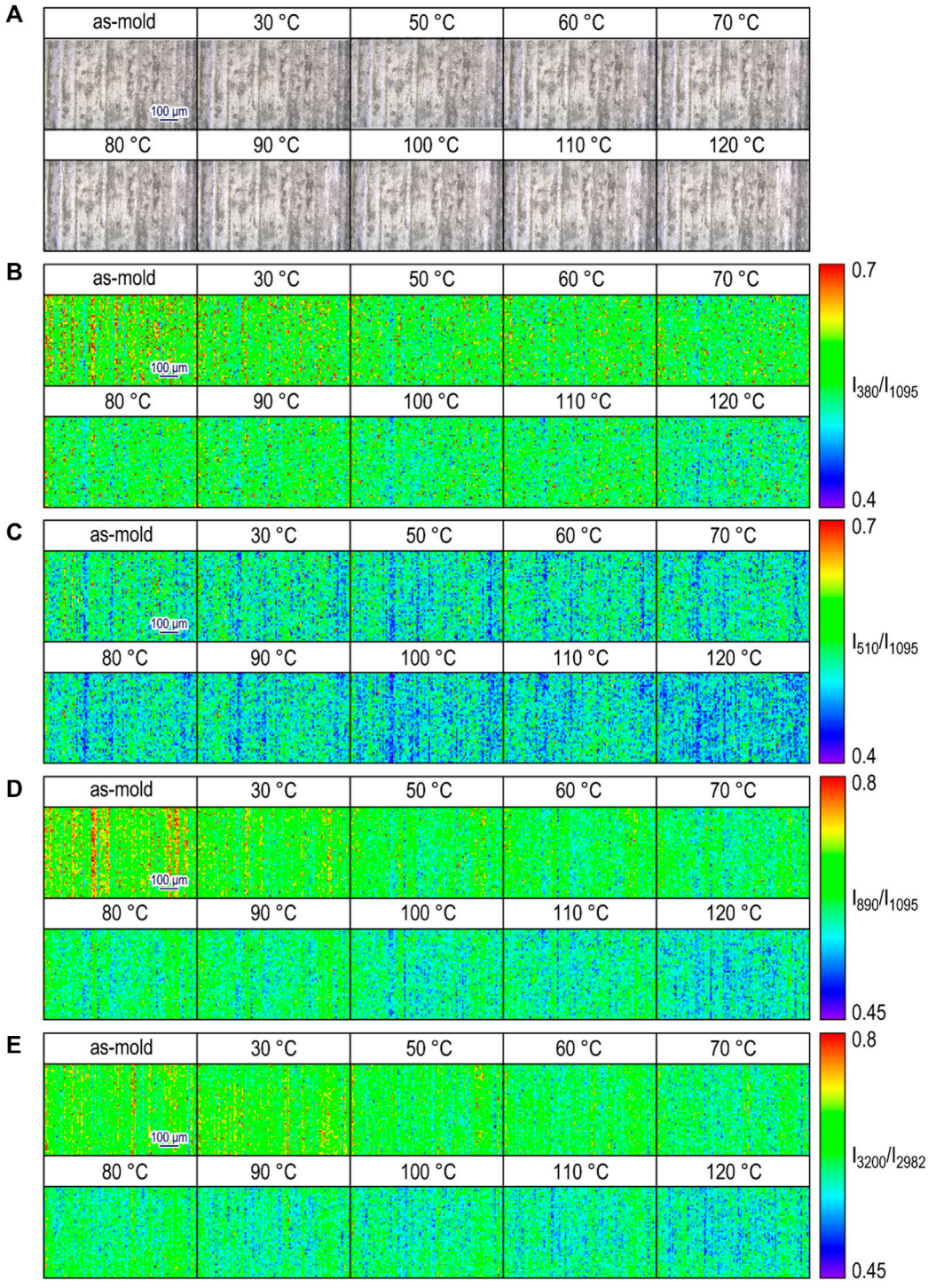


FIGURE 5
**(A)** Optical images of the as-molded and worn surfaces of the CNF molding, and *in situ* Raman-imaging results of **(B)** $I_{380}/I_{1095}$, **(C)** $I_{510}/I_{1095}$, **(D)** $I_{890}/I_{1095}$, and **(E)** $I_{3200}/I_{1095}$ for each temperature in the temperature-rise friction test.

by the formation of a graphitization transfer layer on the counterface material against the DLC coating (Enke, 1981; Memming et al., 1986; Zeng et al., 2015; Okubo et al., 2017; Zhu et al., 2021). Memming et al. (1986) confirmed the formation of a carbon transfer film on the steel side when low friction was observed in the DLC/steel tribo-pair. This low friction was maintained by shifting from sliding between DLC and steel to sliding between DLC and the carbon transfer film. Erdemir et al. confirmed that such a carbon transfer layer was graphitized in the friction state and concluded that the continuous formation of the graphitization-transfer layer resulted in the low-friction behavior of the DLC coating (Erdemir et al., 1995). As shown in Figures 7B, D and G peaks are observed in the Raman

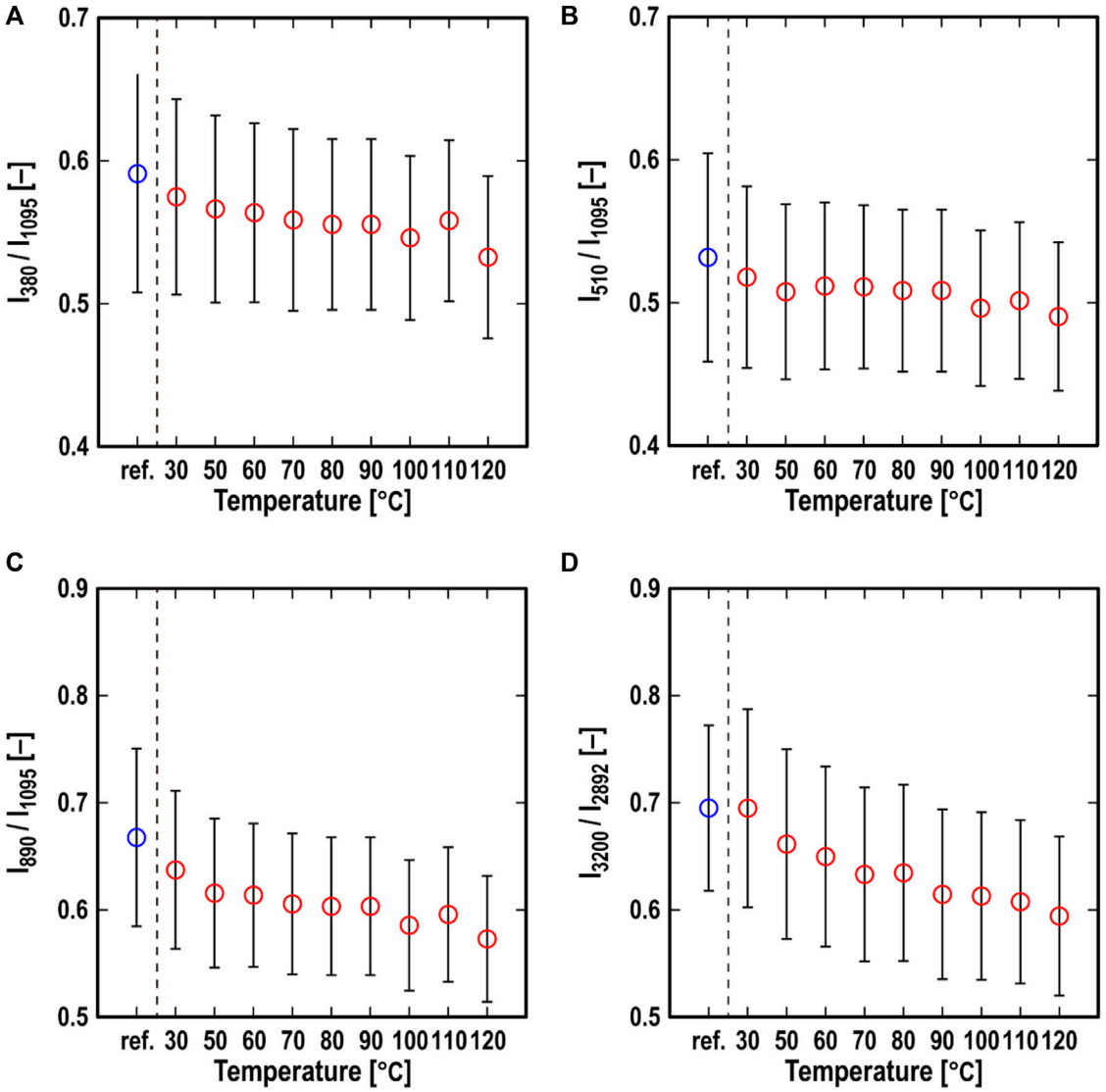


FIGURE 6
Temperature-dependent behavior of the averaged value of all indexes: **(A)** $I_{380}/I_{1095}$, **(B)** $I_{510}/I_{1095}$, **(C)** $I_{890}/I_{1095}$, and **(D)** $I_{3200}/I_{1095}$ (the blue plot is the value for the as-molded surface) in the temperature-rise friction test.

spectra derived from the CNF-derived transfer layer, indicating that the CNF-derived transfer layer is also graphitized during the friction states in a manner similar to that of the DLC coatings (Zeng et al., 2015; Okubo et al., 2017). Figure 9 shows the Raman imaging of the $I_{1352}/I_{1057}$ and $I_{1580}/I_{1057}$ ratios of the relatively low frictional transfer film ($\mu < 0.03$) and high frictional transfer film ($\mu > 0.08$), which are defined by the amount of the $sp^2$ carbon in the CNF-derived transfer film. The low and high frictional transfer films were obtained after the friction test at a test temperature of 120°C and 30°C, respectively. As shown in Figures 9A, B, the two transfer films exhibit different values for both the ratios, although the formation of the transfer film is observed in both the low- and high-friction cases. Both ratios of the low-friction transfer film are higher in a large part of the film than those of the high-friction transfer film, indicating that the low-friction CNF-derived transfer film contains a larger amount of $sp^2$ carbon than the high-friction film.

Many researchers have reported that the graphitization of cellulose is induced by its thermal activation energy (Erdemir et al., 1995; Chen et al., 2018; Morosawa et al., 2021; Romero Millán et al., 2023). Morosawa et al. reported that strong thermal and optical effects occurred during the graphitization of CNF films when they were irradiated with femtosecond laser pulses (Rubentheren et al., 2016). Romero Millán et al. (2023) also reported that an iron-catalysis assistance and high-thermal energy (test temperature of 1,000°C–2000°C) promoted the graphitization of cellulose materials (Snad et al., 2023). Chen also reported that high-pressure (test pressure: 20 MPa) conditions and metal catalysis accelerated the graphitization of cellulose materials (Chen et al., 2018). Previous studies have suggested that cellulose materials can easily transform into graphitic carbon under high-temperature and high-pressure conditions. Furthermore, this transformation is accelerated in the presence of a metal catalyst. In this study, the maximum contact Hertzian pressure was approximately 50 MPa, which is much higher than the applied

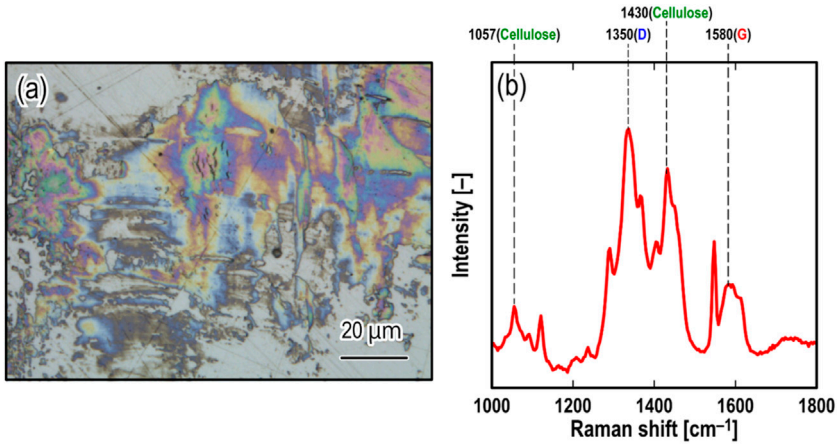


FIGURE 7
**(A)** Optical images of the worn surfaces of the steel disk after the temperature-rise friction test, and **(B)** the Raman spectrum of the transfer region.

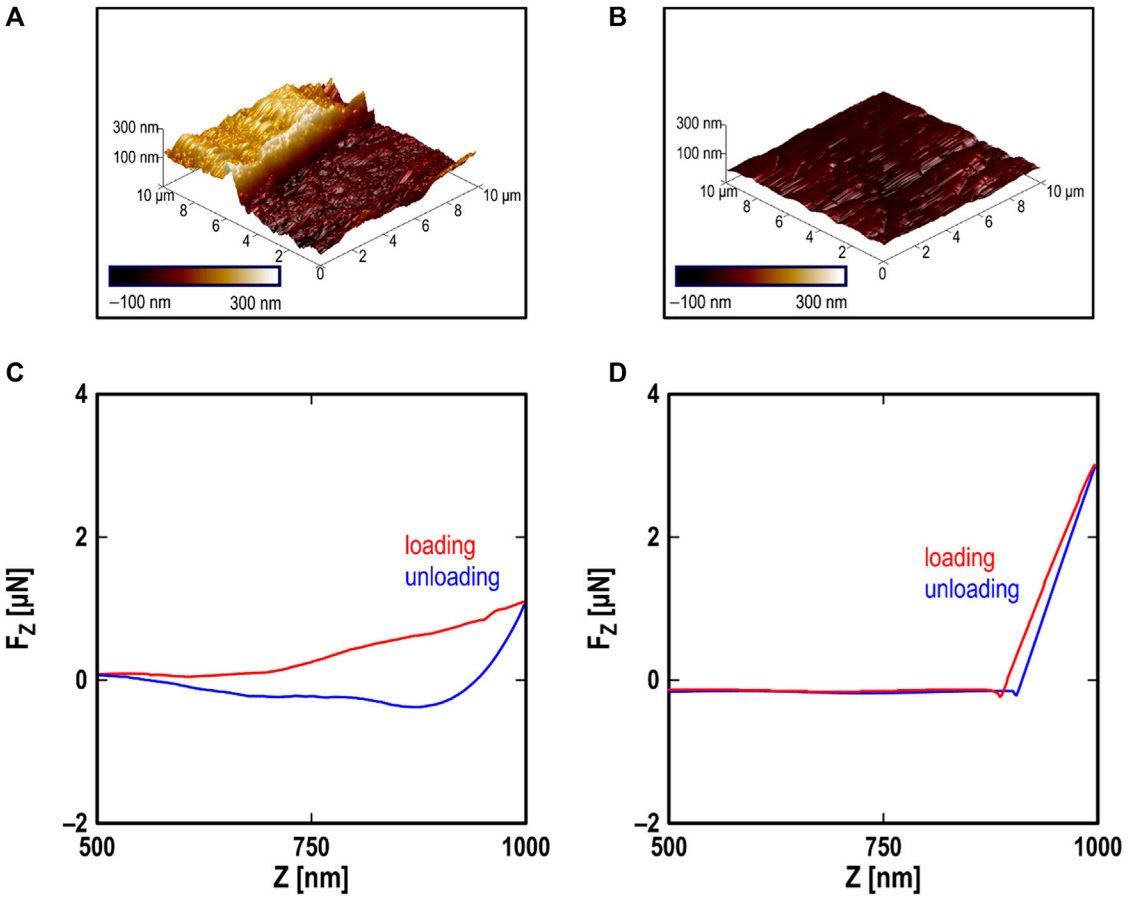


FIGURE 8
AFM topographical images of **(A)** the transfer film region and **(B)** the out-of-the-transfer film region, and AFM force-distance curves of the **(C)** transfer film region and **(D)** out-of-the-transfer film region.

pressure considered in most previous studies. The counter-faced material of the CNF molding, that is, the steel surface, might act as a catalyst. Moreover, the flash temperature, which is a friction-induced temperature increase, should be considered when discussing the thermal effects during friction. This is calculated using the following equation (Rabinowicz, 1965):

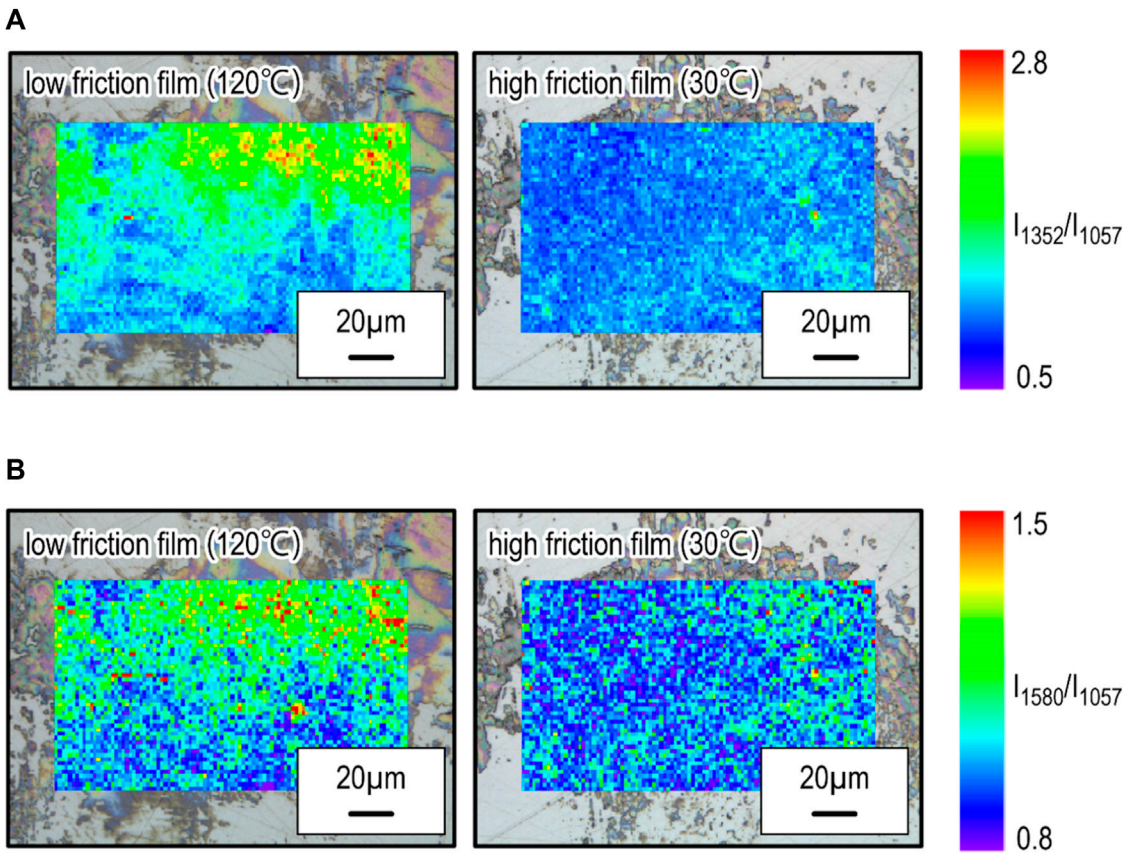


FIGURE 9
Raman images of **(A)** $I_{1352}/I_{1057}$ and **(B)** $I_{1580}/I_{1057}$ for the low friction (120°C) and high friction (30°C) transfer film on the steel surface.

$$\Delta T = \frac{\mu W V}{4Ja(k_1 + k_2)}$$

where $\Delta T$ is the change in the friction-induced temperature, $\mu$ is the friction coefficient, $W$ is the applied load, $V$ is the sliding speed, $J$ is the heat equivalent, $a$ is the contact radius, and $k_{1,2}$ is the thermal conductivity of each sliding material. At the asperity contacts of the CNF/steel tribo-pair surfaces, the above equation can be rewritten as follows.

$$\Delta T_{\mathrm{CNF/steel}} = \frac{\mu_{\mathrm{CNF/steel}} W V}{4Ja_{\mathrm{real}}(k_{\mathrm{CNF}} + k_{\mathrm{steel}})},$$

where $\Delta T_{\mathrm{CNF/steel}}$ is the change in the friction-induced temperature of the CNF/steel tribopair, $\mu_{\mathrm{CNF/steel}}$ is the friction coefficient of the CNF/steel tribopair, $a_{\mathrm{real}}$ is the real contact radius estimated from the AFM topographical image (Figure 8) and equals 10 nm, $k_{\mathrm{CNF}}$ is the thermal conductivity of the CNF molding and equals 2.0 W/(m/K), and $k_{\mathrm{steel}}$ is the thermal conductivity of the bearing steel [80 W/(m/K)]. According to rough parameter estimations, $\Delta T_{\mathrm{CNF/steel}}$ was approximately 300°C–900°C, depending on the friction coefficient and asperity size. Therefore, the thermal energy input into the sliding surface is sufficient to graphitize the CNF molding surface.

Based on the above results and estimations, Figure 10 shows a schematic of the mechanisms by which the thermally activated ultralow friction was generated in the CNF/steel tribopair. Frictional shear or thermal energy breaks the hydrogen and glycosidic bonds in cellulose molecular chains, resulting in the formation of glucose monomers or oligomers (Wang et al., 2021). This tendency is illustrated in Figures 5, 6. The formed glucose is then aromatized, and C=O groups are formed by the dehydration of the hydroxyl groups in the monomer (Wang et al., 2021). C=C bonds are formed via keto–enol tautomerism or intramolecular dehydration, whereas aromatic molecules are formed via intramolecular condensation or aldol reactions (Wang et al., 2021). Finally, microcrystalline graphite and aromatic clusters are formed at the frictional interfaces. Based on the above pathway, the graphitization of CNF molding proceeds at the frictional interface, and a low-frictional transfer film forms on the counter-face steel surface, resulting in ultralow friction of the CNF/steel tribopair at relatively high temperatures.

Generally, many researchers have reported that the graphitization of cellulose requires large amounts of thermal activation energy (Chen et al., 2018; Morosawa et al., 2021; Romero Millán et al., 2023). On the other hand, in this study, the test temperature that the graphitization of cellulose is observed is just 120°C although the set temperature to cause the graphitization of cellulose is above 1,000°C in the previous study. This indicates that the friction-assisted graphitization method proposed in this study, which is efficient and requires low energy, has the potential to be a novel method for efficiently producing graphitic carbon from biomass.

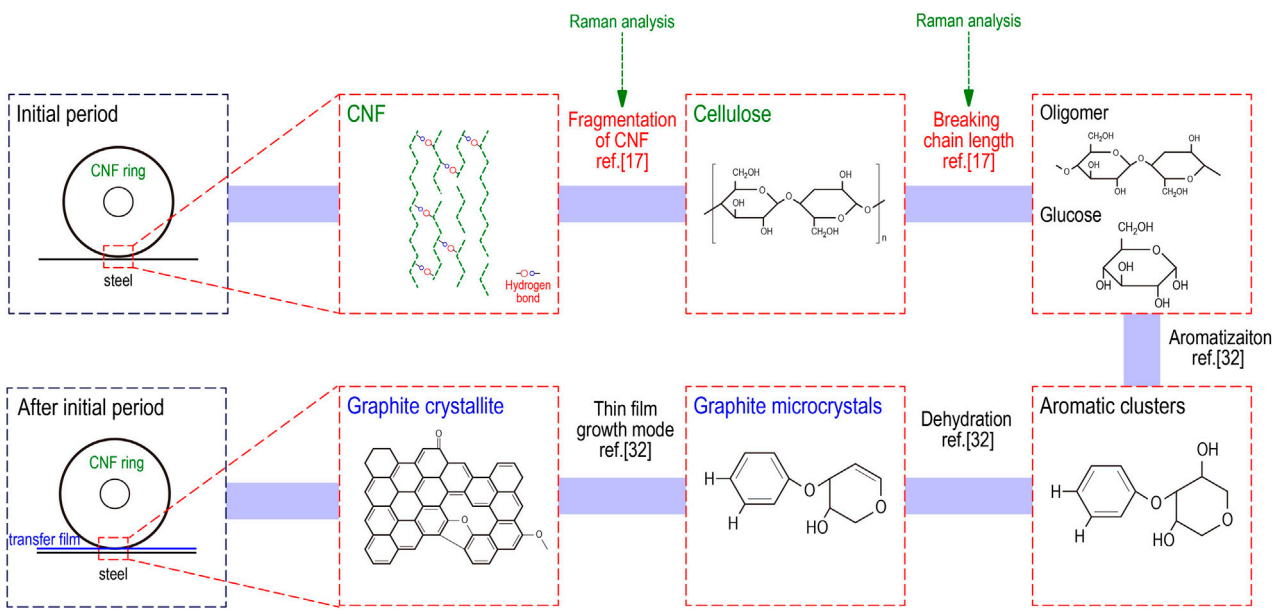


FIGURE 10
Schematic of the formation of ultralow frictional graphitized CNF-transfer film.

## 5 Conclusion

In this study, the effect of the test temperature on the tribological properties of CNF molding was investigated using *in situ* Raman monitoring for friction-induced CNF structural changes. In particular, the mechanisms of thermally activated ultralow friction in CNF molding were examined. The conclusions are as follows.

1. A CNF molding exhibits an ultralow friction coefficient below 0.04 at temperatures exceeding 100°C.
2. The crystallinity and the length of the COC glycosidic chain of a CNF molding gradually decreases at the frictional interfaces as the test temperature increases.
3. The formation of a graphitized CNF transfer film plays an important role in achieving ultralow friction in a CNF molding at high temperatures.

## Data availability statement

The original contributions presented in the study are included in the article/Supplementary Material, further inquiries can be directed to the corresponding author.

## Author contributions

HO: Conceptualization, Investigation, Visualization, Writing–original draft, Writing–review and editing. TI: Investigation, Writing–review and editing. HH: Investigation, Resources, Writing–review and editing. TI: Investigation, Resources, Writing–review and editing. KN: Supervision, Writing–original draft, Writing–review and editing.

## Funding

The author(s) declare that financial support was received for the research, authorship, and/or publication of this article. This study was supported by ACT-X (JPMJAX23D4) from the Japan Science and Technology Agency (JST), and the Transmission Research Association for Mobility Innovation (22B2-01).

## Conflict of interest

Authors HH and TI were employed by Chuetsu Pulp & Paper Co Ltd.

The remaining authors declare that the research was conducted in the absence of any commercial or financial relationships that could be construed as a potential conflict of interest.

## Publisher's note

All claims expressed in this article are solely those of the authors and do not necessarily represent those of their affiliated organizations, or those of the publisher, the editors and the reviewers. Any product that may be evaluated in this article, or claim that may be made by its manufacturer, is not guaranteed or endorsed by the publisher.

# References


Agarwal, U. P., Reiner, R. S., and Ralph, S. A. (2010). Cellulose I crystallinity determination using FT-Raman spectroscopy: univariate and multivariate methods. *Cellulose* 17, 721–733. doi:10.1007/s10570-010-9420-z

Agustin, M. B., Nakatsubo, F., and Yano, H. (2016). The thermal stability of nanocellulose and its acetates with different degree of polymerization. *Cellulose* 23, 451–464. doi:10.1007/s10570-015-0813-x

Azizi Samir, M. A. S., Alloin, F., and Dufresne, A. (2005). Review of recent research into cellulosic whiskers, their properties and their application in nanocomposite field. *Biomacromol* 6, 612–626. doi:10.1021/bm0493685

Bondeson, D., Mathew, A., and Oksman, K. (2006). Optimization of the isolation of nanocrystals from microcrystalline cellulose by acid hydrolysis. *Cellulose* 13, 171–180. doi:10.1007/s10570-006-9061-4

Chen, C., Sun, K., Wang, A., Wang, S., and Jiang, J. (2018). Catalytic graphitization of cellulose using nickel as catalyst. *BioRes* 13 (2), 3165–3176. doi:10.15376/biores.13.2.3165-3176

Chuetsu Pulp and Paper Co. *Chuetsu Pulp and Paper Co, Nanoforest Ltd* (2021), Available at: https://www.chuetsu-pulp.co.jp/wordpress/wp-content/uploads/2021/05/nanoforest.pdf (Accessed June 16, 2022).

Enke, K. (1981). Some new results on the fabrication of and the mechanical, electrical, and optical properties of i-carbon layers. *Thin Solid Films* 80, 227–234. doi:10.1016/0040-6090(81)90226-1

Erdemir, A., Bindal, C., Pagan, J., and Wilbur, P. (1995). Characterization of transfer layers on steel surfaces sliding against diamond-like hydrocarbon films in dry nitrogen. *Surf. Coat. Technol.* 76–77, 559–563. doi:10.1016/02578-9729(50)25189-

Gan, P. G., Sam, S. T., Abdullah, M., and Omar, M. F. (2020). Thermal properties of nanocellulose-reinforced composites: a review. *J. Appl. Polym. Sci.* 137, 48544. doi:10.1002/app.48544

Iwamoto, S., Abe, K., and Yano, H. (2008). The effect of hemicelluloses on wood pulp nanofibrillation and nanofiber network characteristics. *Biomacromol* 9, 1022–1026. doi:10.1021/bm701157n

Li, Q., and Renneckar, S. (2011). Supramolecular structure characterization of molecularly thin cellulose I nanoparticles. *Biomacromol* 12, 650–659. doi:10.1021/bm101315y

Liu, Q., Chen, J., Yang, X., Qiao, C., Li, Z., Xu, C., et al. (2020). Synthesis, structure, and properties of N-2-hydroxylpropyl-3- trimethylammonium-O-carboxymethyl chitosan derivatives. *Int. J. Biol. Macromol.* 144, 568–577. doi:10.1016/j.ijbiomac.2019.12.125

Memming, R., Tolle, H. J., and Wierenga, P. E. (1986). Properties of polymeric layers of amorphous hydrogenated carbon produced by a plasma-activated chemical vapour deposition process I: spectroscopic investigations. *Thin Solid Films* 143 (3), 279–289. doi:10.1016/0040-6090(86)90181-1

Miklozic, K. T., and Spikes, H. A. (2005). Application of atomic force microscopy to the study of lubricant additive films. *J. Tribol.* 257, 405–415. doi:10.1115/1.1843159

Morosawa, F., Hayashi, S., and Terakawa, M. (2021). Femtosecond laser-induced graphitization of transparent cellulose nanofiber films. *ACS Sustain. Chem. Eng.* 9, 2955–2961. doi:10.1021/acssuschemeng.0c09153

Niskanen, I., Zhang, K., Karzarjeddi, M., Liimatainen, H., Shibata, S., Hagen, N., et al. (2022). Optical properties of cellulose nanofibre films at high temperatures. *J. Polym. Res.* 29, 187. doi:10.1007/s10965-022-03019-0

Okubo, H., Hashiba, H., Inamochi, T., Sato, K., Sasaki, S., Yamada, K., et al. (2023b). Novel environmentally superior tribomaterial with superlow friction: 100% cellulose nanofiber molding. *Tribol. Lett.* 71, 83. doi:10.1007/s11249-023-01754-z

Okubo, H., Nakae, R., Daisuke, I., Yamada, K., Yao, S., Nakano, K., et al. (2023a). Tribological properties of 100% cellulose nanofiber (CNF) molding under dry- and boundary lubrication-conditions at CNF/steel contacts. *Cellulose* 30, 6887–6905. doi:10.1007/s10570-023-05309-2

Okubo, H., and Sasaki, S. (2017). *In situ* Raman observation of structural transformation of diamond-like carbon films lubricated with MoDTC solution: mechanism of wear acceleration of DLC films lubricated with MoDTC solution. *Tribol. Int.* 113, 399–410. doi:10.1016/j.triboint.2016.10.009

Okubo, H., Sasaki, S., Lancon, D., Frederic, J., and Thiebaut, B. (2020b). Tribo-Raman-SLIM observation for diamond-like carbon lubricated with fully formulated oils with different wear levels at DLC/steel contacts. *Wear* 454–455, 203326. doi:10.1016/j.wear.2020.203326

Okubo, H., Tadokoro, C., Hirata, Y., and Sasaki, S. (2017). *In situ* Raman observation of the graphitization process of tetrahedral amorphous carbon diamond-like carbon under boundary lubrication in poly-alpha-olefin with an organic friction modifier. *Tribol. Online* 12, 229–237. doi:10.2474/trol.12.229

Okubo, H., Tadokoro, C., and Sasaki, S. (2020a). *In situ* Raman-SLIM monitoring for the formation processes of MoDTC and ZDDP Tribofilms AT steel/steel contacts under boundary lubrication. *Tribol. Online* 15, 105–116. doi:10.2474/trol.15.105

Okubo, H., Tadokoro, C., Sumi, T., Tanaka, N., and Sasaki, S. (2019). Wear acceleration mechanism of diamond-like carbon (DLC) films lubricated with MoDTC solution: roles of tribofilm formation and structural transformation in wear acceleration of DLC films lubricated with MoDTC solution. *Tribol. Int.* 133, 271–287. doi:10.1016/j.triboint.2018.12.029

Posada, P., Velásquez-Cock, J., Gómez-Hoyos, C., Serpa Guerra, A. M., Lyulin, S. V., Kenny, J. M., et al. (2020). Drying and redispersion of plant cellulose nanofibers for industrial applications: a review. *Cellulose* 27, 10649–10670. doi:10.1007/s10570-020-03348-7

Rabinowicz, E. (1965). *Friction and wear of materials*. Hoboken, NJ. HardcoverWiley & Sons Ltd

Romero Millán, L. M., Ghogia, A. M., White, C. E., and Nzihou, A. (2023). Iron nanoparticles to catalyze graphitization of cellulose for energy storage applications. *ACS Appl. Nano Mat.* 6, 3549–3559. doi:10.1021/acsanm.2c05312

Rossetti, A., Paciaroni, A., Rossi, B., Bottari, C., Comez, L., Corezzi, S., et al. (2023). TEMPO-oxidized cellulose nanofibril/polyvalent cations hydrogels: a multifaceted view of network interactions and inner structure. *Cellulose* 30, 2951–2967. doi:10.1007/s10570-023-05058-2

Rubentheren, V., Ward, T. A., Chee, C. Y., Nair, P., Salami, E., and Fearday, C. (2016). Effects of heat treatment on chitosan nanocomposite film reinforced with nanocrystalline cellulose and tannic acid. *Carbohydr. Polym.* 140, 202–208. doi:10.1016/j.carbpol.2015.12.068

Sanad, M. N., Farouz, M., and ElFaham, M. M. (2023). Recent advancement in nano cellulose as a biomass-based adsorbent for heavy metal ions removal: a review of a sustainable waste management approach. *Adv. Eng. Lett.* 2 (4), 120–142. doi:10.46793/adeletters.2023.2.4.1

Wang, D. C., Yu, H. Y., Qi, D., Wu, Y., Chen, L., and Li, Z. (2021). Confined chemical transitions for direct extraction of conductive cellulose nanofibers with graphitized carbon shell at low temperature and pressure. *J. Am. Chem. Soc.* 143, 11620–11630. doi:10.1021/jacs.1c04710

Yang, W., Gao, Y., Zuo, C., Deng, Y., and Dai, H. (2019). Thermally-induced cellulose nanofibril films with near-complete ultraviolet-blocking and improved water resistance. *Carbohydr. Polym.* 223, 115050. doi:10.1016/j.carbpol.2019.115050

Zeng, Q., Eryilmaz, O., and Ali Erdemir, A. (2015). Superlubricity of the DLC films-related friction system at elevated temperature. *RSC Adv.* 5, 93147–93154. doi:10.1039/C5RA16084G

Zhang, X., Li, H., Zhang, W., Huang, Z., Tsui, C. P., Lu, C., et al. (2019). In-situ growth of polypyrrole onto bamboo cellulose-derived compressible carbon aerogels for high performance supercapacitors. *Electrochimica Acta* 301, 55–62. doi:10.1016/j.electacta.2019.01.166

Zhu, L., Dong, J., and Zeng, Q. (2021). High temperature solid/liquid lubrication behaviours of DLC films. *Lubr. Sci.* 33, 229–245. doi:10.1002/ls.1540

frontiers | Frontiers in Mechanical Engineering

TYPE Systematic Review
PUBLISHED 09 July 2024
DOI 10.3389/fmech.2024.1412137

Check for updates

OPEN ACCESS

EDITED BY
Steven Chatterton,
Polytechnic University of Milan, Italy

REVIEWED BY
Saša Milojević,
University of Kragujevac Faculty of Engineering, Serbia
Andrea Vania,
Polytechnic University of Milan, Italy
Edoardo Gheller,
Polytechnic University of Milan, in collaboration with reviewer AV

*CORRESPONDENCE
Florian Michael Becker-Dombrowsky,
florian_michael.becker@tu-darmstadt.de

RECEIVED 04 April 2024
ACCEPTED 13 June 2024
PUBLISHED 09 July 2024

CITATION
Becker-Dombrowsky FM and Kirchner E (2024), Electrical impedance based condition monitoring of machine elements–a systematic review.
*Front. Mech. Eng* 10:1412137.
doi: 10.3389/fmech.2024.1412137

COPYRIGHT
© 2024 Becker-Dombrowsky and Kirchner. This is an open-access article distributed under the terms of the Creative Commons Attribution License (CC BY). The use, distribution or reproduction in other forums is permitted, provided the original author(s) and the copyright owner(s) are credited and that the original publication in this journal is cited, in accordance with accepted academic practice. No use, distribution or reproduction is permitted which does not comply with these terms.

# Electrical impedance based condition monitoring of machine elements–a systematic review

Florian Michael Becker-Dombrowsky * and Eckhard Kirchner

Department for Mechanical Engineering, Institute for Product Development and Machine Elements, Technical University of Darmstadt, Darmstadt, Germany

Condition monitoring of machine elements becomes more important over the last years. Different approaches to detect failures in mechanical components have been developed. All these methods are located at a distance from the point of interest, the observed machine element. This leads to uncertainties in the data, which influences the data quality negatively. Using the electrical impedance for condition monitoring enables *in situ* measurement with reduced uncertainties and higher data quality. In the last years, research considering this topic was done, but a systematic overview is missing. In this article, a systematic literature research according to the PRISMA approach is fulfilled. The main questions are, what application fields for electrical impedance-based condition monitoring approaches exists and which research gaps are not addressed yet. At the end, 21 articles are categorized in their application fields. Analyzing their content, research questions are identified which have to be addressed in further investigations.

KEYWORDS

**electrical impedance, condition monitoring, systematic review, load measurement, condition detection, electric properties, EHL**

## 1 Introduction

Rolling element bearings are one of the most important machine elements in mechanical engineering. They are widely used and a crucial component in most technical systems (Hamrock and Dowson, 1981; Harris, 2001; Kirchner, 2007). Therefore, a damaged rolling element bearing can cause critical damages in a machine or apparatus, which lead to unplanned downtimes and reduced reliability (Schaeffler Monitoring Services GmbH, 2019; Peng et al., 2022). Hence, there is an increasing interest in the detection of harmful bearing conditions and the identification of bearing damages.

The state of the art for damage detection in machine elements for rotary machines is vibration analysis (Davies and Davies, 1998; Jardine et al., 2006; Schenk, 2010; Randall, 2011; Lei, 2016; Schaeffler Monitoring Services GmbH, 2019). Other techniques are thermography, shaft speed analysis, endoscopy and lubricant analysis (Davies and Davies, 1998; Miller and Kitaljevich, 2000; Jardine et al., 2006; Schenk, 2010; Randall, 2011; Schaeffler Monitoring Services GmbH, 2019). Alternative condition monitoring approaches utilize the stator currents in electrical machines (Cameron et al., 1986; Thomson and Barbour, 1998). All these methods have the same disadvantage. They are located outside the point of interest, so the signal path from the damaged bearing to the sensor or observation point is affected by uncertainties (Engelhardt, 2012; Mathias, 2016; Vorwerk-Handing, 2020; Becker-Dombrowsky et al., 2023a). This influences the measurement results and reduces the information density. To increase information density.

The usage of machine learning approaches for analyzing the sensor data is also common (Lei et al., 2008; Lei, 2016; Akpudo and Hur, 2020).

To avoid this disadvantage, sensory utilizable machine elements (SuME) can be used to enable *in situ* measurement. SuME use the electric properties of machine elements to enhance the functionalities of a component to become a sensor itself (Kraus et al., 2020; Kraus et al., 2021). One widespread measurement category of SuME is the electric impedance. Impedance-based condition monitoring approaches are already in use, e.g., for insulation observation (Jameson et al., 2017; Joseph and Krishnan, 2021; Zheng et al., 2021), condition monitoring of stator windings (Kohler et al., 2002; Zhang et al., 2022) and fuel cell observation (Beer et al., 2015; Boškoski et al., 2017; Mahlangu and Barendse, 2021; Jiang et al., 2023). By measuring the electric impedance of a rolling element bearing, different kinds of information can be achieved and the bearing becomes a sensor, which enables condition monitoring of itself and of the surrounding system (Becker-Dombrowsky et al., 2023a; Prashad, 1988; Schirra et al., 2018).

The idea of using the electric properties of machine elements is not new, e.g., Prashad already investigated their opportunities (Prashad, 1988). Many researchers study different kinds of applications for impedance measurement. A structured overview of the state of research in the context of impedance-based condition monitoring for machine elements such as rolling bearings is still missing. Therefore, the aim of this work is to get an overview of this topic and two answer the following two main questions:

1. What are applications of impedance based condition monitoring approaches?
2. Which research gaps exists for the identified approaches?

To do so, scientific literature will be investigated and summarized systematically. Other review articles in this field are focused on harmful currents in drivetrains and electrical induced bearing damages (Johns-Rahnejat et al., 2023; Schneider et al., 2022b) or on film thickness detection techniques (Peng et al., 2022). A broader application field for using the electric properties of bearings, e.g., to detect damages is not considered so far. This article is looking at the topic of impedance-based condition monitoring approaches in general.

In the following section, the fundamentals outlining the basics of the electrical impedance and the electric properties of rolling elements bearings will be addressed. Afterwards, the research method is presented. Then, the results are discussed and a conclusion will be drawn.

# 2 Fundamentals

In this section, the fundamentals of electrical impedance and the elasto-hydrodynamic lubrication (EHL) contacts are given. In addition, the electric analogous model of rolling element bearings will be explained.

## 2.1 The electric impedance

Electrical impedance is the impedance of an element through which alternating current flows. It is determined in the complex plane. The real part R represents the effective resistance, the imaginary part the circular frequency-dependent reactance X. The latter can have both capacitive and inductive components. Therefore, the impedance can be described completely via amplitude and phase (Keysight Technologies, 2014).

The impedance $\boldsymbol{Z}$ is calculated according to Hufschmid as follows in Eq. 1 (Hufschmid, 2021).

$$\boldsymbol{Z} = \boldsymbol{R} + \boldsymbol{jX} \tag{1}$$

The amplitude of the impedance $|\boldsymbol{Z}|$ can be determined using Pythagoras' theorem written in Eq. 2. The phase angle $\boldsymbol{\varphi}$ results from the geometric observation of the impedance vector in the complex plane using the tangent in Eq. 3 (Hufschmid, 2021).

$$|\boldsymbol{Z}| = \sqrt{\boldsymbol{R}^2 + \boldsymbol{X}^2} \tag{2}$$

$$\boldsymbol{\varphi} = \tan^{-1}\left(\frac{\boldsymbol{X}}{\boldsymbol{R}}\right) \tag{3}$$

The reactance $\boldsymbol{X}$ can exhibit both capacitive and inductive behavior. In the case of inductive behavior, the reactance is calculated taking into account the angular frequency, where $\boldsymbol{L}$ is the inductance and $\boldsymbol{\omega}$ is the electrical angular frequency shown in Eq. 4 (Rinderknecht, 2017).

$$\boldsymbol{X} = \boldsymbol{j\omega L} \tag{4}$$

The reactance is calculated in the case of capacitive behavior according to Eq. 5; the capacitance is described by the letter $\boldsymbol{C}$ (Rinderknecht, 2017).

$$\boldsymbol{X} = \frac{\boldsymbol{1}}{\boldsymbol{j\omega C}} \tag{5}$$

The geometric relations describing the electric impedance are pictured in Figure 1.

In general, components show a frequency dependent behavior under alternating current and can exhibit different behaviors. The phase angle for ideal capacitance is–90° until the natural resonant frequency is reached. The phase angle of ideal inductors, on the other hand, is +90° below the natural resonant frequency. Ideal resistors have an angle of 0°. The natural resonant frequency is the frequency at which the reactance of inductance and capacitance are equal and have a phase angle of $\varphi = 0°$. The components then exhibit resistive behavior. After the natural resonance frequency is exceeded, the sign of the respective phase angle changes and the components change their behavior (Keysight Technologies, 2014; Furtmann et al., 2016).

## 2.2 EHL contact

The theory of elasto-hydrodynamic lubricated contact (EHL contact) considers the elastic deformation of the contact partners in the rolling contact, taking into account Hertzian theory in combination with the influence of temperature and pressure on the lubricant viscosity in the lubrication gap. This is an extension of the theory of hydrodynamic contact (HD) (Brüser, 1972; Hamrock and Dowson, 1981; Hertz, 1881; Dahlke, 1994; Steinhilper and Sauer, 2012a).

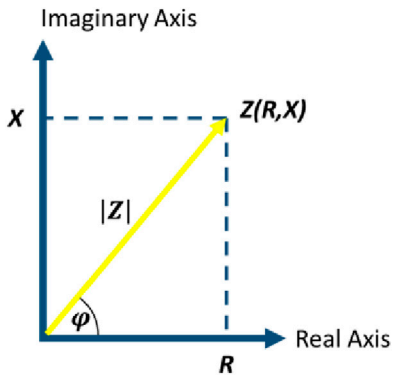


FIGURE 1
The Pythagoras theorem explaining the electrical impedance according to (Keysight Technologies, 2014).

The EHL theory can be used to determine the minimum lubricant film thickness in the rolling contact (Hamrock and Dowson, 1981). This is particularly interesting with regard to the question of sufficient lubricant supply, but also for the electrical properties of the rolling bearing, which will be discussed in more detail later.

The EHL theory is based on the use of several dimensionless parameters, which record the prevailing operating conditions in the rolling contact and thus enable the calculation of the lubrication gap height. Isothermal operating conditions and smooth surfaces of the contact partners are assumed (Hamrock and Dowson, 1981).

According to Hamrock/Dowson, the dimensionless minimum lubricant film thicknes $H_{min}$ is calculated using the following Eq. 6 (Hamrock and Dowson, 1981).

$$H_{min} = 3,63U^{0,68}G^{0,49}W^{-0,073}\left(1 - e^{-0,68k}\right) \quad (6)$$

It is made up of the dimensionless parameters for load $W$, speed $U$ and material $G$, as well as the ratio of the elliptical semi-axes of the Hertzian contact $k$ (Hamrock and Dowson, 1981).

The EHL effect is created by the transportation of lubricant through the lubrication gap. On the inlet side, the lubricant adhering to the bodies is introduced into the lubrication gap. On the outlet side, the lubricant is pressed out of the gap by the prevailing load. Consequently, this is also where the maximum pressure acting in the lubrication gap is located. As a result of the movement and load on the lubricant, shearing of the lubricant occurs. This leads to friction and energy dissipation. This circumstance is not taken into account in the theory according to Hamrock/Dowson. This can be remedied by using correction factors to extend the equation of the minimum lubricant film thickness. However, these are not discussed further here, but reference is made to the relevant literature (Hamrock and Dowson, 1981).

## 2.3 The electric behavior of machine elements

As Furtmann explained, machine elements can exhibit different electrical behavior under alternating current and can be modeled accordingly as circuit elements. He regards shafts as electrical conductors whose electrical behavior corresponds to a serial connection of resistance and inductance between each machine element applied (Furtmann et al., 2016).

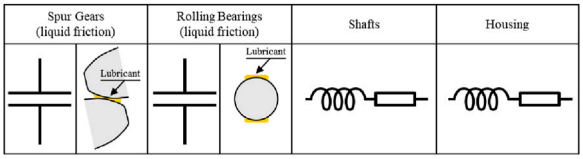


FIGURE 2
Common machine elements and their equivalent electrical components according to (Becker-Dombrowsky et al., 2023a), modified by author.

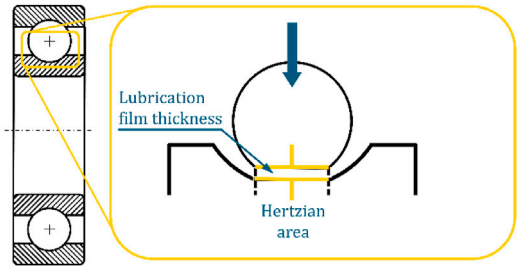


FIGURE 3
Electric model of the EHL contact in a ball bearing (Schirra, 2021).

EHL contact area building machine elements such as rolling bearings and spur gears show a capacitive behavior under hydrodynamic lubrication. They can be modeled as a plate capacitor in case of liquid friction (Becker-Dombrowsky et al., 2023a; Furtmann et al., 2016; Prashad, 2006). Machine elements like housings, screws and shafts are modeled as a serial connection of inductance and ohmic resistance. This is based on the pure metallic structure of this components, which does not allow other electric behavior (Becker-Dombrowsky et al., 2023a; Furtmann et al., 2016). Figure 2 summarizes the central machine elements for rotating machinery and their equivalent electrical components.

As the results in Section 4 show, researchers in the field of impedance-based condition monitoring are focused on rolling element bearings. Therefore, only the electric analogous model of rolling element bearings will be presented in the next section.

## 2.4 The electric analogous model of rolling element bearings

Rolling bearings in an AC circuit can be described as series and parallel connections of capacitors and resistors. The arrangement of the elements and thus the overall electrical behavior change according to the lubrication conditions within the bearing (Prashad, 1988).

The rolling contact is electrically modeled as a plate capacitor with the capacitance $C_{Hz}$ (Prashad, 2006). Figure 3 shows the rolling contact as a capacitor with the associated influencing factors.

The capacitance is calculated according to the equation for plate capacitors Eq. 7 as follows (Gemeinder, 2016).

$$C_{Hz} = \varepsilon_0 \varepsilon_r \frac{A_{Hertz}}{h_0} \tag{7}$$

This shows that the capacitance and consequently the impedance of the rolling contact depend on the lubricant properties (relative permittivity $\varepsilon_r$), the lubricant film thickness $h_0$ and the contact geometry in the form of the Hertzian surface $A_{Hertz}$. The latter in turn is related to the load distribution, which is not constant across all rolling elements during operation (Schirra, 2021).

As can be seen from Figure 3, the equation above does not take into account the boundary influence zone. Barz and Gemeinder use a correction factor $k_c$ for this shown in Eq. 8 (Barz, 1996; Gemeinder, 2016).

$$C_K = k_c C_{Hz} \tag{8}$$

Schirra has already proposed an approach for the corresponding model extension. It replaces the static factors for considering the edge zone by calculating the capacity in this zone. In addition, the unloaded rolling elements are included in the analysis in a similar way. The calculations carried out by him correspond to the empirically determined values and therefore represent a sufficiently accurate model description (Schirra, 2021).

In case of the EHL contact, the contact partners are completely separated and the bearing exhibits capacitive behavior if a high-resistance lubricant is used. The capacitance of the contact depends on the contact geometry, the number of rolling elements, the lubricant film thickness and the electrical properties of the lubricant, which acts as a dielectric (Gemeinder, 2016; Bechev et al., 2020).

Figure 4 shows the exemplary replacement model of a rolling contact with a single rolling element in the bearing under alternating voltage $U_{Lager}$. The metallic components are shown as ohmic resistors for the outer ring $R_{AR}$, the inner ring $R_{IR}$ and the rolling element $R_{WK}$. The contact areas are described as impedance from the rolling element to the inner ring $Z_{IR}$ and to the outer ring $Z_{AR}$. They are modeled as a parallel connection in the case of the EHL contact. The lubricant areas that are not involved in the rolling contact can be assumed as a series connection of three parallel circuits consisting of ohmic resistance and capacitor. The circuits close to the bearing rings with the impedance $Z_{MS}$ describe the interaction between the lubricant and the metal of the rolling bearing rings. The middle parallel circuit with impedance $Z_S$ describes the lubricant behavior without further influences. The variable impedance $Z_{Kontakt}$ represents approximations and contacts of the bearing rings as a result of vibrations and similar phenomena (Furtmann, 2017).

Depending on the lubrication conditions in the rolling contact, three different electrical behaviors can be determined within the lubrication gap. These are primarily related to the lubrication gap height. Figure 5 illustrates this relationship.

In the area of solid-state friction, there is direct metallic contact between the rolling element and the respective raceway, so that the contact zone can be modeled as an ohmic resistance $R_p$. With increasing lubrication and thus increasing lubrication gap height, the contact partners are separated and, in addition to the resistive

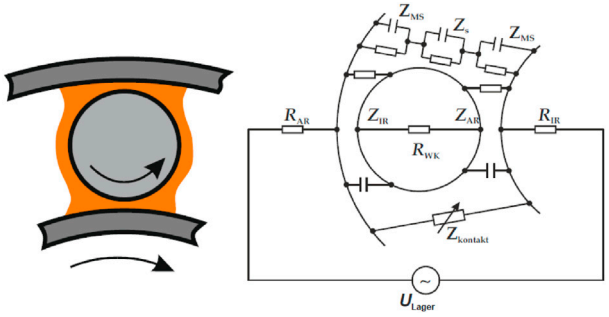


FIGURE 4
Equivalent model of a contact consisting of a rolling element and inner or outer ring (Furtmann, 2017).

behavior, capacitive behavior also occurs within the lubrication gap, whereby voltage flashovers can occur again and again due to insufficient lubrication as a result of contact with roughness peaks (Gemeinder, 2016; Furtmann, 2017).

As can be seen in the middle section of Figure 5, two different phenomena can occur with a thin lubricant film, which are related to the breakdown voltage. According to Gemeinder, the latter is the product of the breakdown field strength of the lubricant and the lubricant film height (Gemeinder, 2016). If the lubricant film height is sufficient or if the voltage at the rolling contact is below the breakdown voltage, the phenomenon described for the EHL contact of the parallel connection of capacitance $C_p$ and high-impedance resistance $R_{p,EHL}$ occurs. As soon as the breakdown voltage is exceeded, The lubricant resistance decreases to $R_{p,EDM}$ and spark-erosive currents occur in the contact area, EDM currents for short, which have a damaging effect and can lead to earlier failure of the rolling bearing. Besides EDM currents, currents in the electric machine lead through the bearings can cause microstructural changes in the metal matrix like White Etching Cracks (WEC), which reduce the bearings operational time. These phenomena are investigated due to the increasing importance of electric mobility and wind power plants (Muetze, 2003; Tischmacher and Gattermann, 2012; Radnai et al., 2015; Gemeinder, 2016; Tischmacher, 2017; Loos et al., 2021; Schneider et al., 2021; Harder et al., 2022; Peng et al., 2022; Johns-Rahnejat et al., 2023; Schneider et al., 2022b).

The bearing current density is decisive for the damaging effect of currents. The bearing current depends on the magnitude of the applied voltage and the bearing impedance (Prashad, 1988), which in turn is related to the contact conditions within the lubrication gap (Gemeinder, 2016). The bearing current density is defined as the quotient of the current and the effective Hertzian area (Muetze, 2003). A bearing current density below 0.1 A/mm$^2$ is considered uncritical (Radnai et al., 2015). A damaging effect cannot be ruled out between 0.1 A/mm$^2$ and 1 A/mm$^2$. Larger bearing currents, on the other hand, have a damaging effect (Radnai et al., 2015). As soon as liquid friction is present, an insulating lubricating film forms between the contact partners and the EHL contact occurs with the behavior described above (Gemeinder, 2016).

As the fundamentals show, impedance measurement and capacitance calculation enable different monitoring approaches to

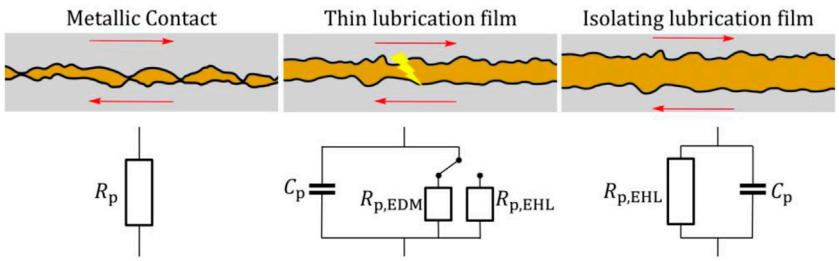


FIGURE 5
Electric model of the EHL contact as a function of the lubrication film thickness (Martin, 2021).

machine elements and especially to rolling bearings. A systematic classification of the applications for impedance measurement in machine element observation has not been fulfilled yet. Also, analyzing possible research gaps and further opportunities of this technique is still missing. Therefore, a systematic literature research is fulfilled in this work to classify the different application fields in impedance based machine element observation and to find possible research questions. In the next section, the method of this literature research is presented.

## 3 Study design

The aim of this work is to get an overview of impedance-based condition monitoring methods. This includes all kinds of machine elements in mechanical engineering topic. The focus is on the observation of classic machine elements like spur gears and rolling element bearings. Specialized applications like fuel cell observation mentioned in Section 1 are not included. Articles about electrical induced damages in rolling element bearings and harmful bearing currents are not included as well. The topics are connected to each other, but electrical induced damages of machine elements are a specific and own field. A literature review according to the PRISMA approach is applied to check different databases about possible literature.

PRISMA is an abbreviation for "Preferred Reporting Items for Systematic Reviews and Meta-Analyses." This approach is a systematic method to analyze different databases to get an overview of the state of research on a certain topic. PRISMA is already used for literature research in medical and clinical contexts (Liberati et al., 2009; Page et al., 2021).

The proceeding in this work is according to Fett et al. (2023), which also used the PRISMA approach for a review in a mechanical engineering topic. The investigated databases Inspec, ProQuest, TEMA and Web of Science are common in mechanical engineering. Additionally, articles found from other sources like Research Gate and Google Scholar are included as well. The databases are searched using their internal search engine. The results are saved in an internal database, where they are clustered manually.

As a search term for the title the following string was used. The restrictions to the title were included using Boolean operators. For the single database, some details had to be changed, but not in a significant manner. Only the titles are investigated to get a reasonable amount of articles. Otherwise, a lot of improper literature has to be investigated. In the first search, spur gears and other machine elements were included, but no literature was found. So, the search term was changed to reduce the amount of improper literature.

1. TITLE ("Impedance" or "Electrical Impedance" or "Impedance Measurement*" or "Real Part" or "Imaginary Part" or "Phase Angle" or "Absolute Value" or "Capacitance" or "Impedanz" or "Elektrische Impedanz" or "Impedanzmessung*" or "Impedanzmessverfahren" or "Realteil" or "Imaginärteil" or "Phasenwinkel" or "Impedanzbetrag" or "Betrag der Impedanz" or "Kapazität")
2. TITLE ("Rolling Element Bearing*" or "Roll* Bearing" or "EHL" or "EHL contact" or "Machine Element*" or "Condition Monitoring" or "Lubrication Condition" or "Wälzlager" or "Maschinenelement" or "Zustandsüberwachung")

After getting the title from the databases, the duplicates are removed and the remaining titles are screened. Titles that do not include condition monitoring using the electric properties of classic machine elements as their topic are excluded. Included are articles, which enable the usage of impedance-based condition monitoring of machine elements by fundamental research. After excluding improper titles, the proper articles are screened and read in detail. Improper articles, articles in unusual languages and not available articles have been removed. In the end, twenty articles are further investigated. Figure 6 summarizes the investigation process. The number of articles in every step is mentioned as well.

## 4 Results

As mentioned in Section 3, twenty articles are identified as proper for this review. Analyzing the publication year, the increasing interest in the topic of impedance based condition monitoring techniques can be seen. In Figure 7 the trend is illustrated. The first article on this topic was published by Heemskerk et al. (1982). In the last years, the increase of interest in the electric impedance can be seen. As yet, the amount of publications has its maximum in 2023 with five articles.

After analyzing the articles' content, three main topics can be differentiated. The first one is about load measurement using the

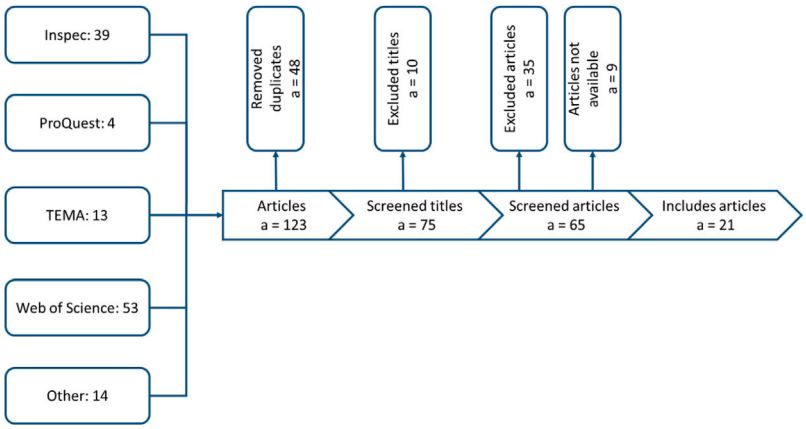


FIGURE 6
Literature investigation process according to PRISMA approach.

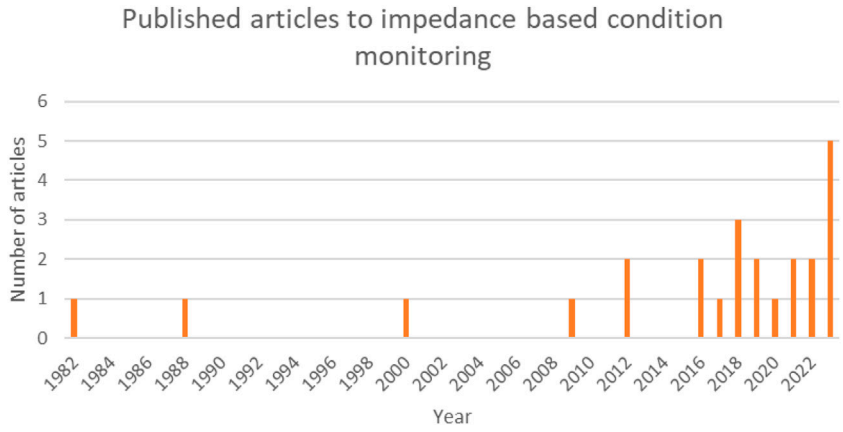


FIGURE 7
Published articles to impedance based condition monitoring of machine elements over their publication years.

electrical impedance. Using load measurement as an instrument for condition monitoring is based on the idea of detecting the loads affecting a machine element and calculating the remaining useful life (Schirra et al., 2018; Schaeffler Monitoring Services GmbH, 2019; Schirra, 2021). It can be applied to machine elements with a fatigue limit such as spur gears (in case of pit load capacity) and rolling element bearings (Dahlke, 1994; Steinhilper and Sauer, 2012a; Steinhilper and Sauer, 2012b; Deutsches Institut für Normung e.V. Wälzlager, 2021). The second topic contains rolling bearing condition monitoring by analyzing electrical signals, e.g., for damage detection. The third and most commonly investigated topic addresses the lubrication condition monitoring. Further, it can be divided into lubrication film thickness detection and lubricant condition detection. All articles are focused on rolling element bearings as the observed machine element or the EHL contact itself. Other machine elements like spur gears are not part of the investigations. Furtmann described the electrical analogous models for different machine elements, but condition monitoring is not his scope (Furtmann et al., 2016; Furtmann, 2017).

In the following, the articles will be summarized shortly in their topic classes. Figure 8 gives an overview of the identified topics.

## 4.1 Impedance based load measurement

The idea of load measurement using the electrical impedance is initiated by Schirra et al. (2018). They investigate the opportunities of simultaneous load and failure monitoring. The basis is the analogous model of the rolling contact. From the impedance, the capacitance is calculated, which enables estimating the Hertzian area. Using the Hertzian area, the load and the resulting remaining useful lifespan of the rolling bearing can be estimated. For a real sensor application, further investigations are necessary as well as additional sensors, e.g., for temperature and speed gauging. Also, instationary operating conditions are not investigated (Schirra et al., 2018).

Some of the identified challenges of impedance based load measurement are considered by Schirra et al. (2021) in a subsequent

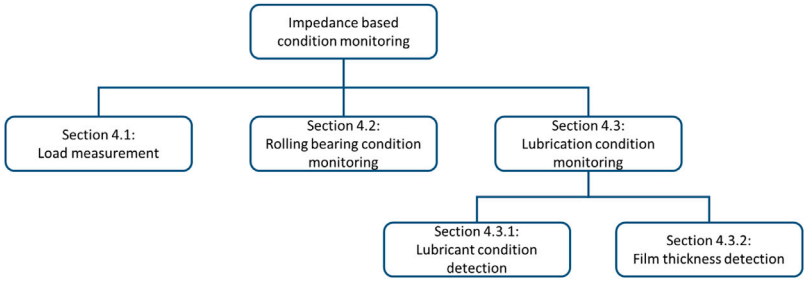


FIGURE 8
Article topics.

TABLE 1 Articles to impedance based load measurement.

| Authors | Title | Year | Reference |
|---|---|---|---|
| Schirra, Tobias; Martin, Georg; Vogel, Sven; Kirchner, Eckhard | Ball Bearings as Sensors for Systematical Combination of Load and Failure Monitoring | 2018 | Schirra et al. (2018) |
| Schirra, T.; Martin, G.; Puchtler, S.; Kirchner, E | Electric Impedance of Rolling Bearings—Consideration of Unloaded Rolling Elements | 2021 | Schirra et al. (2021) |

publication. Their research is taking unloaded rolling elements and the undeflected area into account by enlarging the current models. Their experimental results show an improvement, but differences between measurement and calculation remain (Schirra et al., 2021).

The articles to impedance based load measurement are summarized in Table 1.

## 4.2 Impedance based rolling bearing condition monitoring

Yang et al. (2000) investigated a method to measure the rolling element skew in a tapered roller bearing. The installed two contact potential difference probes at the outer ring and gauged the capacitance between roller and ring. With this capacitance signal, they measure the skew. They were able to determine the correlation between skew, rotational speed and lubrication (Yang et al., 2000).

Tuomas and Isaksson developed an impedance based measurement technique to observe the buildup of the lubrication film in rolling element bearings to identify different operating conditions. Their investigation enables the differentiation between the run-in phase at the beginning of bearing life and the enclosing normal operating state. At the end of bearing life, they are able to identify changes in the signal behavior which indicates additional metallic contacts (Tuomas and Isaksson, 2009).

Schnabel et al. identify the run-in phase of EHL contacts. Further, they studied the correlation between surface roughness and impedance behavior at their ball on disk apparatus. They found out that the contact resistance depends on the surface roughness. The impedance in general was not affected by surface active additives (Schnabel et al., 2016).

Schirra et al. (2018) were already mentioned in Section 4.1. The idea behind the condition monitoring approach is to detect the bearing loads and to calculate the remaining useful lifetime of the observed bearing (Schirra et al., 2018).

Martin et al. (2022) used the impedance signals and changes in the signal to detect pitting damages in the surface. They measured the impedance using a shunt circuit at their rolling bearing test rig in fatigue tests under stationary operating conditions. They also investigate the impedance under artificial surface damages at the inner ring raceway. As a result, detecting and localizing the pitting damages was possible. Also, they are able to measure the pitting length in the raceway (Martin et al., 2022).

Chevallier et al. (2023) compare vibration measurement based condition monitoring to impedance-based condition monitoring approaches. They provide evidence for the possibilities of the impedance method. It can be seen that impedance based condition monitoring has opportunities to be investigated further (Chevallier et al., 2023).

Becker-Dombrowsky et al. (2023b) investigate the data generated by Martin et al. (2022). They identified indicators in the impedance signal using feature engineering approaches, which enables an early detection of pitting damages. The behavior of the identified features in time and frequency domain could be physically explained (Becker-Dombrowsky et al., 2023b).

The articles to impedance based rolling bearing condition monitoring are summarized in Table 2.

## 4.3 Impedance based lubrication condition monitoring

Lubrication condition monitoring is the biggest topic in impedance based condition monitoring. It can be divided into lubrication condition detection and the film thickness detection.

TABLE 2 Articles to impedance based rolling bearing condition monitoring.

| Authors | Title | Year | Reference |
|---|---|---|---|
| Yang, Yeyuan; Danyluk, Steven; Hoeprich, Michael | A Study on Rolling Element Skew Measurement in a Tapered Roller Bearing With a Specialized Capacitance Probe | 2000 | Yang et al. (2000) |
| Tuomas, Roger; Isaksson, Ove | Measurement of Lubrication Conditions in a Rolling Element Bearing in a Refrigerant Environment | 2009 | Tuomas and Isaksson (2009) |
| Schnabel, S.; Marklund, P.; Minami, I.; Larsson, R | Monitoring of Running-in of an EHL Contact Using Contact Impedance | 2016 | Schnabel et al. (2016) |
| Schirra, Tobias; Martin, Georg; Vogel, Sven; Kirchner, Eckhard | Ball Bearings as Sensors for Systematical Combination of Load and Failure Monitoring | 2018 | Schirra et al. (2018) |
| Martin, G.; Becker, F.; Kirchner, E | A Novel Method for Diagnosing Rolling Bearing Surface Damage by Electric Impedance Analysis | 2022 | Martin et al. (2022) |
| Chevallier, Eddy; Boudimbou, Justus Christmaël; Bouzerar, Robert; Garcia, Tania; Bolaers, Fabrice; Chiementin, Xavier | Monitoring of Roller Bearings: electrical vs Vibrational Analysis | 2023 | Chevallier et al. (2023) |
| Becker-Dombrowsky, Florian Michael; Koplin, Quentin Sean; Kirchner, Eckhard | Individual Feature Selection of Rolling Bearing Impedance Signals for Early Failure Detection | 2023 | Becker-Dombrowsky et al. (2023a) |

TABLE 3 Articles to lubricant condition detection.

| Authors | Title | Year | Reference |
|---|---|---|---|
| Zeng, Lin; Wang, Wenqi; Rogers, Foday; Zhang, Hongpeng; Zhang, Xingming; Yang, Dingxin | A High Sensitivity Micro Impedance Sensor Based on Magnetic Focusing for Oil Condition Monitoring | 2020 | Zeng et al. (2020) |
| Shi, Haotian; Zhang, Hongpeng; Huo, Dian; Yu, Shuang; Su, Jun; Xie, Yucai; Li, Wei; Ma, Laihao; Chen, Haiquan; Sun, Yuqing | An Ultrasensitive Microsensor Based on Impedance Analysis for Oil Condition Monitoring | 2022 | Shi et al. (2022) |

### 4.3.1 Lubricant condition detection

Zeng et al. (2020) use the electrical impedance to detect debris in the oil and other abnormalities. The developed sensor is able to detect metallic particles in the lubricant as well as water droplets and bubbles in the oil. Particles between 18 µm (iron) and 75 µm (copper) could be detected. So, the presented system is able to monitor lubricants and systems condition by detecting impurity (Zeng et al., 2020).

Shi et al. (2022) present a similar approach. They have developed an inductance-resistance and capacitance sensing micro sensor. With this sensor, they are able to detect metallic debris, moisture and air bubbles in the observed oil. This enables condition monitoring (Shi et al., 2022).

The articles to lubricant condition detection are summarized Table 3.

### 4.3.2 Film thickness detection

Heemskerk et al. (1982) investigate measuring the lubrication condition in rolling bearings using the electrical impedance. They were able to gauge the film thickness in case of separating lubrication film. They could predict the so-called lift-off speed at the end of the run-in for grease lubrication and named possible application fields (Heemskerk et al., 1982).

Tuomas and Isaksson measured the lubrication condition in rolling element bearings in a refrigerant environment using the electrical impedance. Due to the lower viscosity because of the refrigerant in the oil, a higher amount of metallic contacts in the run-in was expected. They could identify the run-in phase of the bearing by measuring the impedance and the higher amount of metallic contacts in the impedance signal at the bearing's beginning and end of life (Tuomas and Isaksson, 2009).

Glovnea et al. (2012) already published a review about the evaluation of lubrication in EHL contacts using electrical methods. Most approaches were focused on experimental apparatus. They list advantages and disadvantages, but also discuss the opportunities of impedance measurement (Glovnea et al., 2012).

Clarke et al. (2016) investigate the mixed lubrication regime using the electrical contact resistance techniques. It can be shown that the measurement technique was able to monitor the contact conditions and the dependence of the signal from the lubrication film height. Also, the relation between contact resistance, high loads and surface roughness are examined (Clarke et al., 2016).

For lubrication film thickness measurement, Xie et al. (2016) developed an impedance based measurement approach avoiding slip rings and other common contact devices. Therefore, they used two electric field coupling paths. The error between the presented approach and the slip ring method is about 15%, which they declared as sufficient enough for film thickness measurements (Xie et al., 2016).

Jablonka et al. (2012) investigated the electrical analogous model of the ball to raceway contact for a ball on flat configuration. The measurement method based on the impedance is applicable to machine elements like rolling element bearings, but further research is needed. They identify the contact geometry model and the lubricant itself as another research topics (Jablonka et al., 2012).

In a subsequent contribution, Jablonka et al. (2018) transferred their knowledge to radially loaded deep-groove ball bearings. They implemented a quantitative measurement approach for film thickness detection. Modified rolling bearings with ceramic balls and one metallic ball were used to investigate the electric behavior of the single contact in the bearing. So, they were able to investigate lubricant composition, properties and supply, load, temperature and entrainment speed. It could be shown that impedance measurement in rolling bearings allows film thickness detection (Jablonka et al., 2018).

Maruyama and Nakano compared the impedance measurement approach for film thickness evaluation to optical interferometry on a ball-on-disc apparatus. They could confirm that the results of impedance based oil film thickness measurement agreed with the interferometry results. This allows the transfer of the impedance measurement approach to machine elements like ball bearings for EHL contact investigation (Maruyama and Nakano, 2018).

Later, Maruyama et al. (2019) picked up their results and developed an impedance based approach for film thickness monitoring and breakdown ratio of oil films in EHL contacts of ball bearings. It is shown that using the impedance, a parallel observation of breakdown ratio and lubrication film thickness is possible. Also, they compared the calculated film thickness after Hamrock and Dowson (1981) to the measured thickness. In the low-speed range, the measured values agreed with the calculated film heights satisfactorily. For higher speeds, the measured film thickness is thinner than the calculated one, which means that the models have to be optimized (Maruyama et al., 2019).

In 2023, Maruyama et al. (2019) transferred the approach of their research in 2019 to thrust needle roller bearings. The results were similar to the results for ball bearing, which suggests an independence of the measurement technique from the rolling element bearing type (Maruyama et al., 2023).

Cen et al. (2021) created a review on EHL film thickness in rolling element bearings using the capacitance method. Two main approaches for transforming the measured capacitance to an oil film thickness were identified. The first one calculates the capacitance in the Hertzian contact area. The second method uses calibration approaches to transfer the measured capacitance into a film thickness (Cen et al., 2021).

Schneider et al., 2022b present a new capacitance based analytical method for film thickness monitoring. The article includes an approach for measuring and calculating the capacitance of each rolling contact. The novelty of this publication is the calculation of the local lubricant film height of combined loaded bearings with point contact (Schneider et al., 2022a).

Manjunath et al. (2024) describe the Electrical Impedance Spectroscopy (EIS) as an instrument for film thickness measurement in line contact bearings. The research before is focused on film thickness detection in point contact building bearings. For analyzing the generated impedance data, impedance-based and capacitance-based approaches are used. The authors can show that the measured capacitance differs from the calculated capacitance by a factor of 3 up to 11, depending on the parameters like speed and temperature. The presented EIS approach enables to detect the transition from boundary to mixed lubrication and from mixed lubrication to EHL (Manjunath et al., 2024).

The articles to lubricant condition detection are summarized in Table 4.

## 5 Discussion

Using the impedance to measure loads in machine elements, namely, rolling element bearings, works under certain conditions. Mainly, its accuracy depends on the electric analogous model of the EHL contact, which has to be investigated further. Schirra et al. (2021) were able to improve the model, but an error between measurement and calculation still remains (Schirra et al., 2021).

In case of impedance based rolling bearing condition monitoring, two basic topics could be identified. The initial idea was to detect the end of run-in phase and optimal lubrication condition in rolling element bearings to optimize the bearing lifespan (Tuomas and Isaksson, 2009; Schnabel et al., 2016). Later, Schirra et al. (2018) established the idea of condition monitoring over the bearing operational time in general and remaining useful life calculation using the electric analogous model of the EHL contact in combination with the Hertzian theory (Schirra et al., 2018). Martin et al. analyzed the complex impedance signal to find significant changes which leads to pitting damages in the bearings raceways (Martin et al., 2022). They are able to detect and to localize pitting damages and to measure their length in rolling direction. Rycerz et al. (2017); Kunzelmann et al. (2023) developed an approach for rolling contact fatigue prediction, which is based on mathematic models describing the pitting damage progression. They could show that their models can predict the damage progression properly, when the pitting damage has reached a certain dimension. Impedance measurement can detect and measure small pitting damages to use the models described in (Rycerz et al., 2017; Kunzelmann et al., 2023), which is not possible with vibration measurement (Kunzelmann et al., 2023) or ultrasonic reflectrometry (Peng et al., 2022). Becker-Dombrowsky et al. (2023a) continued analyzing the signals of Martin et al. (2022) and could find features in time and frequency domain, which enables the usage of machine learning approaches for damage early detection (Becker-Dombrowsky et al., 2023b; Chevallier et al., 2023) could identify further opportunities for impedance based condition monitoring compared to vibration measurement (Chevallier et al., 2023). Analyzing the different research articles, several open research question can be seen. In fact, the impedance measurement approach is still limited to rolling element bearings. Other machine elements are not taken into account, yet. A first research article to this topic is presented by Becker-Dombrowsky et al. (2023a), but a comparable level to impedance based rolling bearing condition monitoring is not reached. Furthermore, all research was done under stationary operating conditions. Besides, rolling bearings can be operated in mixed lubrication regime, which is not investigated yet. The experiments use standard lubricants without additives. There is the possibility that additives might influence the electric properties by mutating the raceway surfaces (Lugt et al., 2001; Prashad, 2006; Reibung and Schmierung und Verschleiß, 2015; Schnabel et al., 2016; Bukvić et al., 2024). The impedance of the lubricant near the raceway surface differs from the lubricant impedance between the raceways (Furtmann, 2017), which

TABLE 4 Articles to film thickness detection.

| Authors | Title | Year | Reference |
|---|---|---|---|
| Heemskerk, R. S.; Vermeiren, K. N.; Dolfsma, H | Measurement of Lubrication Condition in Rolling Element Bearings | 1982 | Heemskerk et al. (1982) |
| Tuomas, Roger; Isaksson, Ove | Measurement of Lubrication Conditions in a Rolling Element Bearing in a Refrigerant Environment | 2009 | Tuomas and Isaksson (2009) |
| Glovnea, Romeo; Furtuna, Marian; Nagata, Yuichiro; Sugimura, Joichi | Electrical Methods for the Evaluation of Lubrication in Elastohydrodynamic Contacts | 2012 | Glovnea et al. (2012) |
| Clarke, A.; Weeks, I.J.J.; Evans, H. P.; Snidle, R. W | An Investigation into Mixed Lubrication Conditions Using Electrical Contact Resistance Techniques | 2016 | Clarke et al. (2016) |
| Xie, Kai; Liu, Long-Chao; Li, Xiao-Ping; Zhang, Han-Lu | Non-Contact Resistance and Capacitance On-Line Measurement of Lubrication Oil Film in Rolling Element Bearing Employing an Electric Field Coupling Method | 2016 | Xie et al. (2016) |
| Jablonka, Karolina; Glovnea, Romeo; Bongaerts, Jeroen | Evaluation of EHD Films by Electrical Capacitance | 2012 | Jablonka et al. (2012) |
| Jablonka, Karolina; Glovnea, Romeo; Bongaerts, Jeroen | Quantitative Measurements of Film Thickness in a Radially Loaded Deep-Groove Ball Bearing | 2018 | Jablonka et al. (2018) |
| Maruyama, Taisuke; Nakano, Ken | *In Situ* Quantification of Oil Film Formation and Breakdown in EHD Contacts | 2018 | Maruyama and Nakano (2018) |
| Maruyama, Taisuke; Maeda, Masayuki; Nakano, Ken | Lubrication Condition Monitoring of Practical Ball Bearings by Electrical Impedance Method | 2019 | Maruyama et al. (2019) |
| Maruyama, Taisuke; Radzi, Faidhi; Sato, Tsutomu; Iwase, Shunsuke; Maeda, Masayuki; Nakano, Ken | Lubrication Condition Monitoring in EHD Line Contacts of Thrust Needle Roller Bearing Using the Electrical Impedance Method | 2023 | Maruyama et al. (2023) |
| Cen, Hui; Bai, Dan; Chao, Yanpu; Li, Yaohui; Li, Ruihua | EHL Film Thickness in Rolling Element Bearings Evaluated by Electrical Capacitance Method: a Review | 2021 | Cen et al. (2021) |
| Schneider, Volker; Bader, Norbert; Liu, Haichao; Poll, Gerhard | Method for *In Situ* Film Thickness Measurement of Ball Bearings Under Combined Loading Using Capacitance Measurements | 2022 | Schneider et al. (2022a) |
| Manjunath, Manjunath; Hausner, Simon; Heine, André; Baets, Patrick de; Fauconnier, Dieter | Electrical Impedance Spectroscopy for Precise Film Thickness Assessment in Line Contacts | 2024 | Manjunath et al. (2024) |

indicates changes in the electric properties of the bearing using surface mutating additives such as described in (Bukvić et al., 2024).

Investigations under varying loads and speeds are still missing, which is essential for an application in technical systems. Further research is needed here, especially how load and speed changes can influence the signals. It is not clear, if a condition detection can be realized under instationary operating parameters. Another aspect is, if health monitoring is possible under high dynamic conditions. A comparison between states of technique applications like vibration measurement and impedance measurement would be interesting as well.

All tests were carried out in hydrodynamic lubrication regime, but mixed lubrication is not investigated yet. This has to be addressed as well to apply the technique to, e.g., gearboxes. The influence of lubricant additives to the impedance signal is not considered. They can affect the contact partner surfaces, which may cause changes in the impedance signal.

The topic of impedance based lubrication condition monitoring is more investigated than the two topics before, especially film thickness detection. After measuring the lubrication film thickness in ball-on-disc apparatus and other test rigs for single contact investigation (Glovnea et al., 2012; Jablonka et al., 2012; Schnabel et al., 2016; Maruyama and Nakano, 2018), the impedance based approach is applied to rolling element bearings (Heemskerk et al., 1982; Tuomas and Isaksson, 2009; Xie et al., 2016; Maruyama et al., 2019; Schneider et al., 2022a; Maruyama et al., 2023). The results show that the application is transferable from the single contact to the bearing in general, independently from the bearing type with different contact conditions (Maruyama et al., 2019; Maruyama et al., 2023). Still, differences between calculation and measurement remain, which indicates that the contact models need to be improved further. Also, the influence of different lubricants is not investigated yet. Some additives have been researched regarding their influence on the contact impedance, but further research is necessary (Schnabel et al., 2016). A detection of mixed lubrication condition is possible (Heemskerk et al., 1982; Tuomas and Isaksson, 2009; Clarke et al., 2016; Schnabel et al., 2016), but a sufficient film thickness measurement out of the hydrodynamic lubrication regime is not researched as well as varying operation conditions.

For lubricant condition detection, it was shown that different kinds of oil soiling can be detected. This includes metallic particles, moisture and air bubbles (Zeng et al., 2020; Shi et al., 2022). However, tests for lubricant condition detection in machine elements like spur gears and rolling element bearings are still missing. This includes investigations under stationary and instationary operation conditions as well as experiments in the mixed and hydrodynamic lubrication regimes.

As mentioned in Section 4, the research field of impedance based condition monitoring techniques for machine elements can be separated in three main applications summarized in Figure 8. It can be seen that more research in the field of impedance based condition monitoring for machine elements is needed. Mostly, rolling element bearings are in the focus of this techniques.

Other EHL contact building machine elements like spur gears are not investigated deeply in this research area. All in all, the presented approaches are investigated under laboratory conditions. In general, the impedance behavior under instationary operating conditions is not researched yet, independently of its use case. Also, other lubrication regimes beside the hydrodynamic lubrication are not investigated. A transfer to real applications is missing.

## 6 Conclusion

In this review, a systematic literature review according to the PRISMA approach was fulfilled to investigate the topic of electrical impedance based condition monitoring of machine elements. Different databases were studied for literature. The articles found were screened and at the end, 20 articles and their research content were presented.

The research topic of electrical impedance based condition monitoring can be divided in three main section, the load measurement, the rolling bearing condition monitoring and the lubrication condition monitoring. The last one can further be divided into the topics of lubricant condition detection and film thickness detection. It can be seen that the focus of research is on rolling element bearings. This is not surprising, because rolling bearings are one of the central components in drivetrains. The amount of subcategories for the single application fields is interesting, because the identified opportunities for this condition monitoring approach are greater than assumed.

In addition, several research gaps are identified. Other machine elements like spur gears are not taken into account. Based on their electric behavior in the EHL regime, a similar impedance signal behavior can be possible for surface induced damages. Also, the electric properties in the mixed lubrication regime have to be investigated. For rolling element bearings, different lubrication regimes beside the hydrodynamic lubrication are not considered yet. If a damage detection in case of mixed friction is possible has to be investigated further. The influence of surface mutating additives in oil and grease lubrication might change the electric behavior under mixed lubrications in positive or negative manner, which is not considered yet. Furthermore, the presented approaches are tested under stationary operating conditions. A generalization of impedance behavior for different rotational speeds and forces for condition monitoring is missing. Further research has to identify load and speed independent signal characteristic to ensure an overall usage of impedance-based condition monitoring.

In summary, for applying electrical impedance based condition monitoring approaches of machine elements beyond laboratory, further research is necessary. Both research questions are addressed and answered by the results of this literature research. Based on these results, further research regarding impedance-based condition monitoring can be fulfilled.

## Data availability statement

The original contributions presented in the study are included in the article/Supplementary Material, further inquiries can be directed to the corresponding author.

## Author contributions

FB-D: Conceptualization, Formal Analysis, Investigation, Project administration, Supervision, Visualization, Writing–original draft. EK: Project administration, Resources, Supervision, Writing–review and editing.

## Funding

The author(s) declare that no financial support was received for the research, authorship, and/or publication of this article.

## Conflict of interest

The authors declare that the research was conducted in the absence of any commercial or financial relationships that could be construed as a potential conflict of interest.

## Publisher's note

All claims expressed in this article are solely those of the authors and do not necessarily represent those of their affiliated organizations, or those of the publisher, the editors and the reviewers. Any product that may be evaluated in this article, or claim that may be made by its manufacturer, is not guaranteed or endorsed by the publisher.

## References

Akpudo, U. E., and Hur, J.-W. (2020). A feature fusion-based prognostics approach for rolling element bearings. *J. Mech. Sci. Technol.* 34 (10), 4025–4035. doi:10.1007/s12206-020-2213-x

Barz, M. (1996). Die schmierfilmbildung in fettgeschmierten schnellaufenden spindellagern. Diss. (Hannover: Gottfried Wilhelm Leibniz Universität).

Bechev, D., Weicker, M., Schwörer, K., Dellwo, U., and Arnold, D. (2020). "Schädlicher stromdurchgang 2 forschungsvorhaben nr. 650 II," in *Methodik zur praxisnahen Charakterisierung von elektrischen Schmierstoffeigenschaften zur Verbesserung der rechnerischen Vorhersage von Lagerströmen* (Frankfurt: Forschungsvereinigung Antriebstechnik e.V).

Becker-Dombrowsky, F. M., Hausmann, M., Welzbacher, P., Harder, A., and Kirchner, E. (2023a). *Systematic identification of disturbance factors on electric characteristics of mechanical gearboxes*.

Becker-Dombrowsky, F. M., Koplin, Q. S., and Kirchner, E. (2023b). Individual feature selection of rolling bearing impedance signals for early failure detection. *Lubricants* 11 (7), 304. doi:10.3390/lubricants11070304

Beer, C. de, Barendse, P. S., and Pillay, P. (2015). Fuel cell condition monitoring using optimized broadband impedance spectroscopy. *IEEE Trans. Industrial Electron.* 62 (8), 5306–5316. doi:10.1109/TIE.2015.2418313

Boškoski, P., Debenjak, A., and Mileva Boshkoska, B. (2017). *Fast electrochemical impedance spectroscopy*. doi:10.1007/978-3-319-53390-2

Brüser, P. (1972). *Untersuchungen über die elastohydrodynamische Schmierfilmdicke bei elliptischen Hertzschen Kontaktflächen*. Braunschweig: Technische Universität Braunschweig.

Bukvić, M., Gajević, S., Skulić, A., Savić, S., Ašonja, A., and Stojanović, B. (2024). Tribological application of nanocomposite additives in industrial oils. *Lubricants* 12 (1), 6. doi:10.3390/lubricants12010006

Cameron, J. R., Thomson, W. T., and Dow, A. B. (1986). Vibration and current monitoring for detecting airgap eccentricity in large induction motors. *IEE Proc. B Electr. Power Appl.* doi:10.1049/ip-b.1986.0022

Cen, H., Bai, D., Chao, Y., Li, Y., and Li, R. (2021). EHL film thickness in rolling element bearings evaluated by electrical capacitance method: a review. *Tribology-Materials, Surfaces Interfaces* 15, 55–77. doi:10.1080/17515831.2020.1838098

Chevallier, E., Boudimbou, J. C., Bouzerar, R., Garcia, T., Bolaers, F., and Chiementin, X. (2023). *Monitoring of roller bearings: electrical vs vibrational analysis 2023*. doi:10.31224/3295

Clarke, A., Weeks, I., Evans, H. P., and Snidle, R. W. (2016). An investigation into mixed lubrication conditions using electrical contact resistance techniques. *Tribol. Int.* 93, 709–716. doi:10.1016/j.triboint.2014.10.010

Dahlke, H. (1994). *Handbuch wälzlager-technik: bauarten, gestaltung, betrieb*. 1994th ed. Wiesbaden: Springer Fachmedien.

Davies, A. (1998). "Handbook of condition monitoring," in *Techniques and methodology*. Editor A. Davies (Netherlands: SpringerDordrecht).

Deutsches Institut für Normung e.V. Wälzlager (2021). *Dynamische Tragzahlen und nominelle Lebensdauer*.

Engelhardt, R. A. (2012). "Uncertainty Mode and Effects Analysis – heuristische Methodik zur Analyse und Beurteilung von Unsicherheiten in technischen Systemen des Maschinenbaus," in *Technische universität Darmstadt* (Düsseldorf: VDI-Verlag).

Fett, M., Wilking, F., Goetz, S., Kirchner, E., and Wartzack, S. (2023). "Sensor selection and integration for Cyber-Physical Systems in context of Digital Twins – a systematic review of requirements," in 18th Annual System of Systems Engineering Conference (SoSe), 1–7. doi:10.1109/SoSE59841.2023.10178669

Furtmann, A. (2017). *Elektrisches Verhalten von Maschinenelementen im Antriebsstrang* (Hannover: Gottfried Wilhelm Leibniz Universität Hannover).

Furtmann, A., Tischmacher, H., and Poll, G. (2016). "Extended HF equivalent model of a drive train," in XXII international conference on electrical machines (ICEM): SwissTech convention center. Lausanne, Switzerland, 04-07 September, 2016 (Piscataway, NJ: IEEE), 2244–2250.

Gemeinder, Y. (2016). "Lagerimpedanz und Lagerschädigung bei Stromdurchgang in umrichtergespeisten elektrischen Maschinen," in *Technische universität darmstadt* (Bonn: Ingenieurwissenschaftlicher Verlag).

Glovnea, R., Furtuna, M., Nagata, Y., and Sugimura, J. (2012). Electrical methods for the evaluation of lubrication in elastohydrodynamic contacts. *Tribol. Online* 7 (1), 46–53. doi:10.2474/trol.7.46

Hamrock, B. J., and Dowson, D. (1981). *Ball bearing lubrication: the elastohydrodynamics of elliptical contacts*. New York: Wiley.

Harder, A., Zaiat, A., Becker-Dombrowsky, F. M., Puchtler, S., and Kirchner, E. (2022). Investigation of the voltage-induced damage progression on the raceway surfaces of thrust ball bearings. *Machines* 10 (10), 832. doi:10.3390/machines10100832

Harris, T. A. (2001). *Rolling bearing analysis*. 4th ed. New York, NY: Wiley.

Heemskerk, R. S., Vermeiren, K. N., and Dolfsma, H. (1982). Measurement of lubrication condition in rolling element bearings. *A S L E Trans.* 25 (4), 519–527. doi:10.1080/05698198208983121

Hertz, H. (1881). Über die Berührung fester elastischer Körper. *J. für die reine und angewandte Math.* 92, 156–171.

Hufschmid, M. (2021). *Grundlagen der Elektrotechnik: Einführung für Studierende der Ingenieur-und Naturwissenschaften*. Wiesbaden: Springer Vieweg.

Jablonka, K., Glovnea, R., and Bongaerts, J. (2012). Evaluation of EHD films by electrical capacitance. *J. Phys. D Appl. Phys.* 45, 385301. doi:10.1088/0022-3727/45/38/385301

Jablonka, K., Glovnea, R., and Bongaerts, J. (2018). Quantitative measurements of film thickness in a radially loaded deep-groove ball bearing. *Tribol. Int.* 119, 239–249. doi:10.1016/j.triboint.2017.11.001

Jameson, N. J., Azarian, M. H., and Pecht, M. (2017). Impedance-based condition monitoring for insulation systems used in low-voltage electromagnetic coils. *IEEE Trans. Industrial Electron.* 64 (5), 3748–3757. doi:10.1109/TIE.2017.2652359

Jardine, A. K., Lin, D., and Banjevic, D. (2006). A review on machinery diagnostics and prognostics implementing condition-based maintenance. *Mech. Syst. Signal Process.* 20, 1483–1510. doi:10.1016/j.ymssp.2005.09.012

Jiang, P., Chen, J., Jin, L., and Kumar, L. (2023). Adaptive condition monitoring for fuel cells based on fast EIS and two-frequency impedance measurements. *IEEE Trans. Industrial Electron.* 70 (8), 8517–8525. doi:10.1109/TIE.2022.3220843

Johns-Rahnejat, P. M., Rahmani, R., and Rahnejat, H. (2023). Current and future trends in tribological research. *Lubricants* 11 (9), 391. doi:10.3390/lubricants11090391

Joseph, J., and Krishnan, S. T. (2021). Development of severity and location indices based condition monitoring scheme for underground cables by impedance spectroscopy. *IEEE Trans. Power Deliv.* 36 (2), 533–543. doi:10.1109/TPWRD.2020.2984476

Keysight Technologies (2014). *Impedance measurement handbook: a guide to measurement technology and techniques*; Available at: https://www.keysight.com/de/de/assets/7018-06840/application-notes/5950-3000.pdf.

Kirchner, E. (2007). *Leistungsübertragung in Fahrzeuggetrieben: Grundlagen der Auslegung, Entwicklung und Validierung von Fahrzeuggetrieben und deren Komponenten*. Berlin, Heidelberg: Springer-Verlag Berlin Heidelberg.

Kohler, J. L., Sottile, J., and Trutt, F. C. (2002). Condition monitoring of stator windings in induction motors. I. Experimental investigation of the effective negative-sequence impedance detector. *IEEE Trans. Ind. Appl.* 38 (5), 1447–1453. doi:10.1109/TIA.2002.802935

Kraus, B., Neu, M., and Kirchner, E. (2020). *Sensing machine elements as enablers of comprehensive digitization – a review*.

Kraus, B., Schmitt, F., Steffan, K.-E., and Kirchner, E. (2021). *A valve closing body as a central sensory-utilizable component*.

Kunzelmann, B., Rycerz, P., Xu, Y., Arakere, N. K., and Kadiric, A. (2023). Prediction of rolling contact fatigue crack propagation in bearing steels using experimental crack growth data and linear elastic fracture mechanics. *Int. J. Fatigue* 168, 107449. doi:10.1016/j.ijfatigue.2022.107449

Lei, Y. (2016). *Intelligent Fault diagnosis and remaining useful life prediction of rotating machinery*. Oxford, United Kingdom: Elsevier.

Lei, Y., He, Z., and Zi, Y. (2008). A new approach to intelligent fault diagnosis of rotating machinery. *Expert Syst. Appl.* 35 (4), 1593–1600. doi:10.1016/j.eswa.2007.08.072

Liberati, A., Altman, D. G., Tetzlaff, J., Mulrow, C., Gøtzsche, P. C., Ioannidis, J. P. A., et al. (2009). The PRISMA statement for reporting systematic reviews and meta-analyses of studies that evaluate healthcare interventions: explanation and elaboration. *BMJ* 339, b2700. doi:10.1136/bmj.b2700

Loos, J., Bergmann, I., and Goss, M. (2021). Influence of high electrical currents on WEC formation in rolling bearings. *Tribol. Trans.* 64 (4), 708–720. doi:10.1080/10402004.2021.1909789

Lugt, P. M., Severt, R. W. M., Fogelström, J., and Tripp, J. H. (2001). Influence of surface topography on friction, film breakdown and running-in in the mixed lubrication regime. *Proc. Institution Mech. Eng. Part J J. Eng. Tribol.* 215, 519–533. doi:10.1243/1350650011543772

Mahlangu, S., and Barendse, P. (2021). *Online condition monitoring of fuel cells (FC) by implementing electrical impedance spectroscopy using a switch-mode DC-DC converter*, 477–482. doi:10.1109/ECCE47101.2021.9595528

Manjunath, M., Hausner, S., Heine, A., Baets, P. de, and Fauconnier, D. (2024). Electrical impedance spectroscopy for precise film thickness assessment in line contacts. *Lubricants* 12 (2), 51. doi:10.3390/lubricants12020051

Martin, G. (2021). "Die Wälzlagerimpedanz als Werkzeug zur Untersuchung von Oberflächenabweichungen in Wälzlagern," in *Technische universität darmstadt* (Darmstadt: Primary publication).

Martin, G., Becker, F. M., and Kirchner, E. (2022). A novel method for diagnosing rolling bearing surface damage by electric impedance analysis. *Tribol. Int.* 170, 107503. doi:10.1016/j.triboint.2022.107503

Maruyama, T., Maeda, M., and Nakano, K. (2019). Lubrication condition monitoring of practical ball bearings by electrical impedance method. *Tribol. Online* 14, 327–338. doi:10.2474/trol.14.327

Maruyama, T., and Nakano, K. (2018). *In situ* quantification of oil film formation and breakdown in EHD contacts. *Tribol. Trans.* 61 (6), 1057–1066. doi:10.1080/10402004.2018.1468519

Maruyama, T., Radzi, F., Sato, T., Iwase, S., Maeda, M., and Nakano, K. (2023). Lubrication condition monitoring in EHD line contacts of thrust needle roller bearing using the electrical impedance method. *Lubricants* 11 (5), 223. doi:10.3390/lubricants11050223

Mathias, J. (2016). "Auf dem Weg zu robusten Lösungen - Modelle und Methoden zur Beherrschung von Unsicherheit in den frühen Phasen der Produktentwicklung," in *Technische universität darmstadt* (Düsseldorf: VDI Verlag GmbH).

Miller, J. L., and Kitaljevich, D. (2000). "In-line oil debris monitor for aircraft engine condition assessment," in 2000 IEEE Aerospace Conference. Proceedings (Cat. No.00TH8484).

Muetze, A. (2003). "Bearing currents in inverter-fed AC-motors," in *Technische universität darmstadt* (Darmstadt: Shaker-Verlag GmbH).

Page, M. J., Moher, D., Bossuyt, P. M., Boutron, I., Hoffmann, T. C., Mulrow, C. D., et al. (2021). PRISMA 2020 explanation and elaboration: updated guidance and exemplars for reporting systematic reviews. *BMJ* 372, n160. doi:10.1136/bmj.n160

Peng, H., Zhang, H., Shangguan, L., and Fan, Y. (2022). Review of tribological failure analysis and lubrication technology research of wind power bearings. *Polym. (Basel)* 14 (15), 3041. doi:10.3390/polym14153041

Prashad, H. (1988). Theoretical evaluation of impedance, capacitance and charge accumulation on roller bearings operated under electrical fields. *Wear* 125 (3), 223–239. doi:10.1016/0043-1648(88)90115-9

Prashad, H. (2006). *Tribology in electrical environments*. Amsterdam, London: Elsevier.

Radnai, B., Gemeinder, Y., Kiekbusch, T., Weber, J., Hering, J., and Arnold, D. (2015). *Schädlicher Stromdurchgang: Untersuchung des Schädigungsmechanismus und der zulässigen Lagerstrombelastung von Wälzlagern in E-Motoren und Generatoren verursacht durch parasitäre hochfrequente Lagerströme* (Frankfurt am Main: FVA-Heft 1127, Forschungsvorhaben Nr. 650 I, Forschungsvereinigung Antriebstechnik e.V.).

Randall, R. B. (2011). "Vibration-based condition monitoring: industrial," in *Aerospace and automotive applications* (Chichester: Wiley).

Reibung Schmierung and Verschleiß (2015). Reibung, Schmierung und Verschleiß - Forschung und praktische Anwendungen. in *Gesellschaft für Tribologie* (Göttingen: GfT Gesellschaft für Tribologie e.V.).

Rinderknecht, S. (2017). *Einführung in die Mechatronik für den Maschinenbau*. Shaker: Aachen.

Rycerz, P., Olver, A., and Kadiric, A. (2017). Propagation of surface initiated rolling contact fatigue cracks in bearing steel. *Int. J. Fatigue* 97, 29–38. doi:10.1016/j.ijfatigue.2016.12.004

Schaeffler Monitoring Services GmbH (2019). *Condition Monitoring Praxis: Handbuch zur Schwingungs-Zustandsüberwachung von Maschinen und Anlagen*. 1st ed. Mainz: Vereinigte Fachverlage GmbH.

Schenk, M. (2010). *Instandhaltung technischer Systeme: Methoden und Werkzeuge zur Gewährleistung eines sicheren und wirtschaftlichen Anlagenbetriebs* (Berlin: Springer-Verlag).

Schirra, T. (2021). *Phänomenologische Betrachtung der sensorisch nutzbaren Effekte am Wälzlager – Einfluss unbelasteter Wälzkörper auf die elektrische Impedanz: UNSPECIFIED*.

Schirra, T., Martin, G., Puchtler, S., and Kirchner, E. (2021). Electric impedance of rolling bearings - consideration of unloaded rolling elements. *Tribol. Int.* 158, 106927. doi:10.1016/j.triboint.2021.106927

Schirra, T., Martin, G., Vogel, S., and Kirchner, E. (2018). "ball bearings as sensors for systematical combination of load and failure monitoring," in *Design 2018: proceedings of the 15th international design conference, may 2018, dubrovnik, Croatia*. Editors D. Marjanović, M. Štorga, S. Škec, N. Bojčetić, and N. Pavković (Zagreb: Fac: of Mechanical Engineering and Naval Architecture Univ), 3011–3022.

Schnabel, S., Marklund, P., Minami, I., and Larsson, R. (2016). Monitoring of running-in of an EHL contact using contact impedance. *Tribol. Lett.* 63 (3), 35. doi:10.1007/s11249-016-0727-2

Schneider, V., Bader, N., Liu, H., and Poll, G. (2022a). Method for *in situ* film thickness measurement of ball bearings under combined loading using capacitance measurements. *Tribol. Int.* 171, 107524. doi:10.1016/j.triboint.2022.107524

Schneider, V., Behrendt, C., Höltje, P., Cornel, D., Becker-Dombrowsky, F. M., Puchtler, S., et al. (2022b). "Electrical bearing damage," in *A problem in the nano- and macro-range*.

Schneider, V., Liu, H.-C., Bader, N., Furtmann, A., and Poll, G. (2021). Empirical formulae for the influence of real film thickness distribution on the capacitance of an EHL point contact and application to rolling bearings. *Tribol. Int.* 154, 106714. doi:10.1016/j.triboint.2020.106714

Shi, H., Zhang, H., Huo, D., Yu, S., Su, J., Xie, Y., et al. (2022). An ultrasensitive microsensor based on impedance analysis for oil condition monitoring. *IEEE Trans. Industrial Electron.* 69, 7441–7450. doi:10.1109/tie.2021.3100982

Steinhilper, W. and Sauer, B. (2012a). *Konstruktionselemente des Maschinenbaus 2: Grundlagen von Maschinenelementen für Antriebsaufgaben*. 7th ed. (Berlin, Heidelberg: Springer Berlin Heidelberg).

Steinhilper, W. and Sauer, B. (2012b). *Konstruktionselemente des Maschinenbaus 1: Grundlagen der Berechnung und Gestaltung von Maschinenelementen*. 8th ed. (Berlin: Springer Vieweg).

Thomson, W. T., and Barbour, A. (1998). "On-line current monitoring and application of a finite element method to predict the level of static airgap eccentricity in three-phase induction motors," in IEEE Transactions on Energy Conversion. (IEEE), 347–357.

Tischmacher, H. (2017). Systemanalysen zur elektrischen Belastung von Wälzlagern bei umrichtergespeisten Elektromotoren. Dissertation. (Hannover: Gottfried Wilhelm Leibniz Universität Hannover).

Tischmacher, H., and Gattermann, S. (2012). Multiple signature analysis for the detection of bearing currents and the assessment of the resulting bearing wear. in International Symposium on Power Electronics Power Electronics, Electrical Drives, Automation and Motion. 1354–1359.

Tuomas, R., and Isaksson, O. (2009). Measurement of lubrication conditions in a rolling element bearing in a refrigerant environment. *Industrial Lubr. Tribol.* 61, 91–99. doi:10.1108/00368790910940419

Vorwerk-Handing, G. (2020). "Erfassung systemspezifischer Zustandsgrößen – Physikalische Effektkataloge zur systematischen Identifikation potentieller Messgrößen," in *Technische universität darmstadt* (Darmstadt: Publisher's Version).

Xie, K., Liu, L.-C., Li, X.-P., and Zhang, H.-L. (2016). Non-contact resistance and capacitance on-line measurement of lubrication oil film in rolling element bearing employing an electric field coupling method. *Measurement* 91, 606–612. doi:10.1016/j.measurement.2016.05.080

Yang, Y., Danyluk, S., and Hoeprich, M. (2000). A study on rolling element skew measurement in a tapered roller bearing with a specialized capacitance probe. *J. Tribol.* 122 (3), 534–538. doi:10.1115/1.555397

Zeng, L., Wang, W., Rogers, F., Zhang, H., Zhang, X., and Yang, D. (2020). A high sensitivity micro impedance sensor based on magnetic focusing for oil condition monitoring. *IEEE Sensors J.* 20 (7), 3813–3821. doi:10.1109/JSEN.2019.2958872

Zhang, P., Zheng, D., and Lu, G. (2022). The effect and compensation of phase angle deviation along the winding for the online stator insulation condition monitoring. *IEEE Trans. Industrial Electron.* 69 (8), 8440–8451. doi:10.1109/TIE.2021.3108730

Zheng, D., Lu, G., and Zhang, P. (2021). A noninvasive interturn insulation condition monitoring method based on the common-mode impedance spectrum of inverter-fed machines. *IEEE Trans. Ind. Appl.* 57 (5), 4786–4795. doi:10.1109/TIA.2021.3094176

frontiers | Frontiers in Mechanical Engineering

TYPE Original Research
PUBLISHED 21 August 2024
DOI 10.3389/fmech.2024.1456575

Check for updates

OPEN ACCESS

EDITED BY
Satoru Maegawa,
Nagoya Institute of Technology, Japan

REVIEWED BY
Fengshou Gu,
University of Huddersfield, United Kingdom
Milan Bukvic,
Faculty of Engineering, University of Kragujevac, Serbia

*CORRESPONDENCE
Florian Koetz,
florian.koetz@tu-darmstadt.de

RECEIVED 28 June 2024
ACCEPTED 06 August 2024
PUBLISHED 21 August 2024

CITATION
Koetz F, Schmitt F, Kirchner E and Zancul E (2024) Visualising the lubrication condition in hydrodynamic journal bearings using impedance measurement.
*Front. Mech. Eng.* 10:1456575.
doi: 10.3389/fmech.2024.1456575

COPYRIGHT
© 2024 Koetz, Schmitt, Kirchner and Zancul. This is an open-access article distributed under the terms of the Creative Commons Attribution License (CC BY). The use, distribution or reproduction in other forums is permitted, provided the original author(s) and the copyright owner(s) are credited and that the original publication in this journal is cited, in accordance with accepted academic practice. No use, distribution or reproduction is permitted which does not comply with these terms.

# Visualising the lubrication condition in hydrodynamic journal bearings using impedance measurement

Florian Koetz[1]*, Florian Schmitt[1], Eckhard Kirchner[1] and Eduardo Zancul[2]

[1]Institute for product development and machine elements, Technical University of Darmstadt, Darmstadt, Germany, [2]Department of Production Engineering, Escola Politécnica da Universidade de São Paulo, São Paulo, Brazil

**Introduction:** The demand to increase reliability and reduce maintenance costs drives the search for new condition monitoring solutions of machines. Bearings are of special interest in this matter as they are main contributors to machine downtime. Therefore, this article investigates the electric behavior of a hydrodynamic journal bearing using impedance measurement.

**Methods:** For that purpose measurements are taken in boundary lubrication, mixed lubrication and hydrodynamic lubrication of a hydrodynamic journal bearing. In order to interpret the behaviour observed in these measurements, a phenomenological model is developed using the quantitative working space model. The measurement results are also interpreted using analogies to the Stribeck curve as a known tribological model. Additionally, measurements in mixed lubrication are analysed in detail.

**Results:** These measurements show that the electric behaviour of journal bearings changes significantly within the mixed lubrication regime. This change in behaviour shows three distinct states within mixed lubrication which helps to identify destructive operating conditions. Furthermore, the measurements potentially allow the detection of deformation or damage of the bearing in mixed lubrication.

**Discussion:** The quantitative analysis of the electric behaviour of journal bearings is possible in the mixed lubrication regime and can be used in future to extract condition and operating information from a system during operation.

KEYWORDS

**journal bearing, condition monitoring, in-situ measurement, impedance measurement, quantitative working space model**

## 1 Introduction

Within the context of energy crises, efficiency increases emerge as a major requirement for most technical systems. Moreover, retrofitting existing systems, especially productive or energy converting plants, is of great interest for industry and research (Jaspert et al., 2021). As existing technical systems of large scale lack the efficiency of recently developed systems, it is a promising approach to integrate additional functionalities into the system to either increase the efficiency by operating in the most efficient conditions or to prevent damage

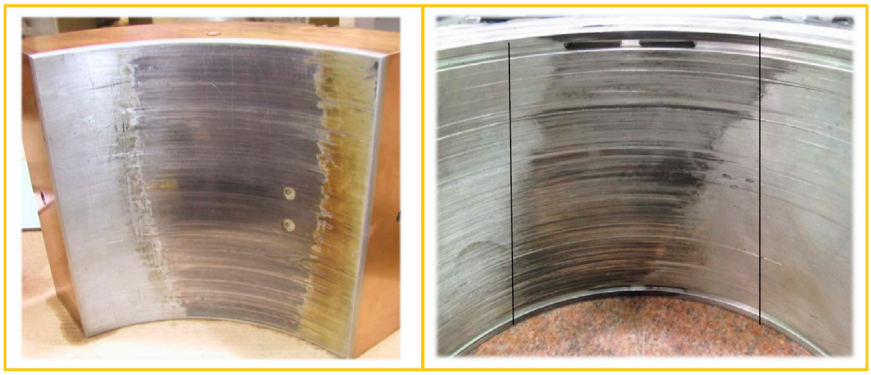

FIGURE 1
Journal bearing segment; left: wear due to operation in mixed lubrication; right: wear due to tilted shaft during operation (Branagan, 2015)

due to unexpected failure of components (Mourtzis et al., 2020). The approach of functional integration as a measure of optimization and increase of reliability drives the research field of condition monitoring (CM). New products as well as existing systems are a focus of research and industry in order to implement CM functions (Surucu et al., 2023). The advancing digitisation of engineering products enables the much needed more reliable and precise solutions for CM (Baszenski et al., 2023). These CM solutions have to provide at least the minimum information necessary to detect and diagnose wear and component failure in the system (Tavner et al., 2008). While some failures can only be detected after their occurrence, others show a time variant behavior (e.g., due to the accumulation of wear) making the prediction of future machine failures especially promising.

Bearings are of special interest for condition monitoring as they show a varying behavior over their lifetime, and their failures are one of the main contributors to machine downtime (Amirat et al., 2009; Dą et al., 2015). Bearing applications comprise a number of characteristics, making them a promising option for implementing various CM functions (Saruhan et al., 2014). Bearings are load carrying elements and, therefore, naturally in the flow of force, which is often function determining and a valuable source of condition information. As bearings run in a variety of operating conditions ranging from high load applications in mixed lubrication to high speed applications in hydrodynamic lubrication, the occurring wear becomes an inherent aspect of their behavior and varies over time and lubrication condition. Additionally, the dimensioning of technical systems is often determined by the dimensioning of bearings and their maintenance cycles. Figure 1 depicts two examples of hydrodynamic bearing segments showing different wear scenarios. The left image is the result of the operation in mixed lubrication, causing significant wear of the gliding surface. This ultimately results in bearing failure and consequently in machine downtime and possibly additional damage to the machine due to increased temperature, wear of the shaft, and vibrations. The right image illustrates the situation of a tilted shaft, visible in the tilted wear pattern. The effects of this wear scenario are similar and have to be avoided in order to avoid a potential bearing or system failure.

Regarding the realization of CM functions, the measurement of state variables, such as temperature or pressure of, e.g., gaseous media, within the system's critical subsystems is a prerequisite (Vorwerk-Handing et al., 2018). A measurement as close as possible to the quantity of interest is called *in situ* measurement (Kraus et al., 2021). Many publications outline the outstanding suitability of bearings for the monitoring of machines as the behavior of bearings is a steady time variant function of the state of wear. Therefore, this behavior can be used as an indicator for the remaining useful life (Okoh et al., 2014) and the need for maintenance. For instance, Manjunath et al. (2024) describe not only the relevance of monitoring bearing conditions for rolling element bearings, but exploring condition monitoring strategies using the impedance of the bearing and the temperature. Both are quantities that are easy to measure compared to measuring the film thickness directly. Other publications such as Fett et al. (2024) show a practical application of the sensor bearing concept in industrial context based on a case study. The influence of material choice is addressed by Kandeva et al. (2016) and Pastukhov and Timashov, (2023). While the importance of monitoring bearing operating and wear condition as a research field becomes apparent based on these publications, the way how to implement a reliable monitoring strategy remains obscure. Bearings can be used to implement reliable measurement functions without altering the predefined and standardized interfaces of machine elements and thus maintaining the same design as a conventional sole mechanical system. The resulting components are referred to as sensing machine elements (Vorwerk-Handing et al., 2020). According to Vorwerk-Handing et al. (2020) both rolling element bearing and hydrodynamic journal bearings can be classified as sensory utilizable machine elements as both machine elements show a capacitive electrical behavior. This inherent electric behavior can be measured to provide information about the state of the system.

These bearing types are common in mechanical systems and the choice between them is often ambiguous. Both hydrodynamic journal bearings and rolling element bearings can operate in a wide range of applications (Childs, 2019). However, hydrodynamic journal bearings offer distinct advantages over rolling element bearings in terms of assembly space and durability in applications with limited start-stop operations and high rotation rates, such as in aircraft turbines (Mokhtari Molk Abadi, 2020), steam turbines (aus der Wiesche and Joos, 2018; Pennacchi and Tanuma, 2022) and ship drive trains (Weychardt

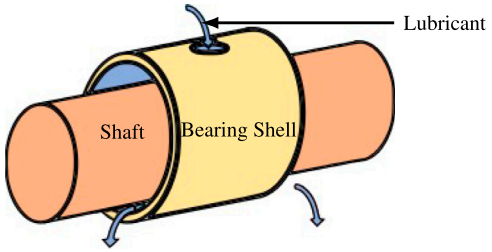


FIGURE 2
Schematic view of a journal bearing.

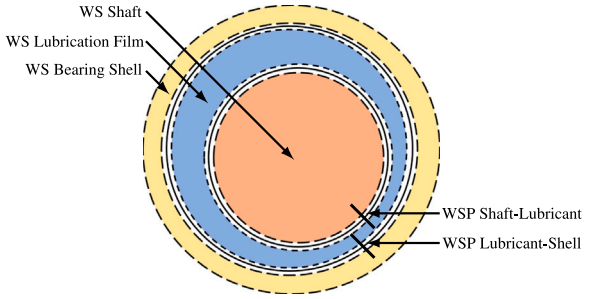


FIGURE 3
Basic working space model for a journal bearing.

et al., 2008). Applications like the ones mentioned benefit from accurate CM solutions that detect dangerous operating conditions before a bearing failure occurs in order to prevent long downtime and ensure the safety of the system.

Therefore, the objective of this contribution is to generate the basis for a CM approach for journal bearings as central components of safety-critical systems, such as aircraft turbines. However, present condition monitoring approaches for journal bearings focus on the detection of already occurred wear (Mokhtari Molk Abadi, 2020). To this point, the classification of the operating conditions based on the electric properties of journal bearings is limited to the description of hydrodynamic lubrication as done by Prashad (Prashad, 1991; Prashad and Rao, 1994; Prashad, 2006) and Furtmann, (2017). However, the detection of mixed lubrication is not discussed as it is assumed that the metal-to-metal contact would invalidate all models of the capacitive behavior of the bearing. It is therefore assumed that the differentiation between hydrodynamic and mixed lubrication is possible as a binary decision. While this differentiation is of considerable value to avoid a high friction coefficient in the boundary lubrication regime, it lacks any kind of information of the mixed lubrication regime. As many high-load applications are constantly or partly operated in mixed lubrication conditions, this regime is of considerable interest.

As the current state of research does not provide a consistent model describing the electric behavior of journal bearings operated in mixed lubrication, this contribution thrives to develop an explanatory approach of how mixed lubrication would propagate over an increasing relative speed of the contact surfaces and how the electric behavior of the bearing is affected by the varying lubrication conditions. To address the lack of information regarding the mixed lubrication regime, a new, volume-based modeling approach, called quantitative working space model (qWSM), is utilized to describe the lubrication film as a three-dimensional space where the physical domains of mechanics, hydrodynamics, and electrostatics interact.

The qWSM is a system representation based on three-dimensional sub-volumes of the observed systems, called working spaces (WS), and it derives the behavior of the supersystem as a function of connected subsystems or working spaces. The behavior of a working space is described by balancing conservation quantities introduced into the working space, e.g., energy, mass or charge. Additionally, the effects of conservation quantities affecting the state of a working space are described, such as the increasing temperature of the lubricant due to friction energy for the working space "lubricant film" (Schmitt and Kirchner, 2022; Schösser et al., 2022). A schematic view of the bearing arrangement is depicted in Figure 2 while a simple qWSM is depicted in Figure 3.

The principles of the qWSM applied to the journal bearing system help to derive an explanatory approach for the electric behavior observed at a journal bearing test rig while operated in a variety of lubrication conditions, ranging from solid state friction throughout the mixed lubrication regime to a hydrodynamic lubrication state. Two mixed lubrication models are derived from the qWSM which offer alternative explanation approaches for effects observed in measurements as described in section 3. This way, the contribution provides new insights in the electrical characteristics of journal bearings within the mixed lubrication regime.These insights are intended to enable users to develop new condition monitoring solutions based on the electric behavior of hydrodynamic journal bearings focusing on the mixed lubrication regime. The visualisation of the operating conditions in mixed lubrication by means of the impedance can be used to optimise the operating strategies. It further allows the detection of improper operating conditions and thus mitigating damage during these operations. The objective of this contribution can therefore be summed up as: *Deriving a new approach to visualize and model the lubrication conditions of hydrodynamic journal bearings.*

The following research hypotheses addressing this objective are underlying this research and will be verified throughout this publication.

H1: *The qWSM serves as a modeling approach to derive a new model of mixed lubrication in hydrodynamic journal bearing in an electric circuit*

H2: *The electric behavior of journal bearings can be described with a continuous function over the relative surface speed rather than a binary distinction between ohmic and capacitive behavior*

In order to evaluate present research approaches on journal bearing CM, the qWSM, and system modeling, the state of research is discussed in the following section.

## 2 Materials and methods

In this section, firstly, the state of research about CM and the electrical behavior of journal bearings is presented. Secondly, the

modeling approach using the quantitative working space model is explained. Thirdly, the journal bearing test bench used for this contribution is described and modelled. Finally, potential modeling approaches for mixed lubrication are outlined.

## 2.1 State of research

Recent publications show that CM is an increasingly important topic to optimise maintenance strategies, improve machine availability, and increase the interconnectivity of machines in relation to Industry 4.0 (Fritz et al., 2001; Tavner et al., 2008; Amirat et al., 2009; Goyal et al., 2019; Baszenski et al., 2023; Sanchez-Londono et al., 2023). Bearings are of special interest for CM as their failure results in downtime and often expensive maintenance (Dą et al., 2015; Rolink et al., 2020). Two established solutions for failure detection are temperature monitoring and acoustic monitoring (Fritz et al., 2001; AlShorman et al., 2021; Baszenski et al., 2023). Both methods can detect faults in a bearing, however, information about the remaining useful life (RUL) cannot be obtained easily (AlShorman et al., 2021). Both approaches are usually applied within corrective maintenance strategies, when a bearing fault has already occurred but before it leads to an increasingly critical failure in adjoining components of the system. An alternative strategy for CM in rolling element bearings consists of using the bearing's impedance as a measurand. The impedance is dependent on the lubrication film thickness and therefore on temperature, bearing load and rotational rate. These state variables can supply information about the bearing's operating state and condition (Jablonka et al., 2018; Maruyama et al., 2019; Schirra et al., 2019; Schneider et al., 2022; Puchtler et al., 2023). However, this research is limited to rolling element bearings and recent publications do not cover the electric behavior of journal bearings.

Another advantage of measuring the impedance of the bearing is that the measuring takes place *in situ* of the process that needs to be assessed. *In-situ* measuring has become increasingly important in recent years with the demand for precise and reliable sensor data (Kraus et al., 2021). Measuring a measurand directly at the point of interest allows the reduction of disturbances and improves data quality (Kraus et al., 2021). Thus, the sensor placement in relation to the process that needs to be measured has to be considered when implementing a measurement strategy (Goyal et al., 2019). However, the majority of existing technical systems have not been designed to provide sufficient, accurate, and reliable information about the system (Vorwerk-Handing, 2021). Moreover, the fitting of additional sensors to machines is often difficult and does not allow the ideal sensor placement. Even in newly designed systems, the available installation space often does not allow the integration of sensors in close proximity to the point of interest (Vorwerk-Handing et al., 2018). The measurement of the bearing impedance does not require the integration of an additional sensor and thus circumvents the problem. In terms of integration complexity, measuring the impedance requires only the insulation of either the bearing's outer ring or the shaft and an individual contact for each electric potential. Thus the insulation can be challenging as well but potentially allows more flexibility in finding appropriate solutions.

Journal bearings and rolling element bearings generally overlap in their use cases. However, journal bearings have advantages over rolling element bearings especially in applications with limited packaging space, rare stoppages, and high rotational rates due to their higher efficiency and smaller dimensions compared to rolling element bearings. Examples of these use cases are steam turbines, aircraft turbines, ship drive trains, and recently also main bearings of wind turbines (aus der Wiesche and Joos, 2018; Pennacchi and Tanuma, 2022; Weychardt et al., 2008; Mokhtari Molk Abadi, 2020; Rolink et al., 2020; Rolink et al., 2022). In the first three use cases, the failure of the bearing directly impacts the safety of the steam turbine, aircraft or shipping vessel and thus CM equipment is important. In the latter case, the failure of a wind turbine main bearing may not pose a threat to human life but causes long downtime and financial losses (Dą et al., 2015; Peng et al., 2023). Additionally, information about the lubrication condition of journal bearings can be obtained by the impedance measurement and thus allows the operator to detect and avoid wear-intensive and inefficient operating conditions such as mixed lubrication.

The operation in mixed lubrication leads to a higher abrasion within the bearing and should thus be avoided as it affects the otherwise very low wear in hydrodynamic bearings compared to rolling bearings. However, the operation in mixed lubrication can not be avoided totally for hydrodynamic bearings, especially when they are facing transient operating conditions during run up or high dynamic loads. Therefore, recent publications investigate mixed lubrication models, in order to describe the mechanical behavior in the mixed lubrication regime more accurately or to derive certain design solutions fit to mitigate the effects of operation in mixed lubrication (Xiao et al., 2021; Guo et al., 2022; Patel et al., 2022; Tang et al., 2023). CM strategies that can detect failures in journal bearings, are among others, the aforementioned temperature and acoustics related fault detection strategies (Fritz et al., 2001; AlShorman et al., 2021; Baszenski et al., 2023). However, they can only detect faults after they have occurred. In order to assess operating conditions and the remaining useful life of the bearing, additional sensors are required to measure load, ambient temperature and rotational rates. With this sensor information an assessment of the remaining useful life can be made (Okoh et al., 2014).

The most critical failure modes of journal bearings occur in relation to mixed lubrication where the corresponding wear is usually caused by insufficient lubrication (Muzakkir et al., 2015). Using the impedance of the bearing for CM offers the chance to directly gain information about the lubrication film thickness and the state of the lubricant over the bearing's lifetime. If, for example, viscosity stabilizing additives are slowly used up over the bearing's lifetime, a reduction of lubrication film thickness would be detected before a failure of the lubricant occurs. Furthermore, the impedance of the bearing is dependent on the bearing load (Furtmann, 2017). Therefore, measuring the impedance allows a qualitative and potentially quantitative assessment of the bearing load.

The capacitive behavior of journal bearings has been known for decades, as described by Prashad, (2006) and Bittner and Kluth, (1995). One addition to Prashad's work is the work of Furtmann, (2017) who extends the capacitive equation of journal bearings with tilt angles. However, Furtmann only covers the electrical behavior and neglects the effects that the tilting has on the hydrodynamic

behavior of the bearing. Furthermore, these publications do not create a relation between CM and the journal bearing impedance. Instead they exclusively focus on the electric behavior of the bearing. The work of Furtmann, Prashad and Bittner et al. is of relevance regarding the electrification of automotive drive trains, which also involves electric leakage currents that can damage bearings and need to be investigated. But this does not take advantage of the CM potential of the electric behavior of the bearing.

In order to analyse the literature in this field, a systematic literature review has been performed using "Web of Science". The string used in "Web of Science" was *capacitance journal bearing OR capacity journal bearing and electric*. This resulted in 32 results which were screened using the abstract. Additionally, google scholar was used to extend the results using the string *capacitance* "*journal bearing*" which resulted in 2,280 results. Of these results, 100 were selected according to their fit to the string and title screened. After this screening 16 results remained which were screened using their abstract. After reviewing the abstracts of the literature found, the literature regarding the load capacity of journal bearings in electrical machines or similar results were discarded as this does not fall into the scope of this contribution. Additionally, eight papers deal with the use of magnetorheological fluids in active journal bearings (Nikolakopoulos and Papadopoulos, 1997; Peng and Zhu, 2006; Bouzidane and Thomas, 2008; Lee, 2015; Zapoměl and Ferfecki, 2021; Kardoudi et al., 2022; Zapoměl and Ferfecki, 2022; Singh et al., 2023). In these papers magnetic fields are used to influence the local viscosity of the lubricant which is not within the scope of this contribution. Two papers cover the electrical damaging of journal bearings as a result of shaft voltages. Other papers offer works on electrical damaging of journal bearings which is also not in the scope of this article (Prashad and Rao, 1994; Muetze, 2010; Golkhandan and Torkaman, 2021). Two works also cover the electric coupling through hydrodynamic journal bearings but do not address condition monitoring opportunities (Dai et al., 2017; Dai et al., 2019). Prashad presents multiple theoretical works on the capacitance of journal bearings (Prashad, 1991) and evaluations of dynamics on two-lobe (Prashad, 1996) and multi-lobe (Prashad, 2006) journal bearings. However, these remain theoretical and do not work towards condition monitoring solutions. Furthermore, the mixed lubrication regime is not covered by these contributions. Similarly, Cui et al. (2014), Cho et al. (1999), Kataoka et al. (2012) and Paranjpe et al. (2000) deal with the measurement of the lubrication film thickness in journal bearings using the electrical capacitance. But they do not cover the systematic behaviour of journal bearings, nor the behaviour in the mixed lubrication regime, nor condition monitoring applications.

The reviewed literature shows a lack of coverage of condition monitoring approaches for journal bearings using the capacitance. Investigating the potential of utilizing the electrical behavior of journal bearings for CM and measurements of the lubrication state and operational parameters is the purpose of this paper. In order to evaluate this potential, a systematic understanding of the electric behaviour of the journal bearing in different lubrication regimes has to be supported. For this purpose, measurements are taken on an existing journal bearing test bench and analyzed. Furthermore, a quantitative working space model of the test bench is created to allow the phenomenological explanation of the behaviour observed in the measurements.

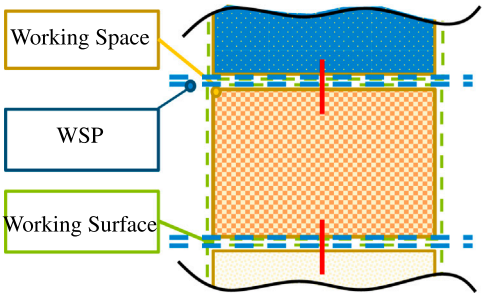


FIGURE 4
Model elements of a qWSM.

## 2.2 Quantitative working space model

The tool that is used to derive the electric model of the journal bearing is the qWSM. This modelling approach uses finite volumes, so-called working spaces, that are distributed throughout the system that is being modelled, which can contain fluids and solids. In the first iteration, the geometry of the working spaces (WS) can resemble the geometry of the individual parts. In later iterations, it may be beneficial to use smaller volumes where needed, leading to a higher resolution by subdividing the working spaces. Between each working space the working space surfaces interact and form working surface pairs (WSP). This interaction is characterized by any kind of energy flow that can be electrical, mechanical, thermal, or volumetric. Therefore, functions can only be conducted, if a WSP is formed, as every functional relation requires a form of energy exchange. In essence, each working space can be considered a subsystem of the overall system with a subsystem boundary. The overall system can be analysed by analysing the energy flow via the WSPs and identifying intended flows, unintended flows, and intended but missing flows. These different categories of energy flow result in intended functions, malfunctions and so-called non-functions. The detection of non-functions by identifying an energy flow is a unique mechanism of the qWSM in the context of product development. The model elements of the qWSM are illustrated in Figure 4.

The quantitative description of the qWSM is achieved by assigning state variables to each WS. State variables are typically quantities such as pressure, charge or temperature of the WS' contents but can also represent more abstract quantities like the lubrication state. Furthermore, coupling equations based on the conservation of energy are assigned to the WSPs as coupling conditions. With these variables and coupling conditions, the state equation of each WS can be formulated dependent on the coupling variables. The resulting model represents the system with state equations and coupling equations for each WS and WSP respectively. The underlying theory is that the state of the overall system can be derived by calculating the state of each individual WS and their interaction (Schmitt and Kirchner, 2022). Assessing uncertainties within the specifications of the detailed embodiment using the qWSM are addressed within (Schmitt et al., 2023) for the example of additively manufactured cooling channels, e.g., used to realize advanced cooling strategies of water-jacked cooled electric drives. Thus, the qWSM provides a modelling

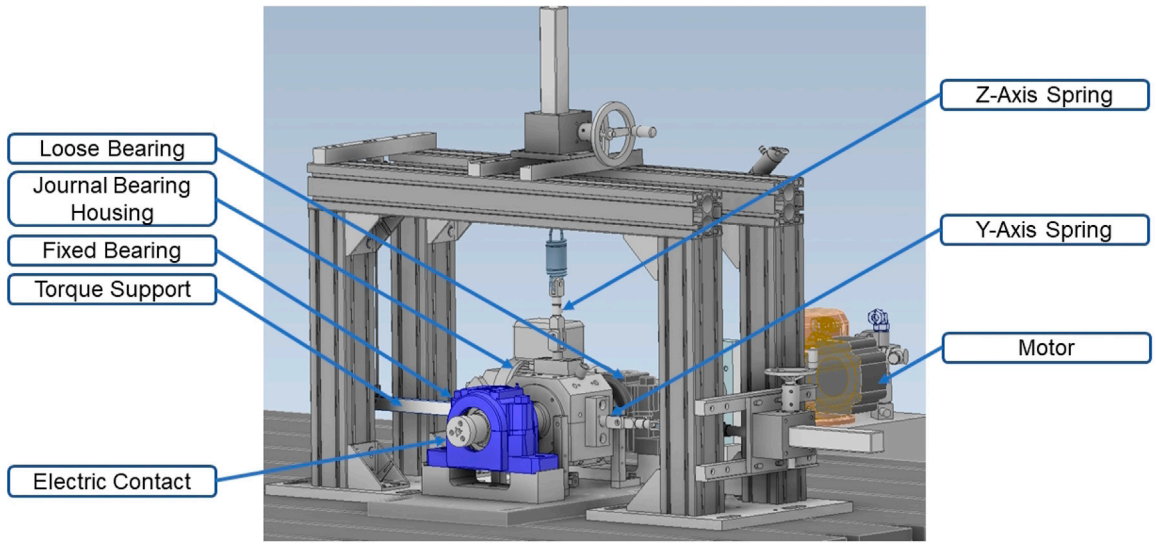


FIGURE 5
Journal bearing test bench.

approach to characterize energy based functions as well as system inherent properties such as surface roughness.

It allows the assessment of varying surface qualities on the system behavior, which becomes of significant relevance for journal bearing applications both for the determination of the detachment point as well as the characterization of mixed lubrication operation and thus is applicable as a model element of the journal bearing qWSM.

## 2.3 Journal bearing test bench

In the following section first the mechanical setup and thereafter the electrical setup of the journal bearing test bench is described.

### 2.3.1 Mechanical setup

The test bench used to operate the journal bearing for measurements is depicted in Figure 5. The test bench consists of a shaft that is supported by two spherical rolling element bearings and powered by an electric motor. The journal bearing is located between the spherical rolling element bearings inside a free swinging housing. The housing is supported only by two spring mechanisms in $z$ and $y$ direction and by a torque stanchion. In real applications of journal bearings, the bearings are used to support a shaft. The weight of the shaft and process-induced forced causes a compressive force in the bottom of the journal bearing. At the test bench applying a tensile force onto the journal bearing housing is necessary to mimic the compressive force inside the journal bearing in real applications. For the purpose of applying tensile forces, the spring mechanisms in $z$ and $y$ direction are used. The torque stanchion only supports the frictional torque inside the journal bearing. The operating parameters measured in the test bench are the horizontal and vertical forces at the spring mechanisms, the force measured at the torque support, the temperature of the journal bearing shell and the position of the journal bearing housing relative to the shaft using four eddy-current sensors. With this setup the test bench is able to operate at up to 1500 $rpm$, between 300 $N$ and 1500 $N$ vertical and horizontal load, with oil temperatures between 30°$C$ and 60°$C$.

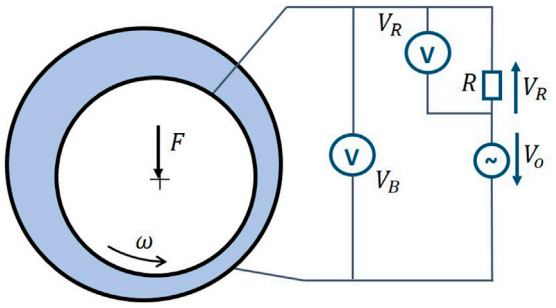


FIGURE 6
Measurement setup of the journal bearing test bench.

### 2.3.2 Electrical setup

The purpose of the test bench is to measure the electrical behaviour of the journal bearing. Therefore, the bearing is connected to an electrical circuit as shown in Figure 6. The electrical circuit is a serial connection between a voltage generator, a reference resistor, the journal bearing housing, the shaft, the electric contact element and again the signal generator. The electrical behaviour can be expected to be capacitive in hydrodynamic lubrication. Therefore, an AC voltage needs to be generated to measure the impedance of the bearing. The frequency and amplitude selection for the voltage signal has to be picked in accordance with an optimization problem. An increase in voltage amplitude may

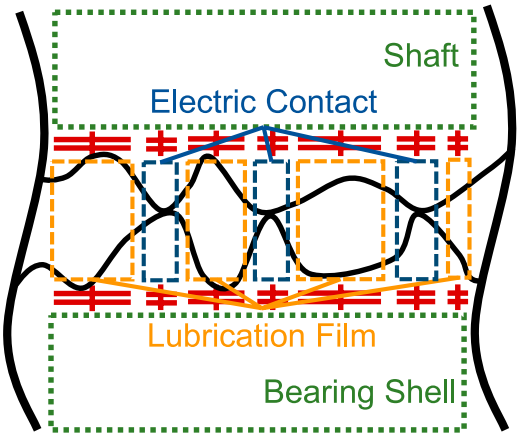


FIGURE 7
Microstructural Working Space model.

result in discharge despite the oil film which may cause damage to the bearing. Therefore, the voltage should be minimised. However, this makes the signal more sensitive to disturbance voltages from the environment. An assessment of the disturbance voltages in the system results in a maximum disturbance voltage of 200 $mV$. The peak voltage is therefore selected to be 2 $V$ in order to limit the influence of disturbance voltages to a maximum of 10% of the signal voltage. The frequency of the AC voltage influences the impedance of the bearing. An increase in frequency lowers the impedance of the bearing and makes the system again more susceptible to disturbances from the outside. In order to analyse the voltage signals measured at the test bench, a Fast-Fourier-Transformation (FFT) is used as explained in section 3. A decrease in frequency lowers the accuracy of the FFT analysis of the measurements due to the reduced frequency resolution. The voltage frequency selected according to this optimization problem is 10 $kHz$.

Lastly, the magnitude of the reference resistor $R$ needs to be selected. The resistor should be as low as possible to make the measurements more sensitive to changes in the impedance of the bearing. It also needs to be high enough to allow the signal generator to generate the 2 $V$ peak when the bearing shows virtually no impedance due to metal to metal contact. The resistance of the reference resistor selected after testing is 1500 Ω. The resulting circuit can be considered a voltage divider between the reference resistor and the journal bearing as long as all other parts of the circuit show a resistance that is significantly smaller than the bearing and the resistor. As measurements show, the combined resistance of the test bench parts is less than 3 Ω and therefore significantly smaller than the impedance of the bearing or the resistance of the resistor. Consequently, the circuit is assumed to be an ideal voltage divider between the journal bearing and the reference resistor.

In order to calculate the impedance of the bearing, the voltage drop over the bearing $V_B$ and the voltage drop over the reference resistor $V_R$ are measured. With the known resistance of the resistor, the impedance of the bearing can be calculated using Equation 1 with the bearing impedance $Z_B$, the reference resistance $R$ as well as the voltage drop over the bearing and the resistor $V_B$ and $V_R$.

$$\frac{Z_B}{R} = \frac{V_B}{V_R} \tag{1}$$

## 2.4 Modelling mixed lubrication using the qWSM

This section presents two approaches that allow the electrical modelling of the journal bearing using the qWSM. In literature, the modelling of mixed lubrication is usually presented through stochastic modelling (Dobrica and Fillon, 2013). The deterministic finite element modelling of mixed lubrication is possible but impractical for large surface applications due to the necessity to map the surface roughness of the contact surfaces. Figure 7 shows the proposed micro-structural model that can accommodate a stochastic surface roughness model. In this model, the metal to metal contact can be represented with one working space each. These working spaces are expected to show a resistive behavior. However, these contact surfaces are expected to carry foreign particles and oil residue. Therefore, the calculation of the resistance of these contact surfaces is currently not possible due to the complexity of the contaminated contact (Vinaricky, 2016). The sections with hydrodynamic lubrication can be described with another working space each. These working spaces are expected to show a capacitive behavior dependent on the distance between the two surfaces and can be modelled as a capacitor. The distribution and number of electric contact working spaces can be calculated stochastically using the models of Greenwood and Williamson (Greenwood and J, 1966) as well as Patir and Cheng (Patir and Cheng, 1979).

However, the measurement results in Section 3.1 show a dynamic electrical behavior that is generally operating with high impedances. These high impedances are frequently disrupted by low impedances. As a result of this observation, a time-varying working space model for mixed lubrication is proposed and depicted in Figure 8. This model largely follows the logic of Heemskerk et al. (Heemskerk et al., 1982) who introduced the percent contact time (PCT) value when measuring the impedance of ball bearings. In this time-varying model, it is assumed that the lubrication condition can exist in either of two states. In state 0 (Figure 8A), it is assumed that boundary lubrication occurs with the asperities of the two contacting surfaces being in direct mechanical contact with each other. This results in a low impedance. In state 1 (Figure 8B), the bearing operates in hydrodynamic lubrication.

To apply these states the time line can be split into constant time windows. To differentiate between the two states, a probability $\chi_0$ can be defined which describes the likelihood that a time window shows boundary lubrication according to state 0. The counter-probability $\chi_1$ describes the likelihood that a time window shows hydrodynamic lubrication according to state 1. The probabilities depend on the operating conditions of the journal bearing, such as the rotation rate $n$, the temperature $T$ and the bearing load $F$. At high rotation rates, for example, the probability $\chi_1$ tends towards 1 as the journal bearing would operate purely in the hydrodynamic regime. The average bearing impedance $Z_{avg}$ can then be calculated using Equation 2 with the impedances in state 0 $Z_0$ and state 1 $Z_1$.

$$Z_{avg} = \chi_0 \cdot Z_0 + \chi_1 \cdot Z_1 \tag{2}$$

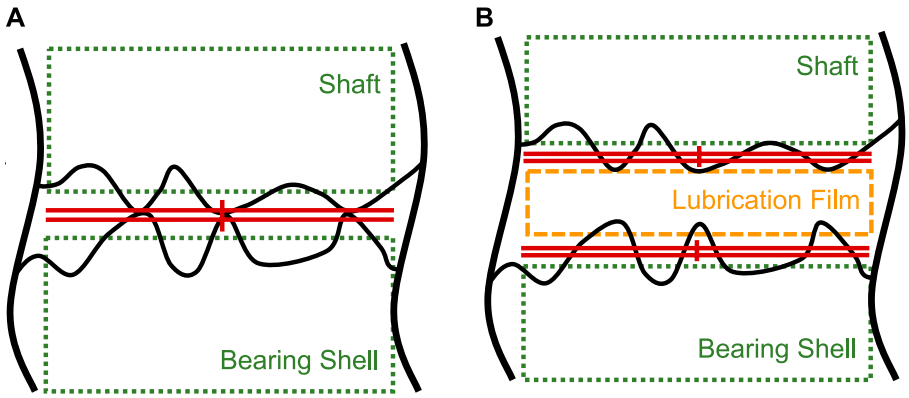


FIGURE 8
Timed Working Space model for **(A)** the state of contact and **(B)** the state of hydrodynamic lubrication.

The impedance of the bearing during the time windows of hydrodynamic lubrication $Z_1$ can be determined numerically. The impedance of the bearing in the boundary lubrication $Z_0$ windows cannot be calculated as the operating conditions resemble a contaminated electrical contact (Vinaricky, 2016). However, for rotational rates close to the release point, it can be approximated that the time windows in boundary lubrication show an impedance $Z_0$ of 0 Ω due to the significantly lower impedance during boundary lubrication compared to hydrodynamic lubrication. The resulting model is able to describe a highly dynamic lubrication condition with a frequently disrupted lubrication film. The average of this behaviour would result in the same average as can be achieved with the stochastic model. However, the stochastic model fails to describe interruptions in the lubrication film that can be observed in section 3.

# 3 Results

In the following section the experimental results will be described. Initially an example measurement will be described to explain the analysis process. Thereafter, the results are taken into context of the known tribological behaviour of journal bearings. Furthermore, the results in mixed lubrication are analysed in detail and interpreted using the qWSM. Each operating condition presented in this contribution has been investigated three times in random order to ensure no statistical inaccuracies in the behaviour. The results presented in this section are a selection of the measurements to improve readability and are representative of the behaviour observed in each of the three test runs.

## 3.1 Determination of the lubrication regime

The measurements in this section are taken over the whole operating regime of the journal bearing including boundary lubrication, mixed lubrication and hydrodynamic lubrication. For the measurements the voltage drops over the bearing $V_B$ and over the reference resistor $V_R$ according to Figure 6 are measured. The voltage signals are alternating with an input peak voltage $V_0$ of 2 $V$ and a frequency of 10 $kHz$. Each voltage is measured with a frequency of 10 $MHz$. For post processing of the measured signals, a FFT is used. The measured voltage signals are first divided into time windows of 0.001 s with 10,000 data points each. Using these 10,000 data points a FFT is performed for each time window. The FFT result at 10 $kHz$ for both voltages is then used to calculate the impedance $Z_B$ of the bearing using the equations for a voltage divider (see Equation 1) with the reference resistance $R$, the voltage drop over the reference resistance $V_R$ and the voltage drop over the bearing $V_B$.

Figure 9 shows the results for the FFT, with each point plotted being the result of one time window. For each measurement, the resulting amplitude of the voltage signals over the reference resistor and the bearing is plotted. Additionally, the phase angle between both voltages is plotted. When the bearing is behaving like a capacitor, the expected phase shift is −90°. From these data points, the bearing impedance is calculated and also plotted. Lastly, the frequency spectrum of the impedance is shown. The operating parameters like oil temperature, bearing load and rotation rate of the bearing were picked to allow the detection of boundary, mixed and hydrodynamic lubrication conditions within the operating range of the test bench. The rotation rates picked for Figure 9 are exemplary for each of the lubrication regimes.

Figure 9A shows the behavior of the bearing at 100 $rpm$. During the operation with a relatively low speed, the expected lubrication condition is boundary lubrication. In this case, the voltage amplitude of the reference resistor is nearing 2 $V$ while the voltage drop over the bearing is almost 0 $V$ as the bearing is not behaving like a capacitor due to the missing lubrication film. The phase shift is about 0°, however, due to the relatively low impedance of the bearing, this calculation is inaccurate and at times shows positive phase angles. These positive phase angles hint at disturbance currents induced by adjacent electric fields. The frequency spectrum of the bearing impedance also does not show any significant information. In Figure 9C the measurements are shown for 700 $rpm$. At this speed the bearing is operating in

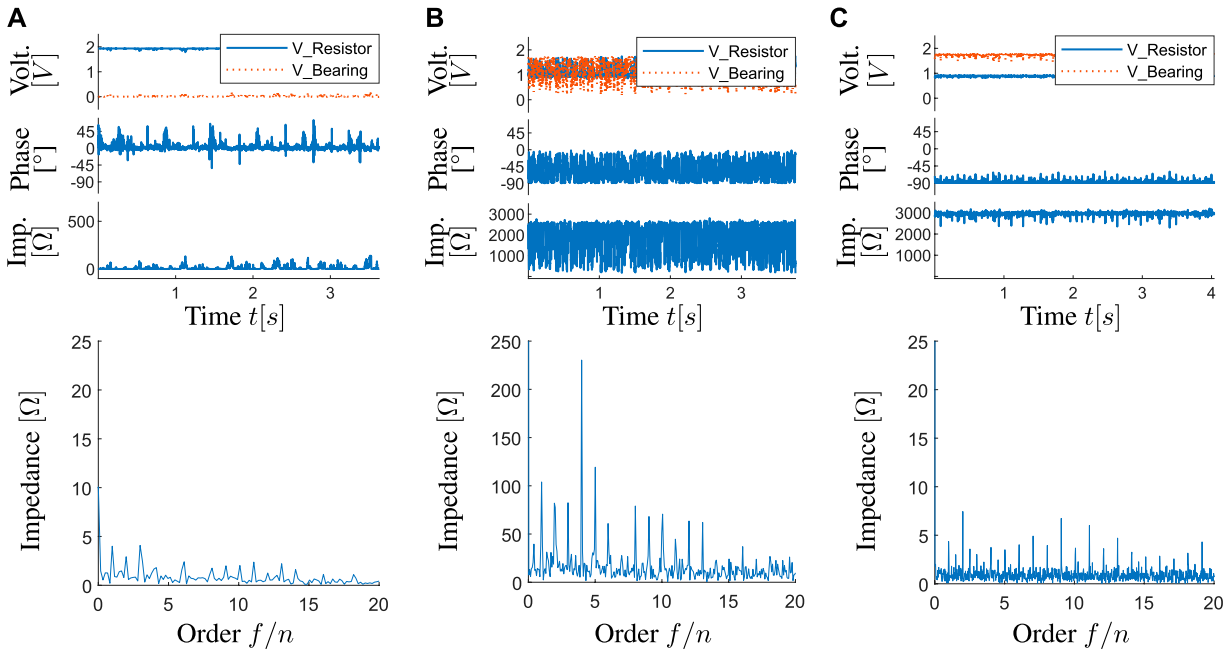


FIGURE 9
Measurement results for 1500 N vertical load, 30°C oil temperature and **(A)** 100 *rpm*, **(B)** 250 *rpm*, **(C)** 700 *rpm*.

hydrodynamic lubrication. In this condition, the bearing is behaving similarly to a capacitor as the phase shift of −90° shows. As a result of the increased bearing impedance, the bearing is now the dominant resistance in the circuit. Additionally, the frequency spectrum of the impedance shows a peak at 11.52 $Hz$ which can be identified as the rotation frequency of the shaft.

Figure 9B) shows the bearing behavior at 250 $rpm$. At this rotation rate of the shaft, the bearing is operating in mixed lubrication. This is indicated by the highly dynamic phase angle that switches between −90° and 0° at a high frequency. The bearing impedance and voltage amplitudes show the same behavior. Additionally, the frequency spectrum shows a noisy impedance signal with distinct frequencies. The first identifiable frequency is at 4.22 $Hz$ with the other frequencies being the harmonics of it. The frequency of 4.22 $Hz$ corresponds to the rotation frequency of the shaft. This measurement suggests that in mixed lubrication condition the bearing is briefly operating in hydrodynamic lubrication but the lubrication film breaks down frequently. The frequency spectrum suggests that this breakdown is most likely occurring at roughly the frequency of each shaft rotation. One explanation for this behavior is that the roundness deviation of the shaft leads to this phenomenon. Ebermann and Prase, (2019) have discovered that roundness deviations lead to a significant decrease in lubrication film thickness. For relatively low rotation rates the reduction of lubrication film thickness could be sufficient to temporarily cause boundary lubrication in the bearing. Consequently, the assumption is that whenever the point of maximum roundness deviation is traversing the point of minimum lubrication film thickness, the reduction in lubrication film thickness is sufficient to cause temporary boundary lubrication.

## 3.2 Interpretation of results using the known stribeck model

Figure 10 shows the mean and standard deviation of the measured impedance's presented in Figure 9 for varying rotation rates at a constant temperature and load. Given this experimental data a good qualitative fit of the measured impedance and the well known model of the Stribeck curve can be observed. This shows a qualitative correlation between the electrical impedance and the lubrication condition within lubricated contacts. This correlation is inverse as the impedance of the bearing increases with increasing revolutions while the friction coefficient decreases with an increase in revolutions until reaching the detachment point. However, this observation is only valid until the detachment point. After the detachment point the impedance signal continues to increase with an increase in revolutions while the friction coefficient reaches its minimum at the detachment point.

It can further be observed that the standard deviation in the mixed lubrication regime remains significant. Considering the measurements presented in Figure 9, it can be assumed that the lubrication regimes can be determined by mainly using the standard deviation as a determining factor. This is due to the standard deviation increasing in mixed lubrication and tending towards zero in boundary and hydrodynamic lubrication. The absolute impedance of a journal bearing on the other hand is dependent on bearing dimensions and the electrical properties of the lubricant. However, a precise detachment point cannot be determined as the reduction in standard deviation from mixed lubrication to hydrodynamic lubrication is continuous and not sudden.

It is further noteworthy, that the observed detachment point of the journal bearing used in this contribution is determined to be at 700 $rpm$ which is significantly later than expected considering

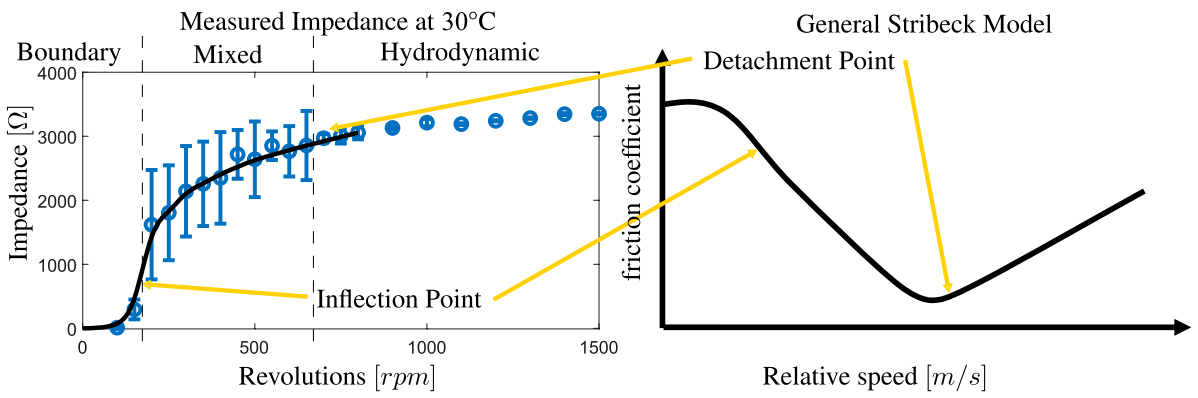


FIGURE 10
Comparison of the measured impedance and standard deviation of the Journal bearing test bench and the Stribeck model according to (Cabrera, 2024) for a run up test at 30°C oil temperature and 10 *kHz* electric frequency.

bearing dimensions and load conditions. At this point the reason for this cannot be determined. On the one hand it is possible that the impedance measurement detects even individual contacts that would otherwise go unnoticed with other condition monitoring methods. On the other hand even the low voltages can cause electrical breakdown that do not necessarily need metal to metal contact. However, so far no damage as a result of electrical breakdowns could be observed at the test bench.

An additional problem of the impedance measurement is that the clear distinction of individual points, i.e., detachment point, is not possible. Instead the measurements show a gradual reduction of standard deviation and a gradual reduction of individual contacts while increasing the rotation rate of the shaft. It is therefore not possible to clearly identify the transition point from boundary lubrication to mixed lubrication and from mixed lubrication to hydrodynamic lubrication using the measurements taken for Figures 9, 10. In the traditional Stribeck model the detachement point is usually described to be reached when the lubrication film thickness reaches three times the root mean square (RMS) of the surface roughness. However, depending on the book or paper, sometimes the ratio between the film thickness and RMS surface roughness is mentioned to be 1.5, 2, 2.5 or 3. This hints at the fact that even in the traditional Stribeck model the change from mixed lubrication to hydrodynamic lubrication is continuous. However, within one lubrication regime a distinction between the regimes can be made according to Figure 9.

## 3.3 Results in mixed lubrication

In this section the electrical behaviour of the journal bearing in the mixed lubrication regime will be analysed in more detail. For this purpose Figure 11 shows measurements taken between 150 $rpm$ and 650 $rpm$ similar to Figure 9. As a basis to determine whether the measurements shown in this section are in mixed lubrication, the results can be compared to Figure 9A at 100 $rpm$. In Figure 9A the phase angle can be determined to be at 0° with occasional positive phase angles due to inaccuracies and electrical disturbances as discussed in section 3.1. In comparison to that Figure 11A at 150 $rpm$ shows a distinctly different behaviour with only occasional positive phase angles. The impedance of the bearing at 150 $rpm$ also shows higher values than at 100 $rpm$. The reduction in phase angle cannot be explained with a simple increase in the contact resistance as this would be an ohmic resistance. Instead the change in phase angle and the increase in impedance show that the bearing has now started entering mixed lubrication.

Some uncertainty lies with the phase angles of up to −30° with a corresponding impedance peak $Z_{Bearing}$ of up to 1000 Ω. This phase angle is defined by Equation 3 and the magnitude of the impedance by Equation 4 and would thus indicate an ohmic resistance inside the journal bearing $R_{Bearing}$ of 1154 Ω (and an impedance as a result of the capacitive behaviour of 1999 Ω). However, the only variable resistance inside the bearing is the ohmic contact resistance combined with the constant metallic resistance of all conductive parts. The constant metallic contact resistance was determined to be < 3 Ω when stationary. This result would imply that the ohmic resistance has increased by more than a factor of 300 which seems unrealistically high. However, calculating the ohmic resistance analytically is not possible due to foreign layers of oxides and oil additives and therefore, the increase of the contact resistance can't be discarded as an explanation.

An alternative hypothesis is the effect that the FFT has on the measurement results. In order to perform the FFT, the measured voltages are divided into time windows of 1 *ms*. If the journal bearing shows partially hydrodynamic and partially ohmic behaviour in the time window, the FFT would create an average of both states. Assuming that in an exemplary time window the bearing shows 0.33 *ms* of hydrodynamic lubrication with an idealized phase angle of −90° and an impedance of 3000 Ω but also 0.66 *ms* of boundary lubrication with a phase angle of 0° and an impedance of 3 Ω, then the resulting average is an impedance of 1000 Ω and an average phase angle of −30°. However, at this point this hypothesis can't be proven.

Another noteworthy difference between Figure 9A at 100 $rpm$ and Figure 11A at 150 $rpm$ is the fact that the rotational frequency of the shaft is visible in the voltage and impedance signal. This is

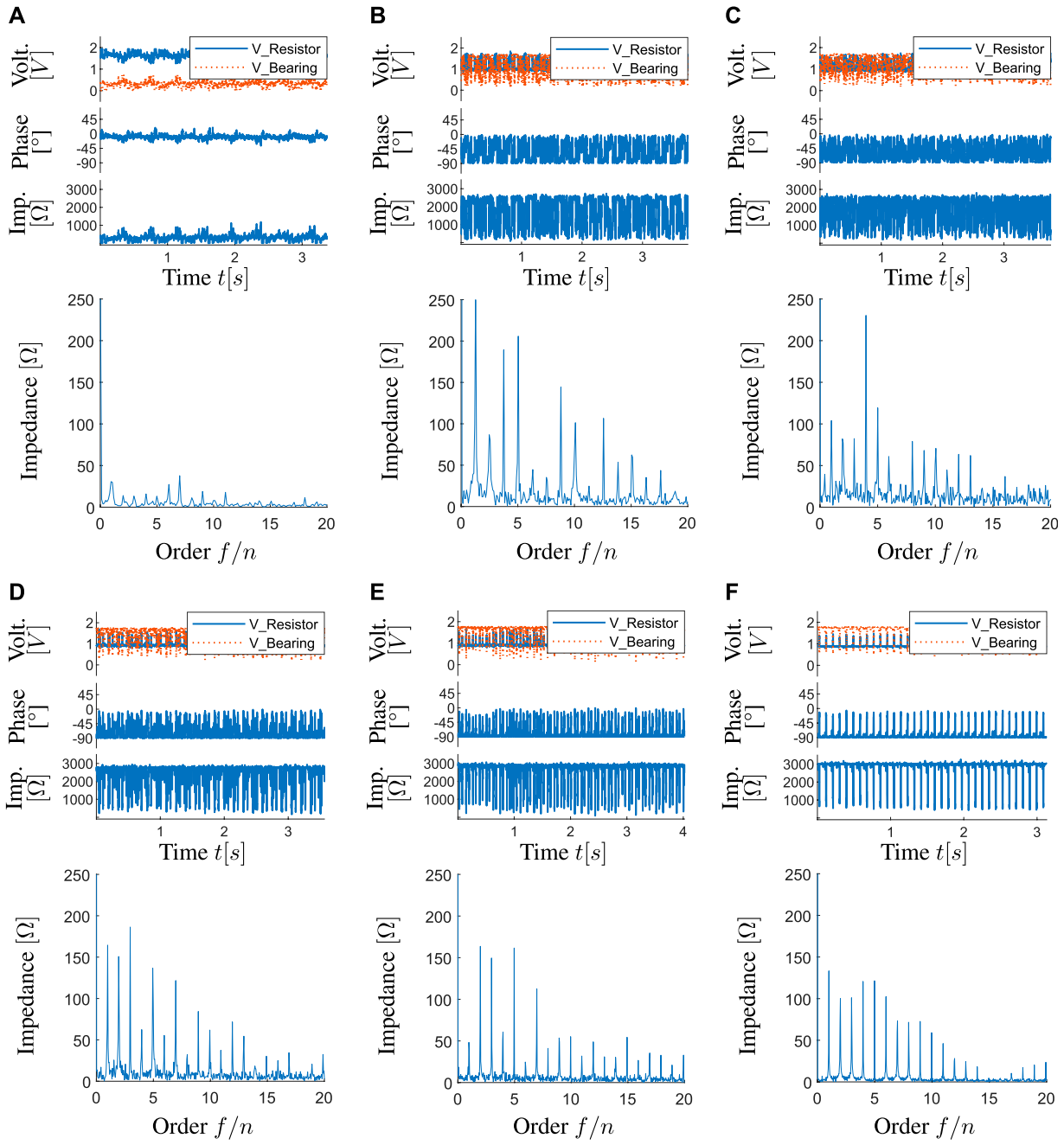


FIGURE 11
Measurement results for 1500 N vertical load, 30°C oil temperature and **(A)** 150 *rpm*, **(B)** 200 *rpm*, **(C)** 250 *rpm*, **(D)** 400 *rpm*, **(E)** 500 *rpm*, **(F)** 650 *rpm*.

reinforced by the order spectrum of the impedance signal. It is worth noting that the order spectrum of the impedance signal of journal bearings in general only shows the rotational frequency of the shaft and its harmonics. This is opposed to impedance measurements taken at ball bearings that show multiple, distinctly different frequencies due to their number of parts. In the case of the journal bearing at 150 $rpm$ (Figure 11A) the impedance signal shows that once per rotation the lubrication condition improves as the higher impedance indicates. However, this improvement cannot be sustained for a full rotation. A further increase in rpm in Figure 11B shows that the peak impedance of 2700 Ω is reached frequently at 200 $rpm$. However, this state still can't be sustained and is interrupted temporarily with the rotation frequency of the shaft. The order spectrum additionally shows more distinct sidebands with the individual peaks which indicates a noisier signal than at lower rpms.

This general behaviour does not change with higher rpms at 250 $rpm$ c.f. Figure 11C), 400 $rpm$ (Figure 11D) and 500 $rpm$ (Figure 11E). However, it can be observed that an increase in rpm results in more measurement points at the impedance peak of

roughly 2900 Ω and less measurement points below 1000 Ω. Likewise the phase angle also tends more towards −90°. It can therefore be assumed that the lubrication condition further improves and the overall time of metallic contact reduces. The sidebands also reduce in amplitude with an increase in rpm as a result of less noise and more stable lubrication conditions.

The measurement with the highest rpm in mixed lubrication (Figure 11F) at 650 $rpm$ shows almost no sidebands. At this rpm the rotation frequency of the shaft is clearly visible even in the impedance signal which shows that exactly once per rotation the lubrication film is interrupted. It was shown by Ebermann Prase, (2019) that this can be the result of manufacturing defects and roundness deviations which reduce the lubrication film.

$$\varphi = \tan \frac{R_{Bearing}}{Z_{Bearing}} \tag{3}$$

$$Z_{total} = \frac{Z_{Bearing} \cdot R_{Bearing}}{\sqrt{Z_{Bearing}^2 + R_{Bearing}^2}} \tag{4}$$

Due to the distinctly different electrical behaviour of the bearing depending on the relative speed, it may be possible to divide the mixed lubrication regime in multiple electrical regimes. In Figure 11A for example, the impedance signal shows a periodic behaviour. In this case the impedance is somewhere between the impedance during boundary lubrication and hydrodynamic lubrication. On the other hand, Figure 11B shows an oscillating behaviour with an increasing amount of hydrodynamic lubrication at higher relative speeds. A further increase in relative speed in Figure 11F shows a reduction in noise but a periodic disruption of the lubrication film. According to Figure 10 this result at 650 $rpm$ still displays a high standard deviation, however, 11f does not display a lot of noise. This can only be observed by looking at the measurement result in detail as opposed to measurements taken between 200 $rpm$ and 500 $rpm$ which show a high standard deviation as well as more noisy signals. Therefore, the division of mixed lubrication in three regimes between 150 $rpm$ and 200 $rpm$, as well as 500 $rpm$ and 650 $rpm$ seems possible.

## 4 Discussion

In summary, this contribution aims to visualise and model the lubrication condition of hydrodynamic journal bearings based on the qWSM and impedance measurements. For this purpose, a journal bearing test bench was operated at constant load and varying speeds. The results show that the impedance measurement is suitable for visualising the lubrication regime of journal bearings. The expected capacitive behaviour of the bearing in hydrodynamic lubrication can be confirmed. The literature assessed in the introduction and state of research is limited to investigations of the electric behaviour of the bearing in hydrodynamic lubrication with the underlying assumptions that the capacitive modelling approach is not suitable for metal to metal contact. This can partially be confirmed as metal to metal contact produces resistive-capacitive behaviour instead of pure capacitive behaviour. However, important qualitative observations can be made even during periods of partial metal to metal contact. The impedance measurement in journal bearing is therefore further suited to observe the behaviour of the bearing in mixed lubrication and allows further interpretation (as discussed in section 3.3). As a result of the detailed analysis of the measurements taken in the mixed lubrication regime, the mixed lubrication regime can be classified into three distinctly different regimes with averaging behaviour (Figure 11A), noisy-oscillating behaviour (Figures 11B–E) and oscillating behaviour Figure 11F.

In order to explain the behaviour of the bearing, the quantitative working space model is used based on the phenomenological observations with the time varying model and based on the state of the art with the microstructural model. Each of these models can be equally valid for condition monitoring approaches as the microstructural model seems more suitable for the aforementioned averaging behaviour while the time-varying model seems more suitable for the oscillating behaviour. H1 can therefore be verified as the qWSM can describe and visualise the electrical behaviour of the journal bearing in all lubrication regimes. Whether the model will be able to support prediction or condition monitoring calculations for the electrical behaviour will have to be investigated in the future. It will also have to be investigated, whether influence factors on the electrical behaviour can be quantified using the qWSM modelling approach. One question that can't be answered currently is whether the measured phase angles of, e.g., −30° are a result of a partially capacitive and partically resistive behaviour of the journal bearing within a measured time window or whether they are representing the actual ratio between resistance and capacitance in the bearing. With the current measurement method the FFT prevents an increase in time resolution beyond 1 $ms$ because an increase in time resolution results in a decrease in frequency resolution. This decrease in frequency resolution also decreases the accuracy of the measured impedance.

One solution to this problem could be a measurement with DC-voltages or offset AC-voltages in which the FFTs of the voltage signals are not required to detect metal to metal contact. This way the frequency resolution of the FFT is no longer a limitation and the time resolution is represented directly by the measurement frequency of the voltages. Alternatively, a curve fitting method could be used to fit a known sine signal to the measured signal which has the potential to improve the time resolution compared to an FFT analysis. In any case, the duration of a single contact within a time window will have to be investigated in future. The measurement results further prove that observing the electric behaviour of journal bearings continuously does not only allow a distinction between ohmic and capacitive behaviour, but it further allows the classification of the mixed lubrication regime. It also allows an assessment of whether the bearing displays averaging, noisy-oscillating or oscillating behaviour. The corresponding state according to the Stribeck curve could therefore be determined more closely using the electrical behaviour observed in this contribution. With this knowledge, small changes in the operating strategy can be made based on the behaviour observed to avoid unintended and unobserved abrasive wear or to improve the lubrication. H2 is therefore also proven right. Further developing descriptive models and the corresponding qWRM could improve the precision of the state determined according to the Stribeck curve.

The main problem with determining the lubrication regime is the difficulty to identify transition points. The results in Figures 9, 11

show different behaviours and measurement results of the bearing. However, the change between the different states is gradual and an individual point cannot be identified. The identification of an individual point, i.e., the detachment point, cannot be made at this time. The definition of a transition point can in theory be made using features like standard deviation according to Figure 10 but this definition is arbitrary and does not explain phenomenological differences between the different types of behaviours displayed by the bearing during measurements. But it may be sufficient depending on the monitoring application. As was pointed out in section 3.2, even analysis based on the friction coefficient according to Stribeck may not allow the identification of transition points between lubrication regimes.

Despite the difficulty to identify the transition point between lubrication regimes and different behaviours in mixed lubrication with the known Stribeck-model, the continuous observation of changes in the electrical behaviour of the journal bearing is possible. Lubrication conditions can deteriorate over time due to physical and chemical processes in the lubricant or due to physical wear of the bearing. Continuously monitoring the electrical behaviour would allow the detection of this deterioration before the detachment point is reached. When operating in mixed lubrication the deterioration could be observed by detecting an increase in the noise level of the oscillating behaviour or by detecting a change from oscillating behaviour to averaging behaviour in the bearing. Which features are suitable to detect changes in the electrical behaviour over time will have to be investigated in the future.

Further research in future will also include quantifying the qWSM models presented in this contribution which can help to describe the electrical behaviour of this bearing. The expansion of these models may allow even prediction of the state of operation of the bearing and assessments about expected bearing behaviour in different operating conditions. It may further allow the developing of wear models and predictive maintenance concepts if the behaviour of the bearing can be predicted to a sufficient accuracy. In this context it is also necessary to answer the question, whether impedance measurement can be beneficial compared to other monitoring solutions (i.e., temperature monitoring) in terms of building space, cost and observation accuracy. Especially cost is an unknown factor in impedance measurement as the electrical insulation required to refit a system with impedance measurement equipment may be negligible or extremely costly and complex depending on the machine and application.

An additional observation of this contribution is that the oscillating behaviour observed indicates roundness deviations as described by Ebermann Prase, (2019). This detection of the suspected roundness deviation or potential damage could further improve the knowledge provided by the measurement of the electrical impedance. This knowledge could improve condition monitoring approaches. It is already possible to mark individual contacts by observing the electrical behaviour. It could also be possible to develop a theory of damage accumulation based on the number of contacts observed under a certain load, speed and temperature for predictive maintenance. However, this possibility will have to be investigated in the future.

## Data availability statement

The raw data supporting the conclusions of this article will be made available by the authors, without undue reservation.

## Author contributions

FK: Conceptualization, Data curation, Investigation, Software, Validation, Visualization, Writing–original draft, Writing–review and editing. FS: Conceptualization, Investigation, Methodology, Project administration, Supervision, Writing–original draft, Writing–review and editing. EK: Funding acquisition, Resources, Writing–original draft, Writing–review and editing. EZ: Writing–original draft, Writing–review and editing.

## Funding

The author(s) declare that financial support was received for the research, authorship, and/or publication of this article. The authors thank the Deutsche Forschungsgemeinschaft (DFG, German Research Foundation), which funded the presented research within the project “Opportunities and limits of the working space model in product development” Funded by the Deutsche Forschungsgemeinschaft (DFG, German Research Foundation) – 443578519.

## Conflict of interest

The authors declare that the research was conducted in the absence of any commercial or financial relationships that could be construed as a potential conflict of interest.

## Publisher’s note

All claims expressed in this article are solely those of the authors and do not necessarily represent those of their affiliated organizations, or those of the publisher, the editors and the reviewers. Any product that may be evaluated in this article, or claim that may be made by its manufacturer, is not guaranteed or endorsed by the publisher.

## References

AlShorman, O., Alkahatni, F., Masadeh, M., Irfan, M., Glowacz, A., Althobiani, F., et al. (2021). Sounds and acoustic emission-based early fault diagnosis of induction motor: a review study. *Adv. Mech. Eng.* 13, 168781402199691. doi:10.1177/1687814021996915

Amirat, Y., Benbouzid, M., Al-Ahmar, E., Bensaker, B., and Turri, S. (2009). A brief status on condition monitoring and fault diagnosis in wind energy conversion systems. *Renew. Sustain. Energy Rev.* 13, 2629–2636. doi:10.1016/j.rser.2009.06.031

S. aus der Wiesche and F. Joos (2018). *Handbuch dampfturbinen: grundlagen, konstruktion, betrieb* (Cham: Springer Fachmedien Wiesbaden and Springer International Publishing AG). doi:10.1007/978-3-658-20630-7

Baszenski, T., Kauth, K., Kratz, K.-H., Gutiérrez Guzmán, F., Jacobs, G., and Gemmeke, T. (2023). Sensor integrating plain bearings: design of an energy-autonomous, temperature-based condition monitoring system. *Forsch. Im. Ingenieurwes.* 87, 441–452. doi:10.1007/s10010-023-00642-1

Bittner, H., and Kluth, T. (1995). Gleitlagerdiagnose mittels magnetfeldmessungen. *Tm. - Tech. Mess.* 62, 346–351. doi:10.1524/teme.1995.62.jg.346

Bouzidane, A., and Thomas, M. (2008). An electrorheological hydrostatic journal bearing for controlling rotor vibration. *Comput. and Struct.* 86, 463–472. doi:10.1016/j.compstruc.2007.02.006

Branagan, L. (2015). Survey of damage investigation of babbitted industrial bearings. *Lubricants* 3, 91–112. doi:10.3390/lubricants3020091

Cabrera, F. (2024). *Electric vehicle tribology: challenges and opportunities for a sustainable transportation future*. auflage edn (Amsterdam: Elsevier Series on Tribology and Surface Engineering Series), 1.

Childs, P. R. N. (2019). *Mechanical design engineering handbook*. second edition edn (Oxford and Cambridge, MA: Butterworth-Heinemann).

Cho, M.-R., Han, D.-C., and Choi, J.-K. (1999). Oil film thickness in engine connecting-rod bearing with consideration of thermal effects: comparison between theory and experiment. *J. Tribol.* 121, 901–907. doi:10.1115/1.2834153

Cui, Z., Yang, C., Sun, B., and Wang, H. (2014). Liquid film thickness estimation using electrical capacitance tomography. *Meas. Sci. Rev.* 14, 8–15. doi:10.2478/msr-2014-0002

Dąbrowski, D., and Natarajan, A. (2015). Assessment of gearbox operational loads and reliability under high mean wind speeds. *Energy Procedia* 80, 38–46. doi:10.1016/j.egypro.2015.11.404

Dai, J., Hagen, S. S., and Ludois, D. C. (2017). *Linear motion system cable elimination via multiphase capacitive power transfer through sliding journal bearings*, 2157–2164. doi:10.1109/APEC.2017.7930998

Dai, J., Hagen, S. S., and Ludois, D. C. (2019). High-efficiency multiphase capacitive power transfer in sliding carriages with closed-loop burst-mode current control. *IEEE J. Emerg. Sel. Top. POWER Electron.* 7, 1388–1398. doi:10.1109/JESTPE.2018.2845385

Dobrica, M. B., and Fillon, M. (2013). "Mixed lubrication," in *Encyclopedia of tribology* (Boston, MA: Springer), 2284–2291. doi:10.1007/978-0-387-92897-5_27

Ebermann, B. H. A., and Prase, M. (2019). *Influence of geometric shape defects on operating parameters in cylindrical journal bearings*. doi:10.1115/IMECE2019-10179

Fett, M., Puchtler, S., Zaiat, A., Bock, M., Melzer, C., Hoffmann, F., et al. (2024). Practical implementation of the sensory utilization of rolling bearing impedance measurement: a case study in machine tool spindle bearings. *Tribol. Trans.*, 1–11doi. doi:10.1080/10402004.2024.2370902

Fritz, M., Burger, W., and Albers, A. (2001). *Schadensfrüherkennung an geschmierten Kontakten mittels schallemissionsanalyse (karlsruhe)*. doi:10.5445/IR/5782002

Furtmann, A. (2017) "Elektrisches Verhalten von Maschinenelementen im Antriebsstrang,". Hannover: Gottfried Wilhelm Leibniz Universität Hannover. Ph.D. thesis. doi:10.15488/8972

Golkhandan, R. K., and Torkaman, H. (2021). Reduction of induced shaft voltage and bearing current in turbo generators: modeling, compensation, and practical test. *IEEE Trans. Industrial Electron.* 68, 4362–4372. doi:10.1109/TIE.2020.2985006

Goyal, D. V., Pabla, B. S., and Dhami, S. S. (2019). Non-contact sensor placement strategy for condition monitoring of rotating machine-elements. *Eng. Sci. Technol. Int. J.* 22, 489–501. doi:10.1016/j.jestch.2018.12.006

Greenwood, J., and J, B. P. W. (1966). Contact of nominally flat surfaces. *Proc. R. Soc. Lond. Ser. A. Math. Phys. Sci.* 295, 300–319. doi:10.1098/rspa.1966.0242

Guo, H., Bao, J., Zhang, S., and Shi, M. (2022). Experimental and numerical study on mixed lubrication performance of journal bearing considering misalignment and thermal effect. *Lubricants* 10, 262. doi:10.3390/lubricants10100262

Heemskerk, R. S., Vermeiren, K. N., and Dolfsma, H. (1982). Measurement of lubrication condition in rolling element bearings. *A S L E Trans.* 25, 519–527. doi:10.1080/05698198208983121

Jablonka, K., Glovnea, R., and Bongaerts, J. (2018). Quantitative measurements of film thickness in a radially loaded deep-groove ball bearing. *Tribol. Int.* 119, 239–249. doi:10.1016/j.triboint.2017.11.001

Jaspert, D., Ebel, M., Eckhardt, A., and Poeppelbuss, J. (2021). Smart retrofitting in manufacturing: a systematic review. *J. Clean. Prod.* 312, 127555. doi:10.1016/j.jclepro.2021.127555

Kandeva, M., Karastoyanov, D., Assenova, E., Jakimovska, K., Simeonov, S., and Vencl, A. (2016). The influence of the valena metal-plating additive on tribotechnical characteristics of the steel–bronze tribological system. *J. Frict. Wear* 37, 187–190. doi:10.3103/S1068366616020082

Kardoudi, M., Nabhani, M., and El Khlifi, M. (2022). Non-Newtonian couple stress lubrication of mhd elastic journal bearings. *Industrial Lubr. Tribol.* 74, 753–762. doi:10.1108/ILT-11-2021-0456

Kataoka, T., Kikuchi, T., and Ashihara, K. (2012). Measurement of oil film thickness in the main bearings of an operating engine using thin-film electrode. *SAE Int. J. Fuels Lubr.* 5, 425–433. doi:10.4271/2011-01-2117

Kraus, B., Schmitt, F., Steffan, K.-E., and Kirchner, E. (2021). A valve closing body as a central sensory-utilizable component. *Procedia CIRP* 100, 109–114. doi:10.1016/j.procir.2021.05.018

Lee, Y.-B. (2015). Behavior analysis of controllable electrorheology fluid plain journal bearings. *J. Dyn. Syst. Meas. CONTROL-TRANSACTIONS ASME* 137. doi:10.1115/1.4029369

Manjunath, M., Hausner, S., Heine, A., de Baets, P., and Fauconnier, D. (2024). Electrical impedance spectroscopy for precise film thickness assessment in line contacts. *Lubricants* 12, 51. doi:10.3390/lubricants12020051

Maruyama, T., Maeda, M., and Nakano, K. (2019). Lubrication condition monitoring of practical ball bearings by electrical impedance method. *Tribol. Online* 14, 327–338. doi:10.2474/trol.14.327

Mokhtari Molk Abadi, N. (2020) "Überwachung hydrodynamischer Gleitlager basierend auf der Körperschallanalyse,". Technische Universität Berlin. Dissertation.

Mourtzis, D., Angelopoulos, J., and Panopoulos, N. (2020). Recycling and retrofitting for industrial equipment based on augmented reality. *Procedia CIRP* 90, 606–610. doi:10.1016/j.procir.2020.02.134

Muetze, A. (2010). On a new type of inverter-induced bearing current in large drives with one journal bearing. *IEEE Trans. Industry Appl.* 46, 240–248. doi:10.1109/TIA.2009.2036672

Muzakkir, S. M., Lijesh, K. P., and Hirani, H. (2015). Failure mode and effect analysis of journal bearing. *Int. J. Appl. Eng. Res.* 10, 37752–37759.

Nikolakopoulos, P. G., and Papadopoulos, C. A. (1997). Controllable misaligned journal bearings, lubricated with smart fluids. *J. Intelligent Material Syst. Struct.* 8, 125–137. doi:10.1177/1045389X9700800203

Okoh, C., Roy, R., Mehnen, J., and Redding, L. (2014). Overview of remaining useful life prediction techniques in through-life engineering services. *Procedia CIRP* 16, 158–163. doi:10.1016/j.procir.2014.02.006

Paranjpe, R. S., Tseregounis, S. I., and Viola, M. B. (2000). Comparison between theoretical calculations and oil film thickness measurements using the total capacitance method for crankshaft bearings in a firing engine. *Tribol. Trans.* 43, 345–356. doi:10.1080/10402000008982350

Pastukhov, A., and Timashov, E. (2023). Procedure for simulation of stable thermal conductivity of bearing assemblies. *Adv. Eng. Lett.* 2, 58–63. doi:10.46793/adeletters.2023.2.2.3

Patel, R., Khan, Z. A., Saeed, A., and Bakolas, V. (2022). A review of mixed lubrication modelling and simulation. *Tribol. Industry* 44, 150–168. doi:10.24874/ti.1186.09.21.11

Patir, N., and Cheng, H. S. (1979). Application of average flow model to lubrication between rough sliding surfaces. *J. Lubr. Technol.* 101, 220–229. doi:10.1115/1.3453329

Peng, H., Zhang, H., Fan, Y., Shangguan, L., and Yang, Y. (2023). A review of research on wind turbine bearings' failure analysis and fault diagnosis. *Lubricants* 11, 14. doi:10.3390/lubricants11010014

Peng, J., and Zhu, K.-Q. (2006). Effects of electric field on hydrodynamic characteristics of finite-length er journal bearings. *Tribol. Int.* 39, 533–540. doi:10.1016/j.triboint.2005.03.017

Pennacchi, P. (2022). "16 - advanced technologies for steam turbine bearings," in *Advances in steam turbines for modern power plants*. Editor T. Tanuma (Oxford and Amsterdam: Woodhead Publishing and Elsevier ScienceDirect), 383–448. doi:10.1016/B978-0-12-824359-6.00009-3

Prashad, H. (1991). Theoretical evaluation of capacitance, capacitive reactance, resistance and their effects on performance of hydrodynamic journal bearings. *J. Tribol.* 113, 762–767. doi:10.1115/1.2920690

Prashad, H. (1996). Evaluation of dynamic coefficients of a two-lobe journal bearing using an electrical analogy approach. *J. Tribol.* 118, 657–662. doi:10.1115/1.2831588

Prashad, H. (2006) "Tribology in electrical environments," in *Tribology and interface engineering series*, 49. Amsterdam: Elsevier.

Prashad, H., and Rao, K. N. (1994). Analysis of capacitive effect and life estimation of hydrodynamic journal bearings on repeated starts and stops of a machine operating under the influence of shaft voltages. *Tribol. Trans.* 37, 641–645. doi:10.1080/10402009408983341

Puchtler, S., van der Kuip, J., and Kirchner, E. (2023). Analyzing ball bearing capacitance using single steel ball bearings. *Tribol. Lett.* 71, 38–10. doi:10.1007/s11249-023-01706-7

Rolink, A., Jacobs, G., Müller, M., Jakobs, T., and Bosse, D. (2022). Investigation of manufacturing-related deviations of the bearing clearance on the performance of a conical plain bearing for the application as main bearing in a wind turbine. *J. Phys. Conf. Ser.* 2257, 012006. doi:10.1088/1742-6596/2257/1/012006

Rolink, A., Schröder, T., Jacobs, G., Bosse, D., Hölzl, J., and Bergmann, P. (2020). Feasibility study for the use of hydrodynamic plain bearings with balancing support characteristics as main bearing in wind turbines. *J. Phys. Conf. Ser.* 1618, 052002. doi:10.1088/1742-6596/1618/5/052002

Sanchez-Londono, D., Barbieri, G., and Fumagalli, L. (2023). Smart retrofitting in maintenance: a systematic literature review. *J. Intelligent Manuf.* 34, 1–19. doi:10.1007/s10845-022-02002-2

Saruhan, H., Sandemir, S., Çiçek, A., and Uygur, I. (2014). Vibration analysis of rolling element bearings defects. *J. Appl. Res. Technol. JART* 12, 384–395. doi:10.1016/S1665-6423(14)71620-7

Schirra, T., Martin, G., Neu, M., and Kirchner, E. (2019). Feasibility study of impedance analysis for measuring rolling bearing loads. *STLE*, 2019.

Schmitt, F., and Kirchner, E. (2022). *Caenorhabditis elegans* as a model for the effects of phytochemicals on mitochondria and aging. *How Prod. Manuf. Des. enable Sustain. Co. Soc. (The Design Society)* 12, 1550. doi:10.3390/biom12111550

Schmitt, F., Sallehsari, K., and Kirchner, E. (2023). "How to control the surface qualities in am channels?," in *Proceedings 34th DFX 2023*, 153–162. doi:10.35199/dfx2023.16

Schneider, V., Bader, N., Liu, H., and Poll, G. (2022). Method for *in situ* film thickness measurement of ball bearings under combined loading using capacitance measurements. *Tribology International* 171, 107524. doi:10.1016/j.triboint.2022.107524

Schösser, F., Schmitt, F., Kirchner, E., and Breimann, R. (2022). Influence of the operation strategy on the energy consumption of an autonomous sensor node. *Journal of Sensors and Sensor Systems* 11, 263–275. doi:10.5194/jsss-11-263-2022

Singh, A. K., Kumar, V., Singh, S. J., and Sharma, S. C. (2023). Performance of hybrid thrust bearing textured surface operating with electro-rheological lubricant. *Proceedings of the Institution of Mechanical Engineers, Part J Journal of Engineering Tribology* 237, 911–925. doi:10.1177/13506501221128110

Surucu, O., Gadsden, S. A., and Yawney, J. (2023). Condition monitoring using machine learning: a review of theory, applications, and recent advances. *Expert Systems with Applications* 221, 119738. doi:10.1016/j.eswa.2023.119738

Tang, D., Xiang, G., Guo, J., Cai, J., Yang, T., Wang, J., et al. (2023). On the optimal design of staved water-lubricated bearings driven by tribo-dynamic mechanism. *Physics of Fluids* 35, 093611. doi:10.1063/5.0165807

Tavner, P. J., Ran, L., Penman, J., and Sedding, H. (2008) "Condition monitoring of rotating electrical machines," in *vol. 56 of* IET power and energy series. London: Inst. of Engineering and Technology. doi:10.1049/PBPO056E

Vinaricky, E. (2016). *Elektrische Kontakte, Werkstoffe und Anwendungen*. Berlin, Heidelberg: Springer Berlin Heidelberg. doi:10.1007/978-3-642-45427-1

Vorwerk-Handing, G. (2021). Erfassung systemspezifischer Zustandsgrößen – Physikalische Effektkataloge zur systematischen Identifikation potentieller Messgrößen *(Darmstadt)*. Gunnar.

Vorwerk-Handing, G., Gwosch, T., Schork, S., Kirchner, E., and Matthiesen, S. (2020). Classification and examples of next generation machine elements. *Forschung im Ingenieurwesen* 84, 21–32. doi:10.1007/s10010-019-00382-1

Vorwerk-Handing, G., Martin, G., and Kirchner, E. (2018). "Integration of measurement functions in existing systems – retrofitting as basis for digitalization," in Design in the era of digitalization *(scotland: the design society)*.

Weychardt, J. H., Thiemke, M., and Christiansen, K. (2008). *Beschreibung der Interaktion maschinen-und schiffbaulicher Komponenten in allen für Beschreibung der Interaktion maschinen-und schiffbaulicher Komponenten in allen für Ausrichtrechnung relevanten Bau-und Betriebszuständen*.

Xiao, Z., Shi, X., Wang, X., Ma, X., and Han, Y. (2021). Lubrication analysis and wear mechanism of heavily loaded herringbone gears with profile modifications in full film and mixed lubrication point contacts. *Wear* 477, 203790. doi:10.1016/j.wear.2021.203790

Zapoměl, J., and Ferfecki, P. (2021), Vibration control of rotors mounted in hydrodynamic bearings lubricated with magnetically sensitive oil by changing their load capacity. *Bulletin of the Polish Academy of Sciences Technical Sciences*. e137988. 1–8. doi:10.24425/bpasts.2021.137988

Zapoměl, J., and Ferfecki, P. (2022). A new concept of a hydrodynamic bearing lubricated by composite magnetic fluid for controlling the bearing load capacity. *Mechanical Systems and Signal Processing* 168, 108678. doi:10.1016/j.ymssp.2021.108678

frontiers | Frontiers in Mechanical Engineering

TYPE Original Research
PUBLISHED 06 September 2024
DOI 10.3389/fmech.2024.1470775

Check for updates

OPEN ACCESS

EDITED BY
Taisuke Maruyama,
NSK Ltd., Japan

REVIEWED BY
Milan Bukvic,
University of Kragujevac, Serbia
Kazumi Sakai,
ENEOS Corporation, Japan

*CORRESPONDENCE
Naoki Yamashita,
naoki@kit.ac.jp

RECEIVED 26 July 2024
ACCEPTED 28 August 2024
PUBLISHED 06 September 2024

CITATION
Yamashita N and Hirayama T (2024) A method for simultaneously measuring friction and gap at metal–lubricant interface by combined use of atomic force microscopy and line-and-space patterned metal films.
*Front. Mech. Eng.* 10:1470775.
doi: 10.3389/fmech.2024.1470775

COPYRIGHT
© 2024 Yamashita and Hirayama. This is an open-access article distributed under the terms of the Creative Commons Attribution License (CC BY). The use, distribution or reproduction in other forums is permitted, provided the original author(s) and the copyright owner(s) are credited and that the original publication in this journal is cited, in accordance with accepted academic practice. No use, distribution or reproduction is permitted which does not comply with these terms.

# A method for simultaneously measuring friction and gap at metal–lubricant interface by combined use of atomic force microscopy and line-and-space patterned metal films

Naoki Yamashita[1]* and Tomoko Hirayama[2]

[1]Department of Mechanical and System Engineering, Kyoto Institute of Technology, Kyoto, Japan, [2]Department of Mechanical Engineering and Science, Graduate School of Engineering, Kyoto University, Kyoto, Japan

In boundary lubrication, adsorbed molecular films formed by lubricant additives on the metal surfaces of sliding parts effectively reduce friction and wear. A method is presented for simultaneously measuring friction and the gap at a metal–lubricant interface under boundary lubrication conditions using atomic force microscopy. In this method, line-and-space patterns are microfabricated in Cu films on Si substrates, and the gap is evaluated from the step height change when scanning in base oil and in base oil with an additive. Neutron reflectometry showed that whereas both stearic acid and stearyl alcohol formed molecular film about 2 nm thick on Cu film in a static state, the gap increased only with stearic acid due to maintaining a molecular film on the Cu film. This demonstrates the feasibility of the proposed method as means for visualizing the gap and shows that there is a difference between the two additives in their film-forming ability in a static state and their durability against friction. The proposed method for simultaneously measuring friction and the gap at a metal–lubricant interface is thus an effective way to investigate the tribological performance of additives under boundary lubrication conditions.

KEYWORDS

**tribology, lubricant additive, boundary lubrication, visualization technique, atomic force microscopy, neutron reflectometry, microfabrication, line-and-space pattern**

## 1 Introduction

Additives in lubricants generally improve the tribological properties of machine sliding parts by acting on metal surfaces (Yu et al., 2023; Cyriac et al., 2024; Nozue et al., 2024; Shu et al., 2024; Xu et al., 2024). Organic lubricating additives suppress friction and wear by simply adsorbing physically or chemically on the metal surface and forming a molecular film without complex chemical reaction due to temperature, pressure, or frictional shear force. This molecular film protects the surface from damage and reduces friction.

There are many types of organic lubricating additives such as fatty acids, amines, alcohols, and polymers (Tang and Li, 2014; Fry et al., 2020; Cyriac et al., 2021), as well as additives with improved adsorption properties (Desanker et al., 2017; Desanker et al., 2018; He et al., 2018; Yamashita et al., 2022; Hou et al., 2023; Oshio et al., 2023). Although the

thickness of the adsorbed molecular film is generally on the nanometer scale, the film often dramatically changes the tribological properties of the sliding parts. Several studies have shown that the frictional properties of the film depend on the molecular structure of the additive, such as its alkyl chain length and the type and number of polar groups (Ries and Cook, 1954; Block and Simms, 1967; Jahanmir, 1985; Tatsumi et al., 2020; Song et al., 2024). These parameters are strongly related to the thickness, stiffness, durability against friction, or stability against temperature rise of the adsorbed molecular film and affect the friction and wear properties.

To understand the tribological properties exhibited by additives, it is necessary to understand the state of the adsorbed film and base oil at the narrow gap between two surfaces in friction. Many studies focused on understanding the mechanism of low friction by simultaneously measuring friction and gap at the metal–lubricant interface. Generally, the measurements have been carried out under elastohydrodynamic lubrication using optical interferometry (Spikes, 1996; Ratoi et al., 2000). However, to accurately measure the gap using optical interferometry, the glass disk must be coated with thin films, such as chromium and silica, and the measurement must be performed under rolling lubrication conditions with a low slip rate to avoid damaging the coating film. A completely different approach is to use a surface force apparatus, which uses optical interferometry for gap measurement (Yamada et al., 2015). This apparatus uses semi-cylindrical glass disks arranged at right angles to each other, and the viscoelasticity of the solid-liquid interface in a narrow gap is investigated in detail by vibrating one of the disks while moving it closer to the other disks. This approach is normally limited to glass or mica specimens to ensure surface smoothness, but recent experiments have been performed using smooth specimens coated with thin metal films (Kasuya et al., 2017; Kurihara, 2019; Song et al., 2023). However, the set-up for the measurements is difficult and requires skilled operation.

Boundary lubrication is a severe lubrication condition in which only a thin oil film is maintained between two sliding surfaces, so the role of the adsorbed molecular film formed by the additive is particularly important. However, few studies have attempted to precisely characterize the tribological properties of the films formed by additives while measuring the gap at the metal–lubricant interface under boundary lubrication conditions with high contact pressure. *In-situ* atomic force microscopy (AFM) observation is now widely used for simultaneous measurement of friction and surface topography in lubricant (Gosvami et al., 2015; Yamashita and Hirayama, 2024). Friction created by AFM probes with sharp tips simulates the single asperity contact of protrusions due to the surface roughness of mechanical sliding parts under boundary lubrication conditions. AFM has been used to evaluate the amount of wear and the reaction rate of anti-wear agents that form a thicker film. However, AFM can measure only the relative change in surface topography, not the absolute thickness of the film. For example, if an adsorbed molecular film is formed over the entire metal surface, not only is it impossible to measure the thickness of the film, but it is also impossible to determine whether a film has actually formed because there is no reference plane corresponding to a height of zero. Campen et al. successfully measured the absolute thickness of island-like adsorbed molecular films formed by physisorption of fatty acids and amines on mica by using dynamic mode AFM observations with low loads to minimize damage to the film structure (Campen et al., 2015a; Campen et al., 2015b). However, contact mode AFM observations showed that the films on the mica were easily removed by friction although a low friction coefficient derived from the film was initially observed. These studies are very interesting in that they evaluated the thickness and durability of the adsorbed molecular films during friction. However, they did not adequately simulate the lubrication conditions of a machine composed mainly of metal, and the adsorption form of the additives was limited to physisorption.

To understand how nanoscale adsorbed films formed by organic lubricant additives reduce friction and wear on metal surfaces under boundary lubrication, it is essential to correlate the durability and load dependence of the film thickness with the tribological properties. Therefore, the aim of this study was to establish a method for measuring the nanometer gap at the metal–lubricant interface with friction under boundary lubrication conditions. There are two challenges in measuring the gap by using AFM. The first is to provide a reference plane invariably corresponding to a height of zero without additive adsorption. The second is to minimize the drift that typically occurs with wide range observation since drift prevents precise height measurement due to the waviness of the observed image. To overcome the first challenge, inactivated Si was used for the reference plane because additives do not easily absorb on it. To overcome the second challenge, a fine metal line pattern was formed to keep the metal plane to be evaluated within a narrow observation range. This was done by microfabricating line-and-space patterns in Cu thin films on Si substrates. The AFM tip was scanned over the pattern in poly-alpha-olefin (PAO) base oil and in PAO containing stearic acid or stearyl alcohol. Since an adsorbed molecular film is not formed on the inactivated Si and the AFM friction measurement is performed under boundary lubrication conditions with almost no oil film between two sliding surfaces, the change in the measured step height from Si to Cu for PAO with/without an additive is equivalent to the gap increase, which reflects the effect of the adsorbed molecular film formed on the Cu film. In this study, friction was measured while measuring the gap between the metal-lubricant interface under boundary lubrication conditions of high contact pressure, which is difficult to achieve conventionally. The proposed method, which utilizes a fine metal line pattern, has the capability to simulate the boundary lubrication of metal sliding parts in machines. Consequently, the relationship between the durability of the adsorbent additive film formed on the Cu surface and the contact pressure dependence of the gap with tribological properties was investigated.

## 2 Fabrication of line-and-space specimens

The specimen fabrication process is schematically shown in Figure 1. ①A 4-inch Si (100) wafer was cleaned using a sulfuric acid-hydrogen peroxide mixture and ultrasonic jet water in a cleaning system (KSC-150CBU, Kanamex). ②The native Si oxide layer on the wafer surface was then removed using a diluted buffered hydrofluoric acid (HF) solution. ③Next, a photoresist (PMGI-SF5S) with a film thickness of 240 nm was deposited as a 1st layer resist using a spin coater, and the Si wafer was baked on a

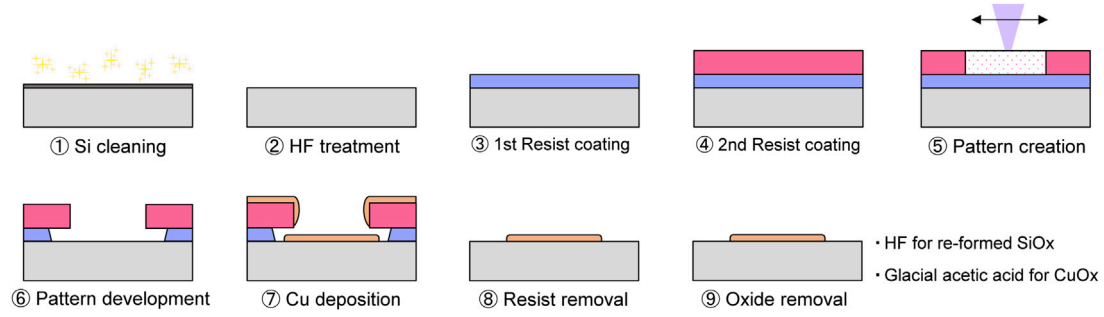


FIGURE 1
Schematic illustration of specimen fabrication process.

hot plate at 180°C for 5 min ④Then, a 2nd layer resist (TDMR-AR80) with a film thickness of 0.95 μm was deposited using a spin coater, and the Si wafer was baked at 90°C for 90 s. ⑤The resist layers were exposed using a UV laser in a direct laser writing system (DWL2000, Heidelberg Instruments), thereby creating a 3 μm line-and-space pattern. The Si wafer was then baked on a hot plate at 110°C for 90 s. ⑥The Si wafer was immersed in 2.38 wt% tetramethyl ammonium hydroxide (TMAH) aqueous solution for 70 s to develop the pattern. Finally, the Si wafer was rinsed with pure water for 60 s and dried with $N_2$ blow. All the processes described above were carried out in a clean room with yellow light.

⑦Next, a vacuum evaporation system (RD-1400, SANVAC) was used to deposit a 2 nm Cr adhesion layer and a 15 nm Cu film on top of it. The deposition rates for both metals were adjusted to be approximately 0.03 nm/s. The Si wafer was stored in a vacuum desiccator until friction measurements to prevent excessive oxidation. Before friction measurement, the wafer was cut into small chips, which were immersed in a 1-methyl-2-pyrrolidinone (NMP) solution at room temperature for 60 min to lift-off the resists and then immersed in another NMP solution heated on a hot plate at 60°C for 60 min to remove the resists more thoroughly. Finally, the chips were ultrasonically cleaned for 10 s in NMP, isopropanol, and ultrapure water and then dried with $N_2$ blow.

⑧To completely remove the photoresists, the chips were immersed in a 1% aqueous solution of TMAH for 1 min and rinsed in ultrapure water for 1 min ⑨The oxide film on the chips, which re-formed during the fabrication process, was again removed by rinsing with HF specially developed to minimize damaging the Cu film (Pure Etch ZE202, Hayashi Pure Chemical) for 1 min, rinsed in ultrapure water and isopropanol, and then dried with $N_2$. As the adsorption of lubricant additives on Cu can vary with the degree of oxidation, the native Cu oxide layer was etched by immersion in glacial acetic acid for 1 min and then dried directly in $N_2$ to improve the reproducibility of the experiment (Chavez and Hess, 2001).

# 3 Experiments

## 3.1 Neutron reflectometry

The structure of the adsorbed additive film formed on the Cu surface in a static state was evaluated by neutron reflectometry. Since hydrogen and deuterium are clearly distinguishable in neutron reflectometry, the thickness and film density of the adsorbed additive film can be evaluated by converting the hydrogen atoms in the additive to deuterium atoms (Hirayama et al., 2012; Hirayama and Yamashita, 2020). This was done using a lubricant with deuterated stearic acid ($C_{17}D_{35}COOH$) or deuterated stearyl alcohol ($C_{18}D_{37}OH$) with a 3 mM concentration, which corresponds to approximately 0.1 wt% in terms of the non-deuterated additive in PAO (30 $mm^2/s$@40°C, Idemitsu Kosan). A mirror-polished Si block (50 × 50 mm, t10 mm) was prepared, and a Cu film was deposited on its surface using an ion beam sputtering system (KUR-IBS) to a 30 nm thickness (Hino et al., 2015).

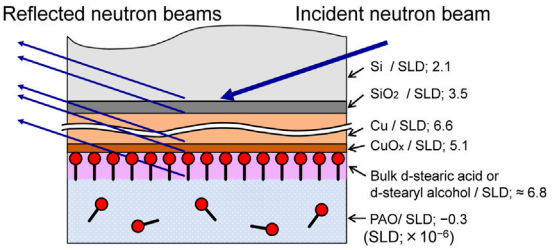


FIGURE 2
Schematic illustration of neutron reflectometry measurement.

Neutron reflectivity measurements were performed using the SOFIA time-of-flight neutron reflectometer in Beamline 16 at the Materials and Life Science Experimental Facility of the Japan Proton Accelerator Research Complex (Yamada et al., 2011; Mitamura et al., 2013). Figure 2 schematically illustrates the neutron reflectometry measurement. The theoretical value of the scattering length density (SLD), which is the coherent nuclear scattering length multiplied by the number density of the constituent atoms, is also shown in the figure. First, a Si block with a Cu film was placed in a holder, and the neutron reflectivity was measured while the Cu surface was immersed in PAO base oil. The base oil was then replaced with PAO containing deuterated stearic acid or deuterated stearyl alcohol. The reflectivity was measured again after 12 h at room temperature. The thickness of the Cu film and the thickness and film density of the adsorbed molecular film formed by each additive were evaluated by fitting

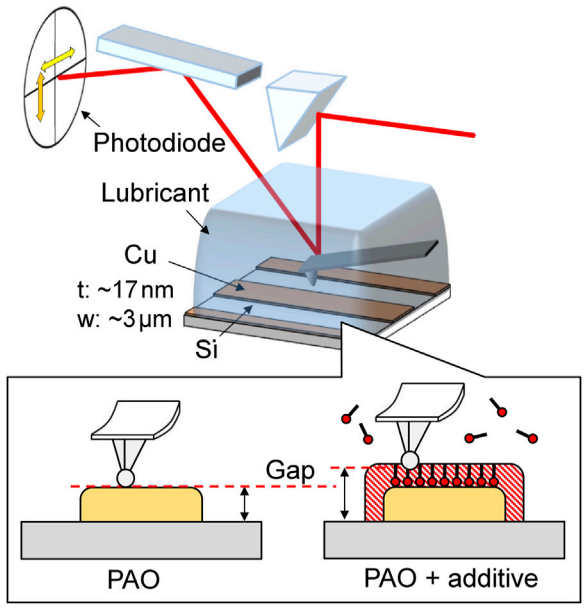


FIGURE 3
Schematic illustration of proposed method using line-and-space specimen.

to the reflectivity profiles obtained from each measurement using analysis software (Nelson, 2006).

## 3.2 AFM observations

AFM observations were first carried out to check that the proposed line-and-space pattern had formed correctly in the Cu film. The observations were carried out using an AFM (SPM-9700HT, Shimadzu) in dynamic mode in air. The maximum operating range of this AFM is 10 μm in the XY plane and 1 μm in the Z direction. The AFM exhibits a resolution of 0.2 nm in the XY plane and 0.01 nm in the Z direction. A point probe type Si cantilever (TAP300AL-G, BudgetSensors; spring constant = 40 N/m, tip radius <10 nm) was used.

A schematic illustration of the simultaneous measurement of friction and gap at the metal–lubricant interface using a specimen with a Cu line-and-space pattern is shown in Figure 3. A sphere-probe-type cantilever made of Si (SD-Sphere-CONT-L, NANOSENSORS), which typically has a 2 μm tip radius, was used for this contact mode AFM observation. Before the experiment, the cantilever was rinsed with specially developed HF for 1 min to inactivate its surface. A 3 μm wide Cu line was formed in the center of the 7.5 μm observation area, and observation was carried out in 50 μL PAO base oil. The applied loads were 25, 75, and 125 nN, with the maximum Hertzian contact pressures on the Cu film corresponding to 200, 280, and 330 MPa, respectively. Next, 50 μL of PAO containing 0.2 wt% of stearic acid or stearyl alcohol was supplied to the same substrate. The lubricant was gently stirred with a pipette, and the concentration of the additive in the lubricant on the substrate was adjusted to 0.1 wt%, after which the same measurements were carried out as for PAO base oil. For the simultaneous measurement of friction and gap at the metal–lubricant interface, 15 successive observations were performed at a load of 75 nN. From each obtained image, the average friction coefficients on the Si block and the Cu film and the step height from the Si reference plane to the Cu line were evaluated.

The AFM images were analyzed using Gwyddion open-source software for AFM data analysis (Nečas and Klapetek, 2012). The height distribution in each image was calculated, and the mean step heights from Si to Cu were found by Gaussian fitting to each height distribution peak. The friction coefficient was obtained by dividing the friction force mechanically calculated from the detected cantilever torsion by the total load of the pushing force calculated from the cantilever deflection and the adhesion force detected in the force curve measurement.

# 4 Results

## 4.1 Neutron reflectometry

The thickness and density of the adsorbed molecular film on the Cu thin film were evaluated by neutron reflectometry. The reflectivity profiles obtained from the measurements are shown in Figure 4. Scattering vector $Q_z$ ($x$-axis) is expressed as the following Equation 1.

$$Q_z = 4\pi/\lambda \sin\theta, \quad (1)$$

where $\lambda$ is the wavelength of the neutron beam and $\theta$ is the angle of incidence (Mitamura et al., 2013).

The SLD profiles obtained by fitting analysis for each reflectivity profile are shown in Figure 5. As the SLD is unique to each material, the film structure can be determined from the depth distribution of the SLD. The thickness of both Cu films formed on the Si blocks was around 30 nm, indicating that the films were successfully deposited at the desired thickness. The thickness of the adsorption film formed on the Cu surface by deuterated stearic acid was 1.9 nm and the film density was 41%. The molecular film formed by deuterated stearyl alcohol had a thickness of 2.2 nm and a film density of 14%. Both the stearic acid and stearyl alcohol has linear chains with 18 carbons, and their molecular length was approximately 2 nm. Therefore, both molecules were in a monolayer state.

## 4.2 Fabricated specimens

The line-and-space patterns observed by optical microscopy and dynamic mode AFM in air with a point probe cantilever are shown in Figure 6. These images show that there was no photoresist or metal residue on the specimen surface and that the target line-and-space pattern was successfully fabricated.

Studies on Si/Si and Si/$SiO_2$ friction measured by AFM have been mostly carried out in air with controlled humidity and in water and have shown that Si-based materials are subject to abnormal wear due to interfacial reactions (Chen et al., 2013; Zhang et al., 2017; Zhang et al., 2018). Although this has not been demonstrated for non-polar solvents such as PAO, the moisture in lubricants may affect wear. In this study, the ambient atmosphere around the lubricant was not controlled, and the moisture content in the lubricant was not monitored. As a result, wear with an average

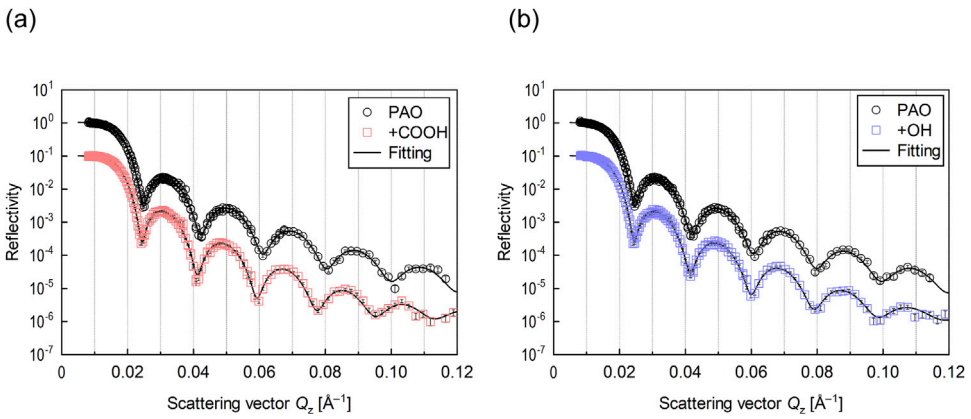


FIGURE 4
Neutron reflectivity profiles for interface of Cu and lubricant **(A)** with stearic acid (+COOH) and **(B)** with stearyl alcohol (+OH).

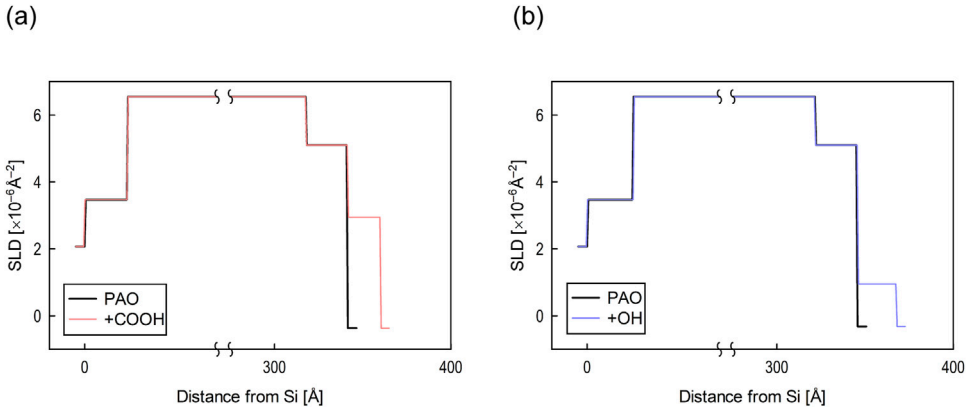


FIGURE 5
SLD profiles obtained by optimum fitting analysis for **(A)** stearic acid (+COOH) and **(B)** stearyl alcohol (+OH).

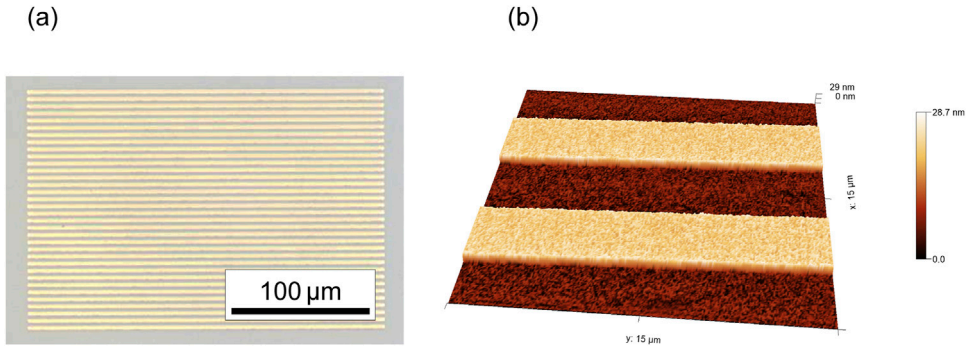


FIGURE 6
Line-and-space patterns observed by **(A)** optical microscopy and **(B)** dynamic mode AFM in air.

depth of about 0.4 nm was rarely observed in the friction area, but data from such cases were not used for evaluation in subsequent experiments. Even if there was sub-nanometer wear that became invisible in the image processing phase, its depth was small compared with the molecular size of the additive and therefore had little effect on the step measurement.

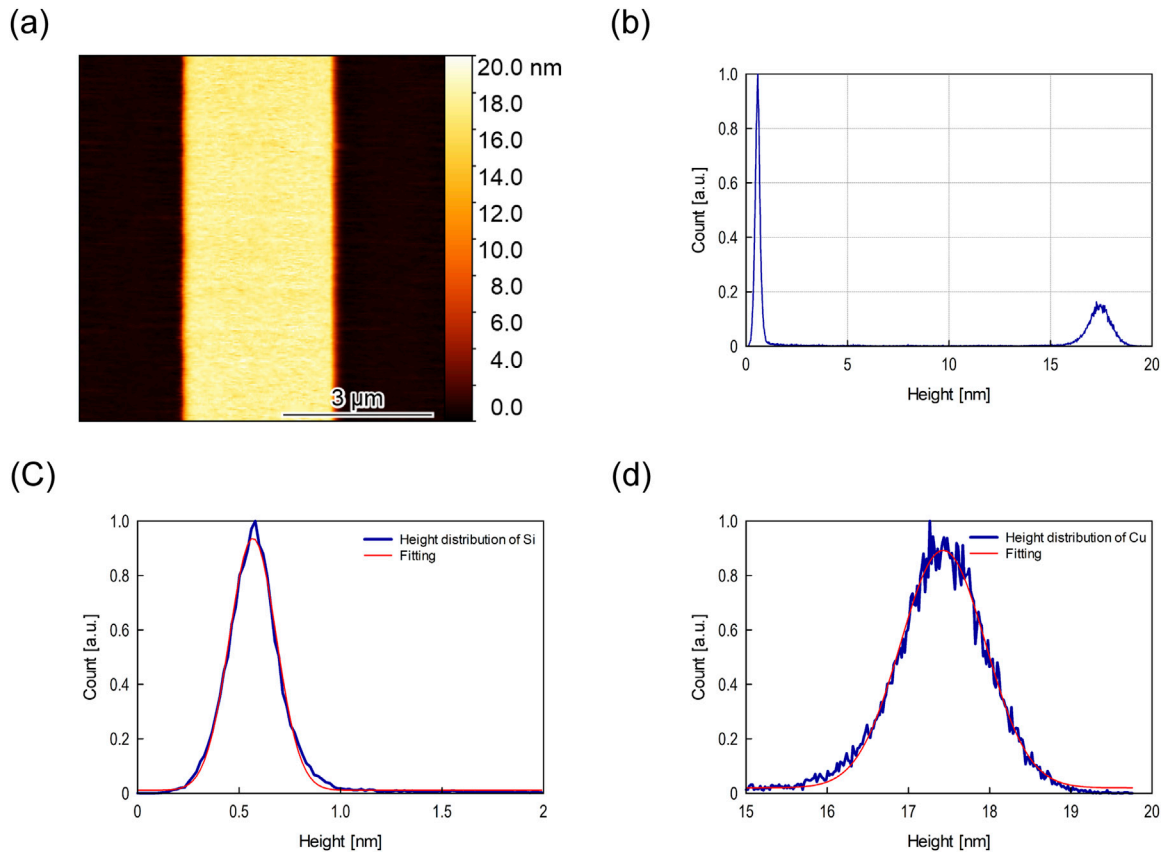


FIGURE 7
Typical example of **(A)** AFM image and **(B)** height distribution in PAO base oil, and Gaussian fittings to height distributions of **(C)** Si and **(D)** Cu.

## 4.3 Load dependence of gap with use of additives

Typical examples of AFM image and height distributions obtained for PAO base oil are shown in Figures 7A, B, respectively. The results of Gaussian fitting to the Si and Cu height distributions in the observed images are shown in Figures 7C, D, respectively. The distances between the peaks correspond to the measured thickness of the Cu film since the minimum oil film thickness calculated using the Hamrock–Dowson equation (Hamrock and Dowson, 1977) is usually extremely small (<10 p.m.). The same analysis was applied to all observed images to obtain an average value. The Cu films used in the experiments were around 17 nm thick for PAO base oil. Experiments were conducted using at least five specimens, and observations were made at five locations for each specimen.

Due to differences in the thickness of the deposited Cu film on each substrate, the average step height for PAO base oil was subtracted from that for PAO with an additive using the same substrate. Since no adsorbed molecular film of an additive was formed on the inactivated Si and since the AFM friction measurements were performed under boundary lubrication conditions with little or no oil film between the two sliding surfaces, the change in the step height from Si to Cu measured for PAO with or without an additive corresponds to the gap generated by the effect of the adsorbed additive film on Cu.

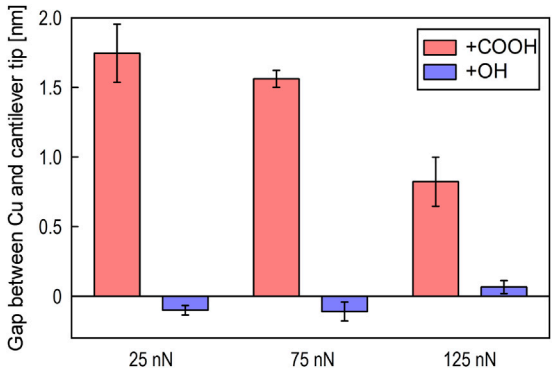


FIGURE 8
Average gap at metal–lubricant interface for each load for PAO with stearic acid (+COOH) or stearyl alcohol (+OH).

The average gap at the metal–lubricant interface obtained from the observations for each load is shown in Figure 8. Gap formation was clearly observed for PAO containing stearic acid, and the gap was greater at lower loads. At the lowest load the gap was approximately the same as the thickness of the adsorbed stearic acid film observed in neutron reflectometry, whereas at a load of 125 nN the gap was about half the thickness. In contrast, PAO containing stearyl alcohol showed a negative gap for the two lowest

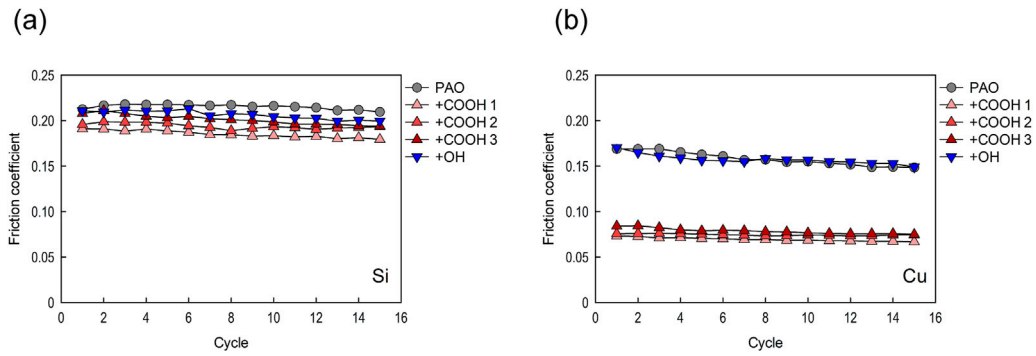


FIGURE 9
Measured friction coefficient for **(A)** Si and **(B)** Cu.

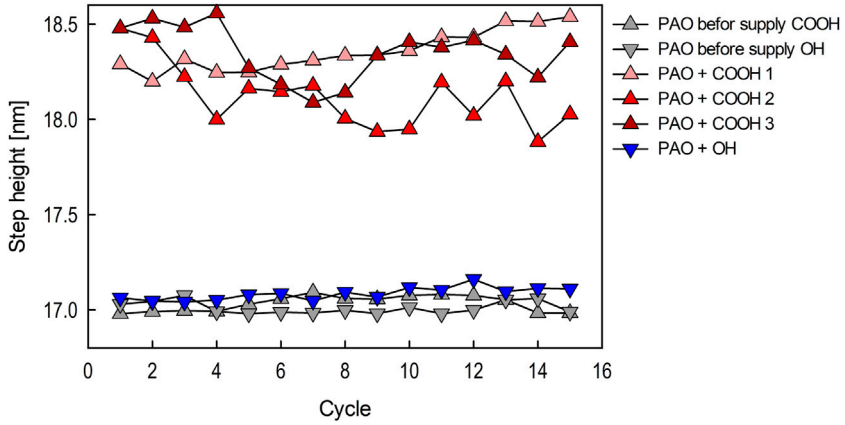


FIGURE 10
Step heights over 15 friction cycles before and after supplying stearic acid or stearyl alcohol.

loads and only a slight gap increase for the highest load. A negative gap, even if the absolute value is small, indicates that stearyl alcohol may have adsorbed on the Si rather than the Cu or that there may have been a small measurement or statistical error.

## 4.4 Simultaneously measurement of friction and gap

Representative friction coefficients for Si and Cu extracted from each 7.5 × 7.5 μm image captured during 15 friction cycles measurement are shown in Figures 9A, B, respectively. The simultaneously measured step heights for PAO containing stearic acid or stearyl alcohol and those for PAO before supplying lubricant for the same specimen are shown in Figure 10. The results for PAO containing stearic acid are shown as three separate results (COOH 1–3) in Figures 9, 10 because the step height showed more variability than those measured for PAO containing stearyl alcohol and PAO base oil.

The step height measurement for PAO base oil showed that the step height was almost unchanged from the initial value, indicating that wear of the Cu does not occur at a load of 75 nN (Figure 10). It can also be seen that stearyl alcohol had no effect on the step height change on Cu. There was no clear difference in the friction coefficient on Cu for PAO base oil and for PAO containing stearyl alcohol (the differences ranged from 0.17 to 0.15). These results indicate stearyl alcohol has insufficient load-bearing capacity against friction for a 75 nN load.

The friction coefficient for Si in PAO containing stearic acid was slightly lower (around 0.19), whereas for PAO base oil and PAO containing stearyl alcohol it was generally around 0.21. According to Campen et al., there is significant friction reduction for lubricants containing stearic acid on mica despite the absence of film formation on its surface (Campen et al., 2015a; Campen et al., 2015b). In this study, the stearic acid slightly reduced the friction coefficient on Si, but the degree of reduction was smaller. This may be because HF treatment inactivates Si surfaces, which makes adsorption of additives more difficult.

For Cu, in PAO containing stearic acid, the friction coefficient was about 0.07, which is a drastic reduction in friction. When stearic acid was used, the step heights were larger than those for Cu film in PAO base oil, indicating that adsorbed stearic acid film on the Cu film increases the gap at the interface. Since the gap varied by 1–1.5 nm during the 15 friction cycles, which is less than the

thickness of the molecular film obtained by neutron reflectivity, the tip of the AFM cantilever is considered to have scanned on or inside the film.

# 5 Discussion

## 5.1 Film properties and gap evaluation

Neutron reflectometry showed that both stearic acid and stearyl alcohol formed adsorbed molecular film about 2 nm thick under static conditions, but the AFM measurements showed no significant step height change on the Cu film when stearyl alcohol was used, even with the lowest load used (Figure 8). Neutron reflectometry revealed that the film density with stearyl alcohol was 14%, which is clearly lower than that of stearic acid (41%). In general, adsorbed molecular film is stronger at higher film densities due to larger interactions between the alkyl chains of the adsorbed additives (Studt, 1981; Hironaka, 1988). Films with lower densities may have a larger contact area with the AFM cantilever probe, resulting in a stronger interaction and thus a higher shear force per unit area and higher friction. It has been suggested that sliding between loosely packed molecular films may cause molecular deformation and greater energy dissipation (Lee et al., 2000). In this study, there were no differences in the friction coefficient and step height for Cu with or without stearyl alcohol. Since the molecular film formed by stearyl alcohol has quite low density, it can be concluded that either the load-bearing capacity was low and could not bear the cantilever tip or that was removed from the Cu surface without any positive or negative effect on friction.

As the results of neutron reflectometry show, the density of the film formed by the stearic acid was relatively high (41%). Furthermore, fatty acids have a high adsorption capacity for Cu, forming a high density molecular film with chemical bonds (Greenhill, 1949). Many studies using steel as a sliding material have shown that fatty acids exhibit a lower friction coefficient than alcohols (Jahanmir, 1985; Studt, 1989; Simic and Kalin, 2013) and that this tendency appears to be basically the same for Cu. The carboxy groups of fatty acids include –OH and C=O groups. Stearic acid can be adsorbed on Cu *via*–OH and C=O groups in a mono- or bidentate mode, and bidentate adsorption increases after the friction-induced tribochemical reaction (Hu et al., 1992; Fischer et al., 1997). Therefore, the adsorption capacity of fatty acids is stronger than that of alcohols, which in principle can only be adsorbed in monodentate mode. For methyl and ethyl esters of fatty acids, the adsorption capacity is reported to be small compared with that of the original fatty acid (Moore, 1951; Studt, 1981; Liascukiene et al., 2012). It is important to have both C=O and –OH groups, and in this study, a stable chemically adsorbed film was formed on Cu, providing substantial friction reduction and a gap increase even under severe friction conditions beneath the AFM cantilever tip.

Figure 8 shows that the durability of the molecular film formed by stearic acid is load dependent. At a load of 25 nN, the change in step height for PAO with/without stearic acid was about 1.7 nm, which is comparable, as revealed by neutron reflectometry, to the film thickness in a static state. This indicates that the molecular film is strong enough to bear an average contact pressure of 200 MPa, in accordance with the Hertzian contact between the Si cantilever and the Cu film, with a contact diameter of 16 nm. At a load of 125 nN, the gap decreased to about 1 nm. That the gap became smaller than the thickness of the molecular film formed in a static state suggests that the film may have been compressed or tilted or that the alkyl chains may have been bent (Salmeron, 2001). However, the gap was still well maintained, indicating that the molecular film formed by stearic acid had a high load-bearing capacity.

In the friction measurement at a load of 75 nN using stearic acid, the friction coefficient remained stable regardless of the number of friction cycles (Figure 9B), and the gap did not decrease due to, for example, removal of the adsorbed molecular film by friction. However, the step height fluctuated around 18–18.5 nm during measurement. Since the step height for PAO base oil exhibited a constant value of around 17 nm (Figure 10), the gap fluctuated significantly with the formation of the adsorbed stearic acid film. Although this measurement technique cannot determine the molecular conformation of the adsorbed stearic acid film during friction, the results indicate that the state of the film may change from moment to moment. The stearic acid adsorbed molecular film on Cu changed to a softer metallic soap state due to friction (Hirayama et al., 2017), suggesting that the cantilever can scan on and within the film.

## 5.2 Effectiveness of proposed method

In the experiments with stearyl alcohol, the neutron reflectometry confirmed film formation under static state conditions, whereas AFM observation simulating single asperity contact did not show any gap increase due to film formation. This indicates that there is a clear difference between film formation ability under static state conditions and maintaining the film under friction conditions. Therefore, to investigate the tribological performance of additives under boundary lubrication conditions, it is highly effective to simultaneously measure the friction and gap at the metal–lubricant interface, as proposed here, in addition to using such methods as neutron reflectometry and quartz crystal microbalance to evaluate adsorption on the metal surface.

Adsorption of an additive can occur to a small extent as long as there is no repulsive force between the substrate and additive. That there was little friction reduction on Si when additives were supplied (Figure 9A) means that weakly and sparsely adsorbed additives are easily removed by applied friction with virtually no effect on the frictional properties. The adsorption of fatty acids, alcohols, and amines on active $SiO_2$ surfaces has been reported in experiments and molecular simulations (Fry et al., 2020; Shi et al., 2020). During the feasibility phase of this study, measurements of friction in lubricant containing stearic acid were performed using Si without HF treatment, and friction reduction was obvious.

In this study, the stearic acid was successfully prevented from adsorbing on Si by removing the Si native oxide film and hydrogen termination by treatment with a special HF, which does not damage Cu, immediately before starting the experiment (as described in Section 2). This indicates that the adsorption of the additive can be suppressed by using inactivated Si. A slight decrease in the friction coefficient was still observed for Si in PAO containing stearic acid (Figure 9A). However, the degree of reduction was much smaller than that for Cu, and no difference in surface topography was observed, suggesting that the amount of adsorption was small.

The feasibility of the proposed method was evaluated using Cu, which can maintain a line-and-space pattern without dissolving or

peeling during HF treatment and is active to the adsorption of additives. In future experiments with other kind of metals, such as iron, it will be necessary to improve the selection of the base material, e.g., by using diamond-like carbon coated Si, which is inactive to additive adsorption (Simič et al., 2014). Future work includes a more detailed evaluation of the contact pressure dependence of the gap at the metal–lubricant interface formed by adsorbed molecular films created by various type of additives on metal films and visualization of the formation of tribofilms and metallic soaps under friction conditions. Simultaneous measurement of friction and gap under various tribological conditions provides a deep understanding of additive properties, facilitating the selection and development of additives that strongly adsorb to metals, resulting in low friction and wear. This method is useful for parameter studies in the field of tribology and contributes to improving the energy efficiency of machines.

## 6 Conclusion

In the proposed method for simultaneously measuring the friction and gap at the metal–lubricant interface of adsorbed molecular films formed on metal surfaces under boundary lubrication conditions using AFM, line-and-space patterns are microfabricated in Cu film on a Si substrate. The gap is evaluated on the basis of the step height change when scanning in base oil and in lubricant with an additive. Neutron reflectometry showed film formation with both stearic acid and stearyl alcohol as additives, but the film density of stearyl alcohol was less than half that formed by stearic acid. The proposed method using AFM confirmed that the molecular film on the Cu film is maintained only with stearic acid and the gap increases under boundary lubrication conditions. This indicates that the adsorbed molecular film of stearyl alcohol, which has low film strength due to low film density and weak adsorption, is easily removed under boundary lubrication conditions and does not contribute to friction reduction. These results are reasonable and support the validity of the evaluation by the proposed method. Therefore, the proposed visualization technique is an effective analytical method for investigating the durability of adsorbed molecular films and the contact pressure dependence of gap at the metal–lubricant interface.

## Data availability statement

The raw data supporting the conclusions of this article will be made available by the authors, without undue reservation.

## Author contributions

NY: Conceptualization, Formal Analysis, Funding acquisition, Investigation, Methodology, Validation, Visualization, Writing–original draft. TH: Methodology, Project administration, Supervision, Writing–review and editing.

## Funding

The author(s) declare that financial support was received for the research, authorship, and/or publication of this article. This study was supported by Transmission Research Association for Mobility Innovation (TRAMI) and NSK Foundation for Advancement of Mechatronics. This work was also supported by JSPS KAKENHI Grant Number 24K07288.

## Acknowledgments

The neutron experiment at the Materials and Life Science Experimental Facility of the J-PARC was performed under a user program (Proposal No. 2023MP-S001). This work was supported by Kyoto University Nanotechnology Hub in "Advanced Research Infrastructure for Materials and Nanotechnology Project" sponsored by the Ministry of Education, Culture, Sports, Science and Technology (MEXT), Japan. We express our sincere gratitude to Professor Masahiro Hino at the Institute for Integrated Radiation and Nuclear Science, Kyoto University, for kindly preparing the Cu films used in the neutron reflectometry experiments (Proposal No. R6114).

## Conflict of interest

The authors declare that the research was conducted in the absence of any commercial or financial relationships that could be construed as a potential conflict of interest.

## Publisher's note

All claims expressed in this article are solely those of the authors and do not necessarily represent those of their affiliated organizations, or those of the publisher, the editors and the reviewers. Any product that may be evaluated in this article, or claim that may be made by its manufacturer, is not guaranteed or endorsed by the publisher.

## References

Block, A., and Simms, B. B. (1967). Desorption and exchange of adsorbed octadecylamine and stearic acid on steel and glass. *J. Colloid Interface Sci.* 25, 514–518. doi:10.1016/0021-9797(67)90062-8

Campen, S., Green, J. H., Lamb, G. D., and Spikes, H. A. (2015a). *In situ* study of model organic friction modifiers using liquid cell AFM; saturated and mono-unsaturated carboxylic acids. *Tribol. Lett.* 57, 18. doi:10.1007/s11249-015-0465-x

Campen, S., Green, J. H., Lamb, G. D., and Spikes, H. A. (2015b). *In situ* study of model organic friction modifiers using liquid cell AFM: self-assembly of octadecylamine. *Tribol. Lett.* 58, 39. doi:10.1007/s11249-015-0514-5

Chavez, K. L., and Hess, D. W. (2001). A novel method of etching copper oxide using acetic acid. *J. Electrochem. Soc.* 148, G640. doi:10.1149/1.1409400

Chen, L., Kim, S. H., Wang, X., and Qian, L. (2013). Running-in process of Si-SiOx/SiO2 pair at nanoscale—sharp drops in friction and wear rate during initial cycles. *Friction* 1, 81–91. doi:10.1007/s40544-013-0007-1

Cyriac, F., Tee, X. Y., and Chow, P. S. (2024). Tribological performance of polymeric friction modifiers under sliding rolling contact condition. *Lubr. Sci.* 36, 119–134. doi:10.1002/ls.1678

Cyriac, F., Tee, X. Y., Poornachary, S. K., and Chow, P. S. (2021). Influence of structural factors on the tribological performance of organic friction modifiers. *Friction* 9, 380–400. doi:10.1007/s40544-020-0385-0

Desanker, M., He, X., Lu, J., Johnson, B. A., Liu, Z., Delferro, M., et al. (2018). High-performance heterocyclic friction modifiers for boundary lubrication. *Tribol. Lett.* 66, 50. doi:10.1007/s11249-018-0996-z

Desanker, M., He, X., Lu, J., Liu, P., Pickens, D. B., Delferro, M., et al. (2017). Alkylcyclens as effective sulfur- and phosphorus-free friction modifiers for boundary lubrication. *ACS Appl. Mater. Interfaces* 9, 9118–9125. doi:10.1021/acsami.6b15608

Fischer, D. A., Hu, Z. S., and Hsu, S. M. (1997). Tribochemical and thermochemical reactions of stearicacid on copper surfaces in air as measured by ultra-soft X-rayabsorption spectroscopy. *Tribol. Lett.* 3, 35–40. doi:10.1023/A:1019109407863

Fry, B. M., Moody, G., Spikes, H. A., and Wong, J. S. S. (2020). Adsorption of organic friction modifier additives. *Langmuir* 36, 1147–1155. doi:10.1021/acs.langmuir.9b03668

Gosvami, N. N., Bares, J. A., Mangolini, F., Konicek, A. R., Yablon, D. G., and Carpick, R. W. (2015). Mechanisms of antiwear tribofilm growth revealed *in situ* by single-asperity sliding contacts. *Science* 348, 102–106. doi:10.1126/science.1258788

Greenhill, E. B. (1949). The adsorption of long chain polar compounds from solution on metal surfaces. *Trans. Faraday Soc.* 45, 625–631. doi:10.1039/TF9494500625

Hamrock, B. J., and Dowson, D. (1977). Isothermal elastohydrodynamic lubrication of point contacts: Part III—fully flooded results. *J. Lubr. Technol.* 99, 264–275. doi:10.1115/1.3453074

He, X., Lu, J., Desanker, M., Invergo, A. M., Lohr, T. L., Ren, N., et al. (2018). Boundary lubrication mechanisms for high-performance friction modifiers. *ACS Appl. Mater. Interfaces* 10, 40203–40211. doi:10.1021/acsami.8b11075

Hino, M., Oda, T., Kitaguchi, M., Yamada, N. L., Tasaki, S., and Kawabata, Y. (2015). The ion beam sputtering facility at KURRI: coatings for advanced neutron optical devices. *Nucl. Instrum. Methods Phys. Res. Sect. A Accel. Spectrom. Detect. Assoc. Equip.* 797, 265–270. doi:10.1016/j.nima.2015.06.046

Hirayama, T., Kawamura, R., Fujino, K., Matsuoka, T., Komiya, H., and Onishi, H. (2017). Cross-sectional imaging of boundary lubrication layer formed by fatty acid by means of frequency-modulation atomic force microscopy. *Langmuir* 33, 10492–10500. doi:10.1021/acs.langmuir.7b02528

Hirayama, T., Torii, T., Konishi, Y., Maeda, M., Matsuoka, T., Inoue, K., et al. (2012). Thickness and density of adsorbed additive layer on metal surface in lubricant by neutron reflectometry. *Tribol. Int.* 54, 100–105. doi:10.1016/j.triboint.2012.04.012

Hirayama, T., and Yamashita, N. (2020). Combined use of neutron reflectometry and frequency-modulation atomic force microscopy for deeper understanding of tribology. *Jpn. J. Appl. Phys.* 59, SN0803. doi:10.35848/1347-4065/ab9c43

Hironaka, S. (1988). Friction properties of C18-fatty acids. *J. Jpn. Petroleum Inst.* 31, 216–220. doi:10.1627/jpi1958.31.216

Hou, J., Tsukamoto, M., Hor, S., Chen, X., Yang, J., Zhang, H., et al. (2023). Molecules with a TEMPO-based head group as high-performance organic friction modifiers. *Friction* 11, 316–332. doi:10.1007/s40544-022-0610-0

Hu, Z.-S., Hsu, S. M., and Wang, P. S. (1992). Tribochemical and thermochemical reactions of stearic acid on copper surfaces studied by infrared microspectroscopy. *Tribol. Trans.* 35, 189–193. doi:10.1080/10402009208982108

Jahanmir, S. (1985). Chain length effects in boundary lubrication. *Wear* 102, 331–349. doi:10.1016/0043-1648(85)90176-0

Kasuya, M., Tomita, K., Hino, M., Mizukami, M., Mori, H., Kajita, S., et al. (2017). Nanotribological characterization of lubricants between smooth iron surfaces. *Langmuir* 33, 3941–3948. doi:10.1021/acs.langmuir.7b00148

Kurihara, K. (2019). Surface forces measurement for materials science. *Pure Appl. Chem.* 91, 707–716. doi:10.1515/pac-2019-0101

Lee, S., Shon, Y.-S., Colorado, R., Guenard, R. L., Lee, T. R., and Perry, S. S. (2000). The influence of packing densities and surface order on the frictional properties of alkanethiol self-assembled monolayers (SAMs) on gold: a comparison of SAMs derived from normal and spiroalkanedithiols. *Langmuir* 16, 2220–2224. doi:10.1021/la9909345

Liascukiene, I., Aissaoui, N., Asadauskas, S. J., Landoulsi, J., and Lambert, J.-F. (2012). Ordered nanostructures on a hydroxylated aluminum surface through the self-assembly of fatty acids. *Langmuir* 28, 5116–5124. doi:10.1021/la2051542

Mitamura, K., Yamada, N. L., Sagehashi, H., Torikai, N., Arita, H., Terada, M., et al. (2013). Novel neutron reflectometer SOFIA at J-PARC/MLF for *in-situ* soft-interface characterization. *Polym. J.* 45, 100–108. doi:10.1038/pj.2012.156

Moore, A. C. (1951). The adsorption of lubricant films: a study by radioactive tracers. *Br. J. Appl. Phys.* 2, 54–56. doi:10.1088/0508-3443/2/S1/320

Nečas, D., and Klapetek, P. (2012). Gwyddion: an open-source software for SPM data analysis. *Open Phys.* 10, 181–188. doi:10.2478/s11534-011-0096-2

Nelson, A. (2006). Co-refinement of multiple-contrast neutron/X-ray reflectivity data using MOTOFIT. *J. Appl. Cryst.* 39, 273–276. doi:10.1107/S0021889806005073

Nozue, T., Itoh, S., Okubo, N., Fukuzawa, K., Zhang, H., and Azuma, N. (2024). Temperature dependence of viscoelasticity of lubricating oil with adsorptive polymer additives sheared in nanogaps. *Tribol. Lett.* 72, 83. doi:10.1007/s11249-024-01884-y

Oshio, T., Minfray, C., Dassenoy, F., Galipaud, J., and Yagishita, K. (2023). Dialkyl phosphonate with carboxylic acid as antiwear additives for ester-base lubricants. *Wear* 530-531, 205042. doi:10.1016/j.wear.2023.205042

Ratoi, M., Anghel, V., Bovington, C., and Spikes, H. A. (2000). Mechanisms of oiliness additives. *Tribol. Int.* 33, 241–247. doi:10.1016/S0301-679X(00)00037-2

Ries, H. E., and Cook, H. D. (1954). Monomolecular films of mixtures: I. Stearic acid with isostearic acid and with tri-p-cresyl phosphate. Comparison of components with octadecylphosphonic acid and with tri-o-xenyl phosphate. *J. Colloid Sci.* 9, 535–546. doi:10.1016/0095-8522(54)90056-2

Salmeron, M. (2001). Generation of defects in model lubricant monolayers and their contribution to energy dissipation in friction. *Tribol. Lett.* 10, 69–79. doi:10.1023/A:1009026312732

Shi, J., Zhou, Q., Sun, K., Liu, G., and Zhou, F. (2020). Understanding adsorption behaviors of organic friction modifiers on hydroxylated SiO2 (001) surfaces: effects of molecular polarity and temperature. *Langmuir* 36, 8543–8553. doi:10.1021/acs.langmuir.0c01386

Shu, J., Espejo, C., Kalin, M., and Morina, A. (2024). Tribological performance of fatty acid, acid/amine additive mixture and ionic liquid. *Proc. Institution Mech. Eng. Part J J. Eng. Tribol.*, 13506501241251524. doi:10.1177/13506501241251524

Simic, R., and Kalin, M. (2013). Comparison of alcohol and fatty acid adsorption on hydrogenated DLC coatings studied by AFM and tribological tests. *Strojniski Vestn.* 59, 707–718. doi:10.5545/sv-jme.2013.1228

Simič, R., Kalin, M., Hirayama, T., Korelis, P., and Geue, T. (2014). Fatty acid adsorption on several DLC coatings studied by neutron reflectometry. *Tribol. Lett.* 53, 199–206. doi:10.1007/s11249-013-0257-0

Song, W., Campen, S., Shiel, H., Gattinoni, C., Zhang, J., and Wong, J. S. S. (2024). Position of carbonyl group affects tribological performance of ester friction modifiers. *ACS Appl. Mater. Interfaces* 16, 14252–14262. doi:10.1021/acsami.3c16432

Song, Y., Fukuzawa, K., Hirayama, T., Yamashita, N., Yamada, N. L., Itoh, S., et al. (2023). Effects of polarity of polymers on conformation and lubricating film formation of adsorbed films. *Macromolecules* 56, 1954–1964. doi:10.1021/acs.macromol.2c02238

Spikes, H. A. (1996). Direct observation of boundary layers. *Langmuir* 12, 4567–4573. doi:10.1021/la950899b

Studt, P. (1981). The influence of the structure of isomeric octadecanols on their adsorption from solution on iron and their lubricating properties. *Wear* 70, 329–334. doi:10.1016/0043-1648(81)90353-7

Studt, P. (1989). Boundary lubrication: adsorption of oil additives on steel and ceramic surfaces and its influence on friction and wear. *Tribol. Int.* 22, 111–119. doi:10.1016/0301-679X(89)90171-0

Tang, Z., and Li, S. (2014). A review of recent developments of friction modifiers for liquid lubricants (2007–present). *Curr. Opin. Solid State Mater. Sci.* 18, 119–139. doi:10.1016/j.cossms.2014.02.002

Tatsumi, G., Ratoi, M., Shitara, Y., Sakamoto, K., and Mellor, B. G. (2020). Effect of organic friction modifiers on lubrication of PEEK-steel contact. *Tribol. Int.* 151, 106513. doi:10.1016/j.triboint.2020.106513

Xu, X., Yang, F., Yang, H., Zhao, Y., Sun, X., and Tang, Y. (2024). Preparation and tribological behaviors of sulfur- and phosphorus-free organic friction modifier of amide–ester type. *Lubricants* 12, 196. doi:10.3390/lubricants12060196

Yamada, N. L., Torikai, N., Mitamura, K., Sagehashi, H., Sato, S., Seto, H., et al. (2011). Design and performance of horizontal-type neutron reflectometer SOFIA at J-PARC/MLF. *Eur. Phys. J. Plus* 126, 108. doi:10.1140/epjp/i2011-11108-7

Yamada, S., Fujihara, A., Yusa, S., Tanabe, T., and Kurihara, K. (2015). Low-friction adsorbed layers of a triblock copolymer additive in oil-based lubrication. *Langmuir* 31, 12140–12147. doi:10.1021/acs.langmuir.5b03620

Yamashita, N., and Hirayama, T. (2024). Effect of atmospheric gas on ZDDP tribofilm formation. *Tribol. Int.* 193, 109400. doi:10.1016/j.triboint.2024.109400

Yamashita, N., Hirayama, T., L. Yamada, N., Shimizu, Y., Oda, K., and Kawamoto, H. (2022). Interfacial structure and tribological property of adsorbed layer formed by dibasic acid ester derivative. *Tribol. Online* 17, 246–256. doi:10.2474/trol.17.246

Yu, H., Chen, H., Zheng, Z., Qiao, D., Feng, D., Gong, Z., et al. (2023). Effect of functional groups on tribological properties of lubricants and mechanism investigation. *Friction* 11, 911–926. doi:10.1007/s40544-022-0630-9

Zhang, P., Chen, C., Xiao, C., Chen, L., Jiang, L., and Qian, L. (2018). Effects of surface chemical groups and environmental media on tribochemical running-in behaviors of silicon surface. *Tribol. Int.* 128, 174–180. doi:10.1016/j.triboint.2018.07.032

Zhang, P., He, H., Chen, C., Xiao, C., Chen, L., and Qian, L. (2017). Effect of abrasive particle size on tribochemical wear of monocrystalline silicon. *Tribol. Int.* 109, 222–228. doi:10.1016/j.triboint.2016.12.050

frontiers | Frontiers in Mechanical Engineering

TYPE Original Research
PUBLISHED 20 September 2024
DOI 10.3389/fmech.2024.1470312

Check for updates

OPEN ACCESS

EDITED BY
Hikaru Okubo,
Yokohama National University, Japan

REVIEWED BY
Saša Milojević,
University of Kragujevac, Serbia
Milan Bukvic,
University of Kragujevac, Serbia

*CORRESPONDENCE
Takayuki Tokoroyama,
takayuki.tokoroyama@mae.nagoya-u.ac.jp

RECEIVED 25 July 2024
ACCEPTED 23 August 2024
PUBLISHED 20 September 2024

CITATION
Tokoroyama T, Okashita M, Zhang R, Murashima M, Tsuboi R, Yoshida T, Shiomi H and Umehara N (2024) The mechanism of small wear particles entrainment in friction under boundary lubrication.
*Front. Mech. Eng.* 10:1470312.
doi: 10.3389/fmech.2024.1470312

COPYRIGHT
© 2024 Tokoroyama, Okashita, Zhang, Murashima, Tsuboi, Yoshida, Shiomi and Umehara. This is an open-access article distributed under the terms of the Creative Commons Attribution License (CC BY). The use, distribution or reproduction in other forums is permitted, provided the original author(s) and the copyright owner(s) are credited and that the original publication in this journal is cited, in accordance with accepted academic practice. No use, distribution or reproduction is permitted which does not comply with these terms.

# The mechanism of small wear particles entrainment in friction under boundary lubrication

Takayuki Tokoroyama[1]*, Masahiro Okashita[1], Ruixi Zhang[1], Motoyuki Murashima[2], Ryo Tsuboi[3], Takuji Yoshida[3], Hiroshi Shiomi[4] and Noritsugu Umehara[1]

[1]Department of Micro-Nano Mechanical Science and Engineering, Graduate School of Engineering, Nagoya University, Nagoya, Japan, [2]Department of Mechanical Systems Engineering, Graduate School of Engineering, Tohoku University, Sendai, Japan, [3]Department of Mechanical Engineering, Graduate School of Engineering, Daido University, Nagoya, Japan, [4]Department of Mechanical System and Engineering, Japan Aerospace Exploration Agency, Nagoya, Japan

When the lubricating oil flowing between the contact surfaces contains simulated wear particles, it is considered that there is a high possibility for the particles to enter between the contact surfaces if the particles are present on the disk side in a friction test between a fixed ball and a rotating disk. For particles with a diameter of 0.8 μm, it has been previously shown that the entrainment frequency changes with the outside oil film thickness, but the effect of the disk material on the amount of particle deposition and the visualization of particle movement direction due to vortices generated between the contact surfaces had not been performed. In this study, by using $SiO_2$ disks and sapphire disks with different Hamaker constants, the effect on the amount of particle deposition in front of the contact surfaces was experimentally clarified by changing the van der Waals forces acting between the particles and the disks. Additionally, assuming that vortices generated in the oil film between the contact surfaces move the particles to the disk surface side, the flow direction of the lubricating oil was visualized using Navier-Stokes simulation.

KEYWORDS

**in-situ, fluorescent staining, Rhodamine B, silane coupling, oil film thickness, Navier-Stokes simulation**

## 1 Introduction

It is not difficult to imagine that abrasive wear particles entraining the contact surfaces and causing abrasive wear can drastically reduce the lifespan of sliding materials. For example, in the wear of the cylinder liner in an automobile engine, material transfer occurs from the aluminum-silicon alloy to the cast iron side. This wear debris gets embedded into the cylinder liner (Milojević et al., 2023; Milojević et al., 2024; Gajevic et al., 2024; Milojević and Stojanović, 2018). When using hard carbon-based thin coatings in lubricating oil (Abdollah et al., 2012; Abdollah et al., 2010), delamination from the substrate (Lee et al., 2019; Lee et al., 2020) and entrainment into the contact surfaces is a significant issue that drastically reduces the material's lifespan (Lee et al., 2018; Kassim et al., 2020; Kassim et al., 2021). The entrainment of particles between contact surfaces depends on the size of the particles, the hardness and material of the contact surfaces, the viscosity and temperature of the lubricating oil or grease, the contact form, and the sliding speed. Dwyer-Joyce et al. have continued to address this issue, reporting that particles drawn into the contact surfaces

scratch the surface and are expelled as wear debris. They explain that particles in the approaching oil layer, where the lubricant oil thickness is about the same as the particle diameter, are drawn into the contact surfaces (Dwyer-Joyce, 1999; Nilsson et al., 2006). Strubel et al. have also continued simulations and experiments on the influx of lubricating oil between contact surfaces (Strubel et al., 2016; Strubel et al., 2017a; Strubel et al., 2017b). Observing the movement of particles within sub-millimeter-sized channels and small pores are challenging, and the use of techniques such as surface-enhanced Raman spectroscopy (SERS) has been considered to enhance particle visibility (Chang et al., 2017; Chang et al., 2019), Quantum Dots method (Azuma et al., 2023), Optical reflectance spectroscopic *in situ* observation to realize the real-time generation of tribofilm (Hashizume et al., 2021), and traditional observation of the surface by optical microscope or SEM (scanning electron microscope) (Aboua et al., 2018a; Aboua et al., 2019; Aboua et al., 2018b). Further developments in this area are anticipated. For particles in the lubricating oil to be drawn into the contact surfaces, they need to be near the solid wall moving towards the contact surface, where an inflow exists. However, when the amount of lubricating oil is high, most particles are eliminated by the reverse flow generated in front of the contact surface. For instance, to improve fuel efficiency in automobiles by reducing the amount of lubricating oil supplied to the bearings or to meet the reduction in oil pumps, it is essential to clarify how particle entrainment into the contact surfaces occurs when the amount of lubricating oil is low. In recent years, it has been reported that mixing carbon nanotubes and nanoparticles into lubricating oil can improve tribological properties (Bukvić et al., 2024). The authors have previously clarified how particles infiltrate the contact surfaces in environments with insufficient lubricating oil (Tokoroyama et al., 2024). They reported that the frequency of particle entrainment changes based on the ratio of the oil film thickness outside the contact point (hereafter referred to as outside oil film thickness *Hi*) to the particle diameter *r*. Particularly, it has been clarified that the number of entrainment particles increases in the range of $1 \leq r \leq 2$, although the mechanism is not yet clear. It is hypothesized that the entrainment frequency increases when particles can stay near the solid wall. Therefore, it is expected that the number of entrainment particles will vary depending on the material of the solid wall. Indeed, the hydrophilicity and lipophilicity of the particles are also considered to be related to their penetration (Ghosh and Böker, 2019), and this is an issue that should be addressed in the future.

In the study by Nikas (2007), Nikas (2020), it was predicted that when the particle size is less than 1 μm, the van der Waals forces on the disk surface become a significant source of force for particle penetration, but this had not been demonstrated. It is important that we should experimentally prove this prediction to be correct. Additionally, in a previous author's paper (Tokoroyama et al., 2024), it was speculated that a reverse flow vortex component forms in the direction away from the disk surface in front of the contact point, but this was only a hypothesis. Therefore, using Navier-Stokes numerical simulations to verify the presence of a vortex exists at a specific location where particles are lifted off the disk surface.

In this study, we investigate the relationship between the amount of particle deposition in front of the contact surfaces and the number of entrainment particles using an *in situ* observation method with fluorescent stained particles, which allows for observation of even microscopic particles that are unobservable due to optical limitations when using an optical microscope of around 1 μm, 0.8 μm is considered the largest particle that can enter between contact surfaces and promote wear while being below the optical limit, making the observation of particles of this size the most important. Transparent materials such as quartz and sapphire were used for the solid wall to enable observation of the contact surfaces. For the friction test conditions, a transparent disk-shaped test piece and a bearing steel ball were used between the two contact surfaces, under elastic contact conditions and boundary lubrication conditions.

Additionally, the particle deposition observed in the aforementioned experiment is considered to be caused by the flow near the disk within the working fluid. Since the presence of vortices that detach particles from the disk surface is deemed most important, Navier-Stokes numerical simulations under poor lubrication conditions were conducted to clarify the positional relationship between the vortices generated within the thin lubrication film and the contact points.

While reducing the supply of lubricating oil in future automotive development is essential for improving fuel efficiency, ensuring a comfortable cabin environment, and reducing lubricating oil consumption, excessive wear on contact surfaces caused by wear particles in thin lubrication environments must be controlled. From this perspective, it is necessary to understand the tribology of particles of practical around μm sizes and their entry into thin lubrication environments that may occur in the future.

## 2 Experimental procedure

### 2.1 Staining silica particles with fluorescent dyes and observation equipment

The detail of staining technique and observation equipment were reported in reference Tokoroyama et al. (2024), the brief and important procedure of staining the silica particles is summarized below. The fluorescent staining of silica particles was accomplished using a combination of a silane coupling agent (KBM-4803 from Shin-Etsu Silicone, Japan) and Rhodamine B (from Fujifilm Wako Pure Chemical Corporation, Japan). These silica particles came in three sizes, with average diameters of 0.8, 1.0, and 3.0 μm (supplied by Potters Ballotine Co., Ltd., Japan).

Friction tests were carried out using an *in situ* observation system called "iFLAT" (Intelligent Fluorescent Light Assisted Tribometer, which equipment can be allowed to use 1.0 N as limitation of normal load, 5.0 mm/s as maximum of sliding speed, and 2,000 fps as frame rate). A schematic of this system is depicted in Figure 1A, with an enlarged view of the observation area shown in Figure 1B. The iFLAT system is equipped with a 532 nm laser source (GLK32200, LASOS, Germany). This laser travels through a light guide from the source, enters an objective lens of an optical microscope, and is directed to the friction area via a sapphire and a quartz disk (1.0 mm thickness, 50 mm diameter, with a surface roughness of approximately 2.0 nmRa, respectively). These transparent materials are used for the visualization of the *in situ*

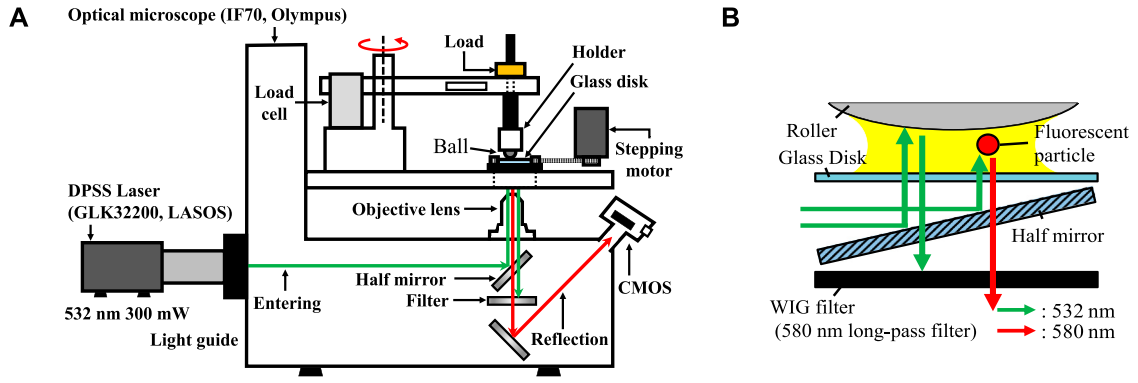


FIGURE 1
**(A)** Schematic of iFlat equipment, **(B)** schematic of inlet laser path through the glass disk to the contact point, and the reflection path through WIG filter.

TABLE 1 Friction test conditions.

| | | |
|---|---|---|
| Normal load *W*, N | 0.2 | |
| Sliding speed *V*, mm/s | 5.0 | |
| Temperature *t*, ℃ | 23 | |
| Frame late *R*, fps | 500 | |
| Disk materials | Glass | Sapphire |
| Surface roughness *Ra*, μmRa | 2.0 | 2.0 |
| Counter material ball | $\phi$8 mm SUJ2 | |
| Surface roughness *Ra*, μmRa | 7.0 | |
| Lubricant | PAO8 | |
| Viscosity $\eta$, mPa·s | 46.0 | |

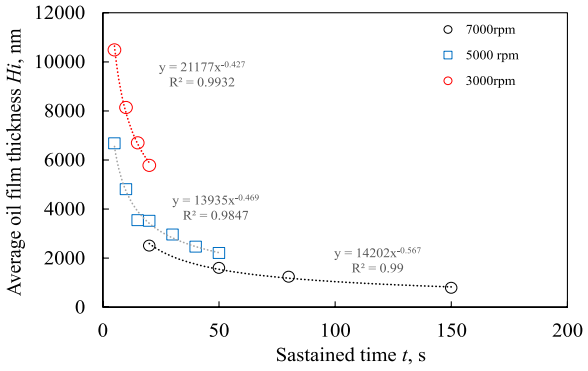


FIGURE 2
Oil film thickness formed at different rotational speeds and times.

observation of the surface, and their surface roughness is smaller than that of actual sliding surfaces (such as honing or coating surfaces). However, by changing the surface roughness of the counterpart material's ball, it will be necessary in the future to clarify the relationship between roughness and particle entry. A fixed SUJ2 bearing ball (approximately 8.0 mm in diameter, with a surface roughness of approximately 7.0 nmRa, it is same property of AISI53200 stainless steel) within a ball holder is placed on a friction cantilever. A dead weight is used to apply a normal load of 0.2 N. The bearing ball reflects the incident laser, and the fluorescently stained particles emit fluorescent light. Both sets of light pass through the sapphire disk before reaching a half-mirror. Subsequently, both lights are directed to a WIG filter, which is a long-pass filter with a cutoff wavelength at 580 nm, effectively eliminating reflected laser light. Finally, the fluorescent light is captured by a CMOS camera, operating at a frame rate of 500 frames per second (fps). The *in situ* observations were conducted multiple times, and we selected 60 frames (0.12 s) that recorded the highest particle counts within the observation area during the observations. The summary of those conditions are listed in Table 1.

## 2.2 Preparation and *in situ* friction test observation procedure

The friction test involved the interaction between an SUJ2 ball and a sapphire or a quartz disk lubricated with PAO8 lubricant, which possesses a viscosity of 46.0 mPs s at 40°C. The i-FLAT system was utilized for this test. In the previous report (Tokoroyama et al., 2024), an outside oil film (*Hi*) was formed by applying a load to the lubricating oil placed between two disks and sliding the two disks to achieve a film of a certain thickness. However, there were issues with the controllability and reproducibility of the oil film thickness. Therefore, a uniform oil film was formed using a spin coater (ACT-220AII). When using a spin coater, the theoretical oil film thickness is calculated by the following Equation 1 (Alfred et al., 1958):

$$h = \frac{h_0}{\sqrt{1 + \frac{4\omega^2 h_0^2 t}{3\nu}}} \quad (1)$$

here, $h$ is the oil film thickness, $h_0$ is the initial film thickness, $\omega$ is the rotational speed, $t$ is the rotational time, and $\nu$ is the kinematic viscosity (Emslie et al., 1958). An oil film was formed using PAO8 at different rotational speeds and times, and the oil film thickness was measured using a reflection spectroscopic film thickness meter. The

results are shown in Figure 2. The calibration curve was created using a power approximation so that it would be a function of time $t$ in the theoretical formula, and the power values of $t$ ranged from −0.427 to −0.567, which were close to the theoretical value of −0.5. The experimental Equations 2–4 obtained from the experiment is shown below.

$$h_{3000\mathrm{rpm}} = 21177t^{-0.427} \quad (2)$$

$$h_{5000\mathrm{rpm}} = 13935\mathrm{t}^{-0.469} \quad (3)$$

$$h_{7000\mathrm{rpm}} = 14202t^{-0.567} \quad (4)$$

The sapphire disk with the lubricant was secured onto the disk holder, with the ball specimen attached to it. A dead weight of 0.2 N was added to the ball specimen. Fluorescently stained particles, comprising a colloidal liquid of ethanol with a volume of 0.1 μL (assuming that the stained particles are Uniformly dispersed in the solvent, the number of particles contained in 0.1 μL is 20,000 when the diameter is 0.8 μm), were applied onto the oil film, positioned at the same radius as the friction test rotation, just ahead of the contact point. Prior to commencing the *in situ* friction test, several minutes were allowed to pass to account for ethanol vaporization. The sliding speed was set at 5.0 mm/s (with a rotation radius of approximately 5.0 mm), and the camera operated at a speed of 500 frames per second (fps). We captured a continuous sequence of 60 frames (0.12 s) to tally the number of particles when the highest concentration of particles was observed near the contact point. The sliding distance covered in these 60 frames was approximately 0.6 mm.

## 2.3 Calculation method for the number of particles deposited between contact surfaces

A friction test was conducted for 5 s until the fluorescent-stained particles were trapped between the contact surfaces, and the area of deposited particles was measured. Since the particles present on the area emit light due to Rhodamine B, the observed images were converted into 256-level grayscale images, and binarization was performed to calculate the area. A threshold value of 60 was used in this process. The projected area created by particles with a diameter of 0.8 μm on the observation area was approximately 0.5 $mm^2$, and even with adjustments of ±2 levels around 60, the particle area fluctuation was less than 1 $mm^2$, so this value was adopted.

## 2.4 Visualization of the flow generated within a thin lubrication film using the Navier-Stokes method

To identify the position where the lubricant generates vortices that cause particles to detach from the disk surface, the flow generated within the thin lubricant film was visualized using Navier-Stokes method simulations. Quartz was used as the disk material, and PAO8 was used as the lubricant. The contact angle between the lubricant and the quartz was set to 11° (the value measured using a contact angle meter). The movement speed of the disk was 5 mm/s, the same as in the experiment, and in the simulation, the lubricant and other test specimens were set to room temperature (23°C).

In the Navier-Stokes simulation (simulations were performed using Ansys Fluent 2020 R1 (ANSYS, Inc., US).), a contact region as shown in Figure 3 was prepared. The outside oil film thickness was set to values ($Hi$ = 0.4 as half of particles, 1.2 as three times thicker than 0.4 μm and it is within the value of $1 \leq r \leq 2$, and 2.0 μm as five times thicker than 0.4 μm and it is the value of $r > 2$). In the figure, i) represents the Hertz contact circle generated between the contacting ball and disk, ii) is a cross-section divided at the center of the Hertz contact circle by the incoming lubricating oil, assuming that the flow occurring in the oil film is symmetrically present. The cross-section of the incoming lubricating oil is represented by iii), and iv) is assumed to symmetrically exist as a pressure outlet. The interface between air and oil was defined as VOF (volume of fluid) = 0.5, assuming that each medium exists in equal amounts.

# 3 Results and discussion

## 3.1 The effect of disk material and outside oil film thickness on the amount of particle deposition on the contact surface

To clarify the effect of outside oil film thickness on the number of particles entering between contact surfaces, friction tests were conducted using glass particles with a diameter of approximately 0.8 μm and employing sapphire disks and quartz disks as counter materials. Figure 4 shows the results of experiments conducted under dry conditions after the solvent dropped before the observation area had dried. The areas covered by particles deposited on the surface of the sapphire disk (Figure 4A) and the quartz disk (Figure 4B) were almost the same, and the numerical results of the areas (Figure 4C) also yielded nearly identical values. The results for when the outside oil film thickness was set to 0.8 μm are shown in Figure 5. It is evident that the number of particles deposited is higher on the sapphire disk and very low on the quartz disk. Next, the results for when the outside oil film thickness was set to 1.4 μm are shown in Figure 6. There was a tendency for the number of particles deposited on the quartz disk to increase compared to the 0.8 μm case. Finally, the results for when the outside oil film thickness was set to 5.0 μm are shown in Figure 7. The number of particles deposited decreased on both the sapphire and quartz surfaces. The relationship between the measured number of particles and the outside oil film thickness is shown in Figure 8. For both the sapphire disk and the quartz disk, the number of deposited particles was the same under conditions without lubricating oil, and the number of particles decreased as the outside oil film thickness increased. However, the number of particles deposited on the quartz disk was consistently lower than on the sapphire disk. From these results, it is shown that the number of deposited particles varies depending on the disk material.

## 3.2 The effect sliding speed, normal load on the deposition amount

It is believed that the flow field generated near the contact point affects the particle's movement speed and retention near the contact point. Since the retention time is considered to be influenced by the

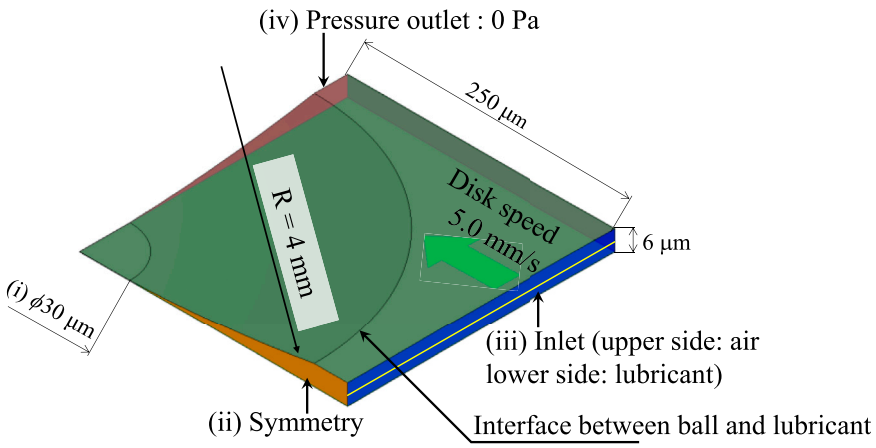


FIGURE 3
Schematic of N-S simulation area.

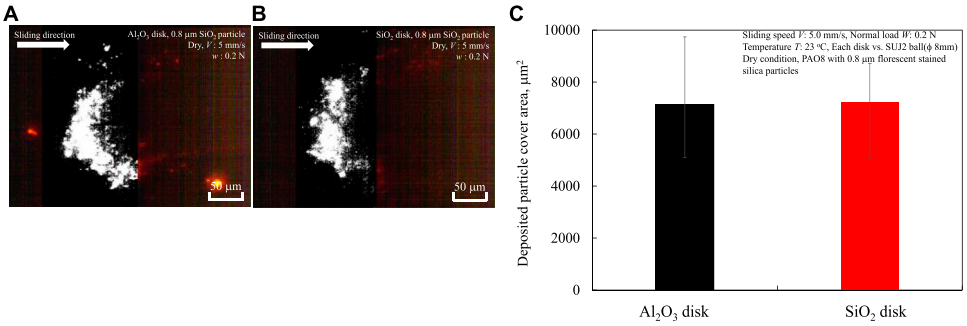


FIGURE 4
Deposition results of 0.8 µm diameter particles between contact surfaces under conditions without lubricant: **(A)** sapphire disk, **(B)** quartz disk, **(C)** particle area deposited on the surface of each disk specimen.

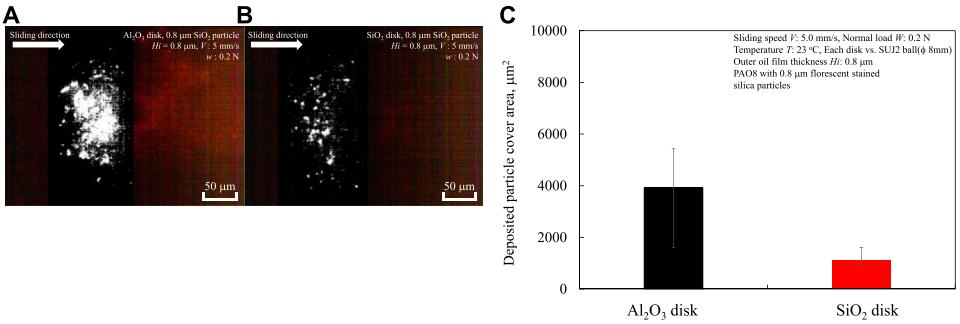


FIGURE 5
Deposition results of 0.8 µm diameter particles between contact surfaces under conditions with lubricant which outside oil film thickness was approximately 0.8 µm: **(A)** sapphire disk, **(B)** quartz disk, **(C)** particle area deposited on the surface of each disk specimen.

rotation speed of the disk specimen, experiments were conducted by reducing the sliding speed from 5 mm/s used in the previous tests to 0.5 mm/s. Additionally, to clarify the effect of normal load acting between the two contact surfaces on the number of particle deposits, experiments were conducted by increasing the normal load to 1.0 N. The results are shown in Figures 9, 10, respectively.

By reducing the rotation speed of the disk from 5.0 mm/s to 0.5 mm/s, the number of particles deposited between the contact

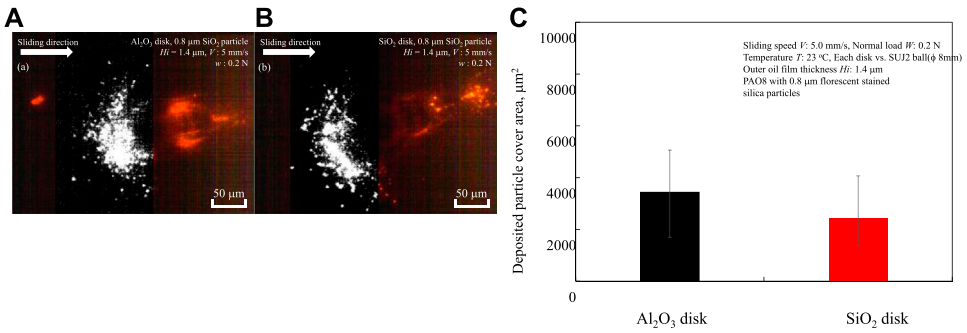


FIGURE 6
Deposition results of 0.8 μm diameter particles between contact surfaces under conditions with lubricant which outside oil film thickness was approximately 1.4 μm: **(A)** sapphire disk, **(B)** quartz disk, **(C)** particle area deposited on the surface of each disk specimen.

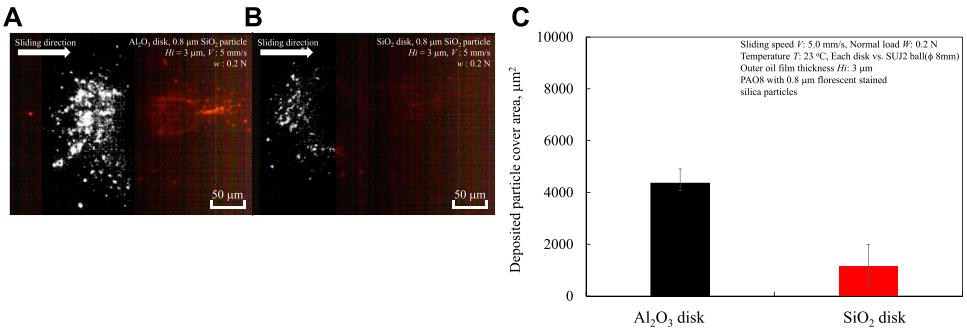


FIGURE 7
Deposition results of 0.8 μm diameter particles between contact surfaces under conditions with lubricant which outside oil film thickness was approximately 5.0 μm: **(A)** sapphire disk, **(B)** quartz disk, **(C)** particle area deposited on the surface of each disk specimen.

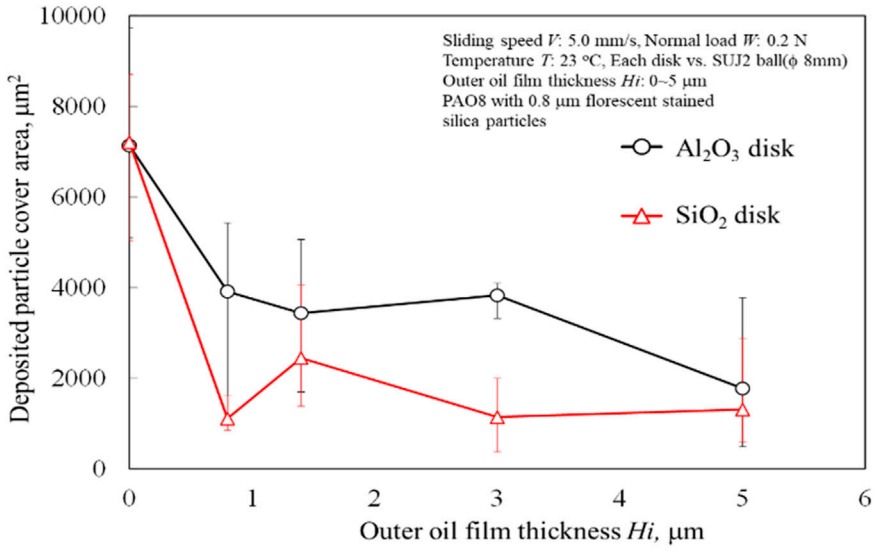


FIGURE 8
The effect of outside oil film thickness on particle deposition area.

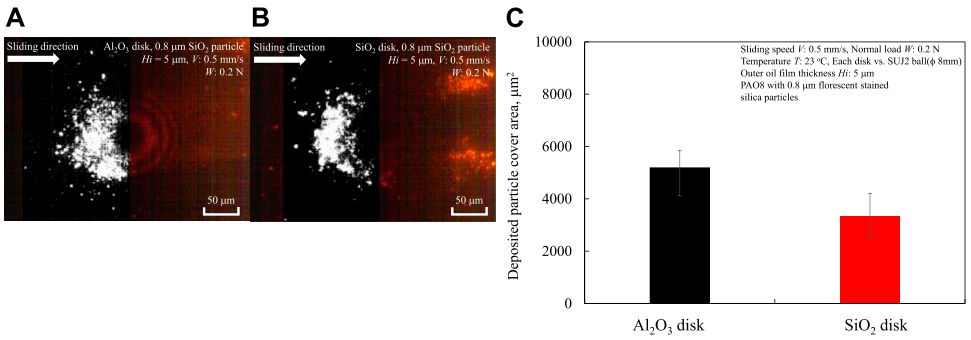


FIGURE 9
Deposition results of 0.8 μm diameter particles between contact surfaces under conditions with lubricant which outside oil film thickness was approximately 5.0 μm using 0.5 mm/s of disk speed: **(A)** sapphire disk, **(B)** quartz disk, **(C)** particle area deposited on the surface of each disk specimen.

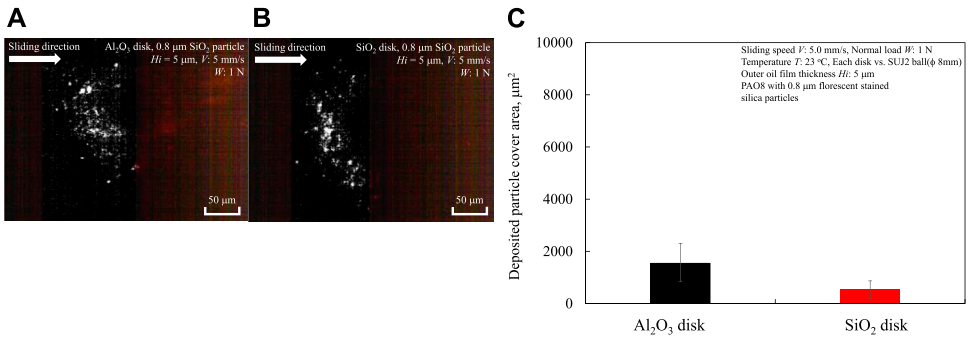


FIGURE 10
Deposition results of 0.8 μm diameter particles between contact surfaces under conditions with lubricant which outside oil film thickness was approximately 5.0 μm using 1.0 N of normal load: **(A)** sapphire disk, **(B)** quartz disk, **(C)** particle area deposited on the surface of each disk specimen.

surfaces increased significantly compared to Figure 6. Approximately twice as many particles were deposited on the sapphire disk, and about 1.5 times as many particles were deposited on the quartz disk. From these results, it can be concluded that the flow generated near the contact surface affects particle deposition.

Next, Figure 10 shows the observation results when the normal load was increased from 0.2 N to 1.0 N under a sliding speed of 5.0 mm/s and an outside oil film thickness of 5.0 μm. Compared to Figure 7, where a similar experiment was conducted at 0.2 N, there are almost small number of particles present between the contact surfaces, similar to the results shown in Figure 7. From these results, it can be concluded that under boundary lubrication conditions, the normal load applied between the contact surfaces does not affect the number of particles entering.

## 3.3 The effect of disk material on the flow near the contact point using a diameter of 0.02 μm

As previously mentioned, it is evident that the number of particles deposited near the contact point varies depending on the material of the disk specimens used and the small outside oil film thickness, using particles with a diameter of 0.8 μm. The different amounts of particle deposition may be due to the inherent physical properties of the disk materials (e.g., van der Waals forces or wettability).

However, it is not clear to what extent these physical properties affect the flow near the contact point. Therefore, particles with a diameter of 0.02 μm were used to observe the flow on the surfaces of sapphire and quartz disks. The results are shown in Figure 11. The yellow circles in the figure indicate positions where the geometric gap between the SUJ2 ball and the disk surface is 0.8 μm. Calculating the particle movement speed on each disk surface from the subtraction between frames, the speed was approximately 5.0 mm/s, which is similar to the disk speed in the sliding direction, indicating that the flow speed is almost the same regardless of the disk material.

## 3.4 The influence of van der waals forces on particle entry into the contact interface

The flow near the contact point is unaffected by the disk material, but the amount of particle deposition near the contact point shows the influence of the disk material. Therefore, it is inferred that van der Waals forces, as inherent material

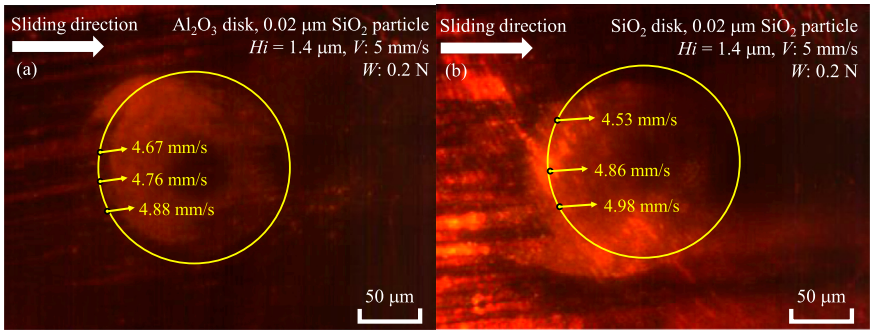


FIGURE 11
The effect of disk material on the flow near the contact point with an outside oil film thickness of 1.4 μm by using 0.02 μm diameter $SiO_2$ particles: **(A)** sapphire, **(B)** quartz.

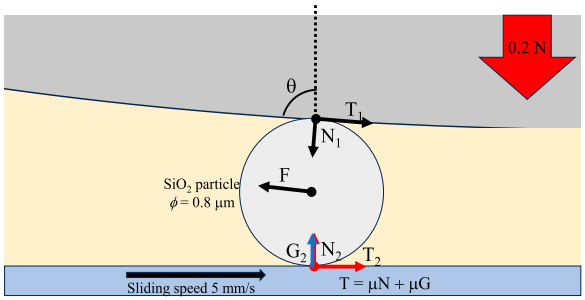


FIGURE 12
The schematics of several force generating to the particle between two surfaces.

properties, play a role (Regarding wettability mentioned earlier, the contact angles of quartz and sapphire with PAO8 are both approximately 11°, showing no difference, thus having no effect.) Nikas et al. has demonstrated through numerical analysis that frictional forces significantly contribute to the trapping of particles between two sliding surfaces, and that for very small particles below 5 μm, the influence of van der Waals forces on particle behavior becomes comparable to fluid forces (Nikas, 2007; Nikas, 2020). Therefore, assuming forces other than the fluid pushing against the deposited particles, Figure 12 shows the geometrical model of the forces acting on a particle when it is trapped. $T$ is the frictional force, $N$ is the normal force, $F$ is the fluid force, $G$ is the van der Waals force acting between the disk and the particle, and $\theta$ is the angle at which the disk and the particle contact at a geometric gap of 0.8 μm. To investigate the change in the number of particles deposited by the disk, the van der Waals force represented by $G$ is assumed to only affect when the distance between the particle and the disk is very close, and it is assumed to act only between the disk and the particle. Under these conditions, it is considered that the particle will be trapped when the sum of the frictional forces $T_1$ and $T_2$ is greater than the reverse fluid force $F$. When a particle is trapped between the sphere and the disk, it is considered that the particle will move into the contact area when the total frictional force of the particles deposited near the contact surface exceeds the horizontally decomposed force of the load.

Here, we use the following Equations 5–7 described in the report by Nikas et al.,

$$F_x = 3\pi\eta_0 \frac{u_1 + u_2}{2}\left[h_c - \frac{\pi}{4}(d - h_c)\right] \tag{5}$$

$$G = \frac{-Hd}{12s^2}\left[\frac{1}{1 + \frac{d}{2.97\sigma}} + \frac{1}{\left(1 + \frac{1.485\sigma}{s}\right)^2}\right] \tag{6}$$

$$H \cong \left(\sqrt{h_d} - \sqrt{h_f}\right)\left(\sqrt{h_p} - \sqrt{h_f}\right) \tag{7}$$

$Fx$ is the fluid force in the sliding direction generated near the contact area, $\eta_0$ is the viscosity of the lubricating oil, $u_1$ and $u_2$ are the velocities of the sliding surfaces, $h_c$ is the minimum gap at the contact area, $d$ is the particle diameter, $G$ is the van der Waals force acting between the particle and the disk, $H$ is the Hamaker constant, and $s$ is the minimum distance between the particle and the disk, and $\sigma$ is the surface roughness. The $h_d$, $h_f$, and $h_p$ are Hamaker constant of each element as disk, fluid, and particle. To calculate the forces acting on the particles, we substituted the values shown in Table 2 for the Hamaker constant, lubricating oil viscosity, and other parameters of the test specimens used in the experiment. As a result, the forces $Fx$ and $G$ moving the particles within the contact surface were $Fx$ = 0.64 nN, $G_{sapphire}$ = 0.18 nN, and $G_{quarts}$ = 0.077 nN, respectively. These results indicate that sapphire disk has higher affection for particles and the force is also same order of fluid force.

## 3.5 Visualization of flow in oil film using Navier-Stokes simulation

The flow direction of lubricating oil containing particles at different outside oil film thicknesses was calculated. The results of averaging the velocity vectors in the vertical direction (defined as the $y$-axis) within the contact surface, accompanying the entry of lubricating oil into the contact surface at an outside oil film thickness $Hi$ = 0.4 μm, are shown in Figure 13A. An air-liquid interface is formed between the two surfaces in contact at a position approximately 95 μm ($x$ = 95 μm) from the centre of the Hertz contact. Assuming that the likelihood of particle entry increases when particles move towards the disc side due to downward flow in

TABLE 2 The physical properties of lubricant, particles and disk specimen.

| | |
|---|---|
| Lubricant dynamic viscosity at 23 C $\eta_0$, mPa· s | 46 |
| Hamaker constant $h_{SiO_2}$; $h_{Al_2O_3}$; $h_{oil}$, $10^{-20}$ J | 8.64 Bergström (1997); 15.2 Bergström (1997); 5 Nikas (2016) |
| Surface speed $u_1$; $u_2$, mm/s | 5; 0 |
| Particle diameter $d$, μm | 0.8 |
| Separation between particle and surface $s$, nm | 0.3 Rabinovich et al. (2000) |
| Surface roughness $\sigma$, μm | 0.006 |
| Min. Oil film thickness $h_c$, nm | 4 Hamrock and Dowson (1981) |

the $y$-axis direction, the flow is strongest downwards around $x$ = 93 μm. However, as will be discussed later, since the geometric distance between the contacting surfaces equals the particle diameter of 0.8 μm at $x$ = 160 μm, in the case of $Hi$ = 0.4 μm, particles with a diameter of 0.8 μm first contact the surface of the SUJ2 ball. Despite the presence of lubricating oil, particles on the disc are assumed to contact the SUJ2 ball in nearly dry conditions, resulting in a similar amount of particle deposition around $Hi$ = 0.4 μm regardless of the change in disc material, as shown in Figure 8.

Next, the results for an outside oil film thickness $Hi$ = 1.2 μm are shown in Figure 13B. The geometric distance between the contacting surfaces equals the particle diameter of 0.8 μm at $x$ = 160 μm. Particles near the disc surface ride the upward flow in the $y$-axis direction at $x$ = 178 μm, but are influenced by the downward flow in the $y$-axis direction in the range of $x$ = 159–174 μm. This downward flow just before particles are geometrically trapped is assumed to push the particles against the disc surface. This result is thought to affect the amount of particle deposition and is consistent with the observation that the number of $SiO_2$ particles deposited peaks around an outside oil film thickness of 1.4 μm, as shown in Figure 8.

Finally, for an outside oil film thickness $Hi$ = 2.0 μm as shown in Figure 13C, an upward flow in the $y$-axis direction is generated at $x$ = 205 μm where the air-liquid interface is formed between the contacting surfaces, suggesting that particles are drawn away from the disc surface. Additionally, an upward flow in the $y$-axis direction occurs again around $x$ = 160 μm where the geometric gap equals the particle diameter, making it difficult for particles to remain.

These results align with the authors' previous findings (Tokoroyama et al., 2024) as shown in Figure 14, which identified the generation of vortices as the cause of a peak in the number of particles entering within the range of $1 \leq r \leq 2$ times the particle diameter, when the outside oil film thickness reaches an extremum.

The results obtained in this study demonstrate how the van der Waals forces and the components that cause particles to separate from the incident flow act when using sapphire and glass disks. However, the effects of the incident flow, the shape, the hardness of the materials, and the hardness of the particles formed on the surfaces of the two contacting faces have not yet been considered. In the future, it will be necessary to widely apply observation techniques to anisotropic particles, ductile metal particles, and biomaterials, making it possible to design structures that suppress particle penetration. Furthermore, the wear particle problems such as human joint which is suffered by wear particles which cause undesirable reaction due to physically and chemically reaction in the body (Kovochich et al., 2018), cell-accelerated corrosion due to metal alloy wear debris (Bijukumar et al., 2020), immune toxicity caused by wear particles (Gill et al., 2012) are the formidable problems to be solved in near future. So, development of observing method of those particles or collecting them (Tokoroyama et al., 2018) should be achieved by several perspectives.

## 4 Conclusion

The prediction of particles' entrainment when the particle size is less than 1 μm, the van der Waals forces on the disk surface become a significant source of force for particle penetration, but this had not been experimentally demonstrated. Furthermore, authors previously reported that a reverse flow vortex component forms in the direction away from the disk surface in front of the contact point, but this was only a hypothesis. Therefore, using Navier-Stokes numerical simulations to reveal the presence of a vortex at a specific location where particles are lifted off the disk surface is required. Using iFLAT, which enables *in situ* observation of particles entering the contact surfaces, the entry of fluorescent-stained particles was observed. Previous research reported that the number of particles entering reached an extreme value when the ratio $r$ of the outside oil film thickness to the particle diameter was $1 \leq r \leq 2$, but the mechanism was unclear. For particles to enter, they need to be present in the layer drawn towards the contact point. In this study, experiments were conducted based on the hypothesis that the proximity to and the amount of deposition on the disk side specimen surface are important parameters. Quartz and sapphire, with different Hamaker constants, were used in the experiments to clarify the effect of materials on the amount of particle deposition. The main conclusions obtained are shown below.

- The amount of particle deposition on the front side of the two contacting surfaces varies depending on the disk material, with sapphire disks consistently accumulating more particles than quartz.
- An experiment was conducted to verify the possibility that the differences in van der Waals forces, which were anticipated before the experiment, could attract particles to the substrate surface. As a result, the amount of particle deposition mentioned above is influenced by the van der Waals forces calculated from the Hamaker constant of the disk material. In

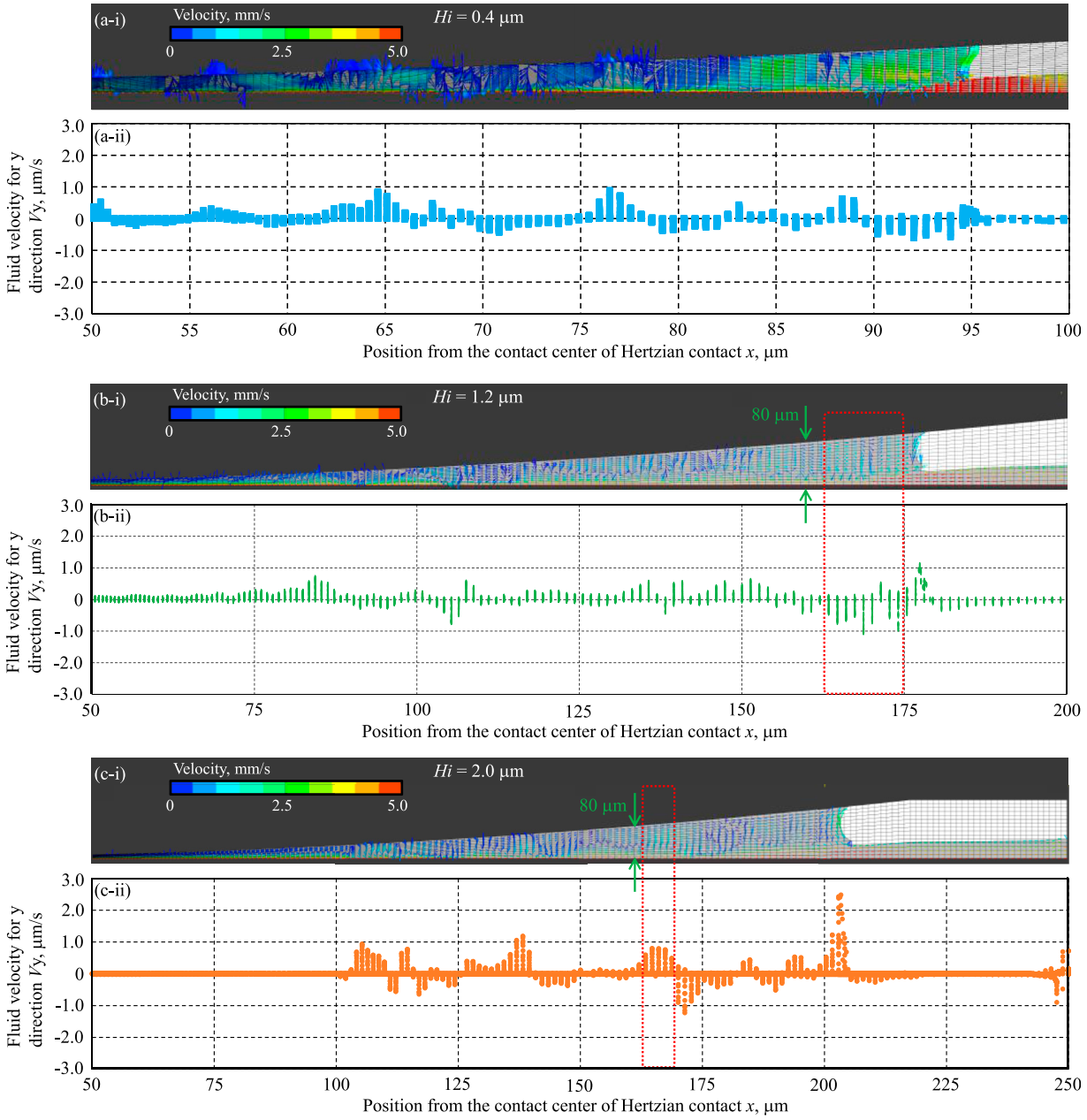


FIGURE 13
The Navier-Stokes Simulation results of different oil film thickness **(A)** *Hi* = 0.4, **(B)** *Hi* = 1.2, and **(C)** *Hi* = 2.0 μm. (i) Shows velocity and direction of oil, (ii) shows average velocity of *y* direction.

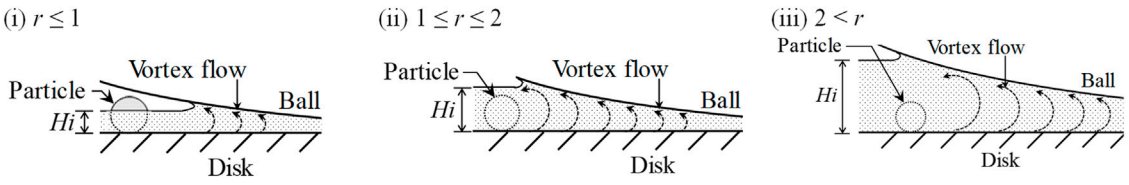


FIGURE 14
Schematic of a particle and vortex flow with different outside oil film thickness (Tokoroyama et al., 2024).

relation to the force $Fx$ = 0.64 nN acting on the particles from the fluid, the van der Waals forces were calculated as $G_{sapphire}$ = 0.18 nN and $G_{quarts}$ = 0.077 nN, respectively.

- Using Navier-Stokes simulation, calculations were performed on the flow between contact surfaces with outside oil film thicknesses of $Hi$ = 0.4, 1.2, and 2.0 μm, and the $y$-axis directional velocity of the lubricant oil was calculated. The results indicated that when the outside oil film thickness was $Hi$ = 1.2 μm, which is comparable to the particle diameter of 0.8 μm, there was a downward flow (i.e., towards the moving disk side) in the range from $x$ = 159–174 μm, including $x$ = 160 μm where the geometric gap between the two surfaces was 0.8 μm. This suggests a high possibility of particles being drawn between the contact surfaces. On the other hand, when the outside oil film thickness was $Hi$ = 2.0 μm, at the position of the liquid-gas interface ($x$ = 205 μm) formed between the lubricating oil and the gas between the contacting surfaces, there was a flow from the disk side towards the SUJ2 ball specimen direction, indicating the possibility of particles moving away from the disk. The above results are presumed to vary depending on factors such as the surface roughness of the counterpart material, the curvature radius of the ball, the viscosity of the lubricant, and the anisotropy of the particles. Therefore, it will be necessary to continue clarifying the entry of particles into the contact surfaces of automotive transmissions and gears in the future.

## Data availability statement

The original contributions presented in the study are included in the article/supplementary material, further inquiries can be directed to the corresponding author.

## Author contributions

TT: Writing–original draft, Writing–review and editing, Formal Analysis, Investigation, Methodology, Visualization. MO: Formal Analysis, Investigation, Methodology, Writing–original draft. RZ: Formal Analysis, Investigation, Methodology, Writing–original draft. MM: Formal Analysis, Investigation, Methodology, Writing–original draft. RT: Formal Analysis, Investigation, Methodology, Writing–original draft. TY: Formal Analysis, Investigation, Methodology, Writing–original draft. HS: Formal Analysis, Investigation, Methodology, Writing–original draft. NU: Supervision, Writing–original draft.

## Funding

The author(s) declare financial support was received for the research, authorship, and/or publication of this article. This paper is based on results obtained from a project, JPNP20004, subsidized by New Energy and Industrial Technology Development Organization (NEDO).

## Acknowledgments

The authors acknowledge the support of Mr. Y. Asada, Mr. T. Sato, and Mr. T. Muramatsu at Univance corporation, Shizuoka, Japan, for supporting research fund and having discussion to perfume this work.

## Conflict of interest

The authors declare that the research was conducted in the absence of any commercial or financial relationships that could be construed as a potential conflict of interest.

## Publisher's note

All claims expressed in this article are solely those of the authors and do not necessarily represent those of their affiliated organizations, or those of the publisher, the editors and the reviewers. Any product that may be evaluated in this article, or claim that may be made by its manufacturer, is not guaranteed or endorsed by the publisher.

## References

Abdollah, M. F. B., Yamaguchi, Y., Akao, T., Inayoshi, N., Miyamoto, N., Tokoroyama, T., et al. (2012). Deformation-wear transition map of DLC coating under cyclic impact loading. *Wear* 274-275, 435–441. doi:10.1016/j.wear.2011.11.007

Abdollah, M. F. B., Yamaguchi, Y., Akao, T., Inayoshi, N., Umehara, N., and Tokoroyama, T. (2010). Phase transformation studies on the a-C coating under repetitive impacts. *Surf. Coat. Technol.* 205 (2), 625–631. doi:10.1016/j.surfcoat.2010.07.062

Aboua, K. A. M., Umehara, N., Kousaka, H., Tokoroyama, T., Murashima, M., Mabuchi, Y., et al. (2018a). Effect of carbon diffusion on friction and wear behaviors of diamond-like carbon coating against Cr-plating in boundary base oil lubrication. *Tribol. Online* 13 (5), 290–300. doi:10.2474/trol.13.290

Aboua, K. A. M., Umehara, N., Kousaka, H., Tokoroyama, T., Murashima, M., Mabuchi, Y., et al. (2019). Effect of carbon diffusion on friction and wear behaviors of diamond-like carbon coating against germanium in boundary base oil lubrication. *Tribol. Lett.* 67 (2), 65. doi:10.1007/s11249-019-1179-2

Aboua, K. A. M., Umehara, N., Kousaka, H., Tokoroyama, T., Murashima, M., Tasdemir, H. A., et al. (2018b). Effect of ZnDTP triboflim's morphology on friction behaviors of DLC coatings: tribofilm characterization by 3D scanning electron microscope observation. *JAMDSM* 12, JAMDSM0129. doi:10.1299/jamdsm.2018jamdsm0129

Alfred, G. E., Francis, T. B., and Leslie, G. P. (1958). Flow of a viscous liquid on a rotating disk. *J. Appl. Phys.* 29, 858–862. doi:10.1063/1.1723300

Azuma, N., Ozeki, H., Miki, K., Fukuzawa, K., Itoh, S., and Zhang, H. (2023). Quantitative measurement of squeeze flow distribution in nanogaps by particle image velocimetry using Quantum Dots. *Tribol. Lett.* 71, 112. doi:10.1007/s11249-023-01783-8

Bergström, L. (1997). Hamaker constants of inorganic materials. *Adv. Colloid Interface Sci.* 70, 125–169. doi:10.1016/S0001-8686(97)00003-1

Bijukumar, D. R., Salunkhe, S., Zheng, G., Barba, M., Hall, D. J., Pourzal, R., et al. (2020). Wear particles induce a new macrophage phenotype with the potential to accelerate material corrosion within total hip replacement interfaces. *Acta Biomater.* 101, 586–597. doi:10.1016/j.actbio.2019.10.039

Bukvić, M., Gajević, S., Skulić, A., Savić, S., Ašonja, A., and Stojanović, B. (2024). Tribological application of nanocomposite additives in industrial oils. *Lubricants* 12 (1), 6. doi:10.3390/lubricants12010006

Chang, S., Eichmann, S. L., Huang, T. Y. S., Yun, W., and Wang, W. (2017). Controlled design and fabrication of SERS-SEF multifunctional nanoparticles for nanoprobe applications: morphology-dependent SERS phenomena. *J. Phys. Chem. C* 121, 8070–8076. doi:10.1021/acs.jpcc.7b00688

Chang, S., Yun, W., Eichmann, S. L., Poitzsch, M. E., and Wang, W. (2019). Magnetic SERS composite nanoparticles for microfluidic oil reservoir tracer detection and nanoprobe applications. *Appl. Nano Mater.* 2, 997–1004. doi:10.1021/acsanm.8b02291

Dwyer-Joyce, R. S. (1999). Predicting the abrasive wear of ball bearings by lubricant debris. *Wear* 233–235, 692–701. doi:10.1016/S0043-1648(99)00184-2

Emslie, A. G., Bonner, F. T., and Peck, L. G. (1958). Flow of a viscous liquid on a rotating disk. *J. Appl. Phys.* 29, 858–862. doi:10.1063/1.1723300

Gajevic, S., Marković, A., Milojević, S., Ašonja, A., Ivanović, L., and Stojanović, B. (2024). Multi-objective optimization of tribological characteristics for aluminum composite using taguchi grey and TOPSIS approaches. *Lubricants* 12, 171. doi:10.3390/lubricants12050171

Ghosh, S. K., and Böker, A. (2019). Self-assembly of nanoparticles in 2D and 3D: recent advances and future trends. *Macromol. Chem. Phys.* 220, 1900196. doi:10.1002/macp.201900196

Gill, H. S., Grammatopoulos, G., Adshead, S., Tsialogiannis, E., and Tsiridis, E. (2012). Molecular and immune toxicity of CoCr nanoparticles in MoM hip arthroplasty. *Trends Mol. Med.* 18 (3), 145–155. doi:10.1016/j.molmed.2011.12.002

Hamrock, B. J., and Dowson, D. (1981). *Ball bearing lubrication: the elastohydrodynamics of elliptical contacts*.

Hashizume, N., Murashima, M., Umehara, N., Tokoroyama, T., and Lee, W. Y. (2021). *In situ* observation of the formation of MoDTC-derived tribofilm on a ta-C coating using reflectance spectroscopy and its effects on friction. *Trib. Int.* 162, 107128. doi:10.1016/j.triboint.2021.107128

Kassim, K. A. M., Tokoroyama, T., Murashima, M., Lee, W.-Y., Umehara, N., and Mustafa, M. M. B. (2021). Wear acceleration of a-C:H coatings by Molybdenum-derived particles: mixing and temperature effects. *Tribol. Int.* 159, 106944. doi:10.1016/j.triboint.2021.106944

Kassim, K. A. M., Tokoroyama, T., Murashima, M., and Umehara, N. (2020). The wear classification of MoDTC-derived particles on silicon and hydrogenated diamond-like carbon at room temperature. *Tribol. Int.* 147, 106176. doi:10.1016/j.triboint.2020.106176

Kovochich, M., Fung, E. S., Donovan, E., Unice, K. M., Paustenbach, D. J., and Finley, B. L. (2018). Characterization of wear debris from metal-on-metal hip implants during normal wear versus edge-loading conditions. *J. Biomed. Mater. Res. Part B* 106B, 986–996. doi:10.1002/jbm.b.33902

Lee, W. Y., Jang, Y. J., Umehara, N., Tokoroyama, T., and Murashima, M. (2020). Effect of defects on wear behavior in ta-C coating prepared by filtered cathodic vacuum arc deposition. *Diam. Relat. Mater* 105, 107789. doi:10.1016/j.diamond.2020.107789

Lee, W. Y., Tokoroyama, T., Jang, Y. J., and Umehara, N. (2018). Effect of substrate bias and temperature on friction and wear properties for ta-C coating prepared under different substrate bias voltages with filtered cathodic vacuum arc deposition. *Tribol. Online* 13 (5), 241–247. doi:10.2474/trol.13.241

Lee, W. Y., Tokoroyama, T., Jang, Y. J., and Umehara, N. (2019). Investigating running-in behavior to understand wear behavior of ta-C coating with filtered cathodic vacuum arc deposition. *J. Tribol.* 23, 38–47. Available at: https://jurnaltribologi.mytribos.org/v23/JT-23-38-47.pdf.

Milojević, S., Glišović, J., Savić, S., Bošković, G., Bukvić, M., and Stojanović, B. (2024). Particulate matter emission and air pollution reduction by applying variable systems in tribologically optimized diesel engines for vehicles in road traffic. *Atmosphere* 15 (2), 184. doi:10.3390/atmos15020184

Milojević, S., Savić, S., Mitrović, S., Marić, D., Krstić, B., Stojanović, B., et al. (2023). Solving the problem of friction and wear in auxiliary devices of internal combustion engines on the example of reciprocating air compressor for vehicles. *Tech. Gaz.* 30 (1), 122–130. doi:10.17559/TV-20220414105757

Milojević, S., and Stojanović, B. (2018). Determination of tribological properties of aluminum cylinder by application of Taguchi method and ANN-based model. *J. Braz. Soc. Mech. Sci. Eng.* 40, 571. doi:10.1007/s40430-018-1495-8

Nikas, G. K. (2007). Effects of operating conditions and friction on the entrapment of spherical debris particles in elliptical contacts. *Proc. Institution Mech. Eng. Part J J. Eng. Tribol.* 221 (6), 727–741. doi:10.1243/13506501JET283

Nikas, G. K. (2016). Algebraic equations for the pile-up geometry in debris particle indentation of rolling elastohydrodynamic contacts. *J. Tribol.* 138 (2), 021503. doi:10.1115/1.4031516

Nikas, G. K. (2020). Particle Entrapment in Line Elastohydrodynamic Contacts and the Influence of Intermolecular (van der Waals) Forces. *Lubricants* 8 (5), 60. doi:10.3390/lubricants8050060

Nilsson, R., Dwyer-Joyce, R. S., and Olofsson, U. (2006). Abrasive wear of rolling bearings by lubricant borne particles. *Proc. Institution Mech. Eng. Part J J. Eng. Tribol.* 220 (5), 429–439. doi:10.1243/13506501J00205

Rabinovich, Y. I., Adler, J. J., Ata, A., Singh, R. K., and Moudgil, B. M. (2000). Adhesion between nanoscale roughs surfaces: I. Role of asperity geometry. *J. Colloid Interface Sci.* 232, 10–16. doi:10.1006/jcis.2000.7167

Strubel, V., Fillot, N., Cavoret, J., Vegne, P., Mondelin, A., and Maheo, Y. (2016). Particle entrapment in hybrid lubricated point contacts. *Tribol. Trans.* 59 (4), 768–779. doi:10.1080/10402004.2015.1106631

Strubel, V., Fillot, N., Ville, F., Cavoret, J., Vergne, P., Mondelin, A., et al. (2017a). Particle entrapment in rolling element bearings: the effect of ellipticity, nature of materials, and sliding. *Tribol. Trans.* 60 (2), 373–382. doi:10.1080/10402004.2016.1168901

Strubel, V., Simoens, S., Vergne, P., Fillot, N., Ville, F., Hajem, M. E., et al. (2017b). Fluorescence tracking and μ-PIV of individual particles and lubricant flow in and around lubricated point contacts. *Tribol. Lett.* 65, 75. doi:10.1007/s11249–017–0859–z

Tokoroyama, T., Kamiya, T., Ahmed, NABH, and Umehara, N. (2018). Collecting micrometer-sized wear particles generated between DLC/DLC surfaces under boundary lubrication with electric field. *JSME Mech. Eng. Lett.* 4, 18–00089. doi:10.1299/mel.18-00089

Tokoroyama, T., Okashita, M., Fusetani, N., Murashima, M., Hashizume, N., Tsuboi, R., et al. (2024). The 1 μm wear particles entrainment *in situ* observation via fluorescent staining silica particles by silane coupling with Rhodamine B. *Front. Mech. Eng.* 10, 1371948. doi:10.3389/fmech.2024.1371948

frontiers | Frontiers in Mechanical Engineering

TYPE Original Research
PUBLISHED 31 October 2024
DOI 10.3389/fmech.2024.1462450

Check for updates

OPEN ACCESS

EDITED BY
Sorin-Cristian Vladescu,
King's College London, United Kingdom

REVIEWED BY
Aleksandar Ašonja,
Business Academy University, Serbia
Saša Milojević,
University of Kragujevac Faculty of Engineering, Serbia

*CORRESPONDENCE
Yasuyoshi Tozaki,
tozaki@mech.kindai.ac.jp

RECEIVED 10 July 2024
ACCEPTED 27 September 2024
PUBLISHED 31 October 2024

CITATION
Tamae H, Ueda N and Tozaki Y (2024) A study of measurement of raceway direct measurement of rolling bearings.
*Front. Mech. Eng.* 10:1462450.
doi: 10.3389/fmech.2024.1462450

COPYRIGHT
© 2024 Tamae, Ueda and Tozaki. This is an open-access article distributed under the terms of the Creative Commons Attribution License (CC BY). The use, distribution or reproduction in other forums is permitted, provided the original author(s) and the copyright owner(s) are credited and that the original publication in this journal is cited, in accordance with accepted academic practice. No use, distribution or reproduction is permitted which does not comply with these terms.

# A study of measurement of raceway direct measurement of rolling bearings

Hiromu Tamae[1], Naoko Ueda[2] and Yasuyoshi Tozaki[1]*

[1]Department of Mechanical Engineering, Faculty of Science and Engineering, Kindai University, Higashiosaka City, Japan, [2]Major in Mechanical Engineering, Graduate School of Science and Engineering, Kindai University, Higashiosaka City, Japan

Demands for improved fuel efficiency in automobiles and other vehicles have led to smaller, lighter power transmission device which result in high surface contact stress and a thin oil film, which in turn tends to cause the temperature of rolling bearings to rise. The most common temperature measurement method is to touch a thermocouple against the inner and outer rings, and this method has been used for many years. However, the method using thermocouples can only measure temperatures in a limited range near the measurement point. The authors applied the Seebeck effect, a phenomenon in which an electromotive force is generated when different metals are connected and a temperature difference is applied to bearings, to a method of measuring bearing raceway temperatures called the dynamic thermocouple method. In the dynamic thermocouple method, the average value of each contact points between the different metals generates the emf (electromotive force), so the temperature rise of all the each rolling elements in contact becomes the average value, and the exact point of temperature rise is not clear. Therefore, all but one rolling element was changed to electrically insulating zirconia balls. With this method, the contact points between many different metals became one, making it possible to identify the locations of temperature rises on the raceway surface. This method makes it possible to directly measure the temperature change of the raceway. The results of temperature measurements of the raceway surface using two types of bearings with different raceway accuracy showed a clear difference of temperature. The bearing with a poor raceway accuracy showed a temperature rise in the unloaded zone, and slippage was observed when the behavior of the rolling element was checked with a high-speed camera. Furthermore, in bearings with good raceway accuracy, the temperature of the raceway surface remained almost constant even in the non-load zone. By using the dynamic thermocouple method and observing the rolling elements with a high-speed camera, it was possible to correlate the bearing temperature rise with the behavior of the rolling elements.

KEYWORDS

**rolling bearing, temperature, seebeck effect, dynamic thermocouple, law of homogeneous, raceway, electromotive force**

## 1 Introduction

As global warming countermeasures, there is a demand for more efficient automobiles and other machines. Tribological optimization of materials is also being considered to improve the sliding surfaces of pistons and cylinders in internal combustion engines, which will contribute to reducing particulate matter emissions by reducing fuel consumption, and

therefore reducing wear on the materials in sliding contact. It contributes to the reduction in harmful gases in the air (Milojevic et al., 2024). Another approach from the lubrication field is to improve lubricants by adding nanotube additives (Bukvic et al., 2024). In addition, efforts are being made to reduce friction loss in rolling bearings for automobiles. There are three technical methods for reducing friction loss in rolling bearings. The first is to change the design of the bearing without changing the main dimensions. The second is to reduce the size of the bearing to reduce torque and weight, and the third is to optimize lubrication in terms of lubricating oil type and bearing materials (Sada, 2017). While two kinds of rolling bearings (ball and roller bearings) are used to reduce friction in internal combustion engine components, allowing rotation and relative motion of mechanical elements, but also, these rolling bearing reducing friction technologies in ICEV automotives are being transferred in electric vehicle design (Farfan-Cabrera, 2019). Due to the development for more compact and lightweight power transmission device and the use of low-viscosity oil to improve fuel efficiency in automobiles and other machines, the temperature of rolling bearings tends to rise due to high contact stress and a thin oil film. Following common rolling bearing failure causes can be classified, with their percentage shares:(1) insufficient amount of lubricant: 15%; (2) inadequate selection of lubricant: 20%; (3) aged lubricant (wear products, additive depletion): 20%; (4) solid particle contamination of lubricant: 20%; (5) liquid contamination of lubricant: 5%; (6) inadequate selection of bearing: 10%; (7) handling induced defects: 5%; (8) mounting faults: 5%; (9) bearing material and production faults: less than 1%. As it can be seen about 80% of bearing failures are associated with the tribological causes (cause 1–5) (Vencl et al., 2017). Reducing friction and wear of rolling bearing elements can be achieved by choosing the right structure, choosing materials with a low friction coefficient and high wear resistance and using appropriate types of lubricants for lubrication (Janic et al., 2015). The fault detection and diagnosis along with condition monitoring and rotating machinery have critical importance for early diagnosis to prevent severe damage of infrastructure in industrial environments. Basic signals used for condition monitoring include vibration, noise, and temperature. Vibration and noise are sensitive to noise, but have the advantage that they can be used for early failure detection and diagnosis. Conversely, temperature cannot be used for early failure detection and diagnosis, but it has the characteristics of being noninvasive and resistant to noise (AlShorman et al., 2020). There are two types of temperature measurement: contact type, which uses thermocouples, *etc.* (Takabi and Khonsari, 2013), and non-contact type, which uses the intensity of infrared rays emitted from an object (Usamentiaga et al., 2014). Contact type measurement is characterized by fixed-point observation and good measurement accuracy, while non-contact type is characterized by the ease of visually understanding the temperature distribution. The most common temperature measurement method is to touch a thermocouple against the inner and outer rings, which has been used conventionally for railroad bearings (Tarawneh et al., 2008) and for development and verification of aircraft engines (Flouros, 2006). However, the method using thermocouples can only determine temperatures in a limited range in the vicinity of the measurement point. Therefore, a technique using infrared rays that detects and visualizes heat to clarify the bearing temperature distribution was used (Jakubek et al., 2021). This method enables visualization of thermal data. In addition, a new technique is the measurement with a sensor that can detect the physical quantity from the amount of wavelength shift, in which the Bragg center reflection wavelength shifts sensitively to temperature by having a short segment in the core of an optical fiber line with a synchronous refractive index modulation of about the wavelength of propagating light (Liu et al., 2013; Dong et al., 2015). Furthermore, a case of temperature measurement by sputtering NiCr and NiSi, which are used as materials for thermocouples, into a thin-film state thermocouple and pressing it onto the edge of a rolling element has been reported (Cui et al., 2022). However, the methods reported so far have not measured the surface temperature of the raceway, which is assumed to be the hottest part of a rolling bearing. Developing a method to continuously measure the surface temperature of rolling bearing raceways is important, as it relates to study into reducing friction loss and improving the reliability of rolling bearings used in automobiles and other machines. Therefore, the authors tried to measure the surface temperature of the raceway surface by using the dynamic thermocouple method, which applies the Seebeck effect, a phenomenon in which an electromotive force is generated. The raceway surface temperature was measured by using the inner ring and rolling elements made of the same material, while the outer ring was made of a different metal. Usually, AISI52100 or carburized steel (AISI4320, AISI9310) is used as the bearing material (Zaretsky, 2012). Basically, the same material is used for the inner ring, outer ring, and rolling elements, but in this study, hardened dissimilar metals were used to generate electromotive force.

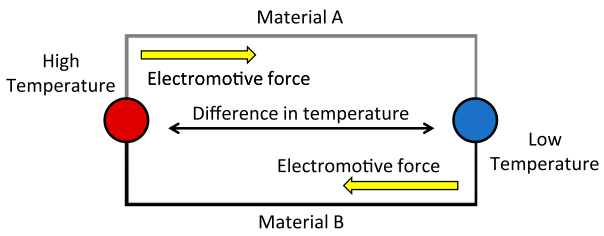


FIGURE 1
Schematic diagram explaining the Seebeck effect.

## 2 Measurement method

This study proposes a dynamic thermocouple method for measuring the temperature of the raceway of rolling bearings. The dynamic thermocouple method is based on the Seebeck effect. The Seebeck effect is a phenomenon in which an electromotive force is generated and an electric current flow when there is a temperature difference between two different metals at each contact point in a closed circuit, as shown in Figure 1.

To apply the Seebeck effect to rolling bearings, different materials were used for the outer ring and rolling element material A and the inner ring material B, so that the rolling element and inner ring raceway temperatures could be measured. Figure 2 shows the details. When measuring raceway temperatures

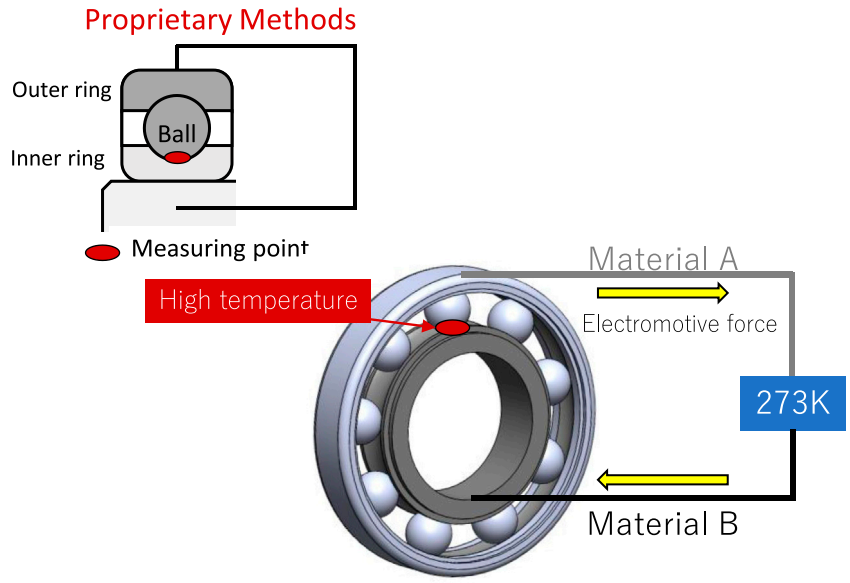


FIGURE 2
Applying method of the Seebeck effect to measuring rolling bearings.

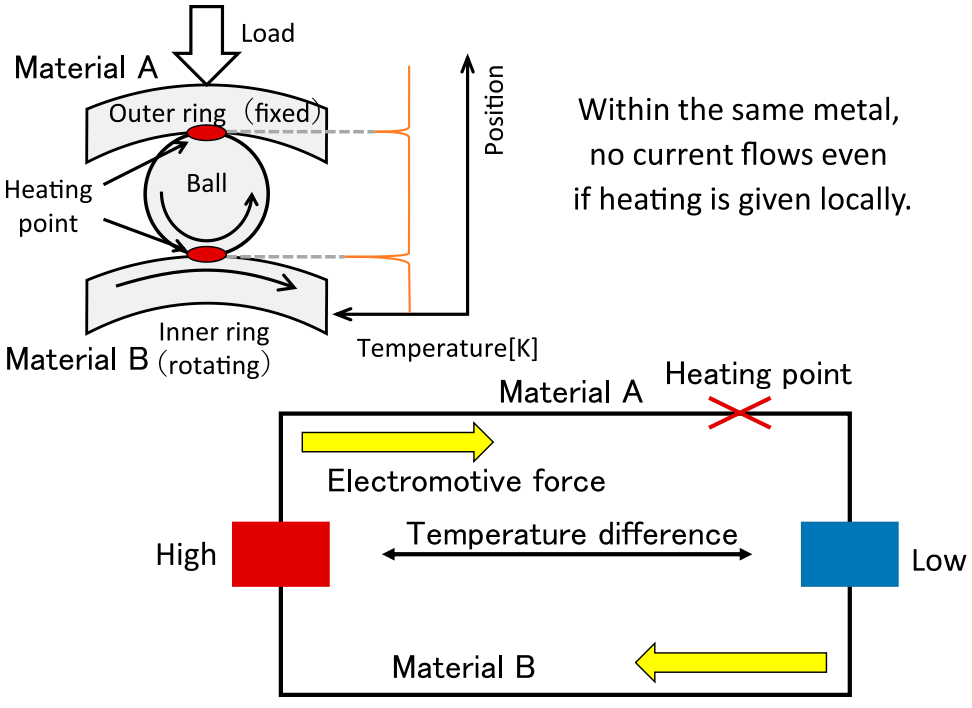


FIGURE 3
Explanation of law of homogeneous circuits.

using the dynamic thermocouple method, the law of homogeneous circuits was used because rolling bearings generate heat at two points: between the inner ring and rolling elements and between the outer ring and rolling elements. The homogeneous circuit law states that when two different metals are assembled in a closed circuit, the emf is affected only by the temperature difference at the contact point and not by heating in the middle of the circuit, even if heating occurs in the middle of the circuit. Therefore, when measuring the temperature of the inner ring raceway, it is not affected by the heat generated by the outer ring raceway. Figure 3 shows an explanation of this. In this case, the outer ring and rolling elements are made of material A and the inner ring is made of

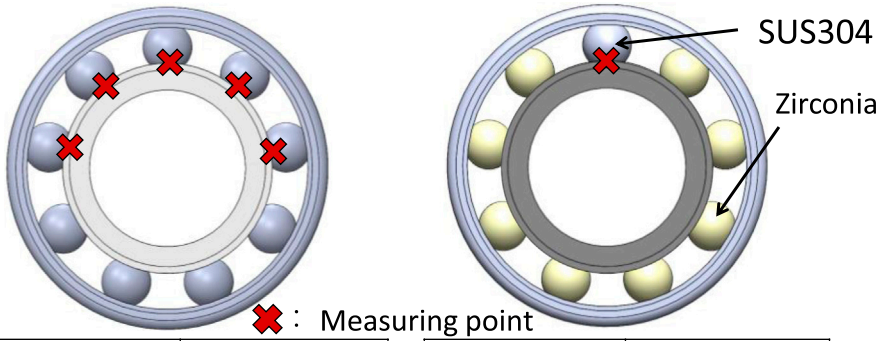


| Bearing Model | No.6207 |
|---|---|
| Outer ring | SUS304 |
| Balls | SUS304 × 9 |
| Inner ring | S55C |

| Bearing Model | No.6207 |
|---|---|
| Outer ring | SUS304 |
| Balls | SUS304 × 1<br>Zirconia × 8 |
| Inner ring | S55C |

This study

FIGURE 4
Configuration of measurement bearing.

material B. The heat generated between the outer ring and rolling elements does not affect the measurement on the inner ring raceway surface because the heat generated is within the same material.

## 2.1 Composition of rolling bearings

In the dynamic thermocouple method, the average value of each contact points between the different metals generates the emf (electromotive force), so the temperature rise of all the each rolling elements in contact becomes the average value, and the exact point of temperature rise is not clear. Therefore, all but one rolling element was changed to electrically insulating zirconia balls. With this method, the contact points between many different metals became one, making it possible to identify the locations of temperature rises on the raceway surface. This method made it possible to directly measure the temperature change of the raceway. As shown in Figure 4, the contact point between the different metals became one, and the temperature rose point on the raceway surface could be identified. The breakdown voltage of the zirconia sphere used in this study was large. The voltage measured in this study was on the order of 10 mV at the maximum, which did not exceed the breakdown voltage, and thus was considered sufficient for insulation. The metal material specifications in the figure are those of JIS (Japanese Industrial Standards).

## 2.2 Calibration of electromotive force

Connect the test piece and the metal wire in the following combinations. Combine the test piece (JIS S55C) and metal wire (JIS S60C) and the test piece (JIS SUS304) and metal wire (JIS SUS304) in a crisscross pattern as shown in Figure 5. Insert the combined test piece and thermometer into a beaker filled with oil. Place the thermos in a heater filled with water. To make the zero contact, fill the thermos with ice water and check that the temperature is 273 K with a thermometer. Insert a metal wire other than the one connected to the test piece into the thermos (zero contact point) at the connection point of the extension cord. Insert and connect the tester to the other end of the extension cord. The emf at the starting temperature of the calibration test was measured, the temperature of the oil in the beater was increased by the heater in 5K increments from 298 to 348K, and the emf was measured at each temperature. The relationship between the obtained temperatures and emf was shown in Figure 5. The test to confirm the law of homogeneous circuits using the test specimens was conducted in the same manner as the emf calibration test described above. Here, the thermometer used was MT-851, MOTHERTOOL, Japan, and the tester was MS8218, MASTACH, China.

The electromotive force at each temperature is measured, and at the same time, the law of homogeneous circuits was confirmed to be valid by heating the middle point of the metal wire S60C and SUS304 with a heat gun. Figures 6, 7 below show a schematic diagram of the homogeneous circuit law verification test using a test specimen and the actual test. The relationship between temperature and emf did not change when the middle point was heated with a heat gun.

## 2.3 Raceway surface temperature measurement test

Figure 8 shows the experimental setup for a test to measure the raceway temperature of a rolling bearing using the dynamic

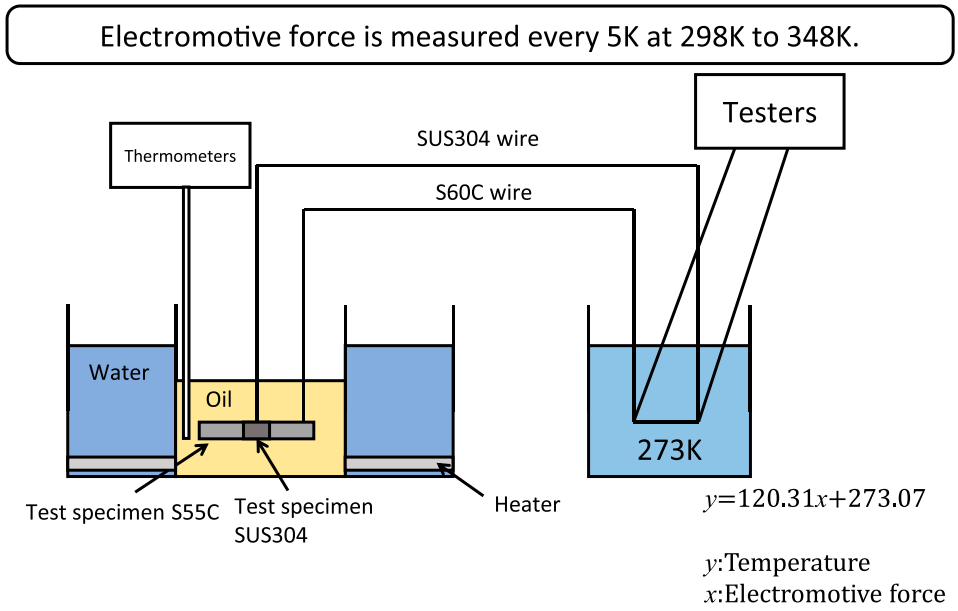


FIGURE 5
Calibration method of this study.

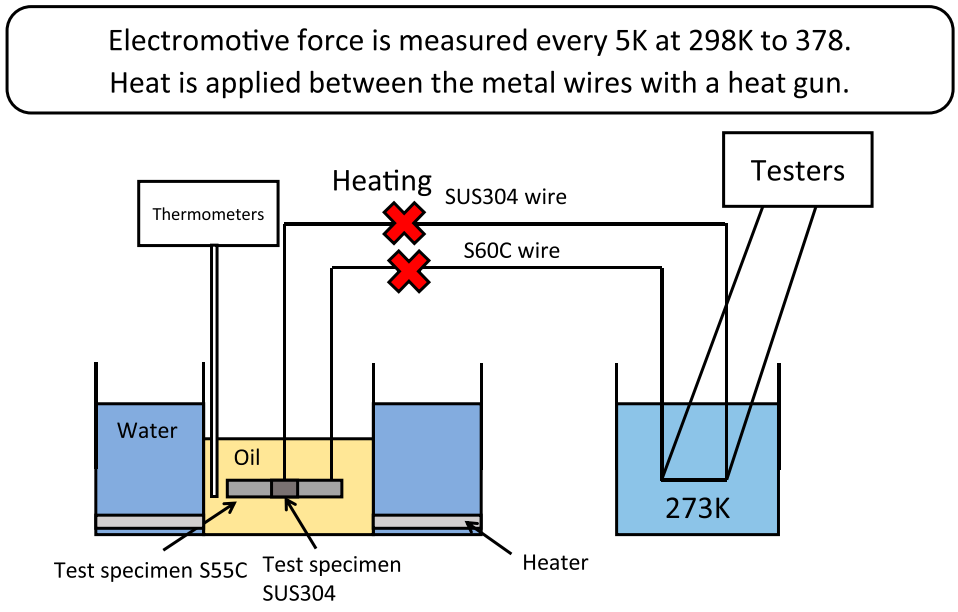


FIGURE 6
Confirmation method of law of homogeneous circuits.

thermocouple method. The shaft was fixed to the motor, and the load was varied by applying a load to the bearing measuring a load cell. The test bearing and the test shaft must be insulated. An insulating coupling was used between the test shaft and the motor, and a ceramic ball bearing was used as the bearing supporting the test shaft. A slip ring was attached to the other end of the test shaft to extract the electromotive force from the rotating element. A data recorder was used to measure the emf. A schematic diagram of the test apparatus is shown in Figure 9. Here, the tachometer used was HT-5500, Ono Sokki Co., LTD., Japan, the data recorder was DC-004P, Tokyo Measuring Instrument Co., Ltd., Japan, and the load cell was LUK-A-5KNSA1, KTOWA ELECTRONIC INSTRUMENT Co., LTD., Japan. The test was conducted with a bearing load of 100 N and a rotational speed of 60 rpm. The load and rotational speed conditions were set so that test could be carried out safely, since a safety cover could not be

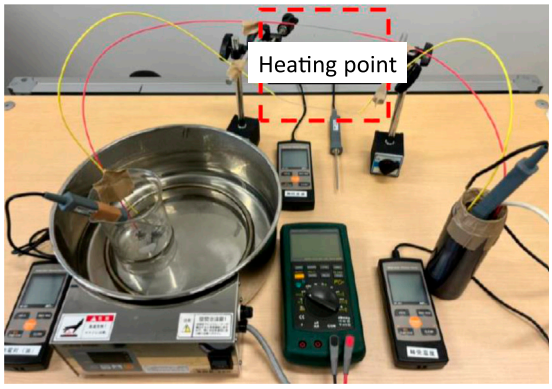


FIGURE 7
Actual test situation of law of homogeneous circuits.

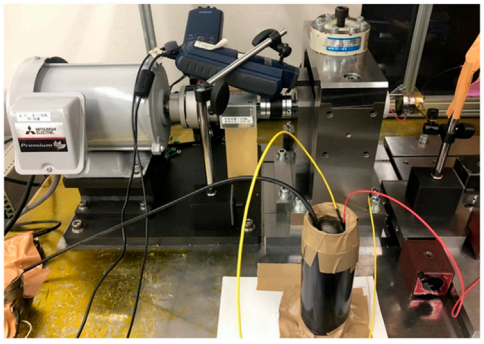

FIGURE 8
Actual test apparatus.

attached in order to measure temperature and the rotational speed of the rolling elements.

## 3 Temperature and rolling element behavior measurement test

The test focused on the accuracy of the bearing outer ring and compared two types of bearings. To improve the accuracy of the bearing inner and outer rings, the bearing material was also changed. Basically, the same procedure was used to prepare for the test as for the material with poor bearing accuracy. The material differences are shown in Table 1.

Next, a comparison of the roundness of the bearing outer rings is shown in Figure 10. The accuracy of the inner ring has also improved (4.73 μm ⇒ 0.35 μm). However, the inner ring rotates and the outer ring is stationary under the operating conditions and the roundness of the outer ring is extremely poor (24.82 μm ⇒ 1.03 μm). Figure 11 shows the installation method of the outer ring with poor bearing accuracy. The bearing load is applied at 0°, and the left and right. The angle was determined to be −60°. The point where the circularity increases was set to −60°.

### 3.1 Temperature measurement test results

To compare the temperature rise caused by differences in raceway accuracy, Figure 12 shows the results for bearings with poor and good accuracy. Figure 12 shows that when bearing accuracy is poor, the temperature rises outside the load distribution area or at points where the rolling element load is small. By observing Figure 12, it was confirmed that the temperature rise pattern differs depending on the bearing

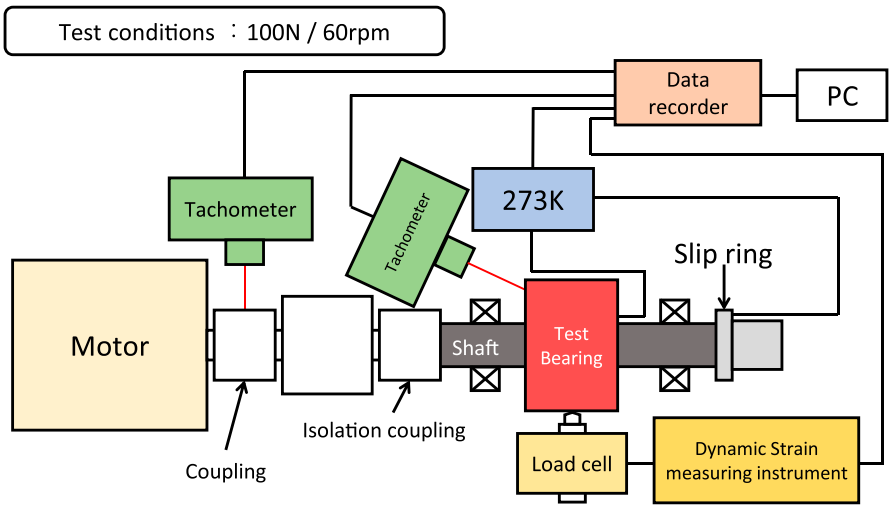


FIGURE 9
Schematic diagram of testing machine.

TABLE 1 Comparison of bearing specifications.

| Accuracy | Inner ring | Rolling elements | Outer ring | Measuring position |
|---|---|---|---|---|
| Poor | JIS S55C | JIS SUS304 × 1<br>Zirconia × 8 | JIS SUS304 | Inner ring surface |
| Good | JIS SUJ2 | JIS SUS440C × 1<br>Zirconia × 8 | JIS SUS440C | Inner ring surface |

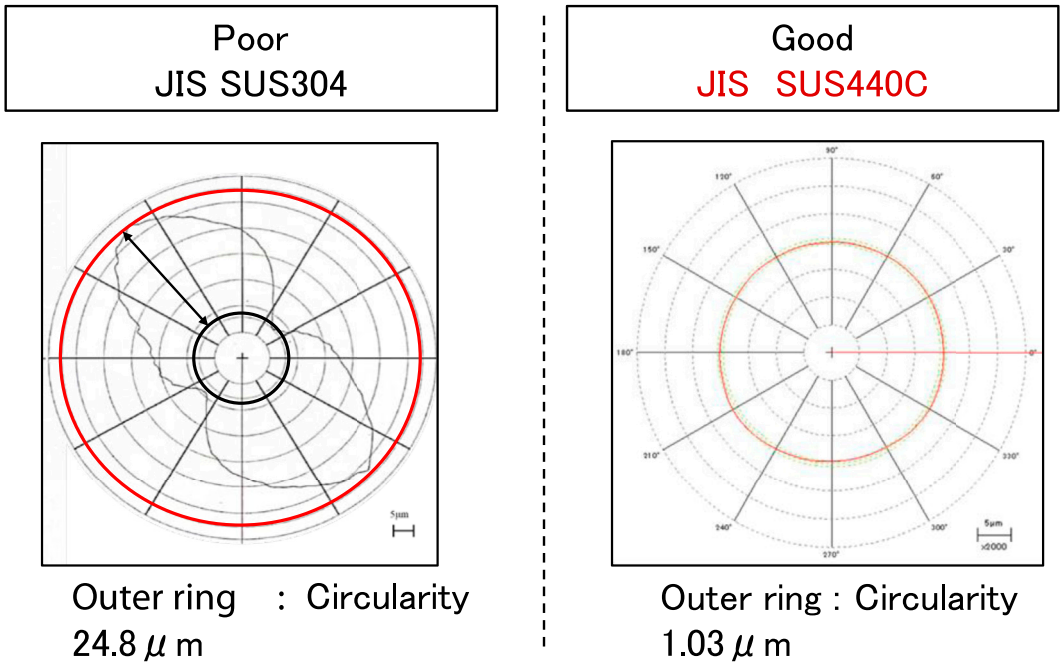


FIGURE 10
Comparison of outer ring circularity.

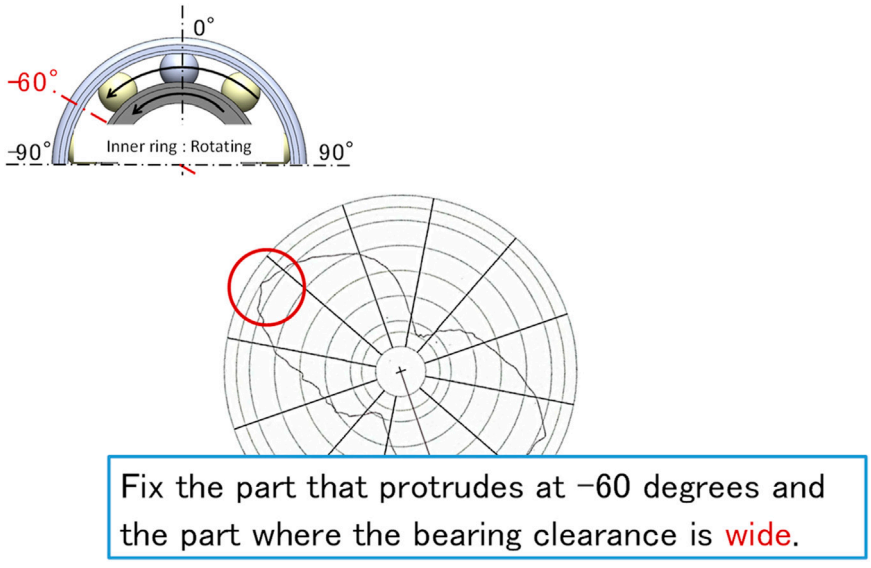


FIGURE 11
Poorly accurate outer ring installation method.

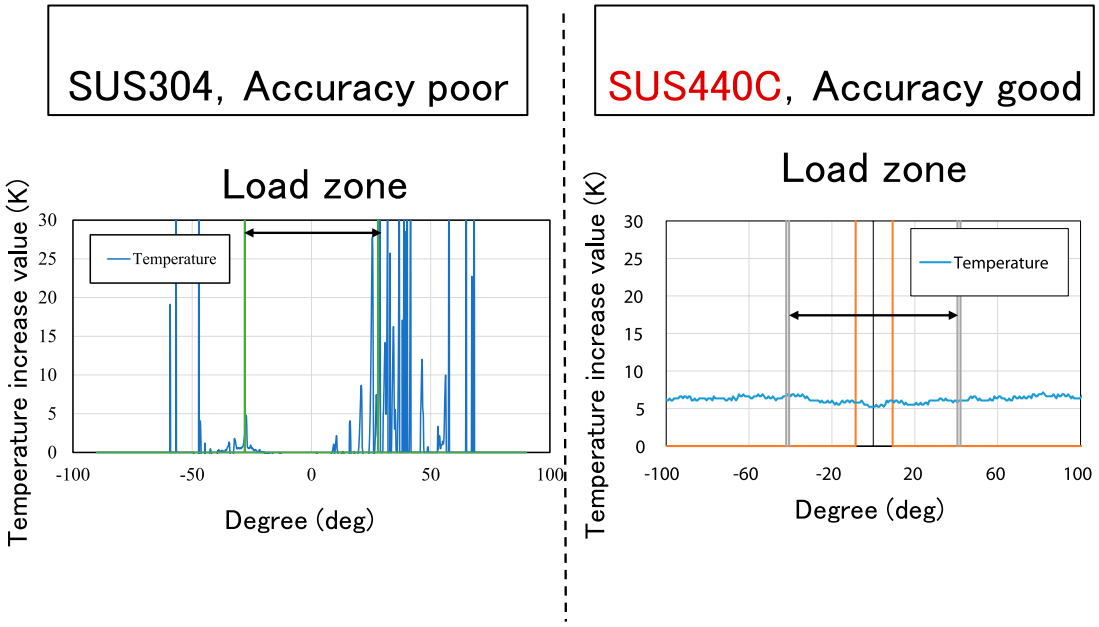


FIGURE 12
Changes in temperature generation due to bearing accuracy.

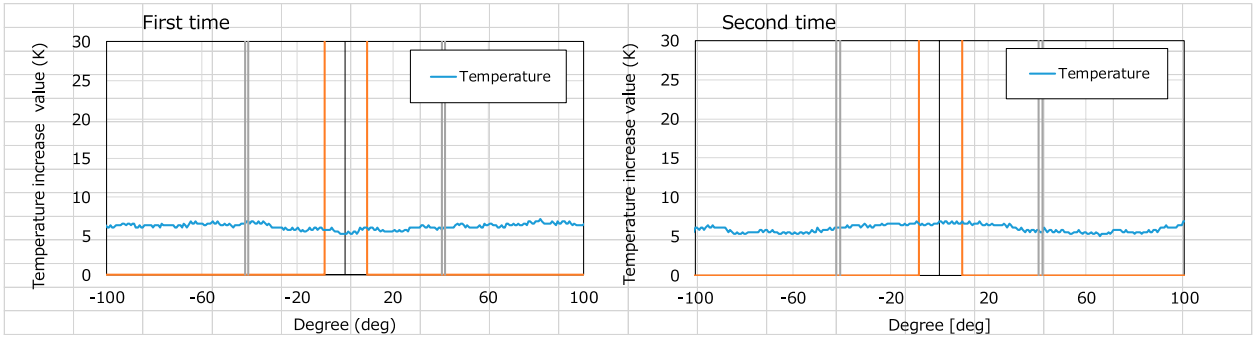


FIGURE 13
Confirmation of reproducibility.

accuracy. In the case of poorly accurate bearings, the rolling elements showed a large amount of slippage in the load zone, which was thought to be the cause of the increase in temperature on the raceway surface.

## 3.2 Confirmation of reproducibility

To confirm the reproducibility of the temperature measurement, we confirmed the reproducibility under the condition of good accuracy. The results are shown in Figure 13. The temperature rise value was almost the same for the first and second measurements, and reproducibility was confirmed. No difference in reproducibility due to noise or the like was observed. In this test, the low-pass filter used for temperature measurement was 50 Hz, and no high-pass filter was set.

## 3.3 Rolling element behavior measurement methods

Figure 14 shows a schematic of the apparatus used to measure the rolling element behavior. The rolling elements (zirconia balls) were marked to make their behavior easier to understand during the observation. A high-speed camera was used to check the rolling element behavior of the bearing by taking pictures through a mirror as shown in Figure 15.

## 3.4 Rolling element behavior measurement results

Figure 16 shows the results of the observation of the rolling element behavior in the lateral portion of the bearing with good

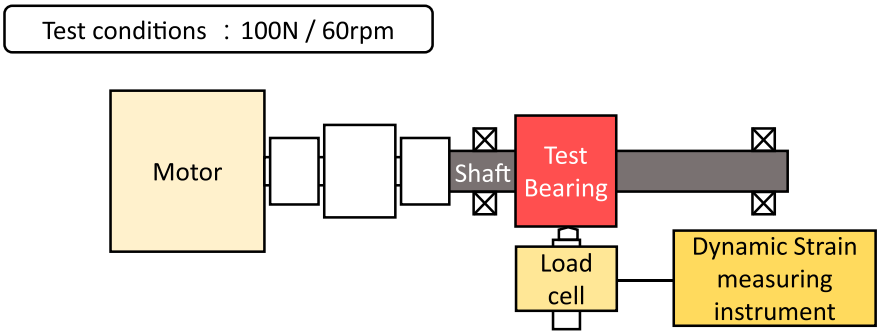


FIGURE 14
Overview of the rolling element movement measuring device.

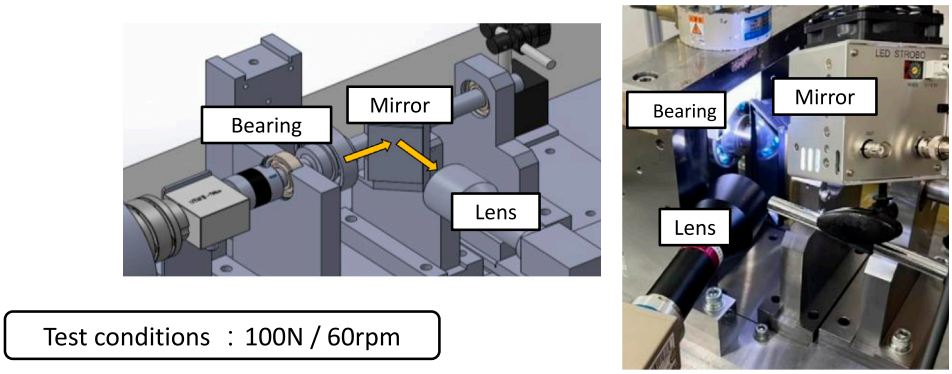


FIGURE 15
Detail of rolling element movement mesuring device.

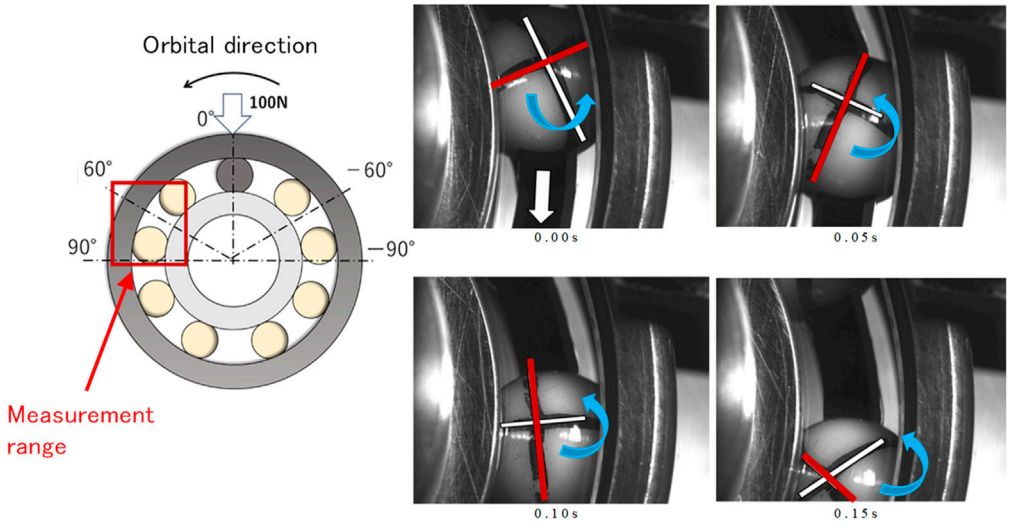


FIGURE 16
Results of the of the observation of rolling element movement.

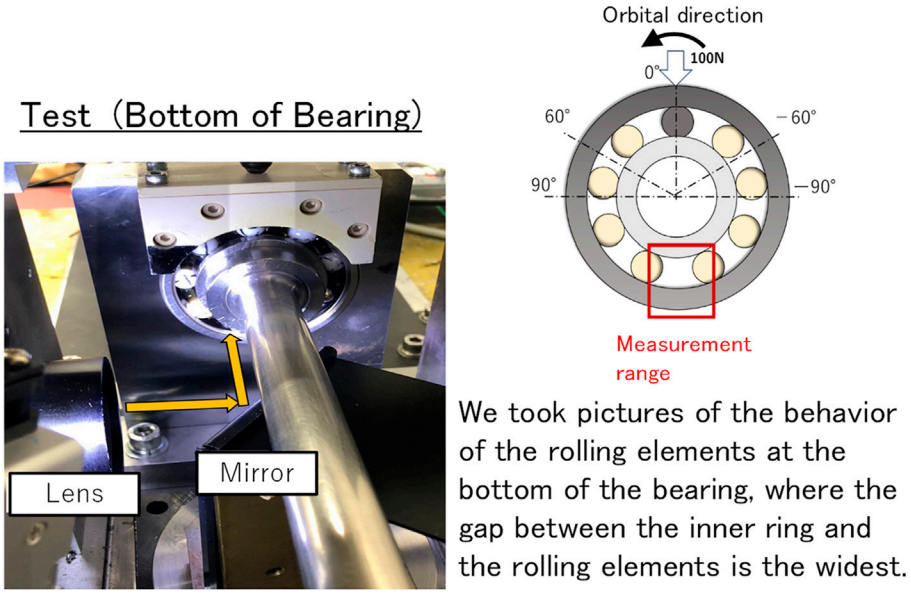


FIGURE 17
Detail of the rolling element movement at the bottom of bearing.

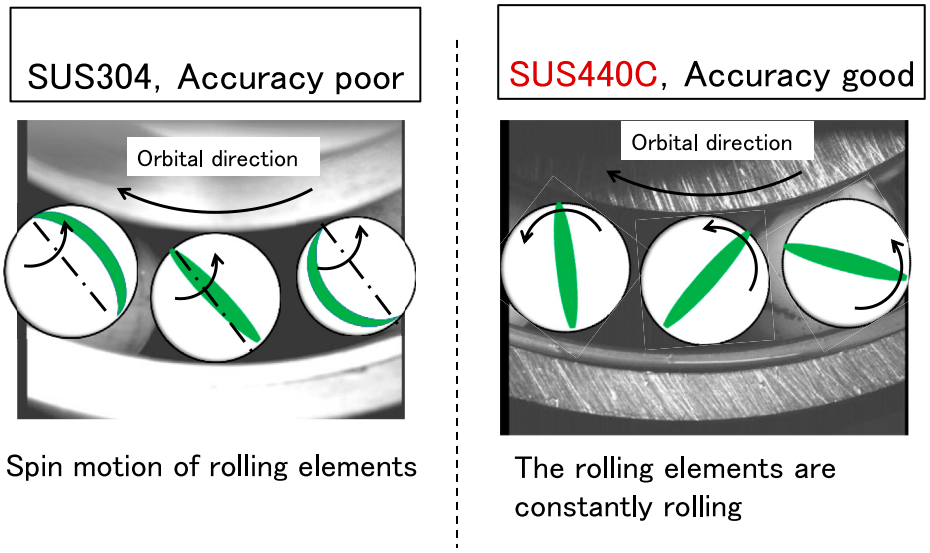


FIGURE 18
Changes in movement of rolling element due to bearing accuracy.

accuracy. The measurement start time was set at 0.000 s, and the results were recorded every 0.050 s. Note that the image was taken through a mirror, so the direction of rotation is reversed from the actual direction of rotation. When we checked the behavior of the rolling elements on the side of the bearing, we found that they were rotating with almost no slippage. Figure 16 shows the method used to observe the rolling element behavior at the bottom of the bearing. The measurement start time was set at 0.000 s, and the data was recorded every 0.050 s. The image was taken through a mirror, so the direction of rotation was reversed from the actual direction of rotation. Figure 17 shows the measurement results. It was confirmed that the rolling element did not slide much even at the bottom of the bearing when the raceway accuracy was good, and that the rolling element was almost rolling. From Figure 18, it can be seen that in bearings with poor raceway surface accuracy, the rolling elements spin and slip along an axis perpendicular to the direction of revolution.

## 4 Research results

Due to various backgrounds, rolling bearings are used more and more in harsh environments, and damage is more likely to occur on the raceway. In this study, we focused on the cause of damage to the raceway from the viewpoint of temperature rise, and measured the temperature of the raceway using the dynamic thermocouple method and the homogeneous circuit law. The temperature rise of the bearing raceways was also compared with different bearing raceway accuracy.

1) For bearings with poor raceway accuracy, the temperature rose in the non-loading zone, and slippage was observed when the rolling element behavior was checked by a high-speed camera. For bearings with good raceway accuracy, the temperature of the raceway remained almost constant in the non-loading zone.
2) When the behavior of the rolling elements in the lower part of the bearing (non-loading zone) was checked with a high-speed camera, the rolling elements in the bearing with a poor raceway accuracy exhibited spinning and sliding motion around an axis perpendicular to the orbital direction. In the case of a bearing with a good raceway accuracy, the rolling element was observed to be in pure rolling motion.

The above results indicate that if the accuracy of the raceway surface is poor, the bearing clearance changes significantly and no load is applied in the unloaded zone, and the direction of rotation is not constant. In addition, the temperature of the raceway cannot be detected because contact between the inner ring and rolling elements is unlikely to occur. The better the raceway accuracy and the smaller the bearing clearance, the more constant the direction of rotation becomes even in the unloaded range. Therefore, the temperature was considered to be almost constant because there was little sliding of the rolling elements. Therefore, it is concluded that the accuracy of the bearing raceway has a significant effect on the temperature rise of the raceway.

## 5 Conclusion

A useful method to continuously measure the surface temperature of the raceway of rolling bearings was developed, and confirmed that the temperature generation patterns differ depending on whether the bearing accuracy is good or bad. This method will contribute to improving design or calculating methods for reducing friction and confirming reliability of rolling bearings. The Seebeck effect and the law of homogeneous metals are common knowledge in the world of physics, but by appropriately combining these two laws, we were able to propose a method for continuously measuring the temperature of rolling bearing raceways, which was previously very difficult. We believe that the fact that we have demonstrated a quantitative evaluation method for areas where no suitable measurement method existed previously will lead to useful developments in mechanical engineering.

## Data availability statement

The original contributions presented in the study are included in the article/Supplementary Material, further inquiries can be directed to the corresponding author.

## Author contributions

HT: Investigation, Methodology, Validation, Visualization, Writing–review and editing. NU: Data curation, Investigation, Validation, Visualization, Writing–review and editing. YT: Conceptualization, Methodology, Project administration, Supervision, Writing–original draft.

## Funding

The author(s) declare that financial support was received for the research, authorship, and/or publication of this article. This research is supported by JSPS Grant-in-Aid for Scientific Research (C) 21K03843.

## Conflict of interest

The authors declare that the research was conducted in the absence of any commercial or financial relationships that could be construed as a potential conflict of interest.

## Publisher's note

All claims expressed in this article are solely those of the authors and do not necessarily represent those of their affiliated organizations, or those of the publisher, the editors and the reviewers. Any product that may be evaluated in this article, or claim that may be made by its manufacturer, is not guaranteed or endorsed by the publisher.

## Supplementary material

The Supplementary Material for this article can be found online at: https://www.frontiersin.org/articles/10.3389/fmech.2024.1462450/full#supplementary-material

## References

AlShorman, O., Irfan, M., Saad, N., Zhen, D., Haider, N., Glowacz, A., et al. (2020). A review of artificial intelligence methods for condition monitoring and fault diagnosis of rolling element bearings for induction motor. *Shock Vib.* 2020, 1–20. Article ID 8843759. doi:10.1155/2020/8843759

Bukvic, M., Gagevic, S., Skulic, A., Savic, S., Asonja, A., and Stojanovic, B. (2024). Tribological application of nanocomposite additives in industrial oils. *Lubricants* 12 (6), 1–21. doi:10.3390/lubricants12010006

Cui, Y., Gao, P., Tang, W., Mo, G., and Yin, J. (2022). Adaptive thin film temperature senor for bearing's elements temperature measurement. *Sensors* 22 (2838), 1–17. doi:10.3390/s22082838

Dong, Y., Zhou, Z., Liu, Z., and Zheng, K. (2015). Temperature field measurement of spindle ball bearing under radial force based on fiber Bragg grating sensors. *Adv. Mech. Eng.* 7 (12), 1–6. doi:10.1177/1687814015620332

Farfan-Cabrera, L. I. (2019). Tribology of electric vehicles: a review of critical components, current state and future improvement trends. *Tribol. Int.* 138 (2019), 473–486. doi:10.1016/j.triboint.2019.06.029

Flouros, M. (2006). Correlations for heat generation and outer ring temperature of high speed and highly loaded ball bearings in an aero-engine. *Aerosp. Sci. Technol.* 10 (2006), 611–617. doi:10.1016/j.ast.2006.08.002

Jakubek, B., Grochalski, K., Rukat, W., and Sokol, H. (2021). Thermovision measurement of rolling bearings. *Measurement* 2021, 1–25. doi:10.1016/measurement.2021.110512

Janic, N., Adamovic, Z., Nikolic, D., Asonja, A., and Stojanovic, B. (2015). Impact of diagnostics state model to the reliability of motor vehicles. *J. Balkan Tribol. Assoc.* 21 (2), 452–463.

Liu, M., Zhang, E., Zhou, Z., Tan, Y., and Liu, Y. (2013). Measurement of temperature field the spindle of machine tool based on optical fiber Bragg grating sensors. *Adv. Mech. Eng.* 2013, 1–6. Article ID 940626. doi:10.1155/2013/940626

Milojevic, S., Glisovic, J., Savic, S., Boskovic, G., Bukvic, B., and Stojanovic, B. (2024). Particulate matter emission and air pollution reduction by applying variable systems in tribologically optimized diesel engines for vehicles in road traffic. *Atmosphere* 15 (184), 184–225. doi:10.3390/atmos15020184

Sada, T. (2017). Loss reduction of rolling bearings for automobile. *Tribol. Online* 12 (3), 94–98. doi:10.2474/trol.12.94

Takabi, J., and Khonsari, M. M. (2013). Experimental testing and thermal analysis of ball bearings. *Tribol. Int.* 60 (2013), 93–103. doi:10.1016/j.triboint.2012.10.009

Tarawneh, C., Cole, K., Wilson, B., and Alnaimat, F. (2008). Experiments and models for the thermal response of railroad tapered-roller bearings. *Int. J. Heat Mass Transf.* 51 (25-26), 5794–5803. doi:10.1016/j.ijheatmasstransfer.2008.05.011

Usamentiaga, R., Venegas, P., Guerediaga, J., Vega, L., Molleda, J., and Bulnes, F. G. (2014). Infrared thermography for temperature measurement and non-destructive testing. *Sensors* 2014 (14), 12305–12348. doi:10.3390/s140712305

Vencl, A., Gasic, V., and Stojanovic, B. (2017). Fault tree analysis of most common rolling bearing tribological failures. *IOP Conf. Ser. Mater. Eng.* 174, 012048–12110. doi:10.1088/1757-899X/174/1/012048

Zaretsky, E. V. (2012). *Rolling bearing steels-a technical and historical perspective*. NASA/TM-2012-217445, 1–21.

frontiers | Frontiers in Mechanical Engineering

TYPE Original Research
PUBLISHED 05 November 2024
DOI 10.3389/fmech.2024.1456618

Check for updates

OPEN ACCESS

EDITED BY
Hikaru Okubo,
Yokohama National University, Japan

REVIEWED BY
Shouhei Kawada,
Kansai University, Japan
Satoshi Momozono,
Tokyo Institute of Technology, Japan

*CORRESPONDENCE
Steffen Puchtler,
office@pmd.tu-darmstadt.de

RECEIVED 28 June 2024
ACCEPTED 17 October 2024
PUBLISHED 05 November 2024

CITATION
Puchtler S, van der Kuip J, Becker-Dombrowsky FM and Kirchner E (2024) Impedance measurement of rolling bearings using an unbalanced AC wheatstone bridge. *Front. Mech. Eng.* 10:1456618. doi: 10.3389/fmech.2024.1456618

COPYRIGHT
© 2024 Puchtler, van der Kuip, Becker-Dombrowsky and Kirchner. This is an open-access article distributed under the terms of the Creative Commons Attribution License (CC BY). The use, distribution or reproduction in other forums is permitted, provided the original author(s) and the copyright owner(s) are credited and that the original publication in this journal is cited, in accordance with accepted academic practice. No use, distribution or reproduction is permitted which does not comply with these terms.

# Impedance measurement of rolling bearings using an unbalanced AC wheatstone bridge

Steffen Puchtler*, Julius van der Kuip, Florian Michael Becker-Dombrowsky and Eckhard Kirchner

Institute for Product Development and Machine Elements, Technical University of Darmstadt, Darmstadt, Germany

Industry 4.0 drives the demand for cost-efficient and reliable process data and condition monitoring. Therefore, visualizing the state of tribological contacts becomes important, as they are regularly found in the center of many applications. Utilizing rolling element bearings as sensors and monitoring their health by the electrical impedance method are promising approaches as it allows, e.g., load sensing and detection of bearing failures. The impedance cannot be measured directly, but there are various methods available. This paper discusses advantages and disadvantages and suggests the AC Wheatstone bridge as a reliable way of measuring impedances with low phase angles at sampling rates in the kHz range. The corresponding equations are introduced, a simulation built, an uncertainty mode and effects analysis carried out and sample measurement results of real rolling elements shown. It can be demonstrated that the AC Wheatstone bridge meets the proposed requirements for sensory utilization and condition monitoring when the bearing is operated in the hydrodynamic regime.

KEYWORDS

**bearing, impedance, measurement, visualization, condition monitoring**

## 1 Introduction

### 1.1 Impedance measurement of rolling bearings

Rolling bearings are central components in many machines. Because of their crucial role in leading process forces into the machine structure, bearing failures cause nearly 20% of all machine breakdowns (Harris and Kotzalas, 2007; Schaeffler Technologies AG and Co. KG, 2000; Becker-Dombrowsky and Kirchner, 2024). With the arising e-mobility, another bearing fault type gets into the focus of research, namely, surface damages based on harmful electric bearing currents (Harder et al., 2022a). In both cases, the electric impedance can give information about the bearing condition.

**Abbreviations:** AC, alternating current; BNC, bayonet nut connector; DUT, device under test; EDM, electrical discharge machining; EHL, elasto hydrodynamic lubrication; SNR, signal-to-noise ratio; UMEA, uncertainty mode and effects analysis.

To avoid unexpected system faults of machines, a precise knowledge about the mechanical and electrical bearing loads as well as health conditions is essential. Martin et al. (2022) showed that measuring the bearing impedance allows to detect damages in the runway surfaces like pittings. Becker-Dombrowsky et al. (2023) used the data generated by Martin et al. and investigated it in time and frequency domain. Three different phases in rolling bearing lifetime were identified and the end of bearings' life could be detected. So, impedance based condition monitoring of rolling element bearings is possible. The gauging principle is based on the description of the electrical behavior of the rolling contact, which is regarded in the next section.

## 1.2 Electrical behavior of rolling contacts

Depending on the lubrication film thickness, three different electrical equivalent models can be described. In case of dry friction, a direct metallic contact between rolling elements and runways exists. The observed electrical behavior is equivalent to an ohmic resistance. With increasing lubrication film thickness, an elasto hydrodynamic lubrication (EHL) contact is built between the rolling elements and the runways. Now, the equivalent circuit can be extended by a capacitor in parallel connection. The capacitor is the Hertz'ian contact zone, which is formed by the bearing loads (Prashad, 1988; Muetze, 2003; Gemeinder, 2016; Schneider et al., 2022a; b). If the lubrication film thickness is insufficient, breakdown voltages like in electrical discharge machining (EDM) machines harm the surfaces of the contact partners. The reason is, that the electric field strength in the Hertz'ian area is high enough to overbear the dielectric strength in the EHL contact, so a harmful current can be transmitted through the lubrication gap. When a sufficient lubrication film separates the contact partners completely, the EHL contact zone can be modeled as the described parallel connection of ohmic resistance and capacitor, in which the capacitive part prevails (Prashad, 1988; Muetze, 2003; Gemeinder, 2016; Schneider et al., 2022a; b). The rolling bearing impedance is a result of the impedance of the single rolling element contact to the runway. These single contacts are connected in parallel. The single contact itself is modeled as a serial connection of two plate capacitors, each in parallel connection to an ohmic resistance. Knowing the electrical properties of rolling element bearings enables their usage as sensors or their usage as condition monitoring device. To do so, the impedance has to be measured during the operation of the bearing. In the next section, impedance measurement approaches will be presented.

## 1.3 Impedance measurement methods

Currently, impedance measurement is used for lubrication film thickness observation (Barz, 1996). Martin et al. could show the possibilities of using the electric bearing properties for condition monitoring. They were able to observe the pitting growth after initial damage in the rolling bearing raceways and to gauge the damage dimensions (Martin et al., 2022). Becker-Dombrowsky et al. expanded the analysis of Martin et al. in the time and frequency domain to enlarge the amount of data using feature engineering techniques (Becker-Dombrowsky et al., 2023). They are able to distinguish three rolling bearing operational time phases and to detect bearings end of life (Becker-Dombrowsky et al., 2023). The impedance measurement can also be used to identify the load condition in the bearing (Schirra et al., 2018). So, the rolling bearing becomes an active element in the measurement circle. When the impedance is used to explain harmful electric conditions in the rolling contact, it is a reacting or passive element. For both approaches, the Hertz'ian contact area has to be calculated according to Equation 1 (Prashad, 1988):

$$C_{\mathrm{Hertz}} = \varepsilon_0 \cdot \varepsilon_{\mathrm{r}} \cdot \frac{A_{\mathrm{Hertz}}}{h_{\mathrm{c}}}, \tag{1}$$

where $C_{\mathrm{Hertz}}$ is the measured capacitance, $\varepsilon_0$ the vacuum permittivity, $\varepsilon_r$ the relative permittivity, $A_{\mathrm{Hertz}}$ the Hertz'ian contact area and $h_c$ the lubrication film thickness in the EHL contact. Approaches for the calculation of the capacitance contributors are discussed by Puchtler et al. (2022). Based on the Hertz'ian theory, the load in the rolling contact can be calculated, which enables more suitable durability analysis and failure monitoring (Schirra et al., 2019). Maruyama et al. (2023) are using the impedance measurement approach to detect lubricants condition in rolling contact. This application field is not addressed in this article. The following section gives a short introduction into different impedance measurement approaches.

### 1.3.1 Charging curve detection

This measurement method is used for lubrication film thickness detection. It utilizes direct current as a carrier signal. To get the impedance of the EHL contact, the known current is let through the bearing. Then the time is measured until a defined voltage level is reached. With this information, the capacitance and the impedance can be calculated. The capacitance is proportional to the time (Barz, 1996).

### 1.3.2 Current and voltage measurement

This gauging method is based on the Ohm's law for the alternating current (AC) circuit. By measuring the bearing voltage over the time and the current through the bearing, the impedance can be calculated (Keysight Technologies, 2020). It is applicable for measurement frequencies between 10 kHz and 100 MHz. Its accuracy depends on the voltage and current measurement systems, which is defined by the working frequency of the gauging device (Keysight Technologies, 2020). The measurement errors can be corrected or minimized, when the inner ohmic resistance of the device is lower than the measured impedance. So, this method is mainly used for detecting higher impedances (Plaßmann and Schulz, 2016).

### 1.3.3 Voltage comparison

The voltage comparison is able to minimize measurement errors, because it is based on a voltage divider. That means, it needs a known reference impedance $\underline{Z}_{\mathrm{ref}}$ to detect the unknown impedance $\underline{Z}_{\mathrm{x}}$. The voltages over the reference impedance $\underline{v}_{\mathrm{ref}}$ and the generator voltage $v_{\mathrm{gen}}$ are measured and the searched impedance is calculated by following equation (Lerch, 2016):

$$\underline{Z}_{\mathrm{x}} = \left(\frac{\underline{v}_{\mathrm{gen}}}{\underline{v}_{\mathrm{ref}}} - 1\right)\underline{Z}_{\mathrm{ref}}. \tag{2}$$

The equivalent circuit is shown in Figure 1A. The advantage of this method is, that systematic errors will be minimized (Lerch, 2016). But the inner resistance of the voltage gauging device has to be higher than the observed impedance. If it is not possible to realize this, the reference impedance has to be in the same range as the observed impedance to reduce measurement errors.

### 1.3.4 Measurement bridge

Measurement bridges are able to use direct and alternating current as carrier signal. They need three known reference impedances to detect the unknown fourth impedance. The generator voltage and the bridge voltage are measured using an oscilloscope or equivalent device (Lerch, 2016). The unknown impedance is calculated by transforming Equation 3 for the searched impedance (Lerch, 2016):

$$\underline{v}_{\mathrm{m}} = \frac{\underline{Z}_{\mathrm{x}}\underline{Z}_2 - \underline{Z}_1\underline{Z}_3}{(\underline{Z}_1 + \underline{Z}_{\mathrm{x}})(\underline{Z}_2 + \underline{Z}_3)} v_{\mathrm{gen}}. \tag{3}$$

An equivalent circuit of a measurement bridge is shown in Figure 1B. The inner resistance of the measurement device and the resistance of the wires can lead to errors, which has to be considered. The main advantage of this measurement principle is its robustness against environmental influences (Plaßmann and Schulz, 2016) and its sensitivity (Mitvalsky, 1964). According to the measurement task, an AC Wheatstone bridge can be configured in different ways (Cone, 1920). Another variant is the balanced AC Wheatstone bridge, where a reference impedance is tuned until the bridge voltage is zero $\underline{v}_{\mathrm{m}} = 0\,\mathrm{V}$ (Takagishi, 1980). For further research into AC Wheatstone method, Gupta et al. (2020) and Rybski et al. (2015) and for its application, Chattopadhyay et al. (2012) should be mentioned.

### 1.3.5 Comparison of measurement methods

In this subsection, the suitability of the single impedance measurement methods for the single contact measurement and the rolling bearing operational time observation will be discussed. The charging curve detection can lead to currents when metallic contacts occur. Thus, a constant signal during the operational time will not be possible. So, the charging curve detection is not suitable for the aim of this paper. The current and voltage measurement method needs a lower inner ohmic resistance of the measurement devices than the observed impedance to reduce measurement errors. The inner resistance of the used oscilloscope is higher than one mega ohm. The rolling bearing impedance for a carrier signal of 20 kHz is about several kilo ohms, which means it is lower than the inner resistance. So this method is not applicable for this case. The voltage comparison method has been used to detect rolling bearing damages by Martin et al. (2022). The bearing seat isolation of the test rig chamber was used as a reference impedance, which can be influenced by the environment and the tests themselves. The carrier signal was about 2.5 MHz. This reference impedance can not be adapted to the expected rolling bearing impedance, so a possible measurement error can not be reduced. An external reference impedance could be adapted and avoid measurement errors. This would be able with a measurement bridge. Because of its robustness against environmental influences, an alternating voltage measurement bridge is more suitable for the single contact and operational time observation. So the measurement bridge is chosen as a new impedance measurement approach. It will be compared to the voltage comparison method in this paper as state of the art in the next sections. In general, the electrical parameters have to be chosen carefully, because all kinds of currents might be harmful to the bearing when the current density in the contact zone is to high (Muetze, 2003; Harder et al., 2022b). In this research, the current density is low enough to avoid harmful currents.

## 1.4 Contributions of this paper

In this paper, the approach of the AC Wheatstone bridge is investigated and refined for rolling bearing applications. The necessary equations to calculate the complex impedance from the measurement while taking the loading effect into account are derived. Furthermore, the procedure to retrieve the reference impedances from measurements on the assembled AC bridge are presented. An uncertainty mode and effects analysis (UMEA) systematically exposes uncertainties of the method. A simulation is used to gain information of the influence of noise and the

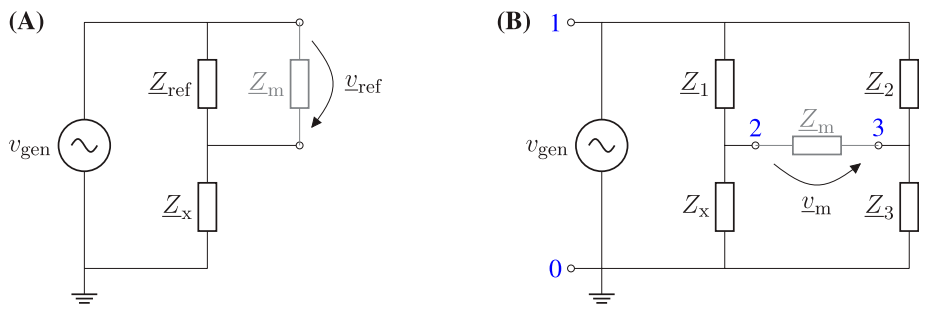


FIGURE 1
Circuit diagrams of **(A)** the voltage comparison method and **(B)** the AC Wheatstone bridge.

frequency response of the method. Lastly, two examplary use cases of impedance measurement of rolling bearings are presented to show the usability of the measurement method for the intended use case.

# 2 Materials and methods

## 2.1 Alternating voltage measurement bridge function

In the following, the AC Wheatstone bridge as described in Section 1.3.4; Figure 1B is enhanced. To take the loading effect of the differential oscilloscope probe measuring $\underline{v}_\mathrm{m}$ into account, the probe's impedance $\underline{Z}_\mathrm{m}$ is introduced. Then, solving for $\underline{Z}_\mathrm{m}$ the following equation can be derived,

$$\underline{Z}_\mathrm{x} = \underline{Z}_1 \frac{\underline{Z}_3\underline{Z}_\mathrm{m} + \left[(\underline{Z}_2 + \underline{Z}_3)\underline{Z}_\mathrm{m} + \underline{Z}_2\underline{Z}_3\right]\underline{v}_\mathrm{m} \Big/ v_\mathrm{gen}}{\underline{Z}_2\underline{Z}_\mathrm{m} - \left[(\underline{Z}_2 + \underline{Z}_3)(\underline{Z}_\mathrm{m} + \underline{Z}_1) + 1\right]\underline{v}_\mathrm{m} \Big/ v_\mathrm{gen}}. \tag{4}$$

The generator voltage phase is defined as $\arg(v_\mathrm{gen}) = 0°$ and therefore, $v_\mathrm{gen}$ is a real number. $\underline{Z}_1$, $\underline{Z}_2$, $\underline{Z}_3$ and $\underline{Z}_\mathrm{m}$ are known and considered constant. Thus, only the complex voltage ratio $\underline{v}_\mathrm{m}/v_\mathrm{gen}$ must be measured during the experiment. This is done by a digital differential oscilloscope with the sampling rate $f_\mathrm{m}$ or sampling interval $T_\mathrm{m} = 1/f_\mathrm{m}$. A subscript $k$ will be assigned to each sample. A phase information cannot be derived reliably from a single sample, therefore, a moving sum is used which covers a number of $N$ samples symmetrically around $k$. Then, a discrete cross-correlation (Alessio, 2016) over these $N$ samples is carried out. The correlation with the generator voltage delivers the real part of $\underline{v}_\mathrm{m}/v_\mathrm{gen}$ with a multiplication with $2/(N\hat{v}^2)$ which yields the correct amplitude of the voltage ratio. For the calculation of the imaginary part, a 90° phase shifted signal of the input voltage $v^\star_\mathrm{gen}$ is calculated.

$$\mathrm{Re}\left\{\underline{v}_{\mathrm{m},k} \Big/ v_{\mathrm{gen},k}\right\} = \frac{2}{N\hat{v}^2} \sum_{i=k-N/2}^{k+N/2} \underline{v}_{\mathrm{m},i} v_{\mathrm{gen},i}, \tag{5}$$

$$\mathrm{Im}\left\{\underline{v}_{\mathrm{m},k} \Big/ v_{\mathrm{gen},k}\right\} = \frac{2}{N\hat{v}^2} \sum_{i=k-N/2}^{k+N/2} \underline{v}_{\mathrm{m},i} v^\star_{\mathrm{gen},i}\,. \tag{6}$$

Subsequently, a first order low pass filter at $f_\mathrm{m}/2$ is applied to remove any remaining ripple and to avoid any false interpretation of the signal, as higher frequencies will not be reliably measured. To reduce the effect of any stray capacitances and cable inductances, an open-short adjustment is carried out. Therefore, the impedance is measured with the device under test (DUT) removed ($\underline{Z}_\mathrm{open}$) and shorted ($\underline{Z}_\mathrm{short}$). These values are used in Equation 7 to retrieve the DUT's impedance from the measured impedance $\underline{Z}_\mathrm{x}$, Equation 4, (Mühl, 2020),

$$\underline{Z}_\mathrm{DUT} = \frac{\underline{Z}_\mathrm{x} - \underline{Z}_\mathrm{short}}{1 - (\underline{Z}_\mathrm{x} - \underline{Z}_\mathrm{short}) \Big/ (\underline{Z}_\mathrm{open} - \underline{Z}_\mathrm{short})}. \tag{7}$$

Finally, the parallel capacitance $C_\mathrm{DUT}$ and resistance $R_\mathrm{DUT}$ of the equivalent circuit at the carrier frequency $\omega = 2\pi f_\mathrm{gen}$ can be calculated as

$$C_\mathrm{DUT} = -\frac{\mathrm{Im}\{\underline{Z}_\mathrm{DUT}\}}{\omega \quad |\underline{Z}_\mathrm{DUT}|^2}, \tag{8}$$

$$R_\mathrm{DUT} = \mathrm{Re}\{\underline{Z}_\mathrm{DUT}\} + \frac{\mathrm{Im}\{\underline{Z}_\mathrm{DUT}\}^2}{\mathrm{Re}\{\underline{Z}_\mathrm{DUT}\}}. \tag{9}$$

### 2.1.1 Measurement uncertainty

The impedances $\underline{Z}_1$, $\underline{Z}_2$, $\underline{Z}_3$ and $\underline{Z}_\mathrm{m}$ cannot be measured directly once the bridge is assembled and connected to the oscilloscope. As these cables contribute to the impedances, they cannot be measured before assembly. The assembled bridge is a four-terminal circuit, hence, the six impedances between the terminals can be calculated from six measurements between different terminals each. The four poles are denominated as 0, 1, 2 and 3, *cf.* Figure 1B. The impedance $\underline{Z}_{ij}$ describes the single impedance between poles $i$ and $j$. The impedance $\underline{Z}_{\mathrm{m},ij}$, Equation 10, describes the measured capacitance between the poles $i$ and $j$ including the effects of all other impedances in the network,

$$\underline{Z}_{\mathrm{m},ij} = \frac{\underline{Z}_{ij}\left[\underline{Z}_{jk}\underline{Z}_{jl}\left(\underline{Z}_{ik} + \underline{Z}_{kl} + \underline{Z}_{ij}\right) + \underline{Z}_{ik}\underline{Z}_{ij}\left(\underline{Z}_{jk} + \underline{Z}_{jl} + \underline{Z}_{kl}\right) + \underline{Z}_{kl}\left(\underline{Z}_{jl}\underline{Z}_{ik} + \underline{Z}_{jk}\underline{Z}_{ij}\right)\right]}{\underline{Z}_{ij}\left(\underline{Z}_{jk} + \underline{Z}_{jl}\right)\left(\underline{Z}_{ik} + \underline{Z}_{ij}\right) + \underline{Z}_{kl}\left(\underline{Z}_{jk} + \underline{Z}_{ik}\right)\left(\underline{Z}_{jl} + \underline{Z}_{ij}\right)}$$
$$+\underline{Z}_{ij}\underline{Z}_{kl}\left(\underline{Z}_{jk} + \underline{Z}_{jl} + \underline{Z}_{ik} + \underline{Z}_{ij}\right) + \underline{Z}_{jk}\underline{Z}_{jl}\left(\underline{Z}_{ik} + \underline{Z}_{ij}\right) + \underline{Z}_{ik}\underline{Z}_{ij}\left(\underline{Z}_{jk} + \underline{Z}_{jl}\right)$$
$$\text{with } i, j, k, l \in \{0, 1, 2, 3\}. \tag{10}$$

Using the trust-region dogleg algorithm implemented as fsolve in Matlab, all $\underline{Z}_{ij}$ can be retrieved by the measured $\underline{Z}_{\mathrm{m},ij}$. For the AC Wheatstone bridge used, the following values were retrieved, corresponding to an RC-equivalent according to Equations 8, 9.

- $\underline{Z}_{12} \Rightarrow C_1 = 990.56\,(3)$ pF $\quad R_1 = 15805\,(879)$ kΩ
- $\underline{Z}_{13} \Rightarrow C_2 = 989.29\,(6)$ pF $\quad R_2 = 11594\,(1034)$ kΩ
- $\underline{Z}_{03} \Rightarrow C_3 = 1059.54\,(2)$ pF $\quad R_3 = 890\,(2)$ kΩ
- $\underline{Z}_{23} \Rightarrow C_\mathrm{m} = 4.22\,(4)$ pF $\quad R_\mathrm{m} = 28236\,(5700)$ kΩ

The impedance $\underline{Z}_{01}$ is parallel to the power source and therefore not considered. $\underline{Z}_{02}$ is parallel to the DUT and will be therefore considered by the open measurement. In case, the open measurement cannot be carried out, this value can be used as $\underline{Z}_\mathrm{open}$.

## 2.2 Uncertainty consideration

The UMEA methodology is used for the analysis of uncertainties in the context of product development. It is divided into five steps, which are briefly described below. Figure 2 schematically shows the procedure for this methodology.

The first step is an environment and target analysis, in which the systems to be considered are defined by means of system boundaries and differentiated from other systems (Engelhardt, 2012). Interfaces to other systems are named and their influences on the system under consideration are taken into account. This is followed by the identification of uncertainties, in which these are named, and their causes are investigated. For this, system models are necessary in order to be able to describe the influences sufficiently precisely (Engelhardt, 2012). Then the uncertainty effects are determined, which is followed by the penultimate step of the UMEA methodology, the uncertainty evaluation. Based on


FIGURE 2
UMEA approach process.

this, a final decision is made regarding the countermeasures to be applied (Engelhardt, 2012).

First, the investigated system is described. On the basis of this description, the necessary system boundaries are defined and the disturbance, input, output and secondary variables acting on it are identified. The definitions of these quantities given below follow that of Mathias and are briefly presented here (Mathias, 2016).

- The **input variable** is a desired quantity which is converted into an output quantity based on the system behavior. Thereby real input quantities can differ from the desired ones.
- An **output variable** is a desired variable that is formed from the input variables and the disturbance variables as a result of the system behavior. The goal is that the system produces an output variable that corresponds to the desired output variable. Deviations are possible in this regard.
- **Disturbance** variables represent undesirable effects on the system, which can thus cause deviations in the output variables.
- **Secondary variables** are unwanted variables that result from the system behavior. They can in turn act as disturbance variables on neighboring systems.

As can be seen from the definitions, disturbance variables and secondary variables have largely the same effect and can therefore be regarded as equivalent (Mathias, 2016). Thus, no distinction is made between them in the identification of disturbances by means of lists.

## 2.3 Simulation model

A Matlab Simulink model was developed to investigate the behavior of the AC Wheatstone bridge in ideal conditions. Figure 3 shows the diagram of the model. The parallel connection of a variable capacitor and a resistor simulates the DUT. The impedances $\underline{Z}_1$, $\underline{Z}_2$ and $\underline{Z}_3$ are modeled using a real capacitor with a parallel resistance of the values retrieved in Section 2.1.1. Similarly, the oscilloscope is modeled by an ideal voltage sensor in parallel with a real capacitor. The voltage signals of bridge voltage $v_m$ and the generator $v_{gen}$ are then sampled with the sampling rate $f_s$ and resolution (12 bit) of the oscilloscope used. For some tests, a white noise is added to the measured bridge voltage simulating electric interference. The resulting signal is then processed with the same scripts later used for measurements in the real application. The simulation of 10 ms is

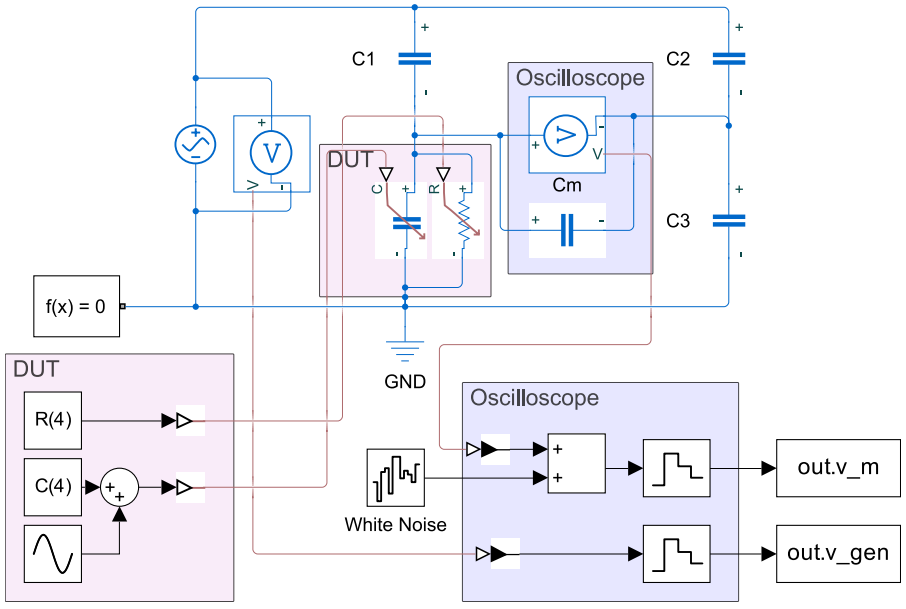


FIGURE 3
Matlab Simulink simulation model of the AC Wheatstone bridge.

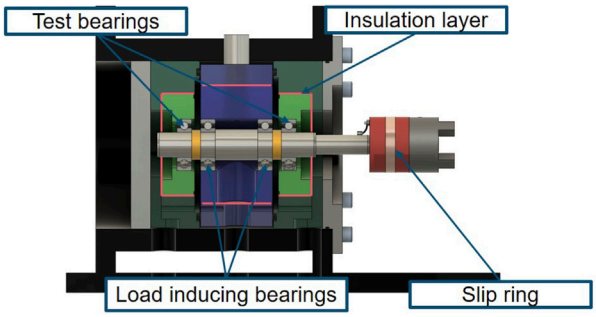


FIGURE 4
Cross section of one rolling bearing test rig chamber. According to (Becker-Dombrowsky et al., 2024)

then carried out using Matlab's ode14x solver with a fixed step size of $0.05/f_s$.

## 2.4 Application tests

### 2.4.1 Rolling bearing test rig

The rolling bearing test rig has four test chambers which can be operated independently. Four rolling element bearings are run in a single chamber. All bearings are loaded radially and in addition, two bearings can be loaded axially if necessary. Each chamber is equipped with an own recirculating oil lubrication system, so oil lubrication besides grease lubrication can be investigated. For test observation, axial and radial vibration sensors and four temperature sensors are located at the chamber. In addition, the motor speed and torque is monitored to enlarge the system information spectrum. Figure 4 shows a cross-section of one chamber. The two rolling bearings in the center induce the radial loads to the two outer bearings. The outer bearings can be loaded axially by the hydraulic actuator on the left side. The radial load induction is also realized by a hydraulic actuator above the chamber.

To avoid parasitic currents and other disturbing factors based on electric phenomena, the steel bearing seats are surrounded by a 50 mm thick isolation layer made from fiber glass. For the electrically investigated bearings, the isolation is over-bridged using contact pins. The shaft is contacted by a slip ring.

### 2.4.2 Single contact test

An application of the impedance measurement method described is testing single steel ball bearings. Therefore, a ceramic ball of a hybrid bearing is replaced by a steel ball of the same diameter, as first described by Jabłonka et al. (2018). Thus, the impedance of a single ball can be measured. Some test results as well as the calculation of the changed mechanical behavior due to different elasticities and thermal expansion coefficients of steel and ceramic, is described in Puchtler et al. (2023a). For small load angles $\beta = \tan(F_a/F_r)$ a high change of capacitance during an orbit of the steel ball is expected due to the distinct load zone. Thus, a capacitance maximum will appear with each cage revolution.

### 2.4.3 Fatigue tests

To investigate the applicability of the new measurement approach, fatigue tests were run at the test rig described in Section 2.4.1. Two different rolling bearing types are used, deep groove ball bearings (6205) and angular deep groove ball bearings (7205). Both bearing types have the same dimensions. All bearings are loaded by a resulting load ratio of $C/P = 1.6$ with changing load angle $\beta$. The rotational speed is stationary at 5,000 $\text{min}^{-1}$. Fully lubrication is applied using the recirculating oil lubrication system of the test chamber with an oil flow of 10 L $\text{min}^{-1}$. The tests are run until the sensor system of the test rig detects a damage. Tests with a duration more than 300 h are ended and will not be investigated in this research. The results of the fatigue tests are compared to the data of Martin et al. The data quality is important as well as the accuracy based on the calculations.

# 3 Results and discussion

## 3.1 UMEA

In this section, the predominant disturbance variables are identified. For this purpose, system boundaries are defined first and then the disturbance variables acting on the respective system are determined. These are evaluated in accordance with the methodology described in Section 2.2. This is followed by an explanation of possible solutions for dealing with the disturbance variables.

### 3.1.1 Disturbance identification

The analyzed system consists of the measuring system for determining the impedance of the test bearings, which includes the signal lines and the oscilloscope. It also includes the connection contacts of the bearing seats and the associated measuring leads. In addition, the lines of the carrier signal, which is generated by a signal generator, and the signal generator itself are counted as part of the system. The measurement system mentioned here must be distinguished from the systems installed in the test bench for test bench operation.

The measuring system for impedance measurement considered in this paper uses an AC voltage as a carrier signal, from whose changes conclusions are drawn about the states of the test bearings. Thus, this electrical signal represents an input variable for the measuring system. In order to operate the measuring system, components such as the oscilloscope require electrical energy, which therefore also represents an input variable. The measuring system perceives the changes in the impedance, whereby it generates electrical signals as an output variable, which are further processed by software after analog-to-digital conversion. The identified disturbance factors are displayed in Figure 5.

The determination of external disturbances is based on the use of checklists. The identified disturbance variables are now presented here and their effects will be evaluated.

#### 3.1.1.1 Material-bound waves

Neighboring test stands and test setups as well as test chambers can result in the transmission of sound waves. These occur in the

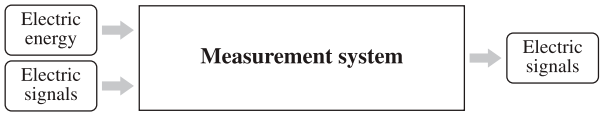


FIGURE 5
Input and output parameters of the measurement system.

form of structure-borne sound when they are transmitted via the foundation to the test stand and thus the test station. Furthermore, structure-borne sound can be transmitted to the test chamber through the base plate on which the motor and test chamber are mounted. In addition, structure-borne noise is transmitted between the test stations by the test stand frame. Another possibility is transmission as airborne sound directly to the test station and test chamber. The sound can cause vibrations that can be reflected in the measurement signal.

#### 3.1.1.2 Electricity and magnetism

In the systems of the test station, the test chamber and the measuring system, electrical operating currents are present during normal operation, as are current changes and fluctuating electrical voltages. Since all measurement methods in question use a carrier signal in the form of an electrical voltage, this can be affected by changes in current, normal operating currents and voltage changes. A greater interference potential results from unequal charge levels. This can result in unintended current flows that affect the measurements as such. Grounding problems are also assigned to this area. Galvanic coupling of the signal generator used and the test stand may occur due to a ground loop. This occurs when the respective housings are grounded via the protective contacts of their mains connections because of the protection against contact. As a result, interference currents are induced, which can directly influence the carrier signal and therefore also the measurement. Since electric motors are used to generate the speeds required for the tests, electromagnetic fields can also occur which affect the measuring system. Likewise, influences by neighboring test stands, which work with stronger electromagnetic fields, are possible. In order to be able to make more detailed statements on this, field measurements must be carried out in the test hall.

#### 3.1.1.3 Motion-based phenomena

Because the test rig is located in the Earth's gravitational field, Newtonian gravity is present for all systems. However, this has no direct effect on the measurements and affects all systems equally. Thus, gravity is not considered further as a disturbance variable.

#### 3.1.1.4 Foreign solids and liquids

Due to dusts in the ambient air, deposits of these may occur on the system under consideration. The same applies to greases and oils. Since the measuring system is not encapsulated from the environment, it is subject to the humidity of the environment. All the factors mentioned have an equal effect on the system, and their effect on the measurement must be questioned.

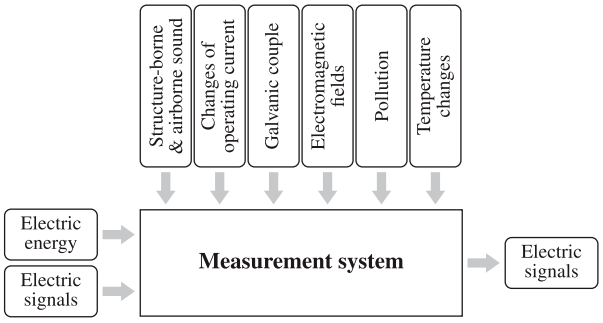


FIGURE 6
Disturbance factors on the measurement system.

Nevertheless, there is a risk of measurement system failure due to ingress of foreign matter such as dust particles into the measurement equipment. However, these problems are usually solved on the manufacturer's side, so they will not be discussed in detail here. In the case of slip ring contacting, contamination up to the formation of an oxide layer can occur. These can influence the measurement signal.

#### 3.1.1.5 Thermodynamics

Due to the environment and the operation of the test stand itself, the phenomena of heat dissipation and heat supply occur. These can result in changes in resistance, which can lead to falsification of measurement results. The following Figure 6 summarizes the findings with regard to the disturbance variables acting on the measurement system.

### 3.1.2 Disturbance evaluation

Structure-borne and airborne noise have a medium uncertainty level and a medium effect, since they reach the measurement point over longer distances or components with damping material properties lie in between. A direct influence on the measurements cannot be excluded. The impact is classified as medium, since vibrations due to structure-borne and airborne noise are part of the operating conditions of bearings. Since the slip ring is directly in the signal flow, the effects due to contamination on the measurement signal are high. However, the uncertainty level is low because contaminants are removed by rotation as a result of operation. Electromagnetic fields are able to induce currents (Schwab and Kürner, 2007), so their effects are classified as very high. However, since there are distances through air between the sources and the measurement system, the uncertainty level is considered low. Changes in temperature can result in changes in resistance, which directly influence the electrical behavior of the measuring section (Mühl, 2020). Therefore, they have a medium effect on the measurement quality, whereas the uncertainty level is to be classified as high. The reason for this is the non-enclosed environment of the test stand and the measuring system, whereby changes in the environmental influences have a direct effect on the systems. Unknown or not fully known reference variables are to be classified as high in amount and impact. Since they are directly included in the evaluation, all

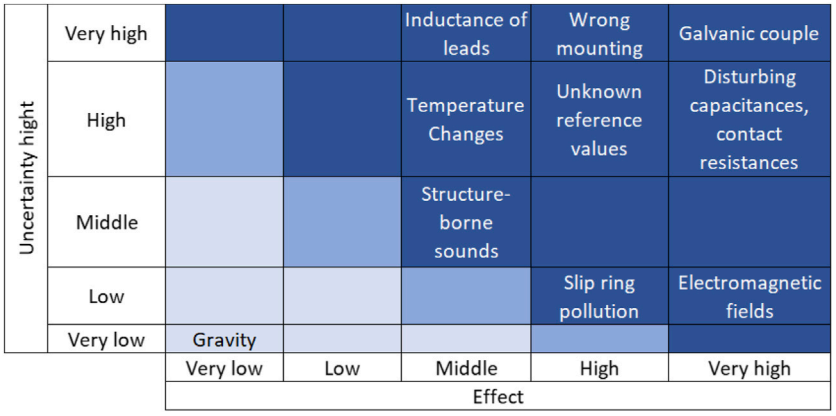


FIGURE 7
Disturbance factor assessment.

uncertainties associated with them are therefore also included in the result. Interference capacitance and contact resistances have a direct effect on the electrical path and can thus cause undefined current flows that directly influence the electrical behavior. Therefore, their effects on the measurement are very high. Due to the test chamber design, their uncertainty level is considered high. Line inductance and the associated line resistances occur in almost all test leads, and their uncertainty level must therefore be classified as very high. Their effects are not negligible because they conduct the electrical signals to the evaluation equipment. Incorrect mounting of bearings has to be classified high in its effect, because it may cause changed operating conditions, which do not correspond to the rule. In case of insufficient mounting skills and knowledge, their uncertainty level is very high. As the previous evaluations make clear, uncertainties acting directly in or on the signal flow are to be considered very high in their effects. Therefore, undefined current flows, grounding problems and also damaged or insufficient insulation are extremely critical in their effect. They allow for changes in the electrical operating behavior, making the models on which the measurement is based only partially or no longer reflect the behavior. Since undefined current flows as a result of several factors and a grounding problem are given by the current technical status of the test chamber, its uncertainty level is very high. This also applies in the case of insulation, if damage is present. Figure 7 summarizes the results of the evaluation.

### 3.1.3 Disturbance handling

In the following, only disturbance variables that have been classified as critical or no longer acceptable according to the Zurich hazard analysis method are considered with regard to their controllability. In order to find approaches for dealing with the disturbance variables, Mathias' catalog of principles is used at this point (Mathias, 2016). Priority is given to the elimination of the disturbance variable or its influence, since an influence on the measurement can thus be excluded and consideration in the evaluation is no longer necessary.

#### 3.1.3.1 Material-bound waves

Structure-borne sound waves due to adjacent test equipment can be reduced or suppressed by decoupling the rolling bearing test rig from the ground (Mathias, 2016). This is already done. The extent to which the effects on measurement were prevented cannot be assessed at this point.

#### 3.1.3.2 Electricity and magnetism

To reduce the influence of electromagnetic fields, it is recommended to shield the electrical conductors of the measuring system or to use shielded cables (Mathias, 2016). Currently, bayonet nut connector (BNC) cables are mainly used as measuring lines. They are a form of coaxial cable and are suitable for the low-loss transmission of high-frequency signals (Rossmann, 2018). However, they exhibit parasitic effects which cannot be neglected (Schwab and Kürner, 2007). Therefore, these must be taken into account in the evaluation of the impedance signals. Another problem with coaxial cables is the effect they have on ground loops (Schwab and Kürner, 2007). Therefore, appropriate countermeasures must be taken. In order to reduce the influence of ground loops, a separate housing grounding of the test chamber is provided for the endurance tests. This is not grounded via a mains connection, but connected to a grounding bar subsequently installed in the test field. In this way, interference currents from the enclosure are to be discharged directly via the building ground and only have a minor effect on the carrier signal. The effect of this consideration will be checked in the course of this paper in later tests.

#### 3.1.3.3 Thermodynamics

All three systems considered are subject to the same climatic conditions. Therefore, the influences on the impedance measurement caused by temperature changes are to be taken into account and compensated by the measurement and evaluation procedure. Measuring bridges generally have the advantage that they can compensate for disturbing influences such as temperature changes and also have a high measuring sensitivity (Mühl, 2020). In addition, the compensation of the resistances of the BNC lines is provided in the evaluation algorithm.

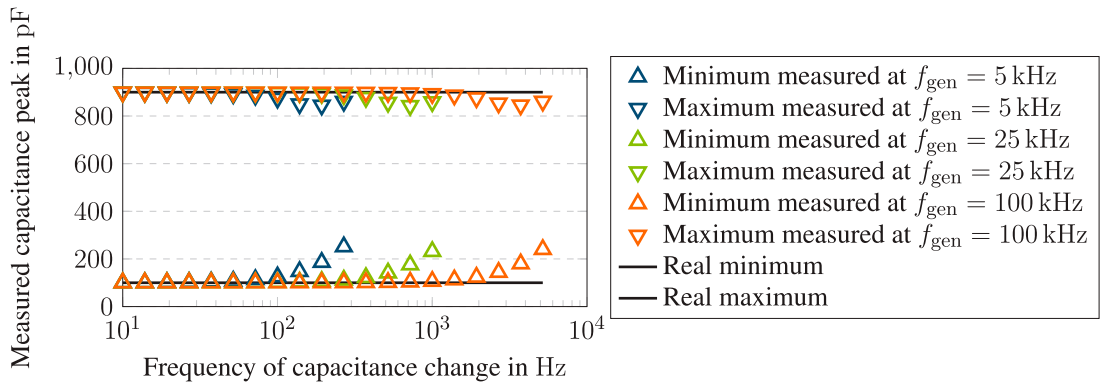


FIGURE 8
Simulation results of a sinusoidal changing capacitance $C_{DUT}$ = 100 . . . 900 pF at a rate of 10 . . . 5,000 Hz measured with a generator frequency of $f_{gen}$ = 5 kHz, 25 kHz and 100 kHz. Displayed are the minimal and maximal values of the sinusoidal capacitance retrieved from the simulated measurement with the sampling frequency $f_s = 36 \cdot f_{gen}$.

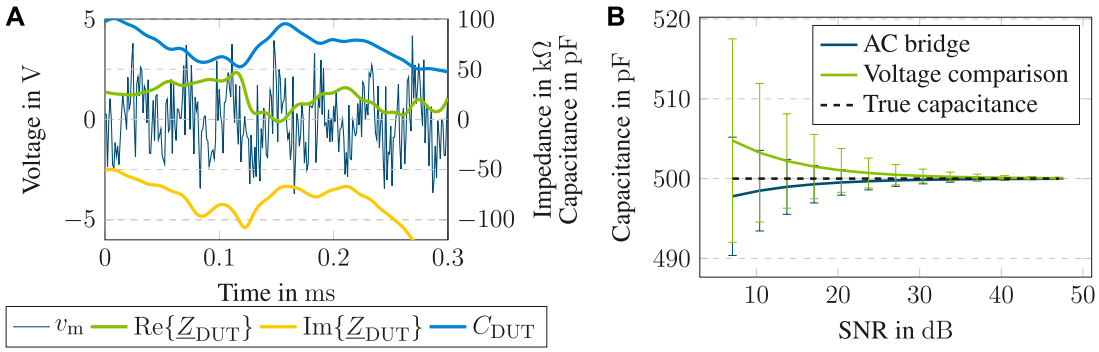


FIGURE 9
Simulation results of the AC Wheatstone bridge with additional white noise on the measured bridge voltage with a generator frequency of $f_{gen}$ = 25 kHz and a sampling frequency $f_s$ = 900 kHz **(A)** Bridge voltage signal $v_m$ with white noise (−4 dB SNR) and resulting DUT impedance $Z_{DUT}$ and capacitance $C_{DUT}$ **(B)** Mean capacitance and standard deviation of the simulated measurement of the proposed AC wheatstone bridge method in comparison with the voltage comparison method and the true capacitance. A higher SNR corresponds to a lower white noise power.

## 3.2 Simulation tests

In the following, results retrieved from the Matlab/Simulink simulation model of the AC Wheatstone bridge as introduced in Section 2.3 are presented.

### 3.2.1 Frequency influence

First, the frequency range in which capacitance changes can be measured reliably is investigated. Figure 8 shows simulation results of the Matlab/Simulink model described in Section 2.3. The capacitance was sinusoidally varied with a mean value of 500 pF, an amplitude of 400 pF and a varied frequency of 10 . . . 500 Hz as depicted on the $x$-axis. The $y$-axis shows the results of the peak simulated measurements as triangles and the true peaks of 100 pF and 900 pF as lines. It can be shown that the relative deviation $w_C = (C_{real} - C_{meas})/C_{real}$ of the real values at a 10th of the balance capacitance is linearly dependent on the generator frequency $f_{gen}$. It can be shown that this error can be approximated for a given capacitance change frequency $f_C$ as

$$w_C = 1000 \cdot \left(\frac{f_C}{f_{gen}}\right)^2. \tag{11}$$

Thus, a limit frequency can be derived for a maximum error of 5% at $f_C = f_{gen}/141$ or for a maximum error of 0.1% at $f_C = f_{gen}/1000$ according to Equation 11.

### 3.2.2 Noise influence

Then, a white noise signal was added to the measured bridge voltage $u_m$ as seen in Figure 3 to investigate the effect of possible disturbances in the real system, cf. Section 3.1. Figure 9A shows the effect of a high noise amplitude resulting in a signal-to-noise ratio (SNR) of −4 dB. Even though the noise power is greater than the signal power and the actual sine-like signal is barely visible, still the resulting calculated capacitance is right order of magnitude though significantly below the true value of 100 pF. It can be also seen that the real part of the impedance briefly dips below 0 Ω. Therefore, it is possible to retrieve negative real parts of impedance if there is a lot of noise compared to the signal. In real applications as later shown in

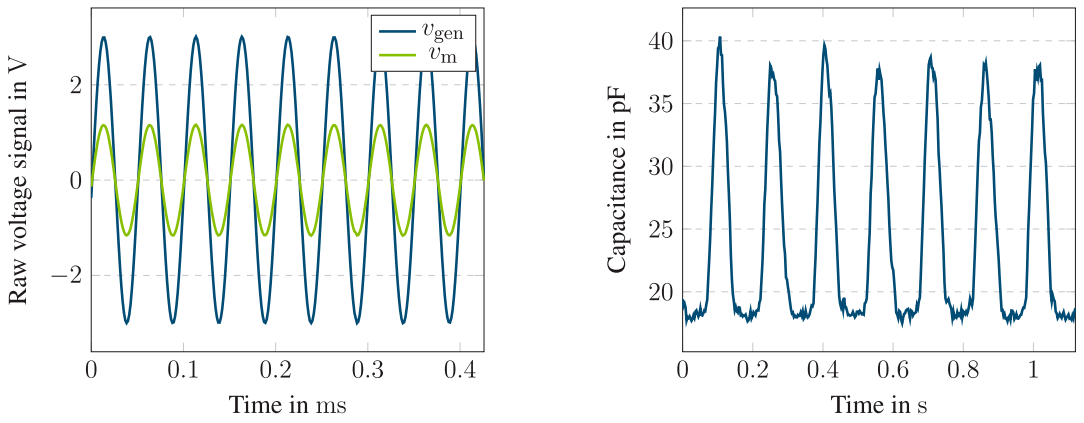


FIGURE 10
Raw **(A)** and calculated **(B)** results of a single steel ball bearing at $T_{Oil}$ = 30°C, $n$ = 1000 min$^{-1}$, $f_{gen}$ = 20 kHz, and $F_r$ = 2525 N.

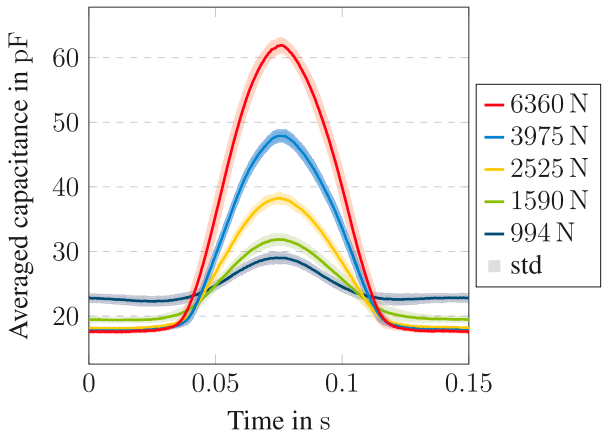


FIGURE 11
Averaged capacitance measurements of single steel ball bearing at $T_{Oil}$ = 30°C, $n$ = 1000 min$^{-1}$, $f_{gen}$ = 20 kHz, and multiple radial forces.

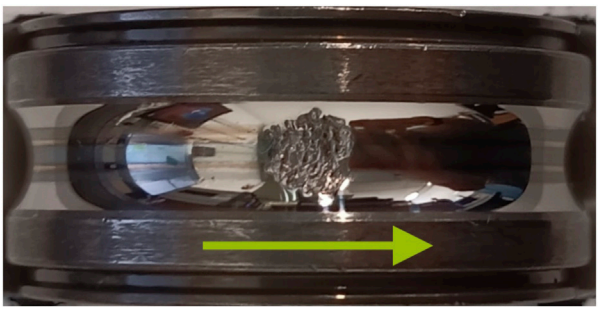

FIGURE 12
Pitting damage at the inner ring of bearing A, bearing type 6205, radial load $F_r$ = 9375 N, load ratio $C/P$ = 1.6, load angle $\beta$ = 0°, rotational speed $n$ = 5000 min$^{-1}$, oil flow of 10 L min$^{-1}$. The arrow indicates the rolling direction.

Figure 10A, the SNR is much better. Figure 9B shows the influence of a rising SNR on the measured capacitance mean, which converges towards the true value of 500 pF and the standard deviation shown as error bars reducing continuously.

For comparison, a simulation model of the voltage comparison method, Figure 1A, was developed. The Simulink model, Figure 3, was adapted to the corresponding circuit, using a 7.5 kΩ reference resistor to achieve the same balance impedance at $f_m$ = 25 kHz as $C_1$ for the AC bridge circuit. The evaluation procedure of the simulation results is mostly analog to the one described in Section 2.1. Firstly, the voltage ratio $\underline{v}_m/v_{gen}$ is calculated according to Equations 5, 6. Then, after applying a first order lowpass filter at $f_m/2$, the reciprocal value is used in Equation 2 to calculate the capacitance.

It can be seen that for all signal-to-noise ratios, the AC Wheatstone bridge shows a smaller deviation from the true value than the voltage comparison method. Similarly, the standard deviation of the results is smaller for the newly proposed method.

## 3.3 Single contact test

Measuring a single steel ball deep groove ball bearing (6205) with the alternating voltage measurement bridge under load results in two voltage signals, which are depicted in Figure 10A. The voltage signal $v_{gen}$ shows the chosen sinusoidal curve with an amplitude of 6 V and a frequency of 20 kHz. The measured voltage signal $\underline{v}_m$ shows the same frequency and no phase shift, with a lower amplitude of approximately 1.15 V. The reduced amplitude results from the electrical circuit of the used measurement bridge (Figure 1B) combined with the altered electrical behavior of the single steel ball bearing.

Using the proposed methods of Section 2.1 the capacitance signal over time can be calculated from the raw $v_{gen}$ and $\underline{v}_m$ signals (Figure 10B). Each cage rotation can be easily separated by a significant peak in capacitance. As the steel ball reaches the load zone, the gap between the steel surfaces of the ball and raceway gets smaller and thus the capacitance increases. Outside the load zone, the geometrically restricted gap between the ball and raceway induces a minimum capacitance of 18 pF. The noise and variation observed when comparing each rotation stem from system distortions, as discussed in Section 3.1.

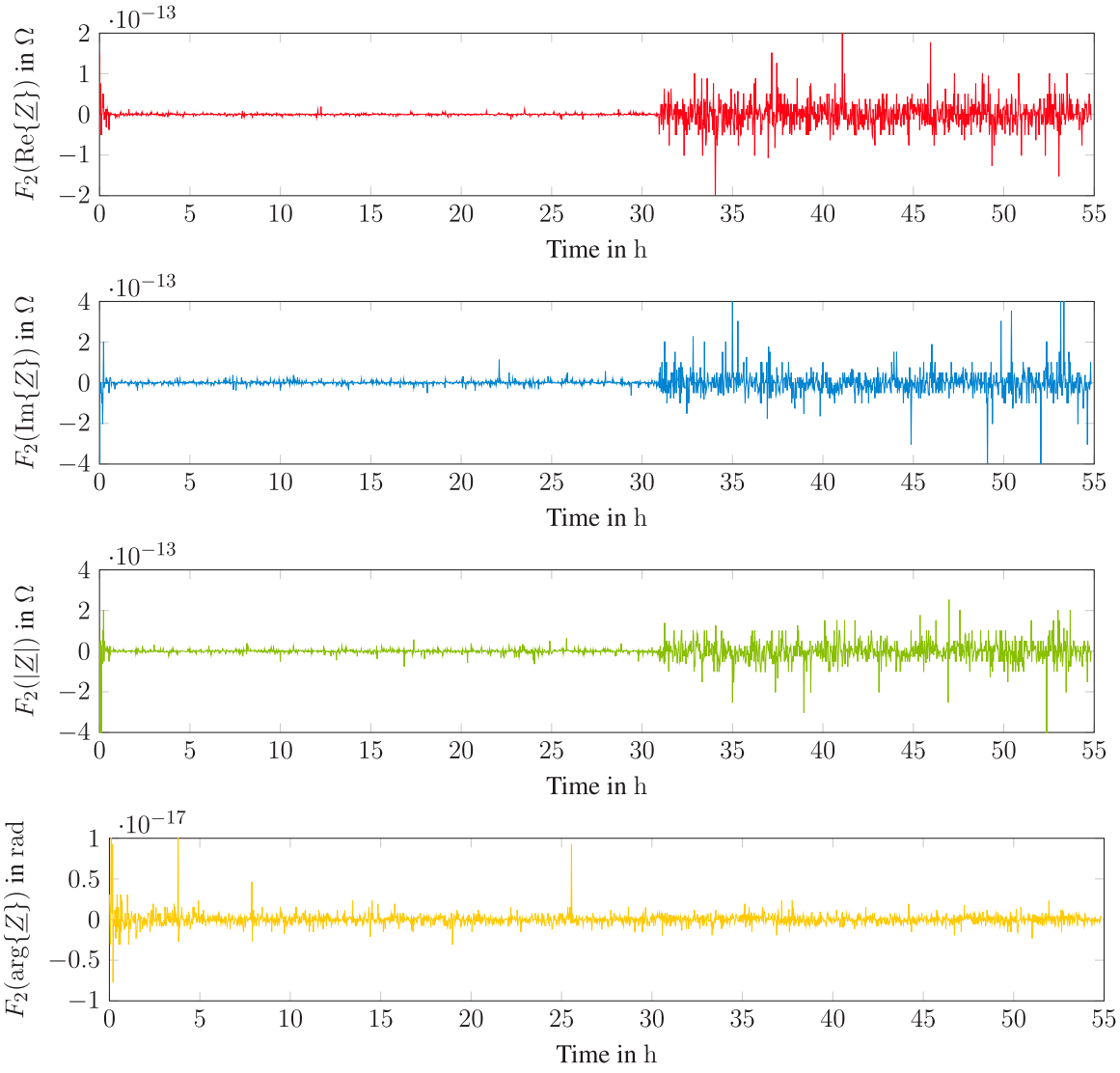


FIGURE 13
Frequency feature $F_2$ - central frequency - for real part (Re{$\underline{Z}$}), imaginary part (Im{$\underline{Z}$}), absolute value ($|\underline{Z}|$) and phase angle (arg{$\underline{Z}$}) over operational time of bearing A, bearing type 6205, radial load $F_r$ = 9375 N, load ratio $C/P$ = 1.6, load angle $\beta$ = 0 °, rotational speed $n$ = 5000 min$^{-1}$, oil flow of 10 L min$^{-1}$. According to (Becker-Dombrowsky et al., 2024)

Separating each rotation of the ball bearing, an averaged capacitance signal can be extracted for different load conditions. In Figure 11 multiple averaged capacitance measurements are depicted with varying radial force $F_r$ and constant oil temperature $T_{Oil}$, rotation speed $n$ and measurement frequency $f_{gen}$. The measuring time was 15 s. At a rotational speed of $n$ = 1000 min$^{-1}$, 250 shaft revolutions and around 99 orbits of the steel ball were captured and averaged. Increasing radial forces result in higher capacitances inside the load zone, as already discussed. However, capacitances outside the load zone are decreasing with rising radial forces. This effect is caused by the deflection of the balls under load. Higher loads result in a more deflected ball inside the load zone, thus more space on the other side of the ball bearing is present. This larger gap induces a lower capacitance compared to ball bearings under less radial force.

Similar results are present using a calculation model, which mathematically describes the geometrical correlation of the ball bearing components and lubricant. Good agreement of calculated and measured results indicates that the simulation model (Section 2.3) used to extract the capacitance of the system is accurate and reliable. Due to mathematical boundaries, only the hydrodynamic regime with oil lubrication can be considered (Puchtler et al., 2023b).

## 3.4 Fatigue tests

Investigations of the data generated by using the alternating current measurement bridge show that three different phases can be identified in bearings' operating life in the frequency domain. According to Martin et al., a run-in phase, a normal

operation phase and a failure phase can be detected, which ensures the usage of the new measurement approach Martin et al. (2022). In time domain, the real part of the impedance data of Martin et al. is negative Martin et al. (2022). In contrast, the real part of the signals generated with this measurement approach is not negative. That makes sense, because a negative real part would implicate an energy gain in the system, which is physically implausible. In general, the measured signals have a high repeatability in their absolute value under the same operating conditions. The bearings for these test were operated under a load ratio $C/P = 1.6$ and rotational speed $n = 5000\,\mathrm{min}^{-1}$. For pure radial loads 13 fatigue test were run (Becker-Dombrowsky et al., 2024). Figures 12, 13 show exemplary the results of one fatigue test. Comparing different bearing types and different load angles, it can be said that the results are independently of the bearing type. In case of additional axial load, the signal changes indicating bearing's operational life end occur later compared to pure radial loads. But the significance of the signal changes still enables a damage detection using this approach (Becker-Dombrowsky et al., 2024). Therefore, the alternating measurement bridge can be used as an observation approach Becker-Dombrowsky et al. (2023).

Figure 12 shows the pitting damage after the bearing test rig was stopped by the internal vibration observation. The pitting was not detected sufficiently enough by the internal vibration observation system of the test bench, which can be seen in its dimensions.

Investigating the electrical impedance signals of the fatigue test with the pitting damage shown in Figure 12 in time and frequency domain increases the information density for condition monitoring. It is essential to detect the damage phase and to differentiate between run-in phase and damage phase. As described by Martin et al. (2022) and Becker-Dombrowsky et al. (2023), the run-in phase is dominant in the pure impedance signal over the operational time. Therefore, different approaches are used to optimize the signal. To do so, the impedance signal is transformed into frequency domain and different features have been calculated and plotted over the operational time to identify significant signal changes. Figure 13 shows exemplary the behavior of the frequency feature $F_2$, the central frequency, according to Table 2 of Becker-Dombrowsky et al. (2023) for the real part ($\mathrm{Re}\{\underline{Z}\}$), imaginary part ($\mathrm{Im}\{\underline{Z}\}$), absolute value ($|\underline{Z}|$) and phase angle ($\arg\{\underline{Z}\}$) over the test time (Becker-Dombrowsky et al., 2023).

The feature signals of real part, imaginary part and absolute value behave different for run-in phase, normal condition phase and damage phase. Due to a higher number of metallic contacts in the run-in phase, the phase angle tends temporary to zero and back again to $-90°$. Therefore, the central frequency changes significantly at the first hours, which can be seen in the yellow graph in Figure 13. This allows the differentiation between these three phases and enables the phase classification using machine learning approaches. In addition, the feature changes significantly hours before the test was stopped by the test-rig internal vibration observation, which indicates the possibility of a damage early detection before vibration observation detects damages. Therefore, the alternating current measurement bridge approach can be seen as an instrument for damage early detection for rolling element bearings.

## 4 Conclusion

In this paper, a visualization technique for rolling bearings, the impedance measurement, was improved. A suitable measurement principle was identified and developed to measure the impedance of rolling element bearings at a several kHz sampling rate and high disturbance resilience, confirming the axpectations and assumptions initially made. First, different impedance measurement principles were introduced and an UMEA was carried out for the most promising approach, the unbalanced AC Wheatstone bridge. A simulation model was developed to study disturbance on the measurement and to investigate the edge frequency up to which a frequency domain analysis of the measured impedance is meaningful. To estimate the latter, an equation was derived. Then, the measurement bridge was physically built and tested in two practical applications. Firstly, measuring the impedance of single steel ball bearings to measure the contact capacitance of a single ball in a radial deep groove ball bearing. Secondly, the impedance of a normal radial deep groove ball bearing was measured over its lifetime in an accelerated fatigue test. In both tests, the AC Wheatstone bridge delivered low-noise and high-frequency impedance signals and therefore proofed suitable for its application in measuring rolling bearing's impedance. This enables the visualization of rolling contact characteristics in a broad range of fields. Wherever a shaft can be electrically accessed with a slip ring and the bearing seat can be isolated, the bearing's impedance can be measured, independent of the application. In future research, remaining useful life models will be developed for better exploitation with reduced maintenance costs at the same time. Additionally, the impedance can be used to retrieve valuable process information, like the applied load.

## Data availability statement

The raw data supporting the conclusions of this article will be made available by the authors, without undue reservation.

## Author contributions

SP: Conceptualization, Data curation, Formal Analysis, Investigation, Methodology, Software, Validation, Visualization, Writing–original draft, Writing–review and editing. JK: Data curation, Formal Analysis, Investigation, Validation, Visualization, Writing–original draft, Writing–review and editing. FB-D: Conceptualization, Data curation, Formal Analysis, Investigation, Methodology, Validation, Writing–original draft, Writing–review and editing. EK: Funding acquisition, Resources, Supervision, Writing–review and editing.

## Funding

The author(s) declare that no financial support was received for the research, authorship, and/or publication of this article.

## Conflict of interest

The authors declare that the research was conducted in the absence of any commercial or financial relationships that could be construed as a potential conflict of interest.

The handling editor HO is currently organizing a Research Topic with the author FB-D.

## Publisher's note

All claims expressed in this article are solely those of the authors and do not necessarily represent those of their affiliated organizations, or those of the publisher, the editors and the reviewers. Any product that may be evaluated in this article, or claim that may be made by its manufacturer, is not guaranteed or endorsed by the publisher.

## References

Alessio, S. M. (2016). *Digital signal processing and spectral analysis for scientists*. Cham: Springer International Publishing.

Barz, M. (1996). *Die schmierfilmbildung in fettgeschmierten schnellaufenden spindellagern*. Hannover: Gottfried Wilhelm Leibniz Universität Hannover. Dissertation.

Becker-Dombrowsky, F. M., and Kirchner, E. (2024). Electrical impedance based condition monitoring of machine elements – a systematic review. *Front. Mech. Eng.* 10. doi:10.3389/fmech.2024.1412137

Becker-Dombrowsky, F. M., Koplin, Q. S., and Kirchner, E. (2023). Individual feature selection of rolling bearing impedance signals for early failure detection. *Lubricants* 11, 304. doi:10.3390/lubricants11070304

Becker-Dombrowsky, F. M., Schink, J., Frischmuth, J., and Kirchner, E. (2024). Investigation of the electrical impedance signal behavior in rolling element bearings as a new approach for damage detection. *Machines* 12, 487. doi:10.3390/machines12070487

Chattopadhyay, S., Banerjee, M., and Pal, S. (2012). Modified ac whetstone bridge network for accurate measurement of pressure using strain gauge type pressure sensor. *Sensors and Transducers* 136, 25–34.

Cone, D. I. (1920). Bridge methods for alternating-current measurements. *J. Am. Inst. Electr. Eng.* 39, 640–647. doi:10.1109/joaiee.1920.6591779

Engelhardt, R. A. (2012). *Uncertainty Mode and Effects Analysis – heuristische Methodik zur Analyse und Beurteilung von Unsicherheiten in technischen Systemen des Maschinenbaus*. Technische Universität Darmstadt. Dissertation.

Gemeinder, Y. (2016). *Lagerimpedanz und Lagerschädigung bei Stromdurchgang in umrichtergespeisten elektrischen Maschinen*. Technische Universität Darmstadt. Dissertation.

Gupta, N., Patel, S., and Hmurick, L. V. (2020). "Using an un-balanced ac whetstone bridge to measure capacitance and inductance," in 2020 international Conference on computational performance evaluation (ComPE) *(IEEE)*, 266–268.

Harder, A., Zaiat, A., Becker-Dombrowsky, F. M., Puchtler, S., and Kirchner, E. (2022a). Investigation of the voltage-induced damage progression on the raceway surfaces of thrust ball bearings. *Machines* 10, 832. doi:10.3390/machines10100832

Harder, A., Zaiat, A., Becker-Dombrowsky, F. M., Puchtler, S., and Kirchner, E. (2022b). Investigation of the voltage-induced damage progression on the raceway surfaces of thrust ball bearings. *Machines* 10, 832. doi:10.3390/machines10100832

Harris, T. A., and Kotzalas, M. N. (2007). Essential concepts of bearing technology, *vol. 1 of* Rolling bearing analysis/Tedric A. Harris Michael N. Kotzalas. fifth edition edn. Boca Raton, London, New York: CRC Press.

Jabłonka, K., Glovnea, R., and Bongaerts, J. (2018). Quantitative measurements of film thickness in a radially loaded deep-groove ball bearing. *Tribol. Int.* 119, 239–249. doi:10.1016/j.triboint.2017.11.001

Keysight Technologies (2020). *Impedance measurement handbook: a guide to measurement Technology and techniques*. 6. edn.

Lerch, R. (2016). Elektrische Messtechnik: Analoge, digitale und computergestützte Verfahren. 7.

Martin, G., Becker, F. M., and Kirchner, E. (2022). A novel method for diagnosing rolling bearing surface damage by electric impedance analysis. *Tribol. Int.* 170, 107503. doi:10.1016/j.triboint.2022.107503

Maruyama, T., Radzi, F., Sato, T., Iwase, S., Maeda, M., and Nakano, K. (2023). Lubrication condition monitoring in ehd line contacts of thrust needle roller bearing using the electrical impedance method. *Lubricants* 11, 223. doi:10.3390/lubricants11050223

Mathias, J. (2016). *Auf dem Weg zu robusten Lösungen - Modelle und Methoden zur Beherrschung von Unsicherheit in den frühen Phasen der Produktentwicklung*. Technische Universität Darmstadt. Dissertation.

Mitvalsky, V. (1964). The maximum sensitivity of the unbalanced wheatstone bridge. *J. Sci. Instrum.* 41, 454–457. doi:10.1088/0950-7671/41/7/310

Muetze, A. (2003). *Bearing currents in inverter-fed AC-motors*. Technische Universität Darmstadt. Dissertation.

Mühl, T. (2020). *Elektrische messtechnik: grundlagen, messverfahren, anwendungen*. Wiesbaden: Springer Vieweg.

Plaßmann, W., and Schulz, D. (2016). *Handbuch Elektrotechnik: Grundlagen und Anwendungen für Elektrotechniker*. Wiesbaden: Springer Vieweg, 7. , neu bearbeitete auflage edn.

Prashad, H. (1988). Theoretical evaluation of impedance, capacitance and charge accumulation on roller bearings operated under electrical fields. *Wear* 125, 223–239. doi:10.1016/0043-1648(88)90115-9

Puchtler, S., Maier, R., Kuhn, M., and Burkhardt, Y. (2023a). "Der initiale elektrische Durchschlag: Einflüsse und Auswirkungen," in *Gleit-und Wälzlagerungen 2023* (Düsseldorf: VDI Verlag GmbH), VDI-Berichte. 21–29.

Puchtler, S., Schirra, T., Kirchner, E., Späck-Leigsnering, Y., and de Gersem, H. (2022). Capacitance calculation of unloaded rolling elements – comparison of analytical and numerical methods. *Tribol. Int.* 176, 107882. doi:10.1016/j.triboint.2022.107882

Puchtler, S., van der Kuip, J., and Kirchner, E. (2023b). Analyzing ball bearing capacitance using single steel ball bearings. *Tribol. Lett.* 71, 38. doi:10.1007/s11249-023-01706-7

Rossmann, A. (2018). *Strukturbildung und Simulation Technischer Systeme: Band 2, Teil 2: Elektrische und Mechanische Dynamik*. Berlin, Heidelberg: Springer Berlin/Heidelberg.

Rybski, R., Kaczmarek, J., and Kontorski, K. (2015). Impedance comparison using unbalanced bridge with digital sine wave voltage sources. *IEEE Trans. Instrum. Meas.* 64, 3380–3386. doi:10.1109/tim.2015.2444255

Schaeffler Technologies AG and Co (2000). Wälzlagerschäden: Schadenserkennung und Begutachtung gelaufener Wälzlager.

Schirra, T., Martin, G., Neu, M., and Kirchner, E. (2019) "Feasibility study of impedance analysis for measuring rolling bearing loads (Nashville)," in *74th STLE annual meeting*.

Schirra, T., Martin, G., Vogel, S., and Kirchner, E. (2018). "Ball bearings as sensors for systematical combination of load and failure monitoring," in *Design 2018*. Editors D. Marjanović, M. Štorga, S. Škec, N. Bojčetić, and N. Pavković (Glasgow, UK: Zagreb: Fac. of Mechanical Engineering and Naval Architecture Univ), 3011–3022. doi:10.21278/idc.2018.0306

Schneider, V., Bader, N., Liu, H., and Poll, G. (2022a). Method for *in situ* film thickness measurement of ball bearings under combined loading using capacitance measurements. *Tribol. Int.* 171, 107524. doi:10.1016/j.triboint.2022.107524

Schneider, V., Behrendt, C., Höltje, P., Cornel, D., Becker-Dombrowsky, F. M., Puchtler, S., et al. (2022b). Electrical bearing damage, A problem in the nano- and macro-range. *Lubricants* 10, 194. doi:10.3390/lubricants10080194

Schwab, A. J., and Kürner, W. (2007) *Elektromagnetische Verträglichkeit; mit 15 Tabellen*, 5. Berlin: Springer.

Takagishi, E. (1980). On the balance of an ac wheatstone bridge. *IEEE Trans. Instrum. Meas.* 29, 131–136. doi:10.1109/tim.1980.4314886

frontiers | Frontiers in Mechanical Engineering

TYPE Original Research
PUBLISHED 06 November 2024
DOI 10.3389/fmech.2024.1489311

Check for updates

OPEN ACCESS

EDITED BY
Michel Fillon,
UPR3346 Institut P' Recherche et Ingénierie en Matériaux, Mécanique et Energétique (Pprime), France

REVIEWED BY
Milan Bukvic,
University of Kragujevac, Serbia
Liang Guo,
SKF, Netherlands
Petr Sperka,
Brno University of Technology, Czechia

*CORRESPONDENCE
Taisuke Maruyama,
maruyama-ta@nsk.com

RECEIVED 31 August 2024
ACCEPTED 22 October 2024
PUBLISHED 06 November 2024

CITATION
Maruyama T, Kosugi D, Iwase S, Maeda M, Nakano K and Momozono S (2024) Application of the electrical impedance method to steel/steel EHD point contacts.
*Front. Mech. Eng.* 10:1489311.
doi: 10.3389/fmech.2024.1489311

COPYRIGHT
© 2024 Maruyama, Kosugi, Iwase, Maeda, Nakano and Momozono. This is an open-access article distributed under the terms of the Creative Commons Attribution License (CC BY). The use, distribution or reproduction in other forums is permitted, provided the original author(s) and the copyright owner(s) are credited and that the original publication in this journal is cited, in accordance with accepted academic practice. No use, distribution or reproduction is permitted which does not comply with these terms.

# Application of the electrical impedance method to steel/steel EHD point contacts

Taisuke Maruyama[1,2]*, Daichi Kosugi[1,2], Shunsuke Iwase[1,2], Masayuki Maeda[1,2], Ken Nakano[3] and Satoshi Momozono[2]

[1]Core Technology R&D Center, NSK Ltd., Fujisawa, Japan, [2]NSK Tribology Collaborative Research Cluster, Tokyo Institute of Technology, Yokohama, Japan, [3]Faculty of Environment and Information Sciences, Yokohama National University, Yokohama, Japan

The authors have previously developed the electrical impedance method which simultaneously measure the thickness and breakdown ratio of oil films in EHD (elastohydrodynamic) contacts. Furthermore, using a ball-on-disc-type apparatus, the authors have also confirmed that the accuracy of oil film measurement by the developed method is comparable to that of optical interferometry (i.e., glass-steel contacts). In this study, we discussed the experimental results obtained by applying the electrical impedance method to steel-steel contacts using a steel disc instead of a glass disc. It was found that under the mixed lubrication regime where wear occurs, the oil film thickness obtained by this method is calculated to be significantly thicker than the theoretical value. This can be attributed to the increase in the apparent dielectric constant of the lubricant due to wear particles in the lubricant.

KEYWORDS

**electrical impedance method, condition monitoring, oil film thickness, breakdown ratio, elastohydrodynamic lubrication, wear, steel/steel contact**

## 1 Introduction

In recent years, with the background of global warming, there has been a demand for further reduction of torque in rolling bearings used in the sliding parts of various machines. To reduce bearing torque, measures such as lowering the viscosity of lubricants or reducing the amount of lubricant filled into the bearing have been implemented. However, these approaches can promote the breakdown of oil films in EHD (elastohydrodynamic) contacts (Gohar and Cameron, 1967) of the rolling bearings, potentially causing various surface damages (Tallian, 1967; Zhu et al., 2007; Maruyama et al., 2017). Of course, various additives are used to improve lubrication properties (Bukvić et al., 2024), but oil film breakdown should be avoided as much as possible. Therefore, the ideal lubrication condition for achieving further torque reduction in rolling bearings is one where the oil film in EHD contacts is as thin as possible without causing metallic contact. Thus, the thickness and breakdown ratio of oil films in EHD contacts are particularly important parameters for visualizing the lubrication condition.

Various studies have been conducted on the visualization techniques of lubrication conditions in EHD contacts (Albahrani et al., 2016). In particular, optical interferometry (Johnston et al., 1991; Yagi and Vergne, 2007; Maruyama and Saitoh, 2010) can accurately measure the oil film thickness in EHD contacts. However, it requires the use of light-transmitting materials, making it difficult to

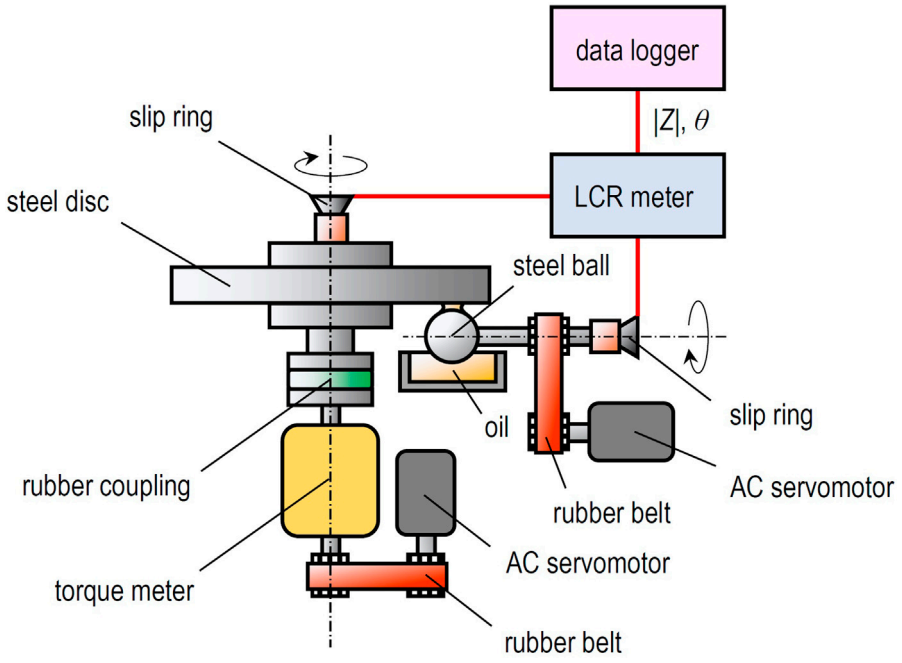


FIGURE 1
Schematic diagram of ball-on-disc-type apparatus for steel/steel contacts.

understand the lubrication conditions in practical rolling bearings. As a visualization technique for lubrication conditions in steel-steel contacts, electrical methods (Lord and Larsson, 2008; Jablonka et al., 2018; Spikes, 2020; Schirra et al., 2021; Shetty et al., 2022; Esmaeili et al., 2022; Schneider et al., 2022; Puchtler et al., 2023) have been highlighted. Recently, the electrical impedance method (Nakano and Akiyama, 2006; Manabe and Nakano, 2008; Nihira et al., 2015), which applies an AC voltage to EHD contacts and simultaneously measures the thickness and breakdown ratio of oil films from the complex impedance response, has been proposed. Maruyama and Nakano (2018) applied both optical interferometry and the electrical impedance method to a ball-on-disc-type apparatus and confirmed that the oil film measurement accuracy of the developed method is comparable to that of optical method (i.e., glass-steel contacts). Furthermore, improvements were made to apply this method to practical deep groove ball bearings (Maruyama et al., 2019) and thrust needle roller bearings (Maruyama et al., 2023) (i.e., steel-steel contacts), and it was confirmed that the results were almost consistent with the theoretical oil film thickness under hydrodynamic lubrication. However, in the case of steel-steel contacts, the experimental results for thickness and breakdown ratio of oil films fluctuated under the mixed lubrication regime, suggesting that wear might have influenced the measurement accuracy. Additionally, since multiple rolling elements are used in rolling bearings, the obtained experimental results represent averaged values for all EHD contacts, which is not suitable for investigating the causes of fluctuations in the results.

Therefore, in this study, ball-on-disc tests using steel discs were conducted to simplify the experimental results obtained when applying the electrical impedance method to steel-steel contacts. It is expected that this paper can contribute to a better understanding of lubrication condition monitoring when applying the electrical impedance method to practical rolling bearings. Furthermore, this method is expected to not only contribute to the improvement of rolling bearing performance and the prediction of lubrication life (time until oil film breakdown) but also to the advancement of lubrication theory.

# 2 Experimental details

## 2.1 Apparatus

Figure 1 shows a schematic diagram of ball-on-disc-type apparatus used in this study for steel/steel contacts. In this setup, the rotating ball specimen is pressed against the rotating disc specimen from below. An AC voltage from an LCR meter is applied to the EHD contact area via slip rings attached to the ends of both rotational axes. Lubricating oil is supplied to the contact area from an oil bath as the ball specimen rotates. Additionally, a torque meter is connected to the rotational axis of the disc specimen, allowing the measurement of the friction coefficient in the EHD contact.

## 2.2 Materials

### 2.2.1 Test specimens

The ball specimen used in this study (diameter: 25.4 mm, arithmetic mean roughness: $R_{a1}$ = 8.2 nm, root mean square

TABLE 1 Test oil properties.

| Oil | Poly-α-olefin oil | Poly-α-olefin oil |
|---|---|---|
| Additive | – | – |
| Density, g/mm$^3$ | 0.826 | 0.850 |
| Kinematic viscosity at 40°C, mm/s$^2$ | 30 | 396 |
| Pressure-viscosity coefficient at 25°C, Gpa$^{-1}$ | 12.5 | 16.3 |
| Relative permittivity | 2.10 | 2.10 |

roughness: $R_{q1}$ = 13.9 nm) was made of AISI 52100 steel (Young's modulus: 207 GPa, Poisson's ratio: 0.30). Similarly, the steel disc specimen (diameter: 100 mm, thickness: 10 mm, roughness: $R_{a2}$ = 0.6 nm, $R_{q2}$ = 2.2 nm) was made of the same material as the ball specimen.

### 2.2.2 Test oils

Table 1 shows two types of PAO (poly-α-olefin oil) used as test oils, with viscosities of $\nu$ = 30 mm$^2$/s and $\nu$ = 396 mm$^2$/s at 40°C. For both lubricants, the oil film thickness was calculated using the same dielectric constant $\varepsilon = \varepsilon_{oil}\,\varepsilon_0 = 2.10\,\varepsilon_0$ F/m, where $\varepsilon_0 = 8.85 \cdot 10^{-12}$ F/m is the dielectric constant in vacuum.

## 2.3 Procedures

In this study, all tests were conducted at room temperature (approximately 25°C). Prior to the tests, the oil bath, ball and disc specimen were cleaned with petroleum benzene using ultrasonic cleaning. After cleaning, the oil bath and each specimen were mounted on the ball-on-disc-type apparatus. The lubricating oil was applied to the ball specimen, which was then pressed against the disc specimen. Using an LCR meter (RMS amplitude: $I_e$ = 50 μA, frequency: $f$ = 1.0 MHz), initial values ($|Z_0|$ [Ω], $\theta_0$ [deg]) under the stationary contacts (i.e., $\alpha$ = 1) were first measured. Subsequently, the ball specimen was separated from the disc specimen, and while rotating, they were brought into contact again to measure the magnitude of the complex impedance $|Z|$ [Ω] and the phase angle $\theta$ [deg] in the dynamic contacts. From these measured values in the stationary and dynamic contacts ($|Z_0|$, $\theta_0$, $|Z|$, $\theta$), the average oil film thickness $h$ [m] and the breakdown ratio of oil film $\alpha$ [–] were calculated using the following Equations 1, 2 (Maruyama and Nakano, 2018), respectively.

$$h = \frac{(1-\alpha)^2 c^2}{2r} \Big/ \mathfrak{W}\left(\frac{(1-\alpha)c^2}{2r^2}\exp\left(1 - \frac{\sin\theta}{2\pi\varepsilon\omega r|Z|}\right)\right) \quad (1)$$

$$\alpha = \frac{|Z_0|\cos\theta}{|Z|\cos\theta_0} \quad (2)$$

Here, $c$ [m] denotes the Hertzian contact radius, $r$ [m] is the radius of the ball specimen, $\omega$ [rad/s] is the angular frequency of the AC voltage, and $\mathfrak{W}(x)$ represents the Lambert function defined implicitly as $x = \mathfrak{W}(x)\exp(\mathfrak{W}(x))$ (Lambert, 1758). Furthermore, in this study, the friction coefficient $\mu$ [–] occurring in the EHD contact was also measured. The average oil film thickness $h$ obtained using this method was compared with the central oil film thickness derived from the Hamrock–Dowson equation (Hamrock and Dowson, 1977a) to verify the accuracy of the oil film measurement. The $h$- and $\alpha$-values were measured using an LCR meter at a sampling rate of 20 kHz for 0.05 s, and error bars representing the standard deviation of the measurement results are displayed in all graphs shown in this study. However, due to the constraints of the testing apparatus, the measured $\mu$ was plotted as a single point for each test condition.

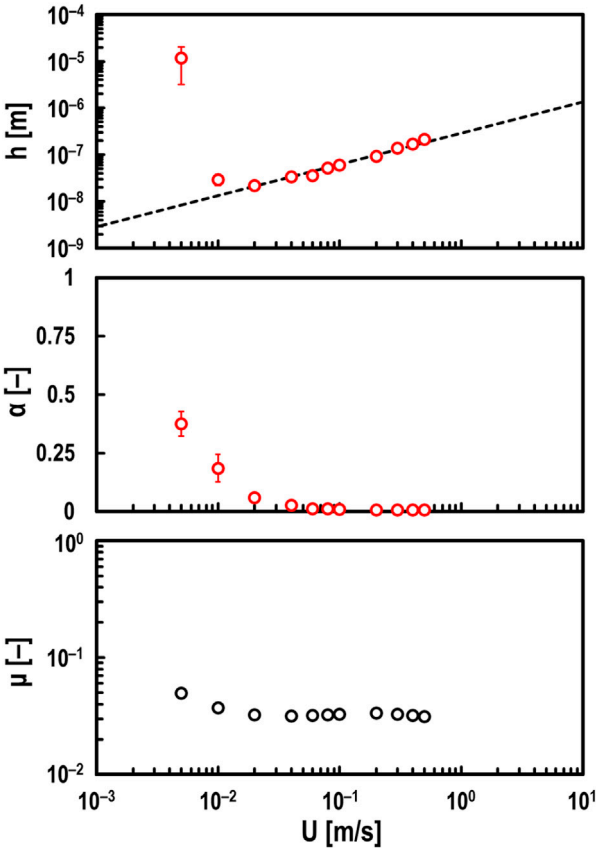


FIGURE 2
Measured values of oil film thickness $h$ (top), breakdown ratio $\alpha$ (middle), and friction coefficient $\mu$ (bottom) for varying entrainment speed $U$ under steel/steel contacts; oil: PAO (viscosity at 40°C: $\nu$ = 30 mm$^2$/s), normal load: $F_z$ = 10 N, and slide-to-roll ratio: $\Sigma$ = 2; red open circles in top and middle graphs: measured values by electrical method; black dashed line in top graph: theoretical prediction by Hamrock and Dowson.

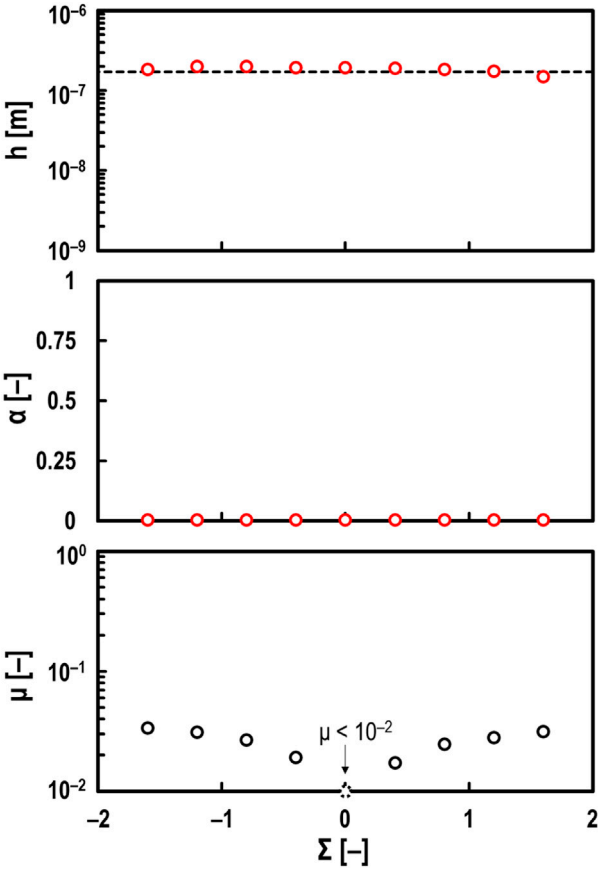


FIGURE 3
Measured values of oil film thickness $h$ (top), breakdown ratio $\alpha$ (middle), and friction coefficient $\mu$ (bottom) for varying slide-to-roll ratio $\Sigma$ under steel/steel contacts; oil: PAO (viscosity at 40°C: $\nu$ = 30 mm$^2$/s), normal load: $F_z$ = 10 N, and entrainment speed: $U$ = 0.5 m/s; red open circles in top and middle graphs: measured values by electrical method; black dashed line in top graph: theoretical prediction by Hamrock and Dowson.

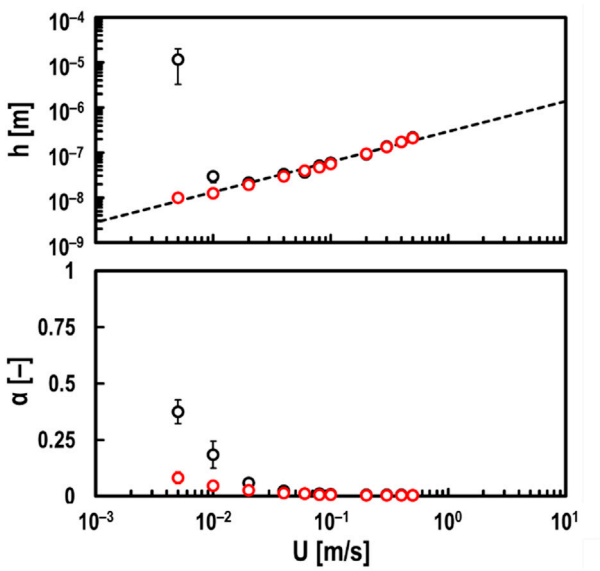


FIGURE 4
Measured values of oil film thickness $h$ (top) and breakdown ratio $\alpha$ (bottom) by electrical method for varying entrainment speed $U$ under steel/steel contacts; oil: PAO (viscosity at 40°C: $\nu$ = 30 mm$^2$/s), and normal load: $F_z$ = 10 N; red open circles in graphs: measured values under pure rolling contacts (i.e., $\Sigma$ = 0); black open circles in graphs: measured values under pure sliding contacts (i.e., $\Sigma$ = 2); black dashed line in top graph: theoretical prediction by Hamrock and Dowson.

# 3 Experimental results

## 3.1 Influence of entrainment speed $U$

First, $h$, $\alpha$ and $\mu$ were measured when the entrainment speed $U$ [m/s] was varied from $U$ = 0.005–0.5 m/s. This range of $U$ was selected because it represents the operational capabilities of the testing apparatus. The measurement results are shown in Figure 2. Here, low-viscosity PAO (viscosity at 40°C: $\nu$ = 30 mm$^2$/s) was used as the test oil, and the normal load $F_z$ = 10 N was held constant. Only the ball specimen was rotated (i.e., slide-to-roll ratio $\Sigma$ = 2.0), and the speed was gradually reduced from $U$ = 0.5 to 0.005 m/s. The red plots in Figure 2 show the experimental results using the electrical impedance method, and the black dashed line is the theoretical central oil film thickness obtained from the Hamrock-Dowson equation (Hamrock and Dowson, 1977a). From Figure 2, it was confirmed that $h$ measured using the electrical method is in close agreement with the theoretical value under the hydrodynamic lubrication regime (i.e., $\alpha \approx 0$). In other words, it was shown that the average oil film thickness measured by the electrical method is equivalent to the theoretical predictions, and it was suggested that the minimum oil film thickness in the EHD contact (Hamrock and Dowson, 1977a) does not significantly affect the oil film measurement accuracy of this method. On the other hand, for $U \leq$ 0.02 m/s, both $\alpha$ and $\mu$ increased, suggesting that this speed range is the mixed lubrication regime. In other words, this developed method can quantitatively evaluate $\alpha$ even in steel/steel contacts. However, $h$ under the mixed lubrication regime was calculated thicker than the theoretical value. In particular, the measured $h$ was extremely thick and had significant variability at the lowest speed condition (i.e., $h \geq 10^{-5}$ m at $U$ = 0.005 m/s).

## 3.2 Influence of slide-to-roll ratio $\Sigma$

Figure 3 shows the experimental results only when $\Sigma$ was varied while keeping $U$ = 0.5 m/s. From Figure 3, it can be confirmed that the measured $h$ using developed method is almost consistent with the theoretical value even when $\Sigma$ is varied. Moreover, it is evident that $\mu$ is significantly affected by $\Sigma$. Additionally, the measured $\alpha$ using this method suggest that these tests were conducted in the hydrodynamic lubrication regime. In other words, it was confirmed that the electrical method does not affect the oil film measurement accuracy even when the lubricating oil is sheared in the hydrodynamic lubrication regime.

Meanwhile, Figure 2 indicates that the measured $h$ using this developed method is significantly thicker than the theoretical value in the mixed lubrication regime when $\Sigma$ = 2. Therefore, to investigate the effect of $\Sigma$ on measured values in detail, $h$ and $\alpha$ at $\Sigma$ = 0 were measured when $U$ was varied from 0.005 to 0.5 m/s.

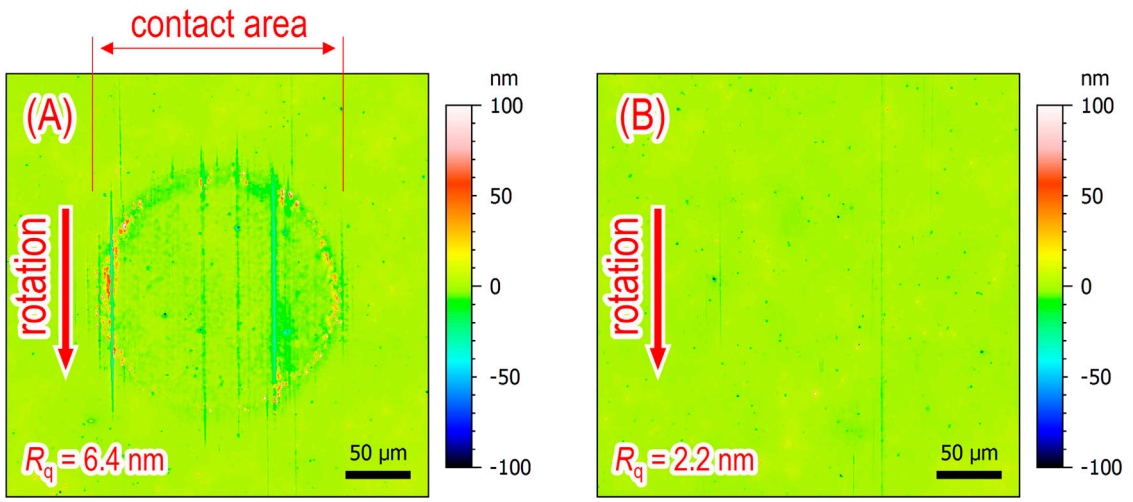


FIGURE 5
Surface roughness images of steel disc specimens after tests at varying entrainment speeds $U$ from 0.005 to 0.5 m/s; oil: PAO (viscosity at 40°C: $\nu$ = 30 mm$^2$/s), and $F_z$ = 10 N; **(A)** surface roughness image at $\Sigma$ = 2 and **(B)** surface roughness image at $\Sigma$ = 0; red arrows: rotational directions of steel ball specimens.

The red plots in Figure 4 show the experimental results at $\Sigma = 0$. On the other hand, the black plots in Figure 4 are the results at $\Sigma = 2$ and are the same as the red plots shown in Figure 2. Figure 4 shows that $h$ measured using the electrical method is almost equal to the theoretical values even in the mixed lubrication regime when $\Sigma = 0$. Furthermore, it was found that $\alpha$ at $\Sigma = 0$ is smaller than that at $\Sigma = 2$. It is thought that in the case of $\Sigma = 2$, running-in wear (Ludema, 1984; Grabon, 2018) occurred on the sliding surfaces, increasing the real contact area. Therefore, the surface roughness of the disc specimens after tests were measured using an optical interference microscope, as shown in Figure 5. Figure 5A confirmed that the surface roughness increased due to wear in the case of $\Sigma = 2$ (for more detailed surface roughness parameters, see Supplementary Material). This suggests that when wear occurs in the EHD contact, the $h$ measured using the developed method is evaluated to be thicker than the theoretical oil film thickness.

## 3.3 Influence of normal load $F_z$

Figure 6 shows the experimental results when $F_z$ was varied from 1.4 to 59 N. It was confirmed that this developed method can accurately measure the oil film thickness even when $F_z$ (i.e., Hertzian contact circle radius $c$ [m] shown in Equation 1) is varied.

Next, the thickness $h$ and the breakdown ratio $\alpha$ of oil films were measured under various normal load conditions ($F_z$ = 1.4, 10 and 59 N) while varying the entrainment speed $U$. However, as shown in Figure 4, under the mixed lubrication regime (i.e., $\alpha \geq 0$) in steel/steel contacts, the measured $h$ values are known to be significantly thicker than the theoretical values. Therefore, the tests were conducted under conditions where wear is unlikely to occur (i.e., $\Sigma = 0$), as shown in Figure 7. Here, the blue plots show the results for $F_z$ = 1.4 N, the green plots show the results for $F_z$ = 10 N, and the red plots show the results for $F_z$ = 59 N. From Figure 7, it was confirmed that varying $F_z$ from 1.4 to 59 N had little effect on the oil film thickness $h$. However, it was found that $h$ becomes slightly thinner as $F_z$ increases. This is evident from the Hamrock-Dowson equation (Hamrock and Dowson, 1977a).

On the other hand, it was found that the breakdown ratio $\alpha$ is greatly affected by $F_z$. This load dependency of $\alpha$ at $\Sigma = 0$ is not considered to be due to wear, as the increase in $h$ shown in Figure 4 was not observed in the mixed lubrication regime.

## 3.4 Influence of viscosity $\nu$

Finally, tests were conducted using high-viscosity PAO (viscosity at 40°C: $\nu$ = 396 mm$^2$/s) with varying speeds from $U$ = 0.005–0.5 m/s, as shown in Figure 8. It was confirmed that in the range of $U \leq 0.1$ m/s, measured $h$-values using the electrical method were found to be in close agreement with the theoretical values.

On the other hand, in the range of $U \geq 0.2$ m/s, it was found that the measured $h$-values were thinner than the theoretical values. Furthermore, it was confirmed that $\mu$ increases in the range of $U \geq 0.2$ m/s. Although direct observations of the EHD contact area were not possible because a steel disc specimen was used as the upper specimen instead of a glass disc specimen, it is expected that the starved lubrication (Hamrock and Dowson, 1977b; Cann et al., 2004; Maruyama and Saitoh, 2015; Nogi, 2015) occurs in this high-speed range, as $h$ decreases and $\mu$ increases. Specifically, the decrease in $h$ leads to an increase in shear rate within the EHD contact, resulting in an increase in $\mu$ (Ali et al., 2017). In other words, the increase in $\mu$ also supports the occurrence of starved lubrication.

# 4 Discussion

## 4.1 Validation of measured oil film thickness

Figure 4 shows that measured $h$-values using this electrical method are significantly thicker than the theoretical values in the

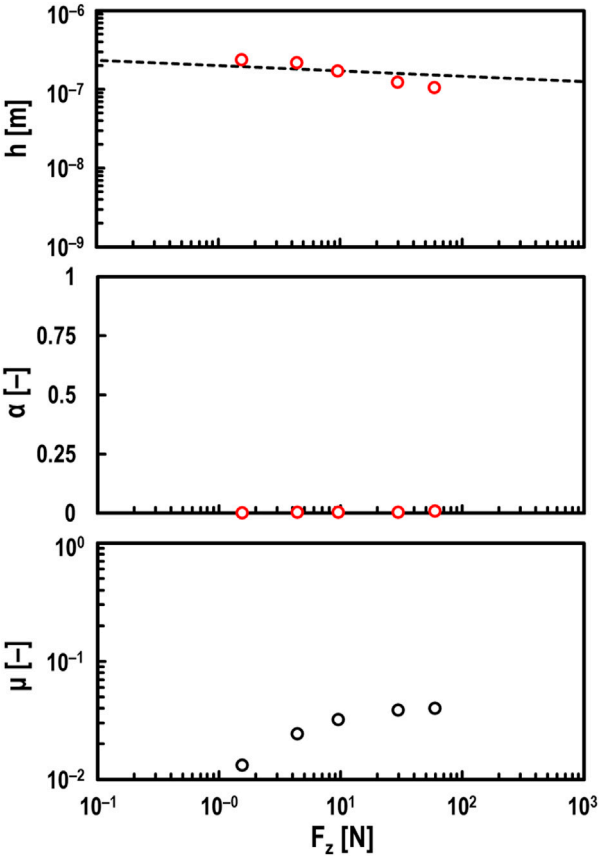


FIGURE 6
Measured values of oil film thickness $h$ (top), breakdown ratio $\alpha$ (middle), and friction coefficient $\mu$ (bottom) for varying normal load $F_z$ under steel/steel contacts; oil: PAO (viscosity at 40°C: $\nu$ = 30 mm$^2$/s), entrainment speed: $U$ = 0.5 m/s, and slide-to-roll ratio: $\Sigma$ = 2; red open circles in top and middle graphs: measured values by electrical method; black dashed line in top graph: theoretical prediction by Hamrock and Dowson.

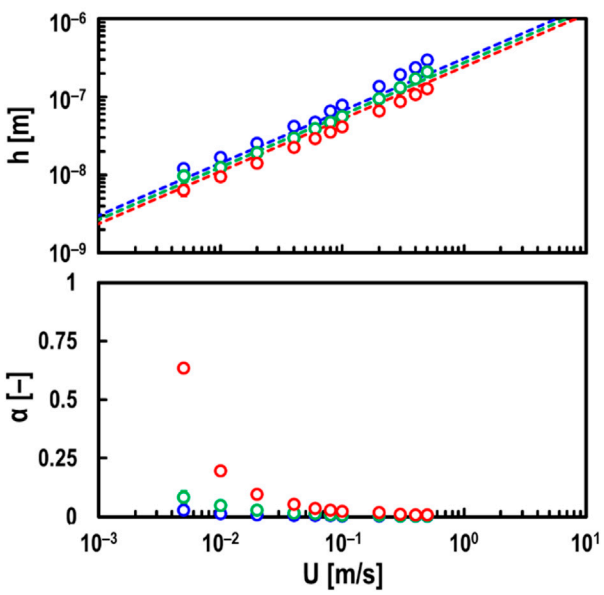


FIGURE 7
Measured values of oil film thickness $h$ (top) and breakdown ratio $\alpha$ (bottom) by electrical method for varying entrainment speed $U$ and normal load $F_z$ under steel/steel contacts; oil: PAO (viscosity at 40°C: $\nu$ = 30 mm$^2$/s), and slide-to-roll ratio: $\Sigma$ = 0; red open circles in graphs: measured values at $F_z$ = 59 N; green open circles in graphs: measured values at $F_z$ = 10 N; blue open circles in graphs: measured values at $F_z$ = 1.4 N; dashed lines corresponding to each color of $F_z$ in top graph: theoretical predictions by Hamrock and Dowson.

mixed lubrication regime ($\alpha \geq 0$) when $\Sigma$ = 2. Conversely, when $\Sigma$ = 0, the measured $h$-values are found to be almost equal to the theoretical values in all speed ranges. Also, the measured $\alpha$-values in the low-speed ranges at $\Sigma$ = 2 were larger than those at $\Sigma$ = 0, suggesting that the wear in the EHD contact area occurred, as shown in Figure 5A. In other words, it is considered that the wear in the contact area may have had some effect on the oil film measurement accuracy of the electrical impedance method. From Equation 1, the oil film thickness obtained by this electrical method is affected by the dielectric constant of the lubricating oil, so it is thought that the wear particles generated in the contact area may have affected the dielectric constant of the lubricating oil. Originally, we should investigate the relationship between the iron powder concentration and the dielectric constant using test oil. However, because the iron powder precipitates when measuring the dielectric constant of oil mixed with iron powder, we substituted the test oil with grease. Commercially available grease (base oil: mineral oil, thickener: Li-soap, base oil viscosity at 40°C: $\nu$ = 100 mm$^2$/s, worked penetration: 280) was mixed with iron powder (material: cementite, particle diameter: 70–150 μm, hardness: HV870). Figure 9 shows the dielectric constant of the grease when iron powder was added. Here, $\varphi_{Fe}$ [vol%] is the volume fraction of iron powder in the grease, and $\varepsilon_{grease}$ [–] is the relative permittivity of the grease. Figure 9 shows that as $\varphi_{Fe}$ increases, $\varepsilon_{grease}$ also increases. This means that the apparent dielectric constant increases when iron powder is dispersed in the grease.

The simulation result of the oil film thickness $h$' [m] obtained using the electrical impedance method (see Equation 1), assuming that the dielectric constant $\varepsilon$ of the test oil changes to the apparent dielectric constant $\varepsilon$' [F/m], is shown in Figure 10. Here, $f$ = 1.0 MHz, $\varepsilon$ = 2.10 $\varepsilon_0$ F/m, $c$ = 0.09 mm, and $r$ = 12.7 mm, and it is assumed to be in hydrodynamic lubrication (i.e., $\alpha$ = 0, $h$ = 100 nm, $\theta$ = −90 deg). Figure 10 shows that simulated $h$'-value increases exponentially with increasing $\varepsilon$'. In other words, according to Figures 9, 10, it is suggested that the very thick $h$-value obtained by the developed method (see Figure 4) in the mixed lubrication regime (i.e., $\alpha \geq 0$) when $\Sigma$ = 2 is due to wear within the EHD contact area, which increases the apparent dielectric constant of the lubricant. From Figure 4, it is clearly unnatural for both $h$ and $\alpha$ to increase simultaneously, and we believe that when such results are obtained, it can be judged that wear is occurring in the contact area. Therefore, we estimated the apparent dielectric constant $\varepsilon$' [F/m] of the lubricant at $\Sigma$ = 2, assuming that the actual oil film thickness at $\Sigma$ = 2 in Figure 4 is the same as the experimental results at $\Sigma$ = 0. Figure 11 shows that $\varepsilon'$ increases at low-speed ranges, especially at $U$ = 0.005 m/s, where the apparent dielectric constant of the lubricant increases about 10 times due to wear shown in Figure 5A. This suggests that the lower the velocity, the more wear particles are mixed in the lubricant due to wear occurring in the EHD contact area.

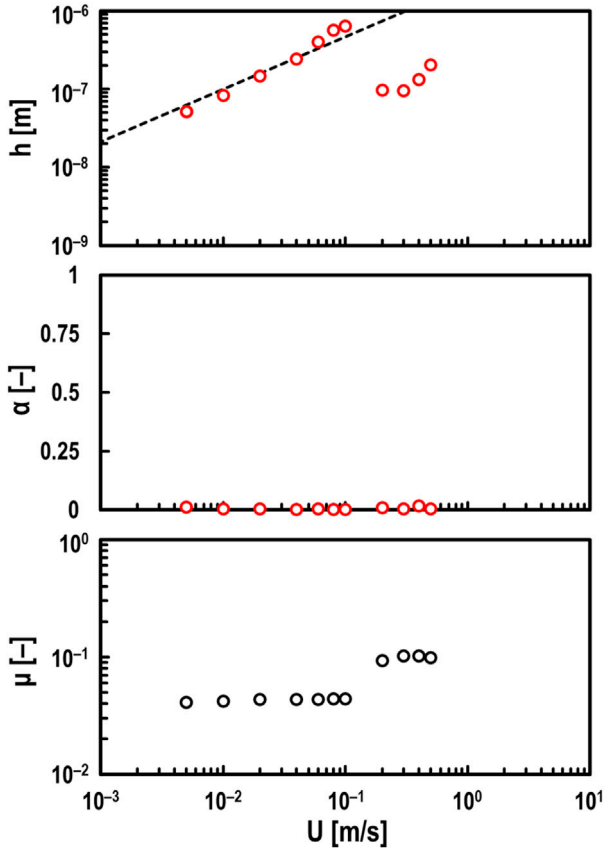


FIGURE 8
Measured values of oil film thickness $h$ (top), breakdown ratio $\alpha$ (middle), and friction coefficient $\mu$ (bottom) for varying entrainment speed $U$ under steel/steel contacts; oil: PAO (viscosity at 40°C: $\nu$ = 396 mm$^2$/s), normal load: $F_z$ = 10 N, and slide-to-roll ratio: $\Sigma$ = 2; red open circles in top and middle graphs: measured values by electrical method; black dashed line in top graph: theoretical prediction by Hamrock and Dowson.

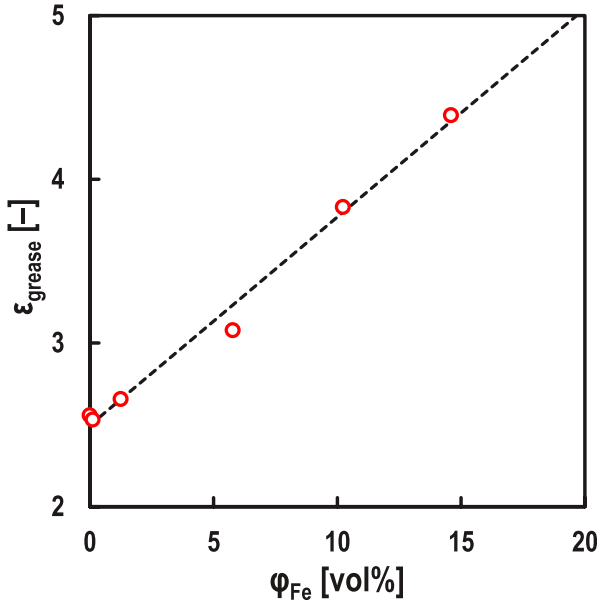


FIGURE 9
Relationship between volume fraction of iron particles in grease $\varphi_{Fe}$ and relative permittivity of Li-soap grease $\varepsilon_{grease}$; black dashed line: fitted curve by linear function fitted curve by linear function.

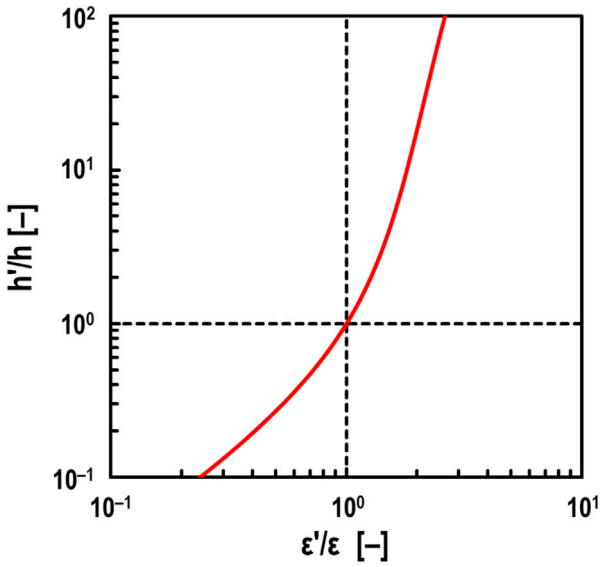


FIGURE 10
Effect of dielectric constant on measured oil film thickness under $F_z$ = 10 N with no breakdown area (i.e., $\alpha$ = 0); $\varepsilon$: true dielectric constant of oil ($\varepsilon$ = 2.10 $\varepsilon_0$ F/m), $\varepsilon'$: estimated dielectric constant of oil, $h$: true oil film thickness ($h$ = 100 nm), $h'$: theoretical measured oil film thickness obtained by electrical method; black dashed vertical line: $\varepsilon' = \varepsilon$, black dashed horizontal line: $h' = h$.

By the way, in the case of glass/steel contact (Maruyama and Nakano, 2018), it has been confirmed that this electrical method can accurately measure the oil film thickness under the mixed lubrication regime (i.e., $\alpha \geq 0$) even when $\Sigma$ = 2. In other words, the measured oil film thickness was not evaluated to be thicker than the actual oil film thickness (i.e., the measured values obtained by optical interferometry or the theoretical values by Hamrock–Dowson equation). This is likely because, in the case of glass/steel contact, adhesion wear (Kalin and Vizintin, 2006) does not occur as much as in steel/steel contact due to the contact between dissimilar materials, resulting in minimal impact on the measurement accuracy of the oil film thickness by the developed method. However, note that the extremely thick measured $h$-values may be influenced not only by the generation of wear particles but also by changes in surface roughness (see Supplementary Material). Additionally, it is already known that the capacitance around the EHD contact can affect the accuracy of oil film measurement (Jablonka et al., 2018; Maruyama and Nakano, 2018). However, it has been theoretically shown that as the oil film becomes thinner, the influence of the capacitance around the contact becomes very small (Maruyama and Nakano, 2018). In other words, under conditions where the oil film is thin enough for wear to occur, we believe that the influence of wear particles around the contact on the measurement accuracy is minimal.

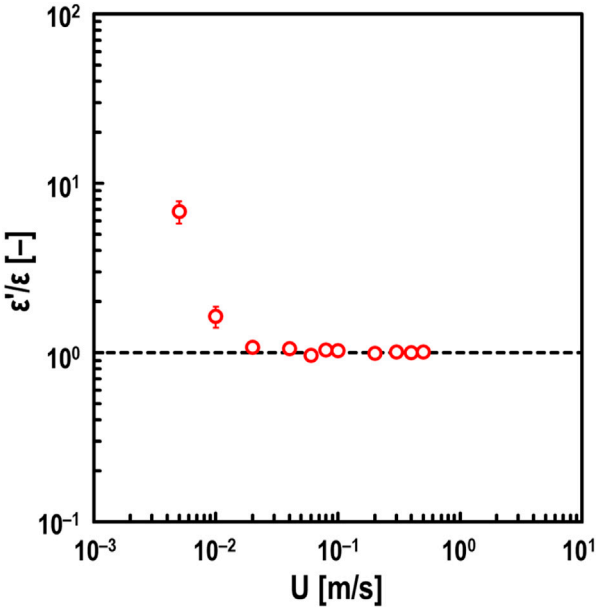


FIGURE 11
Estimated values of dielectric constant of oil ε′ under pure sliding steel/steel contacts for varying entrainment speed $U$; oil: PAO (viscosity at 40°C: $\nu$ = 30 mm²/s), and normal load: $F_z$ = 10 N; black dashed line: ε′ = ε = 2.10 $\varepsilon_0$ F/m.

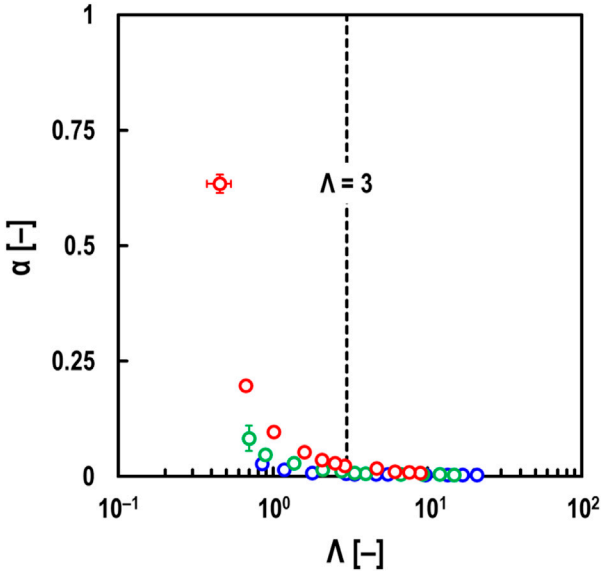


FIGURE 12
Relationship between film parameter $\Lambda$ and breakdown ratio $\alpha$ under steel/steel contacts, oil: PAO (viscosity at 40°C: $\nu$ = 30 mm²/s), entrainment speed: $U$ = 0.005–0.5 m/s, and slide-to-roll ratio: $\Sigma$ = 0; red open circles: measured values at $F_z$ = 59 N; green open circles: measured values at $F_z$ = 10 N; blue open circles: measured values at $F_z$ = 1.4 N; black dashed line: $\Lambda$ = 3.

## 4.2 Validation of breakdown ratio

Next, using the results from Figure 7, the film parameter $\Lambda$ [−], defined as the ratio of oil film thickness to surface roughness, was calculated to investigate its relationship with the breakdown ratio of oil films $\alpha$ in steel/steel contacts. Here, $\Lambda$ is obtained from the following Equation 3 (Tallian, 1967):

$$\Lambda = \frac{h}{\sqrt{{R_{q1}}^2 + {R_{q2}}^2}} \tag{3}$$

where $h$ [m] is the average oil film thickness measured using the electrical method, and $R_{q1}$ [m], $R_{q2}$ [m] are the root mean square roughness of the ball and disc specimen surfaces before tests under non-load conditions, respectively (see 2.2.1 Test specimens). The film parameter $\Lambda$ is often defined using the minimum oil film thickness. However, as the oil film generally becomes thinner, the difference between the minimum and central oil film thickness decreases (Hamrock and Dowson, 1977a). Therefore, in this study, $\Lambda$ was calculated using the average oil film thickness (≈ central oil film thickness) obtained by the electrical method. Tallian (1967) also calculated $\Lambda$ using the central oil film thickness and found that wear occurs in EHD contacts when $\Lambda$ < 3.

The relationship between $\Lambda$ and $\alpha$ is shown in Figure 12. It was found that when $\Lambda$ > 3, the oil film hardly collapsed regardless of $F_z$. On the other hand, when $\Lambda$ < 3, it suggested that the experiments were conducted in the mixed lubrication regime. Johnson et al. (1972) theoretically found that the oil film would collapse when $\Lambda$ < 3, assuming that the number of asperities directly contacting the surface roughness follows a Poisson distribution relative to the oil film thickness. Thus, it was suggested that this method could quantitatively evaluate $\alpha$ even in steel/steel contacts.

Furthermore, it was found that when $\Lambda$ < 3, $\alpha$ increased with increasing $F_z$ even for the same $\Lambda$, as shown in Figure 12. Additionally, from the measured $h$-values shown in Figure 7 ($\Sigma$ = 0), an increase in $h$ as shown in Figure 4 was not observed in the mixed lubrication regime ($\alpha \geq 0$). This indicates that the load dependence of $\alpha$ shown in Figure 12 is not caused by wear. This load dependence is thought to be due to the larger elastic (or plastic) deformation in the real contact area as the load increases. However, as the load increases, the Hertzian contact area also becomes larger, making dielectric breakdown more likely. This could have led to the measured $\alpha$-values being evaluated as larger than the real contact area. Further investigation is needed to determine the cause of this load dependence.

# 5 Conclusion

In this study, ball-on-disc tests using a steel disc were conducted to verify whether the electrical impedance method, developed in previous research, can be applied not only to element tests in glass-steel contacts but also to practical bearing tests in steel-steel contacts. The findings are as follows:

1. Tests were conducted by varying the entrainment speed, slide-to-roll ratio, normal load, and viscosity. Then, the oil film thickness measured by the electrical impedance method was compared with the theoretical values calculated using Hamrock-Dowson equation. As a result, except under the mixed or starved lubrication, it was confirmed that this method can accurately measure the oil film thickness even for steel/steel contacts.
2. When wear occurs within the EHD contacts, the oil film thickness obtained using the developed method was found

to be significantly thicker than the theoretical value. This is believed to be due to the apparent increase in the dielectric constant of the lubricant caused by the inclusion of wear particles. In other words, this method suggests that the occurrence of wear can also be monitored. Specifically, if the unnatural results of both oil film thickness and breakdown ratio increasing simultaneously are obtained, it may indicate that wear is occurring within the EHD contact.

3. When using high-viscosity oil, the oil film thickness was found to be thinner than the theoretical value at high-speed ranges. Since the friction coefficient $\mu$ increased at that time, it suggests that the starved lubrication occurred in the EHD contact. This supports the results obtained using this electrical method, where the oil film thickness was thinner than the theoretical value.
4. The relationship between the film parameter $\Lambda$ and the breakdown ratio $\alpha$ showed that the $\alpha$ increased within the range of $\Lambda < 3$. Additionally, since $\alpha$ and $\mu$ increased simultaneously within the range of $\Lambda < 3$, it suggests that this method can quantitatively evaluate the $\alpha$ even in steel/steel contacts. Therefore, it was considered that the number of asperities directly contacting the surface roughness might follow a Poisson distribution relative to the oil film thickness.
5. It was confirmed that the breakdown ratio of oil films $\alpha$ increased with larger normal loads within the range of $\Lambda < 3$. This is thought to be because the larger the load, the greater the elastic (or plastic) deformation at the asperity in real contact area, leading to an increased $\alpha$.

In summary, this study reports on the interpretation of the measurement results obtained when applying the electric impedance method to steel-steel contacts where wear occurs. We hope that this paper can contribute to a better understanding of lubrication condition when applying the electrical method to actual rolling bearings.

## Data availability statement

The raw data supporting the conclusions of this article will be made available by the authors, without undue reservation.

## Author contributions

TM: Writing–original draft, Writing–review and editing, Conceptualization, Data curation, Formal Analysis, Investigation, Methodology, Project administration, Resources, Supervision, Validation, Visualization. DK: Supervision, Writing–review and editing. SI: Supervision, Writing–review and editing. MM: Data curation, Investigation, Validation, Writing–review and editing. KN: Conceptualization, Data curation, Investigation, Methodology, Project administration, Supervision, Validation, Writing–review and editing. SM: Project administration, Supervision, Writing–review and editing.

## Funding

The author(s) declare that no financial support was received for the research, authorship, and/or publication of this article.

## Acknowledgments

In writing this paper, I received much advice through discussions conducted with Guajardo Duenas Guillermo Andres, Fumiaki Aikawa and Yohei Murata of NSK Ltd. I would like to express my gratitude to these people.

## Conflict of interest

Authors TM, DK, SI, and MM were employed by NSK Ltd.

The remaining authors declare that the research was conducted in the absence of any commercial or financial relationships that could be construed as a potential conflict of interest.

## Publisher's note

All claims expressed in this article are solely those of the authors and do not necessarily represent those of their affiliated organizations, or those of the publisher, the editors and the reviewers. Any product that may be evaluated in this article, or claim that may be made by its manufacturer, is not guaranteed or endorsed by the publisher.

## Supplementary material

The Supplementary Material for this article can be found online at: https://www.frontiersin.org/articles/10.3389/fmech.2024.1489311/full#supplementary-material

## References

Albahrani, S. M. B., Philippon, D., Vergne, P., and Bluet, J. M. (2016). A review of *in situ* methodologies for studying elastohydrodynamic lubrication. *Proc. Institution Mech. Eng. Part J J. Eng. Tribol.* 230, 86–110. doi:10.1177/1350650115590428

Ali, F., Křupka, I., and Hartl, M. (2017). Effects of out-of-contact lubricant channeling on friction and film thickness in starved elastohydrodynamic lubrication point contacts. *Proc. Institution Mech. Eng. Part J J. Eng. Tribol.* 201, 145–150. doi:10.1177/1350650115576943

Bukvić, M., Gajević, S., Skulić, A., Savić, S., Ašonja, A., and Stojanović, B. (2024). Tribological application of nanocomposite additives in industrial oils. *Lubricants* 12 (1), 6. doi:10.3390/lubricants12010006

Cann, P. M., Damiens, B., and Lubrecht, A. (2004). The transition between fully flooded and starved regimes in EHL. *Tribol. Int.* 37, 859–864. doi:10.1016/j.triboint.2004.05.005

Esmaeili, K., Wang, L., Harvey, T. J., White, N. M., and Holweger, W. (2022). Electrical discharges in oil-lubricated rolling contacts and their detection using electrostatic sensing technique. *Sensors* 22, 392. doi:10.3390/s22010392

Gohar, R., and Cameron, A. (1967). The mapping of elastohydrodynamic contacts. *ASLE Trans.* 10, 215–225. doi:10.1080/05698196708972181

Grabon, W. A. (2018). A new approach to the description of height distribution of plateau honed cylinder liner surface texture during the initial stage of wear. *Wear* 408-409, 34–42. doi:10.1016/j.wear.2018.04.019

Hamrock, B. J., and Dowson, D. (1977a). Isothermal elastohydrodynamic lubrication of point contacts: Part III-fully flooded results. *ASME J. Lubr. Technol.* 99 (2), 264–275. doi:10.1115/1.3453074

Hamrock, B. J., and Dowson, D. (1977b). Isothermal elastohydrodynamic lubrication of point contacts: Part IV-starvation results. *ASME J. Lubr. Technol.* 99, 15–23. doi:10.1115/1.3452973

Jablonka, K., Glovnea, R., and Bongaerts, J. (2018). Quantitative measurements of film thickness in a radially loaded deep-groove ball bearing. *Tribol. Int.* 119, 239–249. doi:10.1016/j.triboint.2017.11.001

Johnson, K. L., Greenwood, J. A., and Poon, S. Y. (1972). A simple theory of asperity contact in elastohydro-dynamic lubrication. *Wear* 19 (1), 91–108. doi:10.1016/0043-1648(72)90445-0

Johnston, G. J., Wayte, R., and Spikes, H. A. (1991). The measurement and study of very thin lubricant films in concentrated contacts. *Tribol. Trans.* 34, 187–194. doi:10.1080/10402009108982026

Kalin, M., and Vizintin, J. (2006). The tribological performance of DLC coatings under oil-lubricated fretting conditions. *Tribol. Int.* 39 (10), 1060–1067. doi:10.1016/j.triboint.2006.02.040

Lambert, J. H. (1758). Observationes variae in mathesin puram. *Acta Helvetica Physico-mathematico-anatomico-botanico-medica* 3, 128–168.

Lord, J., and Larsson, R. (2008). Film-forming capability in rough surface EHL investigated using contact resistance. *Tribol. Int.* 41 (9-10), 831–838. doi:10.1016/j.triboint.2007.11.006

Ludema, K. C. (1984). A review of scuffing and running-in of lubricated surfaces, with asperities and oxides in perspective. *Wear* 100 (1-3), 315–331. doi:10.1016/0043-1648(84)90019-x

Manabe, K., and Nakano, K. (2008). Breakdown of oil films and formation of residual films. *Tribol. Int.* 41, 1103–1113. doi:10.1016/j.triboint.2008.02.001

Maruyama, T., Maeda, M., and Nakano, K. (2019). Lubrication condition monitoring of practical ball bearings by electrical impedance method. *Tribol. Online* 14 (5), 327–338. doi:10.2474/trol.14.327

Maruyama, T., and Nakano, K. (2018). *In situ* quantification of oil film formation and breakdown in EHD contacts. *Tribol. Trans.* 61 (6), 1057–1066. doi:10.1080/10402004.2018.1468519

Maruyama, T., Radzi, F., Sato, T., Iwase, S., Maeda, M., and Nakano, K. (2023). Lubrication condition monitoring in EHD line contacts of thrust needle roller bearing using the electrical impedance method. *Lubricants* 11, 223. doi:10.3390/lubricants11050223

Maruyama, T., and Saitoh, T. (2010). Oil film behavior under minute vibrating conditions in EHL point contacts. *Tribol. Int.* 43, 1279–1286. doi:10.1016/j.triboint.2009.11.004

Maruyama, T., and Saitoh, T. (2015). Relationship between supplied oil flow rates and oil film thicknesses under starved elastohydrodynamic lubrication. *Lubricants* 3, 365–380. doi:10.3390/lubricants3020365

Maruyama, T., Saitoh, T., and Yokouchi, A. (2017). Differences in mechanisms for fretting wear reduction between oil and grease lubrication. *Tribol. Trans.* 60, 497–505. doi:10.1080/10402004.2016.1180469

Nakano, K., and Akiyama, Y. (2006). Simultaneous measurement of film thickness and coverage of loaded boundary films with complex impedance analysis. *Tribol. Lett.* 22 (1), 127–134. doi:10.1007/s11249-006-9074-z

Nihira, T., Manabe, K., Tadokoro, C., Ozaki, S., and Nakano, K. (2015). Complex impedance measurement applied to short-time contact between colliding steel surfaces. *Tribol. Lett.* 57, 29. doi:10.1007/s11249-015-0478-5

Nogi, T. (2015). An analysis of starved EHL point contacts with reflow. *Tribol. Online* 10 (1), 64–75. doi:10.2474/trol.10.64

Puchtler, S., van der Kuip, J., and Kirchner, E. (2023). Analyzing ball bearing capacitance using single steel ball bearings. *Tribol. Lett.* 71, 38. doi:10.1007/s11249-023-01706-7

Schirra, T., Martin, G., Puchtler, S., and Kirchner, E. (2021). Electric impedance of rolling bearings - consideration of unloaded rolling elements. *Tribol. Int.* 158, 106927. doi:10.1016/j.triboint.2021.106927

Schneider, V., Bader, N., Liu, H., and Poll, G. (2022). Method for *in situ* film thickness measurement of ball bearings under combined loading using capacitance measurements. *Tribol. Int.* 171, 107524. doi:10.1016/j.triboint.2022.107524

Shetty, P., Meijer, R. J., Osara, J. A., and Lugt, P. M. (2022). Measuring film thickness in starved grease-lubricated ball bearings: an improved electrical capacitance method. *Tribol. Trans.* 65, 869–879. doi:10.1080/10402004.2022.2091067

Spikes, H. A. (2020). Triboelectrochemistry: influence of applied electrical potentials on friction and wear of lubricated contacts. *Tribol. Lett.* 68, 90. doi:10.1007/s11249-020-01328-3

Tallian, T. E. (1967). On competing failure modes in rolling contact. *ASLE Trans.* 10 (4), 418–439. doi:10.1080/05698196708972201

Yagi, K., and Vergne, P. (2007). Abnormal film shapes in sliding elastohydrodynamic contacts lubricated by fatty alcohols. *Proc. Institution Mech. Eng. Part J J. Eng. Tribol.* 221, 287–300. doi:10.1243/13506501jet253

Zhu, D., Martini, A., Wang, W., Hu, Y., Lisowsky, B., and Wang, Q. J. (2007). Simulation of sliding wear in mixed lubrication. *ASME J. Tribol.* 129 (3), 544–552. doi:10.1115/1.2736439

frontiers | Frontiers in Mechanical Engineering

TYPE Original Research
PUBLISHED 07 November 2024
DOI 10.3389/fmech.2024.1471045

Check for updates

OPEN ACCESS

EDITED BY
Antonio Papangelo,
Politecnico di Bari, Italy

REVIEWED BY
Liran Ma,
Tsinghua University, China
Iakov A. Lyashenko,
Technical University of Berlin, Germany
Saša Milojević,
University of Kragujevac Faculty of Engineering, Serbia

*CORRESPONDENCE
Chiharu Tadokoro,
tadokoro@mail.saitama-u.ac.jp

RECEIVED 26 July 2024
ACCEPTED 09 October 2024
PUBLISHED 07 November 2024

CITATION
Tadokoro C, Kobayashi H, Sueda M, Nagamine T, Vlădescu S-C, Reddyhoff T and Nakano K (2024) Controlling windscreen wiper vibration through yaw angle adjustments: a study of dynamic contact behavior using fluorescence observation.
*Front. Mech. Eng.* 10:1471045.
doi: 10.3389/fmech.2024.1471045

COPYRIGHT
© 2024 Tadokoro, Kobayashi, Sueda, Nagamine, Vlădescu, Reddyhoff and Nakano. This is an open-access article distributed under the terms of the Creative Commons Attribution License (CC BY). The use, distribution or reproduction in other forums is permitted, provided the original author(s) and the copyright owner(s) are credited and that the original publication in this journal is cited, in accordance with accepted academic practice. No use, distribution or reproduction is permitted which does not comply with these terms.

# Controlling windscreen wiper vibration through yaw angle adjustments: a study of dynamic contact behavior using fluorescence observation

Chiharu Tadokoro[1,2,3]*, Hiroaki Kobayashi[1], Miwa Sueda[1], Takuo Nagamine[1], Sorin-Cristian Vlădescu[2], Tom Reddyhoff[3] and Ken Nakano[4]

[1]Department of Mechanical Engineering, Saitama University, Saitama, Japan, [2]Department of Engineering, Faculty of Natural, Mathematical and Engineering Sciences, King's College London, London, United Kingdom, [3]Department of Mechanical Engineering, Imperial College London, London, United Kingdom, [4]Faculty of Environment and Information Sciences, Yokohama National University, Yokohama, Japan

Friction-induced vibration in the wiper system of passenger cars not only causes impaired visibility as a result of uneven water film distribution on the windscreen surface, but also leads to noise problems by transmitting vibrations as sound to the passengers. In this study, a novel experimental apparatus was developed to simulate the wiper system, enabling the change in normal support stiffness and the precise adjustment of the yaw angles of a shortened rubber blade and its flexible base relative to the drive direction of a glass plate. The use of fluorescence observation provided a significant advantage, enabling precise measurements of the position of the rubber blade tip and the water film thickness in the contact area of the rubber blade and the glass plate during operation. In conjunction with this, an accelerometer and a gap sensor were employed to measure the normal and tangential motions of the support structures, respectively. This comprehensive setup allows for precise control of blade support conditions, and provides accurate measurement for motions of rubber blade and support structures, making it a powerful tool for investigating friction-induced vibration in the wiper system. The experimental results clearly demonstrated the effectiveness of applying large yaw angles to both the rubber blade and the flexible base in suppressing friction-induced vibration, resulting in smooth motion at any drive speed. These findings have the potential to improve wiper performances under actual operating conditions.

KEYWORDS

**wiper, soft material, friction, vibration, fluorescence observation**

## 1 Introduction

The wiper system of vehicles is designed to maintain clear visibility for drivers by moving a rubber blade pressed against a windshield with a wiper arm in reciprocating motions. During these wiping motions, the friction between the rubber blade and the windshield can cause a self-excited vibration known as friction-induced vibration. If the rubber blade forms an uneven water sheet failing to sweep water drops, the refraction of

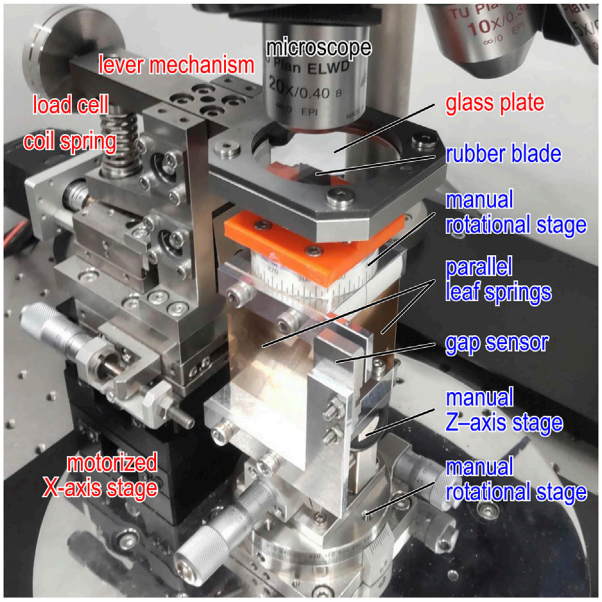


FIGURE 1
Photograph of experimental apparatus; red words: components in drive part; blue words: components in driven part.

light hinders clear view (Kitayama et al., 2012). Friction-induced vibraion can also result in noise problems if the sound of the vibration is transmitted to passengers (Wang et al., 2023). This problem is particularly pronounced in electric vehicles, where the lower levels of interior sound and vibration compared to those in internal combustion engine vehicles make friction-induced vibration and noise more noticeable (Farfan-Cabrera, 2019; Li and Xu, 2023). Therefore, research on suppressing friction-induced vibration contributes not only to traffic safety by maintaining clear visibility but also to user comfort by reducing noise.

To suppress the friction-induced vibration in the wiper system, it is crucial to understand the vibration mechanism in detail. The types of vibration in the wiper system can be categorized as follows (Goto et al., 2001; Reddyhoff et al., 2015): (1) high-frequency vibration, called squeal noise, around 1 kHz, generated at the rubber blade (Goto et al., 2001; Reddyhoff et al., 2015; Le Rouzic et al., 2013; Min et al., 2014; Unno et al., 2017). (2) low-frequency vibration, referred to as chattering, less than 100 Hz, generated in the wiper system including support parts of the rubber blade such as the wiper arm (Suzuki and Yasuda, 1998; Lancioni et al., 2016). (3) impact sound and vibration, called reversal noise, caused by the tip of the rubber blade hitting the glass surface when the wiper changes direction. Regarding (1) and (2), the velocity-weakening friction, which appears in the mixed lubrication regime of the Stribeck curve, is known to cause friction-induced vibration (Reddyhoff et al., 2015; Le Rouzic et al., 2013; Suzuki and Yasuda, 1998). Specifically for squeal noise, the mechanism has been demonstrated theoretically (Goto et al., 2001), experimentally (Reddyhoff et al., 2015; Le Rouzic et al., 2013; Min et al., 2014), and numerically (Unno et al., 2017), showing that the vibrational modes of the rubber blade are excited by the instability caused by the velocity-weakening friction. This phenomenon is independent of the characteristics of the support structure in the wiper system. Several studies have investigated the relationship between friction behavior and noise in terms of the surface roughness, coating treatment, blade material, and wear status (Wang et al., 2023). On the other hand, for chattering, the behavior of the rubber blade tip in friction-induced vibration and the influence of the support structure of the rubber blade are not sufficiently understood to design the wiper system without any vibration and noise problems in advance. In an actual wiper system, not only the velocity conditions but also the yaw support angles of the rubber blade and the deformation direction and stiffness of the wiper arm depend on the position along the rubber blade, complicating the understanding of the phenomenon. It has been demonstrated that the application of a leaf spring support with a yaw angle misalignment between the support deformation direction and the drive velocity can suppress the friction-induced vibration of a tribometer, which is considered a single-degree-of-freedom vibrating system (Kado et al., 2013). In addition, direct observations of water-lubricated elastomer/glass contacts are effective in understanding the mechanism of the velocity-weakening friction (Deleau et al., 2009; Dalzin et al., 2016). Fluorescence observation can be applied to examine the motion of objects with rough surfaces like rubber (Fowell et al., 2014; Vlădescu et al., 2019).

In this study, to understand the influence of the adjustments on yaw angles and support stiffness of the rubber blade on chattering vibration in the wiper system, a custom-made apparatus simulating a wiper system was developed. This apparatus included yaw angle adjustments and support structures in the tangential and normal directions for a short piece of a commercial rubber blade. In addition, to examine the relationship between the motions of the support structure and the rubber blade tip, the in-plane behavior of the rubber blade tip and the distance between the rubber blade tip and glass surface under water lubrication were measured using fluorescence observation. The findings of this study are expected to contribute not only to advancing the fundamental understanding of vibration mechanisms but also to provide insights for the design of quieter and more effective wiper systems.

## 2 Experimental details

### 2.1 Apparatus

The experimental apparatus was designed to simulate the interaction between the rubber blade and glass surface of a wiper system, reproducing the dynamic conditions and frictional behavior observed in practical use. The experimental apparatus allows for precise control of normal load, drive velocity, and yaw angles, enabling detailed study of friction-induced vibration. Figures 1, 2 show a photograph and a schematic diagram of the experimental apparatus, which consists of drive and driven parts that simulate the wiper system, along with an optical setup for monitoring the motion of the rubber blade. A glass plate (material: borosilicate glass, diameter: 50 mm, thickness: 5 mm, and arithmetic average roughness: 4 nm) and a short piece of a commercial rubber blade (made by DENSO WIPER SYSTEMS, INC., model number: AS70GN, width: 10 mm, and arithmetic average roughness: 1 μm) were placed in the drive and driven parts respectively, forming a line contact. In the drive part, the glass plate was mounted on a motorized linear stage (KS101-30R, SURUGA SEIKI, JAPAN) via a holder and a loading mechanism to drive at a constant drive speed $V$. The loading mechanism employed a lever mechanism with a coil spring, including a load cell (stiffness: 2.4 kN/mm, LMB-A-50N, Kyowa Electronic Instruments, JAPAN) above the coil spring to monitor the

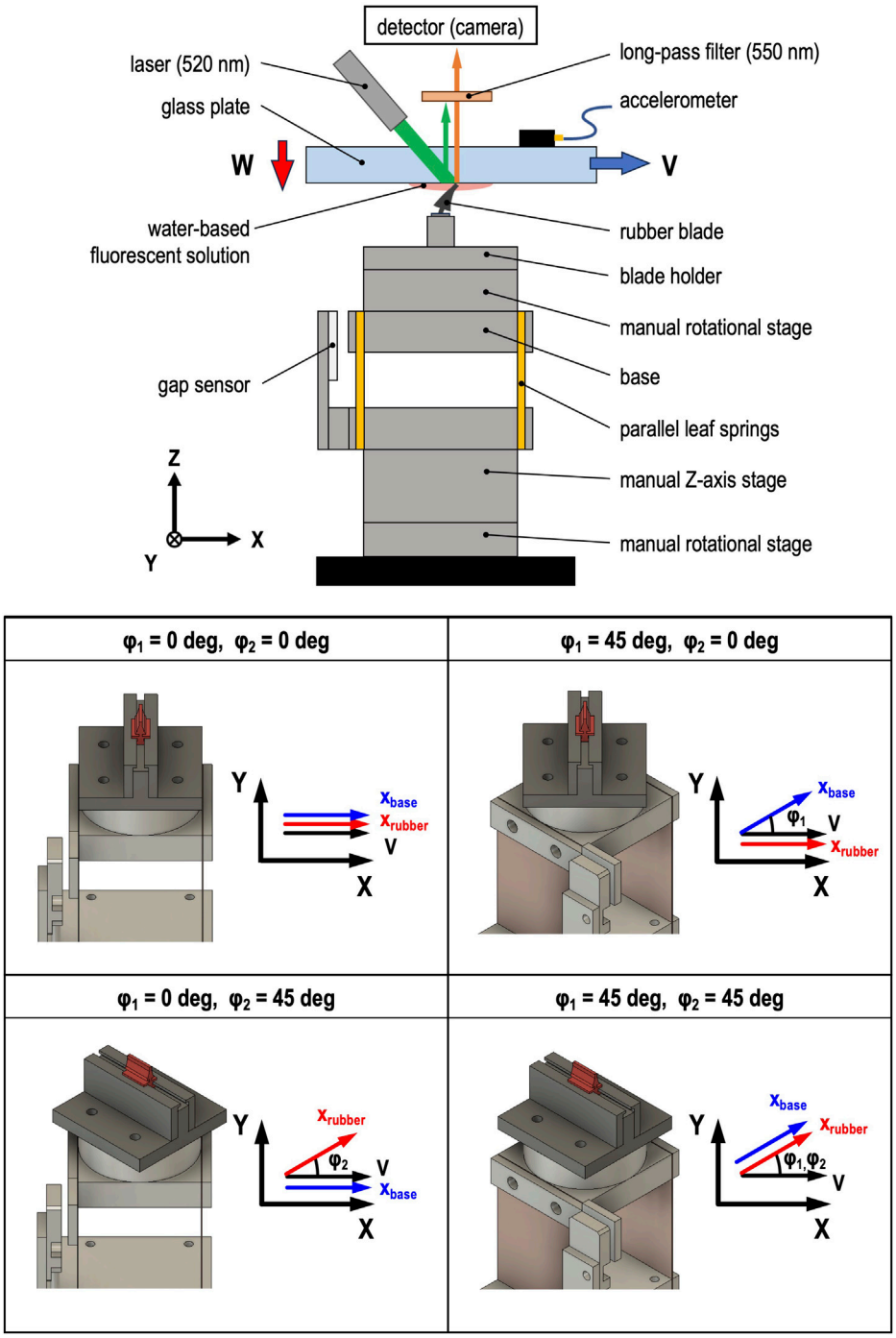


FIGURE 2
Schematic diagram of experimental apparatus; upper diagram: side view of experimental apparatus; lower diagram: configurations of driven part with different yaw angles ($\varphi_1$ and $\varphi_2$).

normal load. The normal load was applied to the contact by the restoring force generated by deforming the coil spring. The coil spring could be replaced with one of three coil springs with different stiffness values ($K$ = 4, 10, and 60 N/mm). This change would adjust the natural frequency of the loading mechanism to $f_L$ = 18, 26, and 40 Hz, respectively. To monitor the $Z$-axis motion of the loading mechanism including the glass plate during the sliding test with the rubber blade, an accelerometer (frequency range: 1 Hz–10 kHz, NP-3211, Ono Sokki, JAPAN) was placed on the opposite surface of the glass plate from the contact. In the driven part, the rubber blade was mounted on a base plate supported by parallel leaf springs (stiffness $k$: 4 N/mm), where the natural frequency of the base structure of the rubber blade was $f_B$ = 29 Hz. The displacement $x_{base}$ of the base plate was measured by a gap sensor (resolution: 0.4 µm, EX-614V, KEYENCE, JAPAN). A manual $Z$-axis stage was placed right under the parallel leaf springs to adjust the height position of the rubber blade tip. A manual rotational stage was placed under the parallel leaf

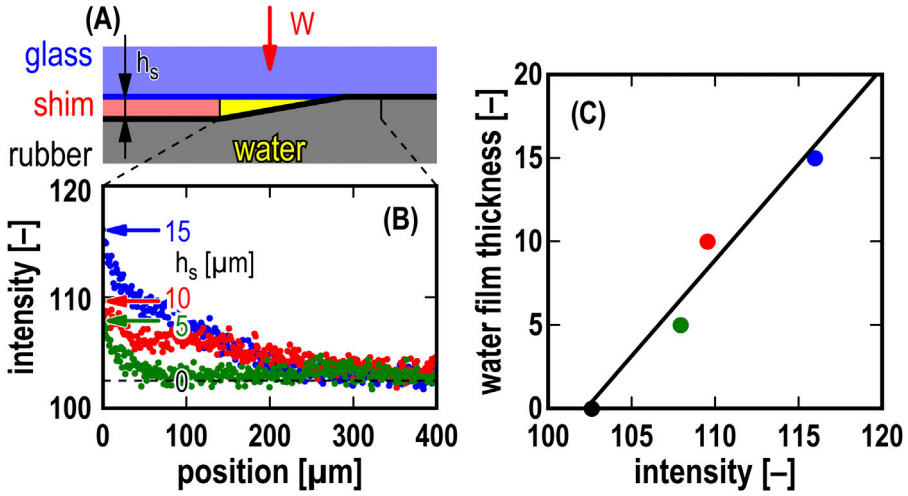


FIGURE 3
Calibration of film thickness measurement; **(A)** schematic of the contact of glass plate and rubber blade with constant-thickness shim ($h_s$ = 5, 10, 15 μm) and water-based fluorescent solution; **(B)** fluorescence intensity measured under the contact; **(C)** water film thickness *versus* fluorescence intensity measured at position of zero.

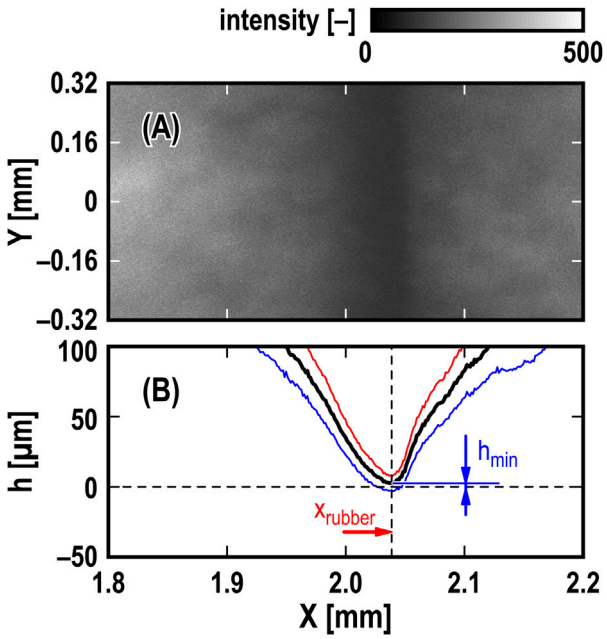


FIGURE 4
Typical result of fluorescence observation for sliding contact of glass plate and rubber blade; **(A)** snapshot of fluorescence observation; **(B)** cross-section of *h versus X*; bold black line: *h* converted from average intensity of snapshot from *Y* = −0.32 to 0.32 mm, red line: *h* + STD, blue line: *h* − STD; *K* = 10 N/mm, $\varphi_1 = \varphi_2$ = 0 deg, and *V* = 5 mm/s; *t* = 0.065 s in Figure 5.

springs to adjust the yaw angle $\varphi_1$ between the direction of drive velocity *V* and the direction of the deformation $x_{base}$ of the parallel leaf springs. Another manual rotational stage was placed between the rubber blade and the base plate to adjust the yaw angle $\varphi_2$ between the direction of drive velocity *V* and the direction of the deformation of the rubber blade.

Fluorescence observation of the contact between the glass plate and rubber blade was performed to measure the water film thickness and the position of the rubber blade tip using the optical setup consisting of a laser (wavelength: 520 nm), microscope, and an intensified CMOS camera (ORCA-Flash4.0 V3, HAMAMATSU PHOTONICS, JAPAN). A fluorescent solution was prepared by adding Rhodamine-B (concentration: 0.3 mol/m$^3$) to pure water, and this solution was used as a lubricant in the contact. The laser beam was directed at the contact area lubricated with the water-based fluorescent solution. The emitted light (wavelength: 570–590 nm) was captured using the camera at a frame rate of 200 fps (exposure time: 1/frame rate) through the microscope equipped with a 5x objective lens and long-pass filter (cut-off wavelength: 550 nm) in the optical path. The resolution of the captured images was 500 × 500 px; the pixel size was 1.28 μm/px; the gradation was 65,536 levels of gray. A manual *XY*-axis linear stage was mounted at the bottom of the microscope to adjust the camera's view to the contact area.

## 2.2 Procedure

The glass plate was cleaned with acetone and hexane for 5 min each using an ultrasonic cleaner, dried with hot air from a blower, and installed into the holder of the drive part. The accelerometer was fixed to the glass plate with solid glue. The rubber blade was wiped by an ethanol-moistened paper towel and then installed onto the base plate via the blade holder. Each yaw angle ($\varphi_1$ and $\varphi_2$) was adjusted to be 0, 15, 30, or 45 degrees using the manual rotational stages, as shown in Figure 2. The contact between the glass plate and rubber blade was made while keeping the glass plate horizontal using the loading mechanism in the drive part and the manual *Z*-axis stage in the driven part. The water-based fluorescent solution of 100 mm$^3$ was injected around the contact. After driving the glass 10 mm at *V* = 20 mm/s, the normal load *W* was adjusted to be 0.17 N while maintaining the glass plate horizontal and the rubber blade bent

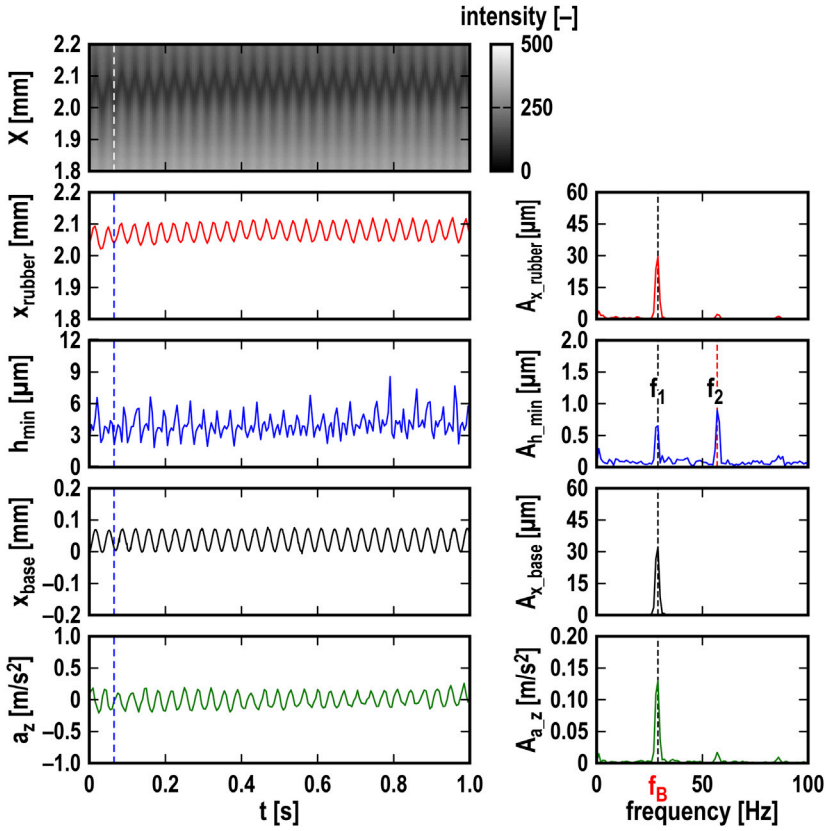


FIGURE 5
Temporal changes and FFT analyses of fluorescence intensity, $h_{min}$, $x_{rubber}$, $x_{base}$, and $a_z$; $K$ = 10 N/mm, $\varphi_1 = \varphi_2$ = 0 deg, and $V$ = 5 mm/s; white and blue dashed lines indicate $t$ = 0.065 s (snapshot in Figure 4); $f_B$ = 29 Hz.

with static friction. The microscope position was adjusted using the manual $XY$-axis linear stage to observe the contact with the camera. The laser beam was then directed at the contact. When the glass was moved 20 mm at $V$ = 5, 10, 15, and 20 mm/s, the displacement $x_{base}$ of the base plate and the acceleration $a_z$ of the glass plate were measured at sampling frequencies of 1,000 Hz and 51.2 kHz, respectively. A signal of 1 V for 0.05 s was used as a trigger to synchronize the start timing of recording $x_{base}$ and $a_z$ and capturing the fluorescence intensity images. The ambient temperature and relative humidity during the experiments were 25°C and 20%–40%, respectively.

# 3 Results and discussion

## 3.1 Calibration of water film thickness under contact between glass plate and rubber blade

Figure 3 illustrates the calibration of film thickness measurements for the water-based fluorescent solution using the images captured by the camera. To calibrate the intensity of the captured images to the water film thickness, a shim film (material: stainless steel) with known thickness $h_s$ of 5, 10, and 15 µm was placed between the glass plate and rubber blade, creating three distinct contact situations: contact via the shim film, contact via the fluorescent water, and direct contact of the glass plate and rubber blade, as shown in Figure 3A. In Figure 3B, green, red, and blue plots represent the fluorescence intensity values measured with shim films of different thicknesses (5, 10, and 15 µm, respectively). Each color plot showed that the fluorescence intensity was maximum at the end of the shim film (position: 0 µm) and decreased with increasing distance from the shim film. The water film thickness at the position where the fluorescence intensity was the maximum was assumed to be equal to the thickness of the shim film. The minimum value of the fluorescence intensity was assumed to indicate the water film thickness of zero. The relationship between the water film thickness and the fluorescence intensity measured at the position of zero using each shim is shown in Figure 3C. The solid back line represents a fitting line with the equation: $h = a\,(I–b)$, where $h$ is the water film thickness, $I$ is the intensity measured by fluorescence observation, and $a$ and $b$ are fitting parameters. The fitting line shown in Figure 3C has parameters $a$ = 1.15 and $b$ = 102.5 (determined by the least squares method, $R^2$: 0.95).

## 3.2 Typical vibration observed in simulated wiper system

Figure 4 illustrates a typical result of fluorescence observation for the sliding contact of the glass and rubber blade at $K$ = 10 N/mm, $\varphi_1 = \varphi_2$ = 0 deg, and $V$ = 5 mm/s, where $t$ = 0.065 s in Figure 5. In the fluorescence intensity image with a grayscale

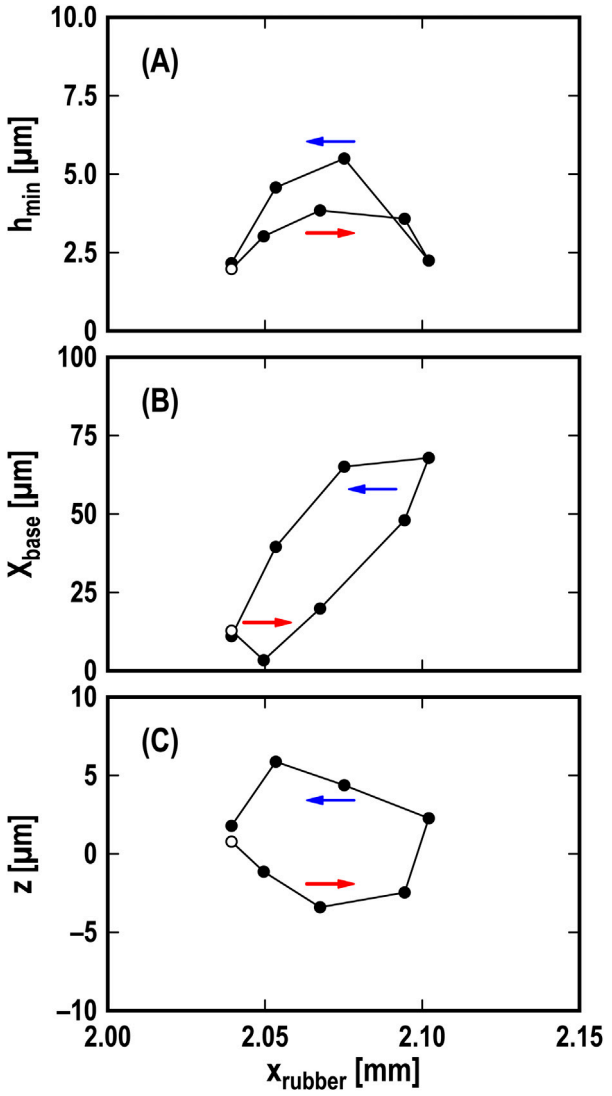


FIGURE 6
Cross-sections of **(A)** $h_{min}$ versus $x_{rubber}$, **(B)** $x_{base}$ versus $x_{rubber}$, and **(C)** $z$ versus $x_{rubber}$; $K$ = 10 N/mm, $\varphi_1 = \varphi_2$ = 0 deg, and $V$ = 5 mm/s; open plot: start point of period ($t$ = 0.065 s); arrows: direction of time progress.

range of 0–500 shown in Figure 4A, the intensity decreased as it approached $X$ = 2.04 mm but did not change significantly along the $Y$-axis direction. The black line in Figure 4B represents the mean values of the film thickness $h$ of water, calculated from the intensity averaged from $Y$ = −0.32 to 0.32 mm. The red and blue lines represent the mean values of $h$ plus and minus standard deviation (STD), respectively, also calculated from $Y$ = −0.32 to 0.32 mm. The variation of $h$ with $X$ shows the tip-corner shape of the rubber blade and the minimum value $h_{min}$ of the water film thickness, which is 2.3 μm at $X$ = 2.04 mm. The position where the minimum film thickness $h_{min}$ was observed is defined as $x_{rubber}$. Considering the STD value shown by the blue line, the value of $h$ at $X$ = 2.04 mm was almost zero, implying that the lubrication regime in the experiment was mixed lubrication.

Figure 5 illustrates temporal changes in fluorescence intensity, $x_{rubber}$, $h_{min}$, $x_{base}$, and $a_z$ as a typical experimental result at $K$ = 10 N/mm, $\varphi_1 = \varphi_2$ = 0 deg, and $V$ = 5 mm/s, where the values from the last one second of the four-second sliding time in the test were extracted. A low-pass filter (cut-off frequency: 200 Hz) was applied to the temporal change in $a_z$. In addition, the spectra shown in the right-hand side column of Figure 5 were obtained using the fast Fourier transform (FFT) method applied to the temporal changes in $x_{rubber}$, $h_{min}$, $x_{base}$, and $a_z$ shown in the left-hand side column of Figure 5. The values of $x_{rubber}$ and $h_{min}$ were obtained from the fluorescence image at the top of the left-hand side column in Figure 5, which was made by combining the intensity profiles averaged in the $Y$-axis direction from each snapshot. $x_{base}$ is the displacement of the base, which was connected to parallel leaf springs. $a_z$ is the acceleration of the glass plate with the lever in the loading mechanism. $x_{rubber}$, $x_{base}$, and $a_z$ showed steady waveforms of 29 Hz, which matched the natural frequency of the base ($f_B$ = 29 Hz), as shown in the spectra, where their amplitudes were 30 μm, 32 μm, 0.13 m/s$^2$, respectively. On the other hand, the waveform of $h_{min}$ contained two components of $f_1$ = 29 Hz and $f_2$ = 57 Hz. The first-order frequency $f_1$ was the same as $f_B$ = 29 Hz, and the second-order frequency $f_2$ was approximately twice $f_B$. The amplitude $A_{h\_min}$ at $f_1$ was 0.63 μm and that at $f_2$ was 0.88 μm.

Figure 6 shows the cross-sections of $h_{min}$, $x_{base}$, and $z$ *versus* $x_{rubber}$ at $K$ = 10 N/mm, $\varphi_1 = \varphi_2$ = 0 deg, and $V$ = 5 mm/s, where the values were extracted at $t$ = 0.065–0.100 s as shown in Figure 5. $z$ is the $Z$-axis displacement of the glass plate, calculated by dividing $a_z$ by $-(2\pi f)^2$, assuming $a_z$ to be a harmonic vibration, where $f$ = 29 Hz as shown in Figure 5. The open plot represents the start point of the period ($t$ = 0.065 s). Regarding the cross-section of $h_{min}$ *versus* $x_{rubber}$ in Figure 6A, the values of $h_{min}$ at the top and bottom end points of $x_{rubber}$ were the minima of 2 μm in one stroke. The value of $h_{min}$ at the center of the backward stroke of $x_{rubber}$ was 6 μm, larger than that at the center of the forward stroke, which was 4 μm. This result suggests that the in-plane motion of the rubber blade tip generated a hydrodynamic effect, such as the wedge effect, increasing the film thickness of water in the middle of the forward and backward strokes where the velocity of the rubber blade tip reached two local maxima in one stroke, causing the $2f_B$ component in $h_{min}$. On the other hand, the cross-section of $x_{base}$ *versus* $x_{rubber}$ shown in Figure 6B displayed a positively inclined elliptical orbit. As the value of $x_{rubber}$ increased, the value of $x_{base}$ also increased, but with a lag relative to the change in $x_{rubber}$. This result suggests that the motion of the rubber blade tip is the origin of the vibration. In addition, the cross-sections of $z$ *versus* $x_{rubber}$ in Figure 6C showed a horizontal elliptical orbit. The difference between the cross-sections of $z$ *versus* $x_{rubber}$ and $h_{min}$ *versus* $x_{rubber}$ indicates that the change in $h_{min}$ was in the $Z$-axis direction but did not affect the $Z$-axis motion of the lever in the loading system.

## 3.3 Influence of drive speed on friction-induced vibration

Figure 7 illustrates the effect of drive speed on the amplitude and frequency of $x_{rubber}$, $h_{min}$, $x_{base}$, and $a_z$ at $K$ = 10 N/mm and $\varphi_1 = \varphi_2$ = 0 deg. The amplitude and frequency were extracted at a predominant frequency in each spectrum, calculated using the FFT method for the temporal change in $x_{rubber}$, $h_{min}$, $x_{base}$, and $a_z$ for 1.0 s, as shown in Figure 5. $A_{x\_rubber}$, $A_{h\_min}$, $A_{x\_base}$, and $A_{a\_z}$ represent the amplitude of $x_{rubber}$, $h_{min}$, $x_{base}$, and $a_z$, respectively. The diameter of circles in Figure 7 represents the amplitude. The

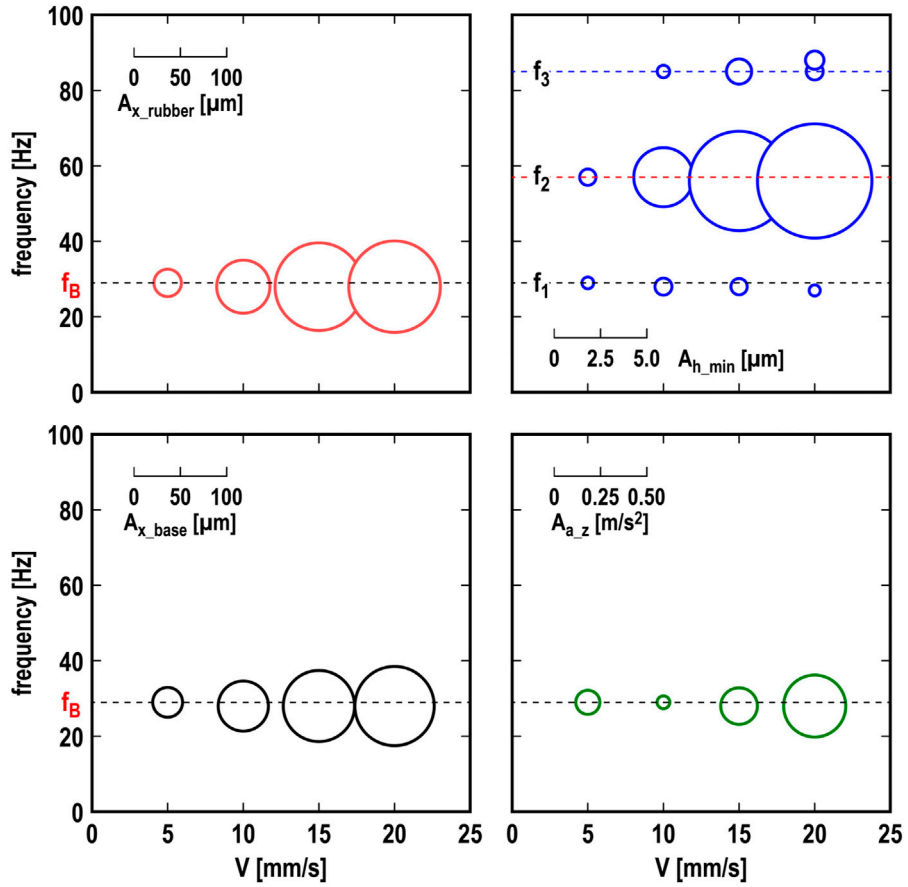


FIGURE 7
Effect of drive speed $V$ on amplitude and frequency of $x_{rubber}$, $h_{min}$, $x_{base}$, and $a_z$; $K$ = 10 N/mm; $\varphi_1 = \varphi_2$ = 0 deg.

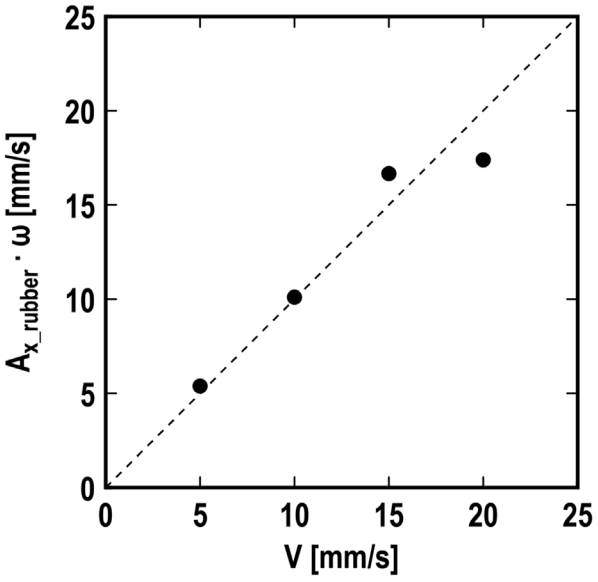


FIGURE 8
Maximum speed $A_{x\_rubber} \cdot \omega$ of rubber blade tip *versus* drive speed $V$; $K$ = 10 N/mm; $\varphi_1 = \varphi_2$ = 0 deg; dashed line: $A_{x\_rubber} \cdot \omega = V$.

thresholds for extracting the predominant components in the spectrum were $A_{x\_rubber}$ = 5 μm, $A_{h\_min}$ = 0.25 μm, $A_{x\_base}$ = 5 μm, and $A_{a\_z}$ = 0.025 m/s$^2$. For $x_{rubber}$, $x_{base}$, and $a_z$, the frequency of the vibration was consistent with $f_B$ = 29 Hz, as shown in Figure 5, and did not change with increasing drive speed $V$. On the other hand, the values of $A_{x\_rubber}$, $A_{x\_base}$, and $A_{a\_z}$ increased with increasing $V$. The tendencies for the vibration frequency to correspond to the natural frequency derived from the supporting structure, rather than the natural frequency of the rubber blade alone, and for the amplitude to increase with drive speed are consistent with the results of Suzuki et al.'s research (Suzuki and Yasuda, 1998). Regarding $h_{min}$, there are three predominant frequencies: $f_1$, $f_2$, and $f_3$. The first-order frequency $f_1$ = 29 Hz was the same as $f_B$ = 29 Hz, the second-order frequency $f_2$ = 57 Hz, as also shown in Figure 5, was approximately 2 × $f_B$, and the third-order frequency $f_3$ = 85 Hz was close to 3 × $f_B$. The values of $f_1$, $f_2$, and $f_3$ did not change with increasing $V$. In contrast, the values of $A_{h\_min}$ at $f_2$ = 57 Hz increased with increasing $V$, but those at $f_1$ = 29 Hz and $f_3$ = 85 Hz did not increase significantly with increasing $V$. Note that the second-order frequency was not the natural frequency of the system's second mode, but could have been caused by the speed-dependent hydrodynamic effect.

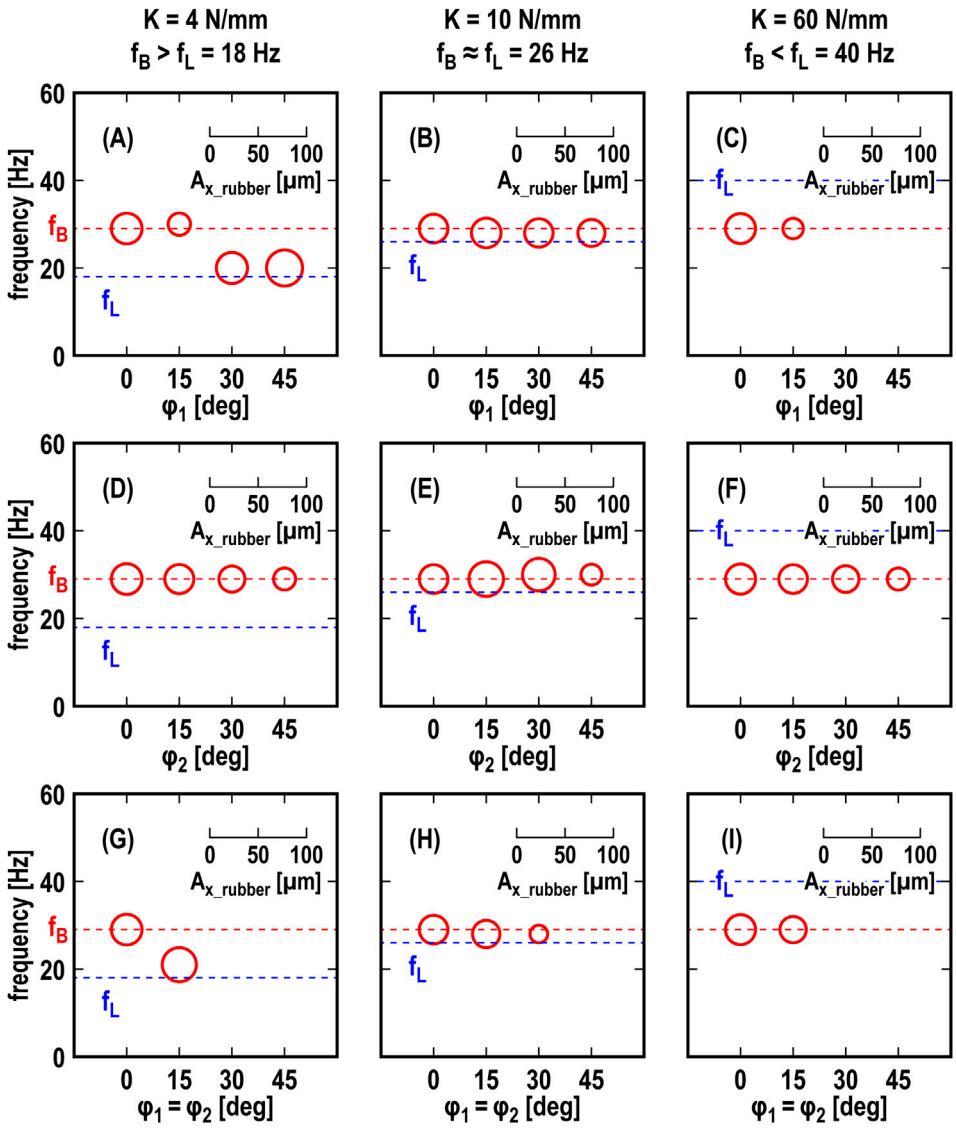


FIGURE 9
Effect of $\varphi_1$ and/or $\varphi_2$ on amplitude $A_{x\_rubber}$ and frequency $F$ of rubber blade tip V = 5 mm/s; top row **(A–C)**: effect of $\varphi_1$ ($\varphi_2$ = 0), middle row **(D–F)**: effect of $\varphi_2$ ($\varphi_1$ = 0), bottom row **(G–I)**: effect of $\varphi_1 = \varphi_2$; left column **(A,D,G)** : $K$ = 4 N/mm ($f_B$ = 29 Hz > $f_L$ = 18 Hz), center column **(B,E,H)**: $K$ = 10 N/mm ($f_B \approx f_L$ = 26 Hz), right column **(C,F,I)** : $K$ = 60 N/mm ($f_B < f_L$ = 40 Hz).

Figure 8 illustrates the comparison between the maximum speed of the rubber blade tip and the drive speed. The maximum speed of the rubber blade tip was calculated with $A_{x\_rubber} \cdot \omega$, where $\omega$ was obtained from $2\pi f_1$. The plot of $A_{x\_rubber} \cdot \omega$ at each $V$ was along the dashed line, which shows $A_{x\_rubber} \cdot \omega = V$. This result implies that the amplitude $A_{x\_rubber}$ of vibration was saturated when the maximum speed $A_{x\_rubber} \cdot \omega$ of the rubber blade tip reached the drive speed $V$.

## 3.4 Effect of yaw support angles and system stiffness on friction-induced vibration

Figure 9 illustrates the effect of the yaw support angles ($\varphi_1$ and/or $\varphi_2$) and stiffness $K$ of the loading system at $V$ = 5 mm/s on the amplitude and frequency of the rubber blade's vibration $x_{rubber}$, which were extracted with thresholds of $A_{x\_rubber}$ = 5 μm. The diameter of circles in Figure 9 represents the amplitude. Figures 9B, E, H show the effect of the yaw support angles ($\varphi_1$ and/or $\varphi_2$) at $K$ = 10 N/mm, where the value of $A_{x\_rubber}$ at $\varphi_1 = \varphi_2 = 0$ was extracted from that shown at $V$ = 5 mm/s in Figure 7. Increasing only $\varphi_1$ ($\varphi_2$ = 0) or $\varphi_2$ ($\varphi_1$ = 0) at $K$ = 10 N/mm as shown in Figures 9B, E, the values of $A_{x\_rubber}$ around 29 Hz did not significantly change. On the other hand, increasing the value of $\varphi_1 = \varphi_2$ at $K$ = 10 N/mm as shown in Figure 9H, the value of $A_{x\_rubber}$ decreased and at $\varphi_1 = \varphi_2$ = 45 deg was lower than the threshold of $A_{x\_rubber}$ = 5 μm. When the stiffness $K$ of the loading system was 4 N/mm, which made the situation $f_B > f_L$, the frequency of the vibration shifted from $f_B$ to around $f_L$ with increasing only $\varphi_1$ (Figure 9A) or both $\varphi_1$ and $\varphi_2$ (Figure 9G). When $K$ = 60 N/mm, which made the situation of $f_B < f_L$ in Figures 9C, F, I, the frequency of the vibration did not change with increasing $\varphi_1$ and/or $\varphi_2$. $A_{x\_rubber}$ decreased with increasing the value of only $\varphi_1$

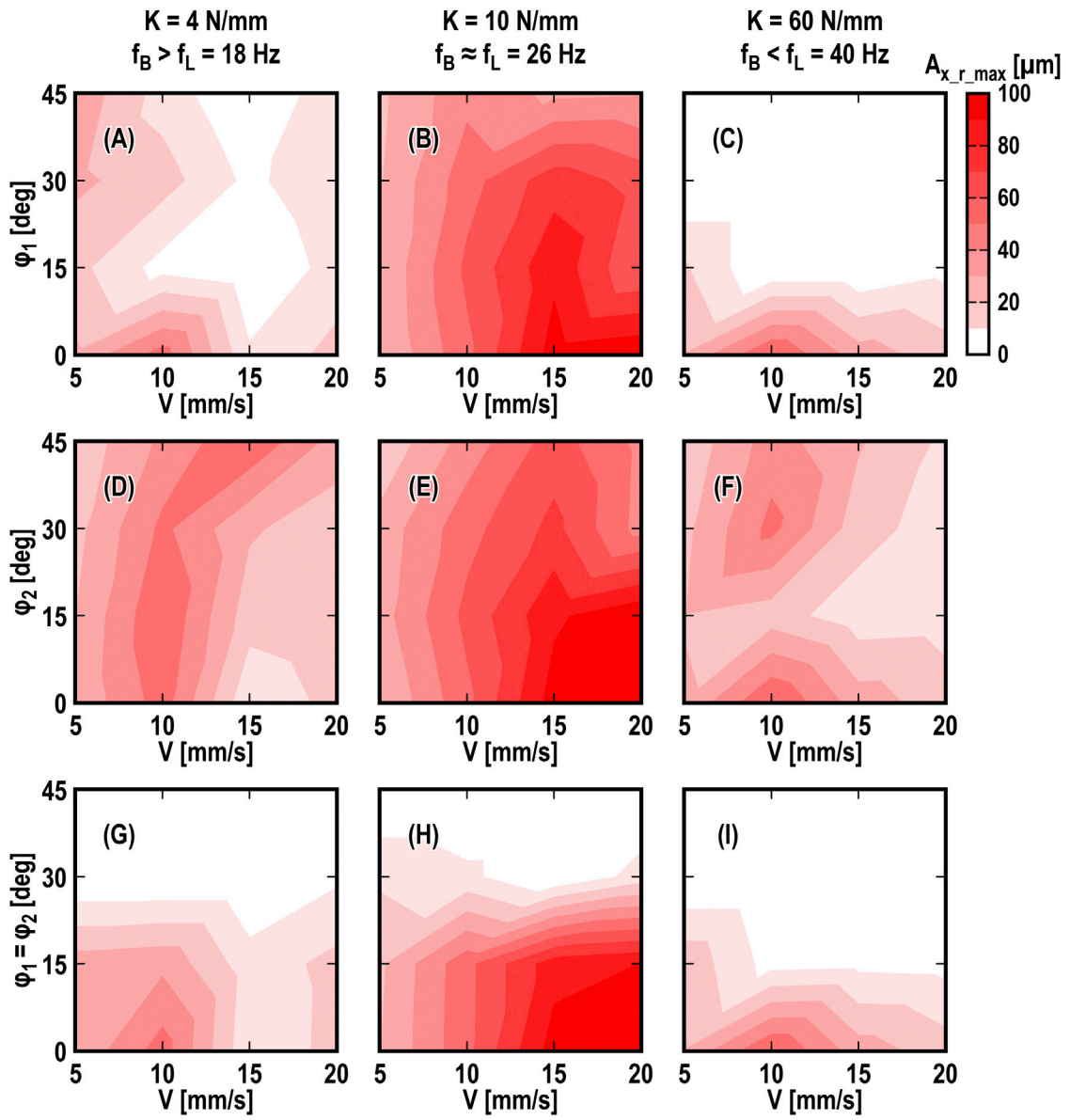


FIGURE 10
Effect of $\varphi_1$, $\varphi_2$, and $V$ on $A_{x\_r\_max}$; top row **(A–C)** : effect of $\varphi_1$ ($\varphi_2 = 0$), middle row **(D–F)** : effect of $\varphi_2$ ($\varphi_1 = 0$), bottom row **(G–I)**: effect of $\varphi_1 = \varphi_2$; left column **(A,D,G)** : $K$ = 4 N/mm ($f_B$ = 29 Hz > $f_L$ = 18 Hz), center column **(B,E,H)**: $K$ = 10 N/mm ($f_B \approx f_L$ = 26 Hz), right column **(C,F,I)**: $K$ = 60 N/mm ($f_B < f_L$ = 40 Hz).

(Figure 9C) or both $\varphi_1$ and $\varphi_2$ (Figure 9I), and disappeared at $\varphi_1 = \varphi_2 > 30$ deg.

Figure 10 illustrates the effect of the yaw support angles ($\varphi_1$ and/or $\varphi_2$), the stiffness $K$ of the loading system, and the drive speed $V$ on the maximum amplitude $A_{x\_r\_max}$ of the rubber blade's vibration $x_{rubber}$, which included the maximum amplitude at a different frequency as shown in Figures 9A, G. Increasing the value of $\varphi_1 = \varphi_2$ in Figures 10G–I, the value of $A_{x\_r\_max}$ decreased under any drive speed and stiffness conditions. When the stiffness of the loading system was relatively high ($K$ = 60 N/mm), the value of $A_{x\_r\_max}$ decreased with increasing only $\varphi_1$ ($\varphi_2 = 0$) in Figure 10C. These results suggest that the yaw support angles in a wiper system could work as the yaw angular misalignment effect (Kado et al., 2013; Nakano et al., 2013-01; Tadokoro et al., 2021), which provides a positive damping effect generated by rotating the friction force vector and suppress the friction-induced vibration. For an actual wiper system in which the wiping motion is in an arc, a parallel misalignment between the drive rotational axis and the driven torsional axis (Tadokoro et al., 2018) could be effective in adding the yaw angular misalignment effect.

## 3.5 Effect of drive speed and yaw support angles on water film thickness and friction coefficient

Figure 11 illustrates the effect of drive speed $V$ on the friction coefficient $\mu$ and average value $h_{min\_mean}$ of $h_{min}$. Black and red plots

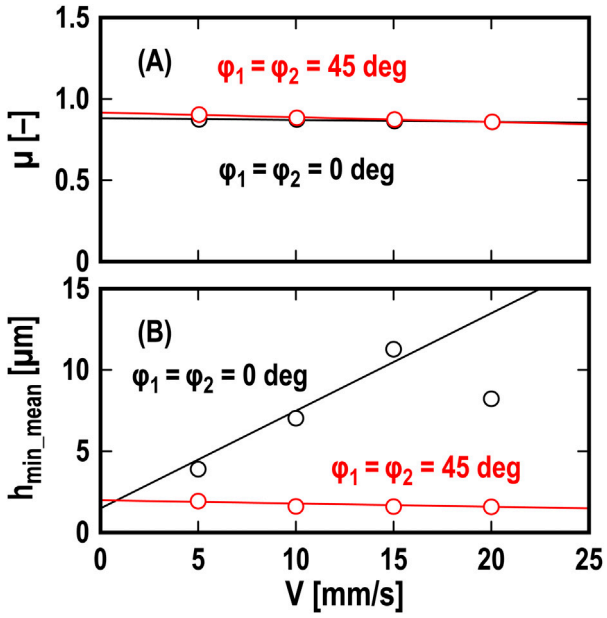


FIGURE 11
Effect of drive speed $V$ on **(A)** $\mu$ and **(B)** $h_{min\_mean}$; black plots: $\varphi_1 = \varphi_2 = 0$ deg and red plots: $\varphi_1 = \varphi_2 = 45$ deg.

represent the values at $\varphi_1 = \varphi_2 = 0$ and 45 deg, respectively. The friction coefficient in Figure 11A was calculated using the following Equation 1 (Kado et al., 2013):

$$\mu = \frac{kx_{base\_mean}}{W \cos \varphi_1} \quad (1)$$

where $x_{base\_mean}$ is the time-averaged value of $x_{base}$. The friction coefficient at $\varphi_1 = \varphi_2 = 0$ and 45 deg showed the velocity-weakening property, with black and red lines representing the fitting lines with the following Equation 2:

$$\mu = \alpha_\mu V + \beta_\mu \quad (2)$$

The black line corresponds to $\alpha_\mu = -0.001$ and $\beta_\mu = 0.88$ ($R^2$: 0.92), and the red line corresponds to $\alpha_\mu = -0.003$ and $\beta_\mu = 0.92$ ($R^2$: 0.99). The slope of the fitting lines at $\varphi_1 = \varphi_2 = 0$ deg was slightly lower than that at $\varphi_1 = \varphi_2 = 45$ deg. In Figure 11B, $h_{min\_mean}$ is the time-averaged value of $h_{min}$. At $\varphi_1 = \varphi_2 = 0$ deg, $h_{min\_mean}$ increased with increasing the drive speed $V$, where the fitting line was adjusted with the following Equation 3:

$$h_{min\_mean} = \alpha_h V + \beta_h \quad (3)$$

The black line corresponds to $\alpha_h = 0.6$ and $\beta_h = 1.5$ ($R^2$: 0.42). On the other hand, at $\varphi_1 = \varphi_2 = 45$ deg, $h_{min\_mean}$ slightly decreased with increasing $V$; the red line corresponds to $\alpha_h = -0.02$ and $\beta_h = 2.0$ ($R^2$: 0.58). These results show that the time-averaging value of $h_{min}$ did not significantly affect the change in the friction coefficient. Also, note that friction-induced vibration causes measurement errors in the friction coefficient (Kado et al., 2013). Therefore, to fully understand the details of the friction-induced vibration in the wiper system, further verifications through numerical approaches are also needed.

## 4 Conclusions

To examine the effects of the yaw support angles and support stiffness in the wiper system on the friction-induced vibration, concurrent measurements were conducted on the tangential displacement of the translational support base and the normal acceleration of the loading mechanism, as well as fluorescence observation to measure the water film thickness and the rubber blade tip position. The main conclusions derived from the results are summarized as follows:

(1) Friction-induced vibration appears as both in-plane vibration at the natural frequency $f_B$ of the base translationally supporting the wiper blade and out-of-plane vibration at $2 \times f_B$ of the wiper blade tip, which is attributed to fluctuations in the water film thickness.
(2) Higher drive speeds lead to increased vibration amplitude, particularly when the natural frequency $f_L$ of the loading mechanism is close to $f_B$.
(3) Friction-induced vibration is suppressed by applying large yaw angles to both the rubber blade and tangential support structure at any drive speed.
(4) At sufficiently high stiffness of the loading mechanism, suppressing friction-induced vibration requires only the addition of the yaw angle of the tangential support structure.

These findings provide valuable insights for improving wiper performances under practical operating conditions. However, further research is necessary to investigate the behavior of different wiper materials under varying environmental conditions, such as temperature, humidity, and wear over extended periods. Further studies should also incorporate numerical simulations and physical models to predict wiper behavior across diverse practical applications.

## Data availability statement

The original contributions presented in the study are included in the article/supplementary material, further inquiries can be directed to the corresponding author.

## Author contributions

CT: Conceptualization, Data curation, Formal Analysis, Funding acquisition, Investigation, Methodology, Project administration, Resources, Software, Supervision, Validation, Visualization, Writing–original draft, Writing–review and editing. HK: Data curation, Formal Analysis, Investigation, Methodology, Writing–original draft, Writing–review and editing. MS: Formal Analysis, Methodology, Validation, Writing–review and editing, Writing–original draft. TN: Conceptualization, Formal Analysis, Methodology, Resources, Supervision, Writing–review and editing, Writing–original draft. S-CV: Conceptualization, Methodology, Supervision, Visualization, Writing–review and editing, Writing–original draft. TR: Conceptualization, Methodology, Supervision, Writing–review and editing, Writing–original draft. KN: Conceptualization, Resources, Supervision, Writing–review and editing, Writing–original draft.

## Funding

The author(s) declare that financial support was received for the research, authorship, and/or publication of this article. This work was partially supported by JSPS KAKENHI Grant Number JP 22KK0236.

## Conflict of interest

The authors declare that the research was conducted in the absence of any commercial or financial relationships that could be construed as a potential conflict of interest.

The author(s) declared that they were an editorial board member of Frontiers, at the time of submission. This had no impact on the peer review process and the final decision.

## Publisher's note

All claims expressed in this article are solely those of the authors and do not necessarily represent those of their affiliated organizations, or those of the publisher, the editors and the reviewers. Any product that may be evaluated in this article, or claim that may be made by its manufacturer, is not guaranteed or endorsed by the publisher.

## References

Dalzin, F., Le Bot, A., Perret-Liaudet, J., and Mazuyer, D. (2016). Tribological origin of squeal noise in lubricated elastomer-glass contact. *J. Sound Vib.* 372, 211–222. doi:10.1016/j.jsv.2016.01.019

Deleau, F., Mazuyer, D., and Koenen, A. (2009). Sliding friction at elastomer/glass contact: influence of the wetting conditions and instability analysis. *Tribol. Int.* 42, 149–159. doi:10.1016/j.triboint.2008.04.012

Farfan-Cabrera, L. I. (2019). Tribology of electric vehicles: a review of critical components, current state and future improvement trends. *Tribol. Int.* 138, 473–486. doi:10.1016/j.triboint.2019.06.029

Fowell, M. T., Myant, C., Spikes, H. A., and Kadiric, A. (2014). A study of lubricant film thickness in compliant contacts of elastomeric seal materials using a laser induced fluorescence technique. *Tribol. Int.* 80, 76–89. doi:10.1016/j.triboint.2014.05.028

Goto, S., Takahashi, H., and Oya, T. (2001). Clarification of the mechanism of wiper blade rubber squeal noise generation. *JSAE Rev.* 22, 57–62. doi:10.1016/s0389-4304(00)00095-3

Kado, N., Tadokoro, C., and Nakano, K. (2013). Measurement error of kinetic friction coefficient generated by frictional vibration. *Trans. Jpn. Soc. Mech. Eng. Ser. C* 79, 2635–2643. doi:10.1299/kikaic.79.2635

Kitayama, T., Kawasumi, M., Yamasaki, H., Nakano, T., Yamamoto, S., Yamada, M., et al. (2012). Method for evaluating performance of wipers based on visibility. *IEICE Trans. Electron.* 95, 1716–1723. doi:10.1587/transele.e95.c.1716

Lancioni, G., Lenci, S., and Galvanetto, U. (2016). Dynamics of windscreen wiper blades: squeal noise, reversal noise and chattering. *J. Non-Linear Mech.* 80, 132–143. doi:10.1016/j.ijnonlinmec.2015.10.003

Le Rouzic, J., Le Bot, A., Perret-Liaudet, J., Guibert, M., Rusanov, A., Douminge, L., et al. (2013). Friction-induced vibration by stribeck's law: application to wiper blade squeal noise. *Tribol. Lett.* 49, 563–572. doi:10.1007/s11249-012-0100-z

Li, Y., and Xu, J. (2023). Dynamic characteristics and generation mechanism of windscreen frameless wiper blade oscillations. *Nonlinear Dyn.* 111, 3053–3079. doi:10.1007/s11071-022-08030-0

Min, D., Jeong, S., Yoo, H. H., Kang, H., and Park, J. (2014). Experimental investigation of vehicle wiper blade's squeal noise generation due to windscreen waviness. *Tribol. Int.* 80, 191–197. doi:10.1016/j.triboint.2014.06.024

Nakano, K., Tadokoro, C., and Kado, N. (2013-01-2069), (2013). Yawing angular misalignment provides positive damping to suppress frictional vibration: basic applicability to disc brake systems. *SAE Int. J. Passeng. Cars-Mechanical Syst.* 6, 1493–1498. doi:10.4271/2013-01-2069

Reddyhoff, T., Dobre, O., Le Rouzic, J., Gotzen, N. A., Parton, H., and Dini, D. (2015). Friction induced vibration in windscreen wiper contacts. *J. Vib. Acoust.* 137, 041009. doi:10.1115/1.4029987

Suzuki, R., and Yasuda, K. (1998). Analysis of chatter vibration in an automotive wiper assembly. *JSME Int. J. Ser. C Mech. Syst. Mach. Elem. Manuf.* 41, 616–620. doi:10.1299/jsmec.41.616

Tadokoro, C., Aso, Y., Nagamine, T., and Nakano, K. (2021). Anti-vibration and traction control of rotary sliding systems by orthogonal rotation providing transverse sliding. *Tribol. Int.* 159, 106992. doi:10.1016/j.triboint.2021.106992

Tadokoro, C., Nagamine, T., and Nakano, K. (2018). Stabilizing effect arising from parallel misalignment in circular sliding contact. *Tribol. Int.* 120, 16–22. doi:10.1016/j.triboint.2017.12.003

Unno, M., Shibata, A., Yabuno, H., Yanagisawa, D., and Nakano, T. (2017). Analysis of the behavior of a wiper blade around the reversal in consideration of dynamic and static friction. *J. Sound Vib.* 393, 76–91. doi:10.1016/j.jsv.2017.01.018

Vlădescu, S. C., Putignano, C., Marx, N., Keppens, T., Reddyhoff, T., and Dini, D. (2019). The percolation of liquid through a compliant seal– an experimental and theoretical study. *J. Fluids Eng.* 141, 031101. doi:10.1115/1.4041120

Wang, Y. S., Guo, H., Yuan, T., Ma, L. F., Liu, N. N., and Sun, P. (2023). Friction-induced noise of vehicle wiper-windshield system: a review. *Results Eng.* 20, 101557. doi:10.1016/j.rineng.2023.101557

frontiers | Frontiers in Mechanical Engineering

TYPE Original Research
PUBLISHED 27 November 2024
DOI 10.3389/fmech.2024.1504347

Check for updates

OPEN ACCESS

EDITED BY
Andras Vernes,
Vienna University of Technology, Austria

REVIEWED BY
Michał Stosiak,
Wroclaw University of Science and Technology, Poland
Milan Bukvic,
University of Kragujevac, Serbia

*CORRESPONDENCE
Shunsuke Iwase,
iwase-sh@nsk.com

RECEIVED 30 September 2024
ACCEPTED 07 November 2024
PUBLISHED 27 November 2024

CITATION
Iwase S, Maruyama T, Momozono S, Maegawa S and Itoigawa F (2024) Studies on dielectric spectroscopy of oxidatively degraded Poly(α-olefin).
*Front. Mech. Eng.* 10:1504347.
doi: 10.3389/fmech.2024.1504347

COPYRIGHT
© 2024 Iwase, Maruyama, Momozono, Maegawa and Itoigawa. This is an open-access article distributed under the terms of the Creative Commons Attribution License (CC BY). The use, distribution or reproduction in other forums is permitted, provided the original author(s) and the copyright owner(s) are credited and that the original publication in this journal is cited, in accordance with accepted academic practice. No use, distribution or reproduction is permitted which does not comply with these terms.

# Studies on dielectric spectroscopy of oxidatively degraded Poly(α-olefin)

Shunsuke Iwase[1,2,3]*, Taisuke Maruyama[1,2], Satoshi Momozono[1,2], Satoru Maegawa[3] and Fumihiro Itoigawa[3]

[1]Core Technology R&D Center, NSK Ltd., Fujisawa, Japan, [2]NSK Tribology Collaborative Research Cluster, Tokyo Institute of Technology, Yokohama, Japan, [3]Nagoya Institute of Technology, Nagoya, Japan

Failures in tribological components such as bearings can significantly affect the performance and lifespan of machinery, necessitating the implementation of effective condition monitoring technologies. This study verified the feasibility of dielectric spectroscopy (DES) as a method for detecting abnormalities before damage occurs. A comparative evaluation was conducted between dielectric relaxation parameters and measurements from size exclusion chromatography, total acid number, and viscosity for oxidatively degraded poly (α-olefin) oils. The results confirmed that DES is an effective method for assessing the oxidative degradation state of lubricants. These findings suggest that DES could be applied to oil film condition monitoring and predictive maintenance.

KEYWORDS

**dielectric spectroscopy, lubricants, oil, degradation, electrical impedance method, condition monitoring, oil diagnosis**

## 1 Introduction

Failures in tribological components such as bearings have a significant impact on the overall performance and lifespan of machinery, necessitating the implementation of appropriate condition monitoring technologies. Traditionally, abnormal vibration sensing has been widely employed to monitor the condition of bearings (Kiral and Karagülle, 2003; Al-Badour et al., 2011; Zarei et al., 2014; Cambow et al., 2018). However, abnormal vibrations typically manifest as a result of damage caused by lubrication failure at the sliding surfaces, and by the time such vibrations are detected, component replacement is often required. In contrast, monitoring the condition of the lubricating oil film offers the potential to detect abnormalities before surface damage occurs. If this method is established, it could allow for methods other than part replacement, such as lubricant replacement, leading to significant reductions in maintenance costs. Additionally, it could serve as a means to identify the specific causes of failure within components, such as incorrect lubricant selection or improper design and installation methods. While optical techniques, such as optical interferometry (Johnston et al., 1991; Kaneta et al., 1993; Sugimura et al., 1998; Maruyama and Saitoh, 2010), are commonly used for monitoring oil films, they cannot be applied to metal components. Therefore, electrical methods have gained attention as potential oil film monitoring techniques for metal-to-metal sliding surfaces.

The capacitance method calculates oil film thickness from the film capacitance and can be applied to thin oil films, ranging from tens to hundreds of nanometers, formed under EHL (elastohydrodynamic lubrication) conditions (Crook, 1961; Prashad, 1988; Jablonka

et al., 2012). Moreover, the impedance method, which builds upon the capacitance technique, allows for high-precision oil film thickness measurement and simultaneously provides information on metal contact (Nakano and Akiyama, 2006; Manabe and Nakano, 2008; Nihira et al., 2015; Schnabel et al., 2016; Maruyama and Nakano, 2018). Consequently, this method has been actively studied in recent years as a predictive maintenance (PdM) technique for rolling bearings (Becker-Dombrowsky and Kirchner, 2024; Maruyama and Nakano, 2018; Maruyama et al., 2024).

Thus, monitoring oil film thickness using electrical methods is considered a promising advanced condition monitoring technology for bearings, but it does not predict lubrication failure leading to metal contact. Generally, lubrication failure is caused by factors such as a decrease in lubricant quantity due to leakage or evaporation, as well as changes in lubricant properties caused by oxidation degradation or contamination. In particular, when lubricant oxidation progresses, it is expected that while the oil film may temporarily thicken due to the increased viscosity of the lubricant based on the Hamrock and Dowson theory (Hamrock and Dowson, 1977), it may simultaneously undergo viscosity reduction due to a rise in temperature caused by increased shear resistance. In other words, monitoring only oil film thickness may not allow for the prediction of damage due to lubrication failure until just before it occurs. If changes in the chemical properties of the lubricant, such as viscosity or acid number, can be monitored, it may become possible to predict the time remaining until lubrication failure during the steady state, when changes in oil film thickness are minimal, thus enabling the realization of PdM for bearings. This means that condition-based maintenance can be implemented, rather than the conventional time-based maintenance. For bearings equipped with oil circulation systems, sensors capable of monitoring lubricant degradation can be installed within the circulation mechanism, making it possible to apply previously reported diagnostic techniques (Patocka et al., 2020). However, particularly in the case of rolling bearings, the lubricant is often sealed, leaving no space to insert a sensor. Therefore, direct sensing in the oil film area is more desirable.

Although there are currently no reported methods for monitoring the chemical property changes of lubricants in oil films formed between metal sliding surfaces, it is possible that existing electrical measurement techniques for bulk lubricants between parallel electrodes could be adapted. Dielectric spectroscopy (DES), which observes the AC frequency response of the complex permittivity, provides direct information on molecular dynamics, making it a promising measurement technique for monitoring chemical property changes, such as lubricant degradation. Guan et al. reported that the total acid number (TAN) and sludge content could be predicted by analyzing DES measurement data (Guan et al., 2011). Additionally, Gong et al. stated that the quantification of nitrogen compounds and sulfur oxides generated in the oil could be achieved by analyzing the temperature dependence of the complex permittivity obtained from two-dimensional DES measurements (Gong et al., 2016; Gong et al., 2017).

However, DES measurements of lubricants reported so far have mainly focused on degradation state prediction based on statistical analysis, and a systematic theoretical framework regarding the underlying physical mechanisms has not yet been sufficiently established. Thus, the challenges associated with applying DES to oil film monitoring remain unclear.

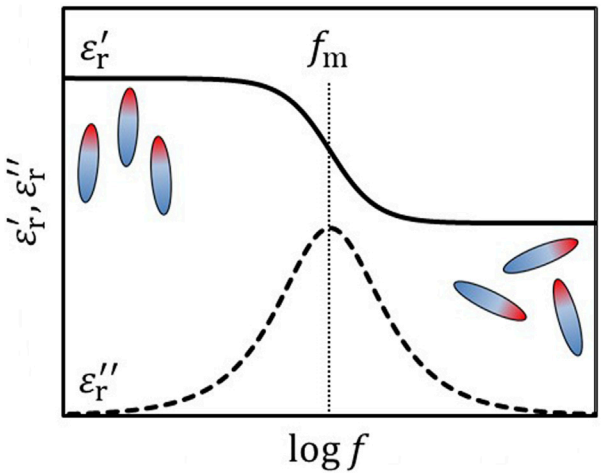


FIGURE 1
Conceptual diagram of DES measurement.

Therefore, in this study, we aim to utilize DES measurements of oil films for the PdM of bearings and consider the information obtained from DES measurements of lubricants under static conditions from the perspective of dielectric relaxation theory. Specifically, we conduct DES measurements of degraded oils using parallel plate capacitors and discuss the relationships between the dielectric properties obtained and the concentration of degradation products, molecular weight, kinematic viscosity, and TAN obtained from various chemical analyses. Additionally, we will discuss the potential for applying oil film DES measurements to PdM and the challenges involved. The insights gained from this report on the dielectric relaxation properties of oils associated with lubricant degradation will contribute to advancements in lubricant degradation monitoring technology for tribological components, further supporting the realization of PdM.

## 2 Experimental details

In this section, we explain the principles and techniques of dielectric spectroscopy. We also explore various models used to describe the relaxation phenomena observed in the frequency characteristics of complex permittivity obtained through measurement, and provide a detailed explanation of the fitting methods applied to these models.

### 2.1 DES and dielectric relaxation

Except for purely non-polar oils, most lubricants contain polar molecules within their components. Examples of such components include ester-based oils, grease thickeners, certain additives, and oxidative degradation products of lubricants. The complex permittivity $\varepsilon^*$ [F/m] of materials that contain internal polar

10.3389/fmech.2024.1504347

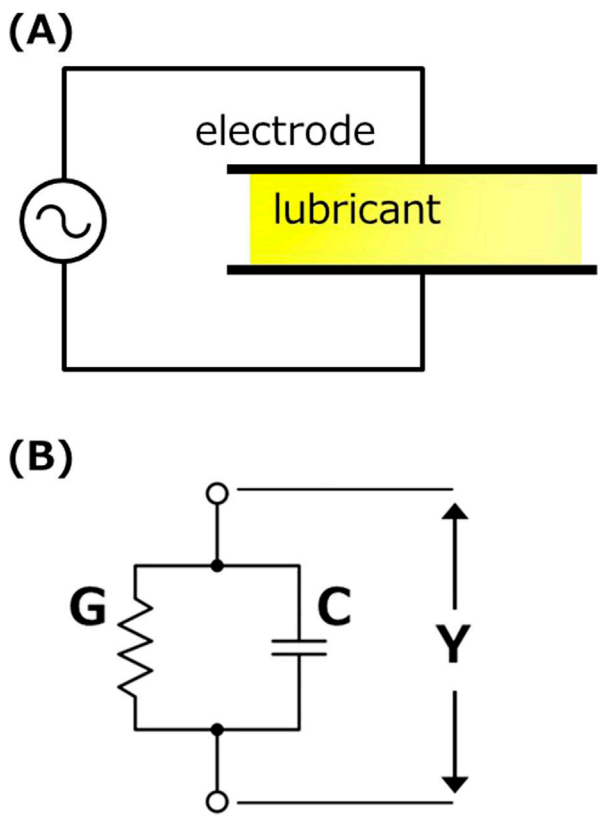


FIGURE 2
DES measurement method for lubricants, **(A)** Schematic diagram, **(B)** Equivalent circuit.

molecules, i.e., permanent dipoles, is expressed by the following equation. For the derivation of this equation, please refer to the relevant literature (Böttcher and Bordewijk, 1980).

$$\frac{\varepsilon^*}{\varepsilon_0} = \varepsilon_r^* = \varepsilon_r' - j\varepsilon_r'' \tag{1}$$

Here, $\varepsilon_r^*$ [-] represents the complex relative permittivity. The real part, $\varepsilon_r'$ [-], is referred to as the storage permittivity, or simply the relative permittivity. The imaginary part, $\varepsilon_r''$ [-], is commonly known as the dielectric loss factor.

Dielectric relaxation refers to the phenomenon where polarization of a dielectric material lags behind the applied alternating electric field. Dielectric relaxation appears as the frequency characteristics of complex permittivity in DES measurements. An example of DES measurements is shown in Figure 1.

In the low-frequency region, the permanent dipoles align with the external electric field, resulting in a high $\varepsilon_r'$ value. As the frequency increases, the permanent dipoles gradually fail to follow the polarity reversals of the external electric field, and at sufficiently high frequencies, $\varepsilon_r'$ asymptotically approaches a low value. $\varepsilon_r''$ reaches its maximum value at the relaxation frequency $f_m$, which corresponds to the inflection point of $\varepsilon_r'$. The relaxation time τ is expressed as $\tau = 1/2\pi f_m$ and represents the time required for the dipoles to reorient.

The equivalent circuit for dielectric spectroscopy measurements of lubricants using parallel plate electrodes is shown in Figure 2.

Since lubricants may exhibit conductivity due to additives or oxidation degradation products, they should be considered as a parallel circuit of a capacitor and a resistor. The complex admittance $Y$ [S] of the dielectric material inserted between the electrodes is generally expressed using conductance $G$ [S] and capacitance $C$ [F] by the following equation.

$$Y = G + j\omega C \tag{2}$$

Here, $\omega$ [rad/s] represents the angular frequency, and using the alternating current frequency $f$ [Hz], $\omega$ is expressed as $\omega = 2\pi f$. Furthermore, Equation 2 can be expressed in terms of the electrode area $S$ [$m^2$] and the distance between the electrodes $d$ [m] as follows.

$$Y = \left(\sigma_0 + \omega\left(\varepsilon_a'' + j\varepsilon'\right)\right)\frac{S}{d} \tag{3}$$

Here, $\sigma_0$ [S/m] represents the DC conductivity, and $\varepsilon_a''$ [F/m] denotes the absorptive dielectric loss caused by relaxation. Additionally, the complex admittance $Y$ can also be expressed using the complex impedance $Z$ [Ω], which is obtained through measurements, as follows.

$$Y = \frac{1}{Z} = \frac{\cos\theta}{|Z|} - j\frac{\sin\theta}{|Z|} \tag{4}$$

Here, $|Z|$ [Ω] represents the magnitude of the impedance of the measured object, and $\theta$ [deg] denotes the phase difference between the applied voltage and the response current. By comparing the real and imaginary parts of Equations 3, 4, Equations 5, 6 can be derived.

$$\varepsilon_r' = -\frac{d\sin\theta}{S\omega|Z|\varepsilon_0} \tag{5}$$

$$\frac{\sigma_0}{\omega\varepsilon_0} + \frac{\varepsilon_a''}{\varepsilon_0} = \varepsilon_r'' = \frac{d\cos\theta}{S\omega|Z|\varepsilon_0} \tag{6}$$

The first term on the left-hand side of Equation 6 represents the conductive dielectric loss due to the conductive component. The equation including the conductive dielectric loss term is also described in the review by Woodward et al.; for further details, please refer to that source (Woodward, 2021).

## 2.2 Curve fitting

In this report, the Cole-Cole relaxation model was adopted to describe the relaxation phenomena. The Cole-Cole relaxation equation is a semi-empirical extension of the theoretical Debye relaxation equation and is commonly used in the analysis of dielectric relaxation (Kremer and Schönhals, 2003). However, the Cole-Cole model addresses only absorptive losses and does not take conductive losses into account. Specifically, it does not include the contribution of the first term on the left-hand side of Equation 6. As mentioned earlier, the conductivity of lubricants, which emerges due to oxidative degradation, can serve as an important indicator for estimating lubricant degradation. Therefore, in this study, the Cole-Cole relaxation

TABLE 1 Test oil properties.

| Oil | Sample ID | Heating time [hour] | TAN [KOH mg/g] | Kinematic viscosity [mm²/s] | | |
|---|---|---|---|---|---|---|
| | | | | At 40°C | At 70°C | At 100°C |
| Low viscosity PAO | L0 | 0[a] | –[b] | 30 | 11 | 6 |
| | L1 | 139 | 4.0 | 51 | 17 | 8 |
| | L2 | 333 | 6.9 | 98 | 28 | 12 |
| | L3 | 446[c] | 12.1 | –[b] | 106 | 35 |
| High viscosity PAO | H0 | 0[a] | –[b] | 124 | 43 | 20 |
| | H1 | 139 | 3.1 | 180 | 57 | 24 |
| | H2 | 333 | 4.6 | 352 | 90 | 35 |
| | H3 | 446[c] | 8.8 | –[b] | 375 | 117 |

[a]New oil was used.
[b]No data available as the value fell below the measurement limit.
[c]To accelerate degradation, the sample amount in the beaker was reduced by half before heating.

model was directly applied to fit $\varepsilon_r'$ (Equation 7), while for fitting $\varepsilon_r''$, a modified version of the Cole-Cole equation with an added term for conductive losses was used (Equation 8).

$$\varepsilon_r{}' = \varepsilon_{r\infty} + \frac{\Delta\varepsilon}{2}\left(1 - \frac{\sinh\beta x}{\cosh\beta x + \cos(\beta\pi/2)}\right) \tag{7}$$

$$\varepsilon_r{}'' = \frac{\sigma_0}{\omega\varepsilon_0} + \frac{\Delta\varepsilon}{2}\frac{\sin(\beta\pi/2)}{\cosh\beta x + \cos(\beta\pi/2)} \tag{8}$$

where $x = \ln 2\pi f\tau$. Here, $\varepsilon_{r\infty}$, $\Delta\varepsilon$, $\tau$, $\beta$ and $\sigma_0$ are fitting parameters, which are explained in detail in Section 4.1. By using these equations, the behavior of dielectric relaxation and the changes in conductivity can be simultaneously evaluated.

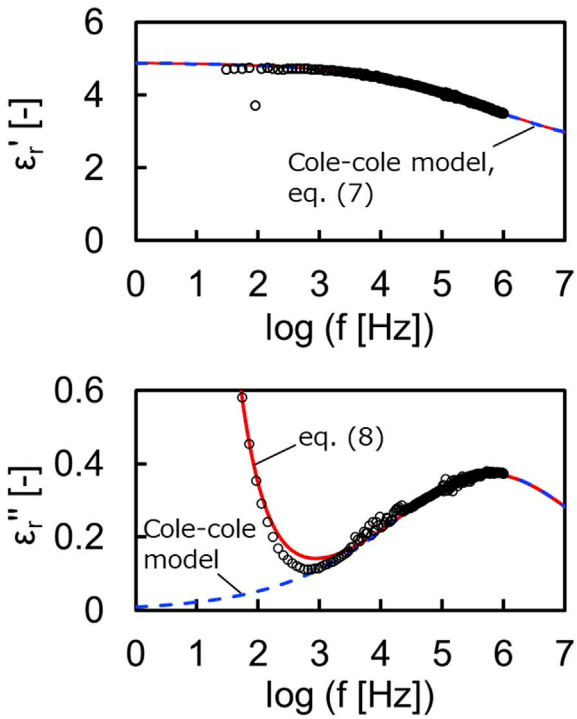


FIGURE 3
Curve fitting results of $\varepsilon_r'$ and $\varepsilon_r''$; The black circle plot shows the dielectric spectroscopy measurements of L3. The red solid line represents the fitting results using Equations 6, 7. The blue dashed line represents the fitting results using the Cole-Cole relaxation model.

# 3 Experimental method

## 3.1 Materials

In this experiment, two types of PAO (Poly (α-olefin)) with different viscosities were used. Each sample was placed in a glass beaker and subjected to thermal degradation by heating in an oven at 160°C. The heating duration and kinematic viscosity of each sample are presented in Table 1. Additionally, the values of TAN, which is commonly used as an indicator of oxidative degradation, are also provided.

## 3.2 Apparatus

The electrodes used in this study were Keysight 16452A. The electrode material was nickel-plated kovar (Fe: 54%, Co.: 17%, Ni: 29%), with an electrode gap of 0.3 mm and an electrode diameter of 38 mm. Complex impedance was measured using the HIOKI IM3536 impedance analyzer. For kinematic viscosity measurements, the Omnitek S-flow 1,200 capillary viscometer was used, following ASTM D445. The total acid number (TAN) was measured according to ASTM D 664, with automatic titration performed using the HIRANUMA COMTITE-550. SEC (size exclusion chromatography) measurements were carried out using the Nexera™ GPC System by Shimadzu, with a Shodex 803L column. Tetrahydrofuran was used as the measurement solvent. A refractive index detector was employed, and the molecular weights were calculated using polyethylene standards for calibration.

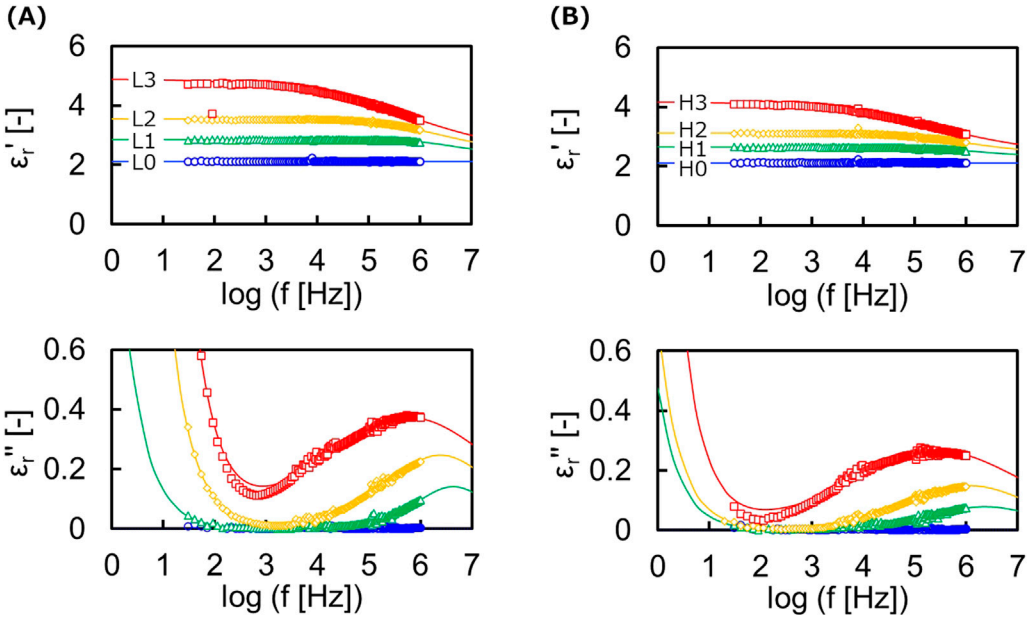


FIGURE 4
The $\varepsilon_r'$ and $\varepsilon_r''$ obtaind from DES measurement; **(A)** Low viscosity PAO: blue circle plot, green triangle plot, yellow diamond plot, and red square plot represent the measurements of L0, L1, L2, and L3, respectively. **(B)** High viscosity PAO: blue circle plot, green triangle plot, yellow diamond plot, and red square plot represent the measurements of H0, H1, H2, and H3, respectively. The solid lines in the figures represent curve fittings based on Equations 7, 8.

## 3.3 Measurement procedure for DES

The complex impedance was obtained using the apparatus described in Section 3.2 and measured by the four-terminal pair method. The applied voltage was set to 1 V, and the AC frequency was swept from 30 Hz to 1 MHz. The cell temperature during measurement was monitored with a thermocouple and maintained at 20°C for all experiments. Moreover, preliminary evaluations confirmed that the variation in complex impedance measurements is negligibly small, with minimal impact on the results. Consequently, all data presented in this paper were derived from a single measurement.

# 4 Results

## 4.1 DES measurements

From the values of TAN and kinematic viscosity shown in Table 1, it can be seen that the degree of oxidative degradation of the prepared samples increased in the order of L0 < L1 < L2 < L3 for the low viscosity oil, and H0 < H1 < H2 < H3 for the high viscosity oil.

Figure 3 shows an example of DES measurements (sample L3) and the results of curve fitting.

When using the Cole-Cole relaxation model, a significant deviation in $\varepsilon_r''$ was observed in the low-frequency region. However, by using Equation 8, a good fit was obtained for $\varepsilon_r''$ across the entire frequency range. This allowed for the quantification of the relaxation parameters $\varepsilon_{r\infty}$ [-], $\Delta\varepsilon$ [-], $\tau$ [s], $\beta$ [-], and $\sigma_0$ [S/m]. Here, $\varepsilon_{r\infty}$ represents the permittivity at the high-frequency limit, and $\Delta\varepsilon$ corresponds to the relaxation strength (the difference between the static permittivity and $\varepsilon_{r\infty}$, i.e., the peak height). $\tau$ is the relaxation time, which, as mentioned earlier, depends on the frequency at the peak of $\varepsilon_r''$. $\beta$ represents the distribution of relaxation times and takes a value between 0 and 1; the closer $\beta$ is to 0, the broader the relaxation peak. $\sigma_0$ is the DC conductivity, and the larger the value, the greater the increase in $\varepsilon_r''$ in the low-frequency region.

TABLE 2 Relaxation parameters of degraded PAO obtained from curve fitting.

| | L1 | L2 | L3 | H1 | H2 | H3 |
|---|---|---|---|---|---|---|
| $\varepsilon_{r\infty}$ [−] | 2.40 | 2.48 | 2.36 | 2.30 | 2.40 | 2.36 |
| $\Delta\varepsilon$ [−] | 0.44 | 1.08 | 2.54 | 0.35 | 0.72 | 1.82 |
| $\tau$ [μs] | 0.037 | 0.066 | 0.27 | 0.069 | 0.13 | 0.52 |
| $\beta$ [−] | 0.73 | 0.55 | 0.36 | 0.55 | 0.50 | 0.36 |
| $\sigma_0$ [nS/m] | 0.07 | 0.52 | 1.3 | 0.02 | 0.04 | 0.11 |

Figure 4A shows the DES measurement results for low viscosity PAO, and Figure 4B shows those for high viscosity PAO. In the undegraded state (L0, H0), $\varepsilon_r'$ remained constant across all frequencies, and $\varepsilon_r''$ was 0 across the entire frequency range. In the oxidatively degraded samples (L1, L2, L3, H1, H2, H3), dielectric relaxation was observed. In addition, high-precision curve fitting was applied to all samples. The relaxation parameters obtained from the fitting are shown in Table 2. As degradation progressed, $\Delta\varepsilon$, $\tau$, and $\sigma_0$ increased, while $\beta$ decreased.

## 4.2 SEC analysis

SEC measurements were conducted to obtain information on the molecular weight and concentration of components generated

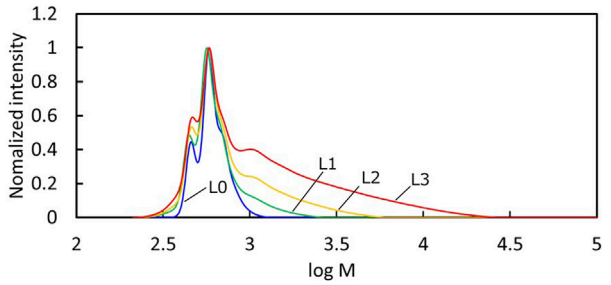


FIGURE 5
SEC results of low viscosity PAO; blue, green, yellow, and red line represent the measurements of L0, L1, L2, and L3, respectively.

TABLE 3 Parameters of degraded components obtained from SEC.

| | L1 | L2 | L3 | H1 | H2 | H3 |
|---|---|---|---|---|---|---|
| $C_d$ [g/mL] | 0.27 | 0.42 | 0.64 | 0.19 | 0.35 | 0.55 |
| $M_w$ [–] | 810 | 1,300 | 2,600 | 2,210 | 4,710 | 11,210 |
| PDI [–] | 1.3 | 1.5 | 2.2 | 2.3 | 3.4 | 6.2 |

by degradation. The results of the SEC measurements for low viscosity PAO are shown in Figure 5. The intensity shown on the vertical axis in Figure 5 was normalized using the peak derived from the fresh component detected around log M = 2.8. Compared to the undegraded sample (L0), an increase in high molecular weight components was observed as degradation progressed. The calculated values of the mass concentration of degraded components, $C_d$ [g/mL], weight-average molecular weight, $M_w$ [-], and polydispersity index, PDI [-], are presented in Table 3. The methods used for $C_d$, $M_w$, and PDI are described in the Supplementary Information.

## 5 Discussion

DES measurements were conducted on oxidatively degraded PAO. As the oxidative degradation progressed, changes were observed in the relaxation strength, $\Delta\varepsilon$, relaxation time, $\tau$, relaxation time distribution parameter, $\beta$, and DC conductivity, $\sigma_0$. In the following sections, the changes in each of these relaxation parameters are discussed using the results from SEC, TAN, and viscosity measurements.

### 5.1 Relationship between $\Delta\varepsilon$ and $C_d$

$\Delta\varepsilon$ is generally known to be proportional to the number of dipoles per unit volume (Kremer and Schönhals, 2003), as shown in Equation 9.

$$\Delta\varepsilon = \frac{1}{3\varepsilon_0}\frac{\mu^2}{k_B T}\frac{N}{V} \tag{9}$$

Here, $k_B, T, \mu, N$ and $V$ represent the Boltzmann constant, absolute temperature, magnitude of dipole moment, number of dipoles, and volume, respectively. Figure 6 illustrates the relationship between $\Delta\varepsilon$ and the mass concentration of degradation products, $C_d$.

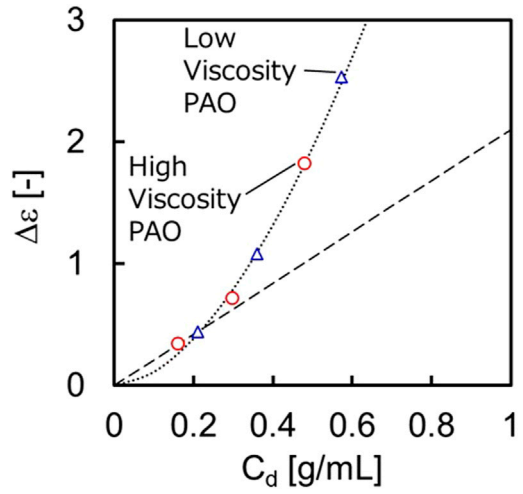


FIGURE 6
Relationship between $\Delta\varepsilon$ and $C_d$; Red circles represent samples H1, H2, and H3, while blue triangles represent samples L1, L2, and L3.

For the two points in the region where $C_d$ is small (H1, L1), a proportional relationship between $\Delta\varepsilon$ and $C_d$ was observed. However, in the region where $C_d$ is large, $\Delta\varepsilon$ exhibited a regular change, approximately following the square of $C_d$. According to studies by Onsager and Kirkwood, it has been reported that when the dipole concentration in a system is high, interactions between the relaxation species become prominent, leading to an increase in $\Delta\varepsilon$ (Böttcher and Bordewijk, 1973). Although the detailed mechanism remains open to further discussion, it has been demonstrated that, at least for PAO-based oils, the concentration of degradation products can be calculated as a simple power function using $\Delta\varepsilon$ obtained from DES measurements, regardless of the initial oil viscosity.

### 5.2 Relationship between $\tau$ and $\eta$

According to Debye's theory (Debye, 1929), $\tau$ is expressed by the following equation.

$$\tau = \frac{4\pi R^3}{k_B T}\eta \tag{10}$$

Here, $R$ represents the effective radius of the dipole. While $\eta$ generally refers to the solvent viscosity, Iwamoto et al. reported that when the solute concentration is high, the interactions between solute molecules become stronger, and it is preferable to use the solution viscosity (Iwamoto and Kumagai, 1998). Therefore, the relationship between the relaxation time $\tau$ obtained from DES and the solution viscosity $\eta$ of each sample was evaluated. $\eta$ was calculated by converting the kinematic viscosity at each temperature (Table 1) to the viscosity at 20°C using Walther's equation, and then multiplying by the measured density (see

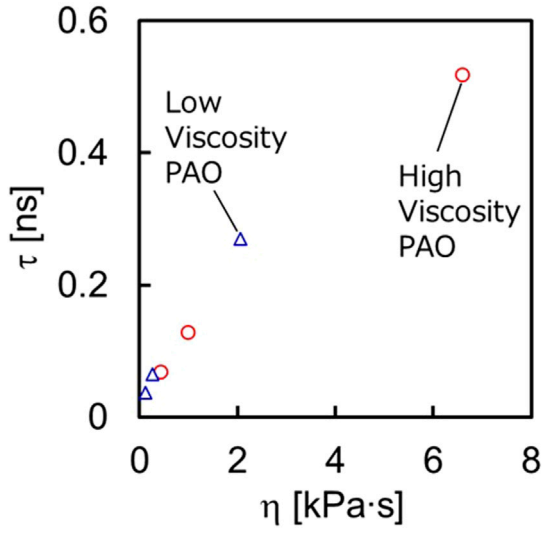


FIGURE 7
Relationship between τ and η; Red circles represent samples H1, H2, and H3, while blue triangles represent samples L1, L2, and L3.

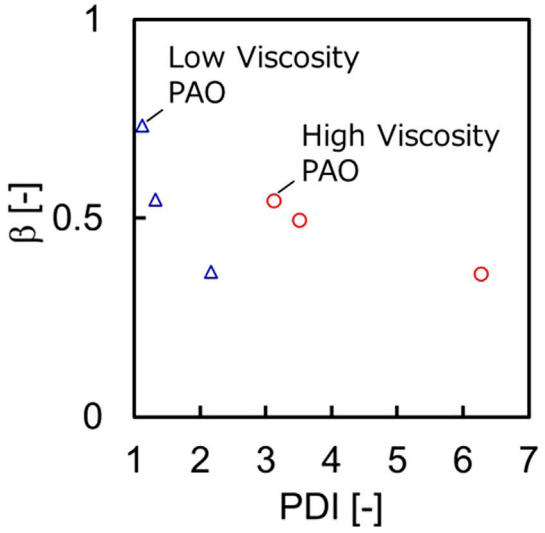


FIGURE 9
Relationship between $\beta$ and PDI; Red circles represent samples H1, H2, and H3, while blue triangles represent samples L1, L2, and L3.

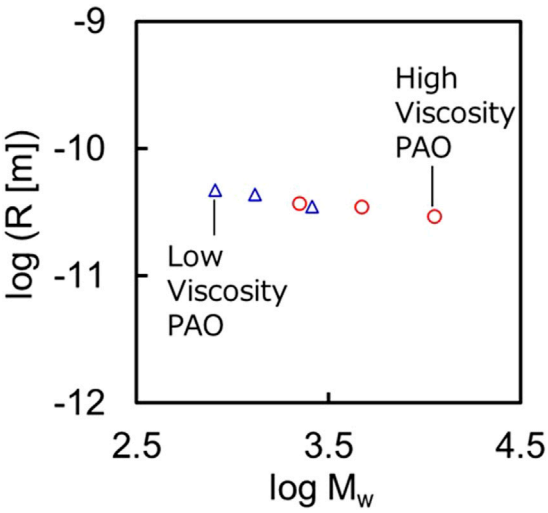


FIGURE 8
Relationship between R and $M_w$; Red circles represent samples H1, H2, and H3, while blue triangles represent samples L1, L2, and L3.

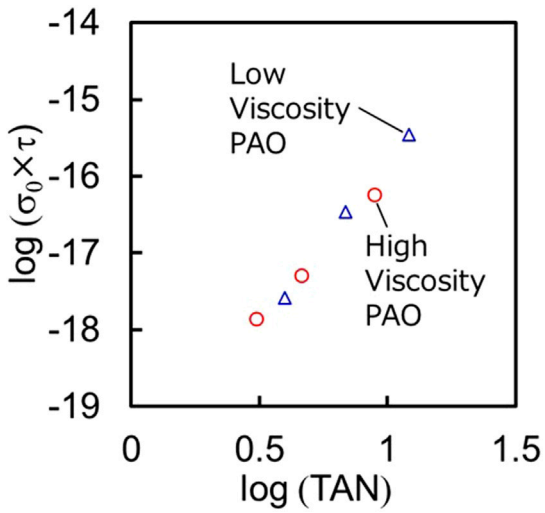


FIGURE 10
Relationship between $\sigma_0\tau$ and TAN; Red circles represent samples H1, H2, and H3, while blue triangles represent samples L1, L2, and L3.

Supplementary Table S1). As shown in Figure 7, $\tau$ generally increased proportionally to $\eta$, regardless of the initial viscosity of the sample. This result suggests that by calculating $\tau$ from DES measurements, it is possible to predict the viscosity of lubricating oil.

As shown in Figure 8, R remained nearly constant value regardless of the weight-average molecular weight, $M_w$ of the degradation products. Although further validation of the accuracy of this value is necessary, it is evident that, at least in the dielectric relaxation phenomena caused by the oxidative degradation of PAO, the domains responding to the electric field are not the entire molecule but rather small units within the molecular chain. Furthermore, it is clear that this response is strongly correlated with the viscosity of the lubricant.

## 5.3 Relationship between $\beta$ and PDI

The parameter $\beta$ indicates the degree of distribution of relaxation times. When $\beta = 1$, this corresponds to a state where only a single relaxation mode is present. However, even in pure substances, $\beta$ rarely equals 1 because dipoles interact with

surrounding molecules, and these interactions vary slightly depending on location. Moreover, in cases like the current study, where multiple relaxation species with different molecular weights and chemical structures exist within the system, $\beta$ is expected to be smaller. The PDI represents the breadth of the molecular weight distribution of polymers, with larger values indicating greater dispersion. As the ester-based polymers generated by lubricant degradation follow a step-growth polymerization mechanism, it is expected that PDI will increase as degradation progresses.

Figure 9 shows the relationship between $\beta$ and PDI. As degradation progressed, PDI increased and $\beta$ decreased. This is likely due to the broadening of the molecular weight distribution and the increased complexity of the constituents as oxidative degradation progressed, resulting in an increase in the number of relaxation modes. On the other hand, when comparing the two types of oils, although the range of PDI variation differed significantly, there was no substantial difference in the range where the value of $\beta$ existed. If the molecules themselves, generated by degradation, were aligning with the electric field, the plots for both oils in Figure 10 would overlap on the same line. Therefore, this result suggests that the size of the relaxation species is not significantly different between the two oils. As mentioned in section 5.2, this indicates that the dielectric relaxation is related to the movement of small segments within the polymer chains, and that these segments, as well as the surrounding environment, do not differ significantly between the two oils.

## 5.4 Relationship between $\sigma_0$, $\tau$ and TAN

TAN is a parameter that indicates the concentration of fatty acids produced by degradation and is widely used as an indicator of oxidative degradation of lubricants. Additionally, the concentration of fatty acids significantly affects the conductivity of the oil (Kajimoto et al., 2003), as it has been reported that the increase in ionicity is due to the high acid dissociation constant (Wada et al., 2014). The conductivity of a solution is generally expressed by equation Equation 11.

$$\sigma_0 = eN_c\mu_c \tag{11}$$

Here, $e$ is the elementary charge, $N_c$ represents the carrier concentration, and $\mu_c$ is the carrier mobility. Furthermore, using the Stokes-Einstein equation, it can be expressed in the form of Equation 12.

$$\sigma_0 = \frac{e^2 N_c}{6\pi r\eta} \tag{12}$$

As mentioned in section 5.2, the viscosity of oxidatively degraded PAO is proportional to the relaxation time $\tau$, leading to the derivation of the following equation.

$$\sigma_0\tau \propto \frac{N_c}{r} \tag{13}$$

Here, assuming that some of the carriers are fatty acid ions, $N_c$ can be regarded as a function of TAN. Consequently, it is expected that $\sigma_0\tau$ would correlate with TAN. Therefore, when plotting the product of $\sigma_0$ and $\tau$ against TAN on a logarithmic scale, a single straight line was obtained, regardless of the initial viscosity (Figure 10).

This suggests that by utilizing two parameters observed in different frequency ranges, the degree of oxidative degradation of PAO can be diagnosed independently of the absolute value of viscosity. In other words, this method implies that when applied to lubricating oil films, it would be possible to diagnose oil degradation in a steady state where there is little change in oil film thickness. However, the plot in Figure 10 shows that $\sigma_0\tau$ depends on approximately the fourth power of TAN, suggesting that the carrier concentration in degraded oil is not solely determined by the concentration of fatty acid ions. There are likely other components that significantly contribute to the increase in conductivity. Potential causes may include the presence of ion species other than fatty acid ions in the degraded oil, as well as an increase in dissolved water content resulting from the increased polarity of the oil; however, the precise mechanisms remain unclear.

# 6 Conclusion

In this study, thermal degradation tests were conducted at 160°C using two types of poly (α-olefin) (PAO) with different viscosities to produce multiple samples with varying degrees of degradation. Dielectric spectroscopy (DES) with a parallel plate capacitor was applied to these samples to obtain detailed measurements of complex permittivity over a wide frequency range (30 Hz–1 MHz). The obtained dielectric relaxation parameters ($\varepsilon_{r\infty}$: permittivity at the high-frequency limit, $\Delta\varepsilon$: relaxation strength, $\tau$: relaxation time, $\beta$: relaxation time distribution, and $\sigma_0$: DC conductivity) were thoroughly analyzed in relation to various properties derived from different analyses ($\eta$: viscosity, TAN: total acid number, $C_d$: mass concentration of degraded components, $M_w$: weight-average molecular weight, and PDI: polydispersity index). The following key findings were obtained:

1. It was demonstrated that $\Delta\varepsilon$ can be used to estimate the concentration of degradation products as a simple power function, regardless of the initial base oil viscosity. This is likely due to the fact that as the dipole concentration of degradation products increases, interactions among dipoles become significant, thereby affecting dielectric relaxation properties. This result suggests a new method for estimating the concentration of degradation products and evaluating the degree of lubricant degradation by measuring $\Delta\varepsilon$.
2. A proportional relationship between $\tau$ and $\eta$ of the degraded oil was identified, consistent with Debye's theory, which states that relaxation time is proportional to the viscosity of the solution. Additionally, comparisons between $\tau$ and $M_w$, as well as between $\beta$ and PDI, indicate that dielectric relaxation observed in oxidatively degraded PAO is due to the motion of small segments within polymer chains. These findings suggest that the viscosity of mixed oils with varying degradation levels can be estimated from $\tau$.
3. The product of $\sigma_0$ and $\tau$ was found to correlate strongly with the TAN of degraded oil. This relationship is attributed to the fact that the conductivity of the oil is determined by the

concentration of ionic substances, such as fatty acids generated by oxidative degradation, as well as by the viscosity at that time. This result implies that by utilizing two parameters appearing at different frequency ranges, the degree of oxidative degradation of PAO can be diagnosed independently of absolute viscosity. In other words, this method can enable the diagnosis of oil degradation in a steady state with minimal changes in oil film thickness if applied to lubricating oil films.

These findings reveal that DES is an effective means of comprehensively evaluating lubricant degradation from the perspective of relaxation phenomena. Although further insights on pressure and temperature effects are needed to apply DES to oil film condition monitoring, the present results suggest the possibility of detecting early signs of lubrication failure, thus supporting the feasibility of implementing predictive maintenance (PdM) for bearings.

## Data availability statement

The original contributions presented in the study are included in the article/supplementary material, further inquiries can be directed to the corresponding author.

## Author contributions

SI: Writing–review and editing, Writing–original draft. TM: Writing–review and editing. SM: Writing–review and editing. SM: Writing–review and editing. FI: Writing–review and editing.

## Funding

The author(s) declare that no financial support was received for the research, authorship, and/or publication of this article.

## Acknowledgments

In writing this paper, I received valuable advice through discussions with Atsumi Koda of NSK Ltd. I would like to express my gratitude to her for the support.

## Conflict of interest

Authors SI, TM, and SM were employed by NSK Ltd.

The remaining authors declare that the research was conducted in the absence of any commercial or financial relationships that could be construed as a potential conflict of interest.

## Generative AI statement

The author(s) declare that no Generative AI was used in the creation of this manuscript.

## Publisher's note

All claims expressed in this article are solely those of the authors and do not necessarily represent those of their affiliated organizations, or those of the publisher, the editors and the reviewers. Any product that may be evaluated in this article, or claim that may be made by its manufacturer, is not guaranteed or endorsed by the publisher.

## Supplementary material

The Supplementary Material for this article can be found online at: https://www.frontiersin.org/articles/10.3389/fmech.2024.1504347/full#supplementary-material

## References

Al-Badour, F., Sunar, M., and Cheded, L. (2011). Vibration analysis of rotating machinery using time–frequency analysis and wavelet techniques. *Mech. Syst. Signal Process.* 25 (6), 2083–2101. doi:10.1016/j.ymssp.2011.01.017

Becker-Dombrowsky, F. M., and Kirchner, E. (2024). Electrical impedance based condition monitoring of machine elements–a systematic review. *Frontiers* 10. doi:10.3389/fmech.2024.1412137

Böttcher, C. J. F., and Bordewijk, P. (1973). "Theory of electric polarization, vol. I," in *Dielectrics in static fields* (Amsterdam, Oxford, New York: Elsevier).

Böttcher, C. J. F., and Bordewijk, P. (1980). "Theory of electric polarization, vol. II," in *Dielectrics in time-dependent fields*. 2nd edn. (Amsterdam: Elsevier Science).

Cambow, R., Singh, M., Bagha, A. K., and Singh, H. (2018). To compare the effect of different level of self-lubrication for bearings using statistical analysis of vibration signal. *Mater. Today Proc.* 5 (14), 28364–28373. doi:10.1016/j.matpr.2018.10.121

Crook, A. W. (1961). Elastohydrodynamic lubrication of rollers. *Nature* 190, 1182–1183. doi:10.1038/1901182a0

Debye, P. (1929). *Polar molecules*. New York: Chemical Catalog Company.

Gong, Y., Guan, L., Feng, X., Zhou, J., Xu, X., and Wang, L. (2017). Low-temperature dielectric spectroscopy characterization of the oxidative degradation of lubricating oil. *Energy and Fuels* 31 (3), 2501–2512. doi:10.1021/acs.energyfuels.6b02795

Gong, Y., Guan, L., Wang, L., and Zhu, L. (2016). Two-channel and differential dielectric spectroscopy characterizationof lubricating oil. *Sensors Actuators A Phys.* 241, 74–86. doi:10.1016/j.sna.2016.02.013

Guan, L., Feng, X. L., Xiong, G., and Xie, J. A. (2011). Application of dielectric spectroscopy for engine lubricating oil degradation monitoring. *Sensors Actuators A Phys.* 168 (1), 22–29. doi:10.1016/j.sna.2011.03.033

Hamrock, B. J., and Dowson, D. (1977). Isothermal elastohydrodynamic lubrication of point contacts: Part III–Fully flooded results. *J. Lubr. Technol.* 99 (2), 264–275. doi:10.1115/1.3453074

Iwamoto, S., and Kumagai, H. (1998). Analysis of the dielectric relaxation of a gelatin solution. *Biosci. Biotechnol. Biochem.* 62 (7), 1381–1387. doi:10.1271/bbb.62.1381

Jablonka, K., Glovnea, R., and Bongaerts, J. (2012). Evaluation of EHD films by electrical capacitance. *J. Phys. D Appl. Phys.* 45 (38), 385301. doi:10.1088/0022-3727/45/38/385301

Johnston, G. J., Wayte, R., and Spikes, H. A. (1991). The measurement and study of very thin lubricant films in concentrated contacts. *Tribol. Trans.* 34 (2), 187–194. doi:10.1080/10402009108982026

Kajimoto, G., Nakamura, M., and Yamaguchi, M. (2003). Changes in organic acid components of volatile degradation products during oxidation of oil, and effects of organic acid on increased conductivity determined by the Rancimat method. *J. Jpn. Soc. Food Sci. Technol.* 50 (3), 223–229. doi:10.4327/jsnfs.50.223

Kaneta, M., Sakai, T., and Nishikawa, H. (1993). Effects of surface roughness on point contact EHL. *Tribol. Trans.* 36 (4), 605–612. doi:10.1080/10402009308983201

Kiral, Z., and Karagülle, H. (2003). Simulation and analysis of vibration signals generated by rolling element bearing with defects. *Tribol. Int.* 36 (9), 667–678. doi:10.1016/s0301-679x(03)00010-0

Kremer, F., and Schönhals, A. (2003). *Broadband dielectric spectroscopy* (Berlin: Springer).

Manabe, K., and Nakano, K. (2008). Breakdown of oil films and formation of residual films. *Tribol. Int.* 41 (11), 1103–1113. doi:10.1016/j.triboint.2008.02.001

Maruyama, T., Kosugi, D., Iwase, S., Maeda, M., Nakano, K., and Momozono, S. (2024). Application of the electrical impedance method to steel/steel EHD point contacts. *Frontiers* 10. doi:10.3389/fmech.2024.1489311

Maruyama, T., Maeda, M., and Nakano, K. (2019). Lubrication condition monitoring of practical ball bearings by electrical impedance method. *Tribol. Online* 14 (5), 327–338. doi:10.2474/trol.14.327

Maruyama, T., and Nakano, K. (2018). *In situ* quantification of oil film formation and breakdown in EHD contacts. *Tribol. Trans.* 61 (6), 1057–1066. doi:10.1080/10402004.2018.1468519

Maruyama, T., and Saitoh, T. (2010). Oil film behavior under minute vibrating conditions in EHL point contacts. *Tribol. Int.* 43, 1279–1286. doi:10.1016/j.triboint.2009.11.004

Nakano, K., and Akiyama, Y. (2006). Simultaneous measurement of film thickness and coverage of loaded boundary films with complex impedance analysis. *Tribol. Lett.* 22 (1), 127–134. doi:10.1007/s11249-006-9074-z

Nihira, T., Manabe, K., Tadokoro, C., Ozaki, S., and Nakano, K. (2015). Complex impedance measurement applied to short-time contact between colliding steel surfaces. *Tribol. Lett.* 57 (3), 29. doi:10.1007/s11249-015-0478-5

Patocka, F., Schneidhofer, C., Dörr, N., Schneider, M., and Schmid, U. (2020). 'Novel resonant MEMS sensor for the detection of particles withdielectric properties in aged lubricating oils. *Sensors Actuators A Phys.* 315, 112290. doi:10.1016/j.sna.2020.112290

Prashad, H. (1988). Theoretical evaluation of impedance, capacitance and charge accumulation on roller bearings operated under electrical fields. *Wear* 125 (3), 223–239. doi:10.1016/0043-1648(88)90115-9

Schnabel, S., Marklund, P., Minami, I., and Larsson, R. (2016). Monitoring of running-in of an EHL contact using contact impedance. *Tribol. Lett.* 63 (3), 35. doi:10.1007/s11249-016-0727-2

Sugimura, J., Jones, W. R., and Spikes, H. A. (1998). EHD film thickness in non-steady state contacts. *J. Tribol.* 120 (3), 442–452. doi:10.1115/1.2834569

Wada, J., Ueta, G., Okabe, S., and Amimoto, T. (2014). Method to evaluate the degradation condition of transformer insulating oil: experimental study on the hydrophilic and dissociative properties of degradation products. *IEEE Trans. Dielectr. Electr. Insulation* 21 (2), 873–881. doi:10.1109/tdei.2013.004204

Woodward, W. H. (2021). "Broadband dielectric spectroscopy—a practical guide," in *ACS symposium series* (Washington, DC: American Chemical Society).

Zarei, J., Tajeddini, M. A., and Karimi, H. R. (2014). Vibration analysis for bearing fault detection and classification using an intelligent filter. *Mechatronics* 24, 151–157. doi:10.1016/j.mechatronics.2014.01.003

frontiers | Frontiers in Mechanical Engineering

TYPE Original Research
PUBLISHED 19 December 2024
DOI 10.3389/fmech.2024.1488803

Check for updates

OPEN ACCESS

EDITED BY
Taisuke Maruyama,
NSK Ltd., Japan

REVIEWED BY
Andriy Zahorulko,
Sumy State University, Ukraine
Saša Milojević,
University of Kragujevac Faculty of Engineering, Serbia

*CORRESPONDENCE
Masayuki Ochiai,
ochiaim@tokai.ac.jp

RECEIVED 30 August 2024
ACCEPTED 30 October 2024
PUBLISHED 19 December 2024

CITATION
Ochiai M and Ohya Y (2024) The effect of inner ring groove on leakage reduction in dry gas seals and its visualization verification. *Front. Mech. Eng.* 10:1488803. doi: 10.3389/fmech.2024.1488803

COPYRIGHT
© 2024 Ochiai and Ohya. This is an open-access article distributed under the terms of the Creative Commons Attribution License (CC BY). The use, distribution or reproduction in other forums is permitted, provided the original author(s) and the copyright owner(s) are credited and that the original publication in this journal is cited, in accordance with accepted academic practice. No use, distribution or reproduction is permitted which does not comply with these terms.

# The effect of inner ring groove on leakage reduction in dry gas seals and its visualization verification

Masayuki Ochiai[1]* and Yuta Ohya[2]

[1]Department Mechanical Systems Engineering, Tokai University, Hiratuka, Japan, [2]Department Mechanical Systems Engineering (Former Student), Tokai University, Hiratuka, Japan

This study investigates the impact of incorporating an Inner Ring Groove (IRG) on the leakage characteristics of dry gas seals, commonly used in turbomachinery such as gas turbines and compressors. The primary objective is to enhance sealing performance and reduce gas leakage, which is critical for improving the efficiency of these machines. The research focuses on various groove shapes, including spiral grooves for single-direction rotation and T-grooves and tree grooves for bi-directional rotation. The experimental setup involved measuring air leakage rates across different seal configurations, both with and without the IRG. The results indicated that while the IRG increased leakage in spiral groove seals, it significantly reduced leakage in T-groove and tree groove seals. Specifically, the IRG reduced leakage by approximately 26% in T-groove seals and 15.8% in tree groove seals, compared to their standard configurations. Additionally, the study employed Particle Image Velocimetry (PIV) to visualize gas flow within the seal gaps. The visualization revealed that the IRG altered the flow dynamics, particularly in T-groove seals, where it redirected the gas flow from a radial to a circumferential direction, thereby reducing leakage. In contrast, the IRG in spiral groove seals promoted radial flow, leading to increased leakage. These findings suggest that the application of IRGs can be particularly effective in bi-directional rotation seals, offering a potential design modification to enhance sealing performance. The study concludes that while IRGs may not be suitable for all groove types, their strategic application can lead to significant improvements in leakage reduction and overall efficiency of dry gas seals.

KEYWORDS

**dry gas seal, non-contacting mechanical seal, visualization, PIV, groove, bai directional rotation seal**

## 1 Introduction

Turbomachinery, such as gas turbines and compressors, are applied to various applications including power plants and transporting systems. Consequently, there is a pressing need to conserve energy and enhance the efficiency of these devices. One approach to augmenting the mechanical efficiency of gas turbines is to increase the compressor's compression ratio. A critical aspect of this is preventing the air compressed by the compressor from leaking into the atmosphere. It has been reported that a 1% reduction in gas leakage from the shaft seal can lead to a 1.7% improvement in engine efficiency for aircraft jet engine compressors (Wilcock et al., 1968). Recently, the supercritical carbon dioxide (sCO2) turbomachinery is the one of the most expected application (Laxander et al., 2019; Zhang et al., 2024; Yuan et al., 2024). As a result, many researcher and engineers are focused on dry gas seals which is known for their minimal gas leakage compared to other non-contact seals.

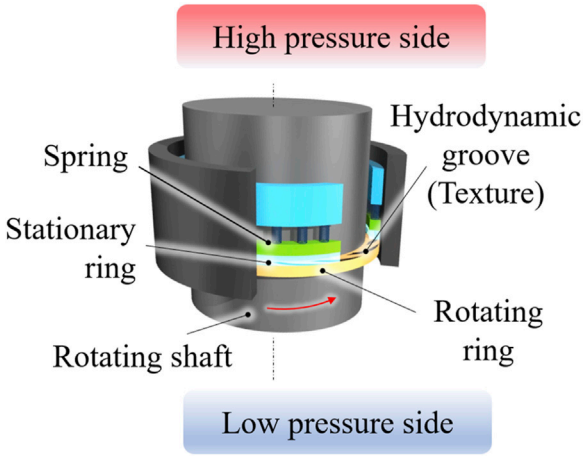


FIGURE 1
Outline of a dry gas seal.

The outline of a dry gas seal is shown in Figure 1 The dry gas seal consists of four main components: a rotating ring, a stationary ring, a spring, and a housing. The rotating ring, equipped with grooves, spins at high velocity to create hydrodynamic pressure and form an air film (Stahley, 2005; Zhang et al., 2024). The performance characteristics of dry gas seals are significantly influenced by the configuration of the hydrodynamic grooves (Chen et al., 1969; Green and Barnsby, 2001; Etsion, 2005; Shahina et al., 2013; Chen, 2024), prompting research into groove shape optimization to improve some characteristics (Hashimoto and Ochiai, 2008; Wang and Chen, 2009; Papadopoulos et al., 2011; Ochiai et al., 2014; Cong et al., 2022; Ochiai and Sato, 2022c).

It is known that the optimized groove designs aimed at minimizing air leakage exhibit superior sealing capabilities. However, sometimes their complex configurations lead to high-precision machining, potentially escalating production costs. Nonetheless, form the one of the optimization results obtained by the cell automaton proposed by the authors reveals a simple ring-shaped groove within a complex structure (Ochiai et al., 2018). This discovery led the author to hypothesize that applying the inner ring groove to previously utilized groove shapes could effectively suppress air leakage. Li et al. analyzed a dry gas seal with grooves in which the spiral groove and the inner ring groove are in, and found that the operation is stable at low speeds and high pressures, but the lifting force is lower and air leakage is increased compared to spiral groove seals (Li et al., 2013). However, there are no studies that apply inner ring grooves to groove shapes in which the inner ring groove and the spiral groove are independent, or to bi-rotating dry gas seals, for example, T-groove shapes. Furthermore, there are no studies that consider the visualization of air flowing through the seal surface when an inner ring groove is applied.

In recent years, Particle Image Velocimetry (PIV) has been applied to fluid lubrication to know the tribological characteristics more specifically (Green et al., 2011; Li et al., 2012; Emden et al., 2016; Richardson et al., 2019). This is a promising method in the field of fluid film lubrication and its applications. Despite the widespread use of Particle Image Velocimetry (PIV) as a flow visualization technique, there have been few instances of its application in Dry gas seals (Suzuki et al., 2016; Ochiai et al., 2019). This is presumably due to the need to capture flow moving at high speeds within extremely thin gaps. However, as previously mentioned, with the recent advancements in measurement equipment and methodologies, it is believed that the application of PIV to fluid lubrication has become possible. Indeed, the authors conducted the PIV analysis against the liquid type of mechanical seals and clarified the effect of rotational direction on leakage characteristics (Ochiai and Sato, 2022a) and the effect of temperature it leads to thermal distortion of seal surfaces comparing the three types of grooved seals (Ochiai and Sato, 2022b). Same as optimization research, it is important to visualize and recognize the actual gas flow between seal surfaces.

Under the background, this study conducted experiments to measure air leakage by incorporating an inner ring groove (IRG) into several types of groove shapes: the spiral groove, typically used for single-direction rotation, and the T-groove and tree groove, suitable for bi-directional rotation. Because the bi-directional rotation type seals are usually inferior to single-directional type seals. Moreover, by using the PIV analysis method of gas lubrication film, comparison of the gas flow vector of the spiral groove seal with T-groove seal was conducted for understanding the mechanism of the inner ring groove (IRG) on the sealing effects.

## 2 Test seals

To ascertain the impact of the inner ring groove, a comparative analysis of six types of seals is conducted. This included three conventional basic seals and seals equipped with newly proposed inner ring grooves. The seal depicted in Figure 2A is a standard seal, while the seal in (a-i) represents a common spiral groove seal designed for single rotation. Conversely, the seals in (a-ii) and (a-iii) are T-groove seals and Tree globe seals, respectively, both designed for bi-directional rotation. Here, $R_1$ denotes the outer radius of the test seal, $R_2$ signifies the inner radius of the test seal, and $R_S$ represents the inner radius of the groove, which we refer to as the seal radius.

In Figure 2B, a thin groove is incorporated on the inner circumferential side of each seal shown in (a). This groove is referred to as the "inner circumference ring groove" throughout this paper. The term $H_i$, as shown in each figure, indicates the inner radius of the inner circumferential ring groove. The dimensions of each test seal are provided in Table 1.

## 3 Gas leakage measurement

### 3.1 Experimental apparatus for amount of gas leakage

A schematic diagram of the experimental apparatus utilized in this study is depicted in Figure 3A, while an external photograph is presented in Figure 3B. A rotor is mounted at the base of this apparatus. It is comprised of a direct drive with an integrated motor, capable of high-speed rotation. The runout around the rotor is constrained to within 5 μm.

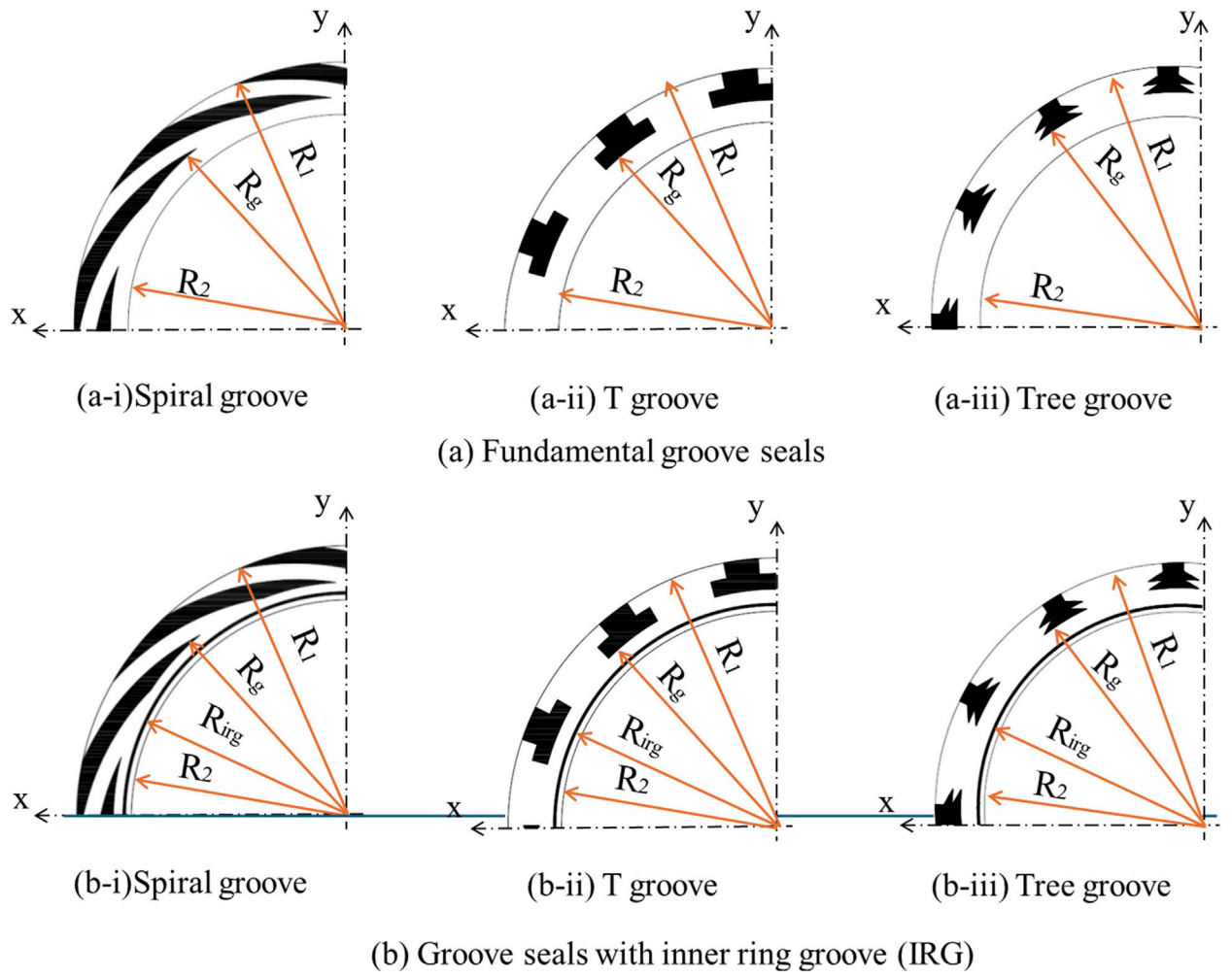


FIGURE 2
**(A)** Fundamental groove seals. **(B)** Groove seals with inner ring groove (IRG).

TABLE 1 Specifications of test seals.

| Parameter | | Spiral groove | T-groove | Tree Groove |
|---|---|---|---|---|
| Number of grooves | N | 10 | 12 | |
| Outer radius | $R_1$, mm | 32 | | |
| Inner radius | $R_2$, mm | 25.6 | | |
| Sealing radius | $R_S$ mm | 27.5 | 28.3 | |
| Groove depth | $h_g$, μm | 8 | | |
| Inner circumferential groove radius | $R_i$, mm | 26.3 | | |
| Inner circumferential groove width | $B_{ig}$, μm | 320 | | |
| Inner circumferential groove depth | $h_{ig}$, μm | 8 | | |

The upper section of the rotor houses the test seal portion, as illustrated in the magnified image in the figure. A gas film is established between the rotor and the test seal surface. An eddy-current displacement sensor is installed within the test seal to gauge the thickness of the gas film. The accuracy of the displacement sensor is 1 μm. A temperature sensor is also incorporated, which is utilized to adjust for the temperature of the eddy-current displacement sensor. The thickness of the gas film can be modified by a micrometer located at the top of the apparatus.

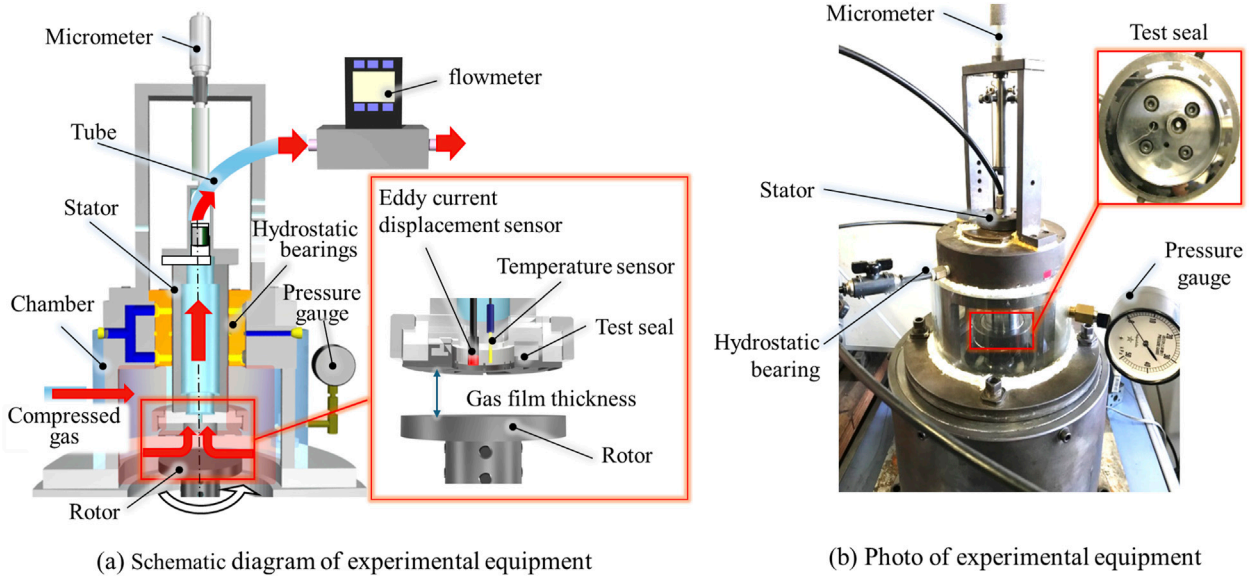


FIGURE 3
**(A)** Schematic diagram of experimental equipment. **(B)** Photo of experimental equipment.

The test seal section is encased within a chamber, to which compressed gas is supplied externally. The pressure within the chamber can be assessed with the pressure gauge depicted in the figure. The compressed gas within the chamber escapes to the inner diameter side of the seal via the gas film formed between the rotor and the test seal surface. The leaked gas travels the interior of the sealed stator and is measured by the flowmeter located in the middle. The test seal can be changed using the attachment, the test seal was appropriately replaced with one of a different groove shape, and the amount of gas leakage was measured.

## 3.2 Experimental method for amount of gas leakage

In this experiment, the amount of air leakage was measured under changing the air film thickness. Initially, air was supplied from the compressor until the pressure within the chamber reached 25 kPa. Subsequently, the height of the test seal can be manipulated using a micrometer, thereby adjusting the thickness of the air film to a predetermined value. The rotor was then set in motion at a speed of 20,000 rpm, and the amount of leakage was measured using a flow meter (M-500, Japan Star Techno Co., Ltd.). The measurement range is 2.5–500 L/min and the accuracy is 0.8% reading + 0.2% full scale. Using this methodology, the thickness of the air film was systematically reduced from 30 μm to 18 μm in increments of 2 μm, and at each stage, 20 separate measurements of the leakage rate was conducted. The thickness of the experiment is large compared with actual dry gas seals, however the ratio of the groove depth hg and gas film thickness $h$, $h_g/h$, is 0.45–0.27 and the obtained tendency from the experiment are applicable to actual applications.

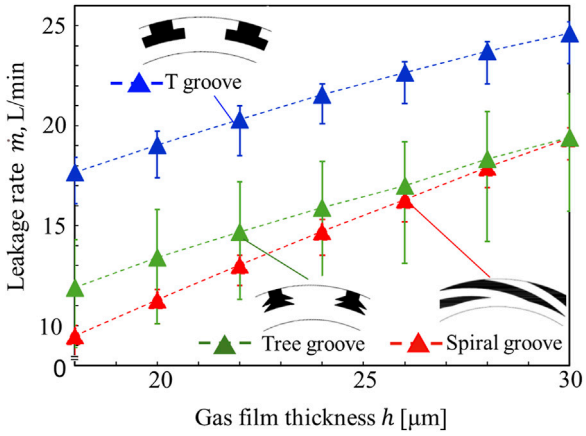


FIGURE 4
Experimental results of leakage rate comparison for three types of dry gas seals.

## 3.3 Experimental results in amount of gas leakage

Initially, we examined the correlation between the leakage rate and the gas film thickness for three types of seals, which are fundamental shapes: the single-rotation spiral groove seal, the T-groove seal, and the Tree groove seal, all of which are designed for bi-directional rotation.

Figure 4 shows the experimental results of amount of gas leakage. Each data plot signifies the average leakage rate following 20 measurements, with the error bars indicating the maximum and minimum measured values. A direct increase in the seal clearance significantly impacts the leakage rate. Comparing the three types of seals, it is evident that the single-rotation spiral

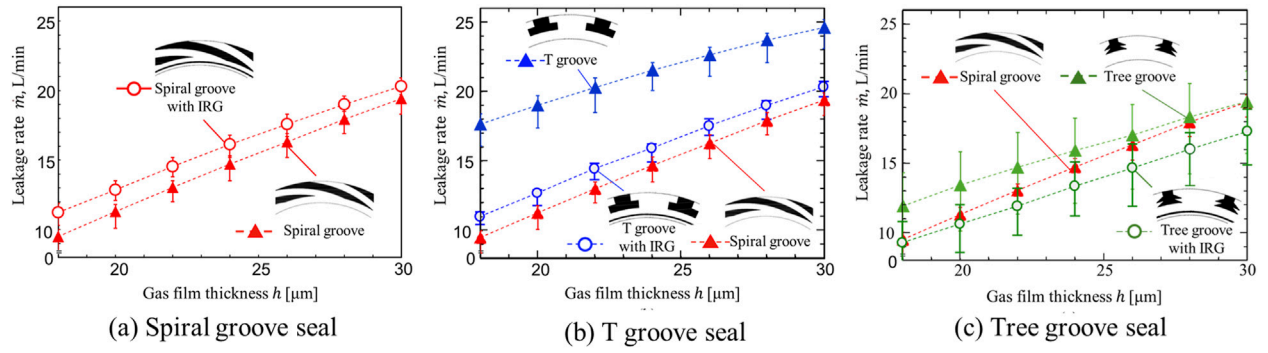


FIGURE 5
**(A)** Spiral groove seal. **(B)** T groove seal. **(C)** Tree groove seal.

groove seal exhibits the least leakage, followed by the tree groove seal. In contrast, the T-groove seal has a considerably higher leakage rate, indicating inferior sealing characteristics. However, since the spiral groove seal cannot generate hydrodynamic pressure during reverse rotation, both rotating grooves offer an advantage, and a bi-directional rotation seal groove may be chosen depending on the machine in use. Regarding the tree groove seal, when the film thickness is substantial, the leakage volume is comparable to that of the spiral groove seal, suggesting its superiority over the T-groove seal.

Then, we compare the leakage quantities with and without inner circumferential ring grooves (IRGs) are incorporated. The results are depicted in Figure 5A, which illustrates the comparative results for a spiral groove configuration. It has been confirmed that the application of an inner ring groove (IRG) to the spiral groove leads to increase of gas leakage. Specifically, when the inner ring groove is present, the larger gas film thickness experiences an increase of leakage rate. This enhancement of amount of gas leakage is nearly identical for a measured wide range of gas film thickness, averaging an increase of 9.3%. In addition, it is suggested that the same tendency remains in thinner gas film same as actual dry gas seals from tendency of this graph. This The underlying rationale can be attributed to the following mechanism: primarily, the leakage quantity originates from the pressure differential across the inner and outer peripheries of the seal interface. Moreover, the presence of a groove on the sealing surface introduces dynamic pressure effects, which in turn generate a pressure distribution impacting the leakage rate. Fundamentally, within the spiral groove, the dynamic pressure induced by the pumped-in flow effect—propelled by rotational motion—is postulated to influence the gas leakage phenomenon.

Conversely, when the inner ring groove is integrated into the T-groove, as illustrated in Figure 5B, a significant reduction in air leakage is confirmed. Quantitatively, the incorporation of the inner ring groove results in an average leakage decreases of approximately 26.0% relative to the fundamental groove configuration without the inner ring groove (IRG). This finding underscores the effectiveness of the inner ring groove in enhancing the sealing performance of T-groove structures. It is quite close to the leakage rate of a fundamental spiral groove seal and it is suggested that the same tendency remains in thinner gas film.

The obtained results can be considered as follows: Within the T-groove configuration, the feature of both rotations generate negative pressure in conjunction with positive pressure to counteract reverse rotation. However, due to the relatively weak generation of positive pressure in the T-groove, the predominant effect of bi-directional rotation is leads to gas flow into the seal interface from the high-pressure outer periphery, resulting in increased leakage with a standard T-groove seal. Conversely, it is considered that the implementation of an inner ring groove (IRG) induces a modification in the flow near the seal's inner circumference, thereby mitigating gas leakage into the seal. This suggests that further research from alternative perspectives may yield additional insights.

Finally, we compared the results of the air leakage measurement experiment when the inner circumferential ring groove was integrated into the tree groove—a groove configuration designed for bi-directional rotation. As depicted in Figure 5C, a significant reduction in leakage is observed with the inner circumferential ring groove compared to the standard tree groove, with an average decrease of approximately 15.8%. Seals featuring tree grooves with IRG not only demonstrated the average leakage rate reduction but also maintained this low rate even at a gas film thickness of $h$ = 30 μm, which is the largest among measured film thickness. Moreover, for a wide measured range of gas film thickness, tree groove with IRG remains most low leakage. However, this advantage might not be remained in thinner area except the measured area. On the other hand, it is suggested that the effect of IRG on tree groove remains in thinner gas film same as T-groove seal.

These findings conclusively demonstrate that the inner ring groove (IRG) contributes to air leakage reduction when applied to a groove designed for dual rotation, thereby enhancing the sealing performance to equal or exceed that of spiral grooves intended for typical single-direction rotation. Then, we specifically investigated the impact of the inner circumferential ring groove (IRG) in isolation. To this end, we measured the leakage rates of a plain seal without any grooves and a seal equipped solely with the IRG. Throughout these experiments, the gas film thickness was maintained at $h$ = 18μm, while the chamber pressure varied from 5 kPa to 35 kPa. The results, as illustrated in Figure 6, indicate that the

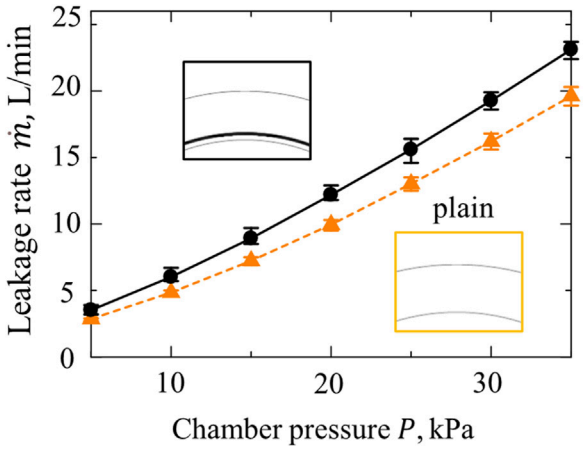


FIGURE 6
Effect of inner ring groove on Leakage rate in plane seal.

gas leakage rate increases with increasing chamber pressure. Notably, at all tested pressures, the seal with the inner ring groove exhibited higher leakage than the plain seal. With the inner ring groove (IRG) alone, it promotes radial flow and gas leakage.

# 4 Visualization of flow in dry gas seals

To elucidate the reasons behind these intriguing findings, we tried to visualize the gas flowing in the seal clearance.

## 4.1 Experimental apparatus for flow visualization and test method

Figure 7A illustrates a schematic diagram of the visualization apparatus, while Figure 7B presents a photograph of the external appearance of the same device. In this experiment, we visualized the airflow through the seal clearance during rotor operation. Initially, we established the zero point of the eddy current displacement transducer by bringing it into contact with the test seal and the rotor in a stationary state. Subsequently, the test seal was secured within an acrylic case, which was then pressurized to 5 kPa. We regulated the rotor's rotational speed to 3,000 rpm at a clearance of 80 μm, and directed a 2 W sheet laser into the gap between the test seal and the rotor. Following this, tracer particles were introduced into the acrylic case, and a high-speed camera positioned atop the case captured the gas flow through the seal gap as shown in Figure 8. A total of 2,000 frames—equivalent to three full rotations of the rotor—were recorded and analysed using Particle Image Velocimetry (PIV). For this phase of the study, a spiral groove seal was chosen to represent single-direction rotation seals, and a

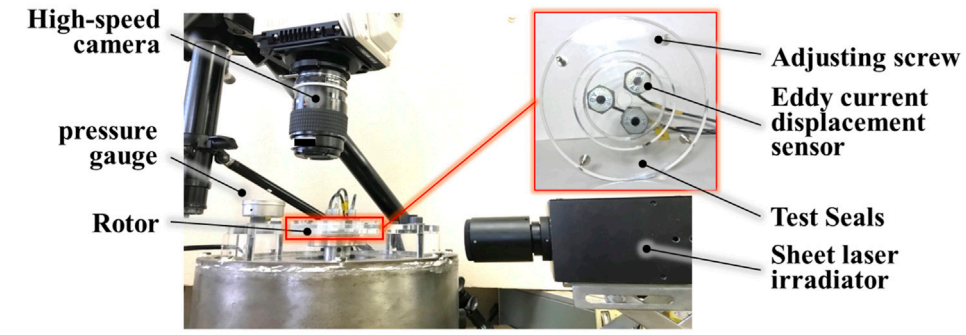


(a) External photo of experimental equipment

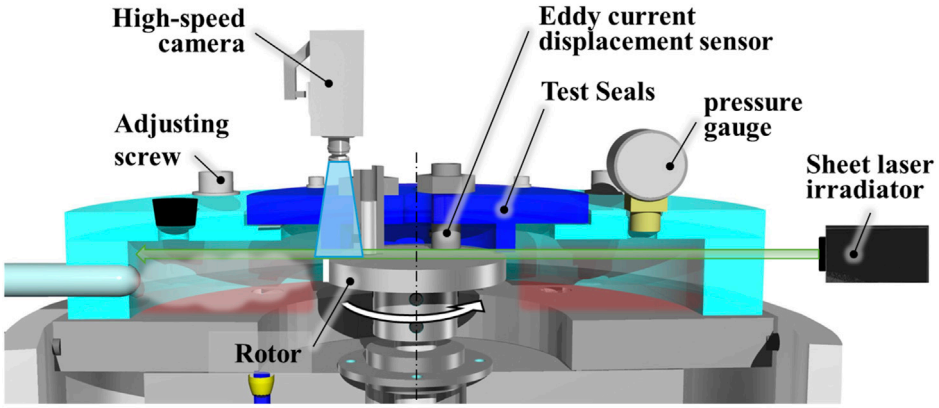


(b) Schematic diagram of experimental equipment

FIGURE 7
Outline of the experimental equipment for visualization **(A)** External photo of experimental equipment. **(B)** Schematic diagram of experimental equipment.

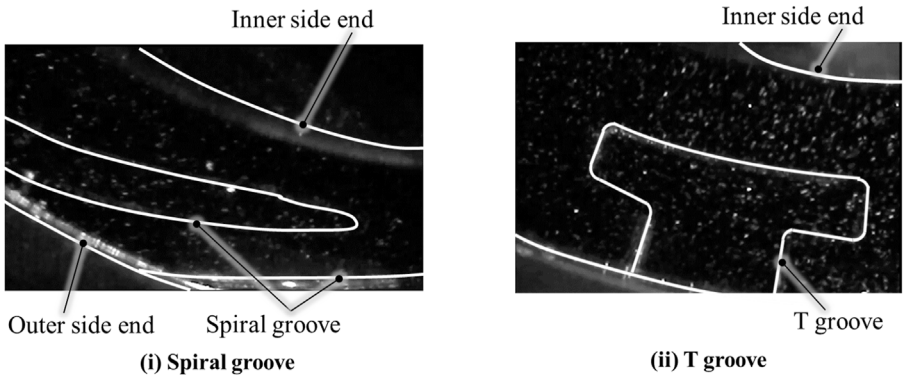


FIGURE 8
Visualization results.

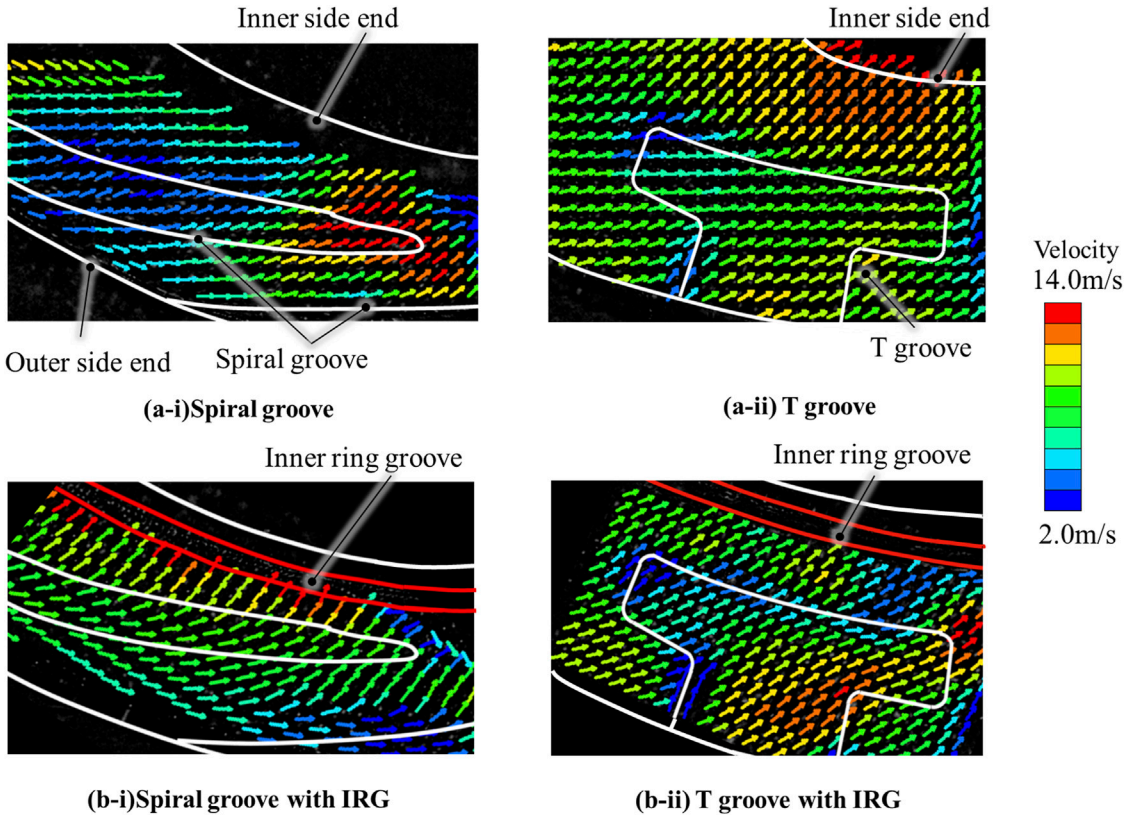


FIGURE 9
Experimental results of PIV comparison with and without IRG.

T-groove seal was selected for bi-directional rotation seals. The experiment aimed to compare the influence of the Inner Ring Groove (IRG) on air leakage around the inner circumference.

## 4.2 Visualization results

The gas flow visualization results of the four types of test seals are shown in Figure 9. Firstly, from the visualization results of velocity vector in Figure 9 (a-i), it is primarily observed that the flow is in the diagonal direction on the spiral groove seal. This is due to the combined effect of the radial flow, which is caused by the pressure difference from the outer periphery to the inner periphery, and the hydrodynamic pressure effect of the groove due to rotation. Outside of the spiral groove, which is observed obliquely lower area in the figure, the circumferential gas flow is dominant. However, the flow varies to follow the groove as it approaches the groove. Conversely, in the flow that enters the groove, the direction of the flow slightly shifts

inward, and this flow direction is generally maintained even after exiting the groove. The velocity magnitude increases slightly with the inner flow exiting the groove.

Additionally, a warm color vector is observed near the tip of the spiral groove, indicating that the flow near the tip has the highest velocity. It is evident how the flow is accelerated within the groove. The gas that exits the tip of the groove appears to flow slightly in the radial direction and exits the interior of the sealing surface while maintaining a relatively high velocity. Generally, the amount of leakage in this vicinity is large, but in other larger areas, the flow is slow in the diagonal direction, suggesting that leakage can be suppressed. In this image, the flow that passes through the interior have not been able to confirm, but it is considered that the above interpretation generally accurate.

Indeed, in the T-groove seal with the basic shape depicted in Figure 9 (b-i), the gas flow significantly differs from that of the spiral groove. Initially, on the outer circumference of the seal, the diagonal flow has already been observed around the outer periphery, and additionally the flow direction is closer in the radial direction compared to the spiral groove. It is noted that the gas flow entering the T-groove slightly alters its direction within the groove. However, upon exiting the groove, it is strongly redirected in the radial direction again and exits inward at a high speed. In comparison to the spiral groove, the warm color area on the inner circumference of the seal is also broader, which is considered contributing to the increase in the amount of leakage.

Then, the impact of the inner circumferential ring groove (IRG) is considered based on the visualization results depicted in Figure 9 (a-ii) and (b-11). Initially, for the spiral groove seal with an IRG as shown in Figure 9 (a-ii), the cold color velocity vector is diminished across the entire sealing surface, and the flow is generally faster. The most characteristic feature is that the gas flow, after traversing the inner circumferential side of the spiral groove, undergoes a strong change in the radial direction and accelerates such that it is drawn into the IRG. In the absence of an IRG, it was possible to suppress the flow to a slow, diagonal direction due to the effect of the spiral groove. However, the installation of an IRG altered the flow direction, which further increased the speed. The flow itself through the inner groove cannot be captured, but it is believed that significant amount of gas is leaking internally due to this flow.

On the other hand, in the double-rotating T-groove, the flow is slightly more intense in the radial direction inside the T-groove due to the influence of the IRG. However, the gas flow that exits the T-groove inward is slightly decelerated, and its direction is also more circumferential compared to the case without an IRG. In the case of the T-groove, the IRG guides the gas flow in the direction of rotation, which is also contribute to the reduction of gas leakage. As depicted in Figure 5 in Chapter 3, it is interesting to note that the flow of the spiral groove without an IRG and the T-groove with an IRG tend to be generally similar.

As described above, from a visualization perspective, we have examined why the Inner Ring Groove (IRG) effect was observed in the T-groove for both rotations, while the IRG was not effective in the spiral groove seal for single rotation. Although the tree groove was not implemented in this instance, the effect of the IRG on the flow is fundamentally considered to be equivalent to that of the T-groove.

## 5 Conclusion

In this study, we experimentally compared the amount of leakage when a simple ring-shaped groove (IRG) was applied to the spiral groove, which is a usual single-rotation seal for dry gas seals, and the T-groove and tree groove for both rotations. In addition, in spiral groove seals and T-groove seals with and without IRG, the gas flow in the seal gap was visualized, and the relationship with the leakage amount was considered. The conclusions reached are as follows.

As a result of comparing the leakage amount of the spiral groove seal for single rotation, the T-groove seal for both rotation, and the tree groove seal, it was confirmed that the spiral groove seal has the lowest gas leakage amount within the experimental range.

When the Inner Ring Groove (IRG) was applied to the spiral groove seal, an increase in the amount of gas leakage was observed. This suggests that the application of an IRG to the spiral groove seal may not be effective in reducing gas leakage.

In the case of the T-groove seal and the tree groove seal, which are both double-rotating grooves, the application of the Inner Ring Groove (IRG) resulted in a significant reduction in the amount of leakage. The leakage rate of the T-groove seal was found to be equivalent to that of the spiral groove seal without an IRG. Interestingly, the leakage rate of the tree groove seal with an IRG was even lower than that of the spiral groove seal. This suggests that the application of an IRG can be particularly effective in double-rotating groove seals.

Based on the visualization of the gas flow within the seal gap, in the spiral groove seal for single rotation, the influence of the Inner Ring Groove (IRG) promoted the flow towards the inner side of the seal surface, leading to an increase in leakage.

In contrast, in the T-groove seal, the influence of the IRG changed the gas flow from the radial direction to the rotational direction, and the speed also decreased. This is thought to have led to a reduction in leakage. These findings provide valuable insights into the design modifications of the addition of an IRG.

These conclusions are applied under our test conditions which are relatively large gas film thickness. However, there is possible to obtain the same tendency in the actual dry gas seals. It is expected to be examined under the actual conditions, for instance in industries.

## Data availability statement

The datasets presented in this study can be found in online repositories. The names of the repository/repositories and accession number(s) can be found in the article/supplementary material.

## Author contributions

MO: Writing–original draft, Writing–review and editing, Conceptualization, Funding acquisition, Investigation, Project administration, Supervision, Validation. YO: Writing–original draft, Data curation, Visualization.

## Funding

The author(s) declare that financial support was received for the research, authorship, and/or publication of this article. This work was supported by JSPS KAKENHI Grant Number JP16K06050.

## Conflict of interest

The authors declare that the research was conducted in the absence of any commercial or financial relationships that could be construed as a potential conflict of interest.

## Publisher's note

All claims expressed in this article are solely those of the authors and do not necessarily represent those of their affiliated organizations, or those of the publisher, the editors and the reviewers. Any product that may be evaluated in this article, or claim that may be made by its manufacturer, is not guaranteed or endorsed by the publisher.

## Supplementary material

The Supplementary Material for this article can be found online at: https://www.frontiersin.org/articles/10.3389/fmech.2024.1488803/full#supplementary-material

## References

Chen, D. (2024). Influence of microtextured parameters of dry gas sealing rings on tribological performance. *Industrial Lubr. Tribol.* 76, 4464–4473. doi:10.1108/ILT-12-2023-0389

Chen, H., Castelli, S. V., and Chow, C. Y. (1969). Performance characteristics of spiral-groove and shrouded Rayleigh step profiles for high-speed noncontacting gas seals. *Trans. ASME. J. Tribol.*, 60–68. doi:10.1115/1.3554900

Cong, Z., Jinbo, J., Wenjing, Z., Jie, J., and Xudong, P. (2022). A comprehensive multi-objective, multi-parameter and multi-condition optimization of a spiral groove in dry gas seals. *J. Braz. Soc. Mech. Sci. Eng.* 44, 206. doi:10.1007/s40430-022-03527-6

Emden, E. V., Venner, C. H., and Morales-Espejet, G. E. (2016). Aspects of flow and cavitation around an EHL contact. *Tribol. Int.* 95, 435–448. doi:10.1016/j.triboint.2015.11.042

Etsion, I. (2005). State of the art in laser surface texturing. *J. Tribol.* 127 (1), 248–253. doi:10.1115/1.1828070

Green, I., and Barnsby, M. R. A. (2001). A simultaneous numerical solution for the lubrication and dynamic stability of noncontacting gas face seals. *J. Tribol.* 123 (1), 388–394. doi:10.1115/1.1308020

Green, T. M., Baart, P., Westerberg, L. G., Lundstrom, T. S., Hoglund, E., Lung, P. M., et al. (2011). A new method to visualize grease flow in a double restriction seal using microparticle image Velocimetry. *Tribol. Trans.* 54, 784–792. doi:10.1080/10402004.2011.604759

Hashimoto, H., and Ochiai, M. (2008). Optimization of groove geometry for thrust air bearing to maximize bearing stiffness. *Trans. ASME, J. Tribol.* 130 (3), 031101. doi:10.1115/1.2913546

Laxander, A., Fesl, A., and Hellmig, B. (2019). Development and testing of dry gas seals for turbomachinery in multiphase $Co_2$ applications, Engineering. *Environ. Sci.* doi:10.17185/duepublico/48878

Li, J. X., Hoglund, E., Westerberg, L. G., Green, T. M., Lundstrom, T. S., Lugt, P. M., et al. (2012). μPIV measurement of grease velocity profiles in channels with two different types of flow restrictions. *Tribol. Int.* 54 (94), 94–99. doi:10.1016/j.triboint.2012.03.007

Li, Y., Peng, Y. S., and Heng, J. X. (2013). Performance analyses of the spiral groove dry gas seal with inner annular groove. *Appl. Mech. Mater.* 420, 51–55. doi:10.4028/www.scientific.net/amm.420.51

Ochiai, M., Aketo, Y., and Hashimoto, H. (2018). A study on surface texturing optimization method using cellular automaton and its application to dry gas seals. *Pro. JSME, Mach. Lubr. Des. Div.* 4, 23–24. doi:10.1299/jsmemdt.2018.18.2C1-7

Ochiai, M., Namai, T., and Hashimoto, H. (2019). Visualization experiment of gas flow on dry gas seal under sinusoidal excitation conditions. *Tribologist*. (in Japanese). doi:10.18914/tribologist.19-00006

Ochiai, M., Sasaki, H., Sunami, Y., and Hashimoto, H. (2014). Experimental and theoretical verification of impact response on air thrust bearing with topological optimized groove. *Tribol. Online* 10 (2), 115–120. doi:10.2474/trol.10.115

Ochiai, M., and Sato, Y. (2022a). Flow visualization of non-contacting mechanical seals with bidirectional rotation. *J. Phys. Conf. Ser. 2217 012028. 16th Asian Int. Conf. Fluid Mach.* 2217, 012028. doi:10.1088/1742-6596/2217/1/012028

Ochiai, M., and Sato, Y. (2022b). Temperature distribution measurement and internal flow visualization in the lubrication film of non-contacting mechanical seals. *Tribol. Lett.* 70, 93. doi:10.1007/s11249-022-01632-0

Ochiai, M., and Sato, Y. (2022c). Groove shape optimization on dry gas seals. *Tribol. Mach. Elem. - Fundam. Appl. Intech Open, Chapter* 9, 179–196.

Papadopoulos, C. I., Efstathiou, E. E., Nikolakopoulos, P. G., and Kaiktsis, L. (2011). Geometry optimization of textured three-dimensional micro-thrust bearings. *Trans. ASME, J. Tribol.* 133 (4), 1–10. doi:10.1115/1.4004990

Richardson, D., Sadeghi, F., Rateick, Jr R. G., and Rowan, S. (2019). Using μPIV to investigate fluid flow in a pocketed thrust bearing. *Tribol. Trans.* 62 (3), 350–361. doi:10.1080/10402004.2018.1556370

Shahina, I., Gadalab, M., Alqaradawic, M., and Badrd, O. (2013). Three dimensional computational study for spiral dry gas seal with constant groove depth and different tapered grooves. *Procedia Eng.* 68, 205–212. doi:10.1016/j.proeng.2013.12.169

Stahley, J. S. (2005). *Dry gas seals handbook*. Tulsa, Oklahoma: PennWell Corporation.

Suzuki, D., Kodama, S., Ochiai, M., Sunami, Y., and Hashimoto, H. (2016). Visualization experiment of gas flow in dry gas seals. *J. Adv. Sci.* 28, 11005–1–11005–5. (in Japanese). doi:10.2978/jsas.11005

Wang, H., and Chen, C. (2009). "Numerical simulation on the geometric parameters of spiral grooved dry gas seals," in *ISECS international colloquium on computing, communication, control, and management*. doi:10.1109/CCCM.2009.5268008

Wilcock, D. F., Bjerklieand, J., and Cheng, H. (1968). Design of floated shoe close clearance seals for supersonic jet engine compressors. *Trans. ASME. J. Tribol.* 90 (2), 500–509. doi:10.1115/1.3601586

Yuan, T., Yang, R., Li, Z., Li, J., Yuan, Q., and Song, L. (2024). Thermal characteristics and cooling effect for SCO2 dry gas seal with multiple dynamic groove types. *Appl. Therm. Eng. Part D.* 236, 121896. doi:10.1016/j.applthermaleng.2023.121896

Zhang, L. D., Wang, X., Zhang, S. S., Ding, J., and Ding, J. (2024). Research progress on the dynamic stability of dry gas seals. *Processes* 12, 575. doi:10.3390/pr12030575

frontiers | Frontiers in Mechanical Engineering

TYPE Original Research
PUBLISHED 21 January 2025
DOI 10.3389/fmech.2024.1469546

Check for updates

OPEN ACCESS

EDITED BY
Thomas Reddyhoff,
Imperial College London, United Kingdom

REVIEWED BY
Jeng Haur Horng,
National Formosa University, Taiwan
Milan Bukvic,
University of Kragujevac, Serbia

*CORRESPONDENCE
Kazuho Takeshima,
takeshima-k@nsk.com

RECEIVED 24 July 2024
ACCEPTED 06 November 2024
PUBLISHED 21 January 2025

CITATION
Takeshima K, Mutoh K, Imanishi K and Oshima S (2025) Mechanisms of cage noise generation in machine tool bearings.
*Front. Mech. Eng.* 10:1469546.
doi: 10.3389/fmech.2024.1469546

COPYRIGHT
© 2025 Takeshima, Mutoh, Imanishi and Oshima. This is an open-access article distributed under the terms of the Creative Commons Attribution License (CC BY). The use, distribution or reproduction in other forums is permitted, provided the original author(s) and the copyright owner(s) are credited and that the original publication in this journal is cited, in accordance with accepted academic practice. No use, distribution or reproduction is permitted which does not comply with these terms.

# Mechanisms of cage noise generation in machine tool bearings

Kazuho Takeshima*, Keisuke Mutoh, Kenji Imanishi and Shunichi Oshima

Technology Development Division Headquarters, NSK Ltd., Fujisawa City, Kanagawa, Japan

Cage instability in ball bearings can lead to torque fluctuations and significant noise. In machine tool spindles, which require high rotational precision, outer ring-guided cages are often preferred over common ball-guided cages. While outer ring-guided cages suppress instability modes caused by sliding friction between the cage and balls, increased interaction between the cage and outer ring can introduce other instability modes, leading to noise. Despite the critical implications of these findings, prior research into this specific type of cage instability, incorporating both experimental and analytical perspectives, remains limited. Therefore, in this study, we utilized a high-speed camera system to conduct visualization tests on cage behavior in grease-lubricated angular contact ball bearings used in machine tools. Through detailed image-processing of the results, we identified specific behaviors associated with cage noise. To facilitate the optimal design of the cage to stabilize these behaviors, we developed a dynamic analysis model focusing on the friction between the cage and the outer ring under grease lubrication, considering fluid pressure effects. The validity of this model was confirmed through experiments at various rotational speeds. This analytical model enabled us to elucidate the underlying mechanisms driving cage instability. The insights gained from this research are expected to significantly enhance the fundamental understanding of cage design principles aimed at eliminating cage noise.

KEYWORDS

**cage instability, cage noise, visualization, high-speed camera system, dynamic analysis, ball bearing, whirl, image processing**

## 1 Introduction

In typical rolling bearings, a cage is utilized to maintain equal spacing among the rolling elements. Interaction occurs between the rolling elements and the cage, where sliding friction between these elements and the rotating cage can induce cage whirl (Kingsbury, 1965). This whirl, when occurring at high speeds, may lead to collisions with the rolling elements, causing deviations from their equidistant arrangements. Such non-repetitive runout compromises the rotational accuracy of the bearing, which is critical in machine tool spindles that require high precision. To mitigate this issue, bearings are often designed with an outer ring-guided cage. This design integrates two distinct types of clearance, as shown in Figure 1. However, challenges arise when the pocket clearance ($c_p$) exceeds the guide clearance ($c_g$), causing the interaction between the cage and outer ring to become dominant. This results in a cage whirl along the shoulder of the outer ring owing to increased sliding

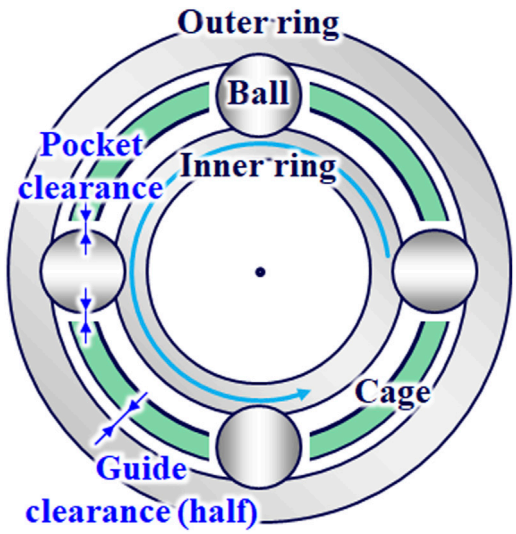


FIGURE 1
Schematic of cage clearance in outer ring-guided type.

friction (Nogi et al., 2018). This whirl is a primary source of severe noise, commonly referred to as cage noise, which significantly degrades the quality of the bearing.

To address and mitigate cage instability, extensive research has been conducted through both experimental (Kingsbury, 1965; Stevens, 1980; Gupta et al., 1986; Boesiger et al., 1992; Kingsbury and Walker, 1994; Stacke and Fritzson, 2001; Servais et al., 2013; Palladino et al., 2017; Chen et al., 2019; Choe et al., 2019; Schwarz et al., 2021; Gao et al., 2022a; Gao et al., 2022b; Liao et al., 2023; Russell, 2023) and analytical methods (Walter, 1971; Kannel and Bupara, 1978; Meeks, 1985; Meeks and Ng, 1985; Gupta et al., 1986; Boesiger et al., 1992; Stacke et al., 1999; Ghaisas et al., 2004; Weinzapfel and Sadeghi, 2009; Ashtekar and Sadeghi, 2012; Nogi et al., 2018; Niu, 2019; Schwarz et al., 2021; Gao et al., 2022a; Gao et al., 2022b; Liao et al., 2023; Russell, 2023). Kingsbury (1965) and Kingsbury and Walker (1994) explored the influence of cage instability on torque variation in rolling bearings. They highlighted the rigid body motion of the cage owing to the sliding friction between the ball and cage as a primary factor causing torque variations. Walter (1971) utilized Euler's equations of motion to describe the non-steady-state dynamics of ball bearings. Kannel and Bupara (1978) investigated the evolution of the cage's rigid body motion without temporal integration, assuming no sliding between the ball and raceways and neglecting the out-of-plane motion of the cage. Their results aligned with the experimental findings of Kingsbury (1965).

Further, Meeks (1985) and Meeks and Ng (1985) performed dynamic analyses on the six degrees of freedom of the cage, assessing the effect of clearance on cage stability. Gupta et al. (1986) developed a comprehensive dynamic analysis program that modeled all the components of a rolling bearing with six degrees of freedom. Boesiger et al. (1992) investigated the impact of a biased cage and operational conditions on cage instability using both experimental and analytical methods. They conducted a dynamic analysis of the rigid-body motion of the cage, considering only planar motion, and confirmed a strong correlation between these results and the experimental results. Ashtekar and Sadeghi (2012) integrated a three-dimensional finite-element model of the cage into a general six-degree-of-freedom bearing dynamics model to examine the effect of elastic deformation of the cage. Servais et al. (2013) developed a method to evaluate cage materials that could potentially reduce cage instability, utilizing the stability map constructed from the coefficients of restitution and friction between the ball and cage.

Choe et al. (2019) conducted an experimental study on the dynamic behavior of a ball bearing cage with mass imbalance in cryogenic environments. Their findings underscore the significant impact of mass imbalance on whirling motion and wear, which align with existing literature. The study also highlights the role of hydraulic forces and suggests that future research should explore the combined effects of mass imbalance and hydraulic forces to enhance understanding of bearing performance. Gao et al. (2022a) developed an advanced dynamic model focusing on cage flexibility and three-dimensional whirling motion in angular contact ball bearings. The model, which neglects fluid pressure effects, divides the self-lubricated cage into segments to assess flexibility and uses multiple coordinate systems to describe ball-cage interactions. The study highlights the need to consider cage flexibility and motion and suggests that future research should address lubricating modes and the impact of varying lubricant amounts on cage behavior. Additionally, Gao et al. (2022b) developed the KH-TEHD model to analyze bearing skidding and cage whirling behavior, incorporating advanced factors such as thermal deformation and elasto-hydrodynamic lubrication, which enhance predictive accuracy in dynamic simulations. This model provides more detailed insights into cage dynamics, particularly under varying operational conditions. However, experimental validation of the cage whirling behavior remains a future research priority to fully confirm the model's effectiveness. Russell (2023) presents an innovative study on the lubrication mechanisms of deep groove ball bearing cages. He introduces the Bearing Cage Friction Test Rig, enabling detailed measurements of friction and lubrication under realistic conditions. The research notably includes a comprehensive model for cage lubrication that addresses cage pocket starvation and varying lubrication environments. Russell's work incorporates extensive computational fluid dynamics (CFD) simulations to analyze lubricant flow and fluid drag within ball bearings, revealing the impact of cage shape on performance. Future challenges include refining lubrication models for high-speed applications and integrating thermal effects into CFD analyses. Nogi et al. (2018) further refined the understanding of cage instability by establishing a critical friction coefficient that determines its occurrence. In addition, it asserts that cage instability could manifest as positive whirl (cage whirls in the direction of its rotation) when $c_p < c_g$ owing to sliding friction with the rolling elements or as negative whirl (cage whirls opposite to its rotation) when $c_p > c_g$ owing to sliding friction with the outer ring.

To optimally design cages that effectively suppress noise in machine tool spindles, it is crucial to utilize a bearing dynamic analysis model that accurately replicates real-world phenomena. Previous research on the generation mechanisms of cage instability, particularly negative whirl in outer ring-guided cages, has been limited. Moreover, these studies have rarely employed a combination of experimental and analytical methods. This study

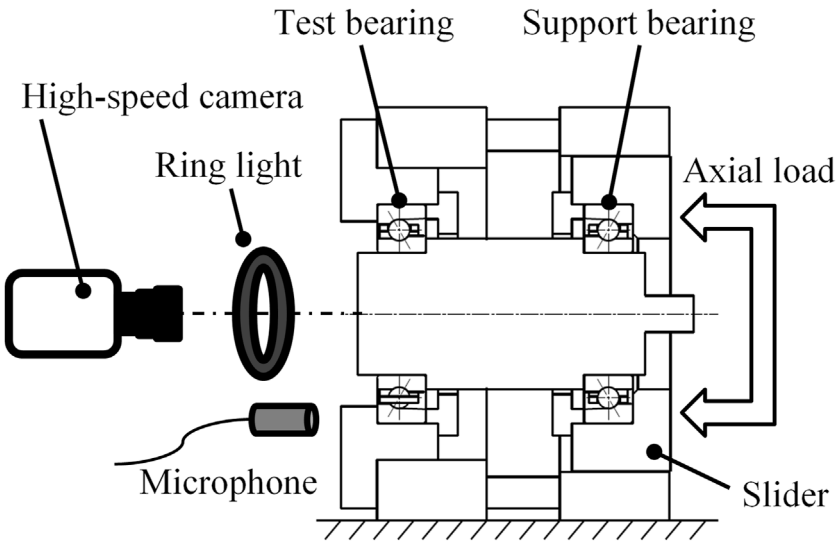


FIGURE 2
Schematic of experimental apparatus.

focuses on grease lubrication, where fluid pressure effects are non-negligible, and includes the experimental validation of a friction model between the cage and the outer ring, which had not been sufficiently verified previously. We intend to achieve this by conducting visualization tests to observe cage behavior directly and applying dynamic analysis.

## 2 Visualization test of cage behavior

### 2.1 Test method

Figure 2 presents a schematic of the testing apparatus used in this study. The apparatus employed an open-type angular contact ball bearing as the test bearing, specified by the bearing dimension series 70. The cage's dimensions include an outer diameter of 110 mm, an inner diameter of 70 mm, and a width of 20 mm. The cage material is phenolic resin with a density of 1,250 kg/m$^3$ and Young's modulus of 9.61 GPa. The cage is a cylindrical type guided by the outer ring, with pocket clearance $c_p$ of 0.555 mm and guide clearance $c_g$ of 0.427 mm. The lubrication was provided by extreme pressure grease, comprising 2.6 g of barium complex soap thickener and mineral oil with a kinematic viscosity of 105 mm$^2$/s at 313 K and 12 mm$^2$/s at 373 K.

The inner ring was mounted on a shaft supported by an angular contact ball bearing of the same series. The outer ring was secured in a fixed housing to restrict its movement. Noise measurement was conducted using a microphone positioned 40 mm from the housing's end face, while a high-speed camera coaxially aligned with the shaft visualized the cage's rigid body motion. High-intensity LED lighting ensured adequate exposure for the camera. An air cylinder attached to the housing exerted a constant axial load ($F_a$), and a motor provided a constant angular velocity ($\omega_z$).

After a 2 h break-in period, sound pressure levels recorded by the microphone and optical images captured by the high-speed camera were synchronously documented. The recording spanned at least 50 shaft rotations, with the camera operating at up to 12,800 frames per second. The recorded area was a 93.75 mm square, equivalent to the diameter of the outer ring shoulder, with an image resolution of 1,024 × 1,024 pixels. This study analyzes results under test conditions of $F_a$ = 687 N and $\omega_z$ ranging from 50 to 8,000 rpm.

It should be noted that, given that the tests were conducted with grease lubrication, the results may be influenced by the characteristics of the grease, such as its viscosity, consistency, and distribution. Therefore, approximately five trials per condition were performed to obtain the data reported in this paper. Within the same test, the occurrence and disappearance of cage noise were repeated, leading to some variability in the frequency of these occurrences. However, it was confirmed that the sound pressure levels during the occurrence of cage noise and the cage whirl velocities, as detailed in Section 2.3, remained relatively consistent under the same conditions. Consequently, this paper presents the most reliable data, including average values and ranges, for comparison with the computational results.

### 2.2 Trajectory of the cage center

To determine the trajectory of the cage center from the test results, image-processing techniques were applied to multiple optical images captured by the high-speed camera. The cage's center of gravity, calculated from its contour in each image, was used to establish the cage's center. This method provided the trajectory data depicted in Figure 3. For each cage rotation, between 200 and 660 optical images were processed. The contour extraction involved binarization, setting a constant brightness threshold for each pixel to ensure the area of the cage contour remained consistent across different frames.

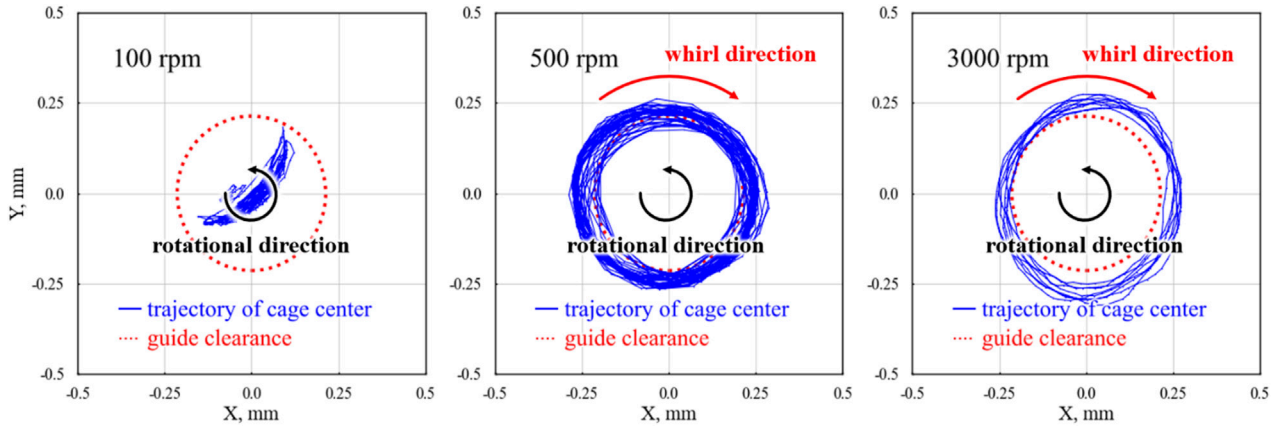


FIGURE 3
Trajectories of cage center during one rotation at $F_a$ = 687 N and $\omega_z$ = 100, 500, and 3,000 rpm in experiment.

In Figure 3, the radial directions of the cage center's inertial coordinates are represented on the vertical and horizontal axes. This presentation shows the results over a single rotation of the cage, including a circle representing the guide clearance diameter. In the present tests, where the rotational speed ($\omega_z$) was incrementally increased in steps, no cage noise was observed at speeds below 100 rpm, whereas cage noise was observed at speeds above 500 rpm. Therefore, the trajectories for conditions at rotational speeds of 100, 500, and 3,000 rpm are shown as representative samples. Notably, the reference origin for each condition is the center of gravity coordinates of the cage trajectory rather than the center of the shaft, considering the convenience of the image-processing technique used.

The observed trajectories suggest that the cage center can exceed the guide clearance owing to the elastic deformation caused by centrifugal forces because of the orbital motion of the cage. At $\omega_z$ = 100 rpm, the cage center exhibits a wobbling motion, forming a crescent-shaped trajectory without generating any detectable noise. At higher speeds, $\omega_z$ = 500 and 3,000 rpm, the cage performs a circular motion within the guide clearance. During one cage rotation, multiple revolutions of orbital motion occurred, with the orbital direction opposite to the rotation direction, indicating negative whirl. Noise associated with the cage was detected under these conditions.

The forces acting on the cage include contact and friction from the rolling elements and outer ring, as well as gravity. In particular, when the relationship between pocket clearance $c_p$ and guide clearance $c_g$ is $c_p > c_g$, the interaction with the outer ring becomes dominant. At $\omega_z$ = 100 rpm, the cage's wobbling is interpreted to center around an equilibrium position where the friction force from the outer ring counterbalances gravity acting in the negative $y$-axis direction. The wobble radius closely aligns with half of the guide clearance ($c_g/2$), suggesting it wobbles along the outer ring shoulder. At $\omega_z$ = 500 and 3,000 rpm, similar forces act, but increased centrifugal force at higher rotational speeds increases the contact and friction forces from the outer ring, thereby making the friction force predominant over gravity, resulting in negative whirl.

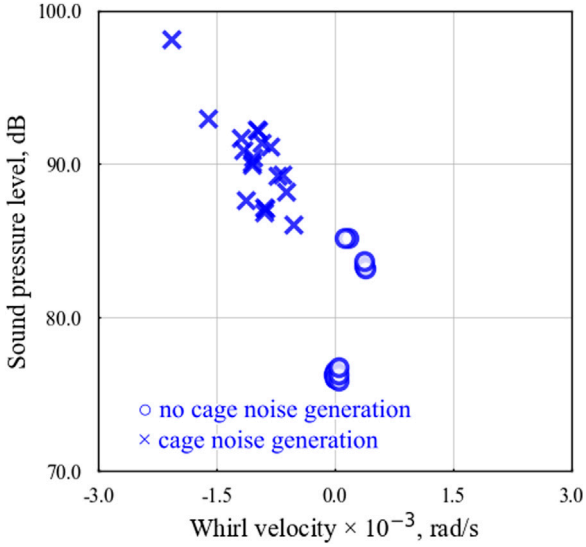


FIGURE 4
Relationship between cage whirl velocity and sound pressure level by microphone at $\omega_z$ = 50–8,000 rpm in experiment.

## 2.3 Effect of cage whirl on cage noise

Analysis of Figure 3 involved calculating the angle between the time-varying cage center coordinates and the origin. The derivative of this angle with respect to time was then used to compute the cage's whirl velocity. These calculations allowed us to determine the time-averaged whirl velocity and time-averaged sound pressure during a single rotation of the cage, as shown in Figure 4. The graph plots time-averaged whirl velocity on the horizontal axis against time-averaged sound pressure on the vertical axis. Positive whirl velocity values indicate the cage orbiting in the same direction as its rotation, whereas negative values indicate an orbit in the opposite direction. Data points are marked with an "x" for cases where cage noise was audibly detected and with an "o" where noise was absent. Given the intermittent nature of the cage noise observed, data points at the beginning, middle, and end of each test condition were plotted.

TABLE 1 Definition of two types of cage motion in this experiment.

| Type of cage motion | Cage noise |
|---|---|
| **Steady**:<br>Absolute value of cage whirl velocity is less than 500 rad/s | Inaudible |
| **Negative whirl**:<br>Cage whirl velocity is less than −500 rad/s. Direction of cage rotation and cage whirl is different | Audible |

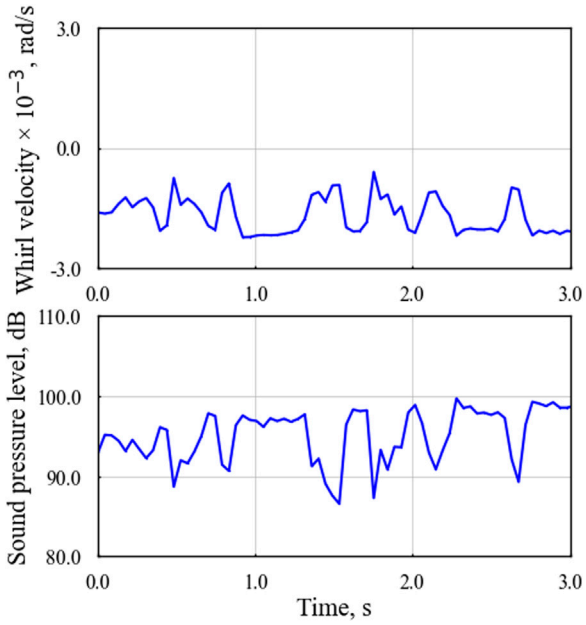


FIGURE 5
Comparison between temporal changes in whirl velocity (first row) and sound pressure level (second row) at $\omega_z$ = 3,000 rpm (negative whirl generation) in experiment.

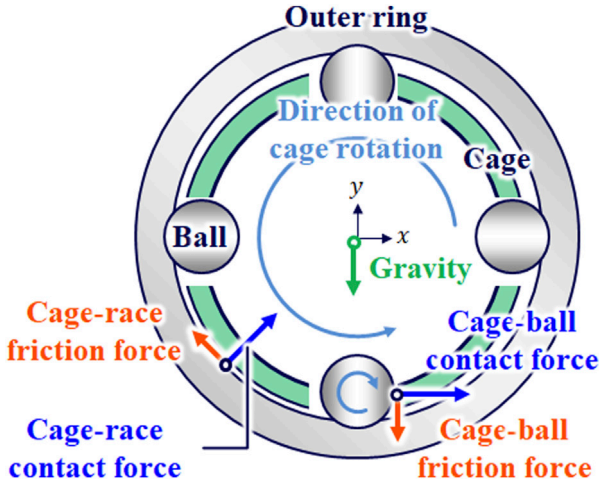


FIGURE 6
Schematic of forces on cage.

From the data represented in Figure 4, test results can be categorized into two distinct types of cage behavior, detailed in Table 1. This categorization has allowed for the clear identification that negative whirl significantly contributes to the generation of cage noise. For a representative condition where negative whirl was observed, we further analyzed the time variations of whirl velocity and sound pressure. These findings are illustrated in Figure 5, where the upper panel shows the time variation of the whirl velocity, and the lower panel shows the corresponding sound pressure variations. The timing of fluctuations in these two measurements generally aligns, corroborating that negative whirl is a principal factor in the generation of cage noise.

# 3 Analytical method

## 3.1 Equations of motion

This section outlines the analytical model developed to replicate the negative whirl observed in experimental settings, effectively capturing the essence of the phenomenon. This approach is instrumental in fundamentally addressing cage noise. To simplify the understanding of the phenomenon and reduce computational costs, a streamlined mechanical model comprising minimal elements is employed. For dynamic analysis of bearing focusing on cage behavior, Kannel and Bupara (1978) and Boesiger et al. (1992) investigated the in-plane motion of a rigid cage, validating this assumption through experimental data. According to Nogi et al. (2018), negative whirl primarily results from sliding friction between the cage and the outer ring. Therefore, this study focuses on the in-plane motion of a rigid cage, disregarding the interaction between the rolling elements and the raceways, with each rolling element theoretically orbiting at equal intervals. Thus, the equations of motion are confined to those of the cage.

The motion of a rigid cage, with two degrees of freedom for translation and one for rotation, is governed by the following equations based on Newton's laws:

$$m\ddot{x} = F_x, \tag{1}$$

$$m\ddot{y} = F_y, \tag{2}$$

$$I_z\ddot{\theta} = M_z, \tag{3}$$

where $m$ is the mass of the cage, $I_z$ is the moment of inertia about its rotational axis, $F_x$ and $F_y$ are the resultant forces in the $x$ and $y$ directions, respectively, and $M_z$ is the resultant moment about the axis of rotation.

A moving coordinate system, fixed at the cage center, facilitates analysis of the forces acting on the cage. The direction of cage eccentricity is denoted as the $\varepsilon$-axis, while the orthogonal direction is termed the $\varphi$-axis. The transformation from the moving coordinate

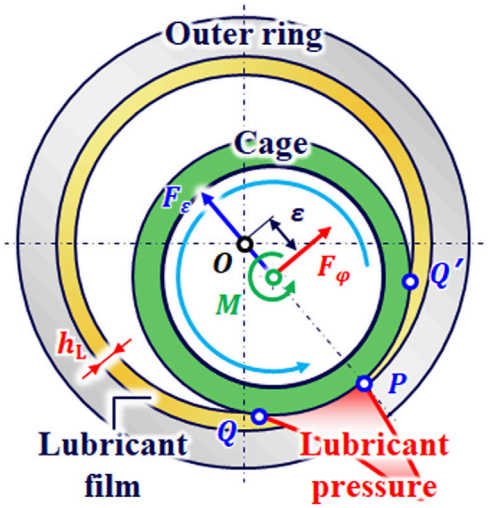


FIGURE 7
Schematic of lubricant forces on cage/race (balls were excluded for visibility).

system to the inertial coordinate system is expressed by the following Equation 4 for the rotation matrix:

$$\begin{bmatrix} F_x \\ F_y \end{bmatrix} = \begin{bmatrix} \cos\varphi & -\sin\varphi \\ \sin\varphi & \cos\varphi \end{bmatrix} \begin{bmatrix} F_\varepsilon \\ F_\varphi \end{bmatrix}, \tag{4}$$

where $\varphi$ is the angle between the $\varepsilon$-axis and the $y$-axis ($0 < \varphi < 2\pi$).

Figure 6 shows the forces acting on the cage, encompassing contact and friction forces from the rolling elements and outer ring, as well as gravity, as outlined in Section 2.2.

## 3.2 Interaction between the cage and rolling elements

The contact state between the cage and rolling elements is effectively modeled by a series connection of the contact stiffness, as determined by Hertzian contact theory, and the deflection stiffness of the cage (Boesiger et al., 1992). Given that the contact stiffness substantially exceeds the deflection stiffness, only the latter is considered significant. A linear Voigt model, consisting of a spring and a dashpot in parallel, is employed as the contact model. The Coulomb friction model is used for the friction calculations.

## 3.3 Interaction between the cage and the outer ring

When examining the interaction between the cage and the outer ring, relying solely on solid contact and Coulomb friction was found to predict a negative whirl velocity approximately ten times greater than what was observed experimentally. Furthermore, to induce negative whirl using a solid friction model, an unrealistically high Coulomb friction coefficient of at least 0.6 was required. Thus, the impact of fluid friction in this interaction cannot be ignored. As shown in Figure 7, the case where the cage center is eccentrically displaced by $\varepsilon$ is considered. Given the study's focus on grease lubrication, it is not assumed that the clearance is consistently filled with grease. It is assumed that a uniform thickness, $h_L$, of lubricant exists on the shoulder of the outer ring, with $h_L$ treated as a constant input value. This model does not account for changes in film thickness due to side leakage or scooping. The presence of lubricant subjects the cage to film pressure and shear force, assumed to act within the geometrically contactable region between the cage and the lubricant (from $\angle POQ$ to $\angle POQ'$). To simplify the representation of cavitation, the film pressure is considered zero in regions of negative pressure.

The analysis also necessitates addressing collision phenomena. The pressure dependency of viscosity in the fluid lubrication model is described by the following equation (Barus, 1893):

$$\eta = \eta_0 \ \exp(\alpha P), \tag{5}$$

where $\eta_0$ is the base oil viscosity, and $\alpha$ is the pressure-viscosity coefficient. Furthermore, owing to potential interference between the cage and the outer ring, contact and friction models are adapted based on the cage's eccentricity, $\varepsilon$. Given that both solid contact and fluid lubrication can occur owing to the surface roughness of the cage, the metal contact ratio $\lambda_r$, as defined by Aihara (1987), is employed in the following Equation 6:

$$\lambda_r = 1 - \exp\left(1.8\Lambda^{1.2}\right), \tag{6}$$

where $\Lambda$ represents the film thickness ratio, calculated as the minimum film thickness between the cage and the outer ring divided by the surface roughness.

Table 2 outlines the friction model between the cage and the outer ring, considering the following three contact states:

1. When $c_g/2 - h_L \geq \varepsilon$:

In this pattern, the cage and lubricant do not geometrically contact, resulting in no interaction between the cage and the outer ring.

2. When $\varepsilon > c_g/2 - h_L$ and $\Lambda > 0$:

This scenario involves geometric contact between the cage and lubricant where the film thickness ratio $\Lambda > 0$. Here, both solid contact and fluid lubrication occur owing to the surface roughness of the cage, linked via the metal contact ratio $\lambda_r$.

3. When $\varepsilon > c_g/2 - h_L$ and $\Lambda \leq 0$:

This signifies geometric contact with a film thickness ratio $\Lambda \leq 0$, indicating interference between the rigid cage and the outer ring. This is considered a transient state where only solid contact is modeled.

The forces acting on the cage, as delineated in Table 2, are formulated under various conditions. Under solid contact, the Voigt model and Coulomb friction, as outlined in Section 3.2, are applied. For fluid lubrication scenarios, the forces derive from Reynolds' equation, considering the dominance of axial flow due to the cage width being typically less than one-fourth of the outer diameter. This scenario applies the theory of short-width journal bearings. The

TABLE 2 Constructed friction model on cage/race.

| Force acting on cage | | Forces acting in each region | | | |
|---|---|---|---|---|---|
| | | $c_g/2 - h_L \geq \varepsilon$ | $\varepsilon > c_g/2 - h_L$ | | |
| | | | $\Lambda > 0$ | | $0 \geq \Lambda$ |
| Fluid lubrication | Force due to lubricant pressure (Reynolds equations) | — | Coupling by metal contact ratio $\lambda_r$ | Adoption | — |
| | Force due to shear (Reynolds equations) | — | | Adoption | — |
| Solid contact | Contact force (Voigt model) | — | | Adoption | Adoption |
| | Friction force (Coulomb friction model) | — | | Adoption | Adoption |

validity of this approach was confirmed through point contact elastohydrodynamic lubrication analysis, focusing on the interaction between the cage and the outer ring, which demonstrated that oil film pressure and tangential forces due to shear do not significantly affect the results.

The Reynolds equation is derived under this assumption, based on Cameron (1971), in the following Equations 7 and 8:

$$\frac{\partial}{\partial y}\left(\frac{h^3}{\eta}\frac{\partial p}{\partial y}\right) = 6(u_1+u_2)\frac{\partial h}{\partial x} + 12\frac{\partial h}{\partial t}, \tag{7}$$

$$h = C(1+\varepsilon\cos\theta), \tag{8}$$

where $h$ is the oil film thickness, $u_1$ and $u_2$ are the surface velocities of the cage and outer ring, $C$ is half the guide clearance, and $\varepsilon$ is the eccentricity, respectively.

Assuming $\eta$ as defined in Equation 5, Equation 7 cannot be solved algebraically using the approach for short-width journal bearings. Based on Cameron (1971), we apply Equation 9 to transform Equation 7. This transformation necessitates the case distinctions described in Equation 10, but the resulting modified Reynolds Equation 11 can then be solved algebraically.

$$q = (1 - e^{-\alpha p})/\alpha. \tag{9}$$

$$p = \begin{cases} -\frac{1}{\alpha}\ln(1-\alpha q) \text{ at } q < 1/\alpha \\ q \text{ at } q \geq 1/\alpha \end{cases} \tag{10}$$

$$\frac{\partial^2 q}{\partial y^2} = \frac{6\eta_0}{h^3}\left((u_1+u_2)\frac{\partial h}{\partial x} + 2\frac{\partial h}{\partial t}\right). \tag{11}$$

Integrating Equation 11 with boundary conditions from Equation 12 yields Equation 13.

$$p(L/2) = p(-L/2) = 0 \tag{12}$$

$$q = -\frac{3\eta_0}{h^3}\left((u_1+u_2)\frac{\partial h}{\partial x} + 2\frac{\partial h}{\partial t}\right)\left(\frac{L^2}{4} - y^2\right) \tag{13}$$

To simplify the representation of cavitation, the pressure is set to zero in regions of negative pressure. From Equations 10, 13, the oil film pressure is derived as

$$p = \begin{cases} \max\left[0, -\frac{1}{\alpha}\ln\left(1 + \frac{3\alpha\eta_0}{h^3}\left((u_1+u_2)\frac{\partial h}{\partial x} + 2\frac{\partial h}{\partial t}\right)\left(\frac{L^2}{4} - y^2\right)\right)\right] \text{ at } q < 1/\alpha \\ \max\left[0, -\frac{3\eta_0}{h^3}\left((u_1+u_2)\frac{\partial h}{\partial x} + 2\frac{\partial h}{\partial t}\right)\left(\frac{L^2}{4} - y^2\right)\right] \text{ at } q \geq 1/\alpha \end{cases} \tag{14}$$

Pressure-induced forces $F_{P-\varepsilon}$ and $F_{P-\varphi}$ acting on the cage center are calculated from the following Equations 15 and 16:

$$F_{P-\varepsilon} = R\int_{-L/2}^{L/2}\int_{\pi-\theta_c}^{\pi+\theta_c} p\cos\theta \mathrm{d}\theta\mathrm{d}y, \tag{15}$$

$$F_{P-\varphi} = R\int_{-L/2}^{L/2}\int_{\pi-\theta_c}^{\pi+\theta_c} p\sin\theta \mathrm{d}\theta\mathrm{d}y, \tag{16}$$

where $\theta_c$ is ∠POQ in Figure 7.

The shear force acting on the cage is calculated based on journal bearing theory (Cameron, 1971), as shown by Equations 17–20. Here, $F_S$ and $M_S$ represent the forces and moments acting on the cage center, respectively. It is important to note that the parameter $p$, which appears in Equation 17, is defined in Equation 14. Consequently, the calculations for Equations 18–20 necessarily require numerical integration.

$$\tau = \frac{\partial p}{\partial x}\frac{h}{2} + \frac{\eta(u_1-u_2)}{h} \tag{17}$$

$$F_{S-\varepsilon} = R\int_{-L/2}^{L/2}\int_{\pi-\theta_c}^{\pi+\theta_c} \tau\sin\theta \mathrm{d}\theta\mathrm{d}y \tag{18}$$

$$F_{S-\varphi} = R\int_{-L/2}^{L/2}\int_{\pi-\theta_c}^{\pi+\theta_c} \tau\cos\theta \mathrm{d}\theta\mathrm{d}y \tag{19}$$

$$M_S = R^2\int_{-L/2}^{L/2}\int_{\pi-\theta_c}^{\pi+\theta_c} \tau \mathrm{d}\theta\mathrm{d}y \tag{20}$$

Thus, the resultant forces acting on the cage from the interaction with the outer ring are detailed in Equations 21, 22.

$$F_\varepsilon = \lambda_r(F_{P-\varepsilon} + F_{S-\varepsilon}) + (1-\lambda_r)F_{DC} \tag{21}$$

$$F_\varphi = \lambda_r\left(F_{P-\varphi} + F_{S-\varphi}\right) + (1-\lambda_r)F_{DF} \tag{22}$$

Here, $F_{DC}$ and $F_{DF}$ represent the contact and friction forces under solid contact, respectively.

## 3.4 Analytical conditions

Table 3 lists the analytical conditions, which correspond to those under which negative whirl was observed in the experiments

TABLE 3 Analytical conditions.

| Parameter | Value | Parameter | Value |
|---|---|---|---|
| Cage mass | 0.01 kg | Number of balls | 25 |
| Cage moment of inertia | $2.05 \times 10^{-5}$ kg m$^2$ | Ball pitch diameter | 89.0 mm |
| Cage outside diameter | 93.3 mm | Pocket clearance | 0.555 mm |
| Cage inside diameter | 87.9 mm | Guide clearance | 0.427 mm |
| Cage contact width with outer ring | 4.0 mm | Frictional coefficient of cage/ball | 0.1 |
| Ball diameter | 8.73 mm | Frictional coefficient of cage/ring | 0.1 |
| Contact stiffness of cage/ball and cage/ring | $1.5 \times 10^6$ N/m | Angular velocity of ball rotation | 1,587 rad/s |
| Contact damping ratio of cage/ball and cage/ring | 0.2 | Angular velocity of ball orbit | 142.5 rad/s |
| Viscosity | 87.2 mPa·s | Initial oil layer thickness on ring | 42.7 μm |
| Pressure-viscosity coefficient | 20 GPa$^{-1}$ | Rms roughness of cage/ring | 1.6 μm |

described in Section 2. Here, the angular velocities of ball rotation and orbit are set to values corresponding to an inner ring rotational speed of $\omega_z$ = 3,000 rpm. The initial conditions are set with the cage center at coordinates $x = 0$, $y = 0$ and the cage's angular velocity at 142.5 rad/s. The analysis period is defined as 100 ms, within which the cage's behavior is expected to stabilize. During this interval, the cage completes approximately 4.5 rotations.

The simulation addresses the dynamic problem of the cage's contact or non-contact with the rolling elements and the outer ring, which varies over time. This variability renders Equations 1–3 as stiff differential equations. To effectively manage these, the LSODA (Petzold, 1983) numerical integration algorithm was utilized. LSODA is an algorithm that automatically switches between the Adams method and the BDF method depending on the stiffness of the ODE, allowing for efficient and accurate solutions to ODEs. It is important to note that although the BDF method selects the optimal scheme to ensure the accuracy and stability of the solution, higher-order schemes are known to increase numerical errors. Therefore, we compared the analysis results obtained using LSODA with those obtained using the Radau method, which is considered less susceptible to errors under similar conditions, and confirmed their consistency. In this study, we adopted LSODA, which has a proven track record in similar bearing dynamic analyses (e.g., Boesiger et al., 1992).

# 4 Analytical results

## 4.1 Cage motion

Figure 8 illustrates the trajectory of the cage center and the temporal changes in cage whirl velocity. It also shows the maximum and minimum whirl velocities observed during negative whirl events, as detailed in the visualization tests described in Section 2. The trajectory of the cage center reveals orbital motion, with trends broadly matching the experimental results shown in Figure 3 (right). The orbital radius remains consistently within the guide clearance, suggesting that the cage stays in contact with the outer ring via the lubricant. It is important to note that this analysis assumes a rigid cage; thus, unlike the experimental results, the cage center does not exceed the guide clearance due to elastic deformation caused by centrifugal force. From 25 ms onward, the whirl velocity remains generally constant and negative, signifying a steady-state condition characterized by continuous negative whirl. A comparative analysis between experimental and analytical whirl velocities indicates a discrepancy ranging from approximately 1.2–2.3 times. In contrast, an analysis based solely on solid contact and Coulomb friction between the cage and the outer ring resulted in a whirl velocity approximately ten times higher than the experimental value, indicating significant enhancements achieved with the analytical model introduced in Section 3.

The model expansion to include more degrees of freedom provides a nuanced representation of the forces driving the cage, encompassing contact, friction, and inertia. While the model discussed in Section 3 initially considered only the radial plane motion of a two-dimensional cage, extending this model to three dimensions allows for the resolution of the driving forces in the axial direction as well. This extension is expected to reduce the absolute value of the whirl velocity, which has been primarily determined within the radial plane, thereby aligning it more closely with the experimental findings.

## 4.2 Forces acting on the cage

Figure 9 shows the time variation of the tangential force $F_\varphi$ acting on the cage center. Under the current analytical conditions, there was no solid contact between the cage and the outer ring; thus, only fluid forces were involved. The force $F_\varphi$ is critical in inducing cage whirl, leading to positive whirl when positive and negative whirl when negative. Specifically, the oil film pressure force $F_{P-\varphi}$ tends to induce positive whirl, whereas the shear force $F_{S-\varphi}$ tends to induce negative whirl. The mechanism by which $F_{S-\varphi}$ induces negative whirl is linked to the direction of the shear force, which opposes the sliding velocity of the cage. This sliding velocity, determined by the rotational and translational speeds of the cage, predominantly aligns

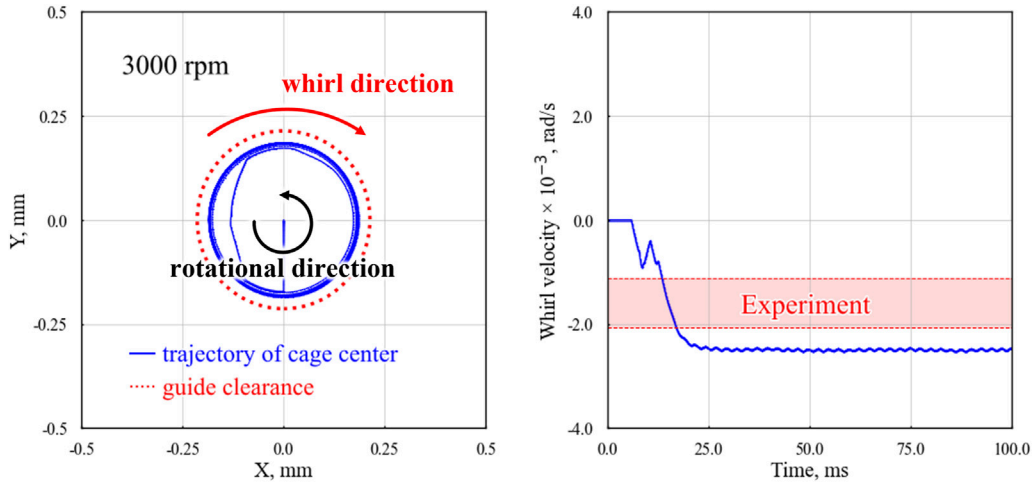


FIGURE 8
Trajectory of cage center (left column) and temporal change in cage whirl velocity (right column) in analysis.

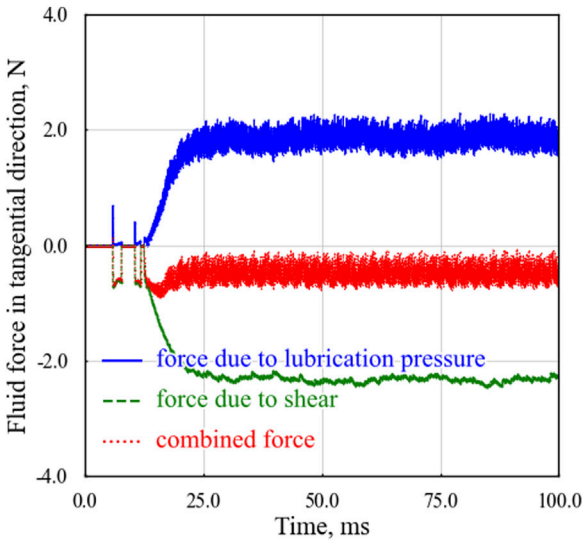


FIGURE 9
Temporal changes in fluid forces on cage/race in tangential direction in analysis.

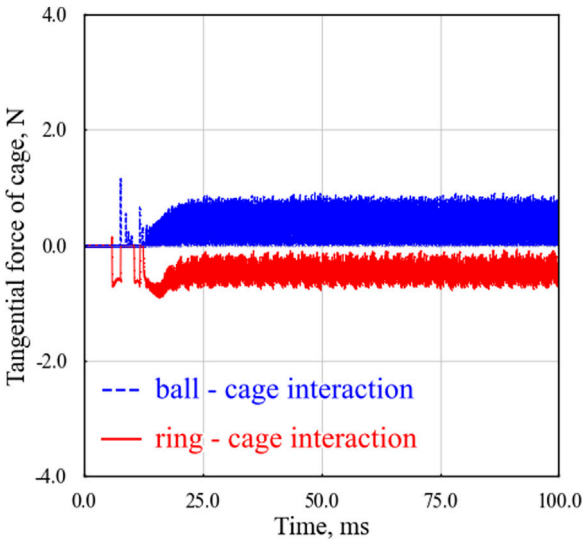


FIGURE 10
Temporal changes in tangential forces of cage by ball/cage interaction and ring/cage interaction in analysis.

with the cage's rotation direction. $F_{S-\varphi}$ acts in the opposite direction thereby inducing negative whirl.

The positive whirl induced by $F_{P-\varphi}$ can be elucidated by Figure 7, where the steady-state oil film pressure is influenced by the wedge effect. This effect generates positive pressure on the entry side and negative pressure on the exit side of the cage. Given the consideration of cavitation, the oil film pressure on the exit side is effectively zero. By integrating the oil film pressure along the arc from $Q$ to $P$, the resultant force aligns with the direction of cage rotation, causing $F_{P-\varphi}$ to induce positive whirl.

Figure 8 reveals that for $t > 25$ ms, a consistent negative whirl velocity occurs, and the forces acting on the cage reach equilibrium. However, focusing on $t \leq 25$ ms in Figure 9, $F_{S-\varphi}$ (inducing negative whirl) rises earlier than $F_{P-\varphi}$ (which counters negative whirl), indicating the initial cause of negative whirl.

In the steady state at $t > 25$ ms, the average value of the resultant force, as shown in Figure 9, is marginally negative. This suggests the presence of a counteracting force that moderates an increase in negative whirl. Figure 10 shows the time variation of the tangential force resulting from the interactions between the outer ring and the cage and between the rolling elements and the cage. The interaction with the rolling elements generates a tangential force that induces positive whirl, effectively balancing the tangential force that induces negative whirl owing to the interaction with the outer ring for $t > 25$ ms.

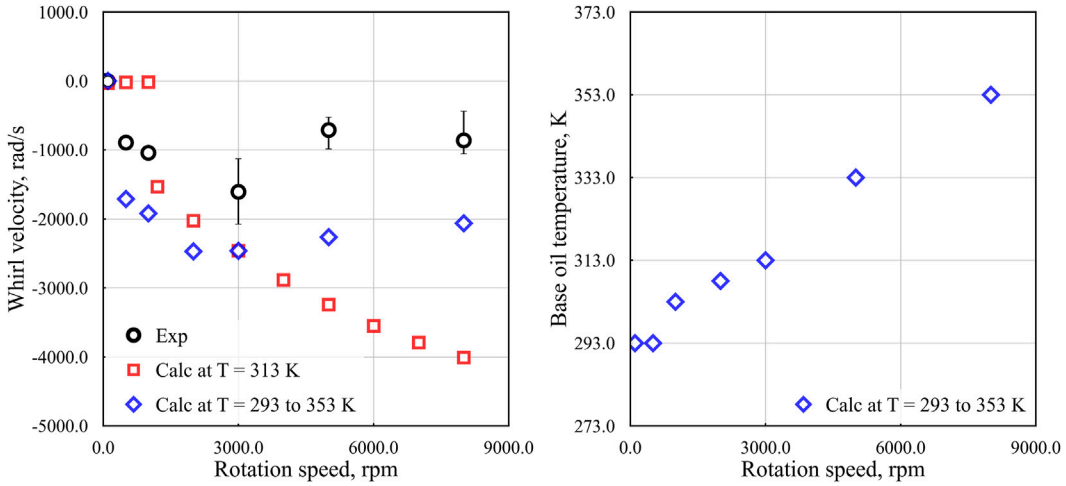


FIGURE 11
Effect of rotational speed on whirl velocity (left column) and base oil temperature used in analysis (right column).

## 4.3 Effect of rotational speed on cage instability

In the content up to Section 4.2, we constructed and validated an analytical model capable of reproducing the negative whirl observed in the 3,000 rpm experiment. In this section, to examine the applicability of this model to other rotational speeds, we evaluated the rotational speed dependency of cage whirl. The analytical conditions were based on those shown in Table 3, with only the angular velocity of ball rotation and orbit adjusted to match the inner ring rotational speed. In the experiment described in Section 2, the cooling effect was not expected due to the influence of grease lubrication, and it is considered that the guide surface experienced heating as the rotational speed increased, potentially leading to a decrease in the viscosity of the base oil on the guide surface. Here, two analytical conditions regarding the base oil temperature were set to identify the parameters needed to reproduce the cage behavior observed in the experiment. Specifically, one condition set a constant temperature regardless of rotational speed, and the other allowed the temperature to vary depending on the rotational speed. It should be noted that the base oil temperatures used in the analysis are reference values, as the guide surface temperatures were not measured in the experiments described in Section 2. The relationship between temperature and viscosity was considered using Walther's equation (ASTM International, 1993).

The analytical results are shown in Figure 11. The left side of the figure shows the rotational speed dependency of the whirl velocity, with the experimental results also included. For each condition, the average values are plotted, and error bars indicating the upper and lower bounds are shown. Regarding the temperature settings in the analysis, the condition of constant temperature used 313 K, as in the content up to Section 4.2, while for the condition where temperature varies with rotational speed, the temperature was explored through trial and error to reproduce the cage behavior observed in the experiment. The right side of the figure shows the base oil temperatures determined for each rotational speed.

The analysis with the base oil temperature fixed at 313 K showed that the cage exhibited stable behavior at rotational speeds below $N < 1{,}100$ rpm, while negative whirl occurred at $N \geq 1{,}100$ rpm. The absolute value of the whirl velocity also tended to increase with increasing rotational speed. However, this result qualitatively differs from the experimental findings, suggesting that the analytical model requires further refinement.

On the other hand, the analysis with the base oil temperature adjusted for each rotational speed indicated that the cage behavior qualitatively matched the experimental results when the temperature increase was determined through trial-and-error adjustments. This observation suggests that the base oil temperature had a significant impact on the experimental outcomes described in Section 2, underscoring the necessity of considering this factor when assessing cage instability in grease-lubricated systems. Additionally, while shear thinning is often considered in the modeling of grease lubrication, it was concluded that this effect could be neglected in this analysis due to the oil film thickness being on the order of tens of micrometers. However, this conclusion may lack sufficient supporting evidence. Therefore, future research should focus on measuring the guide surface temperature, visualizing the lubrication state during testing, and measuring the torque exclusively on the guide surface. These approaches are expected to provide a deeper understanding of cage behavior.

# 5 Conclusion

This study aimed to elucidate the mechanism of cage noise generation in outer ring-guided cages of machine tool spindles. Through visualization tests and bearing dynamic analysis, it was revealed that negative whirl—where the cage whirls in the opposite direction of its rotation—is a significant contributor to cage noise.

These visualization tests showed clear evidence of this phenomenon during noise-generation events.

To accurately simulate this behavior, friction models between the cage and the outer ring, identified as the primary cause of negative whirl, were examined and integrated into a bearing dynamic analysis model. This model successfully replicated cage behaviors that qualitatively matched experimental observations and was validated under various rotational speeds by accounting for the effects of base oil temperature. Furthermore, an examination of the time variation of forces acting on the cage clarified the specific mechanisms responsible for the generation of negative whirl. Understanding these mechanisms enhances the fundamental comprehension of cage design and its implications for noise reduction in machine tool spindles.

Additionally, advancements in analytical methods are expected to reduce prototyping costs and lower environmental impact. The ease of conducting parametric studies is a notable feature of this approach, which could also contribute to shortened development times. These advancements are anticipated to address fundamental issues and enhance the maintainability of the developed bearings.

However, this study focused solely on the in-plane motion of a rigid cage. In practical applications, the three-dimensional motion of the cage, including its deformation and tilt motion, plays a critical role. To achieve higher precision in future analyses, these factors should be incorporated, which can provide a more comprehensive understanding of cage dynamics. For example, as noted in previous research (Ashtekar and Sadeghi, 2012; Gao et al., 2022a; Gao et al., 2022b), treating the cage as an elastic body allows for the consideration of deformation due to centrifugal forces. This approach enables the representation of reduced contact pressure on the guide surface and a decrease in the effective eccentricity of the cage. By integrating this approach with the analytical method proposed in this paper, not only can the friction on the cage guide surface be calculated with greater precision, but this method may also prove to be a powerful tool for investigating the impact of cage material on cage instability.

## Data availability statement

The original contributions presented in the study are included in the article/supplementary material, further inquiries can be directed to the corresponding author.

## Author contributions

KT: Conceptualization, Data curation, Formal Analysis, Investigation, Methodology, Software, Validation, Writing–original draft. KM: Conceptualization, Data curation, Investigation, Methodology, Project administration, Software, Validation, Visualization, Writing–review and editing. KI: Supervision, Writing–review and editing. SO: Supervision, Writing–review and editing.

## Funding

The author(s) declare that no financial support was received for the research, authorship, and/or publication of this article.

## Conflict of interest

Authors KT, KM, SO, and KI were employed by NSK Ltd.

## Publisher's note

All claims expressed in this article are solely those of the authors and do not necessarily represent those of their affiliated organizations, or those of the publisher, the editors and the reviewers. Any product that may be evaluated in this article, or claim that may be made by its manufacturer, is not guaranteed or endorsed by the publisher.

## References

Aihara, S. (1987). A new running torque formula for tapered roller bearings under axial load. *J. Tribol.* 109 (7), 471–477. doi:10.1115/1.3261475

Ashtekar, A., and Sadeghi, F. (2012). A new approach for including cage flexibility in dynamic bearing models by using combined explicit finite and discrete element methods. *ASME J. Tribol.* 134 (10), 041502. doi:10.1115/1.4007348

ASTM International (1993). *Standard practice for viscosity-temperature charts for liquid petroleum products, ASTM d341-93*. West Conshohocken, PA: ASTM International.

Barus, C. (1893). Isothermals, isopiestics and isometrics relative to viscosity. *Am. J. Sci.* 266 (2)–87. doi:10.2475/ajs.s3-45.266.87

Boesiger, E. A., Donley, A. D., and Loewenthal, S. (1992). An analytical and experimental investigation of ball bearing retainer instabilities, ASME J. *Tribology* 114 (7)–531. doi:10.1115/1.2920915

Cameron, A. (1971). *Basic lubrication theory*. London, United Kingdom: Longman.

Chen, S., Chen, X., Zhang, T., Li, Q., and Gu, J. (2019). Cage motion analysis in coupling influences of ring guidance mode and rotation mode. *Jpn. Soc. Mech. Eng.* 13, JAMDSM0054. doi:10.1299/jamdsm.2019jamdsm0054

Choe, B., Kwak, W., Jeon, D., and Lee, Y. (2019). Experimental study on dynamic behavior of ball bearing cage in cryogenic environments, Part II: effects of cage mass imbalance. *Mech. Syst. Signal Process.* 116, 25–39. doi:10.1016/j.ymssp.2018.06.034

Gao, S., Chatterton, S., Pennacchi, P., Han, Q., and Chu, F. (2022a). Skidding and cage whirling of angular contact ball bearings: kinematic-Hertzian contact-thermal-elasto-hydrodynamic model with thermal expansion and experimental validation. *Mech. Syst. Signal Process.* 166, 108427. doi:10.1016/j.ymssp.2021.108427

Gao, S., Han, Q., Zhou, N., Pennacchi, P., Chatterton, S., Qing, T., et al. (2022b). Experimental and theoretical approaches for determining cage motion dynamic characteristics of angular contact ball bearings considering whirling and overall skidding behaviors. *Mech. Syst. Signal Process.* 168, 108704. doi:10.1016/j.ymssp.2021.108704

Ghaisas, N., Wassgren, C. R., and Sadeghi, F. (2004). Cage instabilities in cylindrical roller bearings, ASME J. *Tribology* 126 (10)–681. doi:10.1115/1.1792674

Gupta, P. K., Dill, J. F., Artuso, J. W., and Forster, N. H. (1986). Ball bearing response to cage unbalance. *ASLE Trans.* 30 (1)–55. doi:10.1115/1.3261240

Kannel, J. W., and Bupara, S. S. (1978). A simplified model of cage motion in angular contact bearings operating in the EHD lubrication regime. *ASME J. Tribol.* 100 (7), 395–403. doi:10.1115/1.3453196

Kingsbury, E., and Walker, R. (1994). Motions of an unstable retainer in an instrument ball bearing, ASME J. *Tribology* 116 (4)–203. doi:10.1115/1.2927197

Kingsbury, E. P. (1965). Torque variations in instrument ball bearings. *ASLE Trans.* 8, 435–441. doi:10.1080/05698196508972113

Liao, H., Xie, P., Deng, S., Zhang, W., Shi, L., and Zhao, S. (2023). Investigation of dynamic characteristics experiments and stability evaluation criterion of space ball bearing cage. *Tribol. Trans.* 66 (3), 453–465. doi:10.1080/10402004.2022.2163015

Meeks, C. R. (1985). The dynamics of ball separators in ball bearings - Part II: results of optimization study. *ASLE Trans.* 28 (3), 288–295. doi:10.1080/05698198508981623

Meeks, C. R., and Ng, K. O. (1985). The dynamics of ball separators in ball bearings - Part I: analysis. *ASLE Trans.* 28 (3), 277–287. doi:10.1080/05698198508981622

Niu, L. (2019). A simulation study on the effects of race surface waviness on cage dynamics in high-speed ball bearings. *ASME J. Tribol.* 141 (5), 051101. doi:10.1115/1.4042656

Nogi, T., Maniwa, K., and Matsuoka, N. (2018). A dynamic analysis of cage instability in ball bearings. *ASME J. Tribol.* 140 (11), 011101. doi:10.1115/1.4036451

Palladino, M., Neglia, S. G., and Wygachiewicz, M. (2017). Analysis and monitoring of cage dynamics in ball bearings for space applications. *Procs ESMATS*.

Petzold, L. R. (1983). Automatic selection of methods for solving stiff and nonstiff systems of ordinary differential equations. *SIAM J. Sci. Stat. Comput.* 4 (1), 136–148. doi:10.1137/0904010

Russell, T. C. (2023) *Investigation into the lubrication mechanism of the ball bearing cage*. West Lafayette, Indiana: Purdue University ProQuest Dissertations and Theses. 30741226.

Schwarz, S., Grillenberger, H., Tremmel, S., and Wartzack, S. (2021), Investigations on the rolling bearing cage dynamics with regard to different operating conditions and cage properties, *IOP Conf. Ser. Mater. Sci. Eng.* 1097, 012009. doi:10.1088/1757-899x/1097/1/012009

Servais, C., Duquenne, M., and Bozet, J.-L. (2013). Influence of tribology of cage material on ball bearing cage instability. *ESMATS* 9.

Stacke, L. E., and Fritzson, D. (2001). Dynamic behaviour of rolling bearings: simulations and experiments. *Proc. Instn Mech. Engrs* 215 (Part J), 499–508. doi:10.1243/1350650011543754

Stacke, L. E., Fritzson, D., and Nordling, P. (1999). BEAST - a rolling bearing simulation tool. *Proc. Instn Mech. Engrs* 213 (Part K), 63–71. doi:10.1243/1464419991544063

Stevens, K. T. (1980). *Experimental observations on torque variation caused by ball bearing cage instabilities*, 105. ESA SP-158.

Walter, C. T. (1971). The dynamics of ball bearings. *ASME J. Lubr.* 93 (1), 1–10. doi:10.1115/1.3451516

Weinzapfel, N., and Sadeghi, F. (2009). A discrete element approach for modeling cage flexibility in ball bearing dynamics simulations. *ASME J. Tribol.* 131 (4), 021102. doi:10.1115/1.3063817

frontiers | Frontiers in Mechanical Engineering

TYPE Original Research
PUBLISHED 07 March 2025
DOI 10.3389/fmech.2025.1522524

Check for updates

OPEN ACCESS

EDITED BY
Sorin-Cristian Vladescu,
King's College London, United Kingdom

REVIEWED BY
Qilong Cheng,
Purdue University, United States
Milan Bukvic,
University of Kragujevac, Serbia

*CORRESPONDENCE
Hiroshi Shiomi,
shiomi.hiroshi@jaxa.jp

RECEIVED 04 November 2024
ACCEPTED 15 January 2025
PUBLISHED 07 March 2025

CITATION
Shiomi H and Obara S (2025) An *in situ* experimental method for monitoring the viscosity change and oil amount during the sliding test.
*Front. Mech. Eng.* 11:1522524.
doi: 10.3389/fmech.2025.1522524

COPYRIGHT
© 2025 Shiomi and Obara. This is an open-access article distributed under the terms of the Creative Commons Attribution License (CC BY). The use, distribution or reproduction in other forums is permitted, provided the original author(s) and the copyright owner(s) are credited and that the original publication in this journal is cited, in accordance with accepted academic practice. No use, distribution or reproduction is permitted which does not comply with these terms.

# An *in situ* experimental method for monitoring the viscosity change and oil amount during the sliding test

Hiroshi Shiomi* and Shingo Obara

Research and Development Directorate, Research Unit II, Japan Aerospace Exploration Agency, Tsukuba, Ibaraki, Japan

This study measures the changes in the viscosity and oil volume of lubricants in a vacuum sliding test under starved EHL to evaluate the lubrication life of a small amount of lubricants, and investigates their time transition and a mechanism of lubrication life. Starved EHL is observed in ball bearings lubricated with a small amount of lubricant, which require low friction torque even at high speeds, such as bearings used in artificial satellites. Under starved oil conditions, the oil film formed in the contact area becomes thin, so it is important to accurately estimate the oil film thickness in order to avoid solid contact. Since viscosity and oil volume affect the oil film thickness in the contact area, it is important to know how they change during the test. In this study, a method was proposed to measure viscosity and oil quantity without breaking the vacuum during a sliding test using a small amount of oil in a vacuum. Using this method, changes in viscosity and oil quantity until the end of lubrication life were measured in a sliding test using a small amount of MAC. As a result, an increase in viscosity and a decrease in oil quantity were observed. The measured results discussed the relationship between the increase in viscosity and the frictional work or sliding distance and indicated that the lubrication condition at the end of lubrication life was severely starved.

KEYWORDS

**oil degradation, starved EHL, viscosity measurement, lubrication life, vacuum, visualization test**

## 1 Introduction

Most of the mechanical parts used in satellites orbiting the earth are lubricated with a small quantity of liquid lubricants due to the demand for low torque and other factors. Therefore, the tribological performance of space liquid lubricants has been evaluated on a small quantity of those (Jones and Jansen, 2000; Jansen et al., 2001; Masuko et al., 2010). Mechanical elements lubricated with a small quantity of oil often experience oil starvation in the contact areas, especially at high speeds. In order to avoid solid contact and prevent damage to mechanical elements under starved conditions, it is necessary to predict oil film formation in the contact area. Many studies have experimentally and numerically investigated film thickness under starvation conditions.

The film thickness can be much less than the fully flooded value under starved conditions. Wedeven et al. showed a correlation between the inlet distance of oil meniscus and oil film reduction with an experimental approach using optical interferometry (Wedeven et al., 1971). Hamrock and Dowson (H–D) proposed an equation to calculate the oil film reduction rate using the inlet distance of meniscus

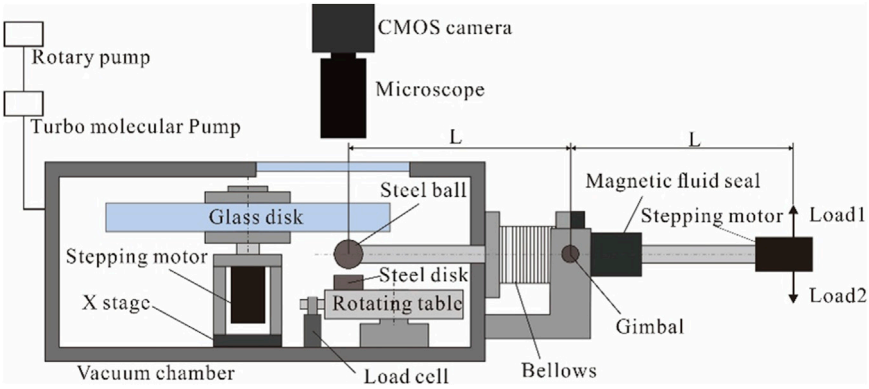


FIGURE 1
Schematic illustration of the test rig.

(Hamrock and Dowson, 1977a). It is necessary to estimate this distance based on the amount of supplied oil and the operating conditions, and many such studies have been conducted both experimentally and numerically. The formula proposed by H–D is effective when the inlet meniscus distance is known, but it is difficult to measure the inlet distance of meniscus for many mechanical elements. Nogi estimated the oil film shape behind the contact zone using the Coyne–Elrod condition, which considers surface tension. Assuming that the oil film shape flows into the inlet side, Nogi calculated the inlet meniscus distance and film thickness numerically and showed that they nearly agreed with H–D's formula (Nogi, 2015a). The formula for inlet distance by Nogi is difficult to apply to severely starved conditions when the inlet meniscus distance is less than 1. Cann et al. proposed a formula to calculate the oil film reduction rate using a dimensionless number called starvation degree (SD) that makes it possible to evaluate the degree of oil starvation up to the severe starvation condition (E Cann et al., 2004). In recent years, many studies have also been conducted on methods for estimating oil film thickness under starvation conditions using computational fluid dynamics (CFD). It is possible to calculate the oil film distribution in front of the contact area from the lubricant volume near the contact area and then use this to predict the oil film shape in the contact area under starvation conditions (Zhang et al., 2023). The oil film reduction rate estimated using the operating conditions and the calculation of film thickness using CFD are effective if the viscosity and amount of lubrication are known. While mechanical elements operate, the lubricant may degrade or evaporate, and the viscosity and oil quantity may change. These must be measured or predicted based on operating conditions.

Multiply alkylated cyclopentane (MAC) is the most-used liquid lubricant for space machinery parts due to its high thermal and chemical stability, especially its ultra-low vapor pressure. Although the chemical stability of MAC is very high, frictional conditions and contact with metals can cause partial decomposition of MAC to form low-molecular weight products such as hydrogen, methane, and ethane (John et al., 2001; Lu et al., 2007). It has been pointed out that the decomposition reaction may lead to contamination of nearby optical components and the loss of lubrication. Masuko et al. conducted reciprocating ball-on-disk tests in a vacuum and found that MAC polymerizes by oxidative polymerization (Masuko et al., 2010). This polymerization increases the viscosity of the MAC oil and reduces the replenishment of the lubricant to the contact area, resulting in the starved condition and loss of lubricity. Although there has been progress in research into the reduction and deterioration of MAC, it is still unknown how these progresses or the degrees of starvation of lubrication life. It is difficult to research changes in viscosity and decreases in oil amount in MAC lubricity evaluation tests because the amount of oil supplied is small, on the order of several mg, and is difficult to measure.

In mechanical elements lubricated with a small amount of MAC operating in a vacuum, the viscosity of the MAC increases and losses due to evaporation occur, further thinning the lubricant film due to oil starvation. In order to use mechanical elements safely over the long term, it is necessary to quantitatively predict the increase in viscosity of the lubricant and the decrease in the amount of lubricant. The purpose of this study is to quantitatively evaluate how degradation progresses when a small amount of MAC is rubbed in a vacuum. A method is proposed to measure the viscosity and oil volume of a small amount of lubricant during a ball-on-disk sliding test in a vacuum without breaking the vacuum. Using the proposed method, the viscosity and oil volume of MAC are measured during pure sliding tests using a small amount of MAC, and the transitions up to the end of its life are obtained. From measuring results, viscosity increases during sliding tests and lubrication state at the end of its lubrication life are discussed.

## 2 Experiment

### 2.1 Sliding test

The sliding tests were carried out in a vacuum chamber with a base pressure of $10^{-4}$ Pa level. The schematic illustration of test rig is shown in Figure 1. This testing machine is characterized by the ability to install two disk test pieces above and below a steel ball. In this study, the upper disk is a glass disk, and the lower disk is a steel disk. Sliding tests are conducted between the steel ball and the steel disk. Sliding is induced by the steel ball rotation. The rotating shaft on which the steel ball is attached is connected to a stepping motor

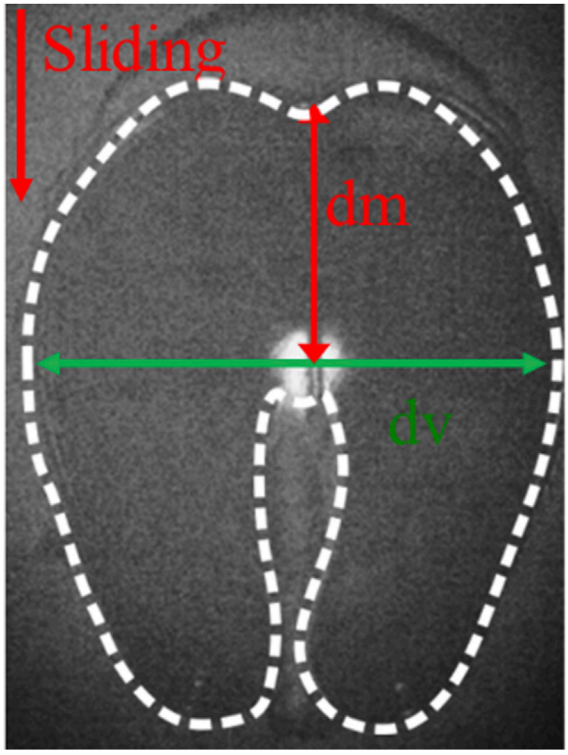


FIGURE 2
Optical image in a visualization test.

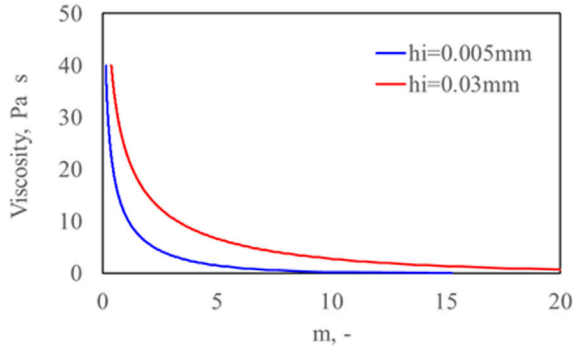


FIGURE 3
Variation of viscosity and inlet distance for $h_i$ = 0.005 and 0.03 mm as the viscosity of the lubricant changes.

outside the chamber via a magnetic fluid seal. The rotating shaft is supported by a single-axis gimbal, and the rotation of the rotating shaft around the center of the gimbal is allowed by the deformation of the bellow. Using a weight, this testing machine can apply a load in the vertical direction to the point where the distance from the gimbal's center of rotation is the same as from the steel ball. The steel ball can contact either the upper or lower disk by switching the direction of the load. When a steel disk and a glass disk are placed below and above the steel ball, respectively, sliding tests can be conducted between the lower steel disk and the steel ball, and the visualization test can be performed by interrupting the sliding test and bringing the upper glass disk and the steel ball in contact.

Sliding in the sliding test and visualization tests is induced by rotating steel ball, and the frictional force during the sliding test is measured with the load cell. By placing the disks symmetrically above and below the steel ball, sliding and visualization tests can be performed on the same track of the steel ball. In this study, the distance of the steel balls from the upper and lower disks is set to 1 mm, and the rotation angle of the shaft required to bring the balls into contact with each disk is less than 1 deg. One optical image from a visualization test is shown in Figure 2.

Physical properties of test specimens and test conditions used in the tests are as follows. The material of the steel ball and the steel disk for the sliding test is SUS440C (Young's modulus 200 GPa, Poisson's ratio 0.3). The glass disk for the visualization test is made of BK7 optical glass (Young's modulus 80 GPa, Poisson's ratio 0.21). The sliding test was performed with a load of 10 N and rotating speed of 10–100 rpm (5.2 mm/s to 52 mm/s). The load and rotational speed are adjusted to those of the sensor bearings, which operate at relatively low rotational speeds among the mechanical components used in satellites.

The visualization test was performed with a load of 1 N to reduce wear during measurement, and the rotating speed was 1–100 rpm (0.52–52 mm/s). The lubricant's MAC (0.2 cst@25°C) was applied to the steel ball before the test began, and the tests were then performed without supplying any more lubricant. After applying MAC to the steel ball, it was rotated at 100, 200, 500, 1,000, and 2,000 rpm for 5 min and then at 3,000 rpm for 10 s to spread it evenly over the ball. The rotation speed and time were selected empirically so that the average initial oil film thickness was several tens of micrometers, similar to that in the test by Masuko et al. (2010). In this study, when the friction coefficient measured during the sliding test exceeded 0.3, it was considered to be at the end of its lubrication life, and the test was stopped.

## 2.2 Measurement of the amount and viscosity of the lubricant

In this study, viscosity is calculated with the dimensionless inlet distance equation proposed by Nogi (2015a), as shown in Equation 1:

$$m = 1.94 H_i^{0.59} H_{cff}^{-0.61} \exp\left(-1.95C^{0.45}\right). \quad (1)$$

Where, $m$ is a dimensionless number obtained by dividing the inlet distance $d_m$ (shown in Figure 2) by the Hertz radius of the contact area. $H_i$ is the amount of oil in the meniscus divided by the area of the meniscus on the glass disk, and the average oil film thickness $h_i$ is made dimensionless using the steel ball diameter and Hertz radius. If the meniscus shape can be measured, $h_i$ can be calculated from the geometric shape between the steel ball and the disk and calculated by Equation 2 using the diameter $d_v$ (shown in Figure 2) at the cross section perpendicular to the sliding direction.

$$h_i = R - R^2 \sin^{-1}\left(\frac{d_v}{2R}\right) \Big/ dv - \sqrt{R^2 - \frac{d_{v^2}}{4}} \Big/ 2. \quad (2)$$

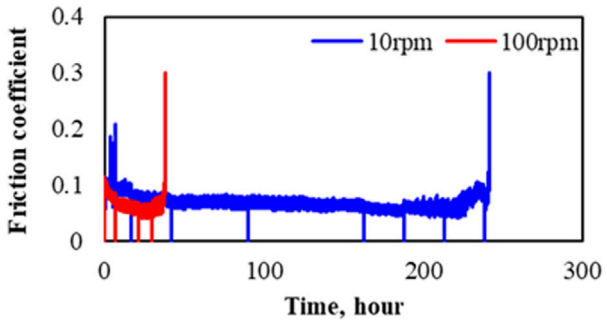


FIGURE 4
Changes in the friction coefficient with time in the sliding test.

$H_{cff}$ is calculated by making $h_{cff}$ (central film thickness in fully flood condition) dimensionless using the steel ball diameter and Hertz radius. In this study, the Johnson dimensionless number was used to determine the region, and $h_{cff}$ was calculated using the Hamrock–Dowson formula for the piezo-viscous elastic region (Equation 3) (Hamrock and Dowson, 1977b; Johnson, 1970).

$$h_{cff} = 4.31R(\eta u/ER)^{0.68}(\alpha E)^{0.49}\left(\frac{w}{ER^2}\right)^{-0.073}\left(1 - e^{-1.23k}\right). \quad (3)$$

$C$ is the capillary number and is expressed by Equation 4.

$$C = \frac{\eta U}{\gamma}. \quad (4)$$

By calculating the average oil film thickness $h_i$ from dv and Equation 2, the relationship between viscosity and dimensionless inlet distance can be obtained from Equations 1, 3. As examples, the variation in viscosity with a dimensionless inlet distance at sliding velocity and $h_i$ = 0.005 mm and 0.03 mm are shown in Figure 3. Figure 3 shows that the inlet meniscus distance decreases with increasing viscosity for the following reasons. The increased viscosity causes insufficient re-flow behind the contact outlet, causing the sideband to move outward. As a result, the amount of oil flowing from the sideband into the contact area near the inlet of the contact area is reduced, and the inlet distance becomes shorter (Nogi, 2015b). Using $h_i$ measured during the test, the relationship diagram between the inlet distance and viscosity is created as shown in Figure 3, and the viscosity is estimated from the measured dimensionless inlet distance. When measuring the viscosity in the visualization test, a velocity was selected such that the dimensionless inlet distance was in the range of 1.5–3. In this study, it is assumed that the surface tension does not change even when the viscosity of the lubricant changes.

# 3 Result and discussion

## 3.1 Changes in the amount and viscosity of oil in the sliding test

Figure 4 shows the changes in friction coefficient over time obtained in sliding with a load of 10 N for the rotation speeds of 10 and 100 rpm. Regardless of the rotational speed, the coefficient of friction increased at the start of the test, then decreased and stabilized at a constant value, and then increased rapidly again, reaching the lubrication life. There was no significant difference in the friction coefficient during the test at either rotating speed, and it is inferred that the sliding test was carried out in the boundary lubrication region. The time to reach the end of its life was shorter at 100 rpm.

The sliding test was stopped mid-test, and a visualization test was performed. When the friction test was stopped, the friction coefficient shown in Figure 4 was 0. In addition, when the friction coefficient exceeded 0.3 and the lubrication life was reached, the visualization test was performed after the sliding test was finished. Figure 5 shows optical images taken at test times of 42, 90, 163, and 242 h during a sliding test at a rotating speed of 10 rpm. In the 47-h and 90-h cases, a closed shape (shape 1) is observed, which ensures that the truck is fully replenished, and in the 163-h case, a butterfly shape (shape 2) is observed, which is seen in situations of oil shortage. These shapes have also been observed in air and are known to change from shape 1 to shape 2 with increasing velocity, viscosity, and decreasing oil amount (Van Emden et al., 2016). The meniscus size and inlet distance gradually decrease as the

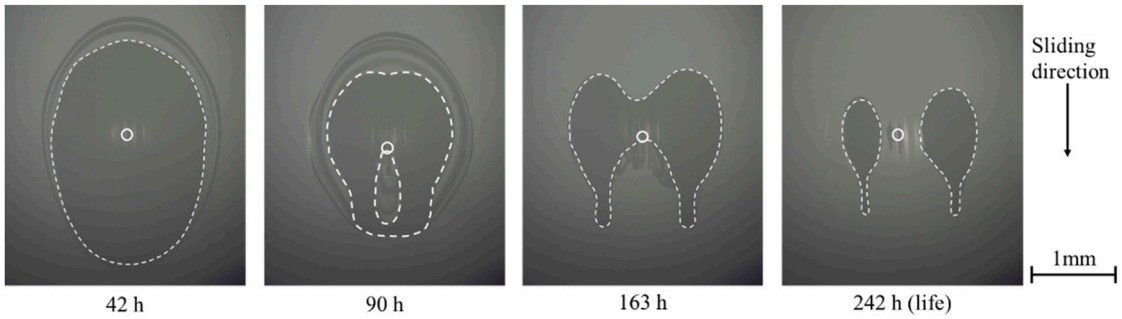


FIGURE 5
Optical images in the visualization test in the sliding test of 10 rpm shown in Figure 4.

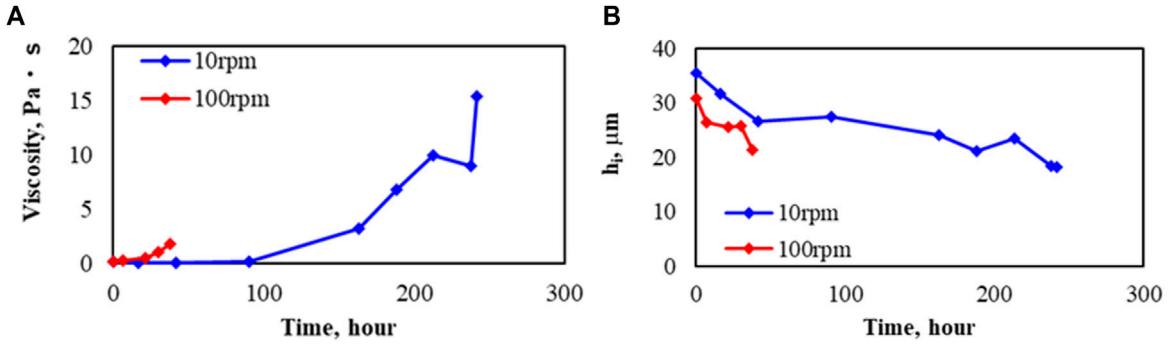


FIGURE 6
Changes in viscosity and average film thickness in the sliding test of 10 rpm and 100 rpm shown in Figure 4. **(A)** Viscosity. **(B)** Average film thickness ($h_i$).

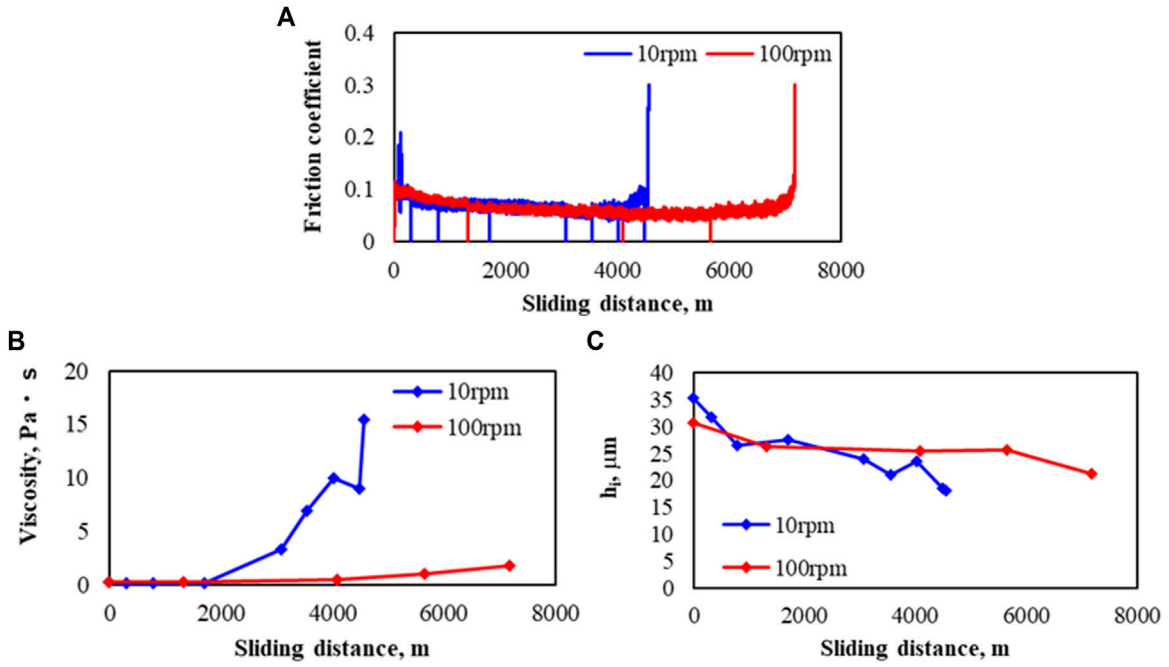


FIGURE 7
Changes in **(A)** friction coefficient, **(B)** viscosity, and **(C)** average film thickness ($h_i$) with sliding distance in the sliding test of 10 and 100 rpm shown in Figures 4, 6.

test progresses. Using the $d_m$ and $d_v$ values measured from each visualization test performed during the sliding tests, the viscosity and average film thickness were calculated using the procedure described in Section 3.2 and are shown in Figures 6A, B. It can be seen that the viscosity gradually increases, and the average film thickness gradually decreases, regardless of the rotating speed. The viscosity at the end of its life increased significantly at 10 rpm over that at 100 rpm. Compared to the initial viscosity, it increased by a factor of 90 at 10 rpm and 10 times at 100 rpm. The rate of change in viscosity over time is faster at 100 rpm. The rate of change of viscosity over time appears to be faster at 100 rpm. The average film thickness at the end of its lubricating life is similar at both speeds; the rate of decrease was faster at 100 rpm, and was roughly constant throughout the test.

## 3.2 Effects of sliding for viscosity increase of MAC

Figure 7 shows the changes in the friction coefficient, viscosity, and average film thickness shown in Figures 4, 6 for the sliding distance. It can be seen that the sliding distance until

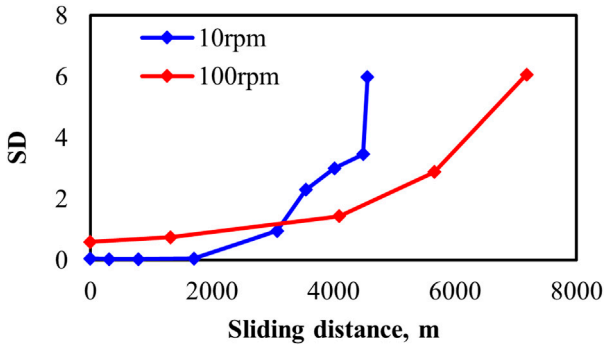


FIGURE 8
Changes in SD with sliding distance in sliding test of 10 rpm and 100 rpm.

the end of the lubrication life is longer at 100 rpm. The rate of change in viscosity and oil volume relative to the sliding distance is smaller at 100 rpm.

The product of the friction force and the sliding distance is called friction work and is used as an index of the energy generated by the friction at the contact area. The friction work up to the end of its life was approximately 3,100 J and 4,600 J in the 10 rpm and 100 rpm tests, respectively. Since the friction force during the test does not differ significantly between the test results at 10 rpm and 100 rpm, the friction work is greater at 100 rpm, which has a longer sliding distance until the end of its life. At 100 rpm, where frictional work is greater, the increase in viscosity is smaller, and no correlation is observed between the increase in viscosity and frictional work. Lu et al. investigated the evolution of low molecular weight gases during vacuum sliding tests of MAC and reported that the rate of gas evolution was determined by the amount of nascent surface rather than the magnitude of friction work (Lu et al., 2007). In a study by Masuko et al., polymerization by oxidation did not occur during sliding tests in air, and it was considered that polymerization requires the generation of nascent surface (Masuko et al., 2010). Lu et al. reported that the gas generation rate is proportional to the sliding velocity. The time integration of the gas generation rate and the sliding velocity results in the amount of gas generated and the sliding distance, so the amount of gas generated is proportional to the sliding distance (Lu et al., 2010). Considering the reports by Lu et al. and Masko et al. together, it is thought that the polymerization of MAC and the associated increase in viscosity require the generation of new surfaces and that the total amount of reaction is proportional to the sliding distance. However, the results of this test show that the viscosity increase was smaller in the 100-rpm test, which has a longer sliding distance, and the viscosity increase cannot be explained solely by chemical reactions at the contact surface. Observation of the test specimens after the test revealed that a large amount of wear debris and powder had been mixed into the MAC. It is known that mixing solid powder into a liquid increases the viscosity. It has been revealed that when grease lubrication is used, in the low speed range, the concentration of the thickener increases near the inlet of the contact area, resulting in increased viscosity and oil film thickness. If something similar to this occurs in this test as a result of an increase in the concentration of wear debris mixed into the lubricating oil, this may explain why the viscosity is higher at 10 rpm than at 100 rpm.

### 3.3 Mechanisms of friction increment at the end of the sliding test

The meniscus observed in the visualization test after the life evaluation test was split into left and right at a rotation speed of 10 rpm, as shown in Figure 5D, and was similar in the life test at 100 rpm. Under these conditions, lubricant flow from the sideband to the contact area does not occur, and it is assumed that the lubricant film ruptures due to insufficient lubricant supply to the contact area, resulting in increased friction. A parameter that indicates the degree of oil starvation is the inlet distance that is used to measure viscosity, but, as there is no meniscus in front of the contact zone, the inlet distance cannot be defined in the present results. Therefore, the starvation degree (*SD*) proposed by E Cann et al. (2004) is used as an indicator of the degree of oil shortage to organize the state of oil shortage during the sliding test; *SD* is expressed by Equation 5:

$$SD = \frac{\eta U a}{h_{\infty} \gamma}, \tag{5}$$

where $h_{\infty}$ is the average oil film thickness, and in this study, *SD* is calculated as $h_{\infty} = h_i$. As the viscosity in this study was calculated on the assumption that the surface tension of the lubricant had not changed due to degradation, the same assumption was made here, and the value of the lubricant before the test was used. The variation in the *SD* calculated using the measured viscosity and average film thickness with respect to the sliding distance is shown in Figure 8. The results for both rotational speeds show that *SD* increases monotonically with sliding distance and reaches its life at approximately 6. In addition to the results shown in Figure 8, life tests were conducted twice at 10 rpm and once at 100 rpm, and the *SD* at the end of life was approximately 6 in these tests. In a small amount of oil lubrication, it is difficult to define the lubrication life because the sliding distance at the end of the life varies depending on the speed. Although it is necessary to confirm this by conducting tests under different test conditions, the *SD* is expected to be a dimensionless parameter that can be used to determine lubrication life.

## 4 Conclusion

In this study, a method was proposed to calculate the viscosity and oil volume during sliding tests with a small amount of MAC by measuring the meniscus shape. Using this method, the changes in viscosity and oil content of MAC during friction tests in vacuum were measured over the life of the lubricant without breaking the vacuum. Under the test conditions in this study, regardless of the rotating speed, the friction coefficient increased at the beginning of the test, remained at a constant value, and then increased rapidly just before the life of the lubricant, reaching the lubrication life. The magnitude of the friction coefficient was similar, regardless of the rotating speed, indicating that the tests were conducted with boundary lubrication. From the

results of sliding tests, the viscosity increases during the MAC sliding test and the lubrication state at the end of its lubrication life were discussed, and the following conclusions were obtained:

- Viscosity gradually increases, and the average film thickness gradually decreases regardless of the rotation speed. Viscosity at the end of its life increases significantly at 10 rpm over that at 100 rpm, and compared to the initial viscosity, it increases by a factor of 90 at 10 rpm and 10 at 100 rpm.
- Past research predicted that the increase in MAC viscosity that occurs during a sliding test would increase as the sliding speed and the sliding distance increase, extending the life of the oil. However, in this study, the viscosity increase was greater for a lower sliding speed and shorter sliding distance until the end of its life. This result indicates that the increase in MAC viscosity is not caused solely by chemical reactions on the nascent surface, and it is necessary to investigate whether the viscosity increase is due to other factors, such as the incorporation of wear particles.
- When MAC reached the end of its lubrication life with a dimensionless inlet distance of less than 1, it entered severe starvation. When the degree of oil starvation was evaluated by *SD*, regardless of rotating speed, *SD* increased monotonically throughout the test, and the value was 6 at the end of the lubrication life.

## Data availability statement

The original contributions presented in the study are included in the article/supplementary material; further inquiries can be directed to the corresponding author.

## Author contributions

HS: conceptualization, data curation, investigation, methodology, validation, visualization, and writing–original draft. SO: writing–review and editing and conceptualization.

## Funding

The author(s) declare that no financial support was received for the research, authorship, and/or publication of this article.

## Conflict of interest

The authors declare that the research was conducted in the absence of any commercial or financial relationships that could be construed as a potential conflict of interest.

## Generative AI statement

The author(s) declare that no generative AI was used in the creation of this manuscript.

## Publisher's note

All claims expressed in this article are solely those of the authors and do not necessarily represent those of their affiliated organizations, or those of the publisher, the editors and the reviewers. Any product that may be evaluated in this article, or claim that may be made by its manufacturer, is not guaranteed or endorsed by the publisher.

## References

E Cann, P. M., Damiens, B., and Lubrecht, A. A. (2004). The transition between fully flooded and starved regimes in EHL. *Tribol. Int.* 35, 859–864. doi:10.1016/j.triboint.2004.05.005

Hamrock, B. J., and Dowson, D. (1977a). Isothermal elastohydrodynamic lubrication of point contacts: Part IV—starvation results. *ASME J. Lubr. Technol.* 99 (1), 15–23. doi:10.1115/1.3452973

Hamrock, B. J., and Dowson, D. (1977b). Isothermal elastohydrodynamic lubrication of point contacts: Part III—fully flooded results. *ASME J. Lubr. Technol.* 99 (2), 264–275. doi:10.1115/1.3453074

Jansen, M. J., Jones, W. R., Predmore, R. E., and Loewenthal, S. L. (2001). *Relative Lifetimes of Several Space Liquid Lubricants Using a Vacuum Spiral Orbit Tribometer (SOT).* NASA TM-2001-210966

John, P. J., Cutler, J. N., and Sanders, J. H. (2001). Tribological behavior of a multialkylated cyclopentane oil under ultrahigh vacuum conditions. *Tribol. Lett.* 9, 167–173. doi:10.1023/a:1018808921623

Johnson, K. L. (1970). Regimes of elastohydrodynamic lubrication. *J. Mech. Eng. Sci.* 12-1, 9–16. doi:10.1243/jmes_jour_1970_012_004_02

Jones, W. R., and Jansen, M. J. (2000). *Space Tribology*. NASA TM-2000-209924, 1189–1216. doi:10.1201/9780849377877-42

Lu, R., Minami, I., Nanao, H., and Mori, S. (2007). Investigation of decomposition of hydrocarbon oil on the nascent surface of steel. *Tribol Lett* 27, 25–30. doi:10.1007/s11249-007-9203-3

Lu, R., Nanao, H., Kobayashi, K., Kubo, T., and Mori, S. (2010). Effect of lubricant Additives on Tribochemical decomposition of hydrocarbon oil on nascent steel surfaces. *J. Jpn. Petroleum Inst.* 53 (1), 55–60. doi:10.1627/jpi.53.55

Masuko, M., Kishi, K., Suzuki, A., and Obara, S. (2010). The lifetime of boundary lubrication performance of small-quantity-applied liquid lubricants for space mechanisms Evaluated with a vacuum reciprocating tribometer. *STLE Tribol. Trans.* 53, 75–83. doi:10.1080/10402000903226374

Nogi, T. (2015a). Film thickness and rolling resistance in starved elastohydrodynamic lubrication of point contacts with reflow. *ASME J. Tribol.* 137, 041502. doi:10.1115/1.4030203

Nogi, T. (2015b). An analysis of starved EHL point contacts with reflow. *Tribol. Online* 10 (1), 64–75. doi:10.2474/trol.10.64

Van Emden, E., Venner, C. H., and Morales-Espejel, G. E. (2016). Aspects of flow and cavitation around an EHL contact. *Tribol. Int.* 95, 435–448. doi:10.1016/j.triboint.2015.11.042

Wedeven, L. D., Evans, D., and Cameron, A. (1971). Optical analysis of ball bearing starvation. *ASME J. Lubr. Technol.* 93 (3), 349–361. doi:10.1115/1.3451591

Zhang, S., Jacobs, G., von Goeldel, S., Vafaei, S., and König, F. (2023). Prediction of film thickness in starved EHL point contacts using two-phase flow CFD model. *Tribol. Int.* 178, 108103. doi:10.1016/j.triboint.2022.108103

# Frontiers in
# Mechanical Engineering

**Explores the design of mechanical systems and their applications**

A multidisciplinary journal which bridges the gaps between areas of research in the mechanical engineering field, from biomechanical engineering to turbomachinery and tribology.

---

## Discover the latest Research Topics

See more →

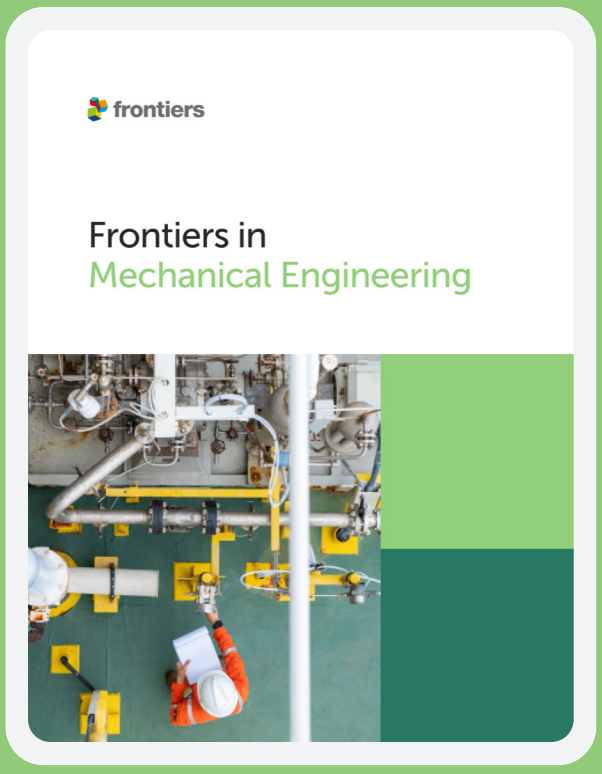


**Frontiers**

Avenue du Tribunal-Fédéral 34
1005 Lausanne, Switzerland
frontiersin.org

**Contact us**

+41 (0)21 510 17 00
frontiersin.org/about/contact